
Calcium Carbonate Biomaterials – Architecture, Design and Nanomechanical Properties of Selected Mollusc, Brachiopod and Echinoderm Skeletal Elements



Dissertation zur Erlangung des Doktorgrades
Dr. rer. nat.

an der Fakultät für Geowissenschaften der
Ludwig-Maximilians-Universität München

Vorgelegt von

Sebastian Hörl

München, 31.07.2025

Betreuer: Prof. Dr. Wolfgang. W. Schmahl

Tag des Antrags auf Zulassung zum Promotionsverfahren: 31.07.2025

Erstgutachter: Prof. Dr. Wolfgang. W. Schmahl

Zweitgutachter: Prof. Dr. Antonio G. Checa

Promotionskommission: Prof. Dr. Wolfgang W. Schmahl

Prof. Dr. Antonio Checa

Prof. Dr. Sandro Jahn

Prof. Dr. Claudia Trepmann

Prof. Dr. Bettina Reichenbacher

Prof. Dr. Stuart Gilder

Tag der mündlichen Prüfung: 22.10.2025

ABSTRACT

Calcium carbonate is a chemical substance that is not only considered the most important compound for biomineralisation in marine organisms and invertebrates, but also has significant implications for industry, the carbon cycle, and biomedicine. Through evolving and adapting to ecological challenges, organisms have developed the ability to biomineralise complex hierarchical structures comprising biopolymers and inorganic minerals. Due to their outstanding material properties, such as high strength and toughness, while retaining a low density compared to the pure inorganic mineral, biomineralised materials have long been a source of inspiration for fabricating and optimising man-made materials. Accordingly, it is of great importance to understand the hierarchical design and biomineralisation principles of calcium carbonate hard tissues. This dissertation presents and discusses in great detail findings related to the microstructure, crystallographic texture, and nanomechanical properties of various calcium carbonate biomaterials. This work focuses mainly on analysing marine invertebrate hard tissues, such as bivalve molluscs shells, rhynchonellate brachiopod shells and sea urchin skeletal elements.

Molluscs, particularly bivalves, are globally widespread and present in highly diverse marine environments. Bivalves are renowned for their high diversity in lifestyles and for generating hard tissues with hierarchical structures. About 15 main calcium carbonate microstructures are recognised today in modern bivalve shells. An important part of the bivalve composite hard tissue is the organic matrix, which regulates and organises the crystallographic orientation and morphology of the inorganic minerals. Bivalve molluscs can secrete four main carbonate polymorphs, namely calcite, aragonite, amorphous calcium carbonate or (rarely) vaterite and use the biomineralised hard tissues mainly for protection of the soft body, but also to pursue diverse lifestyles. To gain insight into the hierarchy, microstructure, and nanomechanical properties of bivalves, I characterised differently cut shells of 30 different species from 11 orders by EBSD analysis, thermogravimetric analysis, electron and confocal laser microscopy imaging, and nanomechanical testing.

The structural results provide a detailed illustration of the microstructure and changeovers between the different layers. If the microstructures feature the same calcium carbonate phase, the changeover is generally smooth, with the initial crystallographic texture being transmitted from the shell portion of the adjacent layer. This biomineralisation mechanism is particularly fascinating for the aragonitic myostraca, the bivalve adductor muscle attachment sites, as their microstructure generation is largely influenced by competitive growth determinants rather than biological control. Bivalve myostraca are not only interesting because they enable the organism to form a strong connection to the adductor muscle fibres, but also because of their outstanding nanomechanical properties, such as a significantly enhanced hardness, compared to other shell layers or geological aragonite. The microstructure and nanomechanical properties of myostraca from different bivalve orders and bivalves

following different lifestyles (such as burrowing, swimming, or attaching to substrates) are characterised. Previous studies have indicated that bivalve myostraca are strictly conservative in microstructure and texture, consistently forming large, prismatic units. However, the measurements presented in this work reveal a broad diversity in myostracal microstructures, demonstrating how the different crystal arrangements, textures, and twinning modes of the myostraca and other shell layers can influence material properties.

Like bivalve molluscs, rhynchonellate brachiopods also use specialised epithelial cells to mediate crystal growth at muscle attachment sites of their calcium carbonate shells. Although rhynchonellates and bivalves share similar living environments, lifestyles and modes of biomineralisation, they are biologically distant organisms. Thus, comparing the microstructural similarities and differences between rhynchonellates and bivalves provides insight into the biological convergence of muscle attachment sites and the different approaches for forming these important organic-inorganic interface structures. High-resolution EBSD measurements for the shells of modern two- and three-layered rhynchonellates show that the general microstructure of brachiopod muscle attachment sites differs strongly from bivalve shells in both calcium carbonate phase and crystal morphology. However, the muscle attachment sites of both invertebrate classes share some characteristics that may be important for a strong muscle-shell attachment. This includes the adoption of crystallographic texture from adjacent shell layers with the same calcium carbonate phase, as well as the co-orientation of crystallographic c-axes parallel to the muscle bundles at muscle attachment sites.

In contrast to the biomineralised hard tissues of bivalved invertebrates, nucleation of calcitic skeletal elements in echinoids involves intracellular processes. The latter usually comprises an intricate arrangement of highly co-oriented trabeculae into various porous, yet robust stereom architectures, historically described as single-crystalline. Applying the unprecedented EBSD data analysis method of pattern matching to different stereom architectures in the tests and spines of *Cidaris cidaris* and *Paracentrotus lividus*, this work reveals the presence and distribution of internal small-angle misorientations. As these misorientations are mostly located at the trabecular junctions, the quality of single-crystallinity appears to be influenced by the respective stereom architecture; however, sea urchin calcite cannot be considered single-crystalline invariably. Furthermore, I demonstrate the presence of poorly co-oriented, polycrystalline areas at both muscle attachment sites of echinoids (at test tubercles and the base of the spines) and the cortex, which encases the primary and secondary spines of *C. cidaris*. The microstructure generation of the cortex is determined by two factors: (i) The cortex crystals nucleate with c-axes oriented perpendicular to the stereom, which functions as a nucleation template. Thus, the smoothness of the outer stereom surface determines the texture of the initial cortex portion. (ii) A competitive growth mechanism determines the further microstructure and texture of the cortex.

Furthermore, this study demonstrates how the EBSD pattern matching method can improve the angular precision and reveal small-angle misorientations within highly co-oriented structures, such as

the sea urchin stereom. By employing this method to other calcium carbonate biomaterials, such as eggshell grains, myostracal prisms or large columns in bivalve shells, I highlight in great detail their crystallographic texture and microstructure, demonstrating the large potential of this data evaluation technique for future studies.

ZUSAMMENFASSUNG

Kalziumkarbonat ist eine chemische Verbindung von zentraler Bedeutung für die Biomineralisierung in Meeresorganismen und wirbellosen Tieren. Darüber hinaus spielt es eine wichtige Rolle in der Industrie, im globalen Kohlenstoffkreislauf und in der Biomedizin. Im Verlauf der Evolution passten sich Organismen an ökologische Herausforderungen an. Dabei entwickelten sie die Fähigkeit, komplexe Strukturen aus Biopolymeren und Mineralien zu bilden. Biomineralisierte Materialien zeichnen sich durch außergewöhnliche Eigenschaften aus: Sie sind zäh und hart, besitzen jedoch im Vergleich zu rein anorganischen Mineralien eine deutlich geringere Dichte. Diese Kombination macht sie seit langem zur Inspirationsquelle für die Entwicklung künstlicher Materialien. Demnach ist es von großer Bedeutung, den hierarchischen Aufbau und die Biomineralisierungsprinzipien von Kalziumkarbonatstrukturen zu untersuchen und verstehen. In dieser Dissertation werden Erkenntnisse über die Mikrostruktur, die kristallografische Textur und die nanomechanischen Eigenschaften verschiedener Kalziumkarbonat-Biomaterialien ausführlich dargestellt und diskutiert. Diese Arbeit konzentriert sich hauptsächlich auf die Analyse des Hartgewebes mariner Invertebraten wie Muscheln, Armfüßern sowie Seeigeln.

Mollusken, insbesondere Muscheln, sind weltweit verbreitet und in sehr unterschiedlichen Meeresumgebungen anzutreffen. Muscheln sind bekannt für ihre vielfältigen Lebensweisen und die Bildung von hierarchisch strukturierten Hartgeweben. In modernen Muschelschalen sind heute etwa 15 Hauptmikrostrukturen aus Kalziumkarbonat bekannt. Ein wichtiger Bestandteil des Hartgewebes von Muscheln ist die organische Matrix, welche die kristallographische Ausrichtung und Morphologie der anorganischen Mineralien reguliert und organisiert. Muscheln sondern hauptsächlich vier polymorphe Karbonatphasen ab, nämlich Kalzit, Aragonit, amorphes Kalziumkarbonat oder (seltener) Vaterit. Die biomineralisierten Karbonatstrukturen werden hauptsächlich zum Schutz des Weichkörpers genutzt, spielen aber auch bei Ausübung verschiedener Lebensweisen eine Rolle. Um die Hierarchie, Mikrostruktur und nanomechanischen Eigenschaften von Muschelschalen zu untersuchen, habe ich 30 Arten aus 11 Ordnungen analysiert. Dazu wurden verschiedene Methoden, wie EBSD-Analyse, thermogravimetrische Analyse, Elektronenmikroskopie, konfokale Lasermikroskopie und Nanoindentation eingesetzt.

Meine strukturellen Ergebnisse liefern eine detaillierte Darstellung der Mikrostrukturen und Übergänge verschiedener Muschelschichten. Weisen zwei benachbarte Mikrostrukturen die gleiche Kalziumkarbonatphase auf, so ist der Übergang generell fließend, wobei die anfängliche kristallografische Textur von der benachbarten Schicht übernommen wird. Dieser Biomineralisationsmechanismus ist besonders faszinierend für die aragonitischen Myostraca, die Ansatzstellen der Muscheladduktoren, da ihre Mikrostruktur weitgehend durch kompetitive Wachstumsfaktoren bestimmt wird, weniger durch biologische Kontrolle. Die Myostraca der Muscheln sind nicht nur interessant, weil sie einen starken Zusammenhalt zwischen Schale und Adduktorenfasern ermöglichen, sondern auch aufgrund ihrer herausragenden nanomechanischen Eigenschaften, wie z. B. einer deutlich erhöhten Härte im Vergleich zu anderen Schalenschichten oder geologischem Aragonit. Diese Arbeit charakterisiert die Mikrostruktur und nanomechanischen Eigenschaften von Myostraca aus verschiedenen Muschelordnungen und von Muscheln mit unterschiedlichen Lebensweisen (zum Beispiel Graben, Schwimmen oder Anhaften an Substraten). Frühere Studien deuteten an, dass Myostraca von Muscheln in Bezug auf Mikrostruktur und Textur streng konservativ sind und generell aus großen, prismatischen Einheiten bestehen. Die in dieser Arbeit vorgestellten Messungen illustrieren jedoch die große mikrostrukturelle Vielfalt der Myostraca und zeigen, wie unterschiedliche Kristallanordnungen, Texturen und Verzwillingungsarten die Materialeigenschaften der Myostraca und anderer Schalenschichten beeinflussen können.

Analog zu Muscheln nutzen auch Brachiopoden der Klasse Rhynchonellata spezialisierte Epithelzellen, um das Kristallwachstum an den Muskelansatzstellen ihrer Kalziumkarbonatschalen herbeizuführen. Obwohl Rhynchonellaten und Muscheln ähnliche Lebensräume, Lebensweisen und Arten der Biomineralisierung teilen, sind sie biologisch kaum verwandt. Der Vergleich der mikrostrukturellen Ähnlichkeiten und Unterschiede zwischen Rhynchonellaten und Muscheln gibt daher Aufschluss über die biologische Konvergenz der Muskelansatzstellen und die unterschiedlichen Ansätze zur Bildung dieser wichtigen organisch-anorganischen Grenzstrukturen. Hochauflösende EBSD-Messungen an den Schalen rezenter zwei- und dreischichtiger Rhynchonellaten zeigen, dass sich die allgemeine Mikrostruktur der Muskelansatzstellen von Brachiopoden sowohl in der Kalziumkarbonatphase als auch in der Kristallmorphologie stark von Muschelschalen unterscheidet. Die Muskelansatzstellen beider Wirbellosen-Klassen weisen jedoch auch ein paar gemeinsame Merkmale auf, die für eine starke Befestigung der Muskeln an der Schale wichtig sein könnten. Dazu gehören die Übernahme der kristallographischen Textur von benachbarten Schalenschichten der gleichen Kalziumkarbonatphase sowie die gemeinsame Ausrichtung der kristallographischen c-Achsen parallel zu den Muskelbündeln an den Muskelansatzstellen.

Im Gegensatz zu den biomineralisierten Hartgeweben zweischaliger Wirbelloser erfolgt die Keimbildung kalzitischer Skelettelemente bei Echinoiden auch durch intrazelluläre Prozesse. Letztere bestehen in der Regel aus einer komplizierten Anordnung hochgradig koorientierter Trabekel in

verschiedenen porösen, aber robusten Stereomarchitekturen, die historisch als einkristallin beschrieben wurden. Durch die Anwendung der neuartigen EBSD-Auswertungsmethode „Pattern matching“ auf verschiedene Stereomarchitekturen in den Tests und Stacheln von *Cidaris cidaris* und *Paracentrotus lividus* zeigt diese Arbeit die Präsenz und Verteilung von feinen Misorientierungen innerhalb des biomineralisierten Gewebes. Da sich diese Misorientierungen meist an den trabekulären Verbindungen befinden, scheint die Einkristallinität vor allem von der jeweiligen Stereomarchitektur abzuhängen; Seeigel-Calcit kann jedoch im Allgemeinen nicht als einkristallin bezeichnet werden. Ferner zeige ich die Präsenz wenig koorientierter, polykristalliner Bereiche sowohl an den Muskelansatzstellen der Echinoiden (an den Testtuberkeln und der Basis der Stacheln) als auch am Kortex, welcher die primären und sekundären Stacheln von *C. cidaris* ummantelt. Die Bildung der Mikrostruktur des Kortex wird durch zwei Faktoren bestimmt: (i) Die Kortexkristalle keimen mit ihren kristallographischen c-Achsen senkrecht zum Stereom, welches als Nukleationsvorlage dient. Somit bestimmt die Struktur und Ebenheit der äußeren Stereomoberfläche die Textur des anfänglichen Kortexteils. (ii) Ein kompetitiver Wachstumsmechanismus bestimmt die weitere Mikrostruktur und Textur des Kortex.

Darüber hinaus zeigt diese Studie, wie die Pattern matching-Methode die Winkelpräzision verbessern und feine Misorientierungen innerhalb koorientierter Strukturen, wie dem Seeigel-Stereom, aufdecken kann. Durch die Anwendung dieser Methode auf andere Kalziumkarbonat-Biomaterialien wie Eierschalen, Myostraca oder die großen Kolumnen mancher Muschelschalen arbeite ich die kristallografische Textur und Mikrostruktur dieser Materialien sehr detailliert hervor und zeige das große Potenzial dieser Datenauswertungstechnik für zukünftige Studien.

LIST OF ABBREVIATIONS

AM	Adductor myostracum
BSE	Backscatter electron
CCL	Complex crossed-lamellar layer
CL	Crossed-lamellar layer
CLSM	Confocal scanning laser microscopy
CNT	Classical nucleation theory
EBS	Electron backscatter diffraction
EBSP	Electron backscatter pattern
EDX/EDS	Energy-dispersive X-ray spectroscopy
FC	Foliated calcite
FE-SEM	Field emission scanning electron microscopy
GD	Growth direction
IS	Inner shell surface
KAM	Kernel average misorientation
Micro-CT	Micro-computed tomography
MUD	Multiple of uniform (random) distribution
MYO	Myostracum
PM	Pallial myostracum
SE	Secondary electrons
SEM	Scanning electron microscopy
TGA	Thermogravimetric analysis
TEM	Transmission electron microscopy

CONTENTS

Abstract	i
Zusammenfassung.....	iii
List of Abbreviations	vii
1 Introduction.....	1
1.1 Biogenic and Non-Biogenic Crystal Nucleation and Growth.....	1
1.2 Principles of Biomineralisation	4
1.2.1 The Biomineralisation Regime in Marine Calcium Carbonate Secreting Organisms	6
1.2.2 The Functionality of Biomineralised Tissues	12
1.3 Biomineralised Microstructures and their Crystal Texture	14
2 Results and Discussion.....	22
2.1 The Biological Crystals in Chamid Bivalve Shells: Diversity in Morphology and Crystal Arrangement Pattern.....	23
2.1.1 Introduction	24
2.1.2 Materials and Methods	26
2.1.3 Results	27
2.1.4 Discussion	39
2.1.5 Conclusions	48
2.1.6 Supplementary Information.....	50
2.2 Crystal Organisation and Material Properties of <i>Chama</i> and <i>Glycymeris</i> Myostraca and Shells	64
2.2.1 Introduction	65
2.2.2 Materials and Methods	67
2.2.3 Results	68
2.2.4 Discussion	86
2.2.5 Conclusions	104
2.2.6 Supplementary Information.....	107
2.3 Correlation between Nanomechanical Properties and Microstructural Design Concepts of Bivalve Muscle Attachment Sites	128
2.3.1 Introduction	129
2.3.2 Materials and Methods	132
2.3.3 Results	135
2.3.4 Discussion	145
2.3.5 Conclusions	162
2.3.6 Supplementary Information.....	166
2.4 Microstructure, Texture and Nanomechanical Properties of Conservative and Non-Conservative Bivalve Myostraca	173
2.4.1 Methods	173
2.4.2 Results and Discussion	174
2.4.3 Conclusions	188
2.5 Crystal Organisation at Muscle Attachment Sites of Bivalved Marine Organisms: A Juxtaposition Between Brachiopod and Bivalve Shells.....	190

2.5.1 Introduction	191
2.5.2 Materials and Methods	194
2.5.3 Results	195
2.5.4 Discussion	210
2.5.5 Conclusions	217
2.5.6 Supplementary Information	220
2.6 Evaluating the Single Crystallinity of Sea Urchin Calcite	227
2.6.1 Introduction	228
2.6.2 Materials and Methods	230
2.6.3 Results	232
2.6.4 Discussion	244
2.6.5 Conclusions	261
2.6.6 Supplementary Information	264
2.7 EBSD Pattern Matching for Characterisation of Biomaterial Texture and Microstructure	272
2.7.1 Methods	272
2.7.2 Results and Discussion	273
2.7.3 Conclusions	291
2.7.4 Supplementary Information	293
3 Conclusions and Outlook	296
3.1 Conclusions	296
3.2 Outlook	302
4 Bibliography	306
Appendices	342
A.1 Terminology	342
A.1.1 Structural and Crystallographic Terminology	342
A.1.2 Biological Terminology	344
A.2 Investigated Samples and Sample Preparation	346
A.2.1 Investigated Samples	346
A.2.2 Sample preparation	349
B Applied Methods	352
B.1 Electron Microscopy	352
B.1.1 Fundamentals of Scanning Electron Microscopy (SEM)	352
B.1.2 Electron Backscatter Diffraction (EBSD) Analysis	354
B.1.3 EBSD Data Evaluation via Pattern Matching	356
B.2 Confocal Scanning Laser Microscopy (CSLM)	358
B.3 Thermogravimetric Analysis (TGA)	359
B.4 Micro-computed Tomography (Micro-CT)	360
B.5 Nanoindentation Testing	361
Acknowledgements	364
List of Publications and Manuscripts	366

1 INTRODUCTION

This work aims to highlight the microstructure and principles of biocrystal growth utilised by organisms when forming calcium carbonate biominerals. Several Ca-carbonate-based biological hard tissues generated by organisms of various species, families, and phyla were investigated. Various analytical techniques were employed to gain an in-depth understanding of the microstructure and texture of the biomineralised tissues, as well as their functional significance for the organism. The scientific results presented in this dissertation aim to broaden our insights into the complex crystal growth mechanisms that control the fabrication of biomineralised calcium carbonates.

1.1 BIOGENIC AND NON-BIOGENIC CRYSTAL NUCLEATION AND GROWTH

Crystals are generally defined as anisotropic solids with a long-range ordered structure (Tilley 2007). Thus, except for local defects or impurities, the atomic arrangement of one point in a crystal is the same as that of any other distant part. Through this periodic organisation, the crystal minimises interatomic energies and maximises its structural stability. The fundamental processes of crystallisation are described by the classical nucleation theory (CNT), a theoretical concept developed by Becker and Döring (1935), which is based on the ideas of Gibbs (1878) and Volmer & Weber (1926). While the CNT was initially derived for the formation of nuclei from supersaturated water vapour, it can also be used to describe crystallisation from a solution (Gebauer & Cölfen 2011).

In principle, there are two mechanisms of primary crystal nucleation: homogeneous nucleation and heterogeneous nucleation. Homogeneous nucleation describes a spontaneous nucleation in the bulk of supersaturated solutions. In contrast, heterogeneous nucleation occurs on a surface or impurity that lowers the nucleation barrier. While heterogeneous nucleation is far more common (Sear 2014), the simplicity of the homogeneous nucleation theory demonstrates which factors promote or impede the growth of a thermodynamically stable nucleus. Since homogeneous nucleation assumes the nucleation and growth of a solid crystal from the disordered liquid phase, it can be regarded as a first-order phase transition. While the bulk free energy of a nascent nucleus is the driving factor for nucleation, the generation of a phase interface, and thus, interfacial tension, impedes nucleus growth. The change in Gibbs free energy ΔG_{total} can, therefore, be described as the sum of interface free energy and bulk free energy, as given by Equation 1.1-1

$$\Delta G_{total} = \frac{4}{3}\pi r^3 \Delta g_B + 4\pi r^2 \sigma \quad 1.1-1.$$

Here, the first term is the volume term, assuming a spherical nucleus of radius r . For crystallisation from a solution, the driving force per unit volume Δg_B is related to the supersaturation S , which is taken as the ratio of the actual ion activity product Q and the ion activity product in equilibrium K_S (solubility product), as expressed by Equation 1.1-2

$$\Delta g_B = \frac{RT}{V_m^c} \ln S = \frac{RT}{V_m^c} \ln \left(\frac{Q}{K_S} \right) \quad 1.1-2$$

where V_m^c is the molar volume of the solid. Generally, as the ion activity product increases, the driving force for nucleation and growth increases. In biomineralisation, the supersaturation is controlled and driven by the mineralising cells of the organism (Kashchiev 2000). As an increase in supersaturation heavily influences physical mechanisms such as agglomeration and decreases the activation energy for nucleation, biological systems need to fine-tune the reaction medium to control the nucleation (Mann 1995; Nudelman & Sommerdijk 2012).

The second term of Equation 1.1-1 represents the surface/interface term, which is proportional to the surface area of a sphere. The surface tension σ between the nucleus and its surroundings (such as a crystalline surface developing in a supersaturated solution) is always positive. For small radii, the surface term dominates, and the Gibbs free energy ΔG_{total} is positive. Hence, small nuclei will dissolve completely. As the volume term is proportional to r^3 and the surface term is proportional to r^2 , there is a radius r^* where the change in total free energy exhibits a maximum, i.e. reaches zero (ΔG^*). Since the volume term outweighs the surface term after reaching this critical radius size, the change in total Gibbs free energy will be negative, and nuclei will grow without limit after this parameter (Fig. 1.1-1). If, however, the nuclei are smaller than the critical radius r^* , the surface term is predominant and the nuclei will dissolve.

The second mechanism of primary crystal nucleation, the heterogeneous nucleation, considers the influence of existing extrinsic interfaces for the initiation of the nucleation process. Since external surfaces, interfaces or structural defects form energetically favourable sites, the energetic barrier of homogeneous nucleation can be overcome more easily. This is due to the critical radius depending on the surface tension σ . Especially low supersaturation conditions, reducing the surface tension and, thus, reducing the critical radius, effectively lead to heterogeneous nucleation and are much more probable than homogeneous nucleation (Kashchiev & Van Rosmalen 2003). Another factor that promotes heterogeneous nucleation is the presence of epitactic growth. Epitaxy describes the presence of structural similarities between the nucleation substrate and the crystallising phase. It can be subdivided into homoepitactic nucleation, where the nuclei and the substrate are formed of the same phase, and heteroepitactic nucleation, where nuclei and substrate comprise different phases. Heteroepitactic nucleation is particularly important for the growth of biological microstructures, as the crystallographic orientations are predefined and are transmitted to the nuclei and growing crystals by organic compounds (e.g., Marin et al. 2007; Checa et al. 2025; Sancho Vaquer et al. 2025).

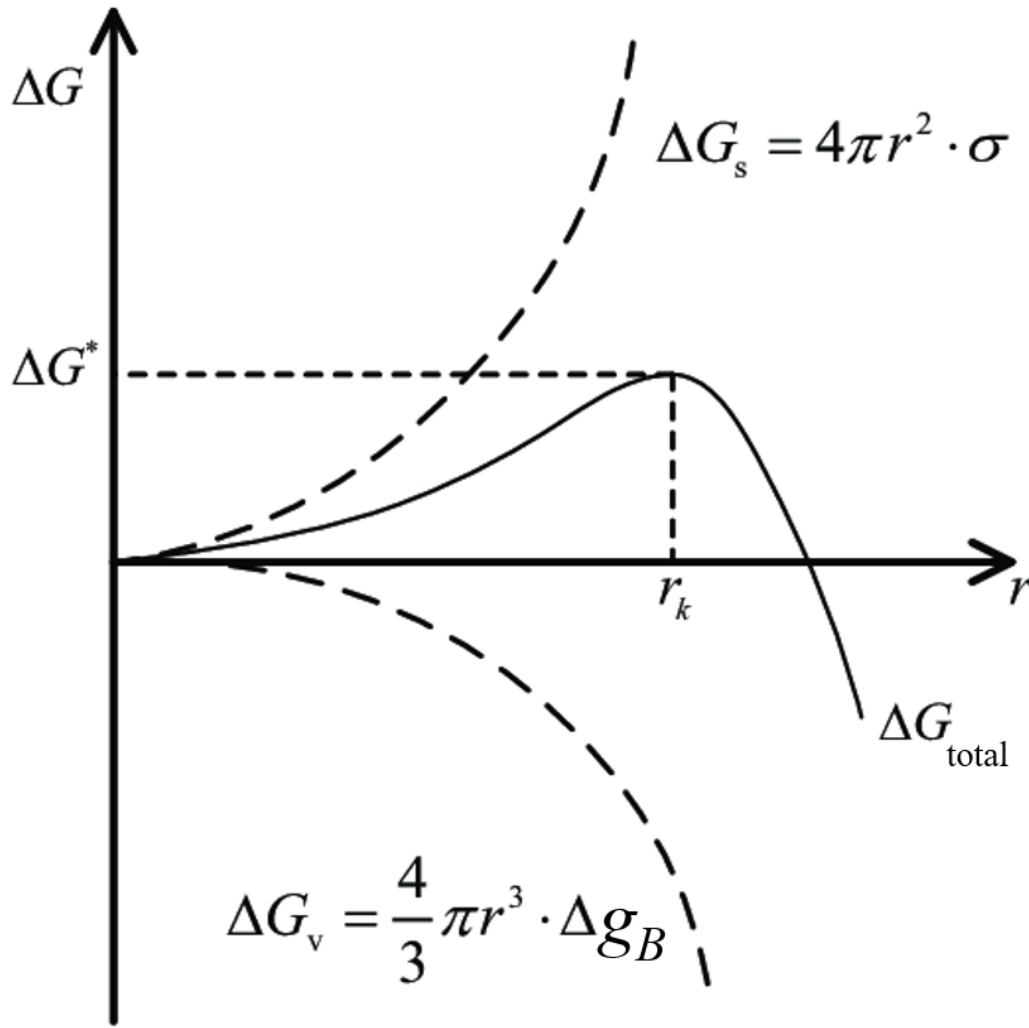


Figure 1.1-1 Schematic diagram of the Gibbs free energy change with increased nucleus radius in a supersaturated medium. Adapted from Peng et al. (2023).

Although the CNT can accurately predict qualitative nucleation phenomena, due to a number of simplifying assumptions (Debenedetti 1997; Sear 2012), some studies suggest that it may fail to quantitatively predict parameters such as nucleation time (Vekilov 2010; Gebauer & Cölfen 2011). Indeed, many examples in complex crystallisation systems cannot be explained by the CNT, but rather point to a non-classical nucleation theory (e.g., Kirner & Sturm 2021; Schlotheuber Née Brunner et al. 2021; Fu et al. 2022; Gebauer et al. 2022; Mandera et al. 2023). The latter proposes that nucleation is not only restricted to a sheer addition of monomers to nuclei and seeds, but also comprises a more advanced set of entities, such as nucleation clusters, nanodroplets and –particles (De Yoreo et al. 2015). A simplified, schematic illustration of classical and non-classical nucleation is shown in Figure 1.1-2. Non-classical nucleation pathways have also been proposed for biogenic mineralisation, suggesting that metastable precursor phases are used to initiate the nucleation of biominerals (Liu et al. 2021; Du et al. 2024). However, the exact mechanisms behind biomineralisation pathways, i.e. for calcium carbonate products, are still not fully understood and controversial (e.g., Andreassen & Lewis 2017; Henzler et al. 2018; He et al. 2023; Mandera et al. 2023; Branson & De Nooijer 2025).

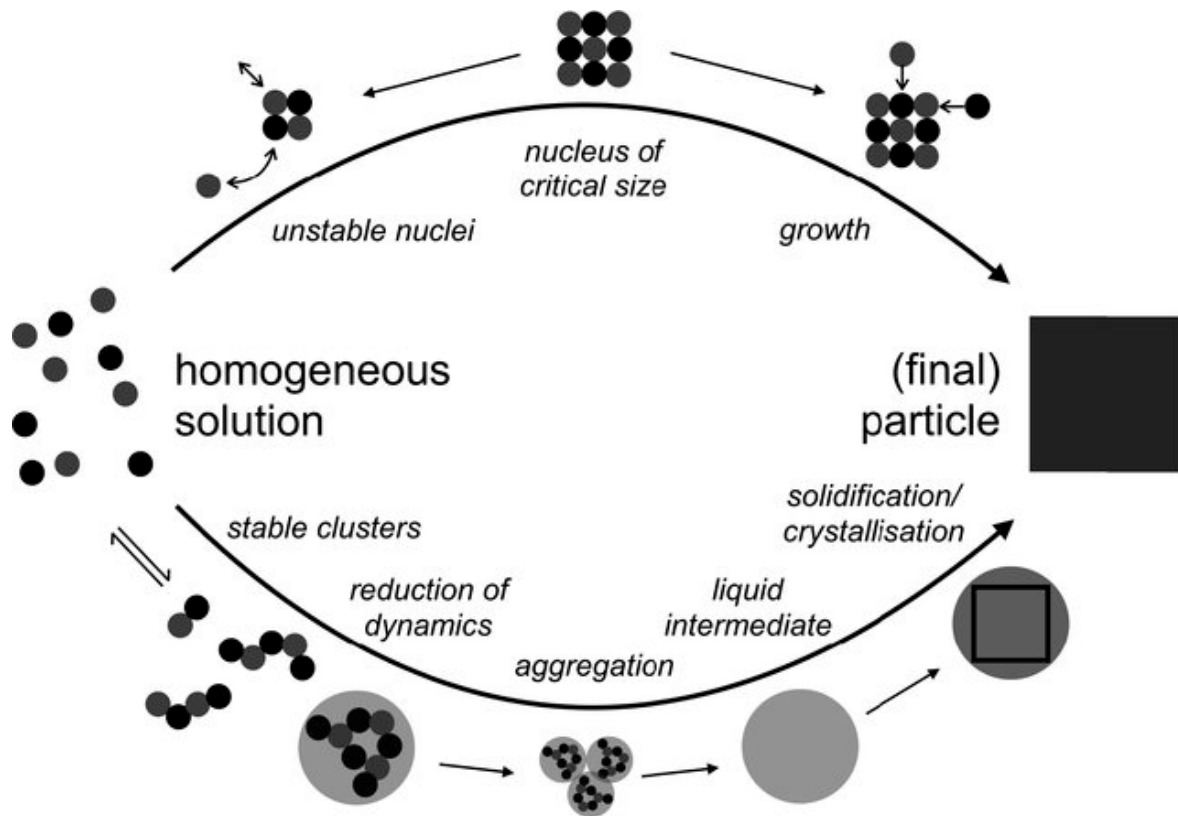


Figure 1.1-2 Simplified illustration of pathways via classical nucleation theory (top) or non-classical nucleation theory (bottom). Adapted from Gebauer et al. (2018).

1.2 PRINCIPLES OF BIOMINERALISATION

Biomineralisation is the process of mineral formation by living organisms, linking hard materials of the solid earth with soft organic tissues (Leadbeater & Riding 1986). The earliest geologically recorded skeletal biomineralisation of CaCO_3 polymorphs dates back almost 550 million years ago and was detected in limestones worldwide (Grant 1990; Grotzinger et al. 2000; Gilbert et al. 2019). As a result of an analogous redevelopment of a past biomineral generation mechanism or an unprecedented lateral genetic transfer during the Cambrian evolutionary explosion, biomineralisation rapidly evolved into a global phenomenon displayed by all major animal phyla (Kirschvink & Hagadorn 2000; Porter 2010; Park et al. 2011). While, today, over 60 different biominerals across various mineral classes can be found in nature (Weiner & Dove 2003), polymorphs of calcium carbonate are the most abundant (Jørgensen & Fath 2008; Demichelis et al. 2018). Table 1.1 gives an overview of the most abundant biotic calcium carbonate polymorphs and lists some examples of phyla that use them for biomineralizing their hard tissues.

Table 1.2.1 Overview of biogenic calcium carbonate polymorphs and the phyla constructing them.

Carbonate polymorph	Chemical formula	Phylum/Kingdom	Reference
Calcite	CaCO_3	Mollusca	(Hahn et al. 2012)
			(Schmahl et al., 2012a)
			(Checa 2018)
		Brachiopoda	(Simonet Roda et al. 2019a)
			(Schmahl et al., 2012b)
			(Casella et al. 2018)
		Foraminifera	(Yin et al. 2021)
			(Lastam et al. 2023a)
		Arthropoda	(Huber et al. 2015)
			(Hild et al. 2008)
Aragonite	CaCO_3	Mollusca	(Peter et al. 2023)
			(Griesshaber et al. 2013)
			(Ritter et al. 2017)
		Cnidaria	(Blamart et al. 2007)
			(Cairns & Macintyre 1992)
		Bryozoa	(Taylor et al. 2015)
			(Wejnert & Smith 2008)
Vaterite	CaCO_3	Chordata	(Falini et al. 2005)
			(Gauldie et al. 1997)
			(Melancon et al. 2005)
		Mollusca	(Wehrmeister et al. 2011)
			(Spann et al. 2010)
			(Frenzel & Harper 2011)
Magnesian calcite	$(\text{Ca}, \text{Mg})\text{CO}_3$	Rhodophyta	(Nash & Adey 2017)
			(Milliman et al. 1971)
			(Nash et al. 2021)
		Arthropoda	(Becker et al. 2005)

			(Fay & Smith 2021)
			(Plotnick 1990)
		Echinodermata	(Wilt 2002)
			(Dickson 2004)
			(James & Klappa 1983)
		Brachiopoda	(Williams et al. 1965)
			(Cusack et al. 2008)
Monohydrocalcite	$\text{CaCO}_3 \cdot \text{H}_2\text{O}$	Pseudomonadota	(Pan et al. 2019)
			(Zhao et al. 2021)
		Plantae	(Levi-Kalisman et al. 2002)
			(Neumann & Epple 2007)
Amorphous calcium carbonate (ACC)	$\text{CaCO}_3 \cdot \text{H}_2\text{O}$	Chordata	(Aizenberg et al. 2002)
			(Lambert & Lambert 1996)
			(Lowenstam & Weiner 1989)
		Arthropoda	(Fabritius et al. 2009)
			(Mergelsberg et al. 2019)
			(Fabritius et al. 2011)
		Plantae	(Levi-Kalisman et al. 2002)
			(Setoguchi et al. 1989)

1.2.1 THE BIOMINERALISATION REGIME IN MARINE CALCIUM CARBONATE SECRETING ORGANISMS

Biom mineralisation is a global phenomenon that is responsible for producing a wide range of molecules that can be broadly separated into the organic biopolymers and the inorganic biominerals. Through biopolymers and the variation of physicochemical parameters (e.g., the osmotic pressure, the temperature, the pH or the biofluid chemistry) at secretion, organisms can exert strong control over many biominerals characteristics: Varying the biominerals composition, biocrystal morphology or crystallographic texture can influence the material properties and help the organisms to adapt and survive in their biological habitats (Meldrum & Cölfen 2008; Schmahl et al. 2012b; Griesshaber et al. 2017). For more than 500 million years, organisms have occupied diverse ecological niches, applying

different biomineralisation principles to develop a variety of optimised materials (Harper 2016). Nonetheless, the generation of biomaterials is more or less always defined by three basic motifs: (i) The interplay and exchange between intracellular and extracellular environments, (ii) the fabrication of components within cells and (iii) the biologically controlled deposition and organisation of these components (Cölfen 2010; Yao et al. 2017; Gal et al. 2018). While there are many biological control parameters, such as fluid chemistry, component transport, material surfaces or soft/hard tissue morphology, the key aspect at biomaterial formation is the portioning of space (Lowenstam & Weiner 1989; Mann 2001; Veis 2005). The importance of forming an intra- or extracellular space partitioning lies in creating a physical boundary that can define the size and shape of the mineral phase through the supramolecular preorganisation of organic molecules (Mann 2001). Through the selective permeability of organic membranes, the spatially defined regions can have distinct chemistries varying from the surrounding environment (Addadi et al. 2003; Kahil et al. 2021). Thus, the controlled environment needed for many biomineralisation principles depends on the presence and activity of biological membranes as well as their interactions with pumps and surfaces. With advancements in evolution, many sophisticated systems have developed, each of which is defined by different interaction mechanisms that employ different biomineralisation strategies (Aidley & Stanfield 2000; Addadi & Weiner 2014).

Subsequently, a short characterisation of the biomineralisation regimes of the three phyla that were investigated in this study, of the molluscs, brachiopods and echinoderms, is provided.

The biomineralisation regime of molluscs

Showing an outstanding ability to adapt to various marine environments, molluscs are a very diverse phylum able to mineralise versatile structures of a large variety of minerals (Simkiss & Wilbur 1989). Within the molluscs, one of the best-understood formation systems for biological hard tissues is that of the bivalves (Checa et al. 2025). Here, the growth of the shell is initiated by the sheet-like mantle tissue, an epidermis covering the visceral mass of the organism (Smolowitz 2021; Checa et al. 2025). As the majority of structures are formed extracellularly by a single layer of epithelial cells, these mantle cells are involved in both the transport of ions to the secretion site as well as the deposition of organic matter. From an invagination of the outer mantle lobe, the periostracum, a robust extracellular membrane, is secreted (Saleuddin & Wilbur 1983). The periostracum comprises highly cross-linked organic molecules and fulfils numerous functions such as enclosing the molluscan mantle tissue and providing a nucleation template for the initial shell deposition (Saleuddin & Wilbur 1983; Wählich et al. 2014; Clark et al. 2020; Huang et al. 2024). Following the free periostracum stage, during which the extruded periostracum emerges from the mantle edge and gradually thickens, the extrapallial space is spatially restricted and shell growth is initiated by the mantle cells (Salas et al. 2012; Checa et al. 2014; Xu & Zhang 2014). The shell formation process is schematically illustrated for a bivalve in Fig. 1.2-1.

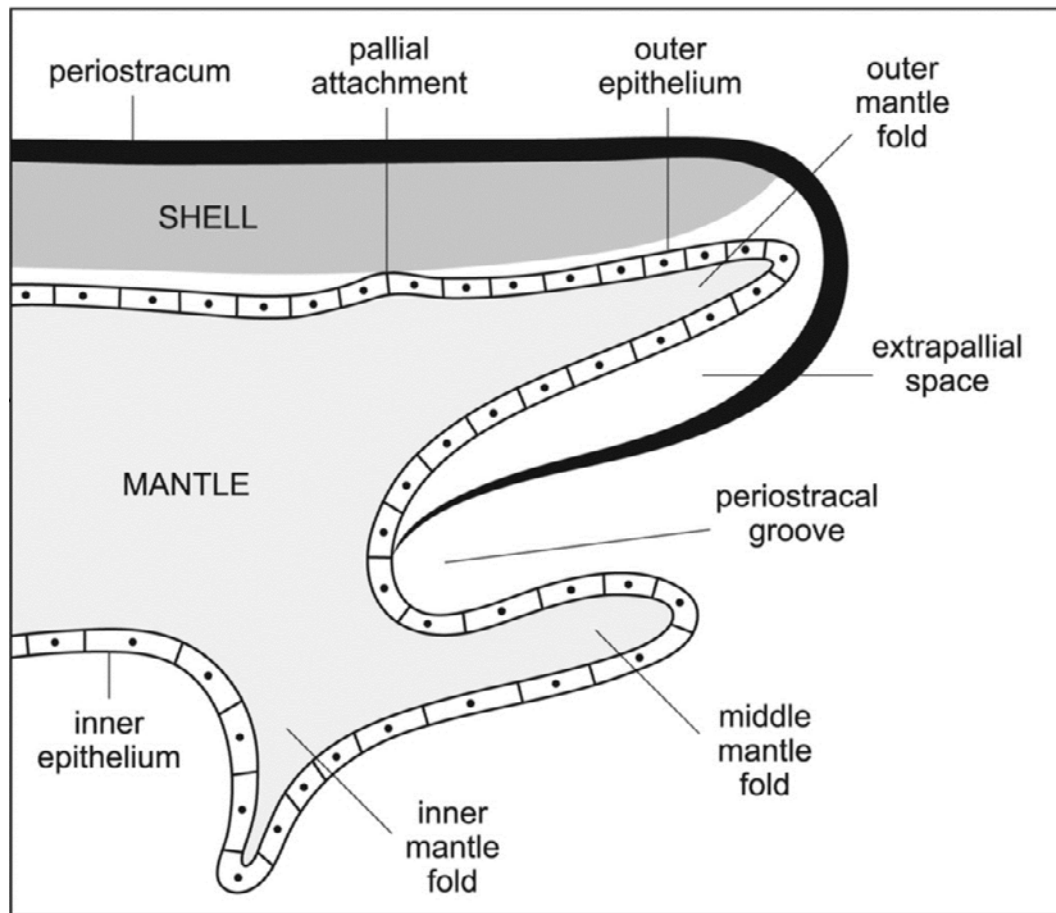


Figure 1.2-1. Schematic overview of a bivalve shell illustrating the biomineral secretion mechanism at the outer shell edge. The illustration highlights the different mantle folds and their relation with the hard tissue, periostracum and extrapallial space. Adapted from Clark et al. (2020).

For almost all mollusc shell layers, the ionic transport and biomineralisation is mediated predominantly by the mantle. As the mantle cells are in close contact to the growth surface, they can precisely control the formation of secreted materials. However, an exception to this mechanism is found at shell-muscle attachment sites (Checa et al. 2025 and references therein). At these sites, the secretion of the hard tissue is mediated by a so-called tendon cell layer that is created by the outer mantle epithelium (Lai-Fook 1967; Reindl 1996; Castro-Claros et al. 2021). At the apical side, the tendon cells are anchored to the extracellular matrix via focal adhesions and at the basal side, they are connected to the extrapallial matrix (Fig. 1.2-2). As the tendon cells are blocked by the extrapallial space and are not in direct contact with the forming crystals, a layer with a specific structure is formed at the muscle attachment sites, the myostracum (Oberling 1964).

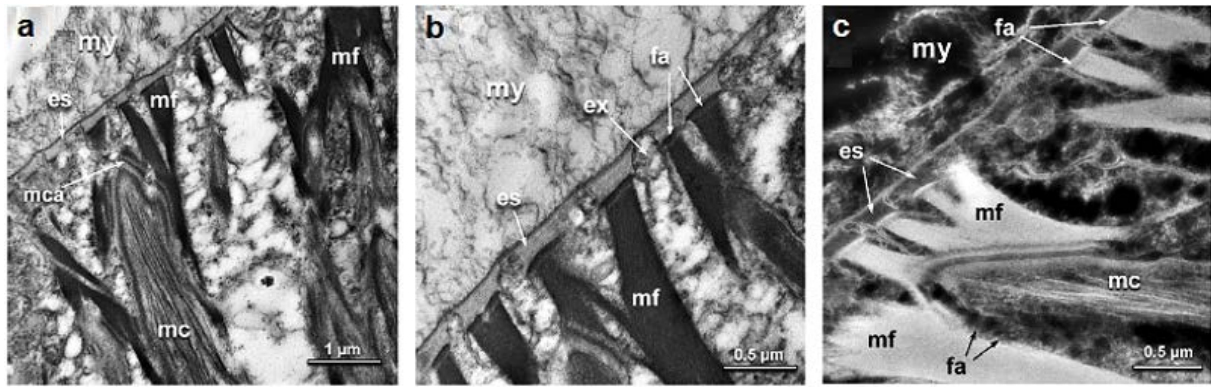


Figure 1.2-2: TEM measurements depicting the attachment of the adductor muscle to the tendon cell layer in *O. stentina* (a-c). em: extracellular matrix; es: extrapallial space; ex: exocytosis of cytoplasmic material; fa: focal adhesions; mc: muscle cell; mca: muscle cell attachment; mf: actin microfilaments; my: myostracum shell layer; nu: nucleus; ve: vesicles. Adapted and modified from Castro-Claros et al. (2021).

The myostracum in bivalves is always aragonitic and, in general, has an invariable and consistent texture and crystal morphology across many bivalve species, termed conservative by Dong et al. (2022). These **Conservative myostraca** appear pale grey or translucent and resemble inorganic aragonite as they do not show thick interprismatic walls between the individual crystals (Kennedy et al. 1969). As highlighted in more detail in Chapters 2.1-2.4 of this thesis, their distinctive crystallographic texture and crystal morphology is largely defined by crystal growth parameters, related to competitive growth. Thus, the conservative myostraca are often characterised by an increasing crystallographic co-orientation and increasing grain size with distance from the nucleation template (Griesshaber et al. 2007; Schmahl et al. 2012b; Crippa et al. 2020a). While conservative myostraca are far more common, this dissertation shows that some molluscs form **non-conservative myostraca**. The latter do not show the typical texture and grain morphology of conservative myostraca, but rather resemble the microstructure of adjacent shell layers. It is also possible to observe **hybrid myostraca**, which show elements of both conservative and non-conservative myostraca. The bivalve shell-muscle anchoring mechanism is among the strongest of invertebrates (Chantler 1983) as the collagen-rich microfilaments can pass through the entire extrapallial space and may even penetrate the shell, becoming incorporated in the myostracal crystals during shell mineralisation (Bubel 1984; Castro-Claros et al. 2021).

The biomineralisation regime of brachiopods

Similar to many bivalves, the benthic or sessile brachiopods are filter-feeders with a bivalved shell. Although brachiopod shells have a mirror plane perpendicular to the commissure, the valves are not mirror images of each other (Rudwick 1970; Schmahl et al. 2012b; Checa et al. 2025). Despite their ecological success during the Paleozoic Era, around 95% of species became extinct at the end of the Permian (Shi & Shen 2000; Peng et al. 2007). Until today, only a fraction of the about 30,000 species described so far is still extant (Williams et al. 1965; Rudwick 1970; Emig 2017). Among the invertebrates, brachiopods are unique as they can secrete both calcium carbonate shells and apatite shells (e.g., LeGeros et al. 1985; Harper et al. 2004; Zhang et al. 2023; Smith et al. 2024). Brachiopod shells

are mineral-biopolymer composites and form a hierarchical structure consisting of up to three layers. Similar to bivalves, brachiopod shells are secreted in a bottom-up process by mantle epithelial cells and into the extracellular space (Simkiss & Wilbur 1989). Starting from the periostracum, which covers the outer shell surface, different shell layers are deposited by different areas of the mantle (Fig. 1.2.3). During mineral secretion in calcitic brachiopod shells, the width of the extracellular space between the mantle cells and the forming shell material is in the range of a few nanometres (Simonet Roda et al. 2022). This enables a precise control of the biomineralised layers. While calcitic shells only feature an organic protein content of around 0.5%, the proteins (mainly chitin) in phosphatic shells may reach up to 25% (Simkiss & Wilbur 1989).

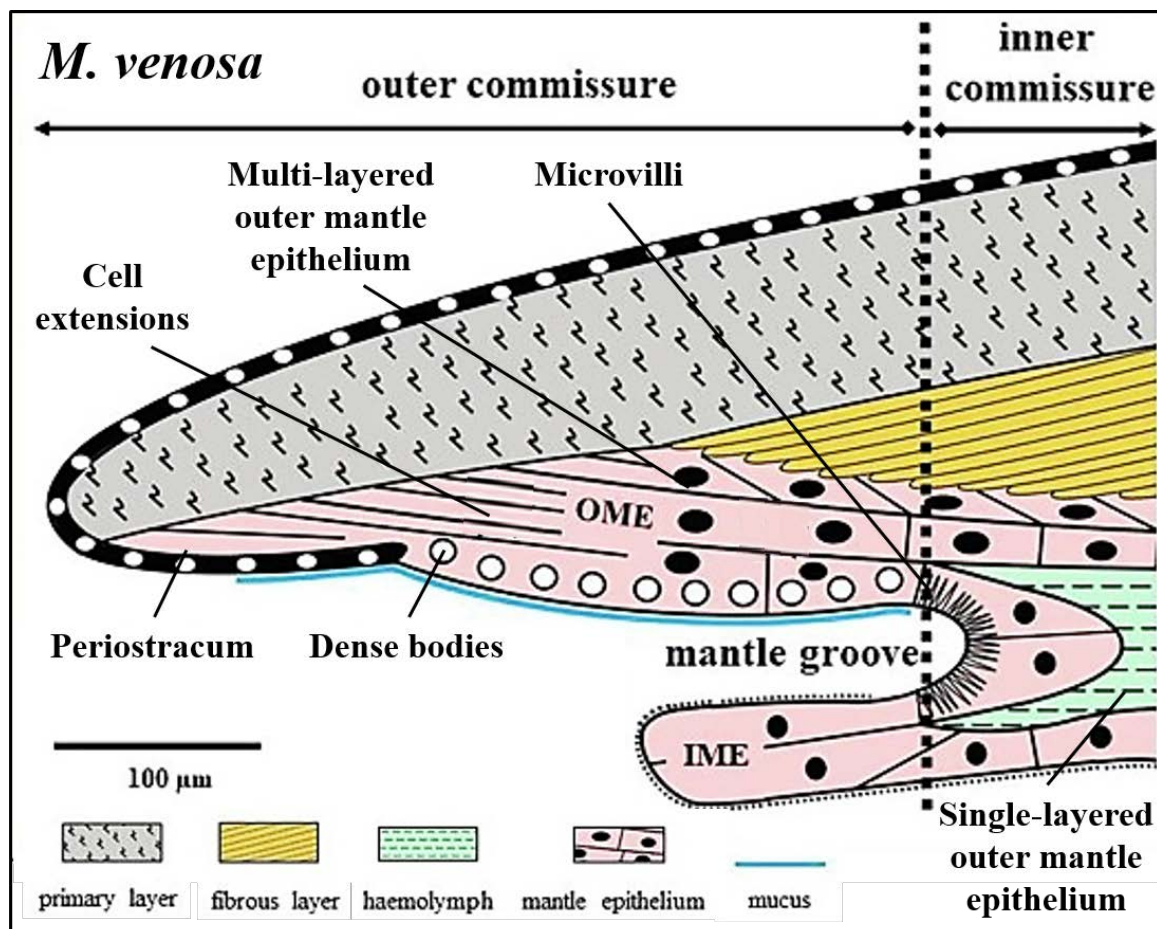


Figure 1.2-3: Schematic illustration of the different layers of a *Magellania venosa* brachiopod shell and its topologic relation with the mantle epithelium. The mantle is structured into the inner mantle epithelium (IME) and the outer mantle epithelium (OME). Based on ultrastructural characteristics, different portions of the outer mantle epithelium can be distinguished and related to different shell layers. Adapted and modified from Simonet Roda et al. (2019).

The biomineralisation regime of echinoderms

Echinoderms comprise a variety of invertebrate marine animals forming their protective hard tissue exclusively of magnesium-rich calcite (Weber 1969; Wilt et al. 2003; Gayathri et al. 2007). In sea urchins, the biomineralised tissue comprises of four main skeleton elements: The two most important features are the circular test and the needle-shaped spines.

Additionally, echinoderms biomineralised a jaw apparatus in the central area of the ventral test region as well as small pedicellariae, which can exist in various shapes and sizes on the test surface (Peters & Campbell 1987; Simkiss & Wilbur 1989; Ameye et al. 1999; Dubois & Ameye 2001). The main portion of the echinoid skeleton, the test, comprises many plates that are interconnected via collagen fibres (Ellers et al. 1998). Distributed along the outer plate surfaces in a Voronoi-like pattern, primary and secondary tubercles fix the spines in a ball-and-socket joint to the test, which allows wide-angle movement of the spines.

Opposed to molluscs and brachiopods, the calcification process of sea urchins is not strictly extracellular, but presumably also involves intracellular processes (Simkiss & Wilbur 1989; Vidavsky et al. 2016). Early mineralisation takes place in vacuoles within syncytial sclerocytes, forming the sea urchin larval skeleton, the teeth and the primary plates of the test (Märkel et al. 1989). For all skeletal elements, the syncytium forms a thin, gelatinous membrane sheath that encloses a matrix-coated cavity (Märkel et al. 1989). Using a concentration gradient and specific channels located in the membrane, Ca^{2+} and CO_3^{2-} -ions are concentrated within the cavities, using active pumps and proteins as anhydrase to remove excessive ions and water during the biomineralisation process (Chen & Lawrence 1987; Weiner & Addadi 2011). Most modern studies suggest that the first precipitation within the cavities comprises highly disordered amorphous calcium carbonate (Politi et al. 2004; Weiner & Addadi 2011; Albéric et al. 2018). This precursor phase is transported to the syncytium, where it is deposited as a calcite single crystal after the membrane degrades (Beniash et al. 1997; Politi et al. 2004; Albéric et al. 2019).

The precipitation and growth of sea urchin magnesium calcite takes place under high biological control, as visible by the unprecedented crystallographic co-orientation and highly functional trabecular arrangement (Okazaki 1960; Moureaux et al. 2010; Kokorin et al. 2014; Shapkin et al. 2017). The trabeculae can construct about 10 different stereom fabrics; however, their type and form can vary even within a single plate (Pearse & Pearse 1975; Smith 1980). Studies suggest that the stereom structure can be influenced by factors such as the growth speed or presence of tissue within the channels (Simkiss & Wilbur 1989). Therefore, extremely rapid growth, i.e. at certain edges of young primary plates, affects the morphology of the outer plate (Märkel et al. 1989) and can weaken the mechanical resistance of the shell, which relates to the density of the sea urchin shell (Moureaux et al. 2010; Lauer et al. 2018; Lauer et al. 2020).

1.2.2 THE FUNCTIONALITY OF BIOMINERALISED TISSUES

Evolving for hundreds of millions of years, the complexity and functionality of biomineralised structures has continuously improved and developed (Yao et al. 2017). Around 810 million years ago, probable protists have formed the first biomineralised hard parts, consisting of simple phosphatic plates formed under active biological control (Wood et al. 2017; Wood 2018). Today, biomineralisation is a key mechanism that is widespread across all six phyla and contain more than 60 different minerals (Sigel et al. 2008; Addadi & Weiner 2014). Through special fabrication strategies that were employed to withstand or utilise environmental factors, organisms have developed advanced hierarchical structures with outstanding material properties that can, in some cases, even outperform man-made materials such as steel or nylon (Launey & Ritchie 2009; Mittal et al. 2018). One of the best examples of the functional evolution of biomineralised hard tissues is nacre, also known as mother-of-pearl. This microstructure comprises small (5-15 μm) aragonite tablets that are arranged into lamellae by an organic matrix. This arrangement has independently evolved in bivalves, gastropods, cephalopods and monoplacopora and generates an outstandingly tough material (Marin et al. 2012; Checa et al. 2025).

While the question about the toughest calcium carbonate microstructure is still disputed (e.g., Currey & Taylor 1974; Currey 1977; Kamat et al. 2004; Li et al. 2017), it is without doubt that their composite nature is the key factor for their mechanical properties that surpass their inorganic counterparts substantially (Loh et al. 2020; Ahamed et al. 2022). In this composites, the minerals provide stiffness and hardness and the surrounding biopolymer matrix provides ductility. The functionality and mechanical properties of a microstructure can be influenced by different factors:

- (i) The crystal morphology and size. Although individual crystals have a periodic structure with precise angles between their flat faces, biomineralisation mechanisms can lead them into various, irregular arrangements to form complex hierarchical structures (Simkiss & Wilbur 1989). Adapted to the function of the biological hard tissue and the lifestyle of the organism, biomacromolecules can form mineral phases with advanced properties (Beniash 2011).

Not only the morphology and structure, but also the size of the biomineralised crystals may impact the functionality of the microstructure. In inorganic materials, smaller grain sizes lead to increased hardness due to the Hall-Petch relation (Salem et al. 2006; Renard & Jacques 2012; Q. Huang et al. 2014; Ding et al. 2019). Although there seems to be no studies about the validity of the Hall-Petch relation in biomineralised hard tissues so far, this effect might still be of considerable influence for the functionality of a biomaterial.

- (ii) The crystallographic orientation. Due to the anisotropy of calcium carbonate biominerals, the material properties such as the nanomechanical hardness of a biomineralised hard tissue depend on the crystallographic texture (Joshi 1993). The highest hardness can be observed when the crystallographic c-axes are oriented perpendicular to the outer surface of the

biomaterial, i.e., the crystallographic preferred orientation observed in most biomineralised hard tissues (Berman et al. 1993; Deng et al. 2023)

- (iii) The distribution of mineral and organic phases. The organic matrix material acts as a glue between biominerals, but its organisation, distribution and ratio compared to the mineral content also have a affect the material properties (Beniash 2011). Depending on the biomineralised microstructure, the organic content, and with it the mechanical properties such as stiffness or hardness, can vary greatly (Piez 1961; Currey & Taylor 1974; Wilt 1999; Currey 2002; Marin et al. 2007b).
- (iv) Crystalline defects and twinning. One of the most effective toughening mechanisms in biomineralised hard tissues is fracture deflection along biomineral grain boundaries. This strategy can be observed in various calcium carbonate layers, e.g., the foliated calcite layer in the bivalve *Placuna placenta* (Li & Ortiz 2014) or the helical microstructure of the gastropod *Clyo pyramidara* (Li et al. 2015). Probably the most effective and famous examples for such a hierarchical structure, however, are the plywood-like structures such as crossed-lamellar layers, which have developed extensively by many bivalves, gastropods, scaphopods and polyplacophorans (Checa et al. 2025). Through a highly functional microstructure comprising first-, second- and third-order lamellae that are tilted at high angles towards each other, fractures are deflected and mechanical damage is constrained. Energy dissipation mechanisms rely on a high number of grain boundaries, substructures or crystalline defects. Thus, an important mechanism for the enhancement of material properties might be the extent, distribution and mode of twinning. In biomineralised calcium carbonate hard tissues, twinning is particularly prominent for aragonitic microstructures (i.e., in bivalve shells, see Crippa et al. (2020) or Sancho Vaquer et al. (2025)), but may also be observed for the calcitic shells and spines of rotaliid foraminifera (Lastam et al. 2023b; Schmahl et al. 2025b). The effects of twin formation are not limited to blocking dislocations and crack propagations, but they also effectively reduce the grain size through the introduction of additional grain boundaries (Shin et al. 2016; Wang & Zhang 2016; Uttam et al. 2020).

1.3 BIOMINERALISED MICROSTRUCTURES AND THEIR CRYSTAL TEXTURE

Many monographs aim to highlight and describe the different microstructures of biomineralised Ca-carbonate hard tissues, i.e. for molluscs (Boggild 1930; Taylor et al. 1969; Taylor et al. 1973; Carter et al. 2012), corals (Struve 1898; Lafuste 1970; Semenov Tian Chansky 1974) or echinoids (Smith 1980; Gorzelak 2021). However, these studies have often focused only on morphological aspects of the biocrystals, such as crystal shape or size, and neglected the crystallographic texture of the different microstructures. Not only do the crystallographic axis orientations of the comprising crystals provide information about the relationship between different skeletal layers or skeletal elements, but they also offer valuable insights into the crystal growth processes and crystal organization-related responses that have led to ecophenotypical variations between different species (Coronado et al. 2015).

Up to now, in calcium carbonate biological hard tissues, seven different crystal texture patterns with varying degrees of crystal co-orientation can be observed. Those seven textures can broadly be divided into three categories: (i) textures with a high degree of crystallographic axes co-orientation, where, at least, one crystallographic axis is clustered in a joint orientation, (ii) textures with a medium degree of crystallographic axes co-orientation, however, with a high degree of local co-orientation between neighbouring crystals and a low co-orientation across the entire microstructure and (iii) textures with poorly defined crystallographic axes co-orientation.

It should be noted that the extremes of these textures, perfectly co-oriented single crystals or untextured and randomly oriented polycrystals, do not exist in biomineralised tissues across an entire microstructure (Table 12.1 in Griesshaber et al. (2017)). Depending on the chosen scale, however, the texture of some calcitic and aragonitic biomaterials comes very close to the texture of non-biological single crystals or polycrystalline assemblies.

Textures with a high degree of crystallographic co-orientation

The strongly co-oriented textures are subdivided into single-crystalline long-range, 3D single-crystal-like and axial/cylindrical textures. The most co-oriented microstructures have a single-crystalline long-range order and have a single joint orientation for all crystallographic axes (Fig. 1.3-1a, b). However, since a “perfect” crystal does not exist in practice, and even the single crystals that are grown under laboratory conditions can comprise lattice defects leading to minute misorientations, pinpointing single crystals is difficult and disputed (Lifshitz 2007; Commins et al. 2019). A commonly accepted definition of a single crystal is “a crystalline entity growing from a single nucleus” (W.W. Schmahl, personal communication, March 3, 2025); however, it is not possible to retrace the complete crystal growth conditions back to the nucleation event, especially for biomineralised hard tissues. While high-resolution EBSD measurements evaluated with modern methods can provide maps with unprecedented

angular precision and highlight small-angle misorientations, defining rigorous critical parameters (such as the maximum allowed misorientation across a certain distance) for single-crystallinity is challenging. In this study, the critical parameters to differentiate a single-crystalline long-range order texture, a single-crystal texture, from a highly co-oriented 3D “single-crystal-like” texture are, therefore, the distribution and degree of internal misorientations as well as the MUD value. The MUD value is calculated by the EBSD software, which quantifies the intensity of the contoured pole figure maxima and indicates quite well the degree of co-orientation. For a half-width of 5° and cluster size of 3° , the MUD value of the contoured pole figures for a measurement across the entire microstructure should be > 700 (Fig. 1.3-1a, b).

A microstructure is considered to have a 3D “single-crystal-like” texture when clear-cut maxima are observed in the pole figures of all crystallographic axes. In contrast to the single-crystalline long-range order texture, orientations may scatter around the clustering directions. A microstructure with a 3D “single-crystal-like” texture can either (i) have all crystallographic axes clustered around a single orientation or (ii) have multiple, distinct maxima, such as the crossed-foliated or the crossed-lamellar layers in molluscs (Fig. 1.3-1c, d). Even though termed 3D “single-crystal-like”, the latter textures may show relatively low MUD values, even below an MUD of 50 (e.g., Fig. 1.3-1c, d).

The texture is considered axial if only one common crystallographic axis is clustered, and the other crystallographic axes are distributed on a circle perpendicular to the clustered axis (Fig. 1.3-1e, f). It is important to mention that there are many different synonymous terms used for this arrangement of crystallographic axes distributions, such as turbostratic (Stolarski et al. 2021), cylindrical (Griesshaber et al. 2010; Lastam et al. 2023a) or fibrous textures (Checa et al. 2020; Berent et al. 2023). Shell microstructures with axial textures are frequent for many marine phyla, such as molluscs (see Chapters 2.1 to 2.4 of this thesis) or brachiopods (see Chapter 2.5 of this thesis), with the crystallographic c-axes of aragonite or calcite, often being arranged parallel to the growth direction. Depending on the scattering of the clustered axis from the texture direction, axial textures can vary in their degree of crystallographic co-orientation, showing MUD values between 50 and well over 400 (e.g., Fig. 1.3-1e).

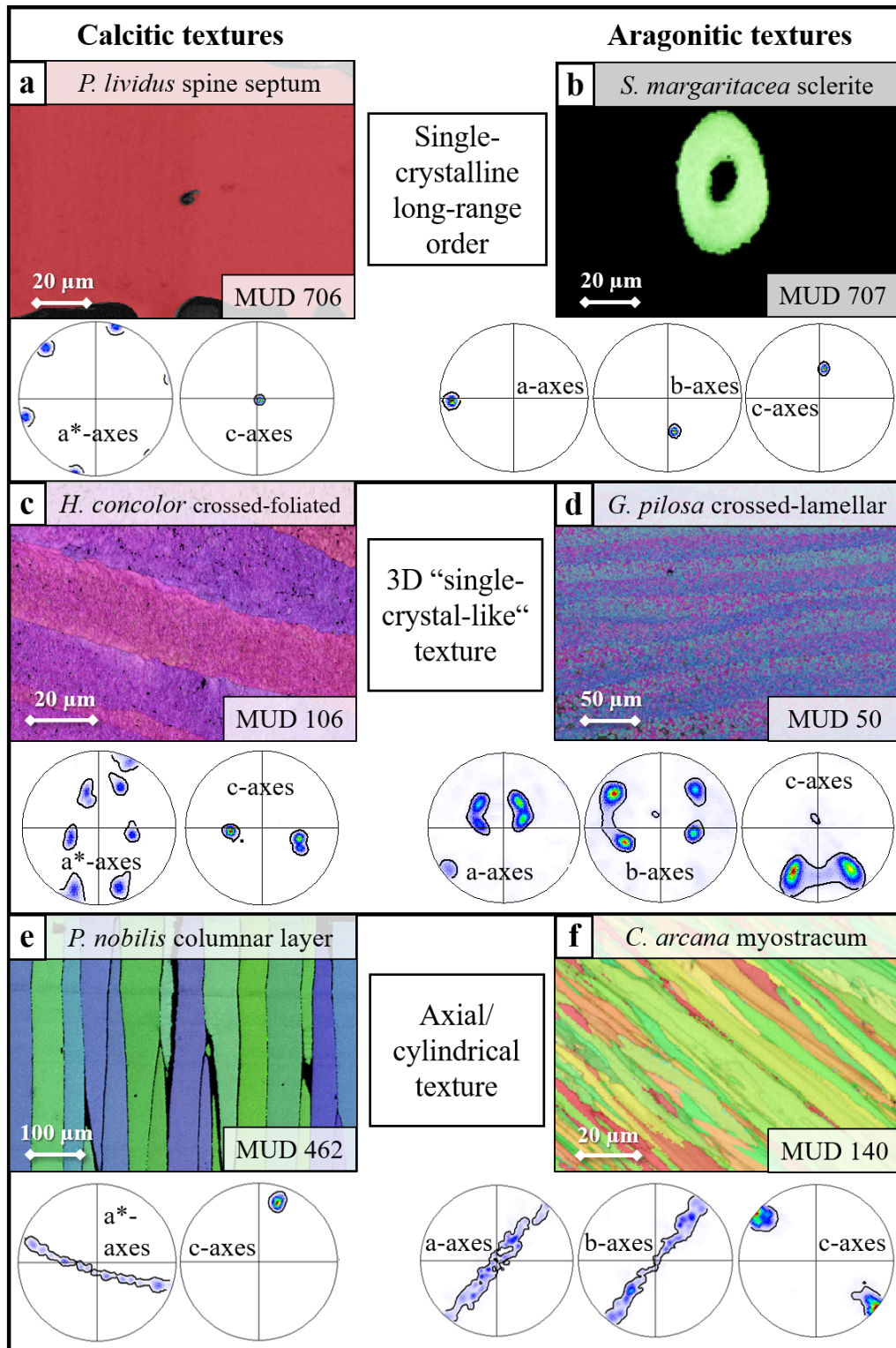


Figure 1.3-1. Compilation of different textures observed in highly co-oriented aragonitic and calcitic microstructures. Microstructures with single-crystalline long-range orders comprise a single orientation along all three crystallographic axes (a, b) and have the highest degree of crystallographic co-orientation (MUD > 700 for a half-width of 5°). Single-crystalline long-range orders in calcium carbonate biomineralised microstructures are uncommon; however, examples are the calcite septa in *Paracentrotus lividus* spines (a) or the aragonitic sclerites of *Simrothiella margaritacea* (b). A 3D "single-crystal-like" microstructure is given for one or more distinct, clustered orientations along all crystallographic axes (c, d). A 3D "single-crystal-like" texture can be observed for the calcitic crossed-foliated layer of *Helcion concolor* (c) or the aragonitic crossed-lamellar layer of *Glycymeris pilosa* (d). Axial textures show clustering in a joint orientation along a single axis, with the orientations of the perpendicular crystallographic axes distributed on a circle perpendicular to the texture axis (e, f). This texture is observed in many microstructures, such as the calcitic columnar layer in *Pinna nobilis* (e) or the aragonitic adductor myostracum in *Chama arcana* (f).

Textures with a medium degree of crystallographic co-orientation

While medium co-oriented microstructures usually have comparatively small misorientation angles between neighbouring crystals (Griesshaber et al. 2025), they typically have low MUD values when considering the entire microstructure (Fig. 1.3-2). Only two texture arrangements have a medium degree of crystallographic axes co-orientation: the “spherulitic-like textures” and the “turbostratic-like” textures. Microstructures with a “spherulitic-like” texture can be found in aragonitic and calcitic biological hard tissues. Similar to non-biological spherulites, e.g. hydrogel-carbonate aggregates (Shtukenberg et al. 2012; Yin et al. 2019), the spherulitic microstructures show a spherical, ring-shaped distribution of the texture axis (usually the c-axis) with the other crystallographic axes varying accordingly (Fig. 1.3-2a, b). The spread of the texture axis orientations, determined with EBSD measurements, depends on the cutting angle through the spherulite, as spherulitic microstructures usually grow from a single, point-like nucleus or nucleation surface and spread evenly in 3D. While this growth mechanism creates homogeneous morphologies in laboratory-grown aggregates (Yin et al. 2019; Chevillotte 2022), the spatial restrictions at biomineralised hard tissue growth generally impose the generation of a three-dimensionally continuous spherulite microstructure. Confinement by neighbouring crystals or uneven nucleation surfaces promotes the growth of some crystals over others. Therefore, biomineralised “spherulitic-like” microstructures often show diverse crystal morphologies, which can influence the texture. Accordingly, pole figures might show maxima for selected crystallographic orientations on the spherulitic orientation ring (see Fig. 1.3-2a). In contrast, others can have broadly distributed orientational density distributions resembling an axial texture (e.g., Fig. 1.3-2b).

The second texture observed for medium co-orientated microstructures is the so-called “turbostratic-like” texture that has only recently been described for a Ca-carbonate hard tissue by Griesshaber et al. (2025). So far, only observed for calcitic foliated and, to some extent, rhombohedral layers of oysters, microstructures with a “turbostratic-like” texture show intricate crystal orientation patterns. In contrast to the axial texture, the c-axes of “turbostratic-like” calcite crystals are not clustered along the growth direction, but their orientation is between 25° to 30° oblique to the growth direction (Runnegar 1984; Checa et al. 2007; Checa 2018). Due to the parallel arrangement of adjacent laths in a folium and the stacked arrangement of folia in a foliated unit, the organisation of calcite c- and a*-axes in foliated units is graded (Schmahl et al. 2025a). Analysis of sequential subsets has revealed that the c-axes of foliated units gradually rotates along a circle perpendicular to the inner shell surface, resembling a spiral (Griesshaber et al. 2025; Sancho Vaquer et al. 2025). The result is a cone-shaped distribution of c- and a*-axes orientations in 3D and a ring-shaped distribution in 2D pole figures. The alignment of the a*-axes perpendicular to the c-axes orientation is not random but rather shows an intricate alignment with a distinct maximum of {105}, {106} directions coincident with the growth direction (Fig. 1.3-2c). While the point-to-point misorientation along grain boundaries is

usually small ($1-5^\circ$, see Griesshaber et al. (2025)), the gradual rotation of c-axes causes the low overall MUD values of “turbostratic-like” microstructures (Fig. 1.3-2c).

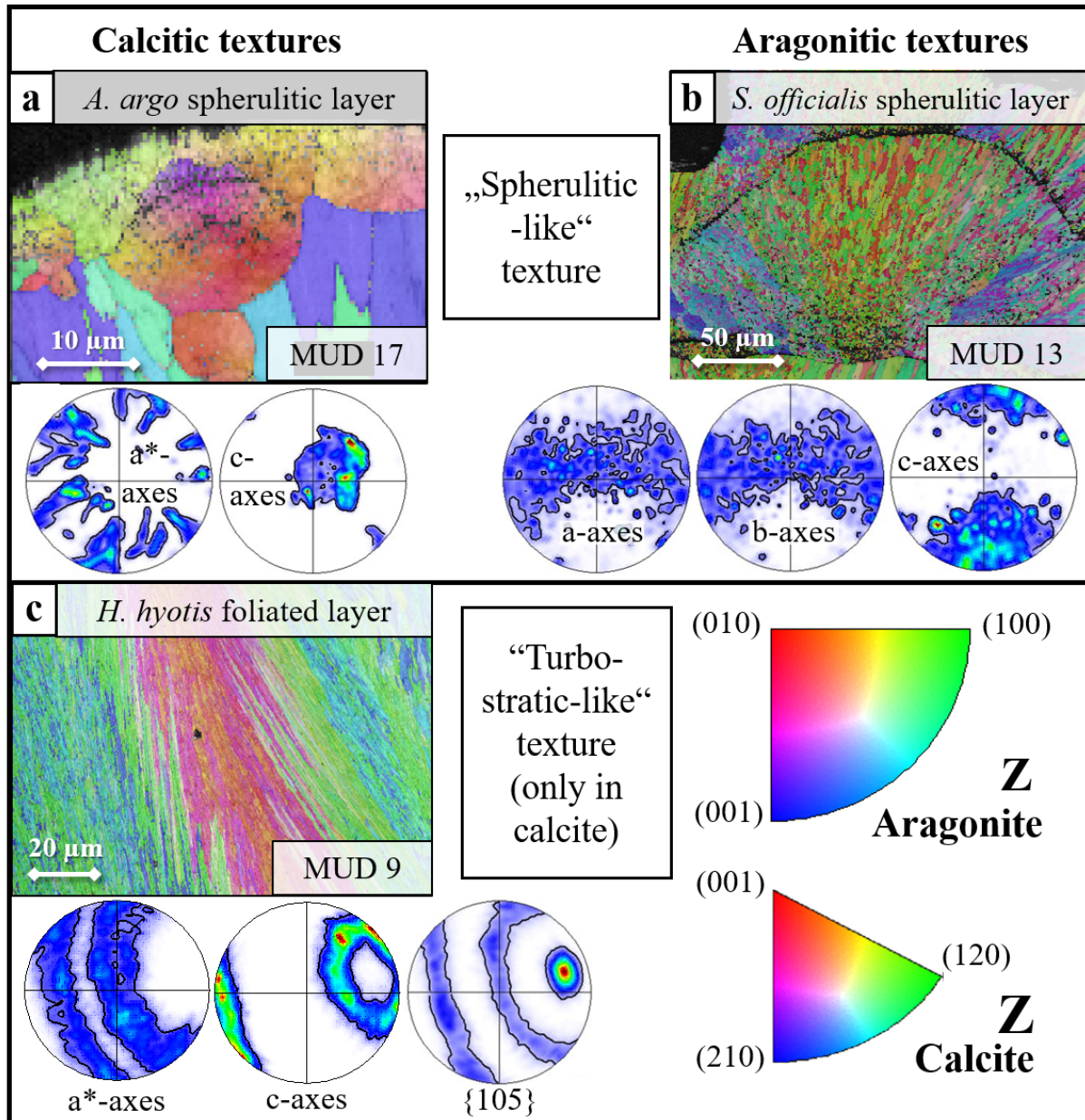


Figure 1.3-2. Textural compilation of different medium co-oriented microstructures with aragonitic and calcitic crystals. A “spherulitic-like” texture is created when crystals grow from a spherical nucleation surface with a texture axis oriented toward crystal growth (a, b). It can be recognised from a ring-shaped orientation distribution maximum, with the other crystallographic axes scattering perpendicular to it. Pole figures may show an uneven (e.g., the spherulitic calcite layer in *Argonauta argo* (a)) or even distribution of maxima (e.g., the spherulitic aragonite layer in *Sepia officinalis* (b)), depending on the crystal size homogeneity. Like “spherulitic-like” textures, the “turbostratic-like” textures have relatively low misorientations compared to the neighbouring crystals/plates. In contrast, the texture of the composite microstructure usually has a low MUD value. So far, “turbostratic-like” textural arrangements have only been observed for calcitic microstructures, such as the foliated and rhombohedral layers in ostreids (e.g., the foliated layer in *Hyotissa hyotis* (c)). The indicated IPF colour-codes give the utilised sample directions of aragonite and calcite for Figs. 1.3-1 to 1.3-3.

Textures with a low degree of crystallographic co-orientation

The poorly co-oriented textures can also be subdivided into two microstructural crystal arrangements: the microstructures with an “axial-like” texture and the “untextured-like” microstructures. Compared to the axial texture, the “axial-like” texture features a broad distribution of crystallographic orientations around the clustered axis. Although the MUD values of microstructures with “axial-like” textures can be as low as 5-10 (Fig. 1.3-3a, b), the pole figures feature areas with a high orientational density and areas with a low orientational density. In contrast to microstructures with a medium degree of crystallographic co-orientation, the “axial-like” microstructures not only show a low co-orientation across the entire measurement but also between neighbouring grains (Sancho Vaquer et al. 2025).

If a microstructure lacks or shows almost no preferred orientation for any crystallographic axis, it is considered an “untextured-like” microstructure. Depending on the size of the EBSD map and the measured crystals, the MUD values of “untextured-like” microstructures can surpass measurements of textures with a medium degree of crystallographic co-orientation (e.g., for the calcitic pillars of *Ostrea edulis* shells, see Fig. 1.3-3c). However, in contrast to the other texture modes, the “untextured-like” microstructures do not show distinct maxima for the pole figures of any crystallographic axis. Up to now, all known microstructures observed for biomineralised calcium carbonate hard tissues feature some degree of preferred crystallographic orientation (Schmahl et al. 2012, A.G. Checa, personal communication, March 22, 2025). The reason for this is most likely that all biologically mineralised materials are composites of polymer and mineral and generated either via heteroepitaxy or oriented nucleation, which also enhance the structural stability (Weiner & Lowenstam 1986). While there are biomineralised examples of both calcitic and aragonitic microstructures with an “untextured-like” orientation distribution (Fig. 1.3-3c, d), it is important to consider the impact of different scales on our perception of crystal textures. For example, the polycrystalline assembly of aragonite crystals in *Acanthopleura vaillantii* spicules appears untextured when considering the spicule as an entity, while an axial-like texture can be recognised on a lower scale (Fig. 1.3-3d).

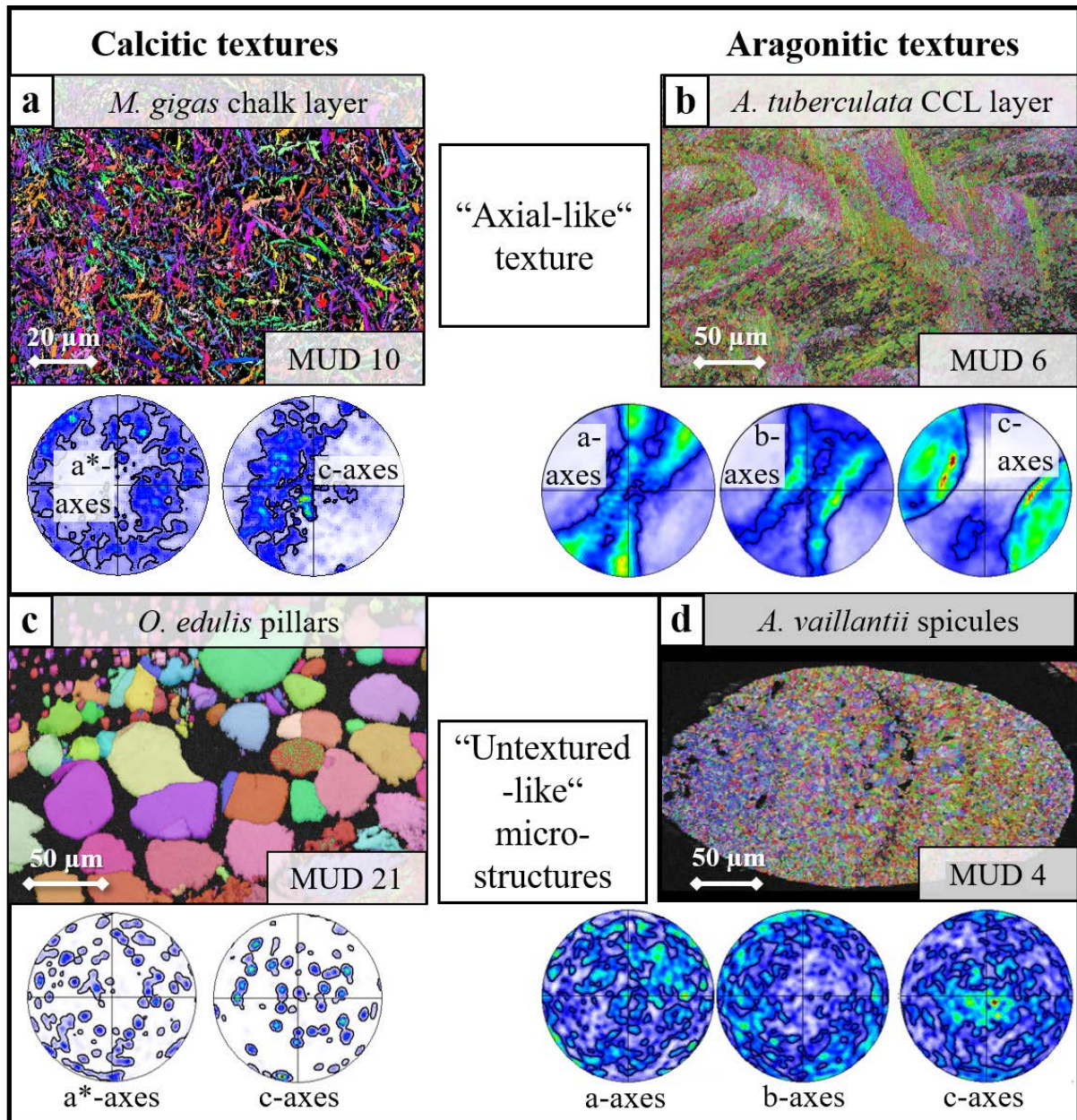


Figure 1.3-3. Compilation of different textures observed in poorly co-oriented aragonitic and calcitic microstructures. An “axial-like” texture is visible in microstructures with a very low crystallographic co-orientation and a weak clustering along a single crystallographic axis (a, b). Depending on the size of the crystals and the measurement, “axial-like” textures usually show low MUD values in the range of 5-20. This texture is present in both calcitic microstructures, e.g., the chalk in *Magallana gigas* shells (a), as well as aragonitic microstructures, e.g., the complex crossed-lamellar layer of *Acanthocardia tuberculata* shells (b). Microstructures with no to almost no crystallographic co-orientation are considered “untextured-like”. Their pole figures show very low MUD values and a broad, practically homogeneous spread of crystallographic orientations for all axes (c, d). Examples of the “untextured-like” microstructures include the calcitic pillar sheets of *Ostrea edulis* shells (c) or the aragonitic spicules of *Acanthopleura vaillantii* spicules (d). Although the *O. edulis* pillars are well-mineralised and show a high internal co-orientation, the misorientation angles between them are almost random (c).

2 RESULTS AND DISCUSSION

Five sections within this chapter are published scientific research journal articles (Sections 2.1, 2.2, 2.3, 2.5, and 2.6). The author is the first author of those five academic publications. Two additional chapters of this chapter (2.4 and 2.7) contain unpublished results. The author has also contributed to three published journal articles, the details of which can be found in the attached publications list.

Section 2.1 Reprinted (adapted) with permission from *Crystals*, 2024, 14 (7), 649. Copyright © 2024 MPDI under the terms of the CC-BY 4.0 license.

Section 2.2 Reprinted (adapted) with permission from *Materialia*, 2024, 36, 213 (2), 107707. Copyright © 2024 Elsevier Inc under the terms of the CC-BY 4.0 license.

Section 2.3 Reprinted (adapted) with permission from *Materials & Design*, 2025, 253, 113845. Copyright © 2025 Elsevier Inc under the terms of the CC-BY 4.0 license.

Section 2.5 Reprinted (adapted) with permission from *Crystals*, 2025, 15 (7), 649. Copyright © 2025 MPDI under the terms of the CC-BY 4.0 license.

Section 2.6 Reprinted (adapted) with permission from *Acta Biomaterialia*, 2025, 198, 334-355. Copyright © 2025 Elsevier under the terms of the CC-BY 4.0 license.

This work aims to highlight the microstructure, texture, crystal growth models and functional significance of various organisms forming calcium carbonate biominerals. The different sections of this chapter are dedicated to understand in great detail the hierarchical structure and small-scale crystal arrangement of different biological hard tissues. The first four sections detail the microstructures, textures and changeovers of various bivalve shell layers, in particular, the myostracum, measured with high-resolution EBSD analysis. Combining EBSD with nanomechanical and thermal analysis techniques, Sections 2.1 – 2.4 show the influence of different microstructural characteristics on the material properties of bivalve shells. Although not closely related, brachiopods form bivalved shells that are superficially similar to the shells of bivalves. Section 2.5 focuses on characterising the microstructure, nanomechanical properties and muscle attachment mechanism of a calcitic brachiopod shell. In contrast to bivalves and brachiopods, sea urchins appear to initiate the nucleation of skeletal elements intracellularly, generating a complex and highly functional hard tissue with a high degree of crystallographic co-orientation. Employing a progressive EBSD data evaluation method, Section 2.6 not only gives an overview about the microstructure and hierarchical development of sea urchin skeletal elements, but also investigates their degree of single-crystallinity. In the final Section 2.7 of this chapter, this novel technique is also applied to other biological hard tissues, revealing internal misorientations and other microstructural features with an unprecedented precision.

2.1 THE BIOLOGICAL CRYSTALS IN CHAMID BIVALVE SHELLS: DIVERSITY IN MORPHOLOGY AND CRYSTAL ARRANGEMENT PATTERN

Sebastian Hoerl ^{1,*}, Erika Griesshaber ¹, Antonio G. Checa ^{2,3} and Wolfgang W. Schmahl ¹

1. Department of Geo- and Environmental Sciences, Ludwig-Maximilians-Universität München, Germany

2. Instituto Andaluz de Ciencias de la Tierra, CSIC-Universidad de Granada, Spain

3. Departamento de Estratigrafía y Paleontología, Universidad de Granada, Spain

Crystals 2024, 14, 649.

<https://doi.org/10.3390/cryst14070649>

Abstract

Chamid bivalves are marine organisms that live in high-energy environments and are cemented to hard substrates. To avoid shell damage, the organisms form thick, densely ornamented shells. Shell material consists of aragonite, and the ornamentation may be either aragonitic or calcitic. The latter can be developed as scaly spines, rows of blades, or comarginal, radial arched lamellae. We investigated biological crystal morphology and mode of assembly of *Chama arcana* and *Chama gryphoides* shells. Structural characteristics were obtained from electron backscatter diffraction (EBSD) measurements, complemented with laser confocal and BSE imaging. We found a wide range of crystal morphologies and sizes, ranging from irregularly shaped calcite and/or aragonite prisms to tiny and thin aragonite laths.

We observed four different modes of crystal assembly patterns: 1. strongly interlocked dendritic calcite units forming the ornamentation blades; 2. aragonite laths arranged to lamellae forming the outer shell layer, the layer adjacent to the calcite; 3. aragonite laths arranged into blocks comprising inner shell layers or aragonitic ornamentations; and 4. shell portions consisting of aragonite prisms, structured in size and crystal orientation, at muscle attachment sites. These four different types of crystal arrangements were observed for the shells of the investigated chamid species; however, they had slightly different strengths of structuring and slight variations in crystal organisation. Additionally, we observed unique microstructural features in *Chama* shells: We report ornamentation crystals resembling idiomorphic calcite and novel, twinned entities found at the changeover between the aragonitic layers. We highlight and discuss these differences and anomalies in this contribution.

Keywords

Bivalves, EBSD, biominerals, microstructure/texture, Chamidae

2.1.1 INTRODUCTION

To protect their soft tissue from environmental hazards (Stanley 1975; Kobayashi 1991; Harayashiki et al. 2020), bivalves form, in general, multi-layered shells. These have different and elaborate crystal arrangement patterns (microstructures). Among invertebrates, bivalves developed one of the strongest muscle–shell attachment mechanisms for valve movement (Castro-Claros et al. 2021). At those valve portions where the muscles attach to the valves, characteristic scars are present at both inner valve surfaces, the muscle scars (Taylor et al. 1969; Liao et al. 2015; Castro-Claros et al. 2021). The muscle scars have a specific optical appearance resulting from their particular microstructure, the adductor myostracum.

Myostracal microstructure and texture appear conservative for species of many bivalve genera. Crippa et al. (2020a), le Moine (2022) and Hoerl (2022) investigated with diffraction measurements myostracal microstructure and texture for 22 bivalve species belonging to 10 orders. Except for the myostracum of three bivalve species (*Arctica islandica*, *Tellina planata*, and *Mytilus edulis*), the myostracum of all the other bivalves had a similar microstructure and texture. Crystal organisation was determined with electron backscatter diffraction (EBSD). The specific mode of myostracal crystal assembly demonstrates that myostracal crystal growth and, hence, myostracal microstructure is formed by a specific growth process, namely the process of competitive growth (Nakahara & Bevelander 1971; Liao et al. 2015; Crippa et al. 2020a; Castro-Claros et al. 2021; le Moine 2022; Hoerl et al. 2024b).

The myostracal valve portion and other mineralised parts of the shell are composite materials consisting of minerals and biopolymers. Bivalve myostraca consists solely of aragonite, even when the adjacent shell layers are formed of calcite (le Moine 2022; Hoerl et al. 2024b). The above-mentioned studies indicate that myostraca comprises, relative to the other shell layers, little organic substance. The aragonite of the myostracum resembles, for many structural characteristics, non-biological aragonite (Kennedy et al. 1969; Taylor et al. 1969; Lee et al. 2011).

Shells of the genus *Chama* are prime examples of the fact that microstructures may vary even among closely related species. *Chama* forms thick (up to 5 mm) shells that are densely covered with ornamentations. These consist of pointy blades arranged for the different species in various ways on the shell surface (Yonge 1967; Matsukuma et al. 1997). *Chama* species are common in warm and tidal waters. Most of them occupy shallow environments, up to a water depth of about 30 m (Beratis 2019); however, some species, such as *C. gryphoides*, live in deeper environments, at about 270 to 280 m water depth (Krylova 2006). Except for a few species that rest freely on loose sediment, most *Chama* shells are cemented to substrates by a byssal complex (Yonge 1967; Matsukuma 1996). *Chama* shells are about 2–3 cm in diameter and have rather irregular shapes and a circular morphology. Some rock-bound *Chama* organisms have enlarged umbonal regions on the left side of the hinge (Allen 1976). An outstanding characteristic of *Chama* organisms is the notably elongated adductor muscles that enable a

rapid and prolonged valve closure despite their notoriously weak hinge (Nicol 1952; Allen 1976; Berezovsky 2021).

With their thick shells, complex shell organisation, use of the two main carbonate phases for shell generation, and a large variety of microstructures, *Chama* is a very suitable genus for investigating the interrelation of calcitic and aragonitic shell microstructures, along with their specific characteristics among different species. Similar to the Ostreidae, the Chamidae show a high morphologic variation due to ecological adaptations of the respective species (Reeve 1847; Pastorino 1991). The focus of this study is to highlight, juxtapose, and discuss structural characteristics, such as crystal morphology and mode of crystal assembly, of the different layers of two *Chama* species. We selected shells of *C. arcana* F. R. Bernard, 1976, and of *C. gryphoides* (Linnaeus, 1758). These bivalves are abundant in many marine environments (Vance 1978; Patton et al. 1991); however, they dwell at slightly different water depths: *C. gryphoides* in deeper (up to 280 m) and *C. arcana* in shallow (up to 30 m) environments, respectively. Crystal structural characteristics, their shape, and their assembly were gained from high-resolution electron backscatter diffraction (EBSD) measurements, complemented with laser confocal microscopy and field emission scanning electron microscopy (FE-SEM) imaging.

Checa (2018) discusses possible modes of molluscan shell microstructure generation. These comprise physical processes, such as competitive growth, chemical controls, such as stereochemical recognition, chemical–biological mechanisms, such as nucleation on and between self-organised polymer templates and solely biological determinants, such as contact recognition at biopolymer and mineral component deposition. These processes enable the overall understanding of mollusc shell microstructure generation; however, they do not provide local structural information on the growth characteristics of carbonate molluscan shells, e.g., the transmission of crystal orientations between adjacent shell layers or the patterns of crystallographic axes alignments of crystals belonging to adjacent shell layers (Schäffer et al. 1997; Feng et al. 1999; Yao et al. 2014) and many more.

Many studies investigated the overall structure of bivalve shells, including *Chama* shells (Harper 1998; Agbaje et al. 2017; Checa 2018); however, few studies focused on small-scale and local carbonate crystal arrangement patterns. The study of Crippa et al. (2020) provides this information for *Glycymeris*, but, to the knowledge of the authors, up to now, there is no such full characterisation for species of the genus *Chama*. Accordingly, the study presented here provides the following:

- (i) An in-depth characterisation of the different shell, ornamentation, and myostracal microstructures and textures for two *Chama* species;
- (ii) Juxtaposes these;
- (iii) Indicates the crystal growth mechanisms for the different shell layers;
- (iv) Our study highlights, in particular, structural characteristics of the myostracal valve sections, including pallial and adductor myostraca. While the microstructure and texture

of pedal and adductor myostraca have been investigated by now using EBSD (for *Glycymeris* species (Crippa et al. 2020a)), the measured pattern of crystal organisation for the pallial myostracum has not been reported yet. The latter is performed in this study;

- (v) Myostracal pillars are prominent structures for Chamidae (Taylor et al. 1969). We characterise the microstructure and texture of these and trace them from the pallial myostracum to the inner shell surfaces.

2.1.2 MATERIALS AND METHODS

Materials

Shell samples investigated in this study were chosen to illustrate differences in shell microstructures within and between different *Chama* species and scanned with EBSD. Several shells were investigated in this project, and we report the results obtained for two specimens for each species. The shell sizes of investigated *C. arcana* samples range from 3 to 5 cm. For *C. gryphoides*, the shells each had a size of about 3 cm. The investigated species are, thus, considered to be fully grown, adult animals.

Specimens of *C. gryphoides* were collected in infralittoral rocks near Benalmádena (Málaga, Spain). The specimens of *C. arcana* were collected in Newport Beach, CA, USA, and obtained from collections of the Natural History Museum London, UK.

Sample preparation for electron backscatter diffraction (EBSD) measurements, field emission scanning electron microscopy (FE-SEM), and laser confocal microscope imaging

The shells were sectioned such that the cut crossed the adductor myostracum and adjacent shell layers. The shells of *C. arcana* were cut either perpendicular to the hinge (cut A, Fig. 2.1-AP1) or transversely through those shell portions where both the anterior and posterior adductor muscles were attached to the valves (cut C, Fig. 2.1-AP1). For *C. gryphoides*, the shells were cut obliquely through the hinge and the adductor muscles (cut B, Fig. 2.1-AP1). Shells were sectioned with a low-speed diamond saw. The cut shells were embedded in EPON epoxy resin and conventionally polished in several mechanical grinding and polishing steps, cloths, and suspensions. For EBSD, sample surfaces were coated with 4–6 nm of carbon. For FE-SEM imaging, sample surfaces were coated with 6–8 nm of Pt/Pd. We show in this study images with BSE contrast.

FE-SEM imaging and EBSD measurements were carried out using a Hitachi SU5000 field emission SEM, Japan, equipped with an Oxford Instruments NordlysNano II EBSD system. For all analytical techniques, the SEM was operated at 20 kV. EBSD measurements were performed with a step

size ranging from 200 to 450 nm. EBSD data were evaluated with the Oxford Instruments AZtecCrystal 3.0 and HKL Channel 5.0 softwares and are presented as colour-coded crystal orientation maps and the corresponding pole figures. For each measurement, the band contrast images and the pole figures depicting the individual data points of the crystal orientations are depicted in Chapter 2.1.6 of this thesis. The specimens of *C. arcana* were scanned with 15 EBSD maps, two of which consisted of three individual measurements that were combined into a single scan. For *C. gryphoides*, nine different measurement positions were chosen, four on each shell sample A and five on shell sample B.

An in-depth terminology of the structural terms used in this work can be found in Appendix Section A.1 of this thesis.

2.1.3 RESULTS

We describe in this contribution structural characteristics and crystal organisation for the different microstructures of *C. arcana* and *C. gryphoides* shells. For each species, we show and discuss two specimens (specimen A and specimen B). For these, we present the changeover between the shell layers and detail the prevailing microstructure and texture. For a comprehensive visualisation of the observed microstructures, each colour-coded crystal orientation map (Figs. 2.1-1 to 2.1-8) is complemented with the corresponding, grey-scaled, band contrast measurement map, which is provided in the Supplementary Information (Figs. 2.1-AP3 to 2.1-AP5, 2.1-AP7, 2.1-AP8 and 2.1-AP11 to 2.1-AP13). Aragonite and calcite textures are shown with pole figures (Figs. 2.1-1 to 2.1-8 provide the contoured version of orientation data; Figs. 2.1-AP3 to 2.1-AP5, 2.1-AP7, 2.1-AP8, and 2.1-AP11 to 2.1-AP13 provide orientation data points). The directions of the cuts and the position of the scans are visualised in overview laser confocal microscopy images, provided in the Supplementary Information (Figs. 2.1-AP1, 2.1-AP2, 2.1-AP6 and 2.1-AP10).

Figures 2.1-1 to 2.1-3 and Supplementary Information Figures 2.1-AP3 to 2.1-AP5 visualise the microstructure and texture of the different layers of a *C. arcana* shell sectioned along cut A. The outer shell surface of *C. arcana* is covered with calcitic ornamentalations. The microstructure of an ornamentation blade is shown in Figure 2.1-1a. A calcitic ornamentation consists of large (up to 50 μm in diameter) crystal units (Fig. 2.1-1a); these are internally structured (Fig. 2.1-1b). The crystallites that form the calcitic units of the ornamentation are well co-oriented (Fig. 2.1-1a, b). Towards the inner shell surface, adjacent to the calcite, is an aragonitic shell layer with crossed-lamellar microstructure (Fig. 2.1-1b). The boundary between the calcite and the aragonite is undulating, a remarkable feature that we observed for all investigated *C. arcana* specimens (Fig. 2.1-1a, b). This characteristic is different from what is found for the boundaries between shell layers of Mytilidae, Glycymerididae, and Anomiidae (le Moine 2022; Peter et al. 2023; Rathi 2023). Crystal orientation changes gradually within a calcitic ornamentation as the first crystals grow with their c-axis orientation perpendicular to the outer shell

surface (Fig. 2.1-1a). The calcite within individual calcitic units is, rather, co-oriented (Fig. 2.1-1b), even though the calcite units are substructured by small-angle boundaries (Fig. 2.1-1b). The interface between the calcitic ornamentation and the aragonitic crossed-lamellar layer is serrated. At the changeover between calcite and aragonite, we observed that some calcitic units show regular (104) growth morphologies; these units resemble idiomorphic crystals (indicated by yellow arrows in Fig. 2.1-2a). Hence, they exhibit crystal morphologies characteristic of non-biological calcite obtained from solution (Fig. 2.1-2a). Idiomorphic shapes for biologically secreted crystals are outstanding and very rarely observed. Adjacent calcite units within an ornamentation blade are interdigitated in 3D, as indicated by the dendrite-like calcite microstructure (Fig. 2.1-2a). This is also a very specific structural feature that has not yet been reported for other modern bivalves.

Adjacent to the calcite of the ornamentation, the interface zone to the crossed-lamellar shell consists of a thin layer formed of minute (average size 1–2 μm^2) aragonite crystallites (Fig. 2.1-2a, b). These are randomly oriented, appear to be granular, and do not show the characteristic crossed-lamellar texture comprising the two sets of first-order lamellae. The well-developed crossed-lamellar microstructure is observable a few micrometres away from the calcite–aragonite boundary (Fig. 2.1-2a, b). From EBSD measurements, we could deduce that the orientations of the first-order lamellae of the crossed-lamellar microstructure are transmitted to the crystals of both the adductor myostracum (Fig. 2.1-2b) and the pallial myostracum (Fig. 2.1-3a). They can also be transmitted from the pallial myostracum onto the initial complex crossed-lamellar portion of the shell (Fig. 2.1-3a). Nonetheless, the crossed-lamellar mode of crystal orientation is eventually lost within the complex crossed-lamellar microstructure (Fig. 2.1-3a). The microstructure of the myostracum (Figs. 2.1-2b and 2.1-3b) is characteristic of crystal growth resulting from a competitive growth mechanism. The first myostracal crystals adopt the texture of the crossed-lamellar layer; however, with distance away from the changeover, a distinct microstructure characteristic evolves for competitive growth (Figs. 2.1-2b and 2.1-3b). The crystal size and co-orientation (quantified by the MUD values) increase with distance away from the changeover, and the microstructure is characterised by prismatic crystals and low organic content (Fig. 2.1-2b). Close to the myostracum, within the crossed-lamellar shell portion, we observed for the investigated *C. arcana* shells the incorporation of large (up to 20 μm), irregularly shaped aragonite units (yellow stars in Fig. 2.1-3a, b). This is a characteristic of *C. arcana* and is not observed in the shells of other *Chama* species. These aragonite units are often twinned and may pierce into the myostracum. Their function and/or advantage for the shell is not yet known.

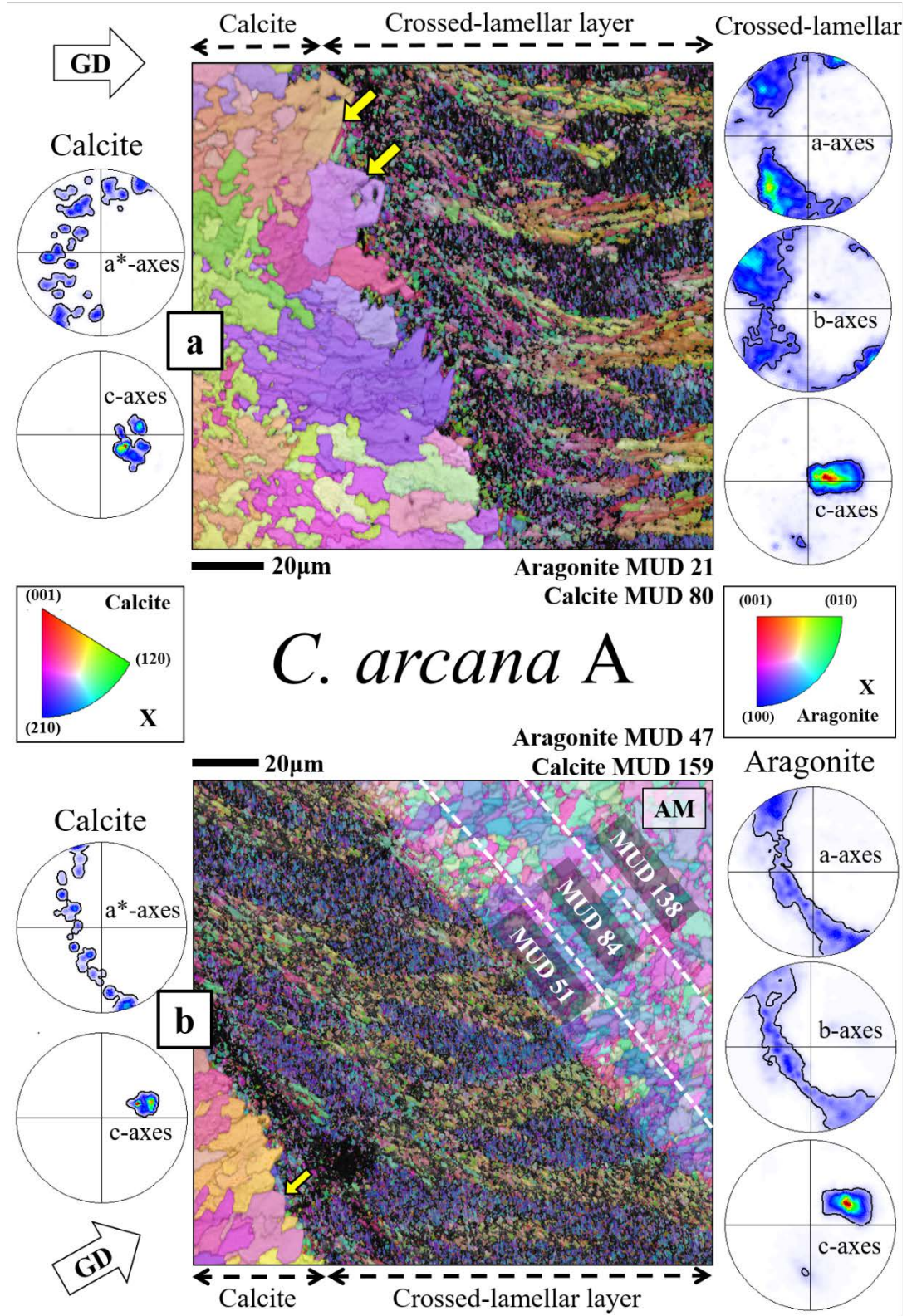


Figure 2.1-2. EBSD scans illustrating the interface between the calcitic layer and the aragonitic crossed-lamellar layer observed for the applied cut A of a *Chama arcana* shell. The crystals within the calcitic layer are substructured and interdigitated in 3D (a). At the serrated interface with the crossed-lamellar layer, some of the calcitic crystals show regular (104) growth faces (yellow arrows in a, b). The maps show that the characteristic crossed-lamellar patterns start to appear only after a few μm from the interface with the ornamentation (b). The increasing crystal co-orientation (displayed by the MUD values of subsets sketched by dotted white lines) within the adductor myostracum (AM) indicates crystal growth by growth competition in the myostracum. The axial pole figures display the respective orientational probability density distributions for the calcitic and aragonitic sections. The growth direction (GD) of each scan is indicated with a white arrow.

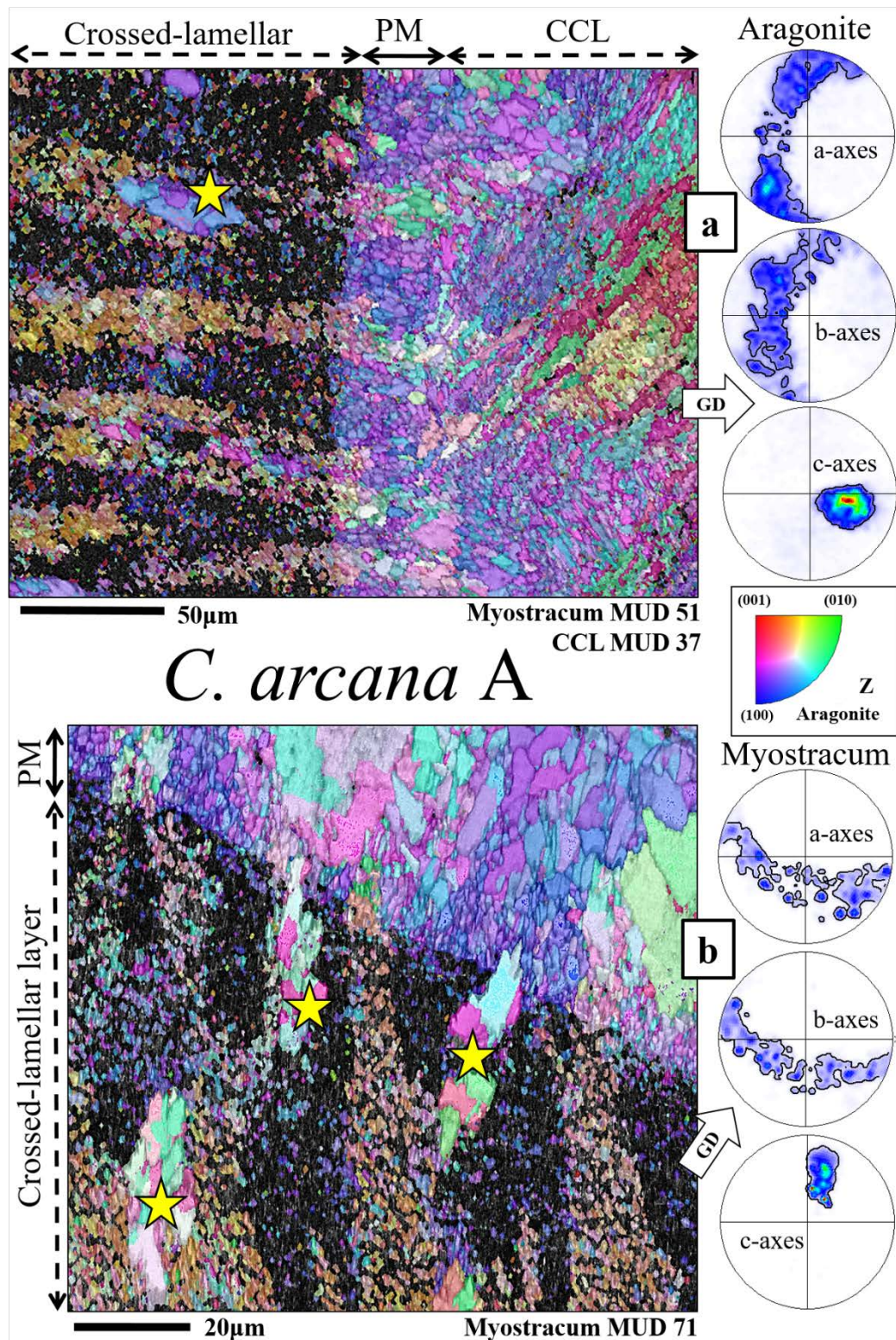


Figure 2.1-3. EBSD scans depicting the interfaces within the different aragonitic layers for the applied cut A of a *Chama arcana* shell. As the fine-grained crystals in the crossed-lamellar layer (CL) are encased by an organic substance (Crippa et al. 2020a), only a fraction of the backscatter Kikuchi patterns are indexed, leading to the patchy appearance of the lamellar sets. The interface between the pallial myostracum (PM) and the complex crossed-lamellar layer (CCL) is indistinct and vague (a). In the thicker adductor myostracum (AM), the crossed-lamellar crystal orientation pattern is maintained for the first few μm until gradually vanishing due to the competitive growth process (b). Highlighted in the two scans is the occasional presence of crystal assemblies consisting of large grains (around $10\text{ }\mu\text{m}$ in length) appearing in the interface region of the crossed-lamellar layer (yellow stars in a, b). The pole figures show the orientational probability density distributions and show an axial texture for the pallial myostracum and complex crossed-lamellar layer (a) and the adductor myostracum (b). The growth direction (GD) of each scan is indicated with a white arrow.

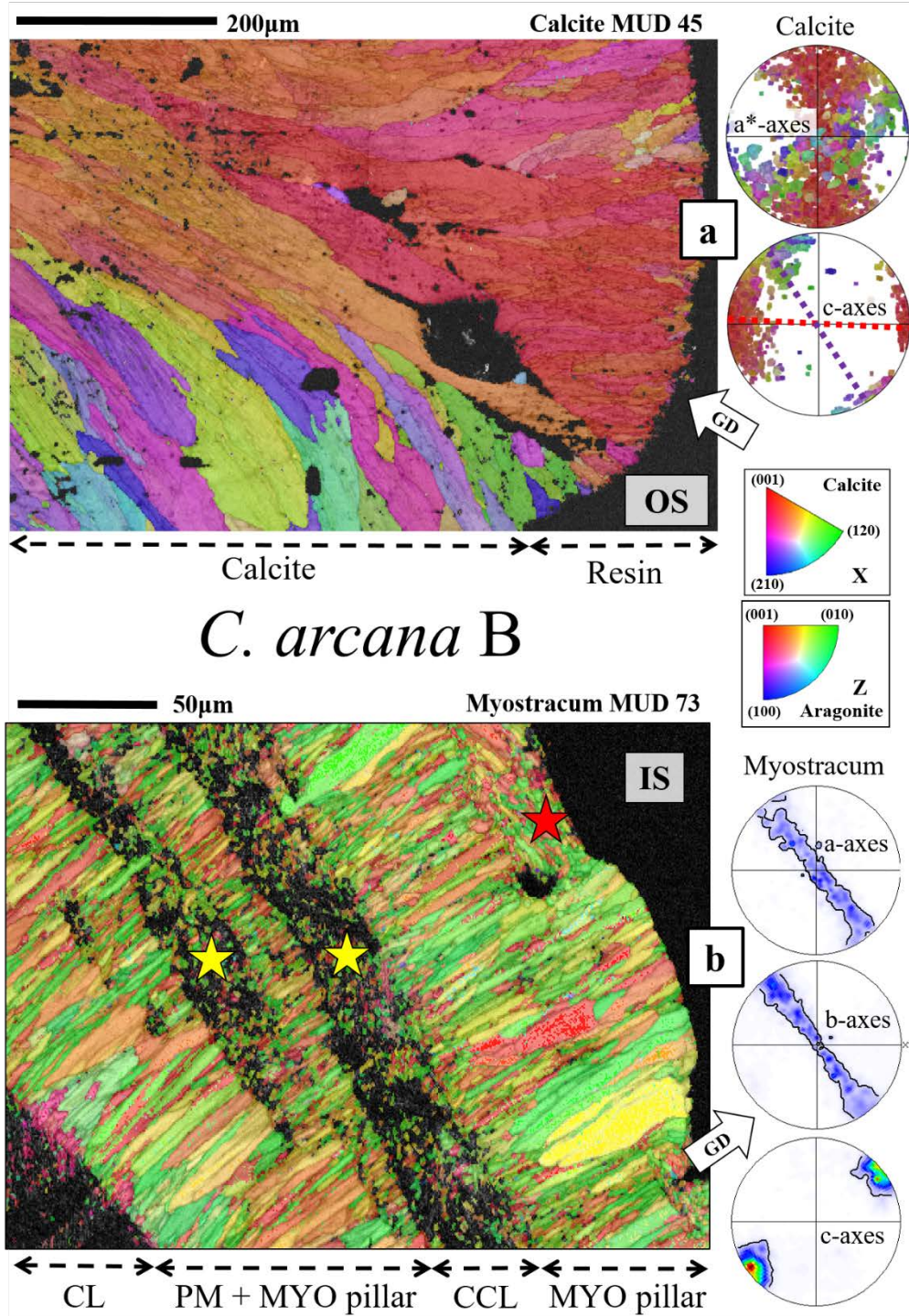


Figure 2.1-4. EBSD scans depicting the different microstructures observed for the applied transverse cut C of a *Chama arcana* shell. The calcitic shell ornamentations comprise internally structured crystal units (a). These units are oriented with their c-axes perpendicular to the outer shell surface (OS), gradually rotating the crystallographic axes as indicated by the colourful dashed lines in the corresponding pole figures (a). The aragonitic pallial myostracum (PM) initially comprises small, spherical crystals (arithmetic mean: 46 µm²) close to the interface with the crossed-lamellar layer (CL, b). Toward the inner shell surface (IS), the growing myostracum crystals (MYO, mean: 83 µm²) are subsequently arranged in a series of pillars with an average thickness of about 50 µm. The changeover from the pallial myostracum into the myostracal pillars is fluent. The pillars traverse the complex crossed-lamellar layer (CCL) that is scarcely found along the inner shell surface (red star in b) or in thin sheets interrupting the myostracal pillars (yellow stars in b). The evolution of the crystal co-orientation statistics in the myostracal pillars depicted in (b) can be found in the Supplementary Information section of this research article (Figure 2.1-AP7). The pole figures indicate the crystal orientation data points for the calcitic layer (a) and the orientational probability density distribution for the myostracal pillars (b), both of which have an axial texture. The growth direction (GD) of each scan is indicated with a white arrow.

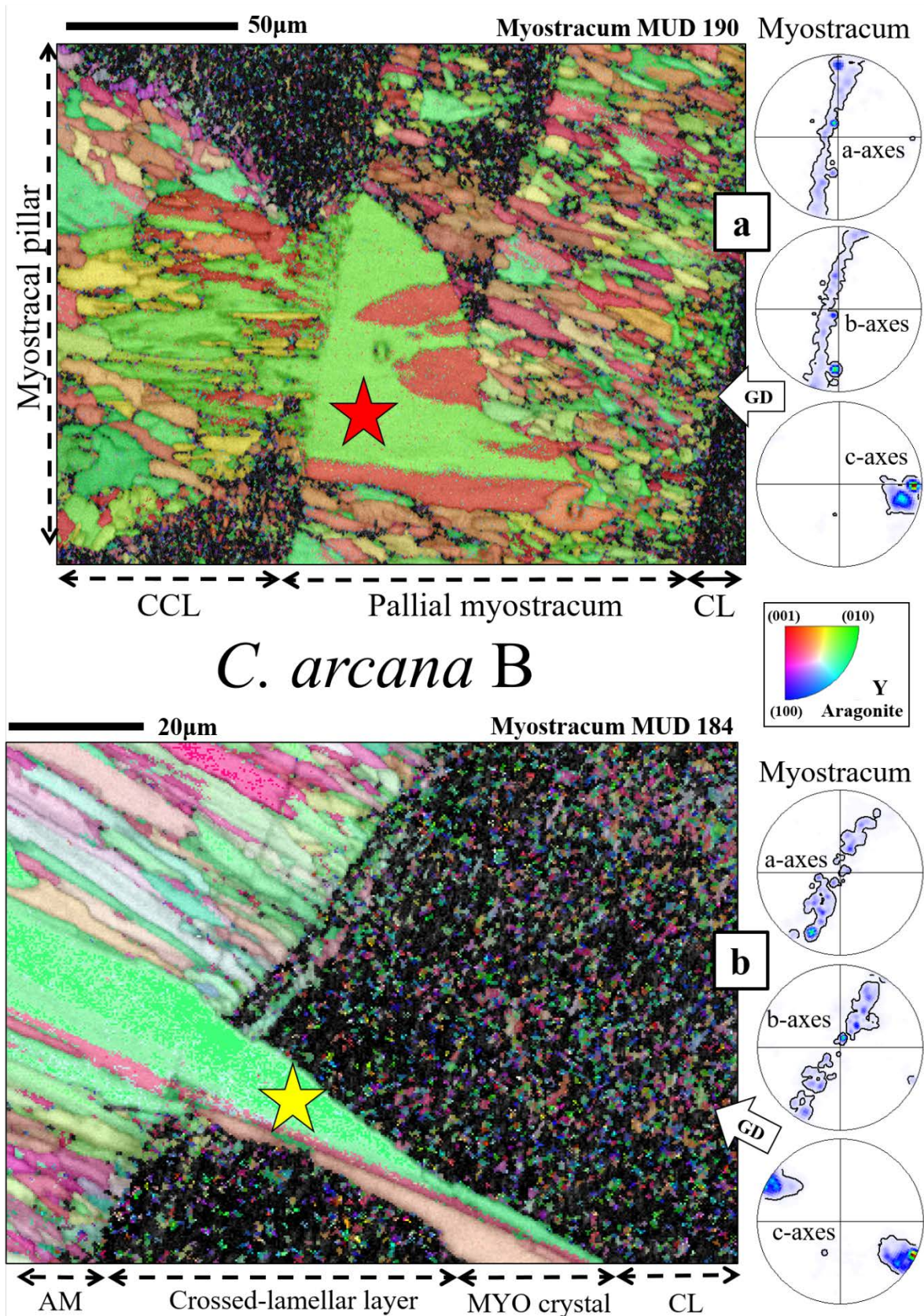


Figure 2.1-5. EBSD scans depicting anomalous single-crystal-like crystals observed for the applied transverse cut C of a *Chama arcana* shell. The highlighted grains have a microstructure similar to the myostracum and can occasionally be found passing into the pallial (red star in (a)) and the adductor myostracum (AM, yellow star in b). It is twinned along a single plane parallel to the growth direction and longer than 50 µm. The pole figures indicating the orientational probability density distribution for the myostracum areas of the two scans depict the axial texture of the pallial and adductor myostracula. The growth direction (GD) of each scan is indicated with a white arrow.

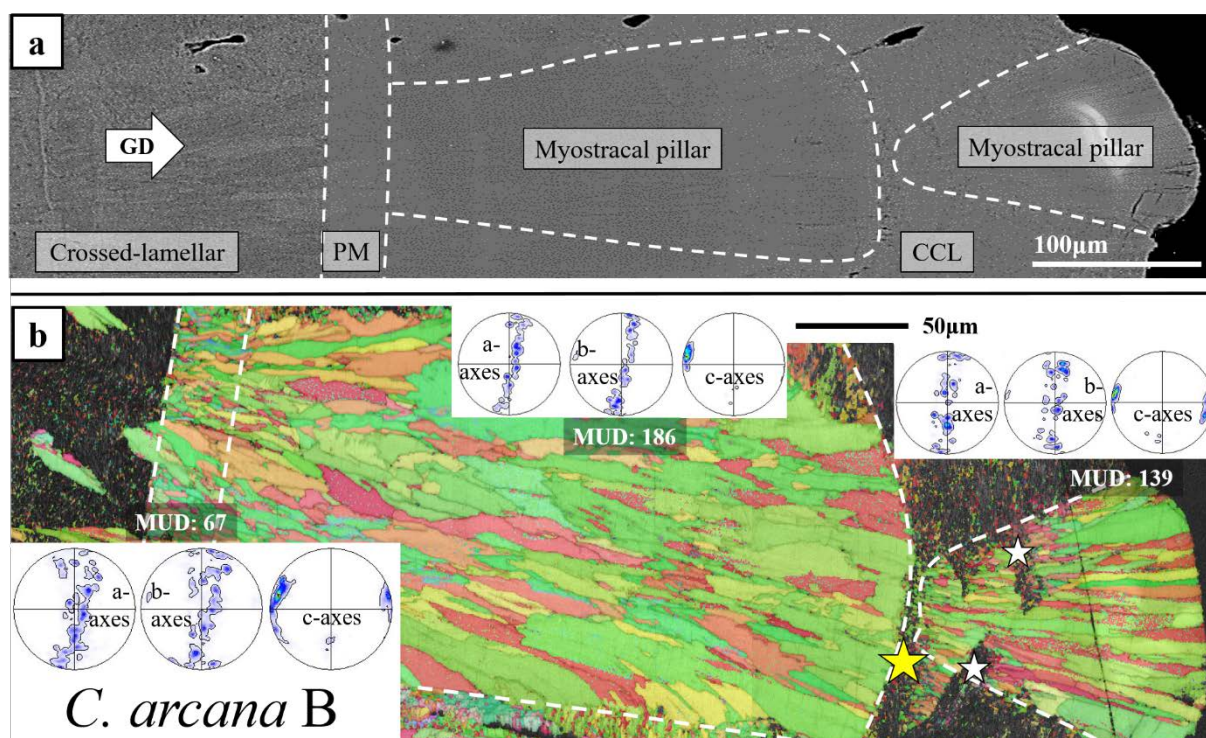


Figure 2.1-6. BSE image and EBSD scans depicting the microstructure and texture of a myostracal pillar for the applied transverse cut C of a *Chama arcana* shell. The BSE image highlights the structure and general layout of the composite shell and shows a large number of prismatic crystal assemblies that protrude from the crossed-lamellar layer into the pallial myostracum (PM, a). They exhibit a length of up to 30 μm and show a high degree of co-orientation, albeit a frequent occurrence of twinning (b). The myostracal pillar grows continuously from the pallial myostracum and comprises large crystals (arithmetic mean: 81 μm^2) that are arranged spherulitically. Continuous complex crossed-lamellar sheets can cause the subsequently formed myostracum to dissociate from the primary pillar, leading to a sharp decrease in crystal size in the subsequent pillar (yellow star in b). If the interrupting layer does, however, not cover the whole pillar, its growth mechanism is not reset (white stars in b). The pole figures indicate the orientational density distributions and MUD value for different sections of the scan separated by white dotted lines. The pallial myostracum has a low crystal co-orientation and broad maximum for the c-axis orientations. In the myostracal pillar, the crystal size and co-orientation increase as the texture becomes strictly axial. After being interrupted by a sheet of complex crossed-lamellar microstructure, the crystal growth mechanism restarts; hence, the crystal co-orientation is decreased (b). The growth direction (GD) is indicated with a white arrow (a).

Figures 2.1-4 to 2.1-6 and Supplementary Information Figures 2.1-AP7 to 2.1-AP9 highlight the structural characteristics of another *C. arcana* specimen. The latter is sectioned along cut C and shows the presence of myostracal prisms in the inner shell layer, in addition to the complex crossed-lamellar microstructure. The outer shell layer of this *C. arcana* specimen also comprises ornamentations consisting of calcite crystals with spherulite-resembling crystal arrangements due to the crystals retaining a high angle to the shell surface (Fig. 2.1-4a). We observed large crystal units that are highly co-oriented with their c-axes pointing perpendicular to the outer shell surface of the ornamentation (Fig. 2.1-4a). Sectioned along a traverse cut, the calcitic crystal units of *C. arcana* appear regular and prismatic. Figure 2.1-4b shows the crystal orientation within the aragonitic myostracal pillars located at the inner shell surface of *C. arcana*. Myostracal pillars mostly comprise large aragonitic prisms, the texture and microstructure of which resemble that of myostracal layers (Fig. 2.1-4b). Within the

myostracal pillars, thin layers of myostracal and complex crossed-lamellar microstructures may alternate parallel to the inner shell surface (yellow stars in Fig. 2.1-4b). In general, the spherulitic pillars and the surrounding complex crossed-lamellar layer coexist and do not disrupt each other up to the inner shell surface (Fig. 2.1-5a). The consistent crystal orientations (red star in Fig. 2.1-5a) show that myostracal pillar crystal orientations derive directly from the pallial myostracum. Similar to the uneven crystal units observed in the first specimen (e.g., yellow stars in Fig. 2.1-4a, b), large prisms are also visible in the myostracal changeover sections of the second specimen (Fig. 2.1-5a, b). They appear close to pallial (red star in Fig. 2.1-5a) and adductor myostraca (yellow star in Fig. 2.1-5b) and are strongly twinned along clear-cut planes. These crystals may exceed 100 μm and often traverse both the crossed-lamellar and the myostracal shell portion (Fig. 2.1-5b).

The microstructure and texture of myostracal pillars in *C. arcana* shells are very intricate (Fig. 2.1-6). This is the first study that shows measured crystal arrangements for these myostracal pillar structures. Adjacent to the crossed-lamellar layer, a row of small crystals and prisms increase in size towards the inner shell surface. In cross-section, we observed an alternation between the microstructure obtained by competitive growth and the complex crossed-lamellar microstructure of the remaining valve (Fig. 2.1-6a). Single myostracal pillars often do not cover the entire shell portion from the pallial myostracum to the innermost shell surface, as continuous sheets of complex crossed-lamellar microstructure can interrupt the growth of myostracal pillars (yellow star in Fig. 2.1-6b). Following this sheet, a further myostracal pillar may form, inheriting the texture of the primary pillar. It appears that non-continuous notches of the complex crossed-lamellar layer do not disrupt the microstructure of myostracal pillars (white stars in Fig. 2.1-6b).

Figures 2.1-7 to 2.1-9 and Supplementary Information Figures 2.1-AP11 to 2.1-AP14 show the structural characteristics and organisation of different microstructures found in two different *C. gryphoides* shells, sectioned along an oblique direction (cut B). In contrast to *C. arcana*, *C. gryphoides* shells are purely aragonitic and construct their ornamentations of aragonite (Fig. 2.1-7a, b). This outermost shell layer comprises first-order lamellae consisting of granular aragonite crystals that have a low degree of crystal co-orientation (Fig. 2.1-7a, b). As it occurs at the outer shell region, we addressed the latter microstructure as a complex crossed-lamellar-type structure (Hoerl et al. 2024b). According to (Taylor et al. 1969) and (Kennedy et al. 1970), the complex crossed-lamellar microstructure is only present at inner valve sections. Towards the inner shell surface, the changeover from a complex crossed-lamellar type to a crossed-lamellar assembly is smooth (Fig. 2.1-7b). However, the texture in the crossed-lamellar layer is rather 3D “single-crystal-like” and shows higher crystal co-orientation than the strictly axial complex crossed-lamellar-type microstructure (Figs. 2.1-7b and 2.1-AP14b).

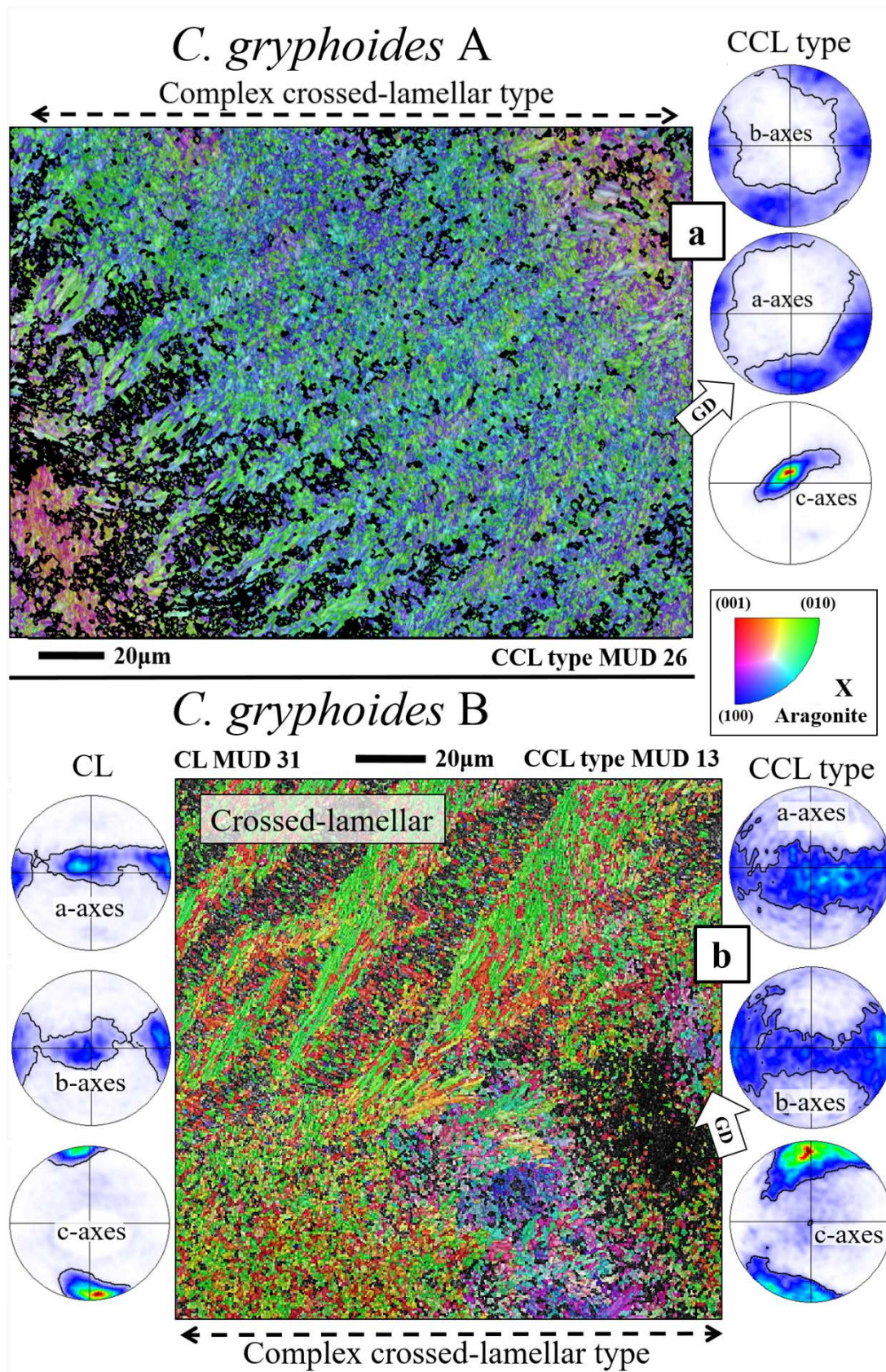


Figure 2.1-7. EBSD scans displaying the microstructure of the complex crossed-lamellar (CCL)-type layer for different shells of *Chama gryphoides* sectioned along the transversal cut C. The complex crossed-lamellar layer comprises first-order-lamellar blocks arranged in a complex pattern (a, b). At the changeover with the crossed-lamellar (CL) layer, differences in texture and microstructure are visible between the two layers (b). The texture is shown by the pole figures indicating the orientational density distributions for the respective layers. The growth direction (GD) of each scan is indicated with a white arrow.

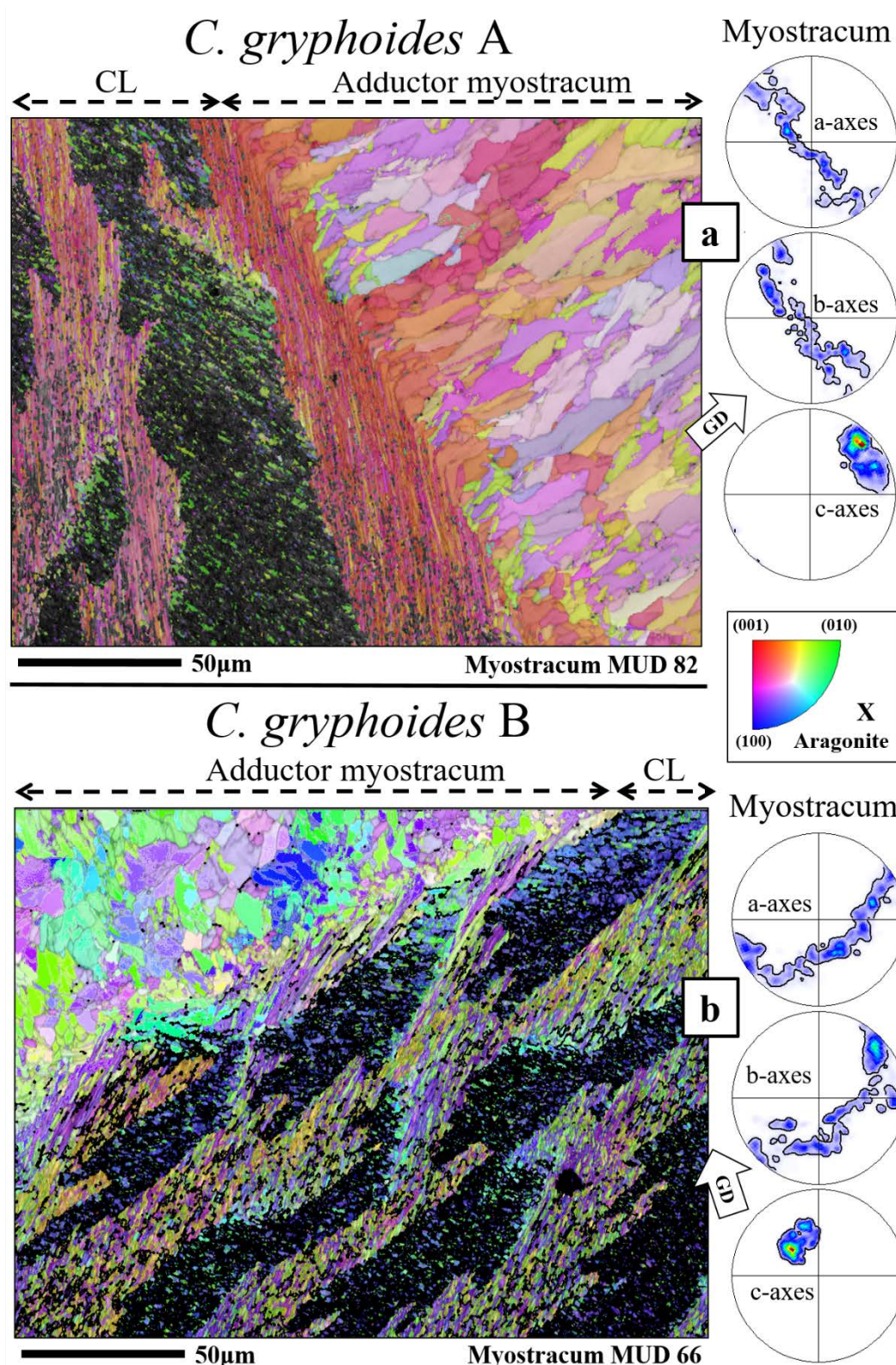


Figure 2.1-8. EBSD scans depicting the interfaces between the crossed-lamellar layer (CL) and the adductor myostracum observed for the two applied sections (cut B) of *Chama gryphoides* shells. The crystals within the crossed-lamellar layer are small (arithmetic mean size 9 µm) and have a fibrous morphology. At the interfaces, the similar colour-coding of the respective layers illustrates the coincident crystal orientation of the crossed-lamellar layer and the myostracum (a, b). The scans illustrate the complex and irregular microstructure of the myostracum, as opposed to the controlled crossed-lamellar microstructure. The pole figures indicate the orientational probability density distribution for the myostracum areas in the two respective scans. The double maxima for the c-axis orientations are a relic of the crossed-lamellar crystal orientation pattern. As opposed to the 3D “single-crystal-like” texture of the crossed-lamellar layer (Figure 2.1-7b), the myostraca have an axial texture (a, b). The growth direction (GD) of each scan is indicated with a white arrow.

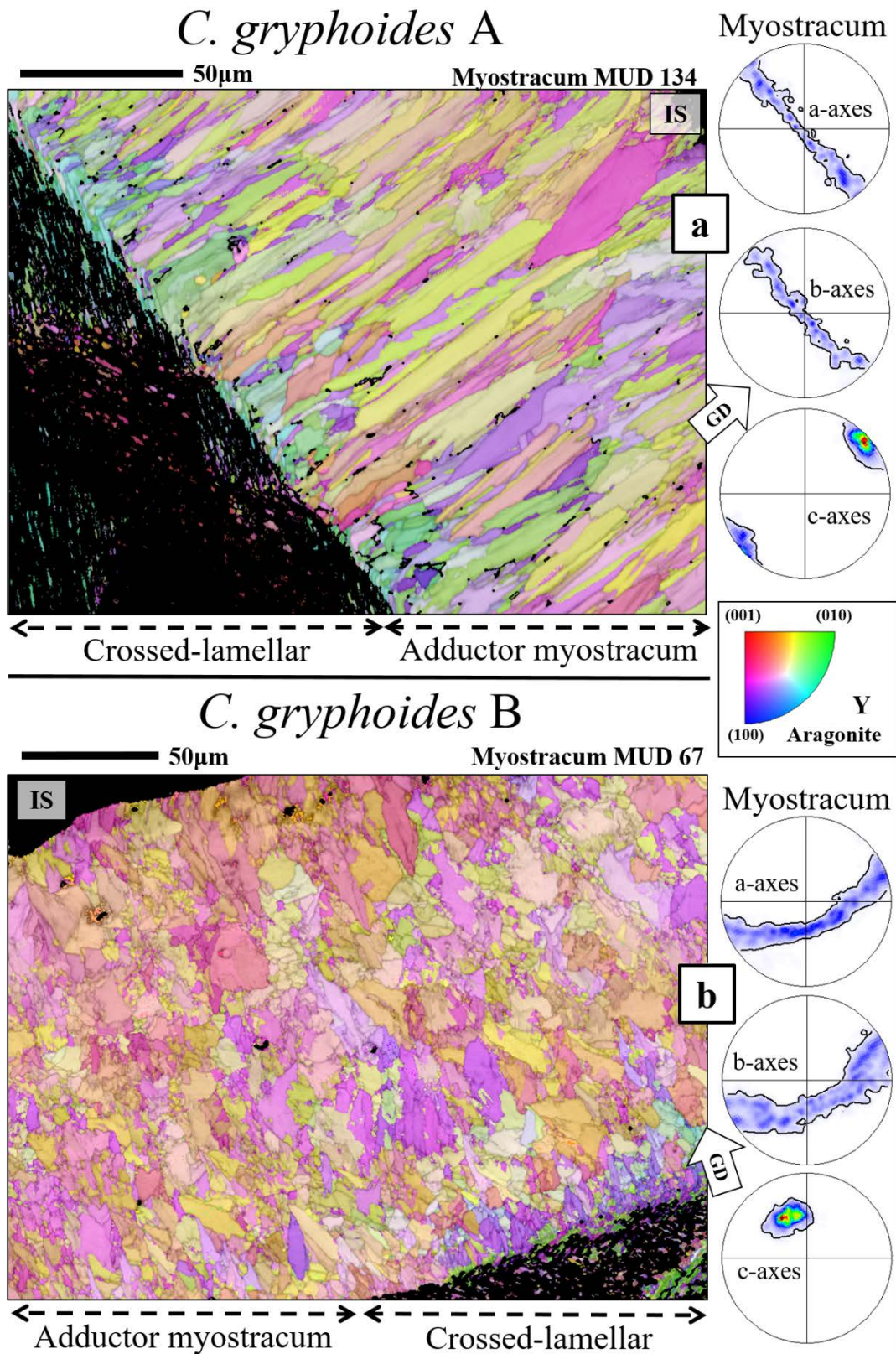


Figure 2.1-9. EBSD scans depicting the microstructures of adductor myostraca observed for the two applied cuts of *Chama gryphoides* shells (cut B). Due to small differences in the cutting directions, the exposed microstructures show different crystal morphologies. The crystals of the first shell appear prismatic and rather co-oriented; however, grain boundaries between the crystals are irregular (a). The second shell comprises irregular grain morphologies of the competitively grown myostracum crystals (b). Towards the inner shell surface (IS), the average grain diameter seems to increase, and crystals appear erratic and anisotropic (b). The pole figures indicate the orientational probability density distribution for the myostracum areas of the two respective scans and show an axial texture in the myostraca. The growth direction (GD) of each scan is indicated with a white arrow.

As opposed to the *C. arcana* specimens (e.g., Fig. 2.1-3a, b) or to other bivalves (le Moine 2022; Hoerl et al. 2024b), the first-order lamellae in *C. gryphoides* run at a high angle to the growth direction (Fig. 2.1-8a, b). At the changeover with the myostracum, the adjacent myostracal crystals adopt epitaxially the crossed-lamellar crystal orientations (Fig. 2.1-8a, b). Towards the inner shell surface, crystals become increasingly large and prism-shaped (Fig. 2.1-9a, b). The myostracal layers in *C. gryphoides* shells show irregular crystal shapes and little-regulated myostracal crystal arrangement patterns (Figs. 2.1-8a, b and 2.1-9a, b). This contrasts significantly with the crystal characteristics that we found for Glycymerididae myostraca (Crippa et al. 2020a; Hoerl et al. 2024b).

2.1.4 DISCUSSION

Bivalve shells vary strongly in shape, size, and internal structure (Kennedy et al. 1969; Iglukowska et al. 2023). To adapt to demands imposed on the organisms by their environment, many bivalves have developed specific shell microstructures (Boggild 1930; Tevesz & McCall 1979; Morton & Machado 2019; Castro-Claros et al. 2021). For carbonate-shelled molluscs, up to now, about 15 basic microstructures are described: granular, fibrous-prismatic, columnar-prismatic, sheeted-nacreous, columnar-nacreous, spherulitic, foliated, crossed-foliated, complex crossed-foliated, lamellar, crossed-lamellar, complex crossed-lamellar, vesicular, myostracal, helical and chalky (e.g., Berezovsky, 2021; Carter et al., 2012; Carter, 1990; Crippa et al., 2020a; Kobayashi and Samata, 2006; MacClintock, 1967; Taylor et al., 1969). While many shell microstructures appear to be highly conservative and recur among various unrelated bivalve species, their origin lies in different evolutionary pathways (Marie et al. 2009; Marie et al. 2012; Popov 2014). The parallel evolution of shell architectures and microstructures for different bivalve classes started in the Cambrian and is most probably related to an increase in selective pressure for the development of stronger and more protective shells (Runnegar & Pojeta 1985; Jackson et al. 2010). Subsequently, we discuss the different microstructures and crystallographic features found in the shells of *C. arcana* and *C. gryphoides*.

The microstructures, textures, and changeover between different crystal assemblies

Figure 2.1-10 gives an overview of the diversity of crystal arrangement patterns and illustrates the microstructures that we observed for the investigated *Chama* species. We found five different microstructures. Prismatic calcite (1) is present in the ornamentations of *C. arcana*; however, it is not present in the aragonitic ornamentations of *C. gryphoides*. The ornamentations of *C. gryphoides* are aragonitic and have a complex crossed-lamellar type microstructure (2). In addition to the microstructures of the ornamentations, both investigated *Chama* species construct their shell of crossed-lamellar (3), myostracal (4), and complex crossed-lamellar (5) aragonite crystal assemblies.

Secretion of bivalve shell crystals takes place by mantle epithelial cells. These are secreted below the periostracum, an organic layer formed of cross-linked proteins, mucopolysaccharides, and lipids, and serve as a template for crystal nucleation (Clark et al. 2020). To achieve the generation of the ornamentations, the nucleation template is folded before mediating the growth of the shell crystals. Crystal growth direction is, in general, normal to the marginal parts of the mantle. The first crystals grow epitaxially from the folded periostracum (Kennedy et al. 1970; Lopes-Lima et al. 2010; Suzuki et al. 2013). Therefore, irrespective of whether the ornamentation is aragonitic or calcitic, ornamentation crystal a- and b-axes orientations scatter on a great circle in the pole figure (Figs. 2.1-2a, 2.1-4a and 2.1-7a, b) instead of having co-oriented a- and b-axes distributions. The ornamentation texture pattern deviates considerably from that of the crossed-lamellar shell layers. These have a 3D “single-crystal-like” texture.

The changeover from the ornamentation to the adjacent crossed-lamellar microstructure and texture highlights how bivalves achieve a drastic change in microstructure and texture without losing the structural integrity of their shell. Figure 2.1-11 gives an overview of the shell layers found in *C. arcana* near the adductor myostracum region. The changeover from prismatic calcite (ornamentation) to crossed-lamellar aragonite (shell) is achieved via an undulating interface consisting of calcite crystals (Figs. 2.1-1, 2.1-2 and 2.1-11b). Along the interface, many calcitic units show regular (104) growth morphologies resembling idiomorphic calcite (yellow stars in Fig. 2.1-3a, b). The regular growth morphologies indicate a lack of biological control during the growth of the ornamentation. This observation is in agreement with the conclusions of (Harper & Checa 2017). The authors investigated the biological influence on the shell growth of euheterodont and pteriomorph species. They found that calcitic euheterodont microstructures, such as the ornamentations in *C. arcana*, feature a low organic content due to the absence of an organic envelope encasing the prisms. Hence, rather than being controlled by biological determinants, the fibrillar prisms of the ornamentations seem to predominantly form under physical controls (Harper & Checa 2017). At the changeover to the crossed-lamellar layer, the spatial restrictions imposed by the neighbouring crystals appear to be cancelled. This could explain the regular (104) growth morphologies found along the serrated interface.

A further specific feature of the above-mentioned changeover from the calcitic ornamentation to the aragonitic crossed-lamellar shell can be observed for the first few micrometres of the crossed-lamellar layer. The microstructure of crossed-lamellar aragonite is usually formed of laths that are assembled into two sets of first-order lamellae. However, we observed instead, at the direct transition from ornamentation calcite into crossed-lamellar aragonite, a thin shell layer (white stars in Fig. 2.1-2a) that is low in crystal co-orientation and rich in organic substance. The latter might be needed to guide aragonite arrangement to form the characteristic crossed-lamellar pattern, as, here, an organic membrane template controlling crystal orientation is absent, and the crystal growth process changes from low

(ornamentation) to high (crossed-lamellar) biological control. Similar structural characteristics have been found for the calcite–aragonite interface in the shell of *Pinctada margaritifera* (Cuif et al. 2023).

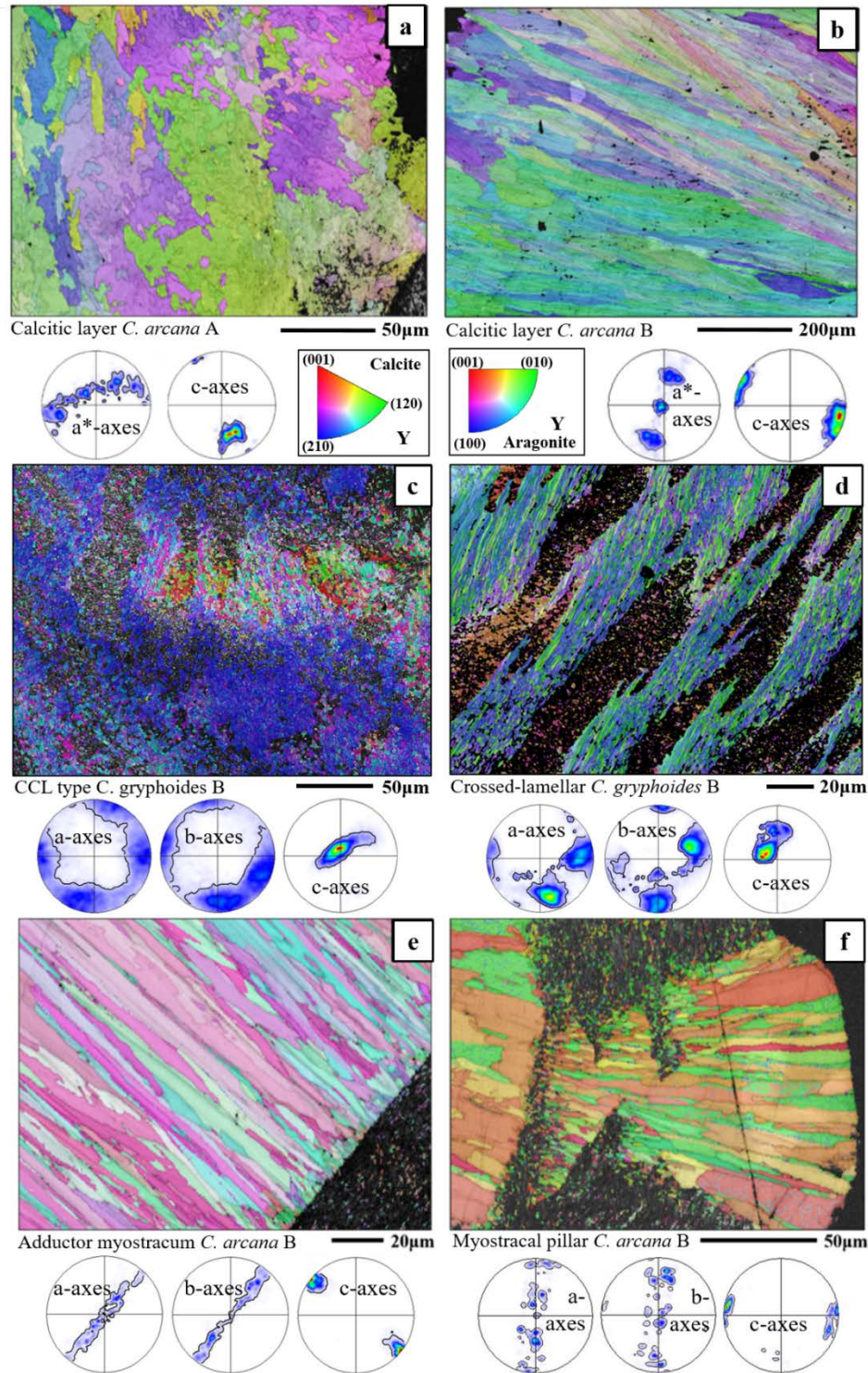


Figure 2.1-10. Compilation of the microstructures of different layers found in *Chama* shells depicted by EBSD measurements. The calcitic ornamentation in *C. arcana* comprises large, irregular prisms that are interdigitated in 3D (a, b). The calcitic ornamentation microstructure is characterised by a lack of an organic envelope encasing the internally substructured prisms (a, b). The aragonitic ornamentations in *C. gryphoides* comprise a complex crossed-lamellar (CCL)-type microstructure (c). Ornamentations and myostraca in *C. arcana* and *C. gryphoides* are separated by a crossed-lamellar microstructure (d). The adductor myostracum is characterised by large, prismatic crystals that increase in size as they grow away from the interface (e). Some *C. arcana* species show myostracal pillars traversing the complex crossed-lamellar layer (f). The pole figures show the orientational probability density distribution for the respective layers (a–f).

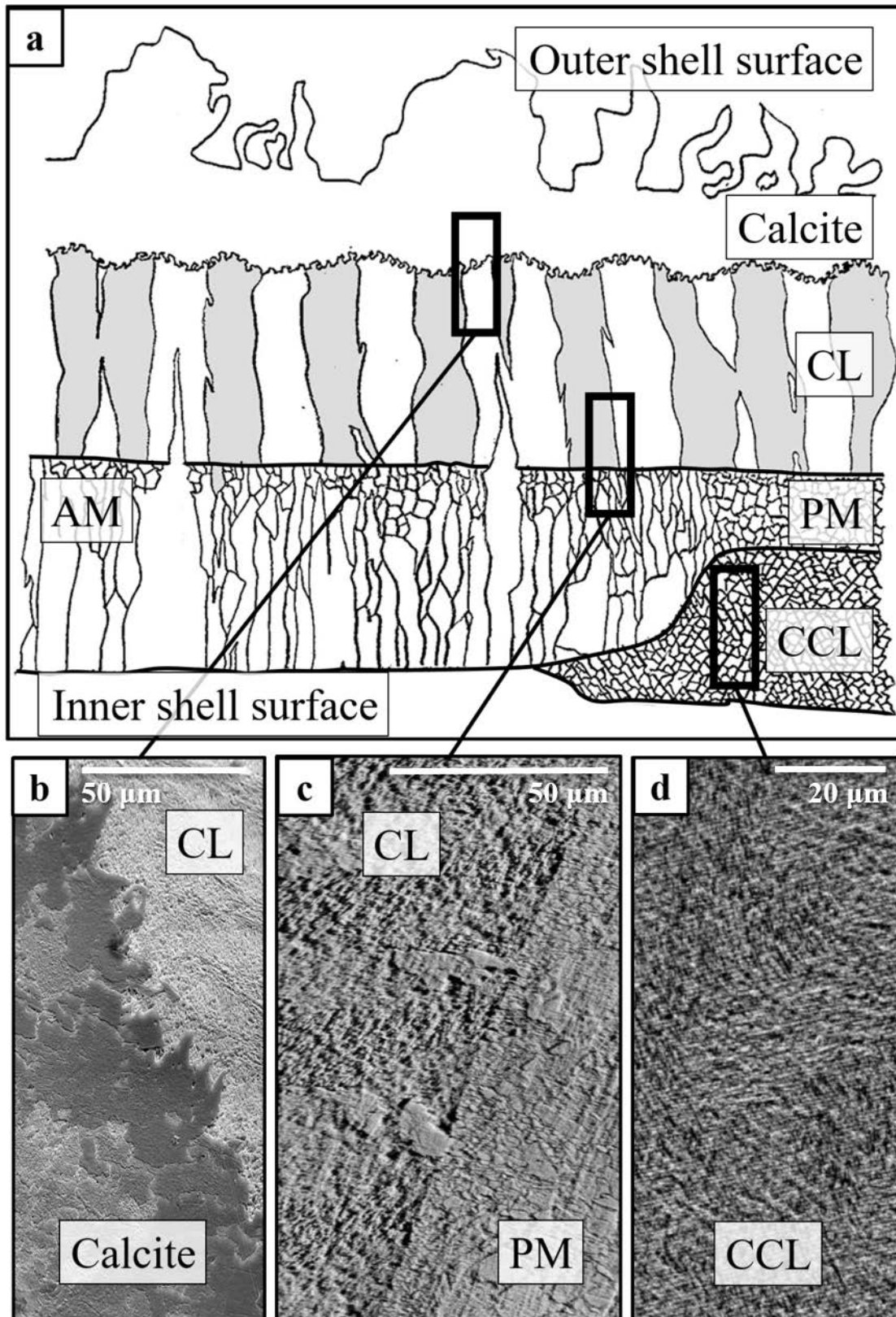


Figure 2.1-11. Schematic overview image displaying the organisation of layers near the adductor myostracum found in *Chama arcana* shells. The myostracal pillars that occur in some *C. arcana* species are not depicted in the graphic. The shell comprises four different microstructures (a). Myostracum may form during shell attachment with different muscles, e.g., forming the thick adductor (AM) or the thin pallial myostracum (PM). The outer shell ornamentations have a prismatic microstructure and a serrated interface with the adjacent crossed-lamellar layer (CL, b). In the changeover region from crossed-lamellar to myostracal layers, large (around 10 µm) and irregular single-crystal prisms are visible (c). The inner layer always comprises a complex crossed-lamellar structure, either as a uniform layer (d) or traversed by myostracal pillars.

In *C. gryphoides*, the entire shell is aragonitic, and there is no changeover from calcite to aragonite. Nonetheless, the microstructures of the layers are quite different. The aragonite crystals may appear as large prisms (myostracum), thin laths arranged in first-order lamellae (crossed-lamellar), or granules (complex crossed-lamellar type). The ornamentation in *C. gryphoides* comprises a complex crossed-lamellar-type microstructure with an axial texture (e.g., Figs. 2.1-7a, b and 2.1-AP14a). The adjacent crossed-lamellar layer shows a 3D “single-crystal-like” texture (Figs. 2.1-7b and 2.1-AP14b). Regarding crystal morphology, the changeover between those two layers is rather sharp; however, it is smooth regarding crystallographic texture. Thus, it appears that the crystal orientation pattern of the ornamentation is initially transmitted to the crossed-lamellar layer and subsequently “filtered” during its growth towards the inner shell surface (Fig. 2.1-7b). This may ensure a strong connection between the two layers while maintaining the tough crossed-lamellar microstructure that always comprises only the two sets of first-order lamellae. The similar crystal orientation patterns of the four different microstructures in *C. gryphoides* interconnect the shell layers without having to construct a metabolically expensive sheet of organic material or losing the microstructural properties of the individual layers.

Our study shows that, for the investigated *Chama* species, the shell layers differ in microstructure and that adjacent microstructures do not merge into one another. There is no intermediate between adjacent microstructures. The contrary is observed for the textures of adjacent shell layers. (i) If adjacent shell layers are formed of different carbonate polymorphs, calcite, and aragonite (Figs. 2.1-1b and 2.1-2b), then the texture pattern is not transferred from one shell layer to the other. In this case, there is always a marked inlay, rich in organic substance, between the calcitic and the adjacent aragonitic shell portions. (ii) If adjacent layers are formed of the same carbonate polymorph, as is the case for *C. gryphoides* solely of aragonite (Figs. 2.1-3a, 2.1-5a and 2.1-7b), then the texture of the one layer is transmitted to the adjacent shell layer at the changeovers. Crystallographic a-, b-, and c-axes of crystals of the adjacent aragonitic layers have very similar orientations at and close to the interface. With distance from the changeover regions, each of the textures becomes more distinct, and differences between the shell layers become visible. All aragonitic microstructures of the observed *Chama* specimens show strong twinning on the (110) plane. Hoerl et al. (2024b) demonstrated the twinning modes in crossed-lamellar, myostracal, and complex crossed-lamellar layers.

Ornamentation morphology and crystallography

Even though most species of Chamidae form a purely aragonitic shell (Taylor et al. 1969), a few *Chama* species, such as *C. arcana*, form their shell of aragonite and the ornamentation of calcite. Bivalve ornamentations not only serve as protection for the soft tissue but also have a variety of other functions. They help the bivalve maintain a stable position in the sediment (Trueman 1966; Kauffman 1969; Aller 1974; Stanley 1981), play an important role during burrowing (Stanley 1969; Stanley 1970; Alexander et al. 1993; Johnson 2020), and add to the general stability of the shell (Kauffman 1969; Aller 1974;

Klompaker & Kelley 2015). Through adaptation to various environments and lifestyles, such as to the site of cementation, exposure to wave action, and encrusting biota, bivalves formed numerous patterns of ornamentation sculptures (Kennedy et al. 1970; Ubukata 2005; Ye et al. 2023). The ornamentations of the two investigated *Chama* species vary in carbonate mineralogy, crystal morphology, microstructure, and texture and are, thus, well suited to demonstrate the structural variety of chamid shells.

The aragonitic ornamentations of *C. gryphoides* comprise a complex crossed-lamellar-type microstructure. Due to its microstructure with first-order-lamellar blocks that comprise small crystals arranged into an intricate pattern (Figs. 2.1-7a, b and 2.1-AP14a), this layer was historically described to have a crossed-lamellar microstructure (Matsukuma et al. 1997). To our knowledge, this is the first study to describe the microstructure of the complex crossed-lamellar-type layer and its changeover to the crossed-lamellar microstructure in great detail, using electron microscopy and EBSD. The changeover is rather sharp, and the pole figures show dissimilar textures for the two layers: While the complex crossed-lamellar-type layer has an axial texture with a- and b-axes orientations varying on a great circle perpendicular to the c-axes, the texture of the crossed-lamellar layer is 3D “single-crystal-like” (Figs. 2.1-7, 2.1-10c, d, and 2.1-AP14). Despite the initial transmission of the crystal orientation pattern from ornamentation to the crossed-lamellar layer in *C. gryphoides* shells, the layers are, thus, distinct, and their crystal growth mechanisms might vary. The homogeneous grain morphology and crystal orientation pattern indicate some degree of organic substance control during the growth of the complex crossed-lamellar-type layer.

In contrast, the calcitic ornamentation layer in *C. arcana* comprises irregular prisms that lack distinct sheaths around the large (up to 200 μm in length) substructured grains. The low degree of organic content and the distinct microstructure indicate a lack of biological control in the ornamentation layer. The latter might induce the internal substructuring and the complex 3D interdigitating dendrite-like calcite crystals as the growing crystals fight for space in the spatially restricted ornamentation. Similar crystallographic configurations have so far been observed for brachiopods and rotaliid foraminifera that comprise interdigitating calcite crystals characterised by dendritic boundaries and low organic content (Goetz et al. 2011; Lastam et al. 2023a). To our knowledge, this study is the first to report this kind of microstructure for bivalve shells. The poorly ordered yet effective calcitic ornamentation serves as a primary layer of protection in a life stage where the soft tissue is most vulnerable to predators and environmental threats (Verween et al. 2007; Pineda et al. 2012). Once the ornamentation is constructed, most *Chama* organisms form the highly controlled crossed-lamellar layer. This could explain the structural variety of ornamentation sculptures that have been observed for the Chamacea (Kennedy et al. 1970). Thus, the ornamentation carbonate and layers may not be mechanically optimised but rather the result of spatial and chemical restrictions imposed by their surrounding environment. Gránásky et al. (2024) support the idea that the physicochemical environment

in which the biomineralisation takes place may be controlled and manipulated by the genetically encoded organic material. Seeing that the metabolic cost of the calcitic foliated, prismatic, and chalk structures is lower than for aragonitic structures (Taylor & Layman 1972), it might be favourable for some species to form calcitic assemblies of crystals. Rather than forming a genetically controlled microstructure with high organic content (as seen, e.g., in Pteriomorphs (Harper & Checa 2017)), calcitic ornamentations in *C. arcana* contain little organic material and can possibly be deposited more quickly (Taylor & Layman 1972; Harper & Checa 2017). Thus, calcitic ornamentations can serve as an efficient alternative to aragonite in turbulent environments.

The mechanical drawbacks of calcitic ornamentations might be counteracted by the particular ornamentation geometry that is predefined by the periostracum: In *C. arcana* shells, the calcitic ornamentations are long and run at high angles to the inner shell surface (Figs. 2.1-AP2 and 2.1-AP6a), whereas the fully aragonitic *C. gryphoides* shows a rather shallow and thin ornamentation layer. Living in different environments, the two observed species, thus, might have developed varying evolutionary strategies for the protection of the soft tissue and survival of the organism.

Microstructural Anomalies

It is quite common that bivalve shells vary in structural characteristics across different species within the same order (Kennedy et al. 1969; Taylor et al. 1969; Sato & Sasaki 2015; Prezant et al. 2022). This is also the case for *C. arcana* and *C. gryphoides*. Those differences usually result from evolutionary processes that cause certain characteristics to appear, disappear, increase, or decrease. However, it is highly unusual to see significant structural differences in a single specimen that do not result from malformation or spatial limitations. In our study, we report two specimens of *C. arcana* that drastically vary in their shell structure and properties. The differences are visible both on a microscopic and on a macroscopic scale, as reported for the two following characteristics:

1. Myostracal pillars or the complex crossed-lamellar layer along the inner shell surface

For the investigated specimens of *C. arcana*, we see striking differences in their respective inner shell layers. While specimen A exhibits a continuous complex crossed-lamellar microstructure along its inner shell surface, specimen B features myostracal pillars that reach lengths of up to 1 mm. The myostracal pillars are embedded in a complex crossed-lamellar microstructure and are also reported for other species of the Chamacea (Taylor et al. 1969; Kennedy et al. 1970). However, to our knowledge, this is the first study to measure and analyse those structures using modern techniques such as scanning electron microscopy and EBSD. The myostracal pillars have an elongated, ovoid morphology and seem to arise directly from the pallial myostracum, assuming its texture and microstructure (Figs. 2.1-4a, 2.1-5a, 2.1-6). Therefore, they comprise large, irregular prisms that have their c-axis orientation normal to the inner shell surface. Similar to the myostraca, the myostracal pillars have a thin organic matrix separating the grains but do

not show well-developed interprismatic protein walls. Their microstructure strongly contrasts the complex crossed-lamellar layer (Kennedy et al. 1970; Hoerl et al. 2024b). The reason why one specimen shows the presence of pillars and the other one does not might be related to the muscular activity of the organisms: Following the detachment of the pallial muscles in specimen B, other muscles are locally attaching to the shell, initiating the growth of the pillars. Periodic attachment/detachment of those muscles would, therefore, explain the alternating sheets of myostracal pillars and the complex crossed-lamellar layer, as observed in our study in some measurements (yellow stars in Figs. 2.1-4b and 2.1-6b).

2. Formation of single crystal-like units in the crossed-lamellar layer

For all *C. arcana* shells, we found the presence of anomalous single-crystal-like aragonite units in the crossed-lamellar layers. They can vary in size from 5 μm to more than 100 μm and are usually oriented with their c-axis perpendicular to the inner shell surface. Most of these crystals are located at or near the changeover into the myostracum and match the texture of the surrounding crossed-lamellar layer. In specimen A of *C. arcana*, aragonite crystals appear to be clustered in scattered units of around 20 μm diameter (yellow stars in Fig. 2.1-3a, b). They comprise differently oriented crystals that are twinned along irregular planes. On the other hand, specimen B of *C. arcana* also shows large crystal entities in addition to the small clusters. Those entities (stars in Figs. 2.1-5a, b and 2.1-AP9) may exceed a length of 100 μm and a thickness of 25 μm . Similar to the small clusters, they are strongly twinned; however, the twin plane is usually a clear-cut and straight boundary. The direction of the cut may affect the appearance of the entities; however, the large divergence in length and thickness between the specimens points towards a structural difference. To our knowledge, this study is the first to report single-crystal-like entities within crossed-lamellar layers in *Chama* shells or even bivalve shells in general. Therefore, their exact origins and growth mechanisms are uncertain. Opposed to the myostracal pillars, they probably do not stem directly from muscle–shell attachment: (i) individual crystal morphologies are irregular and can vary in thickness (e.g., Figs. 2.1-5a, b and 2.1-AP9), (ii) larger crystal entities can penetrate the adductor myostracum without assuming its texture or microstructure and (iii) in contrast to the myostraca, there is no gradient in crystal size, e.g., as is the case for crystal that grow through growth competition (see Fig. 2.1-AP11 in Hoerl et al. (2024b)).

Reviews of Taylor *et al.* (1969, 1973), Kennedy *et al.* (1970) and Ponder *et al.* (2019) highlight the rich portfolio of shell microstructures that bivalves developed throughout the Phanerozoic. The microstructure diversity for bivalves that we see today is far above that of any other calcifying phylum (Carter 1990). Mineralisation by bivalves started in the lower Cambrian with the genera *Fordilla* and *Pojetaia*. The microstructure of these two genera was always foliated aragonite (Runnegar & Bentley 1983). If we take into account all molluscs, then there already was a wide variety of mollusc

microstructures in the Cambrian: fibrous, prismatic, crossed-lamellar (weak evidence), calcitic semi-nacre, foliated calcite, and foliated aragonite (Runnegar & Bentley 1983; Runnegar & Pojeta 1985; Feng et al. 2003; Vendrasco et al. 2010). The nacre in the Cambrian *Mellopegma* (Trueman 1966) was reinterpreted as calcitic semi-nacre (Vendrasco et al. 2010), and the evidence of crossed-lamellar microstructure in *Yuwenia* (Trueman 1966) is very weak. Hence, molluscan nacre was absent in the Cambrian, and the presence of the crossed-lamellar microstructure is very doubtful. Thus, the two main microstructures that we observe today for mollusc shells, the nacreous and cross-lamellar crystal arrangements, were not present in the Cambrian and appeared in the Ordovician. Even though laminated calcite formation by molluscs is reported for the Cambrian (Vendrasco et al. 2010), the increased production of calcitic bivalve shells started in the late Permian to Early Triassic (Stenzel 1971; Guo et al. 2018; Li et al. 2018; Li et al. 2021). Although the cause for mineralised tissue formation is still disputed, one prominent hypothesis is that it was evoked by the onset of predation. The latter called forth the initiation of diverse defensive solutions. These include the development of differently sized and formed shells with various thick shell walls, the formation of layered shells, and the development of diverse crystal orientation patterns for the different shell layers (e.g. Runnegar and Pojeta 1985, Vendrasco *et al.*, 2010).

Mechanical property characterisation of bicarbonate microstructures demonstrated that these are variably suitable for protection against mechanical and chemical external threats. For example, the crossed-lamellar microstructure, the most widely used microstructure by Mollusca today, has a higher fracture toughness and ability to dissipate cracks relative to granular and nacreous crystal arrangements (e.g. Currey and Taylor 1974, Currey and Kohn 1976, Currey 1988, Peter *et al.* 2023). However, the crossed-lamellar structure also has an increased organic contact, as each lath of the first-order lamellae is encased by an organic substance (Fig. 20d, e in Crippa *et al.* (2020)). The organisation of the organic substance in the crossed-lamellar microstructure is more complex and intricate (Fig. S20a–c in Crippa *et al.* (2020)) relative to the organisation of the organic substance in shells with granular structures (e.g., *Arctica islandica*, Figs. 2b and 3b in Casella *et al.* (2017)) and nacreous microstructures (e.g., *Mytilus galloprovincialis*, *Haliotis glabra*, Figs. 3–5 in Peter *et al.* (2023)). Furthermore, the functional significance of calcite, relative to aragonite, is uncertain, as calcitic microstructures are, in general, softer than aragonitic (Taylor & Layman 1972; Troncoso et al. 2020; Lew et al. 2023; Peter et al. 2023; Hoerl et al. 2024b) and do not seem to provide notable benefits regarding shell dissolution or protection from external chemical attacks (Gabriel 1981; Henrich & Wefer 1986; Harper 2000; Cubillas et al. 2005).

Hence, the “best” microstructure for biological hard tissues depends not only on its mechanical properties but also on the metabolic cost and the constraints imposed by the surrounding environment. Thus, we hypothesise that calcite and aragonite seas may play primary roles in determining the initial carbonate mineralogy; however, their subsequent influence on skeletal mineralogy is limited (Avery & Etter 2006; Porter 2010; Thomsen et al. 2015; Conci et al. 2021; Collins et al. 2023).

2.1.5 CONCLUSIONS

For a trade-off between functionality, mechanical properties, and metabolic cost, bivalves can choose from a wide variety of crystal arrangements when forming their hierarchical shell.

Although the Chamidae are mostly sessile, they live in different ecological environments that pose challenges that benefit some subspecies more than others. This phenomenon might explain the significant structural diversity we observed among chamid shells. We found differences not only in the ornamentation, the first-formed layer that is epitaxially controlled by the periostracum, but also in the inner shell layers and the muscle attachment behaviour.

In this contribution, we highlight and discuss differences in shell hierarchy and microstructure between and within different species of *Chama*. From our structural results, we conclude the following:

1. For *C. arcana* and *C. gryphoides*, five distinct microstructures can be observed. From the outer to the inner shell surface, these microstructures are Prismatic calcite (only in the ornamentations of *C. arcana*), complex crossed-lamellar-type aragonite (only in the ornamentations of *C. gryphoides*), and crossed-lamellar, myostracal, and complex crossed-lamellar aragonite.
2. Depending on the type of muscle attachment, myostracal microstructures may appear as thick patches (adductor), as a thin and hollow hemisphere (pallial), or as pillars arising from the pallial myostracum.
3. In some, but not all, shells of *C. arcana*, myostracal pillars traverse the inner complex crossed-lamellar layer. They have a spherulite-resembling shape comprising large aragonite prisms that grow continuously from the pallial myostracum and, most probably, follow a competitive growth mechanism.
4. Myostracal pillars adapt to the texture of the pallial myostracum. Muscular detachment and reattachment can cause myostracal pillars to be interrupted by sheets of complex crossed-lamellar shell material. With further growth of the shell, the competitive growth mechanism restarts and assumes at first the texture of the preceding (in this case, complex crossed-lamellar) layer.
5. The pallial and adductor myostraca follow a competitive growth mechanism. The crystal orientation pattern of the crossed-lamellar layer is transmitted onto the myostracum and onto the complex crossed-lamellar layer. The changeover region from crossed-lamellar to myostracal layers in *C. arcana* shells features large (up to 100 μm), single-crystal-like crystals with irregular morphologies twinned along one or few boundaries. These crystals have not yet been observed in crossed-lamellar layers, and their origin and growth mechanism are not yet known.

6. Ornamentations in chamid bivalves may be either calcitic or aragonitic. Calcitic ornamentations (e.g., in *C. arcana*) comprise a prismatic microstructure of large (up to 200 μm in diameter) crystals that have their c-axes oriented perpendicular to the outer shell surface defined by the periostracum. The aragonitic ornamentations in *C. gryphoides* comprise a complex crossed-lamellar-type microstructure that resembles the inner layer featuring first-order-lamellar blocks that comprise small third-order lamellae.
7. The crystal orientation pattern is transmitted at the changeover from the aragonitic ornamentation to the crossed-lamellar shell in *C. gryphoides*. Since the textures of the complex crossed-lamellar-type ornamentation (axial) and of the crossed-lamellar layer (3D “single-crystal-like”) are different, the crystal orientation pattern is lost a few μm after the interface.
8. The changeover from the calcitic ornamentation to the crossed-lamellar layer in *C. arcana* is sharp and features an organic-rich aragonite sheet that might be needed to mediate the biologically controlled growth of the crossed-lamellar layer and to connect the two layers.
9. The serrated interface between calcitic ornamentations and the aragonitic crossed-lamellar layer in *C. arcana* exposes some regular (104) growth faces of calcite, resembling the morphology of idiomorphic crystals. As indicated by the disordered crystal arrangement and substructured, irregular units, the texture of the calcitic ornamentation does not seem to be directed biologically.

Acknowledgements

We thank E.M. Harper, Department of Earth Sciences, University of Cambridge, Downing Street, Cambridge CB2 3EQ, U.K. and C. Salas and S. Gofas, Departamento de Biología Animal, Facultad de Ciencias, Universidad de Málaga, Málaga, Spain, for the samples. A.G.C. acknowledges the Research Group RNM363 (Consejería de Economía, Innovación, Ciencia y Empleo, Junta de Andalucía) and the Unidad Científica de Excelencia UCE-PP2016-05 (University of Granada).

Author contributions

Conceptualisation, S.H., E.G.; Formal analysis, A.G.C., W.W.S.; Investigation, S.H., E.G.; Methodology, S.H., E.G.; Supervision, E.G., W.W.S.; Validation, A.G.C., W.W.S.; Visualisation, S.H., E.G.; Writing – original draft, S.H., E.G.; Writing – review & editing, A.G.C., W.W.S..

2.1.6 SUPPLEMENTARY INFORMATION

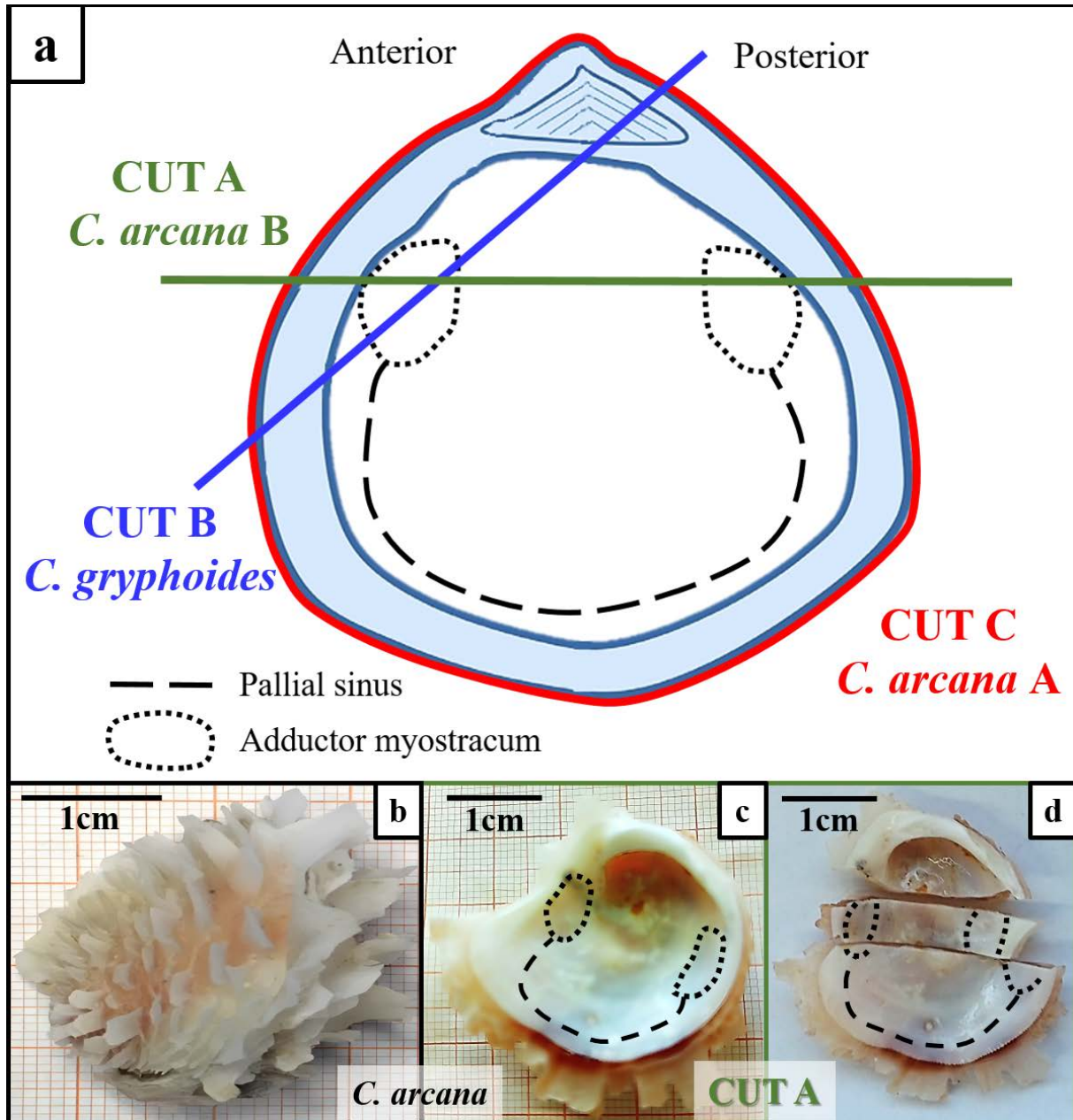


Figure 2.1-AP1. Schematic overview image indicating the direction and position of the different shell cuts performed on the specimens presented in this article (a, modified from Crippa et al. (2020a)). The valves were cut either crossways, exposing the cross- section of the adductor myostraca (*Chama arcana*, cut A), transversely through both adductor myostraca (*C. arcana*, cut C) or obliquely through only one adductor myostracum (*Chama gryphoides*, cut B). Valves were cut to expose the adductor myostraca indicated by a dotted line (a, c, d). The ornamentation details (b) and structural morphology of *Chama* shells (c) is indicated by overview images showing the entire shell. The sectioning along cut A is indicated for a *C. arcana* shell (c, d).

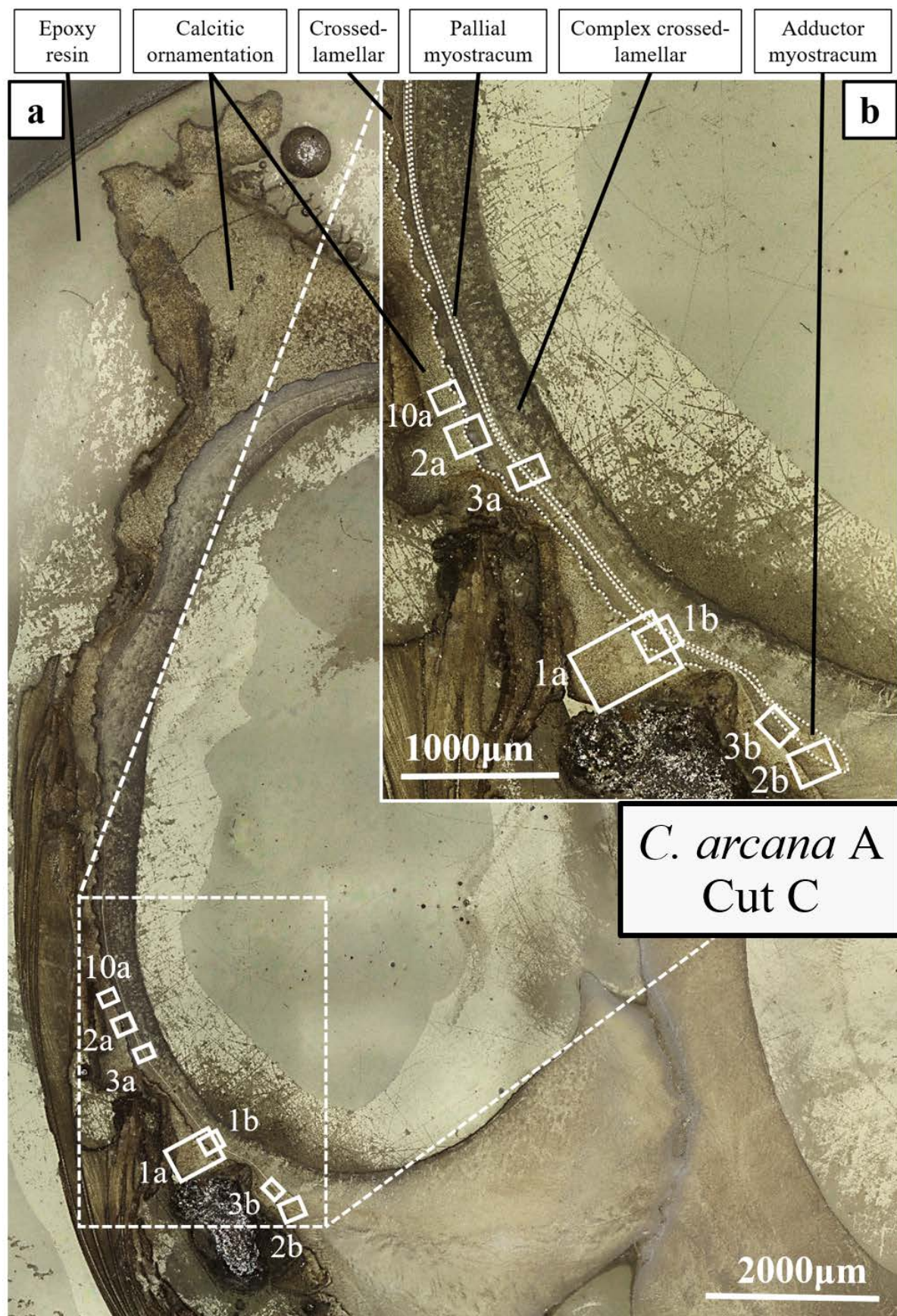


Figure 2.1-AP2. Laser confocal microscopy image depicting the measurement positions for the EBSD scans performed on a *Chama arcana* sample that was sectioned crossways (cut C). The sectioned sample comprises an intricate structure (a) so the measurements were performed in the region near the adductor myostracum. Interfaces of the shell layers are highlighted with dashed white lines in the close-up image (b).

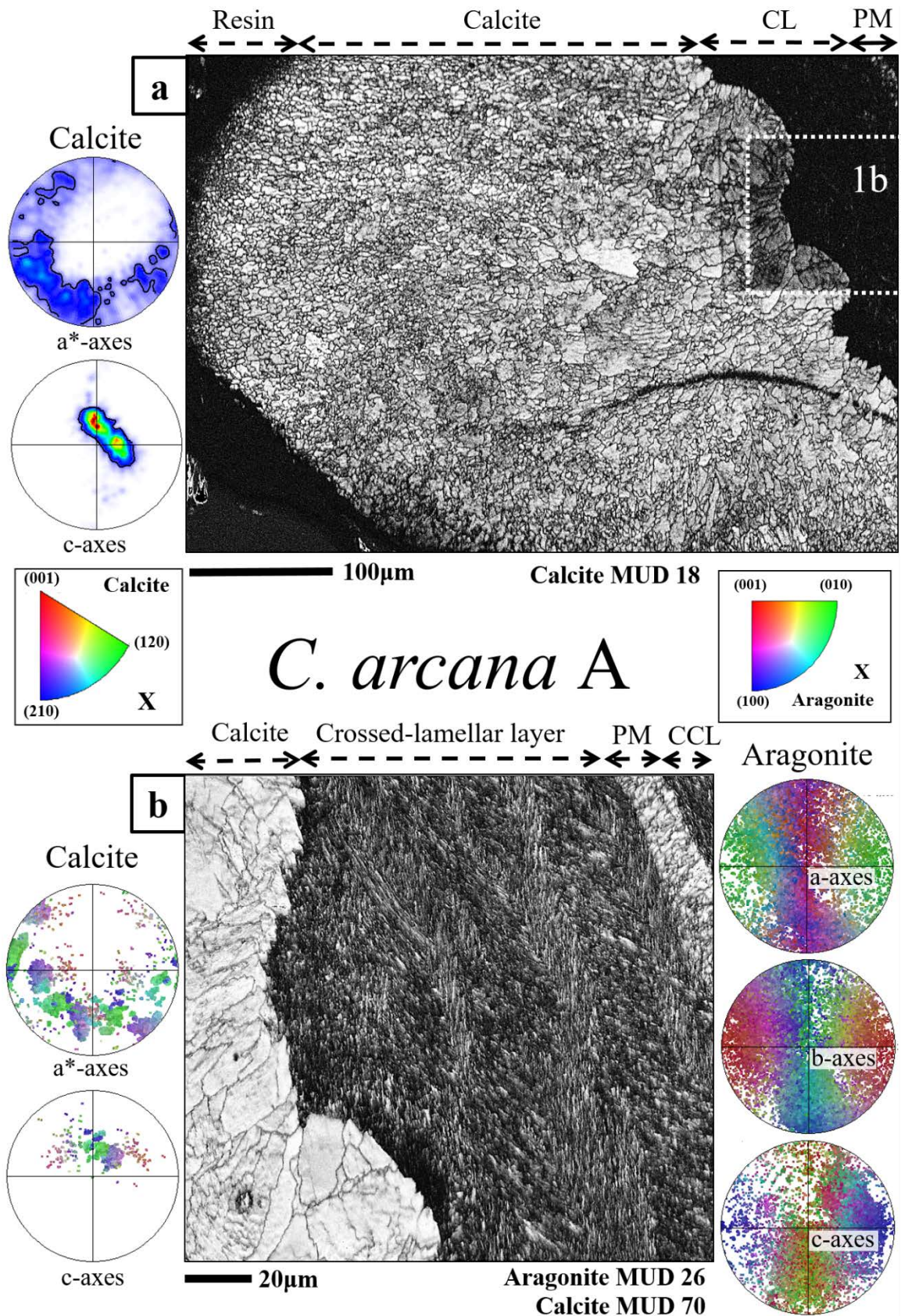


Figure 2.1-AP3. EBSD band contrast images demonstrating the different internal structures present in the applied cut C of a *Chama arcana* shell. The calcitic ornamentalations along the outer shell surface consist of multiple large crystal clusters interlocked into each other (a). The aragonitic crossed-lamellar (CL) layer characteristically comprises multiple sets of differently oriented lamellae, each consisting of small, fibrous crystals (b). The pallial myostracum (MYO) separates the crossed-lamellar layer from the complex crossed-lamellar layer (CCL) on the very inside of the shell (b). The pole figures indicate the individual crystal orientations of the calcitic and aragonitic shell layers (a, b).

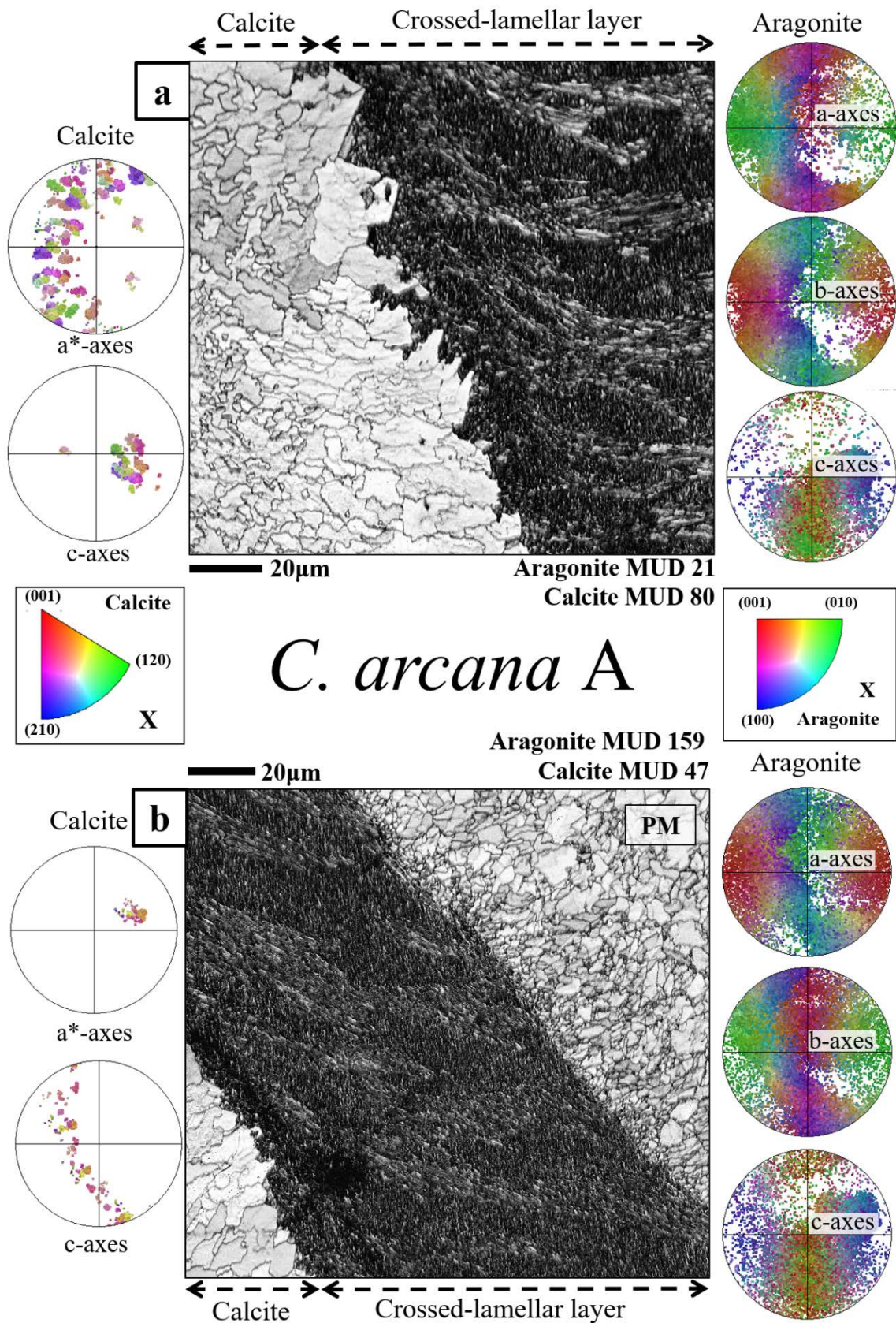


Figure 2.1-AP4. EBSD band contrast images illustrating the interface between the calcitic layer and the aragonitic crossed-lamellar layer observed for the applied cut C of a *Chama arcana* shell. The crystals within the calcitic layer show a complex and fractal-like interpenetration. Towards the inner shell surface, the crossed-lamellar layer transitions into the adductor myostracum (AM, b). The pole figures display the individual data points of the crystal orientations in the calcitic and aragonitic layers. The texture of both layers is axial, however, the calcitic layer is rather co-oriented and aragonitic crystal orientations vary significantly.

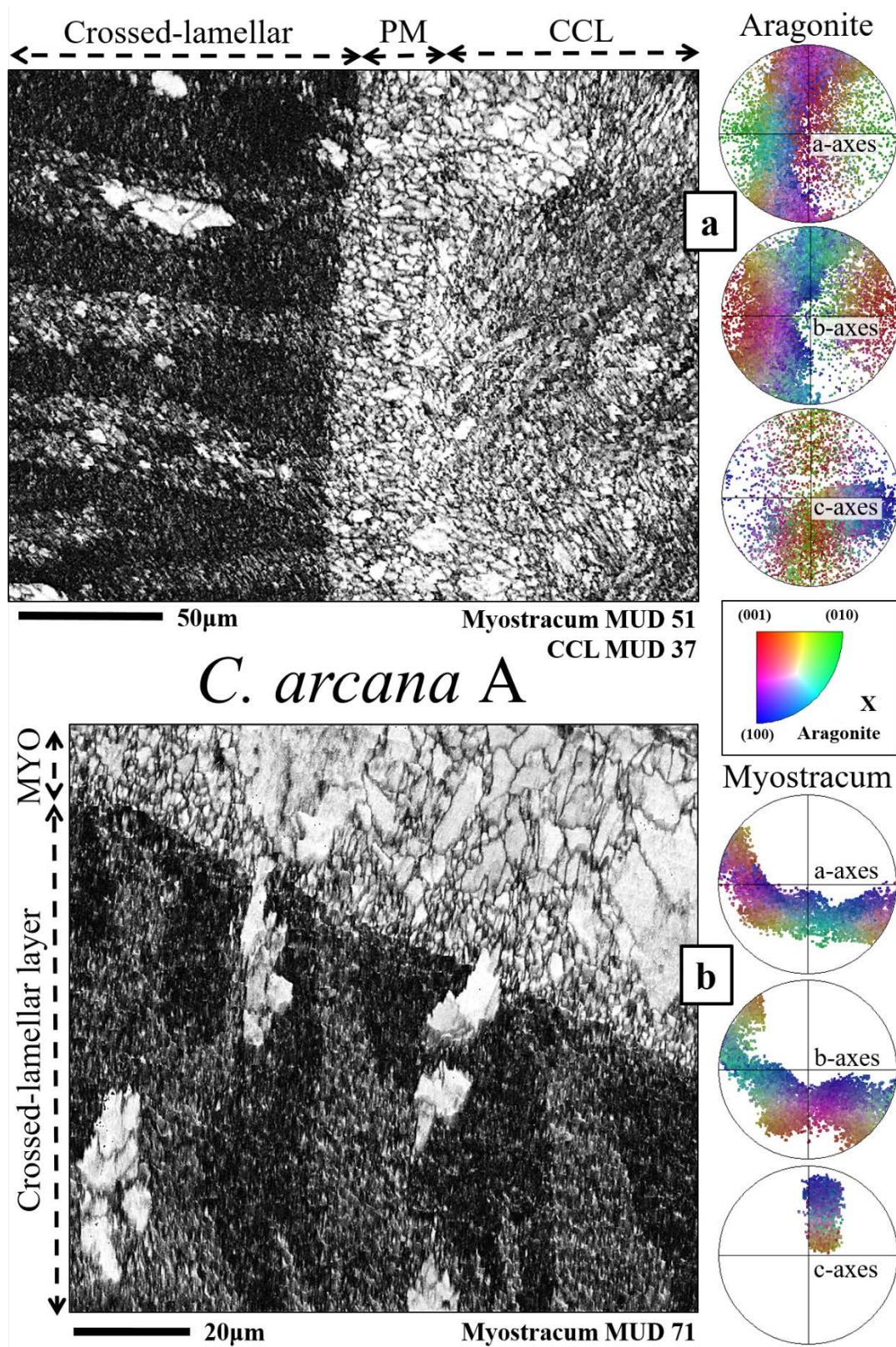


Figure 2.1-AP5. EBSD band contrast images depicting the interfaces within the different aragonitic layers of a *Chama arcana* shell sectioned crossways (cut C). The interface between the pallial myostracum and the complex crossed-lamellar layer (CCL) is indistinct and vague (a). The crossed-lamellar layer, however, shows a straight and rather sharp interface with the pallial (PM, a) and adductor myostraca (AM, b). A peculiarity highlighted in the two scans is the occasional presence of crystal assemblies consisting of large (around 10 μm) grains appearing in the interface region of the crossed-lamellar layer (yellow stars in a, b), their morphology resembling myostracum crystals with high crystal co-orientation and intensity of the Kikuchi bands. The pole figures indicate the individual crystal orientations of the pallial and the adductor myostracum in the two respective scans (a, b).

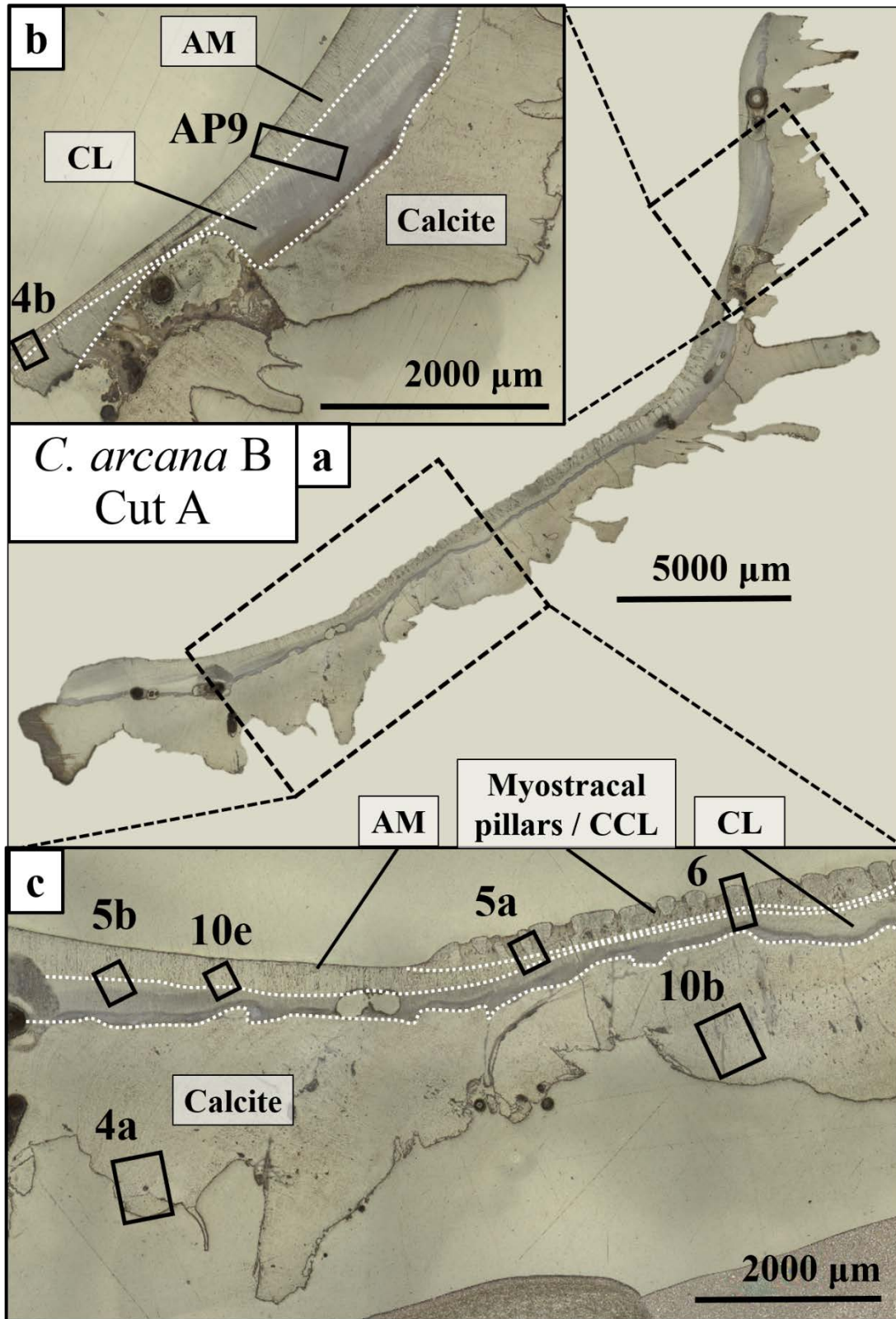


Figure 2.1-AP6. Laser confocal microscopy images depicting the measurement positions for the EBSD scans performed on a transversely cut *Chama arcana* shell (cut A). Two measurements were performed on the posterior (b) and six measurements on the anterior end (c). The interfaces of the respective layers are highlighted with dashed white lines (b, c). AM: Adductor myostracum, CL: Crossed-lamellar layer, CCL: Complex crossed-lamellar layer.

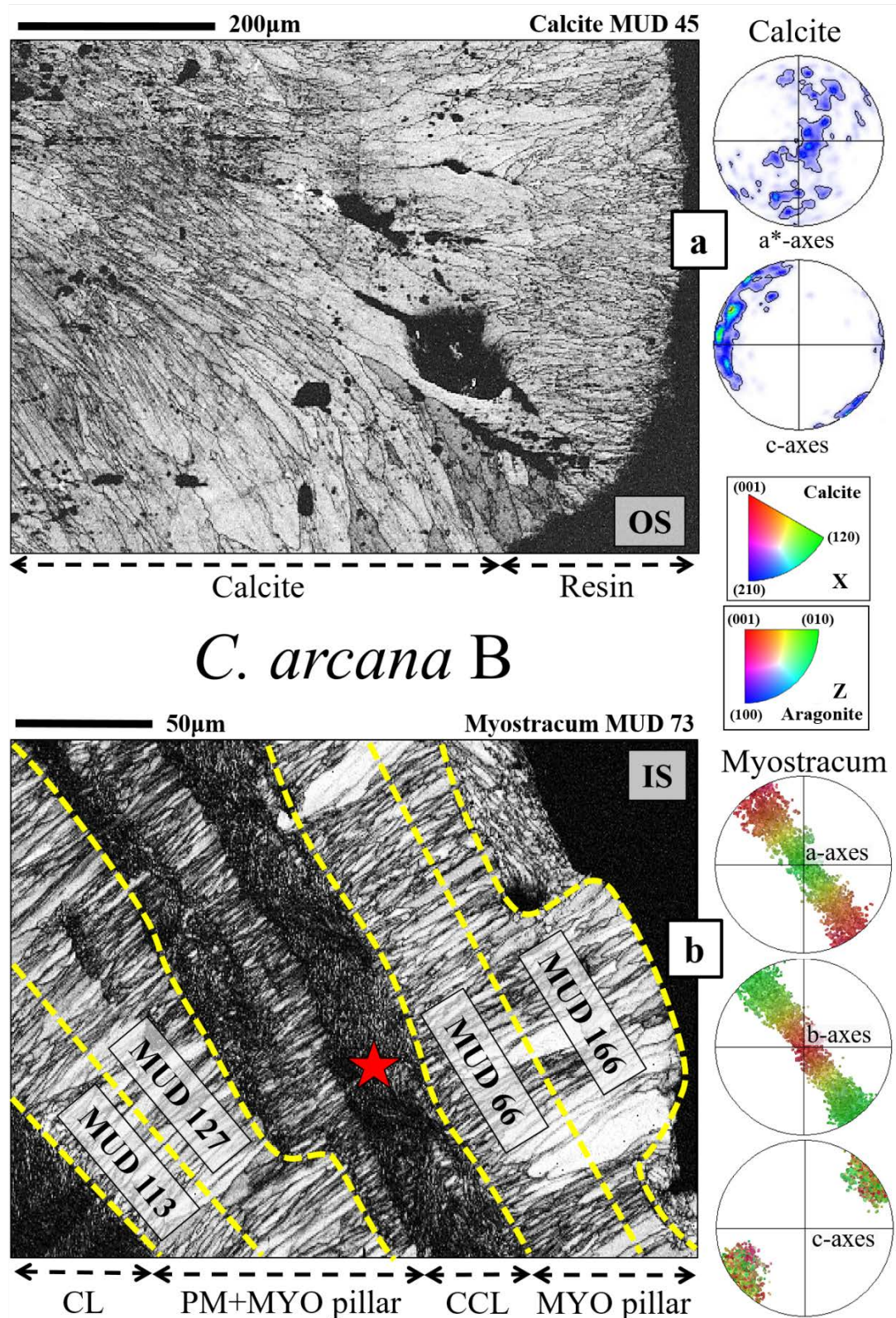


Figure 2.1-AP7. EBSD band contrast images depicting the different microstructures observed for the applied transverse cut A of a *Chama arcana* shell. The calcitic shell ornamentations along the outer shell surface (OS) comprise crystal units that follow an intricate interlocking mechanism (a). In the aragonitic section of the shell, the pallial myostracum (MYO) comprises small, isotropic crystals close to the interface with the crossed-lamellar layer (CL, b). The pallial myostracum exhibits a competitive growth mechanism that causes the overall crystal size and co-orientation strength (indicated by MUD values of subsets indicated by dotted yellow lines) to increase rapidly towards the inner shell surface (IS). When interrupted by a continuous sheet of complex crossed-lamellar (CCL) layer (red star in b), the competitive growth mechanism of the myostracal pillar restarts. The pole figures for the calcitic and myostracum areas of the two scans show an axial texture (a, b).

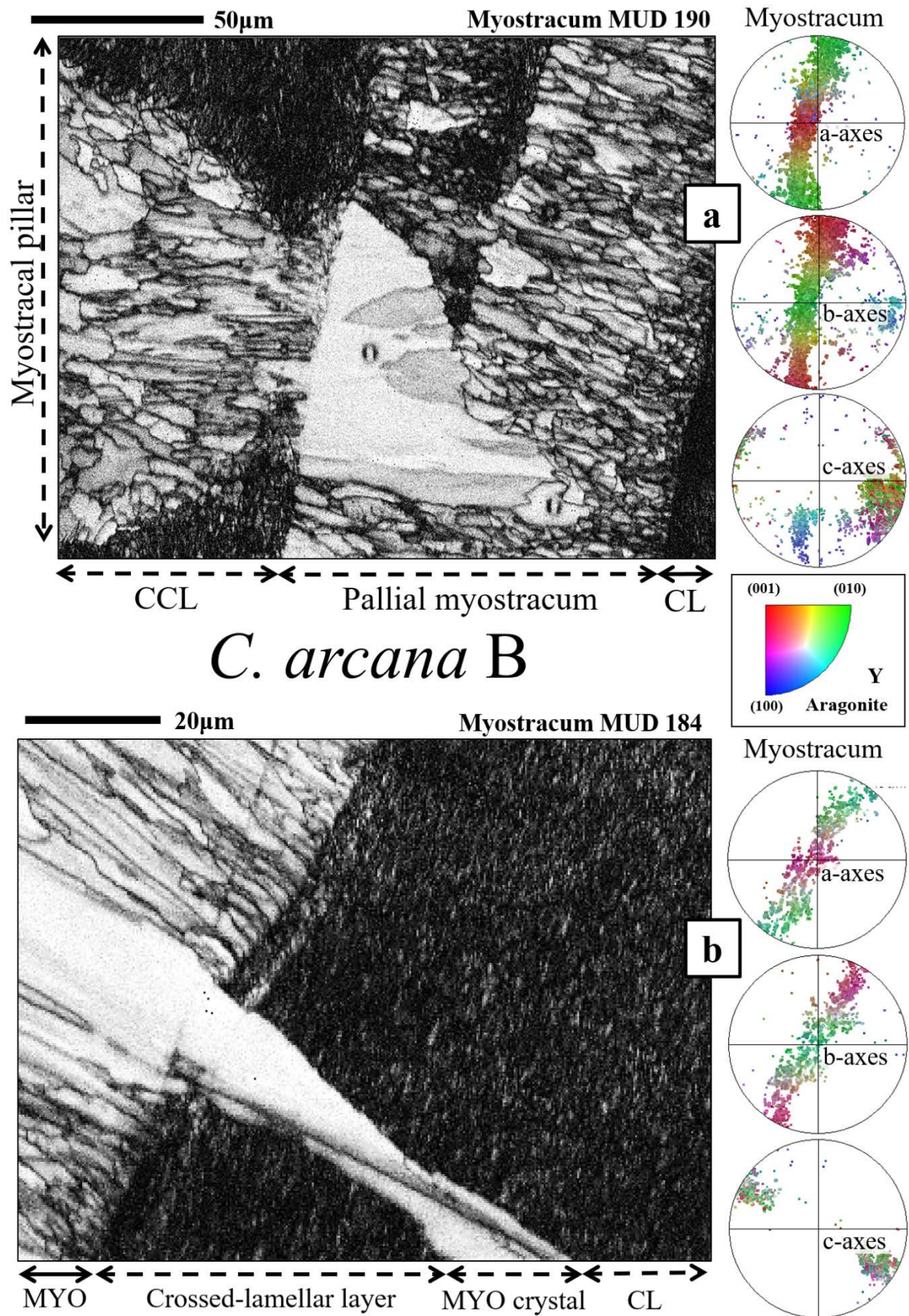


Figure 2.1-AP8. EBSD band contrast images depicting large, anomalous myostracum (MYO) crystals observed for the applied transverse cut A of a *Chama arcana* shell. The highlighted sizeable crystals can occasionally be found in the pallial (red star in a) and the adductor myostracum (AM, yellow star in b) and show a peculiar microstructure. The pole figures display the individual data points of the crystal orientations for the myostracum layers that show an axial texture.

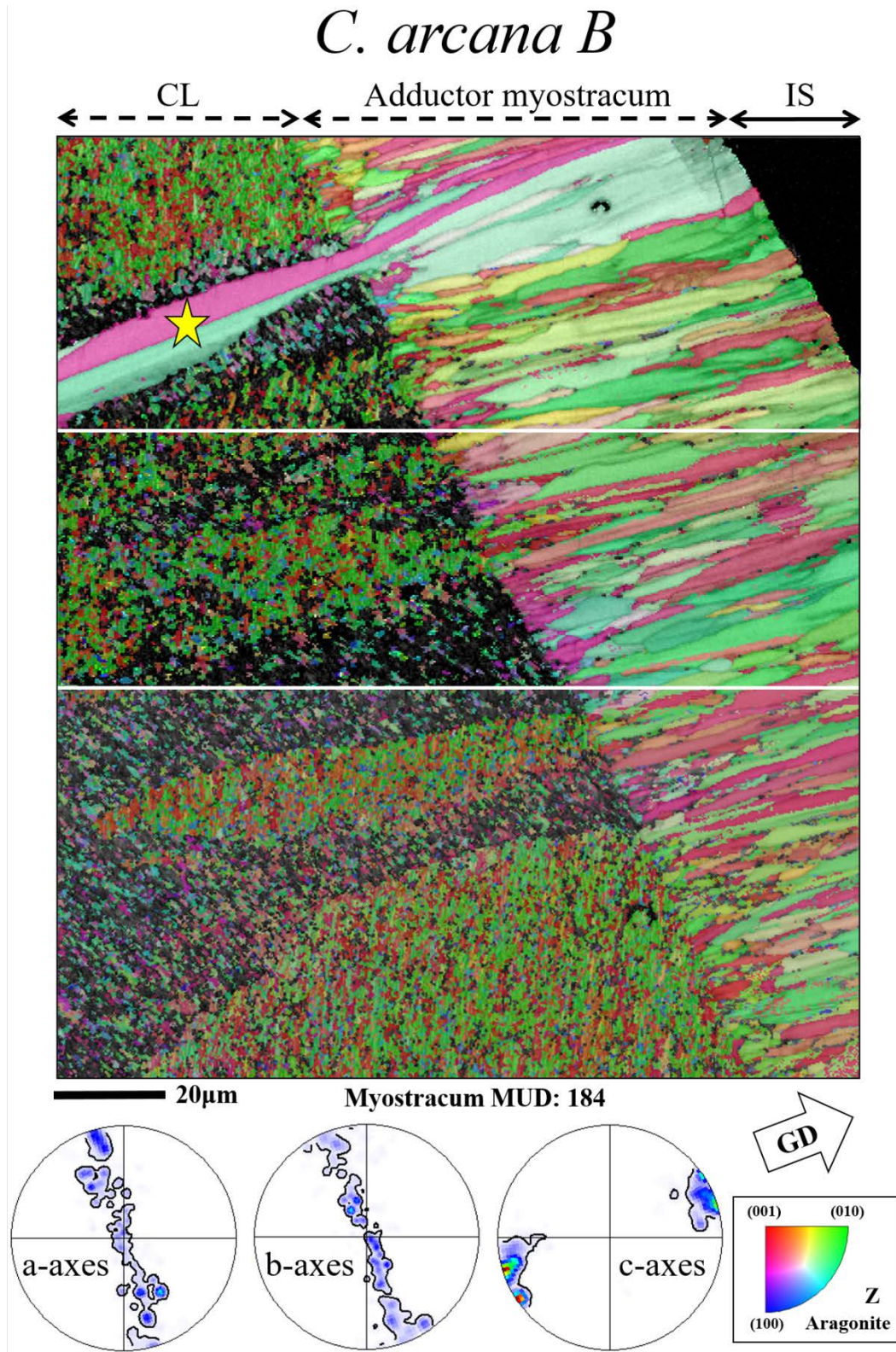


Figure 2.1-AP9. EBSD scans depicting the interface between the crossed-lamellar layer (CL) and the myostracum for the applied transverse cut A of a *Chama arcana* shell. The EBSD map is composed of three individual scans with overlapping positions. The white lines indicate the borders of the respective measurements. The composite map highlights the transition of the crossed-lamellar sets into the myostracum. Along this interface, the orientations of the rearmost crossed-lamellar crystals and the adjacent myostracum crystals correlate. Due to the competitive growth mechanism, the pattern is quickly lost towards the inner shell surface (IS) as the crystals increase in size and prismatic shape. Similar to Figure 2.1-8b, a substantial crystal (indicated by a yellow star) traverses both shell layers. The pole figures show the orientational probability density distribution for the myostracum area of the composed scan and depict an axial texture. The growth direction (GD) is indicated with a white arrow.

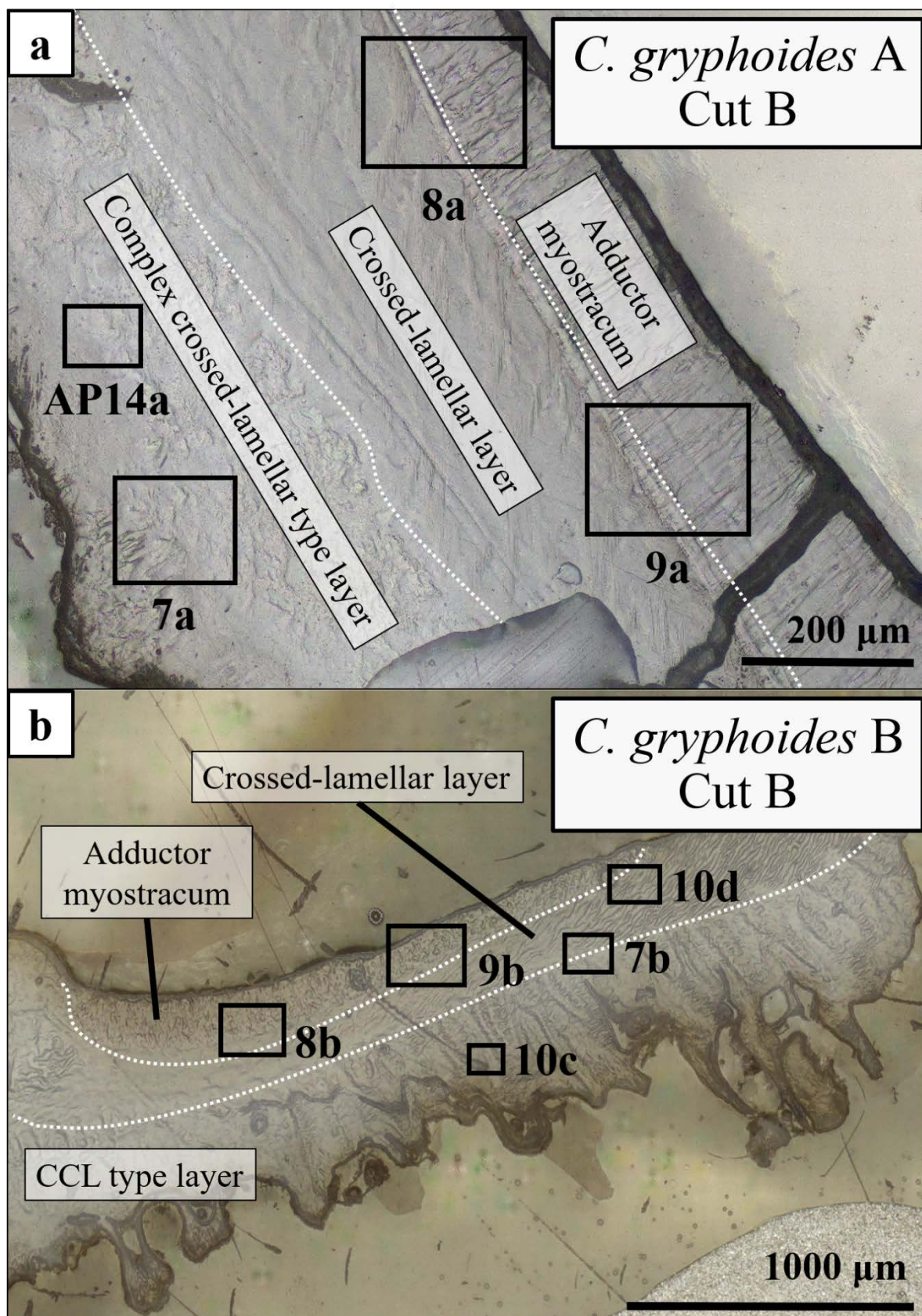


Figure 2.1-AP10. Laser confocal microscopy images depicting the measurement positions for all *Chama gryphoides* EBSD scans. A total of nine measurements were performed on the two samples sectioned obliquely (cut B). The interfaces of the respective layers are highlighted with dashed white lines (a, b). CCL: complex crossed-lamellar.

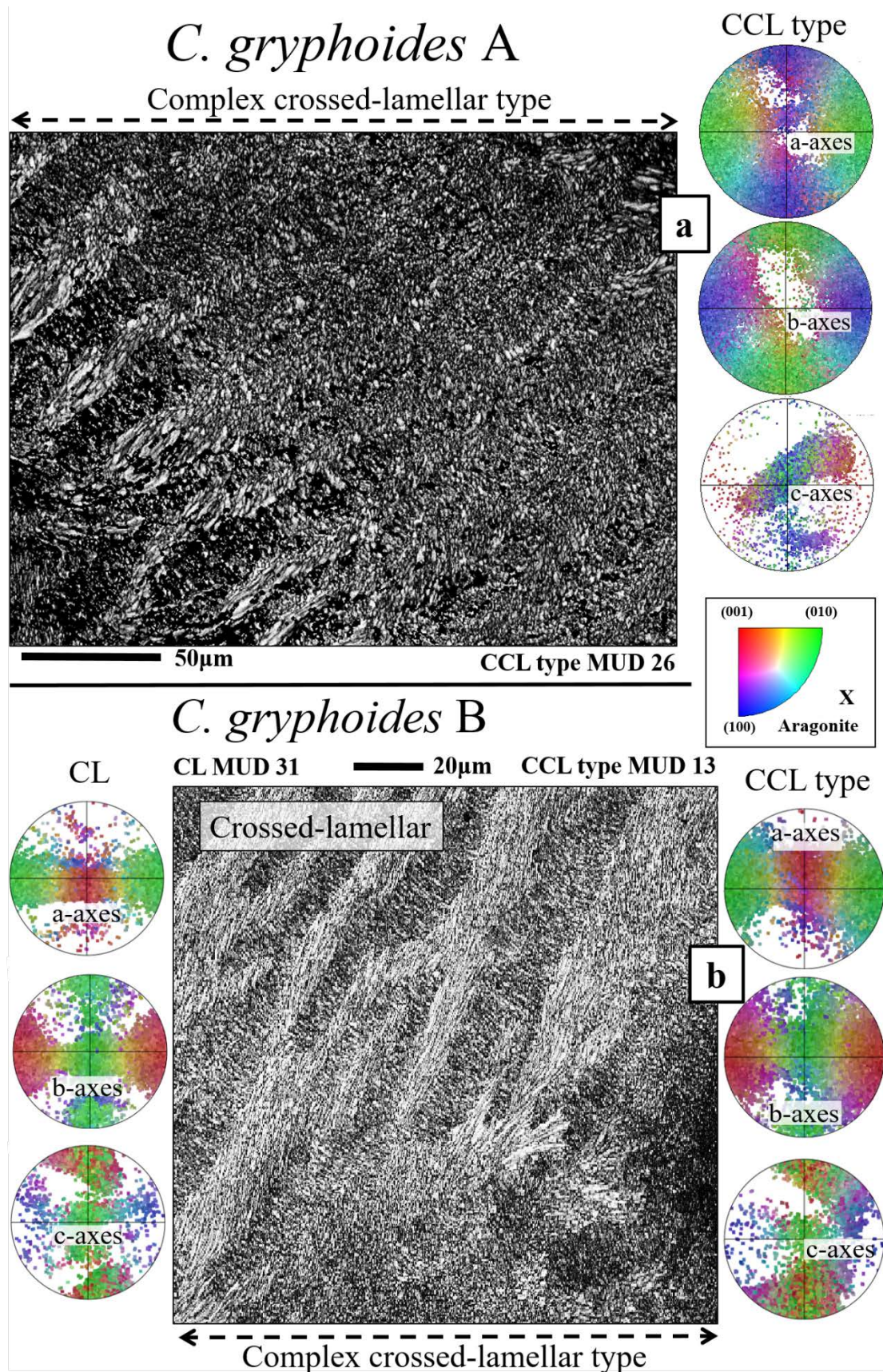


Figure 2.1-AP11. EBSD band contrast images displaying the microstructure of the complex crossed-lamellar (CCL) type layer for different shells of *Chama gryphoides* sectioned obliquely (cut B). The complex crossed-lamellar layer comprises first-order-lamellar blocks arranged in a complex pattern (a) and has a rather smooth changeover into the complex crossed-lamellar layer (b). The texture is shown by the pole figures indicating individual data points of the crystal orientations for the respective layers.

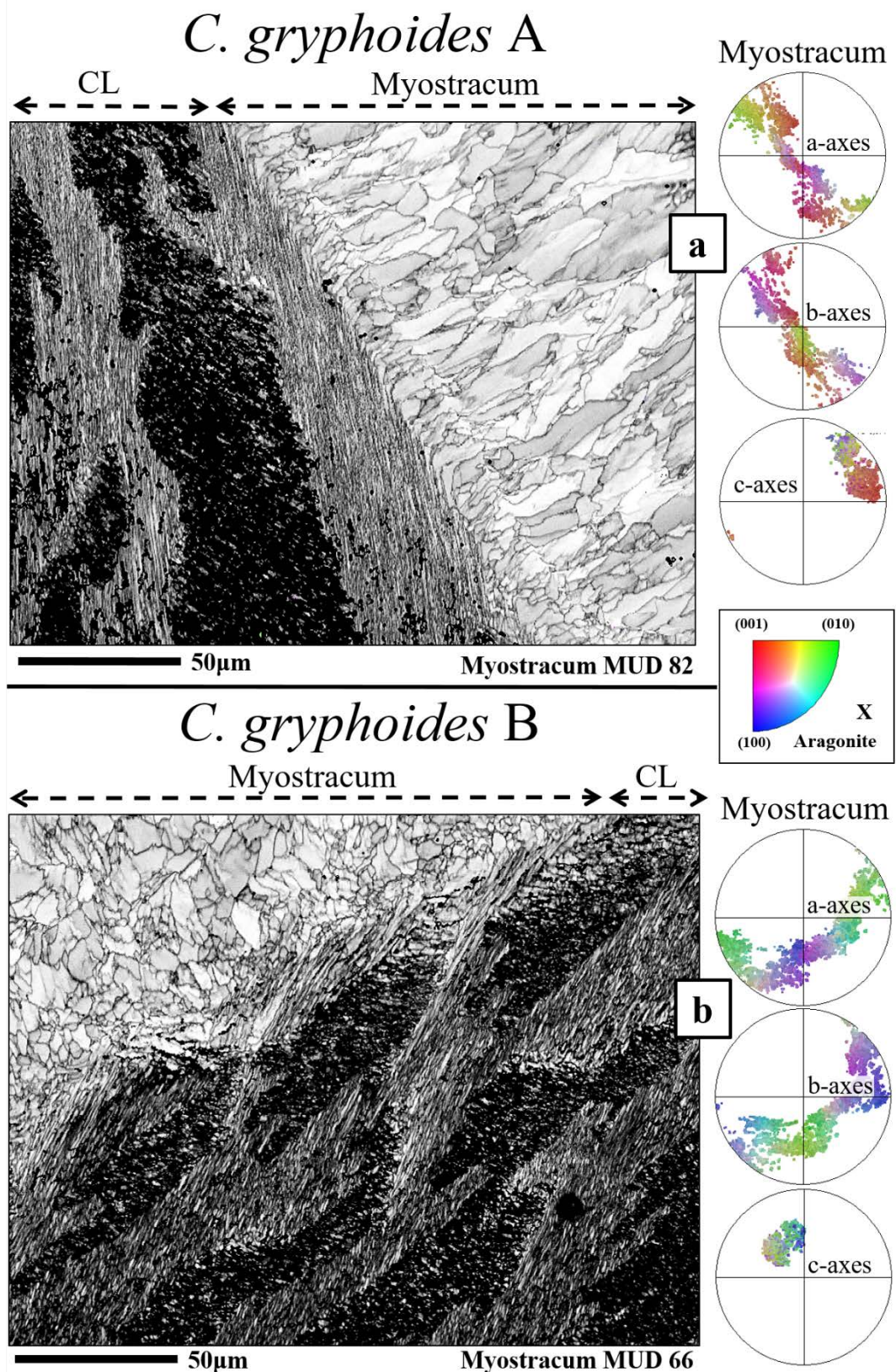


Figure 2.1-API2. EBSD band contrast images depicting the interfaces between the crossed-lamellar layer (CL) and the adductor myostracum observed for the two obliquely sectioned (cut B) *Chama gryphoides* shells. The crystals within the crossed-lamellar layer are small and prismatic, while the competitively grown myostracum crystals get increasingly large towards the inner shell surface (a, b). The pole figures display the individual data points of the crystal orientations for the myostracum sections that show an axial texture. The double maxima for the c-axis orientations are a relic of the crossed-lamellar crystal orientation pattern and the a- and b-axis orientations scatter significantly (a, b).

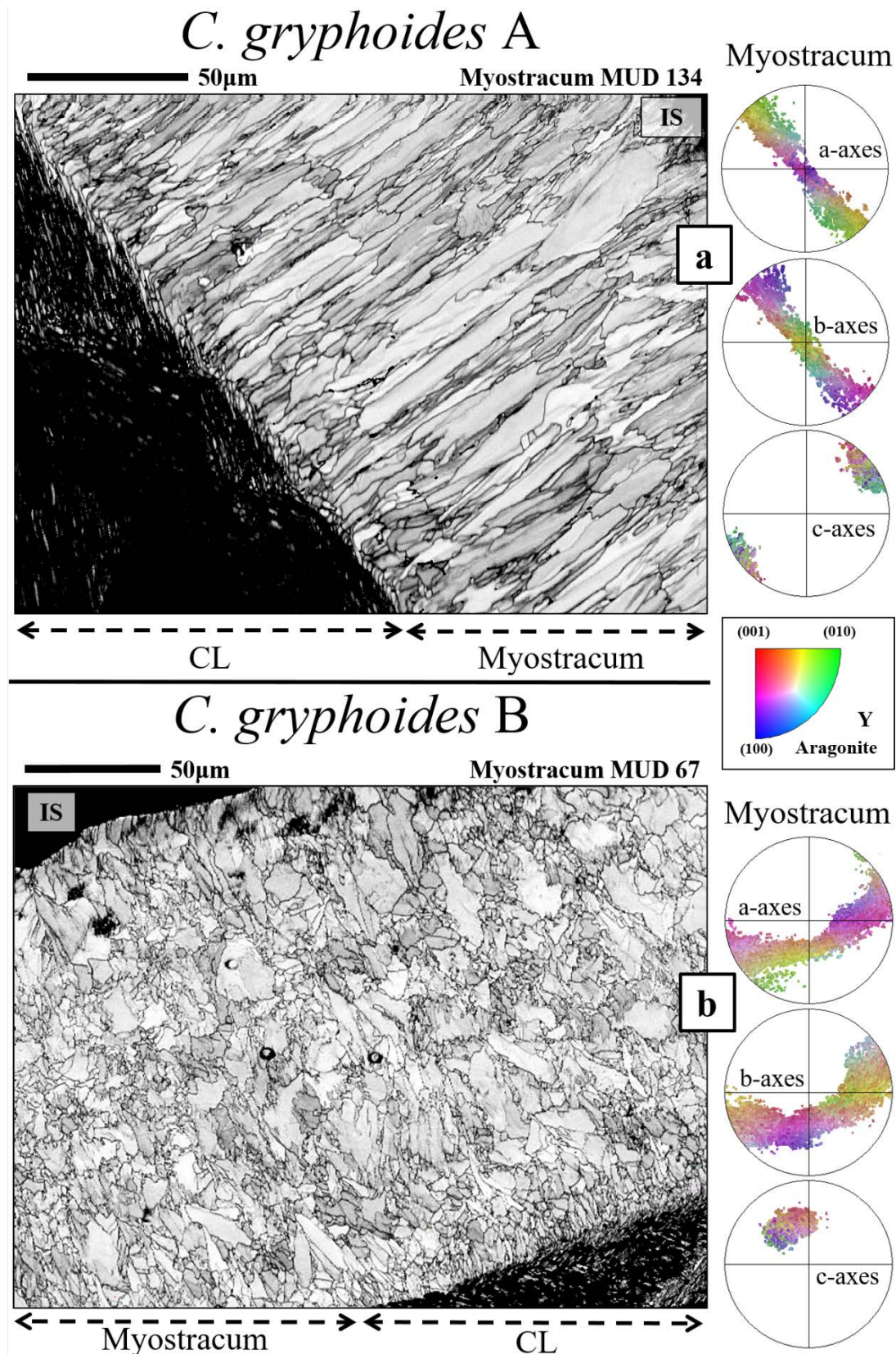


Figure 2.1-AP13. EBSD band contrast images depicting the microstructures of adductor myostraca observed for the applied cut B of two *Chama gryphoides* shells. Due to slightly deviating cutting directions between the two shells, the exposed microstructures depict different crystal morphologies. The crystals of the first shell are prismatic, the EBSD map exemplifies that their grain boundaries appear irregular and disorganized (a). In the second shell, the scan illustrates the irregular grain morphologies of the myostracum crystals (b). The illustrated microstructure of the myostracum in both scans (a, b) results from the competitive growth prevailing towards the inner shell surface (IS). The pole figures display the individual data points of the crystal orientations for both myostracum layers that show an axial texture.

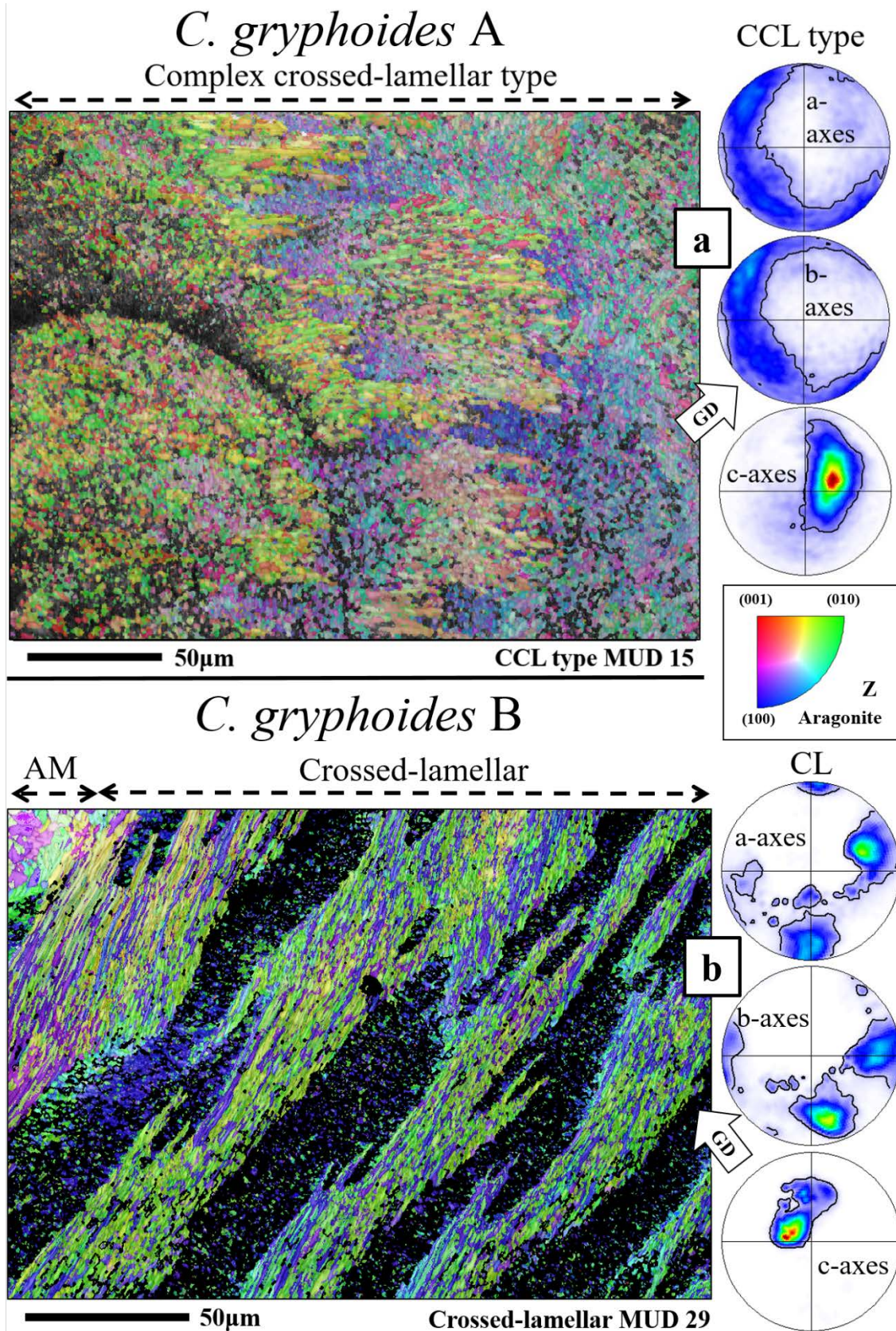


Figure 2.1-AP14. EBSD band contrast images depicting changeovers observed for the applied cut B of two *Chama gryphoides* shells. The first scan depicts the microstructure of the complex crossed-lamellar (CCL) type layer (a). In the second shell, the scan illustrates the microstructure of the crossed-lamellar shell and its changeover into the adductor myostracum (b). The pole figures display the orientational probability density distribution in the CCL type and the crossed-lamellar layers. The CCL type layer has an axial texture (a), and the complex crossed-lamellar layer shows a 3D “single-crystal-like” texture. The growth direction (GD) of each scan is indicated with a white arrow.

2.2 CRYSTAL ORGANISATION AND MATERIAL PROPERTIES OF *CHAMA* AND *GLYCYMERIS* MYOSTRACA AND SHELLS

Sebastian Hoerl^{1,*}, T. le Moine¹, N.J. Peter², S. Amini³, E. Griesshaber¹, J. Wang², E. M. Harper⁴, C. Salas⁵, A. G. Checa^{6,7}, R. Schwaiger², W. W. Schmahl¹

1. Department of Geo- and Environmental Sciences, Ludwig-Maximilians-Universität München, Germany

2. Institute of Energy and Climate Research, IEK-2: Microstructure and Properties of Materials,
Forschungszentrum Jülich GmbH, Jülich, Germany

3. Max Planck Institute of Colloids and Interfaces, Department of Biomaterials, Potsdam, Germany

4. Department of Earth Sciences, University of Cambridge, Downing Street, Cambridge CB2 3EQ, UK

5. Departamento Biología Animal, Facultad de Ciencias, Universidad de Málaga, Málaga, Spain

6. Instituto Andaluz de Ciencias de la Tierra, CSIC-Universidad de Granada, Armilla, Spain

7. Departamento de Estratigrafía y Paleontología, Universidad de Granada, Granada, Spain

Materialia 2024, 36, 102149.

<https://doi.org/10.1016/j.mtla.2024.102149>

Abstract

Movement of bivalve hard and soft tissue requires muscular action. Despite diverse bivalve lifestyles and living environments, the myostracum, a specific hard tissue formed where muscles attach to the shell, appears similar in structure for species of many bivalve orders. We investigated myostracal and non-myostracal, valve, microstructure, texture and material properties of Chamidae and Glycymerididae species with electron-backscatter-diffraction, laser-confocal and backscatter electron imaging and nanoindentation testing. Chamidae and Glycymerididae follow different lifestyles and live in distinct environments. Chamidae are cemented to substrate and live in wave-swept, shallow, waters. Glycymerididae dwell in calm water and burrow into sandy/muddy sediment.

We found that myostracal aragonite of all investigated species has a crystal assembly pattern that reflects crystal growth through growth competition. Aragonite is extensively twinned in the myostracum and non-myostracal, valve, layers, not in the calcitic ornamentation. For myostracal aragonite, we found cyclic twinning, for non-myostracal aragonite the twinning was polysynthetic or polycyclic. We show how twinning and crystallographic texture are transmitted between myostracal and non-myostracal, valve, layers. Relative to non-biological aragonite, myostracal and non-myostracal, valve, indentation elastic modulus is reduced by 10-15% and 15-20%, respectively; myostracal and valve hardness is increased by 15-20% and 5-10%, respectively. Comparing modulus and hardness between aragonitic microstructures, we found that, relative to other microstructures, myostracal modulus is increased by 5% and myostracal hardness by 15%. Hence, the myostracal material shows a

unique and specific microstructure, texture, modulus, and hardness that might be necessary for muscle attachment to enable the lifestyle-controlled requirements posed onto the organism.

Keywords

Myostracum/muscle scar; biomaterials; EBSD; microstructure/texture; nanoindentation; bivalves

2.2.1 INTRODUCTION

Biomineralised tissues are important for understanding the relationship between crystal organisation and properties of materials (e.g. Chen *et al.*, 2012; Raut *et al.*, 2020; Mohammadi *et al.*, 2021; Zhao *et al.*, 2022). Through hundreds of millions of years of natural selection, organisms developed targeted hard- and soft-tissue microstructures and fabrics for purposes such as adherence, motion, locomotion, vision, protection and many more. Called forth by many different lifestyles, derived adaptations of biomaterials were the consequence. These enabled survival in a wide range of habitats (e.g. Stanley, 1975; Brom and Szopa, 2016; Chen *et al.*, 2019).

Of particular interest are the hard tissues of shelled organisms, e.g. molluscs and brachiopods. These are, in most cases, multi-layered and the different shell layers have different modes of crystal organization. Deciphering the arrangement pattern of the crystals and understanding their formation mechanism is of main interest, not only for understanding the diversity of biomaterial generation principles but also as a source of information for the construction of man-made materials with targeted tissue properties (Alves *et al.* 2010; Studart 2012; Yao *et al.* 2017; Venier *et al.* 2019; Tang *et al.* 2021; Wang *et al.* 2021; Zhang *et al.* 2021).

Bivalve shells consist of calcium carbonate crystals that are embedded into an organic matrix of proteins, lipids and polysaccharides. Depending on the shell structure, the fraction of organic substance varies in proportion to the total shell weight (usually 0.1-5 mass %) and amino acid composition (Nakahara *et al.* 1980; Rosenberg & Hughes 1991; Kobayashi & Samata 2006). Bivalve shells often comprise both main carbonate polymorphs, aragonite and calcite, however, never mix them in a single morphological type of shell microstructure. The most widespread bivalve shell microstructure is the crossed-lamellar arrangement of aragonite biocrystals. The nacreous and columnar crystal assemblies are often utilized, but significantly less widespread. Due to the mode of crystal and organic substance organization, the latter three microstructures are well known for their ability to stop crack development and progression and to promote crack deflection within the hard tissue (Currey & Kohn 1976; Z. Huang *et al.* 2014; Almagro *et al.* 2016a; Chan *et al.* 2022).

Bivalves attach their mantle and organs to the shell via muscles: the foot attaches with the pedal, the mantle with the pallial and adductor, and the gill with the retractor muscles (Ponder et al. 2019). At muscle attachment sites a specific layer of carbonate crystals is deposited, referred to as the myostracum. The latter consists solely of aragonite and has a prominent microstructure and texture that is distinct from the other layers of the shell (Taylor et al. 1969; Liao et al. 2015; Crippa et al. 2020b; Crippa et al. 2020a; Castro-Claros et al. 2021). Myostraca can be found within the shell, between the inner and outer shell layers, or as patches along the inner shell surface.

The overall aim of the study presented here is to describe and discuss valve and myostracum microstructures, textures and material property characteristics for Chamidae (order Venerida) and Glycymerididae (order Arcida) shells. We choose animals that belong to different bivalve genera, form thick, but differently-sized shells, live in different habitats and follow distinct lifestyles. *Glycymeris* and *Chama* are abundant in many seas and oceans (Thomas 1975; Vance 1978). *Glycymeris* forms large aragonitic shells (Oliver & Holmes 2006; Carter 2008) that can reach more than 10 cm in diameter (Pope & Goto 1993). Glycymerididae live in turbid, calm, fairly shallow marine environments (up to 200 m) and use their siphonal openings and valves to burrow into the sediment (Thomas 1978; Legac & Hrs-Brenko 1999). With their circular shape and lack of a functional byssus, the shells are perfectly adapted for anterior-posterior rocking locomotion, which is the mode of movement used to traverse the substrate (Thomas 1978; Oliver & Holmes 2006; Koller-Hodac et al. 2010). Chamidae are found in warm, tidal, wave-swept marine environments and live within the upper 30 m of the water column (Krylova 2006). *Chama* bivalves are sedentary; for protection, they form thick, aragonitic, circular shells that are 3-5 cm in diameter (Bernard 1976; Skinner & Weicker 1992). Most *Chama* species form wholly aragonitic shells (Kennedy et al. 1969; Kennedy et al. 1970), however, some species form an outer shell layer that consists of rows of pointy calcitic ornamentations (Yonge 1967; Matsukuma et al. 1997). The valves of juveniles are symmetrical to one another, in contrast to the shells of adult animals (Yonge 1967; Allen 1976). The loss of symmetry of the two valves with increasing age is due to an enlarged umbonal region in the left valve and is called forth by the attachment (Yonge 1967; Allen 1976). Adult *Chama* individuals have large, particularly elongated adductor muscles (Kennedy et al. 1970). These induce and regulate rapid and prolonged closure of the valves and are, obviously, necessary, as the ligament of Chamidae is very weak (Nicol 1952; Allen 1976; Berezovsky 2021).

By using electron backscatter diffraction (EBSD), field emission scanning electron microscopy (FE-SEM), laser confocal imaging and depth-sensing nanoindentation, we characterise shell and myostracum microstructure, texture, hardness and indentation elastic modulus of *Chama* and *Glycymeris* shells. We place particular interest in understanding the structural and material property characteristics of myostraca and the changeover from the non-myostracal, valve, to myostracal microstructures and textures. We investigated the structural characteristics of two myostraca, the adductor myostracum and the pallial myostracum. We discuss first (i) whether the difference in habitat

and lifestyle causes significant differences in non-myostracal valve and myostracum microstructure, texture and material properties. Subsequently (ii), we investigate whether valve activity, coordinated by muscle contraction and release, initiates differences in microstructure and texture of the myostracum at adductor muscle attachment sites. Different bivalve lifestyles, such as cementation to substrate, reclining on substrate surface, burrowing into muddy sediment or active swimming rely on differences in valve movement speed as well as strength and duration of valve closure and opening. At last, (iii) we discuss whether variation in valve action affects myostracal hard tissue microstructure, texture and material properties.

2.2.2 MATERIALS AND METHODS

Materials

We investigated two *Chama* and three *Glycymeris* species, *Chama arcana*, *Chama gryphoides* and *Glycymeris bimaculata*, *Glycymeris nummaria* and *Glycymeris pilosa*, respectively. Care was taken that all investigated specimens were shells of adult organisms. Specimens of *G. bimaculata* were provided by the Bavarian State Collection of Zoology (ZSM) and *G. pilosa* was sampled in the Pasman channel, Adriatic Sea. Specimens of *G. nummaria* were collected from infralittoral environments close to Benalmádena (Málaga, Spain). *C. arcana* was sampled near Newport Beach, CA, USA, and obtained from collections of the Natural History Museum (London, UK).

Sample preparation for electron backscatter diffraction (EBSD) measurements, field emission scanning electron microscopy (FE-SEM), and laser confocal microscope imaging

Figures 2.2-AP1 to 2.2-AP5 indicate the cuts through the shell and the sites where EBSD maps were taken. For all investigated species, the cut through the shell crossed the adductor myostracum, often, the pallial myostracum and the surrounding shell layers. *G. bimaculata*, *G. nummaria* and *G. pilosa* shells were cut in oblique and transverse directions. The shell of *C. arcana* was cut perpendicular to the hinge. The shell of *C. gryphoides* was cut transversely through the sites of both, anterior and posterior adductor muscles. The obtained shell pieces were embedded into EPON epoxy resin and were subjected to several mechanical grinding and polishing steps. The final polishing step consisted of etch-polishing with colloidal alumina (particle size $\sim 0.06 \mu\text{m}$) in a vibratory polisher. Samples were coated with 4–6 nm of carbon for EBSD analysis, with 5 nm Pt/Pd for SEM imaging. For laser confocal imaging and nanoindentation testing, sample surfaces were not coated.

SE, BSE imaging and EBSD measurements were carried out with a Hitachi SU5000 field emission SEM, equipped with an Oxford Instruments NordlyNano EBSD detector and an X-Max 80x80 EDS detector. EBSD scans were taken at 20 kV and were performed with a step size of 200 to 450 nm.

For indexing the aragonite EBSD patterns the unit cell setting: $a_0 = 4.9614(3) \text{ \AA}$, $b_0 = 7.9671(4) \text{ \AA}$, $c_0 = 5.7404(4) \text{ \AA}$ was used. EBSD data were evaluated with the Oxford Instruments AZtecCrystal 3.0 and HKL Channel 5.0 softwares and are presented as colour-coded crystal orientation maps, corresponding band contrast measurement maps and corresponding pole figures presenting individual orientation data points or their density distributions.

For a comprehensive understanding of non-myostracal shell and myostracum microstructure, samples were scanned with many EBSD measurements. On *G. nummaria* and *G. bimaculata* shells, we measured, for each species, 15 EBSD maps. *G. pilosa* shells were mapped with 5 measurements, on *C. arcana* and *C. gryphoides* shells we conducted, on each shell, more than 20 measurements.

Nanoindentation testing

Nanoindentation measurements were conducted on *G. bimaculata* and *G. nummaria* using an MTS Nano Indenter XP (Nano instruments, USA), and on *C. arcana*, geological aragonite and geological calcite using a Nanoindenter G200X (KLA, USA) at Institute for Energy- and Climate Research (IEK-2), Forschungszentrum Jülich GmbH, Jülich, Germany, equipped with a standard diamond Berkovich tip (indentation elastic modulus 1141 GPa, Poisson's ratio 0.07). Before each set of experiments, the tip area function and the frame stiffness were calibrated using a standard reference material, i.e., fused silica (indentation elastic modulus 72.12 GPa, Poisson's ratio 0.179). The quasi-static method was used at a constant indentation strain rate of 0.05 s^{-1} , and the peak holding time was 10 s for each test at a maximum depth of $\sim 300 \text{ nm}$ (XP) or a maximum load of $\sim 9 \text{ mN}$ (G200X) corresponding to a maximum depth of around 300 nm as well. The drift was determined at 90% of the unloading segment (10 % of the maximum load) during unloading for a drift correction. The indentation elastic modulus and the hardness values were determined via the unloading curve according to the Oliver-Pharr method (Anstis et al. 1981; Oliver & Pharr 1992). The *C. gryphoides* samples were tested using a Triboindenter TI-950 nanomechanical tester, Hysitron, USA at the Department of Biomaterials, Max-Planck Institute of Colloids and Interfaces, Potsdam, Germany. A load function of 5s-2s-5s (loading-holding-unloading) with a peak force of 1.2 mN and a holding time of 2 seconds at maximum load was applied at each measurement.

An in-depth terminology of the structural terms used in this work can be found in Appendix Section A.1 of this thesis.

2.2.3 RESULTS

This study details the structural and material property characteristics of *Glycymeris* and *Chama* shells. We describe first the microstructure and texture of the valves (without the myostracal layers and patches) and that of the ornamentations (Figs. 2.2-1 to 2.2-3, 2.2-AP6 to 2.2-AP8). Subsequently, we

describe structural characteristics of adductor and pallial myostraca (Figs. 2.2-4, 2.2-5, 2.2-AP9, 2.2-AP10) and the changeover between valve and myostracal layers (Figs. 2.2-6 to 2.2-8, 2.2-AP11 to 2.2-AP13). At last, we present specific structural and nanomechanical properties of *Glycymeris* and *Chama* valve and myostracal hard tissues, such as the presence and distribution of twinned aragonite and discuss hardness and indentation elastic modulus properties of the valves and of the myostraca (Figs. 2.2-9 to 2.2-12, 2.2-AP14 to 2.2-AP19). For a comprehensive visualisation of the observed microstructures, each colour-coded crystal orientation map (Figs. 2.2-1 to 2.2-10) is complemented with the corresponding, grey-scaled, band contrast measurement map given in the Supplementary Information (Figs. 2.2-AP6 to 2.2-AP13). Aragonite and calcite textures are shown with pole figures (Figs. 1 to 10 give the contoured version of orientation data, and Figs. 2.2-AP6 to 2.2-AP13 give orientation data points).

Irrespective of the myostraca (adductor, pallial), the valves of the investigated *Glycymeris* species comprise *two layers*. The investigated *Chama* species construct their valves with *three layers*, including the ornamentation layer. Myostraca are considered to be additional layers to those of the non-myostracal valves. For all investigated species, the mode of crystal arrangement varies significantly for the different shell layers.

Figures 2.2-1 and 2.2-AP6 visualise *Glycymeris* shell microstructure in the complex crossed-lamellar (inner shell layer) and the crossed-lamellar layer (outer shell layer), respectively. The complex crossed-lamellar layer (Fig. 2.2-1a) exhibits an intricate crystal orientation pattern consisting of numerous, differently oriented, clusters/entities/blocks formed of small, rather granular to prismatic crystals. As the colour-coded EBSD map (Fig. 2.2-1a) shows, these crystal entities/blocks vary considerably, to some degree randomly, in orientation. The crossed-lamellar layer (Fig. 2.2-1b) consists of assemblies of small, lath-shaped, crystals organised into first-order lamellae. A first-order lamella comprises a set of crystallographic orientations. Crystals within the set1 lamella have an opposing inclination to the crystals of the set2 lamella (e.g. Crippa *et al.*, 2020b; Crippa *et al.*, 2020a). In *Glycymeris* shells, the first-order lamellae run almost perpendicular to the inner shell surface and growth lines (Figs. 2.2-1b, 2.2-AP6b). This is not the case for the investigated *Chama* shells (Fig. 2.2-2a).

The shells of *Glycymeris bimaculata*, *Glycymeris nummaria* and *Glycymeris pilosa* consist entirely of aragonite. The shell of *Chama arcana* is formed of aragonite and calcite. The ornamentations of *C. arcana* are calcitic, the layers of the shell are aragonitic. The shell and ornamentation of *Chama gryphoides* are solely aragonitic.

Irrespective of the myostraca (adductor, pallial), the valves of the investigated *Glycymeris* species comprise *two layers*. The investigated *Chama* species construct their valves with *three layers*, including the ornamentation layer. Myostraca are considered to be additional layers to those of the non-myostracal valves. For all investigated species, the mode of crystal arrangement varies significantly for the different shell layers.

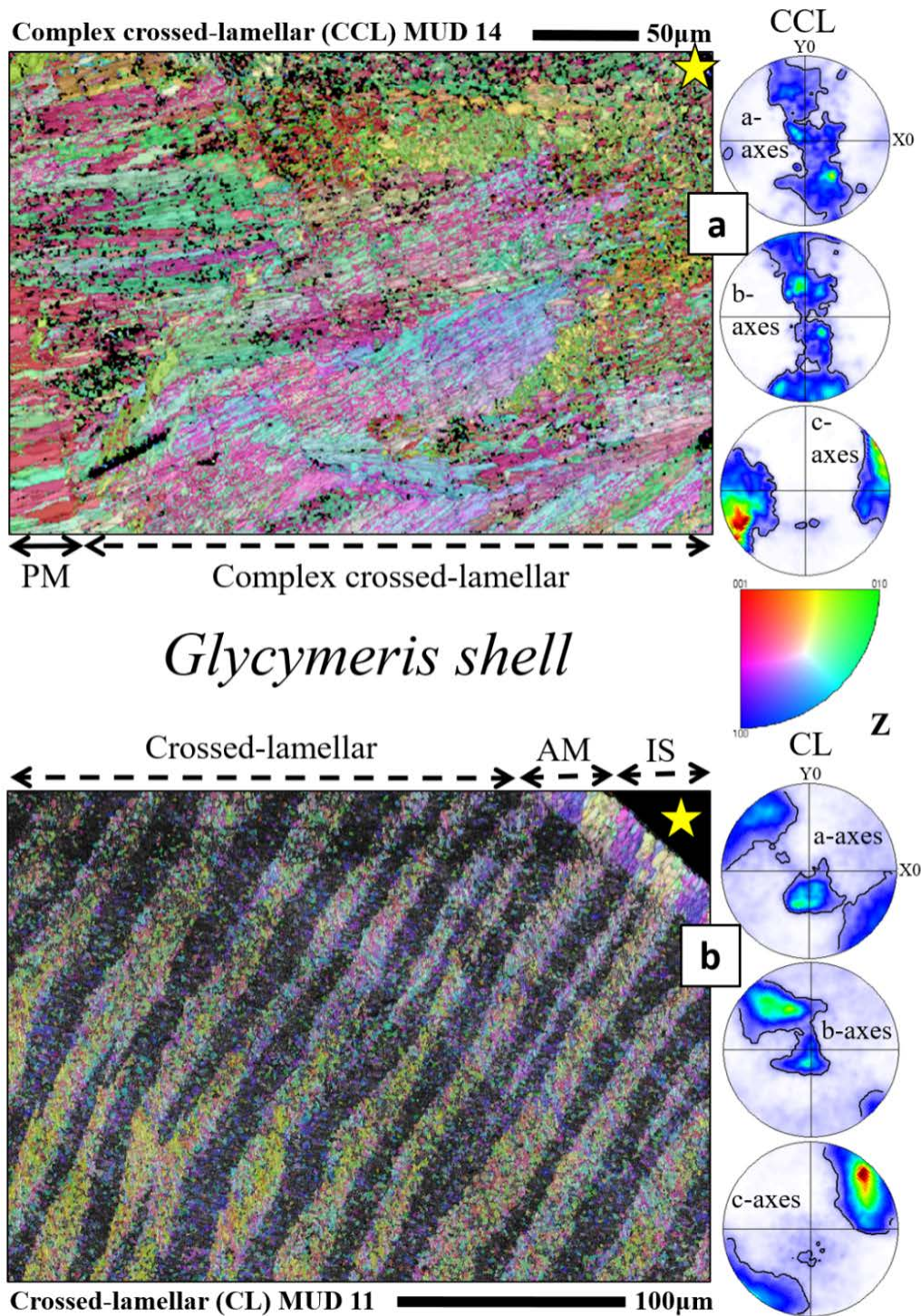


Fig. 2.2-1. EBSD scans depicting the different microstructures of non-myostracal *Glycymeris* shells. (a): a transversely (a) and (b) an obliquely sectioned shell of *G. bimaculata*. IS: inner shell surface, AM: adductor myostracum, PM: pallial myostracum, CCL: complex crossed-lamellar, CL: crossed-lamellar, yellow star in (a) and (b): inner shell surface. From the outer towards the inner shell surface, *Glycymeris* shells comprise a crossed-lamellar (CL), the myostracal (PM = pallial myostracum) and the complex crossed-lamellar shell layer (CCL). The complex crossed-lamellar layer (a) consists of differently oriented clusters/blocks of small prisms and fibres. The crossed-lamellar layer (b) consists of arrays of first-order lamella, with each first-order lamella formed of two sets of lamella (b); the sets are inclined to each other. In *Glycymeris* the first-order lamellae run perpendicular to inner shell surface (b). The pole figures indicate the acquisition coordinate systems and show the orientational probability density distribution for the complex crossed-lamellar (a) and the crossed-lamellar sections (b), respectively. We observe a 3D “single-crystal-like” texture. However, in comparison to the complex crossed-lamellar valve portion, the 3D “single-crystal-like” texture is significantly better developed for the crossed-lamellar layer.

Figures 2.2-1 and 2.2-AP6 visualise *Glycymeris* shell microstructure in the complex crossed-lamellar (inner shell layer) and the crossed-lamellar layer (outer shell layer), respectively. The complex crossed-lamellar layer (Fig. 2.2-1a) exhibits an intricate crystal orientation pattern consisting of numerous, differently oriented, clusters/entities/blocks formed of small, rather granular to prismatic crystals. As the colour-coded EBSD map (Fig. 2.2-1a) shows, these crystal entities/blocks vary considerably, to some degree randomly, in orientation. The crossed-lamellar layer (Fig. 2.2-1b) consists of assemblies of small, lath-shaped, crystals organised into first-order lamellae. A first-order lamella comprises a set of crystallographic orientations. Crystals within the set1 lamella have an opposing inclination to the crystals of the set2 lamella (e.g. Crippa *et al.*, 2020b; Crippa *et al.*, 2020a). In *Glycymeris* shells, the first-order lamellae run almost perpendicular to the inner shell surface and growth lines (Figs. 2.2-1b, 2.2-AP6b). This is not the case for the investigated *Chama* shells (Fig. 2.2-2a).

Chama shells are formed of three layers (Figs. 2.2-2, 2.2-3, 2.2-AP7, 2.2-AP8). For *C. arcana* we observed complex crossed-lamellar aragonite at inner and crossed-lamellar aragonite at outer shell portions (Figs. 2.2-2, 2.2-AP7). The outermost layer is calcitic and its surface is covered by rows of calcitic ornamentations (Figs. 2.2-3, 2.2-AP8). The crossed-lamellar microstructure of *Chama* (Figs. 2.2-2a, 2.2-AP7a) comes close to the crossed-lamellar crystal arrangement of *Glycymeris* shells. In *Chama* as well, crossed-lamellar aragonite is formed of first-order lamellae that comprise two sets of lamella that are arranged at an angle to each other. The two sets of first-order lamellae consist of minute, lath-shaped crystals. Carter (1990) described different types of crossed-lamellar arrangements and suggested that interlacing of first-order lamellae is always given in crossed-lamellar microstructures. When we compared the degree of interlacing between the crossed-lamellar shell of *Glycymeris* and that of *Chama*, we found that, in contrast to *Glycymeris*, in *Chama* shells adjacent lamellae are rarely parallel to each other and more strongly interlaced (compare Figs. 2.2-1b and 2.2-2a). To our opinion, this is not due to a cut effect as, to trace the topological relation of the two sets of a first-order lamella, we sectioned *Chama* shells in different directions and scanned them with EBSD.

The shell of *C. gryphoides* is entirely aragonitic. We found a layer of complex crossed-lamellar aragonite at the innermost shell sections. Adjacent to the latter, towards the outer shell surface, crossed-lamellar aragonite is developed for this *Chama* species as well with, as it is the case for *C. arcana* shells, the set1 and the set2 lamellae being rather interlaced. The outermost shell layer and ornamentation of *C. gryphoides* shells is formed of granular aragonite (e.g., Fig. 2.2-2b) that, only in some instances, comprises differently oriented aragonite clusters/entities. Hence, the microstructure of the outermost shell and ornamentation of *C. gryphoides* resembles, only to some extent, the complex crossed-lamellar arrangement pattern of crystals in the investigated *Glycymeris* and *C. arcana* shells. (Figs. 2.2-2b, 2.2-AP7b). We addressed the latter microstructure as a complex crossed-lamellar type structure that occurs at outer shell layers. According to Taylor *et al.* (1969) and Kennedy *et al.* (1970), the complex crossed-lamellar microstructure for *Chama* and *Glycymeris* is only present at inner valve sections.

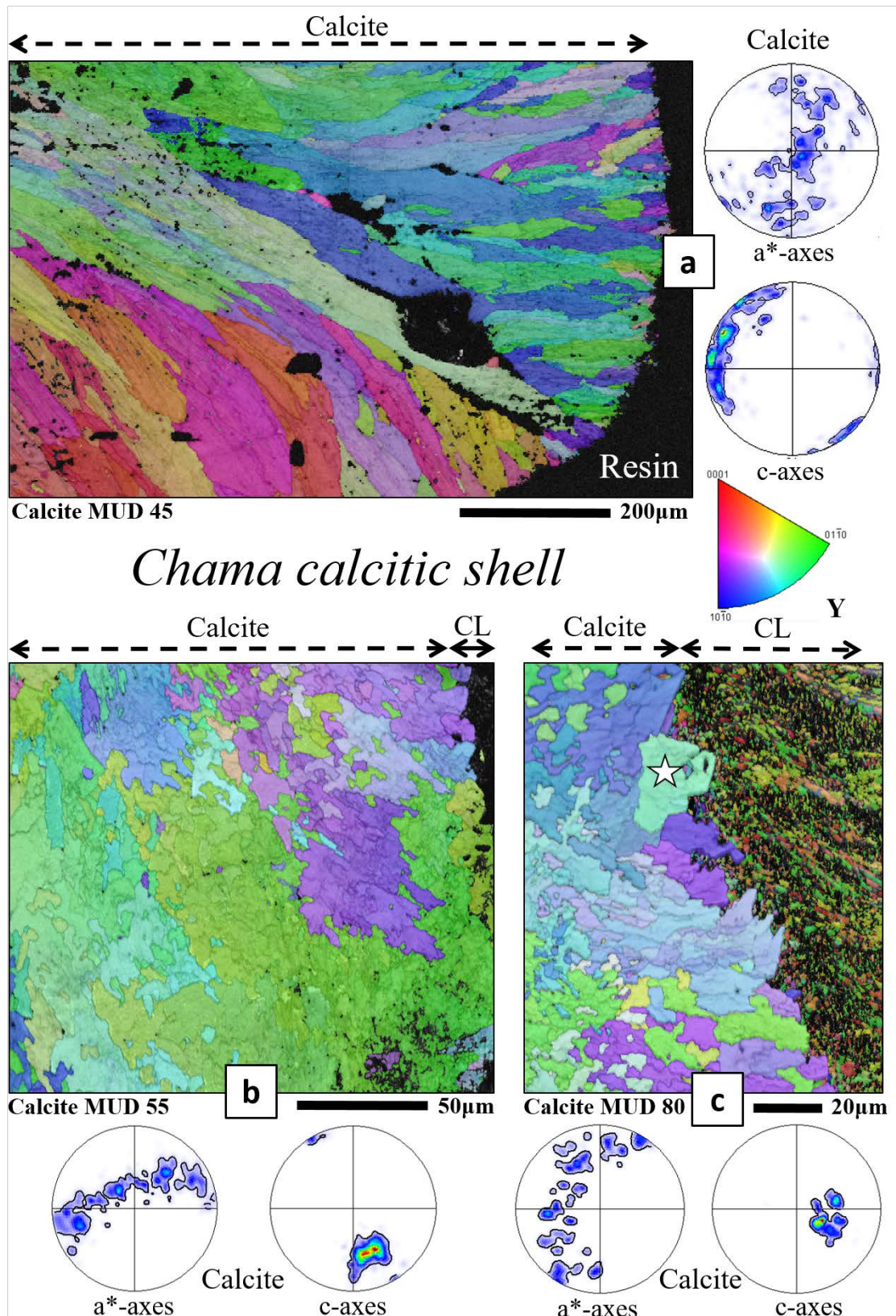


Fig. 2.2-3. EBSD scans depicting the **microstructure of the calcitic ornamentation of *Chama* shells**. The calcitic ornamentations of *C. arcana* comprise large crystal clusters with the calcite c-axis being perpendicular to the ornamentation surface (a). Within the ornamentation, the calcitic crystals interconnect in a complex mode in 3D (b, c). Towards the inner shell, the calcite crystals are interconnected in a complex way with the aragonitic crossed-lamellar layer (CL). The calcite crystals have rhombohedral, idiomorphic, crystal morphologies (b, c). Pole figures show the orientational probability density distribution for the crystals shown in the corresponding EBSD maps and illustrate that ornamentation calcite has an axial (fibre) texture.

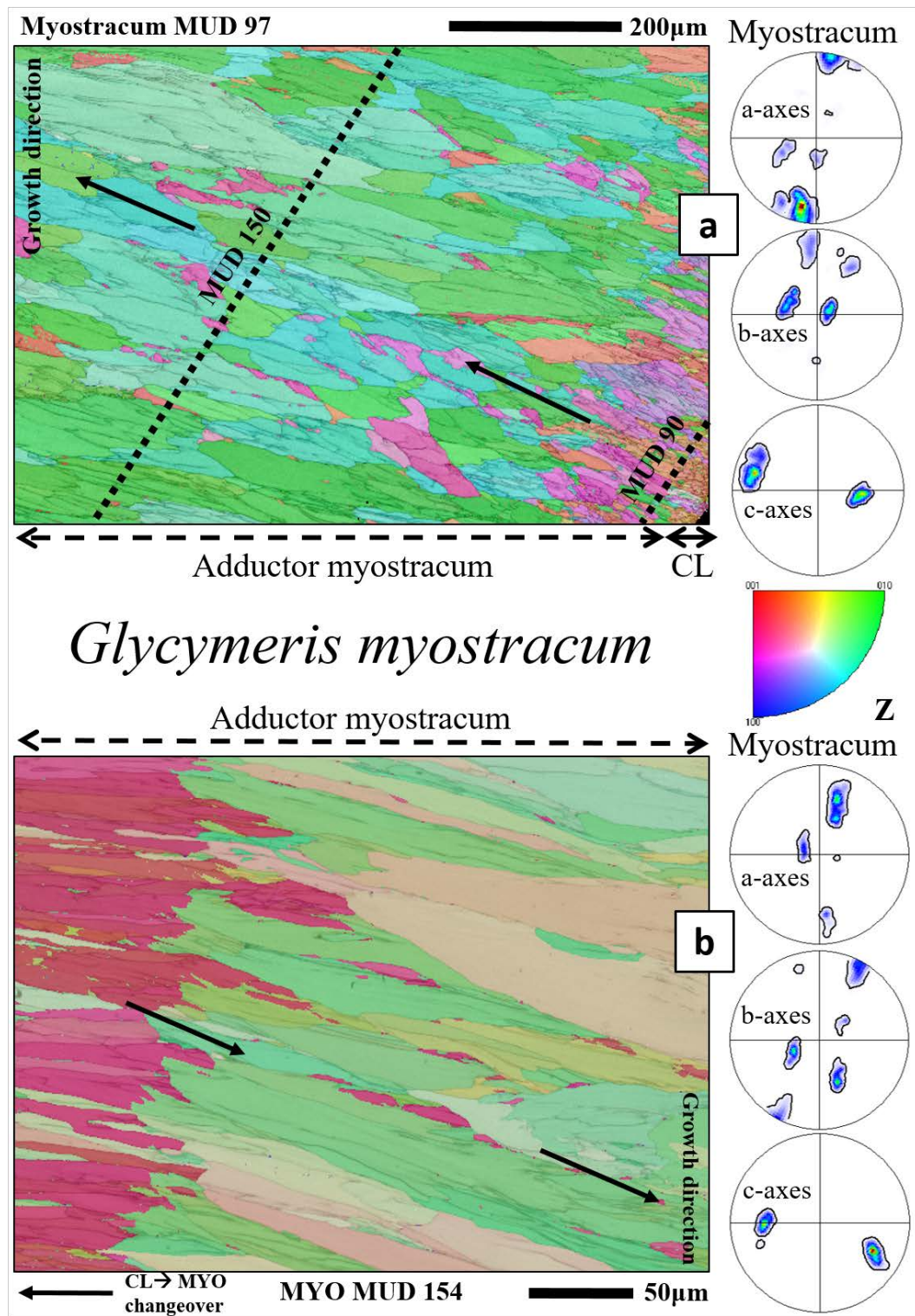


Fig. 2.2-4. EBSD scans visualizing the **microstructure of the adductor myostracum in *Glycymeris* shells**. Visible in (a) is the competitively grown microstructure of *G. bimaculata* adductor myostracum and the interface between myostracal to the crossed-lamellar valve layer (CL). Myostracal crystals close to the crossed-lamellar shell are minute to small (average grain size 25 μm) and isotropic in shape (a). As implied by the MUD values of different subsets, the crystal co-orientation increases towards the inner shell surface. (a). The crystals become larger and assume prismatic shapes towards the growth direction indicated by black arrows (a, b). The second EBSD map depicts the microstructure of the adductor myostracum in *G. nummaria* (b). It features an assembly of large myostracal prisms and a sharp boundary in crystal orientation (b). Pole figures depict the orientational probability density distribution for the respective myostracal layers and show a 3D “single-crystal-like” texture.

For *Glycymeris* and the aragonitic microstructures of the investigated *Chama* species, we found a smooth transition from the crystal orientation pattern of one shell layer into the other. Hence, there is a continuity of aragonite crystal crystallographic axes from one aragonitic microstructure to the other (e.g., Figs. 2.2-1a, b, 2.2-2a). However, we did not observe a smooth transition between calcitic ornamental structures and the aragonitic shell in *C. arcana* (Fig. 2.2-AP4c, 2.2-AP5a, b). In the latter, the calcite of the ornamentation is separated from the aragonitic layers by a thick, layered, organic deposit (grey sheet in Fig. 2.2-AP5b).

The microstructure of the ornamentation ribs of *C. arcana* is very specific and different to the microstructures of the other shell layers (Figs. 2.2-3, 2.2-AP8). We observed a gradual increase in crystal size away from the outer surface of the ornamentation ribs. Hence, the largest crystals of the ornamentation ribs are adjacent to the crossed-lamellar shell layer. We find that calcite c-axes are perpendicular to the outer surface of the ornamentation; they rotate with the curvature of its outer shell surface (Figs. 2.2-3a, 2.2-AP8a). Most interesting is the habitus of crystals that form the ornamentation ribs as well as the nature of their interlinkage (Figs. 2.2-3b, c, 2.2-AP8b, c). The crystals or crystal units have highly fractal morphologies and interlock strongly in 3D (Figs. 2.2-3b, c, 2.2-AP8b, c). In addition, we observed calcite crystals with idiomorphic morphologies in the biologically secreted ornamentation (white star in Fig. 2.2-3c, black star in Fig. 2.2-AP8c and Hoerl et al. (2024a)). The structural characteristics that we found for *Chama* ornamentation ribs are rarely observed for biologically secreted hard tissues and convey some information on the formation process of the ornamentation calcite. Biocarbonate crystals with dendritic-fractal morphologies and the crystals interdigitating strongly in 3D have so far been observed for brachiopod primary shell layer calcite (Goetz et al. 2011) and rotaliid foraminifera shell calcite (Lastam et al. 2023a).

Figures 2.2-4 to 2.2-8 and Supplementary Figures 2.2-AP9 to 2.2-AP13 visualise the microstructure and texture of adductor and pallial myostraca as well as topological characteristics at the changeover of the non-myostracal, valve, structures (crossed-lamellar, complex crossed-lamellar microstructure) to that of the myostraca. In comparison to the non-myostracal layers of the valves, the myostracal layers comprise less organic substance (Crippa et al. 2020b; Crippa et al. 2020a). For all investigated species, adductor myostraca are always adjacent to the crossed-lamellar portion of the shell (Figs. 2.2-6, 2.2-7a, 2.2-8a, 2.2-AP11, 2.2-AP12a, 2.2-AP13a), while the pallial myostracum is always between the crossed-lamellar and the complex crossed-lamellar layers of the valves (Figs. 2.2-7, 2.2-8, 2.2-AP12b, 2.2-AP13b). At the crossed-lamellar - myostracum interface (Figs. 2.2-4a, 2.2-5, 2.2-6), myostracal aragonite consists of minute/small, granular-prismatic, crystals (Average grain size around 10 μm). These increase in size towards the inner shell surface (Average grain size larger than 100 μm). Pole figures (e.g. Figs. 2.2-4, 2.2-6) illustrate that the aragonite c-axes orientation is normal to the inner shell surface. These structural characteristics evidence that *Glycymeris* and *Chama* myostracal aragonite has a ‘competitive growth type’ microstructure. Crystal formation through growth competition implies

that at nucleation, many crystals form close to each other (Figs. 2.2-4a, 2.2-AP11) and, at growth, compete for space. The likelihood for a small crystal to grow to a large entity is inversely proportional to the deviation of the crystal growth direction from an orientation normal to the nucleation template. The result of the growth competition process is a strong decrease in the number of crystals as one moves away from the nucleation substrate, accompanied by an increase in crystal size and generation of a progressively stronger crystallographic preferred orientation (Fig. 2.2-AP11). Thus, at inner shell surface, aragonite c-axes are almost parallel to each other. This structural characteristic is observed in all investigated *Glycymeris* and *Chama* species for pallial as well as adductor myostraca. For *Glycymeris* and *Chama*, Figs. 2.2-7, 2.2-8, 2.2-AP12 and 2.2-AP13 show the changeover from crossed-lamellar to the adductor myostracal layer as well as from pallial myostracal to the complex crossed-lamellar part of the shell. We find assemblies of small/minute crystals always at the transition from crossed-lamellar to the myostracal structure and not at the transition from myostracal to complex crossed-lamellar microstructure. Figures 2.2-4, 2.2-AP9 and Figures 2.2-5, 2.2-AP10 highlight, for the investigated *Glycymeris* and *Chama* species, a significant difference in the morphology of adductor myostracum prisms. This marked difference between *Glycymeris* and *Chama* in myostracal crystal shape is not caused by a cut effect; we checked this with EBSD measurements, carried out on different cuts through the valves and myostraca. We find also that the crystallographic texture, visible from the pole figures, varies between the two genera. *Glycymeris* usually shows a 3D “single-crystal-like” texture (with orientational density maxima and high crystal co-orientation, Figs. 2.2-4, 2.2-AP9), whereas the texture in *Chama* myostraca is mostly axial (fibre texture) with the a- and b-axes orientations varying evenly on a great circle (Figs. 2.2-5, 2.2-AP10).

For *Glycymeris* and *Chama*, Figs. 2.2-6, 2.2-7a, and 2.2-8a highlight the changeover from crossed-lamellar to myostracal layers. It is well observable that crystal orientation is transmitted from one layer to the next (see the white arrows indicating a continuation in colour from one microstructure to the other in Figs. 2.2-6a, 2.2-7a), even though for the two adjacent layers, crystal morphologies, sizes and growth modes are different. Furthermore, as Figs. 2.2-6a and 2.2-7a demonstrate, one can observe the continuation of the first-order lamellar microstructure into the myostracal part of the shell. The crossed-lamellar orientation pattern of crystals is transmitted to the adjacent myostracum and is continued, even with the competitive growth mechanism. In the texture of the myostracum, it is visible that the inherited orientations of the first-order lamellae coincide along one common a-axis (pole figures in Figs. 2.2-6b, 2.2-AP11a). This characteristic is common for the crossed-lamellar orientation pattern and is discussed in more detail in (Wilmot et al. 1992; Almagro et al. 2016b; Almagro et al. 2016a). The interface between the crossed-lamellar layer and the myostracum is not always straight. It can be serrated, with the two latter layers interlocking into one another (Fig. 2.2-7a). Towards the inner shell surface, the transition from the myostracum into the complex crossed-lamellar layer is remarkable (Fig. 2.2-7b). The large prisms, that form during the most advanced stage of myostracal growth, continue vestigially into the first-formed sections of the complex crossed-lamellar shell (yellow star in Fig. 2.2-

7b). These crystals are partially traversed by polycyclic twins (the red pixels indicate the twinning, see the crystal marked with a yellow star in Fig. 2.2-7b) and merge with the microstructure and mode of crystal orientation (texture) of the complex crossed-lamellar structure (Figs. 2.2-7b, 2.2-8b).

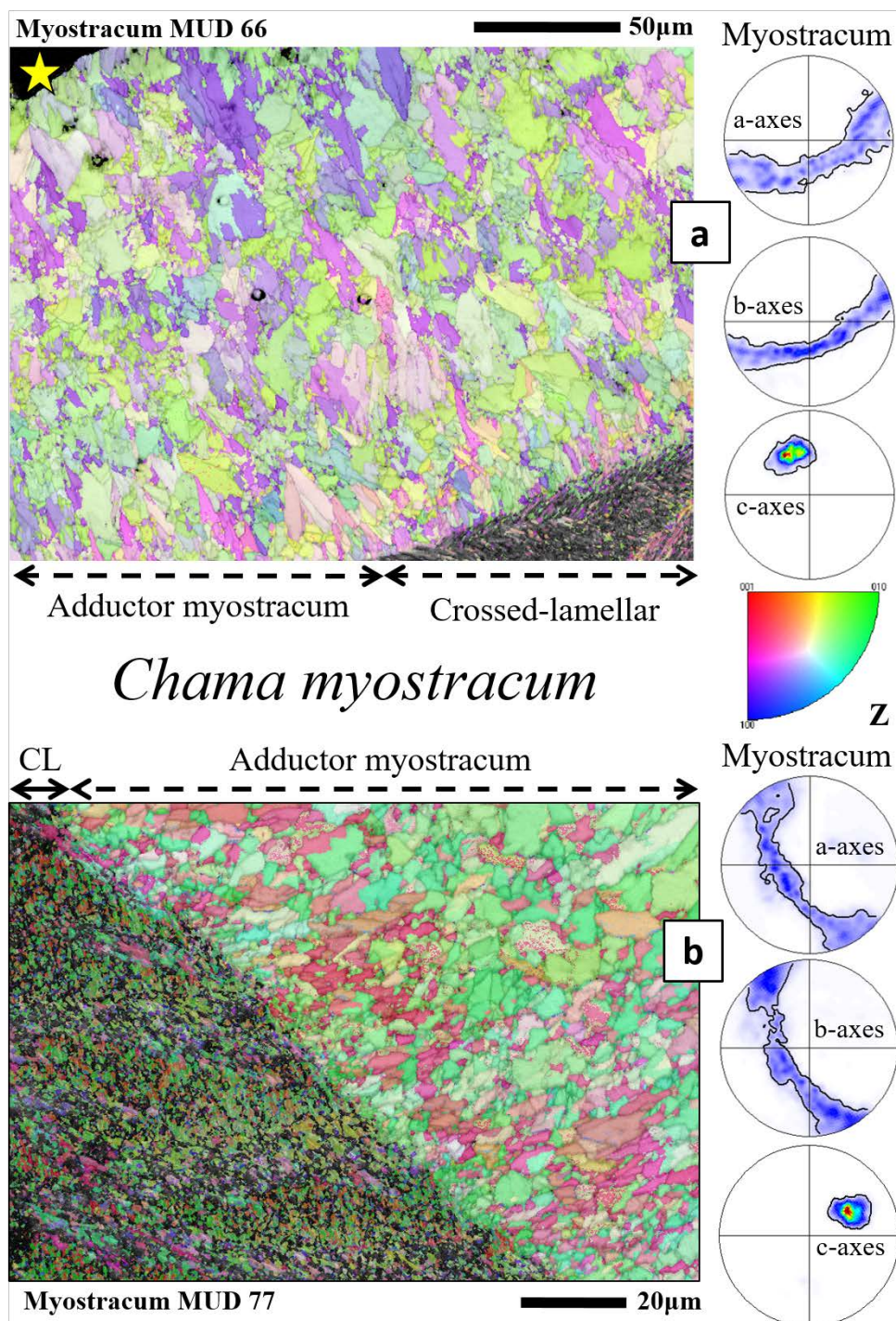


Fig. 2.2-5. EBSD scans depicting the microstructure of the adductor myostracum of *Chama* shells. In (a) we show the competitively grown adductor myostracum of *C. gryphoides*, from the interface with the crossed-lamellar shell (CL) up to the inner shell surface (yellow star in a). In (b) we highlight the adductor myostracum microstructure of *C. arcana*, also starting from the interface with the crossed-lamellar shell. The microstructure of *Chama* adductor myostracum is intricate. Crystal morphologies are very irregular in shape, size and organization and show only vaguely prismatic morphologies. The competitive growth microstructure is not as obvious as it is the case for *Glycymeris* shells (e.g. Fig. 2.2-4a). Pole figures visualise the orientational probability density distribution for myostracal shell portions and highlight for *Chama* adductor myostraca an axial (fibre) texture.

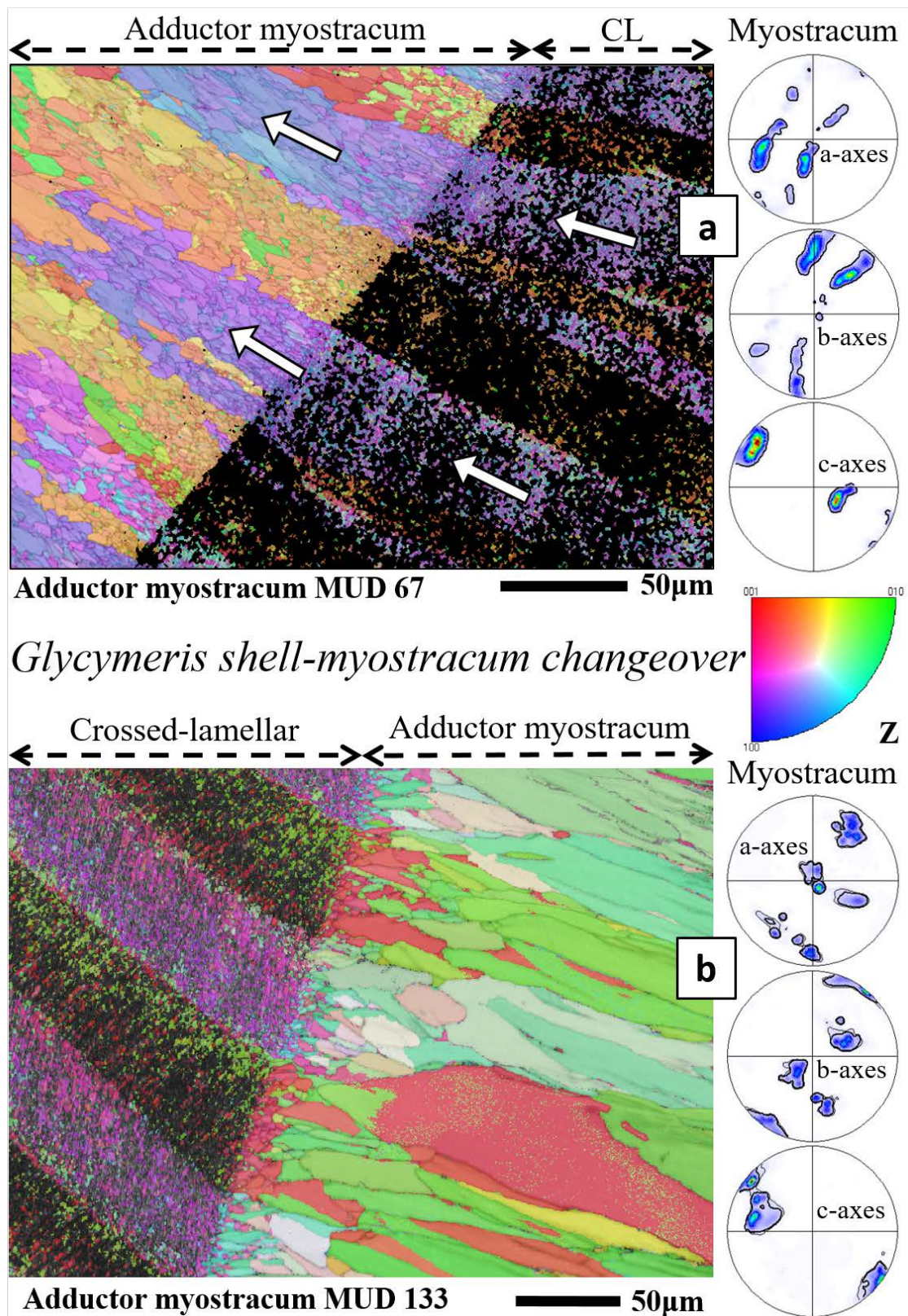


Fig. 2.2-6. EBSD scans visualizing for *Glycymeris* the changeover from crossed-lamellar to adductor myostracal microstructures. (a): *G. bimaculata*, (b): *G. pilosa*. It is well visible in (a) and (b) that the crystal orientation of the two sets of first-order lamellae of the crossed-lamellar (CL) microstructure is transmitted to the adductor myostracum (e.g., white arrows in a). Myostracal crystals close to the interface are granular and minute to small in size (a, b), increase in size and become more prismatic towards the inner shell surface. The evolution of the crystal co-orientation towards the inner shell surface is depicted in Supplementary Figure 2.2-AP11. Pole figures show orientational probability density distribution for the myostraca and depict that these have a 3D "single-crystal-like" texture.

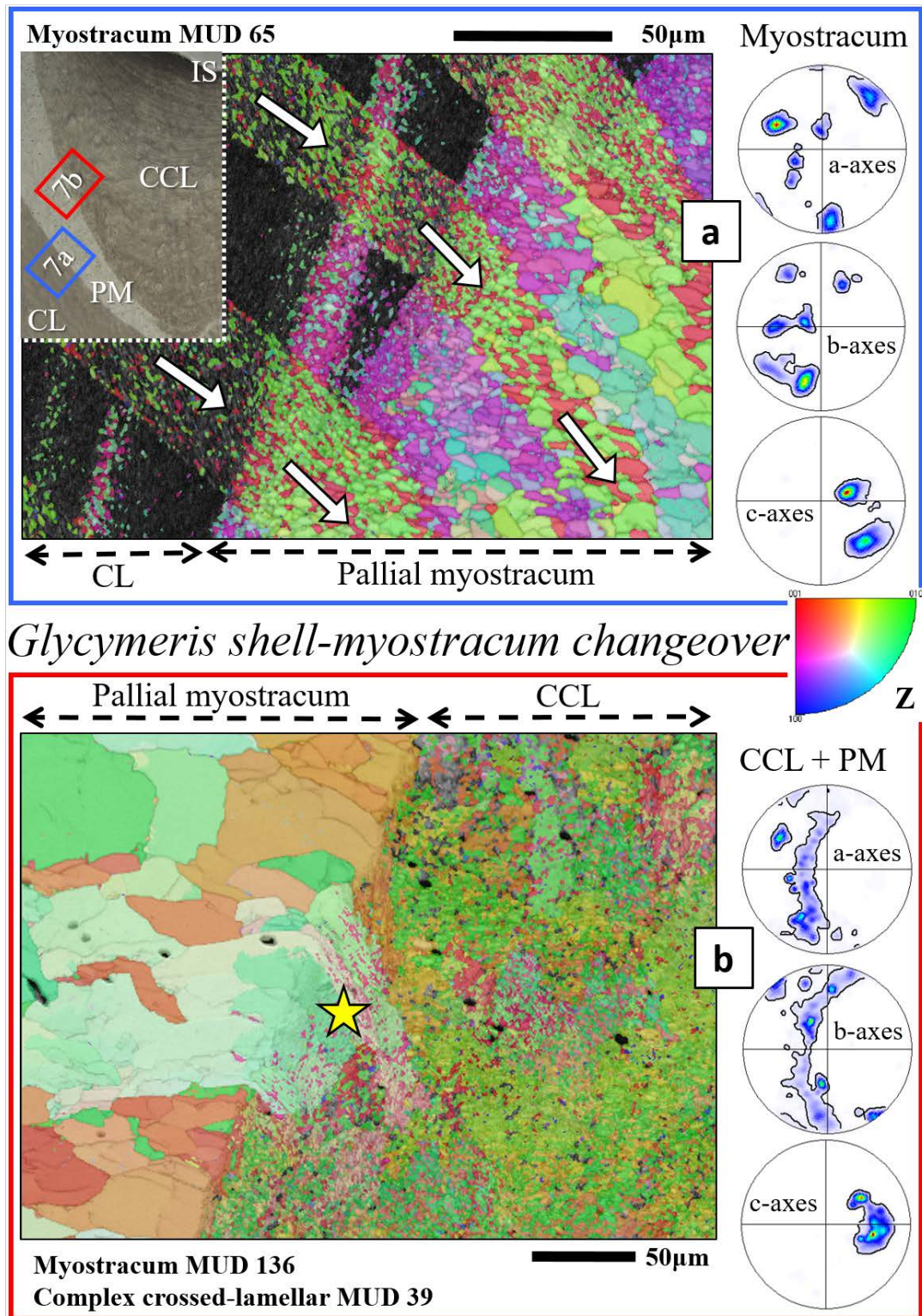


Fig. 2.2-7. EBSD scans visualizing for *Glycymeris* the changeover from crossed-lamellar to pallial myostracal (a) and from pallial myostracal to complex crossed-lamellar microstructures (b). For the position of EBSD scans see insert in (a). We visualize also the interface between crossed lamellar – pallial myostracal and pallial myostracal – complex crossed-lamellar shell portions. The continuation in the orientation of the two sets of first-order lamellae into the myostracum (white arrows in a) is well observable. (b): the transition of the pallial myostracum (PM) into the complex crossed-lamellar layer (CCL) for a *G. nummaria* shell. Large myostracal prisms (yellow star in b) protrude into the complex-crossed lamellar layer. Along the sharp interface, they are interrupted by a boundary of polycyclic twinning on (110) and ($\bar{1}\bar{1}0$) (around 64° misorientation) that commences in the complex crossed-lamellar layer. Pole figures indicate the orientational probability density distribution for the respective, non-myostracal, valve and myostracal layers and depict in (a) a single-crystal li texture and in (b) an axial (fibre) texture.

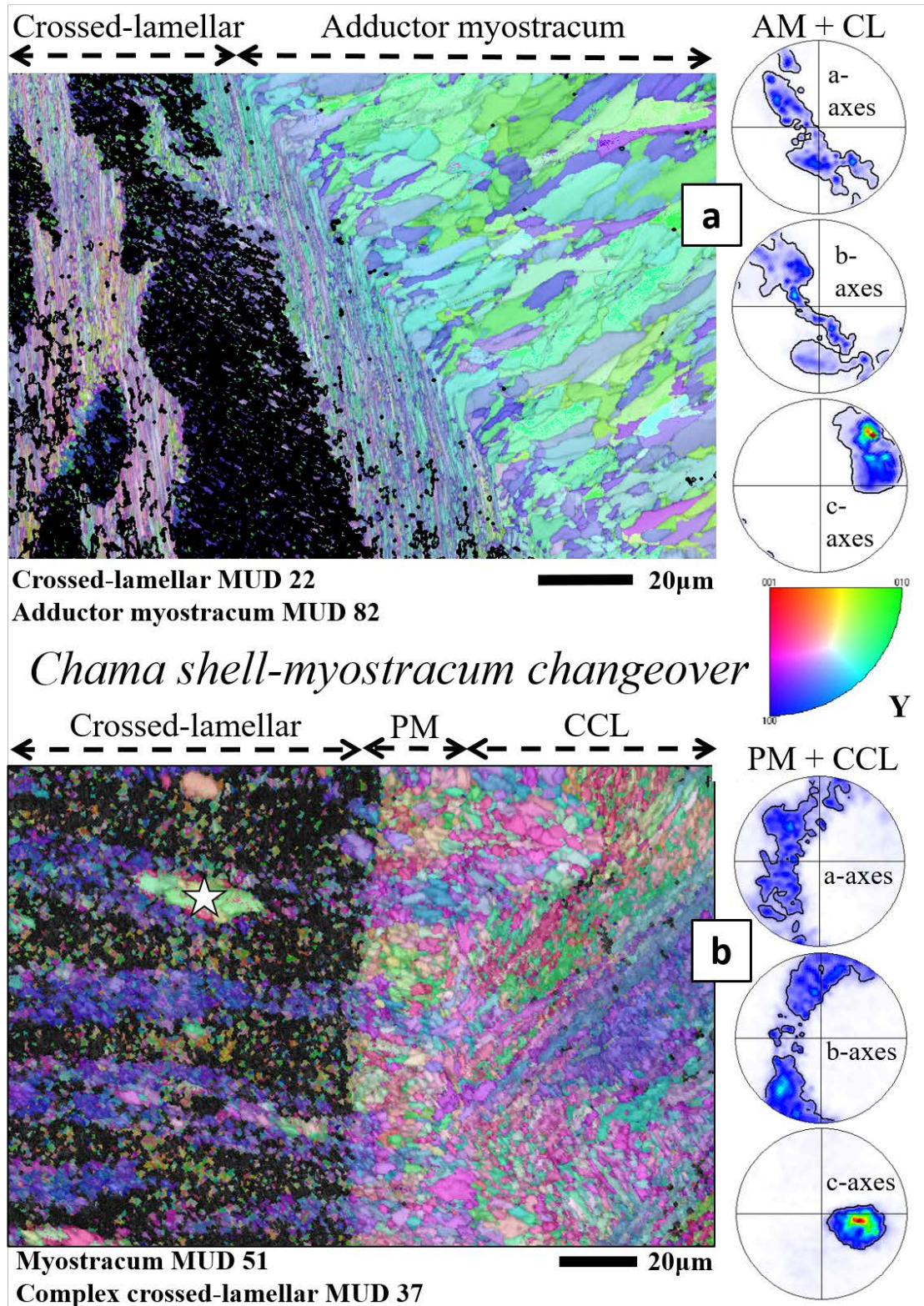


Fig. 2.2-8. EBSD scans depicting for *Chama* the changeover from the crossed-lamellar shell to the pallial myostracum (a). (b): the changeover from the crossed-lamellar shell to the pallial myostracum and from the pallial myostracum to the complex crossed-lamellar shell. (a): *C. gryphoides*, (b): *C. arcana*. CL: crossed-lamellar, CCL: complex crossed-lamellar, AM: adductor myostracum, PM: pallial myostracum. (a): Even though the sets of the crossed-lamellar structure run almost parallel to the interface between the two microstructures, the transmission of the crystal orientation pattern, from the crossed-lamellar to the myostracal shell, is still visible. (b): The crossed-lamellar layer comprises scattered, large single-crystal domains (white star in b) and its texture is transmitted through the pallial myostracum (PM) into the complex crossed-lamellar (CCL) layer. Pole figures show the orientational probability density distribution for the non-myostracal, valve, and the two myostracal layers and depict an axial (fibre) texture.

EBSD measurements allow the determination of misorientation between crystals. Figs. 2.2-9a, 2.2-10a, and 2.2-AP19a show EBSD maps conducted on *G. nummaria*, *C. arcana* and *G. bimaculata*, respectively. The map in Figure 2.2-9a covers the crossed-lamellar, pallial myostracal and complex crossed-lamellar microstructure, the map in Figure 2.2-10a shows the prisms of the adductor myostracum. The map in Fig. 2.2-AP19a depicts the pallial myostracum and the adjacent complex crossed-lamellar valve layer. With white lines, we highlighted the sites where we found a systematic misorientation of $\sim 64^\circ$ between adjacent crystals. At these sites, specific high-angle boundaries are present between adjacent crystals and connect these with a specific orientation relationship. These high-angle boundaries are twin boundaries; crystals connected by twin boundaries are the domains of a twinned crystal. The twin law of aragonite is a mirror reflection on the $\{110\}$ plane, which is also the composition plane (Hahn & Klapper 2013). For aragonite, we find cyclic, polycyclic and polysynthetic twinning. Accordingly, with the white lines in Figures 2.2-9a, 2.2-10a, 2.2-AP14a we document the distribution and abundance of twinned crystals within the different shell layers. For the different layers, we observed differences in the degree of twinning (Figs. 2.2-9b, c, 2.2-10b, c, 2.2-AP14a, b). In *Glycymeris* valves, the complex crossed-lamellar structure appears to be most twinned and the crossed-lamellar microstructure least twinned, respectively (Figs. 2.2-9a, 2.2-AP14a, 2.2-9b, 2.2-AP14b see the relative frequency – misorientation angle diagrams). However, it has to be noted that the relative misorientation frequencies may be affected by the amount of indexed data points for each layer. In the complex crossed-lamellar layer, twinning is mostly polycyclic and very abundant (Figs. 2.2-9a, 2.2-AP14a). Within the myostracum, twinning is between the prismatic crystals and not within them (Figs. 2.2-9a, 2.2-10a, 2.2-AP14a). For the crossed-lamellar layer, we observe polysynthetic twinning within each first-order lamella and cyclic twinning between adjacent set1 and set2 lamellae (Fig. 2.2-9a).

The texture of all valve layers, including the myostracal and ornamentation portions, is either 3D “single-crystal-like” (Figs. 2.2-1b, 2.2-2a, 2.2-4, 2.2-6, 2.2-7a, 2.2-8a) or cylindrical (Figs. 2.2-1a, 2.2-2b, 2.2-3, 2.2-5, 2.2-7b, 2.2-8b). For definitions of the texture modes see Introduction Section 1.3. The pole figures demonstrate the similarity in c-axes orientation between the different valve layers, the different myostraca and the ornamentations (Figs. 2.2-1 to 2.2-8, 2.2-AP6-2.2-AP14). Hence, crystal c-axis orientation is similar from the outermost ornamentation (calcitic or aragonitic), up to the innermost complex crossed-lamellar shell portion (aragonitic).

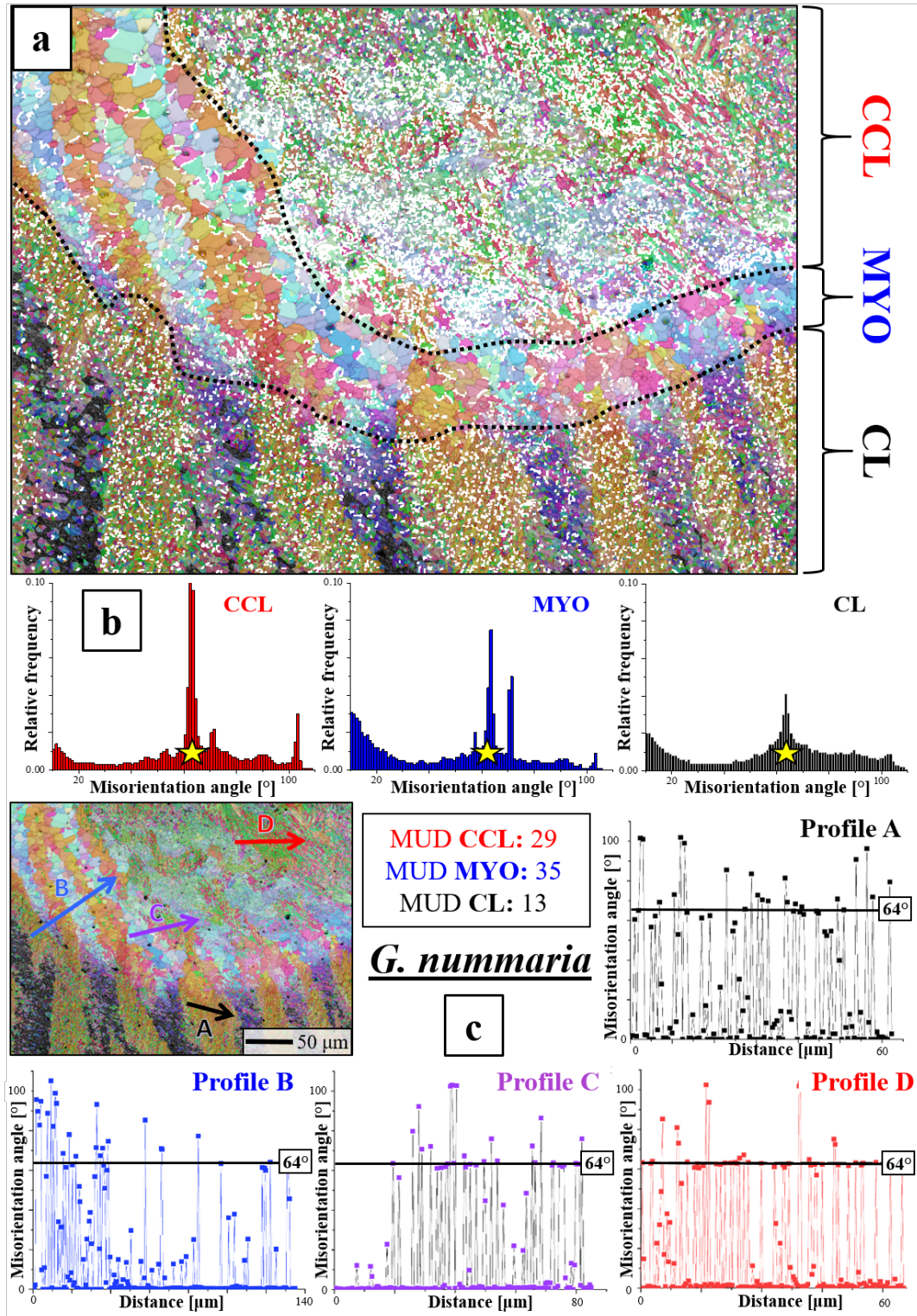


Fig. 2.2-9. Misorientation angle analysis of the different layers in an obliquely sectioned *Glycymeris nummaria* shell. The EBSD map (a) visualizes the three layers that are present in this measurement: Complex crossed-lamellar layer (CCL), myostracum (MYO) and crossed-lamellar layer (CL). Grain boundary angles between 63° and 65° are highlighted with white points in the EBSD map and indicate grain boundaries of twinned aragonite. The misorientation angle plots (b) show for all three layers peaks of varying relative frequency for a misorientation angle of 64° (indicated by yellow stars). Misorientation angle profiles (A-D) traversing the different layers provide further information about the type of aragonite twin (c).

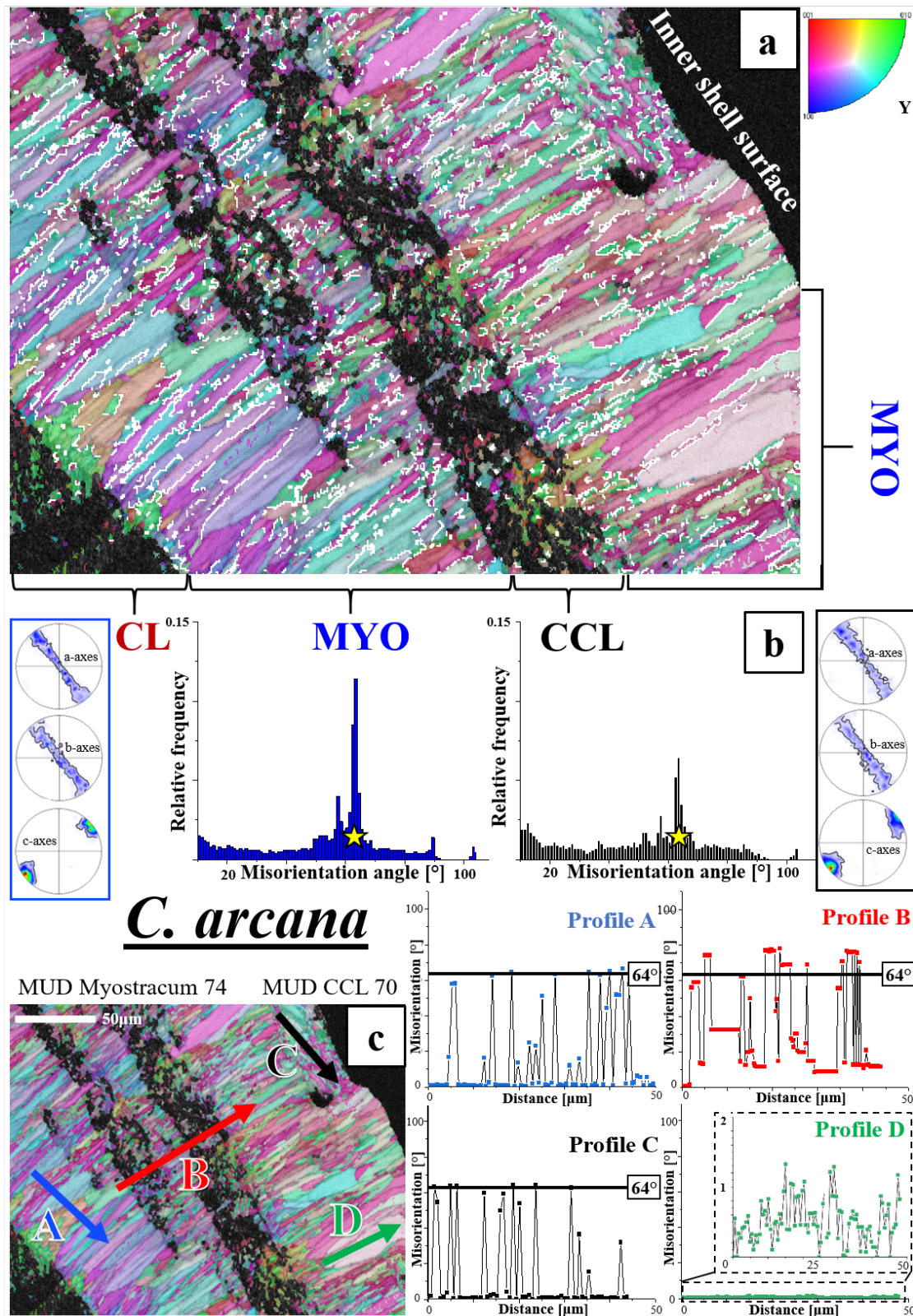


Fig. 2.2-10. Misorientation angle analysis of different layers in a transversely sectioned *Chama arcana* shell. The EBSD map (a) visualizes the three microstructures that are present in this measurement: The crossed-lamellar layer (CL) in the bottom left and, subsequently towards the inner shell surface, the myostracum (MYO) that is traversed with irregular sheets of complex crossed-lamellar microstructure (CCL). Grain boundary angles between 63° and 65° are highlighted with white points in the EBSD map and indicate twinned aragonite grain boundaries. The misorientation angle plots (b) show myostracum and complex crossed-lamellar layer peaks of varying relative frequency for a misorientation angle of 64° (indicated by yellow stars). The misorientation angle profiles (A-D) traversing the measurement provide further information on the twinning mode in the different structures (b).

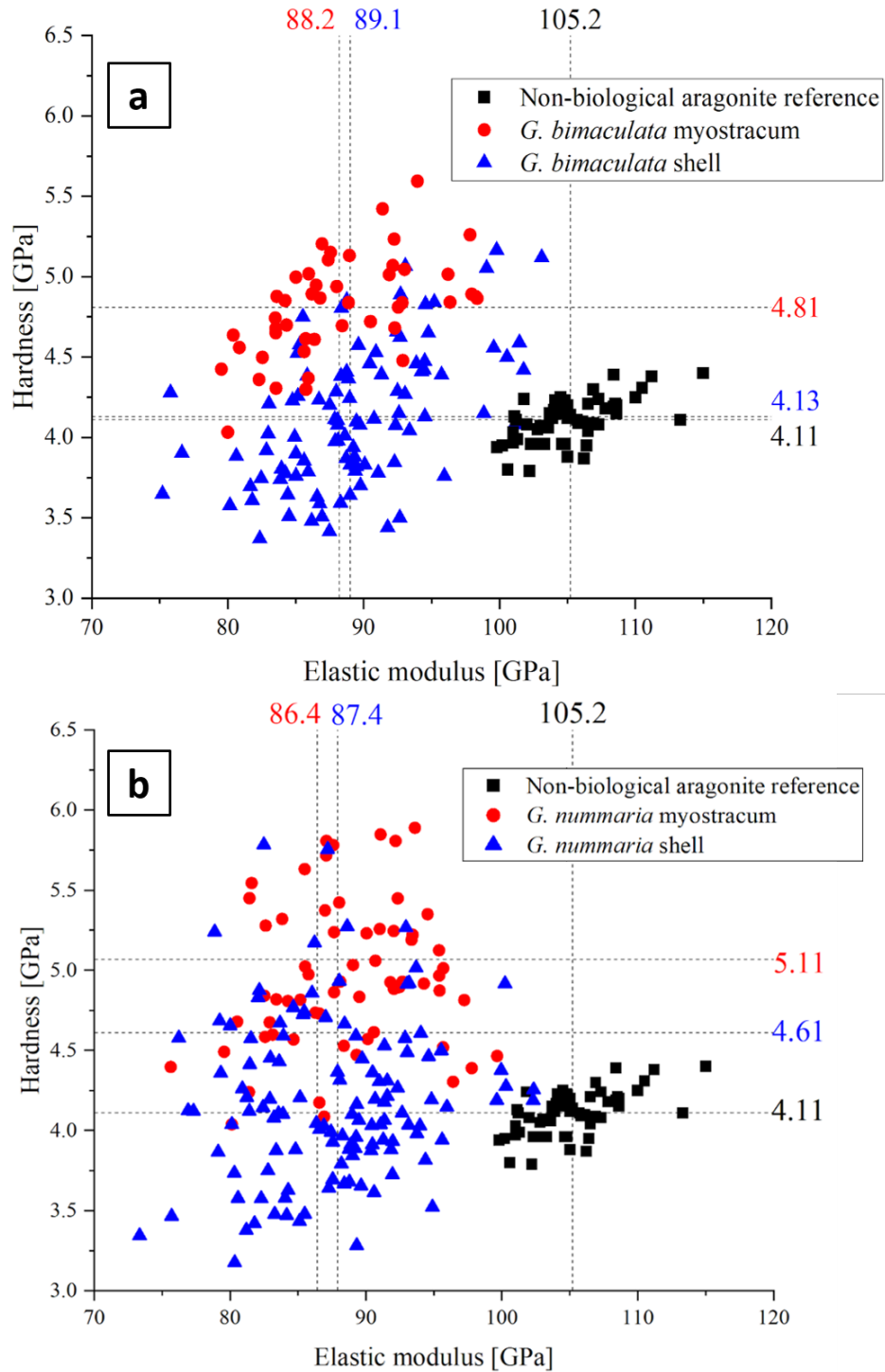


Fig. 2.2-11. The hardness and indentation elastic modulus distribution of different layers of *Glycymeris* samples with a geological aragonite reference. Plot (a) depicts that the myostracum layer (red circles) in *G. bimaculata* samples has a distinctly higher hardness than the aragonitic shell (blue triangles) and a non-biological aragonite reference (black squares). The indentation elastic modulus of myostracum and shell is similar and significantly lower than in geological aragonite. Plot (b) depicts the measured values for *G. nummaria*. The highest average hardness is observed in the myostracum. In the shell, despite the large standard deviation, the average hardness is higher than in the geological reference. Similar to *G. bimaculata*, the observed indentation moduli in the *G. nummaria* shell and myostracum are both similar, yet explicitly lower than the non-biological aragonite reference. Crossed-lamellar and complex crossed-lamellar layers are combined as "shell" due to their similar nanomechanical properties. The given average values have the following standard deviations σ : Hardness: Reference 0.14, *G. bimaculata* myostracum 0.31, *G. bimaculata* shell 0.39, *G. nummaria* myostracum 0.46, *G. nummaria* shell 0.41. Indentation elastic modulus: Reference 3.2, *G. bimaculata* myostracum 5.1, *G. bimaculata* shell 5.2, *G. nummaria* myostracum 5.6, *G. nummaria* shell 6.0. A breakdown of the individual layers and profile positions can be found in the Supplementary Information of this publication (Figs. 2.2-AP15, 2.2-AP16).

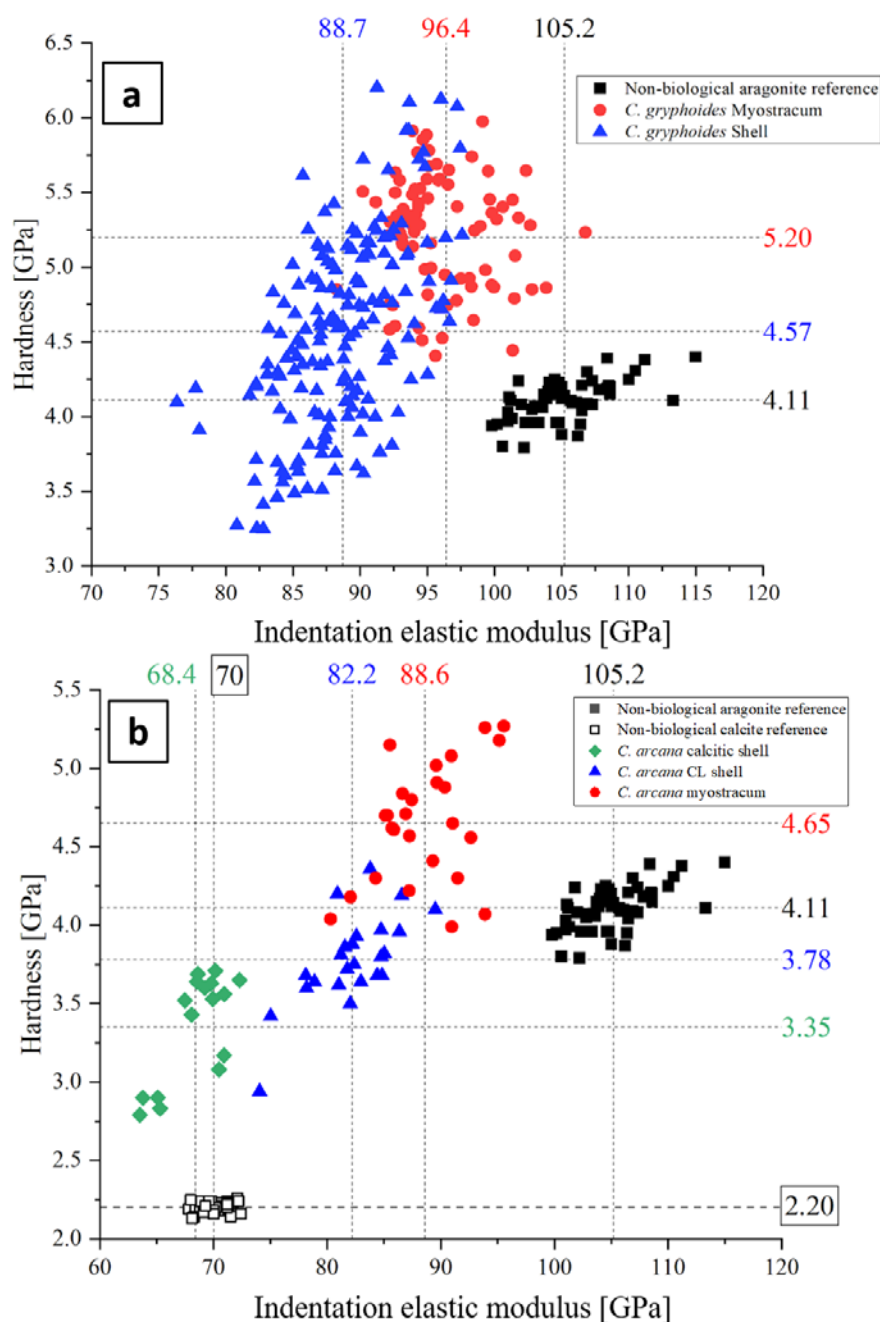


Fig. 2.2-12. The hardness and indentation elastic modulus distribution of different layers of *Chama* samples with a geological aragonite reference. Plot (a) depicts that the myostracum layer (red circles) in *C. gryphoides* samples has a distinctly higher hardness than the aragonitic shell (blue triangles) which is slightly harder than non-biological aragonite reference (black squares). While the indentation elastic modulus of the *C. gryphoides* myostracum is lower than the geological reference, the lowest average value was observed for the shell. The second plot (b) indicates the nanomechanical properties of aragonitic and calcitic layers in *C. arcana*. The crossed-lamellar layer is only slightly softer than the stiff, non-biological aragonite reference. The myostracum has a significantly higher hardness than the other layers and slightly higher indentation elastic modulus than the crossed-lamellar layer. The calcitic shell is harder than the reference while maintaining a similar indentation elastic modulus. The given average values have the following standard deviations σ : Hardness: Aragonitic reference 0.14, calcitic reference 0.03, *C. gryphoides* myostracum 0.59, *C. gryphoides* shell 0.62, *C. arcana* calcite 0.34, *C. arcana* myostracum 0.38, *C. arcana* CL shell 0.29. Indentation elastic modulus: Aragonitic reference 3.2, calcitic reference 1.26, *C. gryphoides* myostracum 4.4, *C. gryphoides* shell 3.8, *C. arcana* calcite 2.6, *C. arcana* myostracum 3.9, *C. arcana* CL shell 3.5. A breakdown of the individual aragonitic shell layers and profile positions is shown in the Supplementary Information of this publication (Figs. 2.2-AP17 to 2.2-AP19).

Figures 2.2-11, 2.2-12, Table 2.2-1 and Supplementary Figures 2.2-AP14 to 2.2-AP19 show the hardness and indentation elastic modulus results obtained from the different layers of *Glycymeris* and *Chama* shells, relative to the non-biological aragonite and calcite analogues. In *G. bimaculata* and *G. nummaria* (Fig. 2.2-11), the hardness of the myostracum surpasses the hardness of the (complex) crossed-lamellar shell layers and, significantly, that of the non-biological reference. When considering the indentation moduli of the investigated materials, it is well visible that, for both species, the myostracum and the (complex) crossed-lamellar layers are distinctly lower in indentation elastic modulus, relative to the non-biological aragonite reference. For both *Glycymeris* species, the range in indentation elastic modulus is similar for the valves and the myostracum (Fig. 2.2-11). For *C. gryphoides* and *C. arcana* myostracum, hardness is increased, relative to (complex) crossed-lamellar shell regions and relative to the non-biological carbonate analogues. When compared to non-biological aragonite, (complex) crossed-lamellar shell layers and the myostracum are lower in indentation elastic modulus, than the reference. In contrast to *Glycymeris*, we observe for *Chama* a slight difference in indentation elastic modulus between (complex) crossed-lamellar layers and the myostracum. Hence, while for *Glycymeris* only the hardness is varied between the (complex) crossed-lamellar and myostracal valve regions, for *Chama*, we find for the myostracum and the rest of the valves a variation in hardness and a slight variation in indentation elastic modulus (Table 2.2-1).

2.2.4 DISCUSSION

Bivalved molluscs live in a wide range of habitats and have developed a variety of lifestyles. While *Chama* is sessile and lives in turbulent waters at depths up to 30 m, *Glycymeris* populates calm waters, burrows superficially in the sediment and lives up to 200m depth. Adjusting to different environments and leading different lifestyles demands adaptations of soft and hard tissue. For bivalves, adaptation include for example variations in shell size, form and thickness, modification of the foot, change in hinge ligament size and resilience, variation in muscle size, number and structure, and adjustments of organs (Taylor et al. 1969; Kennedy et al. 1970; Stanley 1975; Chantler 1983; Ponder et al. 2019). In this study, we investigated structural and material property characteristics of the hard tissue of the non-myostracal and the myostracal parts of the valves for examples of mobile, infaunal, and sessile, epifaunal, bivalves. Of particular interest is to understand structural and nanomechanical property characteristics of those hard tissues where adductor and mantle muscles attach to the shell and to characterise the nature of the transition from non-myostracal, valve, to myostracal structures (Figs. 2.2-13-2.2-16, 2.2-AP14-2.2-AP21). We complemented our discussion with EBSD results on the pedal myostracum of *Glycymeris glycymeris* (Crippa et al. 2020b; Crippa et al. 2020a), an EBSD measurement on the pallial myostracum of *Dosinia scalaris* (Fig. 2.2-15) and an EBSD measurement on the adductor myostracum of the bivalve *Placopecten magellanicus* (Fig. 2.2-AP21).

Exerting control onto valve activity is essential for the survival of bivalves. The speed of valve movement, the time-dependent variation of valve opening and closure, and the strength of valve closure decide on the quality of soft tissue protection (Kier 1988; Guderley & Tremblay 2016). The opening/closing of the valves and the movement of the foot are determined by the action of adductor and pedal muscles (Bowden 1958; Millman 1967; Rüegg 1971; Zange et al. 1989; Odintsova et al. 2007). For bivalves, the movements of muscles involve forces generated by antagonistic muscle contraction, muscle extension and relaxation (Chantler 1983). Hence, depending on the motion in question, e.g., movement of valves and foot at burrowing or keeping the valves open or shut for longer periods, demands contraction and relaxation of the involved muscles, at diverse speeds and for diverse times (Millman 1967; Rüegg 1971; Zange et al. 1989; Odintsova et al. 2006). To facilitate the latter requirements, a particularly strong, and, for the movement, appropriate attachment of the muscles to the valves has to be developed by bivalved organisms.

As described in the introduction, bivalve muscles attach to the hard tissue of the myostracum via a tendon cell layer. Myostracal scars and layers are always aragonitic and have an outstanding and characteristic microstructure that is distinct from that of the remaining shell, and have a specific hardness and indentation elastic modulus. The two sketches in Figure 2.2-13 visualize on a larger scale for *Glycymeris* and *Chama* the interrelation between the observed, non-myostracal, valve and myostracal microstructures. We measured with a large series of EBSD scans (i) the transition from one myostracum into the other (from pallial to adductor and vice versa) and (ii) the myostracum in relation to the crossed-lamellar and the complex crossed-lamellar valve layers. In Figure 2.2-13 we summarized our findings gained from EBSD scans and visualize structural characteristics and the topological relation of the different myostracal and non-myostracal valve crystal assemblies.

Subsequently, we discuss the following questions:

1. Are the microstructure, texture, and material properties of the non-myostracal parts of the valves, similar or different for the investigated *Glycymeris* and *Chama* species?
2. Are myostracal microstructure, texture, and material properties similar or different for the investigated *Glycymeris* and *Chama* species? As described above, Glycymerididae and Chamidae do not share similar habitats and lifestyles.
3. What are the driving factors for structural similarity or difference?

The secreting cells?

The topological relation of muscle (adductor and pallial) and mantle cells to the hard tissue of the myostracum and to that of the non-myostracal valves?

Is a possible difference in the biomineralisation process responsible for the difference in myostracum and valve structure?

The microstructure and texture of the non-myostracal layers

Kennedy *et al.* (1969) and Taylor and Kennedy (1970) reported for *Glycymeris* and non-calcitic *Chama* shells crossed- and complex crossed-lamellar aragonite crystal arrangement patterns. Our results confirm this; however, we observe for some *Chama* shells an additional microstructure. We name the latter as a ‘complex crossed-lamellar type’ microstructure. For the investigated *Glycymeris* and *Chama* species, the non-myostracal (Figs. 2.2-1, 2.2-2) and myostracal (Figs. 2.2-4, 2.2-5) layers do show some comparable microstructural motifs, are, however, not entirely similar.

We observe for both, *Glycymeris* and *Chama*, the formation of first-order lamellae, arranged into two sets, with the latter having distinct crystal orientations. Each of the first-order lamellae comprises lath-shaped third-order lamellae. Despite the similarity in the internal structure of the first-order lamellae, we see, for *Glycymeris* and *Chama*, differences in set1 and set2 lamellae organization and interlinkage (Figs. 2.2-1b, 2.2-2a, 2.2-AP20). For *Glycymeris*, the first-order lamellae run strongly parallel to each other (Fig. 2.2-AP20), while for *Chama*, they are less clear-cut in morphology and, in general, interlaced (Fig. 2.2-AP20). In our opinion, this is most likely not caused by a cut effect, as this interlaced mode of first-order lamella set organisation for *Chama* shells was observed for shells sectioned along various orientations (see Methods Section 2.2.2). A structural effect in lamella orientation, relative to the myostracum, is that in *Glycymeris* first-order lamellae are at an angle of, more or less, 90° to myostracal layers, while in *Chama* first-order lamellae are always at low angles to myostracal layers, occasionally are even almost parallel to the myostracum. The different arrangements of first-order lamellae, relative to the myostraca might contribute to the observed differences between *Glycymeris* and *Chama* in myostracal crystal organization and texture.

The complex crossed-lamellar microstructure of *Glycymeris* consists of laths that, in general, assemble into first-order lamellae with different crystal orientations (Fig. 2.2-1 and Crippa *et al.* (2020a, 2020b). For all investigated *Chama* and *Glycymeris* species, we find the latter type of complex crossed-lamellar aragonite at the innermost valve portions (this study and Hoerl *et al.* 2024a). However, for the fully aragonitic *C. gryphoides*, the aragonite of the ornamentation forms a similar microstructure to the complex crossed-lamellar layer, as defined by Taylor *et al.* (1969). When cut in cross-section, this microstructure forms a large part of the valve. Due to the applied cut, aragonite crystals in the outermost valve layer appear to be granular to prismatic (Figs. 2.2-2b, 2.2-AP7b) and assemble into differently oriented clusters (Figs. 2.2-2b, 2.2-AP7b). It is striking that this microstructure occurs at outer shell portions. According to Taylor *et al.* (1969) and Kennedy *et al.* (1969), the complex crossed-lamellar layer forms always the innermost valve regions. Accordingly, we addressed the microstructure of the outer valve layer and ornamentation of *C. gryphoides* as a ‘complex crossed-lamellar-type’ microstructure.

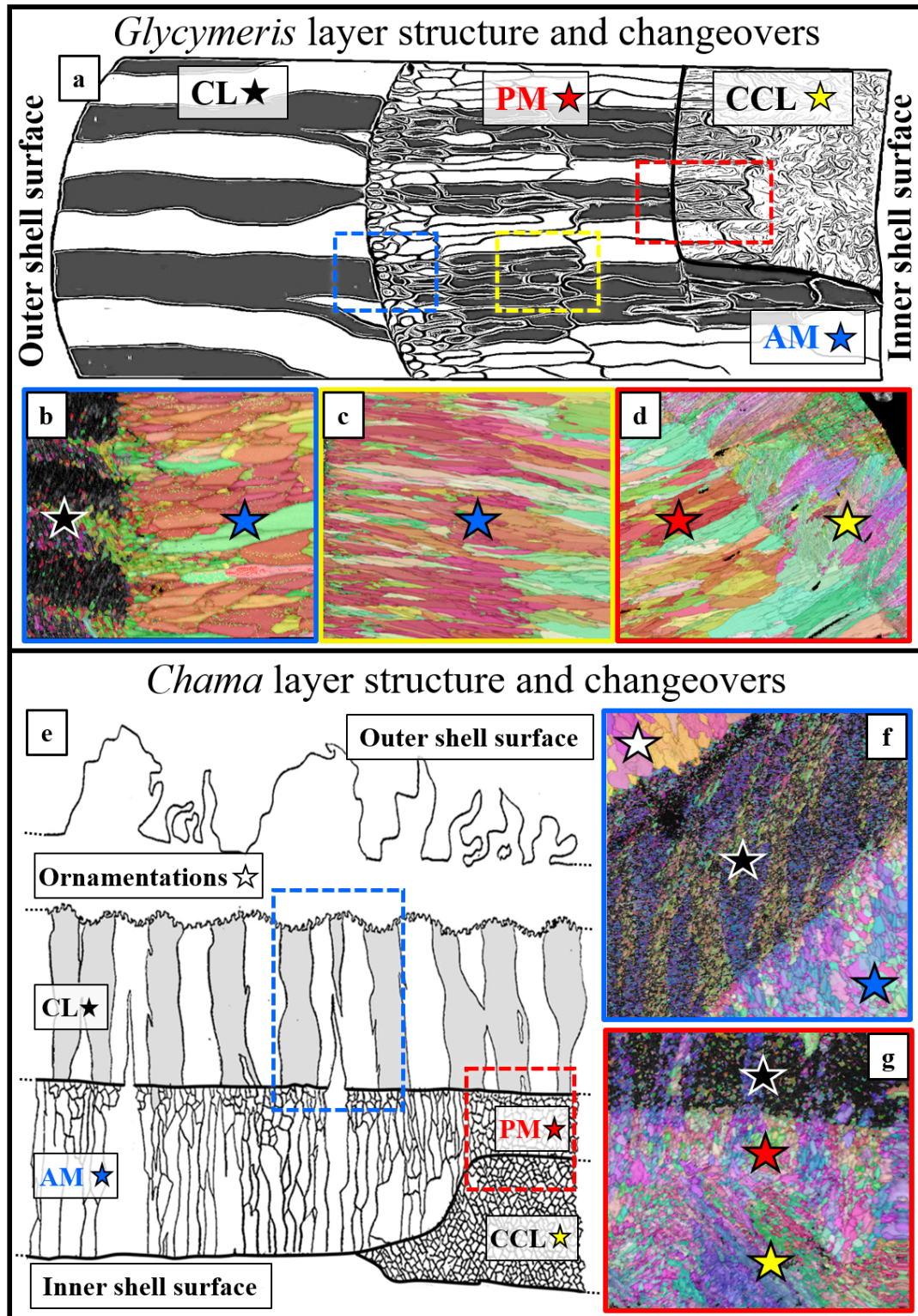


Fig. 2.2-13. Schematic illustrations depicting the general layer structure and transitions of *Glycymeris* (a-d) and *Chama* (e-g) shells. The outer valve layer of investigated *Glycymeris* samples has a crossed-lamellar microstructure (black star in b). The crystal orientation pattern is transmitted (b) and continued (c) in the subsequent, competitively grown adductor and pallial myostracum layers (blue and red stars in b, c, d). At the changeover between the pallial myostracum and complex crossed-lamellar layer (yellow star in d), the large protruding myostracal prisms exhibit extensive polycyclic twinning. While ornamentations in *C. gryphoides* are aragonitic, in *C. arcana* shells, the ornamentations are calcitic (white star in f), and form a three-dimensional interlocking mechanism with the subsequent crossed-lamellar layer (black star in f). The crossed-lamellar crystal orientation is transmitted into the myostracal crystals (blue star in f, red star in g). While the orientation transmitted by pallial myostracum crystals devolves in the first μm of the complex crossed-lamellar layer (yellow star in g), it is eventually lost in the convoluted microstructure of the complex crossed-lamellar layer.

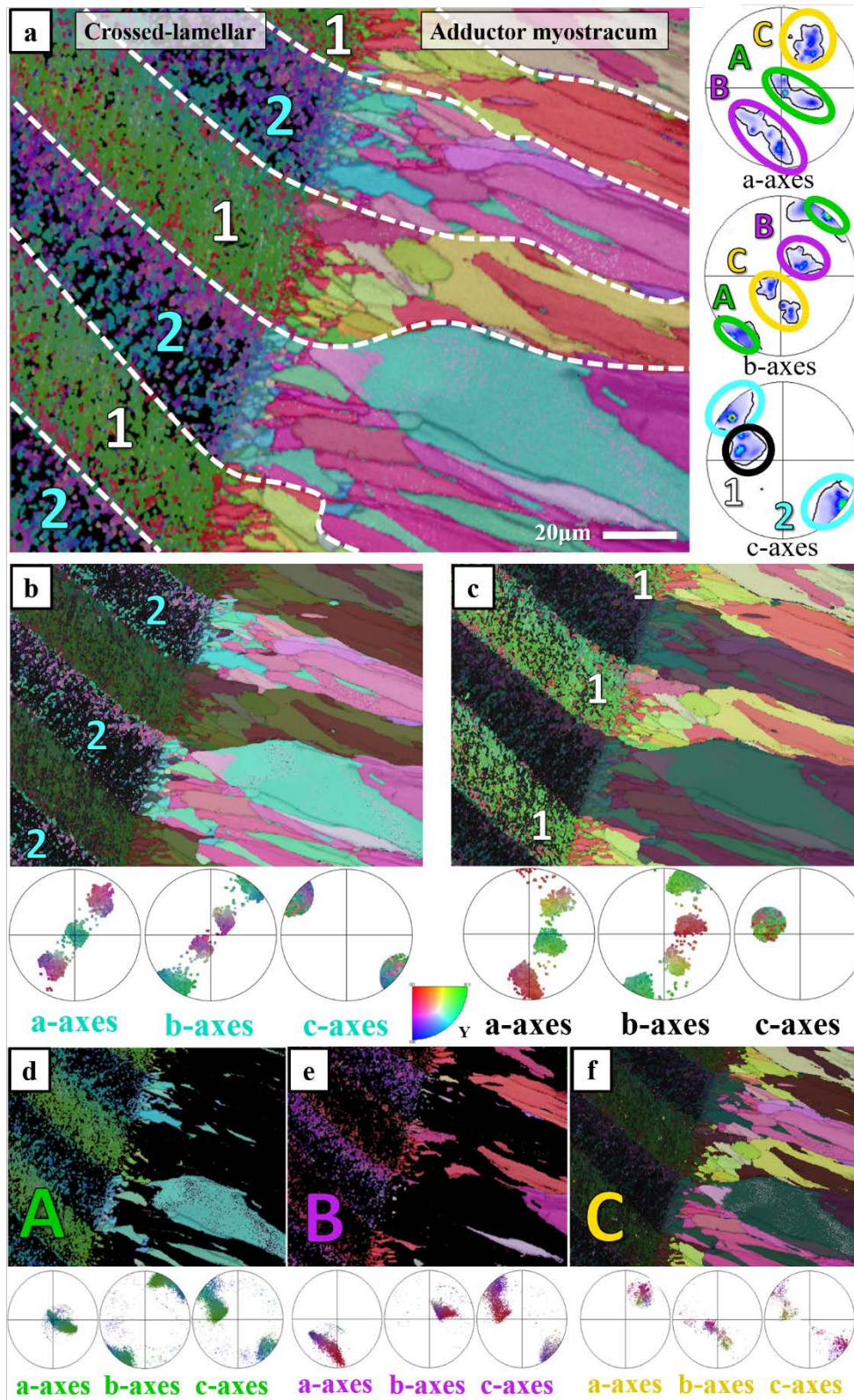


Fig. 2.2-14. Breakdown of crystallographic texture in the non-myostracal, valve-myostracum changeover portion of a transversally sectioned *Glycymeris pilosa* shell. The transmission of the set1 and set2 crystal orientation pattern into the adductor myostracum is highlighted in EBSD maps and pole figures for the entire dataset (a) and various subsets (b-f). The pole figures a-c show that the aragonite c-axes in first-order lamellae set 1 are tilted, relative to aragonite c-axes in set 2 that run almost parallel to the direction of crystal growth. In addition to the two twinned orientations inherited by each of the two first-order lamella sets (d, e), the competitive growth process initiates a third, unique, orientation that is found only in the myostracum and differs in orientation of the a- and b-axes (f). The latter corresponds to the third orientation of the polycyclic twin.

EBSD measurements allow the determination of crystal co-orientation strength for the different shell layers. We observed, for all investigated species of *Glycymeris* and *Chama*, low crystal co-orientation for complex crossed-lamellar and crossed-lamellar shell portions (*Glycymeris*: MUD (CCL) = 14, MUD (CL) = 11; *Chama*: MUD (CCL) = 26, MUD (CL) = 27). Crystal co-orientation strength for the calcitic ornamentation of *Chama* was increased (MUD = 45 / 55 / 80), relative to that of the aragonitic shell. Most increased, for all investigated species, was the co-orientation strength of aragonite within myostracal layers and individual myostracal crystals (*Glycymeris* MUD myostracum = 67 / 97 / 154 / 133; *Chama* MUD myostracum = 64 / 66 / 51 / 77), relative to aragonite co-orientation of the non-myostracal shell. It has been shown for *G. glycymeris* that individual myostracal prisms are single crystals (Fig. 8a, c-e in Crippa *et al.* (2020a)). We also find this for all species that were investigated in this study. The latter might be an indication that individual myostracal prisms contain very little organic substance. It should be noted that myostracal aragonite of *Chama* is less co-oriented than myostracal aragonite of *Glycymeris*.

The microstructure and texture of the myostraca

Kennedy *et al.* (1969) and Taylor and Kennedy (1970) describe that bivalve myostraca are assemblies of aragonite prisms. We observed this as well for *Glycymeris* and *Chama* myostraca, however, based on EBSD measurements, we found further, important, structural characteristics:

- (i) Prism morphology regularity/irregularity is different for *Glycymeris* (Fig. 2.2-4) and *Chama* (Fig. 2.2-5).
- (ii) Crystal co-orientation strength within adductor and pallial myostraca is different for *Glycymeris* and *Chama* (Figs. 2.2-4, 2.2-5).
- (iii) Orientational probability density distribution within myostraca is different for *Glycymeris* and *Chama*, with *Glycymeris*, in most cases, showing 3D “single-crystal-like” (e.g., Figs. 2.2-4, 2.2-6, 2.2-7a) and *Chama* exhibiting, very often, axial (fibre) textures (e.g., Figs. 2.2-5, 2.2-8, 2.2-10).
- (iv) The aragonite of *Glycymeris* and *Chama* pallial, adductor and pedal myostraca has a microstructure that is characteristic of a crystal growth process derived of growth competition (this study and Crippa *et al.* (2020a, 2020b)). Hence, wherever muscles attach to the shell, a hard tissue is formed that has a microstructure that is generated through growth competition. The growth competition process has two important structural effects: (a.) at an advanced stage of the crystallisation process, the crystals are large entities. (b.) with progressive growth, a common growth direction develops for all crystals and a specific crystallographic lattice orientation is attained. This is discussed subsequently.

According to Checa (2018), crystal formation and assembly by growth competition is, in the biological realm, a process that is fully governed by physical controls and contrasts the processes at the formation of other carbonate biomaterial microstructures. In the latter, microstructure development is determined by biological determinants, such as the influence of organic matrix biopolymers or the influence of the secreting cells when in direct contact with the forming crystals (Checa 2018). Castro-Claros *et al.* (2021) describe for *Ostrea stentina* and *Anomia ephippium*, that adductor myostracal mineralisation takes place, among other possible ways, via CaCO_3 -containing vesicles, which become delivered to the extrapallial space (Fig. 5d, e, h in Castro-Claros *et al.* (2021)). This is in contrast to the non-myostracal portion of the shell (of *Ostrea stentina* and *Anomia ephippium*), where, at secretion, mantle cells are in close contact with the forming biocarbonate (Castro-Claros *et al.* 2021). Accordingly, different biomineralisation processes account for the formation of non-myostracal and myostracal Ca-carbonate biomaterials. In essence, based on our structural results, and, in analogy to the findings of Castro-Claros *et al.* (2021), we inferred that the formation of *Glycymeris* and *Chama* myostracal and non-myostracal CaCO_3 is initiated by different crystal formation and growth determinants, however, both controlled by the secreting cells. Nonetheless, the growth competition process has two important structural effects: (i) at an advanced stage of the crystallisation process, the crystals become large entities (up to 50 μm in diameter and 200 μm in length). (ii) with progressive growth, for all crystals, a common growth direction develops and a specific crystallographic axes orientation is attained, with the c-axes being normal to the inner shell surface. This is discussed further subsequently.

Biocrystal formation through growth competition has been reported for species of various marine organism groups, e.g., for *Liothyrella neozelanica* and *Gryphus vitreus* brachiopod columnar calcite (Schmahl *et al.* 2008; Goetz *et al.* 2009; Goetz *et al.* 2011), for *Argonauta argo* and *Argonauta hians* cephalopod shell aragonite (Stevens *et al.* 2017; Checa *et al.* 2021), for rotaliid foraminifera shell calcite (Lastam *et al.* 2023a; Lastam *et al.* 2023b) and for *Glycymeris glycymeris* and *Glycymeris nummaria* bivalve myostracal (adductor, pedal) aragonite (Crippa *et al.* 2020b; Crippa *et al.* 2020a). With this study, we show for *Chama arcana*, *Chama gryphoides*, *Glycymeris bimaculata*, *Glycymeris nummaria* and *Glycymeris pilosa* that adductor and pallial myostracal aragonite forms through growth competition. This study is part of a larger survey of bivalve myostracal microstructure and texture and covers species of the orders Arcida, Mytilida, Venerida, Unionida, Cardiida, Ostreida, Pectinida, Chamidae and Tellinoidea. For most investigated species, we find the competitive-growth-type microstructure for myostracal shell portions; however, we also find different myostracal structures for, e.g. *Mytilus edulis*, *Arctica islandica*, *Tellina planata*, *Venus verrucosa* (see Chapter 2.4 of this thesis).

One important result of our study is that *Glycymeris* and *Chama* non-myostracal and myostracal aragonite are twinned (Figs. 2.2-9, 2.2-10, 2.2-AP14). (Crippa *et al.* 2020b; Crippa *et al.* 2020a) showed for two *Glycymeris* species that the aragonite in their shells is twinned, for *Chama* we describe twinning

of shell carbonate for the first time. We observe polysynthetic, cyclic and polycyclic twinning; for definition see the Terminology Section A.1 and (Hahn & Klapper 2013).

- (i) The crossed-lamellar layer exhibits polysynthetic twinning within the two sets, between the third-order laths that form set1 and set2 of a first-order lamella.
- (ii) For the myostraca, we find cyclic twinning.
- (iii) For the complex crossed-lamellar aragonite we observe polycyclic twinning between and within the first-order blocks/lamellae.

Polysynthetic, cyclic, and polycyclic twins are defined by the number of twin planes and their orientation/co-orientation. If twin planes in a twinned crystal are parallel to each other, the twin crystal is termed as a polysynthetic twin; if twin planes in a twinned crystal are not parallel to each other, the twinned crystal is addressed as a polycyclic twin (Hahn & Klapper 2013).

When aragonite crystals are assembled to form the crossed-lamellar arrangement, the first-order lamellae comprise lath-shaped crystals (the third-order lamellae, see Fig. 13b in Crippa et al. (2020b)) that are inclined to each other and alternate in their respective crystal orientations (see Fig. 13a in Crippa et al. (2020b)). For the crossed-lamellar microstructure, we found twin formation mainly between the third-order laths that comprise a first-order lamella (see 64° misorientation boundaries in Fig. 2.2-9a) and to a lesser extent between the lamellar sets.

When aragonite is assembled to form the complex crossed-lamellar arrangement, several, irregularly shaped and variously oriented, first-order blocks/lamellae are formed. The latter consist of third-order laths and crystals. For the complex crossed-lamellar microstructure, we observed polycyclic twin formation within the blocks/lamellae and to a lesser extent between them (Fig. 2.2-9a). Accordingly, for the complex crossed-lamellar microstructure we detected a high density of 64° misorientations (see Figs. 2.2-9a, b, 2.2-AP15a).

Myostracal (adductor, pallial, pedal) aragonite is cyclically twinned. The 64° misorientations are between adjacent prisms and not within the prisms (Figs. 2.2-9a, 2.2-10a, 2.2-AP15a, 2.2-AP16a). The distinct peak of 64° in the relative frequency–misorientation angle diagram for the myostracum (see Figs. 2.2-9b, 2.2-10b, 2.2-AP19b) is, to some extent, due to the low number of total grain boundaries imposed by the large prism size in the adductor myostracum.

The changeover from non-myostracal, valve, to myostracal crystals

For *Glycymeris* and *Chama*, the transition between the layers of the non-myostracal and myostracal valve portions is continuous. We discuss first the transition from the crossed-lamellar valve to the adductor myostracum and, subsequently, the transition from the pallial myostracum to the complex crossed-lamellar valve portion (Figs. 2.2-6 to 2.2-8, 2.2-9a, 2.2-14, 2.2-15 and 2.2-AP14a, c)

Our EBSD results showed that adductor and pallial myostraca form via two crystallization processes:

- (i) the *very first crystals* form through epitaxial growth onto the crossed-lamellar template
- (ii) *further growth* is guided through the competitive growth process

For *Glycymeris* and *Chama*, the adductor myostracum is always attached to the crossed-lamellar valve portion (Figs. 2.2-6, 2.2-7a, 2.2-8a, 2.2-14a-d), while the pallial myostracum attaches to the crossed-lamellar layer, along its external surface, and to the complex crossed-lamellar microstructure, along its internal surface (Figs. 2.2-7, 2.2-8b, 2.2-9a, 2.2-14e).

Crystal orientation measurements demonstrated, for the crossed-lamellar – adductor myostracum changeover, that crystal size and morphology are not transmitted to the myostracum (Fig. 2.2-14a). However, the lamellar habitus of the crossed-lamellar structure, thus, crystal orientation of the two sets of first-order lamellae, is transmitted and can be well traced within the adductor myostracum (Figs. 2.2-6a, 2.2-7a, 2.2-14a, b, c). Some crystallographic aspects of the crossed-lamellar texture are also transmitted to the adductor myostracum. Hence, crystallographic axes orientation is conferred from crossed-lamellar to adductor myostracal aragonite. Figures 2.2-14d, e show that the very first-formed adductor myostracal crystals grow epitaxially onto the crystals of the first-order lamellae of the crossed-lamellar layer. At this stage of myostracal growth, all crystal orientations of the crossed-lamellar valve are also maintained within the adductor myostracum. With further growth of the myostracum (controlled by the competitive growth process), this changes, as (i) only some orientations of the crossed-lamellar valve are retained and (ii) a new crystal orientation along the a- and b-axes is developed within the adductor myostracum (Fig. 2.2-14f). This newly developed orientation is cyclically twinned, relative to the crystal orientation of the first-order lamellae, and is retained for the entire myostracal growth sequence. The c-axis orientation of the crystals with the new crystallographic orientation is parallel to the c-axis orientation of crystals of the first-order lamellar sets and to the c-axis orientation of the epitaxially-formed adductor myostracum crystals (see pole figures in Fig. 2.2-14d, e, f). This indicates that the restrictions of the polysynthetic twinning in the crossed-lamellar layer no longer apply to the myostracum. Hence, c-axis orientation of all crystals (i) remains similar for the different microstructures (crossed-lamellar and myostracal), (ii) become oriented in parallel along inner shell layers and (iii) is perpendicular to the inner shell surface. (iv) Crystal co-orientation strength is low for the first-formed crystals of the myostracum, however, for the crystals that nucleate on the crossed-lamellar template, crystal co-orientation strength increases significantly towards inner shell surface. (v) The restrictions of polysynthetic twinning within the third-order lamellae of the crossed-lamellar layer are not continued in the adductor myostracal layer. It should be kept in mind that all these structural characteristics and effects are initiated by the competitive growth process.

In summary: (i) the first crystals of the adductor myostracum grow epitaxially onto the crossed-lamellar template (Fig. 2.2-14a, d, e). (ii) further growth of myostracal aragonite is controlled by growth competition. (iii) two c-axes orientations, one for each set of first-order lamellae (see Almagro et al. 2016a; Crippa et al. 2020a, 2020b) and two different a- and b-axes orientations are transferred to the adductor myostracum. (iv) c-axis orientation remains rather conservative for the crossed-lamellar and the adductor valve portion, while a new a- and b-axes orientation develops within the myostracal layer. (v) for the crossed-lamellar layer we find polysynthetic twinning within the first-order lamellae and, only to some extent, twinning between the two sets.

Pallial myostraca are, in 3D, sheet-like structures (Hudson 1968; Nishida et al. 2011) that are incorporated into the valves and separate adjacent hard tissue layers, having specific microstructures (Kennedy et al. 1969). For *Glycymeris* and *Chama*, the pallial myostracum connects, along its outer surface to the crossed-lamellar (Figs. 2.2-8b, 2.2-9, 2.2-15) and along its inner surface to the complex crossed-lamellar microstructure (Figs. 2.2-7b, 2.2-8b, 2.2-15). Figures 2.2-9 and 2.2-15 visualize the corresponding transitions between the microstructure of the pallial myostracum and the two different, non-myostracal valve layers.

(i) *The changeover from the crossed-lamellar valve to the pallial myostracum*

As is the case for the changeover from the crossed-lamellar valve portion to the adductor myostracum, the lamellar habitus of the first-order lamellae and the polysynthetic twinning pattern are transferred from the crossed-lamellar valve to the pallial myostracum. These two structural characteristics continue across the entire extent of the pallial myostracum (see white arrows in Fig. 2.2-15a). As is the case for the adductor myostracum, for the pallial myostracum as well, we observed within the pallial myostracum the generation of an additional crystal orientation of the a- and b-axes (Fig. 2.2-15b-d). It appears that this is the third orientation of the polycyclic twin previously restricted by the mantle. The latter controlled the crossed-lamellar crystal growth, prior to pallial muscle attachment (Fig. 2.2-15d). When based on c-axis orientation, the two orientations of the two first-order lamellar sets carry over from the crossed-lamellar to the complex crossed-lamellar valve portion. Hence, overall, six different aragonite crystal orientations are developed up to the transition from the pallial myostracum to the complex crossed-lamellar layer. They correspond to the two sets of first-order lamellae imposed by the crossed-lamellar layer and the two orientations resulting from polycyclic twinning.

(ii) *The changeover from the pallial myostracum to the complex crossed-lamellar valve*

Figures 2.2-7b and 2.2-15e-h show close-ups of the transition from the pallial myostracum to the complex crossed-lamellar shell. The white dashed line in Figure 2.2-15e indicates the border between myostracal and complex crossed-lamellar layers. We observed the following: (i) The crystals of the complex crossed-lamellar layer (yellow stars in Figs. 2.2-7b, 2.2-15e) grow epitaxially onto the previously formed myostracal crystals. The prismatic microstructure and the formation of large prisms

are carried over from the pallial myostracum into the complex crossed-lamellar valve portion (yellow stars in Figs. 2.2-7b, 2.2-15e). For the latter transition from one microstructure into the other, we observed similar structural characteristics as detected for the transition from crossed-lamellar to pallial myostracum. We found again epitaxial growth of the first-formed crystals of the complex crossed-lamellar, non-myostracal, valve portion onto the prisms (large prisms that form at an advanced stage of crystallization) of the pallial myostracal template. For the complex crossed-lamellar layer we have detected for both, *Glycymeris* and *Chama*, polycyclic twinning. Extensive polycyclic twin formation is started right at the transition from pallial myostracum to the complex crossed-lamellar shell (yellow stars in Figs. 2.2-7b, 2.2-15e) and executed throughout the entire inner shell layer.

The different twinning modes impact the texture of the pallial myostracum and of the complex crossed-lamellar shell layers. We visualised with pole figures (Fig. 2.2-16) the transformation from a 3D “single-crystal-like” to an axial texture. Originating in the crossed-lamellar valve, it is modified in the pallial myostracum and transforms into an axial texture in the complex crossed-lamellar shell. Figure 2.2-16 depicts the mode of crystal arrangement with an EBSD map (Fig. 2.2-16a) and corresponding pole figures (Fig. 2.2-16b), covering the crossed lamellar, pallial myostracal and complex crossed-lamellar layers. Numbers 1 to 5 indicate chosen segments of the map and the corresponding pole figures: 1: crossed-lamellar valve, 2: pallial myostracum, 3: complex crossed-lamellar valve portion directly next to the pallial myostracum, 4 and 5: complex crossed-lamellar portions further away from the myostracum. The pole figure of the crossed-lamellar layer shows four orientation probability maxima for the a- and b-axes (see arrows in pole figure 1 in Fig. 2.2-16b). These correspond to the inclination between the two sets of first-order lamellae and the two, polysynthetically twinned, crystal orientations within each set of a first-order lamella. Due to these maxima, the pole figure of the crossed-lamellar shell conveys a single crystal-like texture. This texture is transferred into the pallial myostracum, however, in the pallial myostracum a third “set” of twinned orientation develops. The latter indicates, most likely, the loss of biological control over aragonite crystal growth during adductor muscle attachment. Most probably, it is not induced on purpose but is rather accidental (pole figure 2 in Fig. 2.2-16b). The pallial myostracum texture is transferred to the first-formed portion of the complex crossed-lamellar layer, the layer directly adjacent to the pallial myostracum, (pole figure 3 in Fig. 2.2-16b and see section 3 in the EBSD map), however, the density maxima (see pole figure 3) are less distinct due to the polycyclic twinning mode in the complex crossed-lamellar layer. Further away from the pallial myostracum, towards inner shell surface (map segments 4, 5 in Fig. 2.2-16a and pole figures 4 and 5 in Fig. 2.2-16b), the texture becomes more and more axial as the c-axes of the lamellar sets merge to a common c-axes orientation (pole figure 5 in Fig. 2.2-16b), that is normal to inner shell surface.

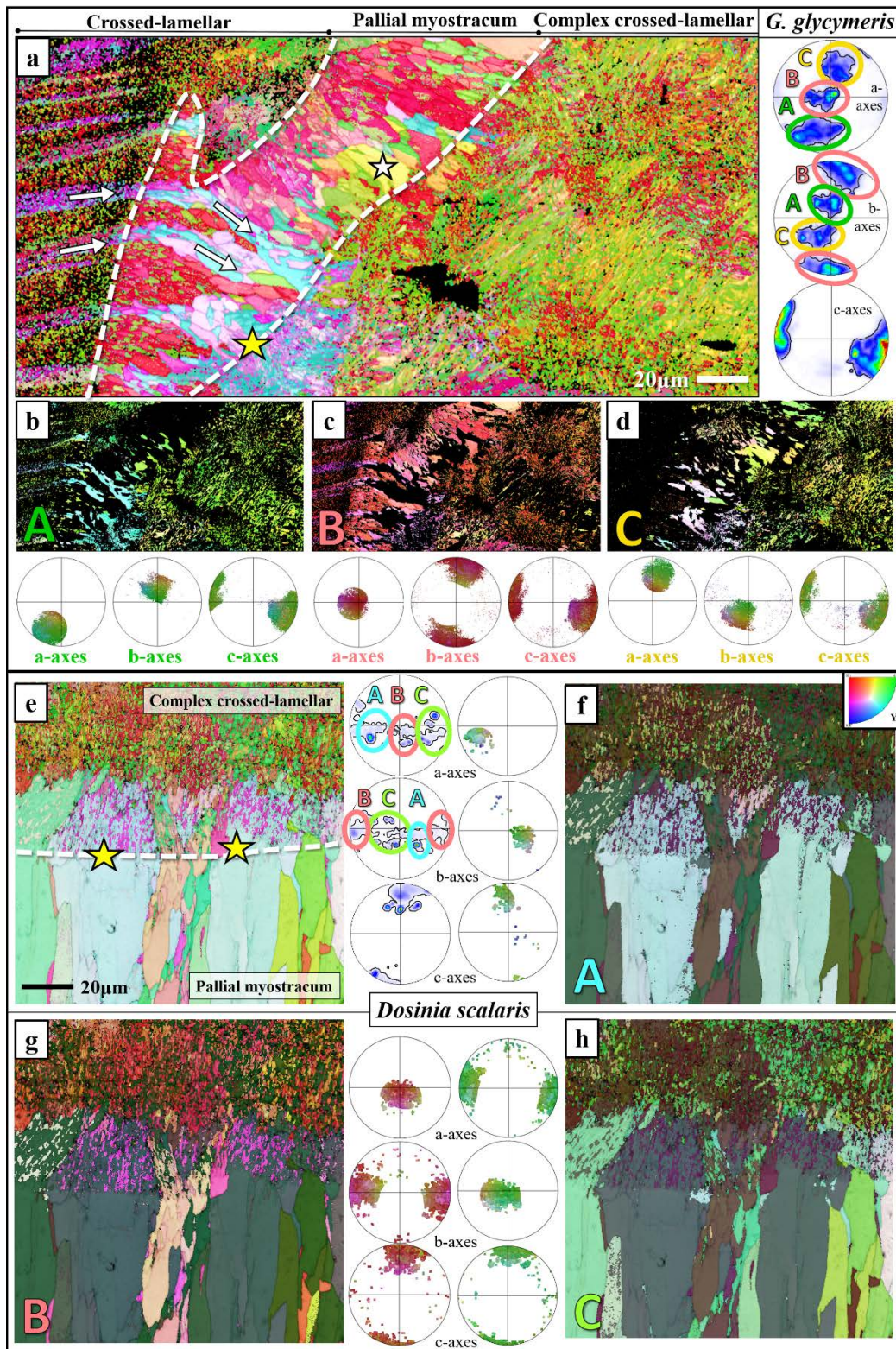


Fig. 2.2-15. Breakdown of the crystallographic texture in the non-myostracal valve-myostracum changeover region of an obliquely sectioned *Glycymeris glycymeris* shell and a transversally sectioned *Dosinia scalaris* shell. In *G. glycymeris*, the crossed-lamellar crystal orientation pattern continues through the pallial myostracum (white arrows in a) and appears to extend into the complex crossed-lamellar layer (b, c, white star in a). Similar to Fig. 2.2-12, a unique set of orientations, that was not transmitted from the texture of the first-order lamellae, is generated in the myostracum and continues into the complex crossed-lamellar layer (d). Similar to Fig. 2.2-7b, at the changeover from pallial myostracum to the complex crossed-lamellar layer a sharp boundary of incipient polycyclic twinning is visible in *D. scalaris* (white stars in e). The 3D “single-crystal-like” crystallographic texture comprises three sets of orientations (f-h) that are generated by the orientation pattern of first-order lamellae and the competitive growth mechanism of the myostracum.

In summary: (i) We observed that both adductor and pallial myostraca have similar structural characteristics. (ii) We observed for both changeovers, from the crossed-lamellar valve to the adductor or pallial myostracum and from pallial myostracum to the complex crossed-lamellar valve, similarities in transmission of crystal orientation, utilization of epitaxial growth and twin formation. (iii) We found significant structural differences between the non-myostracal, valve, and myostracal layers. The above-discussed structural features have not yet been described elsewhere.

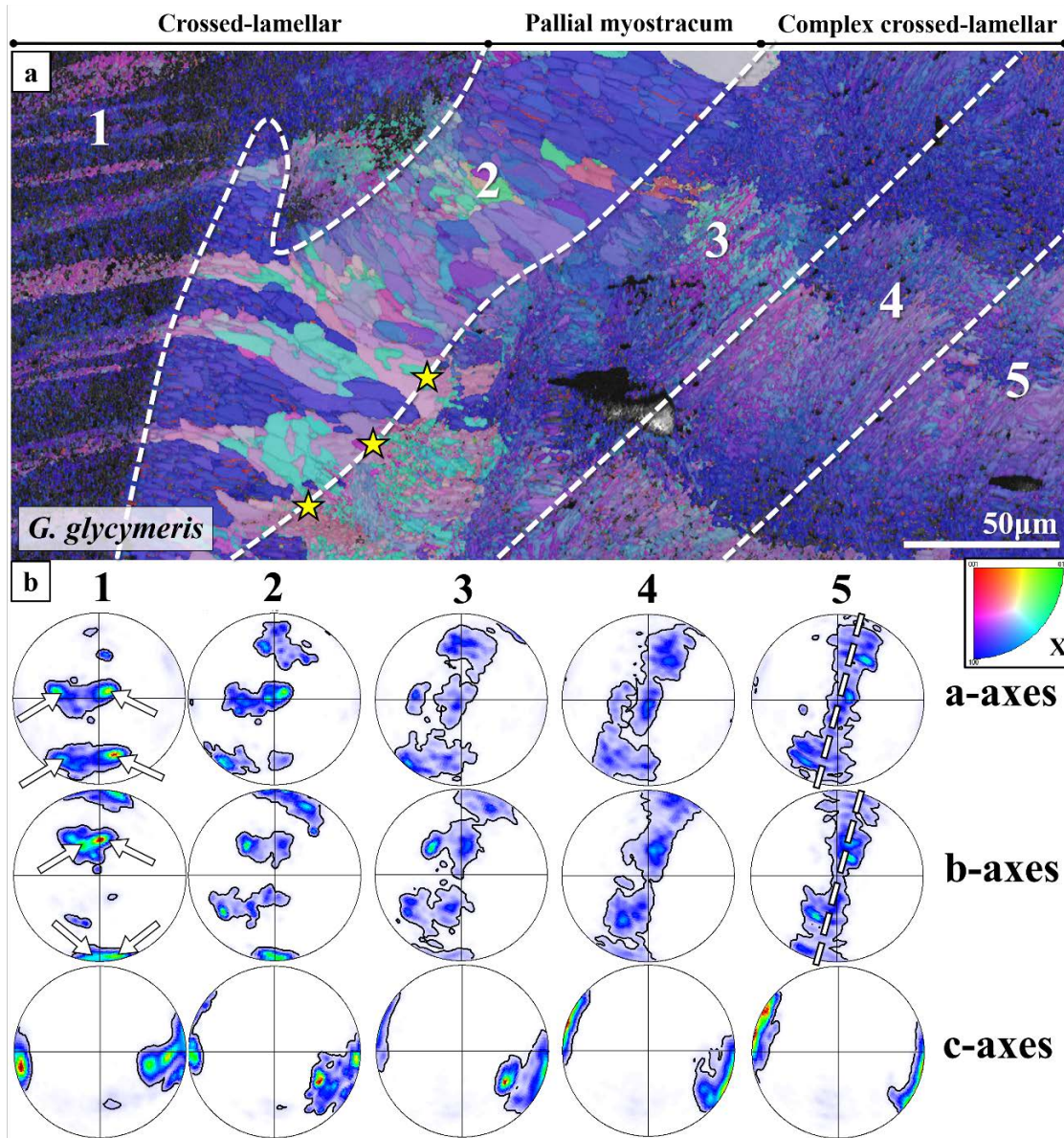


Fig. 2.2-16. Texture evolution for *Glycymeris glycymeris* from the crossed-lamellar (1) via the pallial (2) to the complex crossed-lamellar (3, 4, 5) microstructure, respectively. The measurement is split into five sections, indicated by a white dashed line in the EBSD map (a). The first pole figure (b1) corresponds to the crossed-lamellar layer, the second (b2) to the pallial myostracum and pole figures three to five (b3-5) to different stages of the complex crossed-lamellar layer (b). The pole figure (b1) indicates that the crossed-lamellar layer comprises two sets of orientations, each with a slightly deviating c-axes orientation. This pattern is continued into the pallial myostracum (pole figure b2), however, here an additional a- and b-axes orientation is added through polycyclic twinning, as described in Fig. 2.2-15. While the myostracal texture is initially continued into the first few μm of the complex crossed-lamellar layer (as visible from the EBSD map and pole figure b3), the single crystal-like texture (pole figures b1, b2) gradually transforms into an axial/fibre texture (pole figures b3, b4, b5). This indicates that the initial lamellar crystal orientation pattern of the crossed-lamellar shell is kept in the pallial myostracum, but it is abandoned in the advanced growth stages (parts 4 and 5) of the complex crossed-lamellar layer.

The hardness and indentation elastic modulus of myostracal and valve aragonite

Table 2.2-1 and Figures 2.2-11 and 2.2-12 highlight, for the investigated *Glycymeris* and *Chama* species, that myostracal valve sections are harder in comparison to the non-myostracal valve layers and to non-biological aragonite. Concerning indentation elastic modulus, non-myostracal valve and myostraca show comparable values, although we find species (*C. gryphoides* and *C. arcana*) where myostracal indentation elastic modulus is slightly increased, relative to the indentation elastic modulus of the valves.

Table 2.2-1. Nanoindentation results for profiles on *Glycymeris* and *Chama* shells. The profiles are shown in Figs. 2.2-AP14 to 2.2-AP18. (a): absolute values for hardness and indentation elastic modulus in the aragonitic layers, (b) ratios between the absolute values of two aragonitic layers, (c) first and third rows give absolute values, second and forth rows show the ratios between absolute values of the calcitic layer and the non-biological reference.

a	Shell		Myostracum	Shell		Myostracum	
	Hardness (GPa)		Hardness (GPa)	Indentation elastic modulus (GPa)		Indentation elastic modulus (GPa)	
Glycymeris bimaculata	4.13		4.81	89.1		88.2	
Glycymeris nummaria	4.61		5.11	87.4		86.4	
Chama gryphoides	4.57		5.20	88.7		96.4	
Chama arcana	Aragonite	Calcite	4.65	Aragonite	Calcite	88.6	
	3.78	3.35		82.2	68.4		
	Non-biological calcite H: 2.20 (GPa) E: 70 (GPa) Non-biological aragonite H: 4.11 (GPa) E: 105.2 (GPa)						
b	Aragonite		Myostracum	Myostracum		Myostracum	
	vs Reference	vs Reference	vs Reference	vs Reference	vs Shell		
Glycymeris bimaculata	Hardness (GPa)	Hardness (GPa)	Indentation elastic modulus (GPa)	Indentation elastic modulus (GPa)	Hardness (GPa)	Indentation elastic modulus (GPa)	
Glycymeris nummaria	1.005	1.170	0.847	0.838	1.165	0.990	
Chama gryphoides	1.122	1.243	0.831	0.821	1.108	0.989	
Chama arcana	1.112	1.265	0.843	0.916	1.138	1.087	
	0.920	1.131	0.781	0.842	1.230	1.078	
c	Calcite		Myostracum	Myostracum		Myostracum	
	Hardness (GPa) Shell	Hardness (GPa) Shell vs Reference	Indentation elastic modulus (GPa) Shell	Indentation elastic modulus (GPa) Shell vs Reference			
Chama arcana	3.35	1.523	68.4	0.977			

When hardness and indentation elastic modulus were compared between myostracal, crossed-lamellar, and complex crossed-lamellar aragonite arrangements, we found that, on average, myostracal hardness is increased by 15% and myostracal indentation elastic modulus by 5%, relative to the hardness and indentation elastic modulus of the microstructures of the non-myostracal valves. (Zhao et al. 2015) made nanoindentation measurements on the adductor myostracum of the fast-swimming scallop *Placopecten yessoensis*. Adductor myostracum hardness and indentation elastic modulus are 5.65 GPa and 78.03 GPa, respectively, while hardness and indentation elastic modulus values for the non-myostracal valve are 4.33 GPa and 69.76 GPa, respectively (Zhao et al. 2015). The material property results for *Placopecten* compare well with our material property measurements on *Chama* and *Glycymeris*. Hence, irrespective of the lifestyle of the bivalve (sessile, burrowing or swimming), we observed for the myostraca an increased hardness and a slightly increased indentation elastic modulus relative to the hardness and indentation elastic modulus values that are measured for the respective non-myostracal valve.

Variations in the chemical composition of aragonitic biominerals can affect their mechanical response (Moynihan et al. 2021). However, *Chama* and *Glycymeris* shells share similar chemistry, thus, the question is, what initiates myostracal hardness? Two factors are conceivable: (i) generally, material hardness is related to crystal twinning (Shin et al. 2016; Wang & Zhang 2016; Zhang et al. 2017b; Uttam et al. 2020), as twin boundaries block dislocation and crack propagation and induce delocalization of deformation around the crack tip. Another effect of twinning is the reduction of crystal sizes due to formation and incorporation of additional, new, grain boundaries. In inorganic materials, smaller grain sizes lead to increased hardness due to the Hall-Petch relation (Salem et al. 2006; Renard & Jacques 2012; Q. Huang et al. 2014; Ding et al. 2019); however, our results show superior hardness values for the microstructure with the largest prisms. Furthermore, we find twinning in all three layers and the exact correlation between twinning and the measured nanomechanical properties is uncertain due to the small probe size with respect to the large twin domains.

(ii) The more feasible explanation involves the proportion of mineralised material to organic matter and their distribution within the layers. For *Chama* and *Glycymeris*, myostraca consist of assemblies of large, strongly mineralised, prisms while other valve portions are formed of assemblies of minute, organic substance-coated, laths. Myostracal prisms are also encased in organic matter; however, they are significantly larger mineral entities in comparison to the laths. The observed increase in myostracal hardness values, thus, can be explained by the increased mineralisation of myostracal prisms and the relatively low amount of organic matrix material that surrounds the crystals. The latter prevents indented grains from shifting and rearranging in softer organic matter and leads to a higher measured hardness. To account for crystal anisotropy that can influence the nanomechanical properties of a material (Amini et al. 2014; Gilbert et al. 2022b), the layers were indented both parallel and

perpendicular to the c-axes orientations. For both cases, the myostracum layer shows higher hardness values than the non-myostracal valve (see also Hoerl (2022)).

The effect of myostracal crystal organisation

The topological relation between mollusc muscles and myostracal hard tissue is well-investigated by now (Hubendick 1957; Nakahara & Bevelander 1970; Plesch 1976; Tompa & Watabe 1976; Chantler 1983; Isaji et al. 2002; Castro-Claros et al. 2021). The muscle tissue does not connect directly to myostracal carbonate or insert into myostracal hard tissue. Muscle cells terminate at the basal cellular membrane of a layer of specialized epithelial cells, the tendon cells (e.g. Castro-Claros et al. 2021; Nakahara and Bevelander 1970; Tompa and Watabe 1976). As described by other studies (e.g. Chantler 1983; Nakahara and Bevelander 1970; Tompa and Watabe 1976), the tendon cell layer has hemidesmosome junctions at its basal and apical sides, contains actin, myosin and paramyosin microfilament bundles and has, at its apical side, knob-like microvilli. The microvilli are close to myostracal crystals, however, do not insert into these. A seam of extracellular polymer fibrils, collagen fibrils, derived from or/and connected to the microvilli (e.g. Isaji et al. 2002; Tompa and Watabe, 1976) is the substance that is directly next to myostracal crystals and, even more important, enters into the basal side of the prisms (e.g. Castro-Claros et al., 2021; Isaji et al., 2002; Plesch, 1976; Tompa and Watabe, 1976). Thus, muscle fibres connect to myostracal crystals via the basal tendon cell layer (Tompa & Watabe 1976) and the extracellular actin, myosin and paramyosin fibrils in the myostracal aragonite (Chantler 1983). Hence, bivalve myostracal prisms are biopolymer fibre-reinforced polymer-mineral composites.

The opening and closing of mollusc valves is an interplay between adductor muscle and hinge ligament action (Kahler et al. 1976; Yonge 1978). Contractile activity of the muscles closes the valves, causing the ligament to bend and compress. During muscle relaxation, this energy stored in the ligament opens the valves (e.g. (Millman 1967; Rüegg 1971). Bivalve adductor muscles are among the strongest muscles known for invertebrates and vertebrates (Chantler 1983; Castro-Claros et al. 2021). Bivalve adductor muscles can generate tensions up to 15 kg/cm² to counteract the force of the ligament, which, in some bivalves, takes 1 kg/cm² or more (Chantler 1983). The strong forces that bivalve muscles can exert are achieved through (i) the use of a combination of different muscle types and muscle fibre structures (e.g. thick, thin muscle filaments; striated, smooth muscles (Millman 1967; Chantler 1983)), (ii) a tight connection from muscle to myostracal tissue (e.g. variation in muscle cross-section (Millman 1967; Trotter 1993; Odintsova et al. 2007; Tremblay et al. 2015)) and (iii) the integration of tendon cell-derived biopolymer fibrils into myostracal crystals. From a material property perspective of particular interest is the junction between the apical surface of the tendon biopolymer fibrils and the basal surface of the myostracal crystals. As very dissimilar materials join at this junction, interfacial stress is likely to accumulate here and will lead to fracture. However, Zhao et al. (2015) reported for the scallop *Placopecten yessoensis* that, at forcing the valves apart, rather the adductor muscle itself breaks into

half, instead of being torn away from the myostracal crystals. Hence, as the biopolymer fibrils of tendon cells are anchored within the myostracal crystals, much less interfacial stress accumulates at the fibril-crystal interface. Accordingly, the incorporation of the fibrils into the crystals is the decisive factor for the strength of the myostracum-tendon layer connection.

Myostracal crystals are always aragonitic (e.g., this study and (Crippa et al. 2020a; Hoerl 2022; Le Moine 2022; Hoerl et al. 2024a). Even in entirely calcitic shells, e.g. that of Ostreoida, myostraca are aragonitic (Sancho Vaquer et al. 2023). This might have the following reasons: (i) it is well-documented by now for nacreous and coral aragonite that biologically formed aragonite has biocompatible properties (Lopez et al. 1992; Silve et al. 1992; Zhang et al. 2017a; Rousseau 2018). Hence, in analogy, we can assume that this strong preference for molluscs to produce myostracal crystals solely of aragonite might be rooted in the biocompatible nature of the bioaragonite. (ii) The high Mg^{2+} content in many marine environments due to the large Ca^{2+} consumption (Cheng et al. 2014) may slow down the growth kinetics of calcite, thus, thermodynamically favouring aragonite formation in oceanic environments (Mucci & Morse 1984; Wombacher et al. 2011). (iii) The competitive growth process initiates that large and specifically oriented prisms are adjacent to tendon cell filaments. Hence, a specific crystallographic face of aragonite crystals borders filament ends. This might foster attachment and incorporation of the biopolymer filaments into myostracal aragonite.

The pallial, adductor (this study) and pedal myostraca (Crippa et al. 2020a) of bivalve species that were, so far, investigated with EBSD have a competitive growth-derived microstructure. The result of the latter crystal growth process is that (i) aragonite crystals become oriented in a specific direction and (ii) large crystals face the array of organic fibrils and the apical surface of the tendon cell layer. Tompa and Watabe (1976) and Castro-Claros et al. (2021) discussed and showed that the tendon cell-associated extracellular polymer fibrils insert into myostracal crystals. Through competitive growth, the basal surface of myostracal crystals becomes oriented in parallel to the apical surface of tendon cells. Consequently, with the adductor myostracum – tendon cell – muscle fibre constellation aragonite c-axis orientation is parallel to the morphological, long axes direction of organic fibrils (see pole figures in Figs. 2.2-4 and 2.2-5) and the orientation of aragonite prisms becomes aligned with the direction of the tensile force. Thus, the myostracal microstructure appears to be beneficial for embedding polymer fibres into crystalline materials, as it results in a huge increase in tensional force. However, it is not yet clear, whether this crystal arrangement is derived solely from the lack of cellular control during crystal growth or is due to biological adaptations. For *Anomia ephippium*, it has been shown that collagenous fibrils are arranged in parallel within myostracal prisms (personal communication C. Salas), however, the exact mechanism that initiates the arrangement is, for biologically secreted hard tissues, not yet well understood. For non-biological, polymer fibre–ceramic materials it is shown that the latter can sustain the highest tensional forces when the incorporated polymer fibres are oriented within the crystals in parallel (Donald & McMillan 1976; Eckold 1994). As bivalve adductor and catch muscles are among

the strongest muscles known for organisms, exceeding significantly tensile forces of vertebrate muscles (Chantler 1983), a parallel alignment of biopolymer fibrils within the orchestrated aragonite prisms is most likely (e.g. personal communication C. Salas). Hence, the competitive growth mechanism secures, for the organic fibril–crystal attachment, the right topological relationship between crystals, on one hand, and polymer fibrils, tendon cells, on the other.

Is strength and mode of valve action relatable to the size, form, and structure of the adductor myostracum?

Yonge (1978) suggested that the size, structure and combination of muscle types of mollusc adductor and pedal muscles should be relatable, at least to some extent, to the environment. It is comprehensible that the frequency, speed and duration of valve opening and closure have to be connected to the lifestyle and habitat of the organism.

The many studies on mollusc muscle action show that there is a range of speeds of muscle contraction and relaxation and that these depend on the specific need for muscle utilization. Hence, variation in muscle contraction and relaxation must be paralleled and observable by muscle structure (Millman 1967; Trotter 1993; Tremblay & Guderley 2014; Tremblay et al. 2015; Tremblay & Guderley 2017). Depending on the respective mode of the bivalve's lifestyle (being sessile, burrowing or swimming), the striated or smooth muscle fibres might be developed differently, as a response to the different functional demands of the animal (Hanson & Lowy 1960). Accordingly, variations in the adductor (muscles that close the valves) and pedal (muscles that move the foot) muscle structure might influence the development, size, and crystal arrangement pattern of the muscle imprints, the myostraca.

In our study, we compared adductor myostracal structure, microstructure, texture and material properties of sessile and burrowing species belonging to different bivalve orders. We have deliberately chosen organisms that form thick valves. We complemented our results and discussion with one EBSD measurement made on the adductor myostracum of the swimming bivalve, *Placopecten magellanicus* (Fig. 2.2-AP21). The latter species is one of the strongest swimmers among bivalves. *P. magellanicus* is a scallop and only has the posterior adductor muscle. Nonetheless, we found:

(i) a marked difference in the dimension of the adductor scars. The swimming bivalve species developed the largest adductor scar, relative to the adductor scars of the burrowing and the sessile species. As the scar of the swimming *P. magellanicus* is large in extent, one can differentiate for its adductor scar microstructure (the latter measured with EBSD) between imprints initiated by phasic and by tonic muscles, hence, imprints generated by striated and smooth muscles (Tremblay & Guderley 2017).

(ii) Significant differences in myostracal prism morphology regularity. The sessile *Chama* species form their adductor myostracum with strongly irregularly-shaped prisms, relative to prism morphology developed by the swimming *P. magellanicus* and the burrowing *Glycymeris* species.

(iii) Differences in prism size. This can be well investigated for those bivalve species that form even prism morphologies. The myostracum of the swimming *P. magellanicus* consists of many, very thin, regularly shaped prisms (see Fig. 2.2-AP21), while the adductor prisms of the burrowing *Glycymeris* species are also regular in shape, but significantly thicker (e.g., Fig. 2.2-4b).

Nonetheless, common to all investigated bivalves, irrespective of their lifestyles and habitats, is the development of the competitive growth microstructure for myostracal aragonite. It develops large prisms close to the row of tendon cells, orientation of c-axes normal to the inner shell surface and alignment of aragonite c-axes parallel to the long axis of the extracellular biopolymer fibrils that are associated with the tendon cells. Hence, for the investigated species, myostracal microstructure, texture and material properties are (i) to a large extent determined by a competitive growth process that results from the mantle losing control over crystal growth. However (ii), the investigated *Chama* and *Glycymeris* samples exhibit differences in the organization and texture of the myostracum, including crystal morphologies, thickness, and continuation of the crossed-lamellar orientation pattern. These might be related to the structure of the attached muscles, which is modulated by environmental factors, such as the lifestyle of the bivalve, and the ligament size and strength. Opening and closing the valves is an integrant within the interplay between the resilience and efficiency of the hinge ligament and the resilience and efficiency of the adductor muscle (Ansell & Trueman 1967a; Kennedy et al. 1970; Allen 1976; Stokesbury & Himmelman 1996; Tremblay & Guderley 2014; Tremblay & Guderley 2017).

2.2.5 CONCLUSIONS

The bivalve shell has several functions. It protects the soft tissue of the organism, is involved in the different modes of animal movement (swimming, burrowing, sedentariness) and acts as a skeleton for the attachment of muscles. It also may have hydrodynamic functions related to feeding. The bivalve shell consists of diverse arrangements of well-ordered crystals (microstructures). These comprise all mineralized shell layers, including the myostraca. Nonetheless, despite significant differences in shell microstructure, for the investigated species, we find only two texture patterns. In most cases, the preferred crystallographic orientation (texture) is axial, in some it is three-dimensional “single-crystal-like”.

In this contribution, we highlight and discuss differences in valve and muscle attachment site crystal organization for bivalve species following different lifestyles and living in different environments. From our structural and material property results, we conclude the following:

1. For *Chama* and *Glycymeris*, non-myostracal, valve and myostracal crystal size, type and assembly pattern are distinct. Contrary to the crossed- and complex crossed-lamellar arrangements, pallial and adductor myostracal crystals have an organization pattern that is characteristic of a crystal assembly mode obtained through growth competition. The assembly of non-myostracal, valve crystals is governed by biological, the assembly of myostracal crystals by competitive growth processes, respectively.
2. For *Glycymeris* and *Chama* the adductor myostracum is attached to the crossed-lamellar microstructure, the pallial myostracum is between the crossed- and the complex crossed-lamellar crystal assemblies. Crystal size and morphology are not transferred from the crossed-lamellar microstructure to myostracal layers/portions. The laminated appearance of the crossed-lamellar valve as well as crystal (c-axis) orientation and the twinned nature of the aragonite become transmitted from valve to myostracal layers.
3. For the investigated bivalves, crystallographic texture gradually shifts from a three-dimensionally ordered preferred orientation (“single-crystal-like”) in the crossed-lamellar layer to an axial orientation in the complex crossed-lamellar layer. In *Chama*, the pallial myostracum shows, in most cases, an axial texture, with a- and b-axes orientations distributed homogeneously on a great circle. In the pallial myostracum of *Glycymeris*, a 3D “single-crystal-like” texture is visible. For the latter, the six density distribution maxima of aragonite crystal orientation in the pole figures can be attributed to cyclic twinning.
4. The first-formed myostracal crystals nucleate epitaxially onto the aragonite of the crossed-lamellar microstructure. The crystallographic orientation of valve and myostracal (adductor, pallial) crystals is parallel, it is, thus, transferred from one layer to the other. At slightly advanced stages of myostracal growth, in addition to the aragonite orientation of the first-order lamellae, a further crystal orientation develops within the myostracum and is kept for all additional growth stages. The competitive growth mode of myostracal crystals ensures that aragonite c-axes become oriented normal to inner shell surfaces.
5. Bivalve muscle cells do not attach directly to the microstructures of the valves but utilize a tendon cell layer. The myostracum is secreted during the strong shell-adductor muscle attachment that impedes the mantle from controlling crystal growth biologically. This is caused by collagenous fibres that enter myostracal prisms and prevent direct contact between the mantle and myostracal hard tissue. For most bivalves, the myostracum comprises a specific aragonite arrangement with high hardness and prisms that are parallel to adductor muscle fibres. For the development of the latter two characteristics, two crystal growth processes are utilized: (i) *epitactic nucleation* for acquisition of microstructure and texture of the valve template (not the carbonate phase, e.g. Saruwatari et al., 2009) and (ii) *competitive growth* for adjusting crystal face and c-axes orientation normal to inner shell surface, and to secure that large crystals seam inner shell surfaces. The prismatic myostracal microstructure facilitates the attachment and

insertion of collagen-rich tendon cell fibrils, which in turn, are connected basally to the tendon cells of the muscles by intracellular action filaments.

6. *Chama* and *Glycymeris* shells are twinned in crossed-lamellar, complex crossed-lamellar as well as myostracal layers. The extent and type of twinning are different for valve and myostracal aragonite. The crossed-lamellar microstructure exhibits polysynthetic twinning between third-order lamellae and cyclic twinning between the first-order lamellae. The myostracum shows cyclic twinning and revokes the polysynthetic restrictions imposed by the crossed-lamellar layer. The complex crossed-lamellar layer exhibits the highest amount of relative twinning frequency and features mostly polycyclic twins within first-order lamellae.
7. Through its specific microstructure resulting from adductor muscle attachment, the myostracum exhibits outstanding nanomechanical properties. For *Chama* and *Glycymeris*, the hardness of the valves and myostracum differs by up to 20%. The average value of respective indentation moduli in valve and myostracum is similar across *Glycymeris* shells, is, however, slightly different for *Chama*. For the latter species, it is always lower than the non-biological reference.

Acknowledgements

We thank Prof. N. Lagos Suárez, Centro de Investigación e Innovación para el Cambio Climático – CIICC, Universidad Santo Tomas, Santiago, Chile, Dr. M. Peharda Uljević, Institute of Oceanography and Fisheries, Split, Croatia and Prof. S. Gofas, Departamento de Biología Animal, Facultad de Ciencias, Universidad de Málaga, Málaga, Spain for the samples.

Author contributions

Conceptualisation, S.H., E.G.; Formal analysis, N.J.P., S.A., E.M.H., C.S., A.G.C., W.W.S.; Investigation, S.H., T.I.M., N.J.P., S.A., E.G., J.W.; Methodology, S.H., E.G., E.M.H., C.S.; Supervision, N.J.P., S.A., E.G., W.W.S.; Validation, A.G.C., W.W.S.; Visualisation, S.H., E.G.; Writing – original draft, S.H., E.G.; Writing – review & editing, T.I.M., N.J.P., S.A., J.W., E.M.H., C.S., A.G.C., R.S., W.W.S..

2.2.6 SUPPLEMENTARY INFORMATION

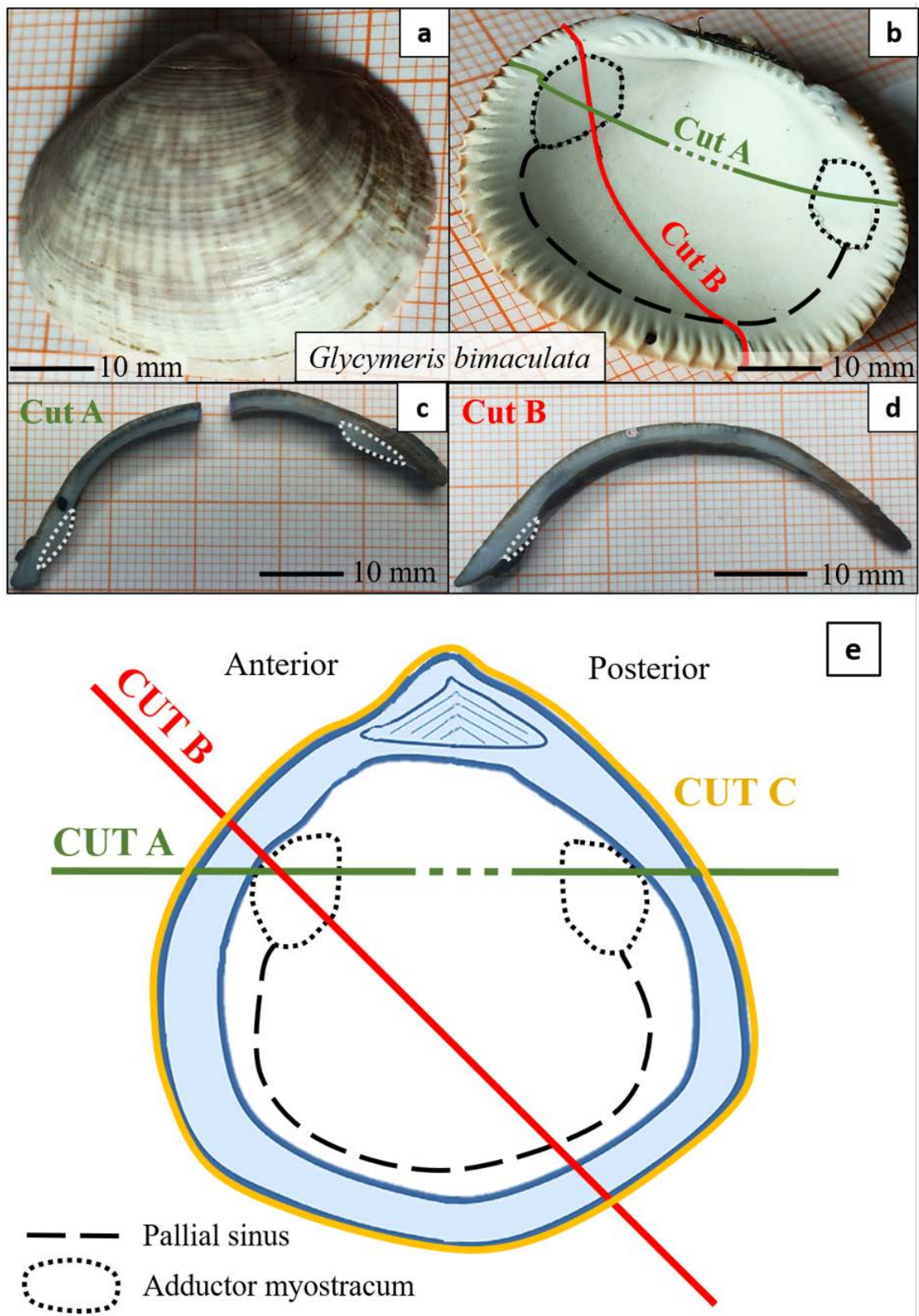
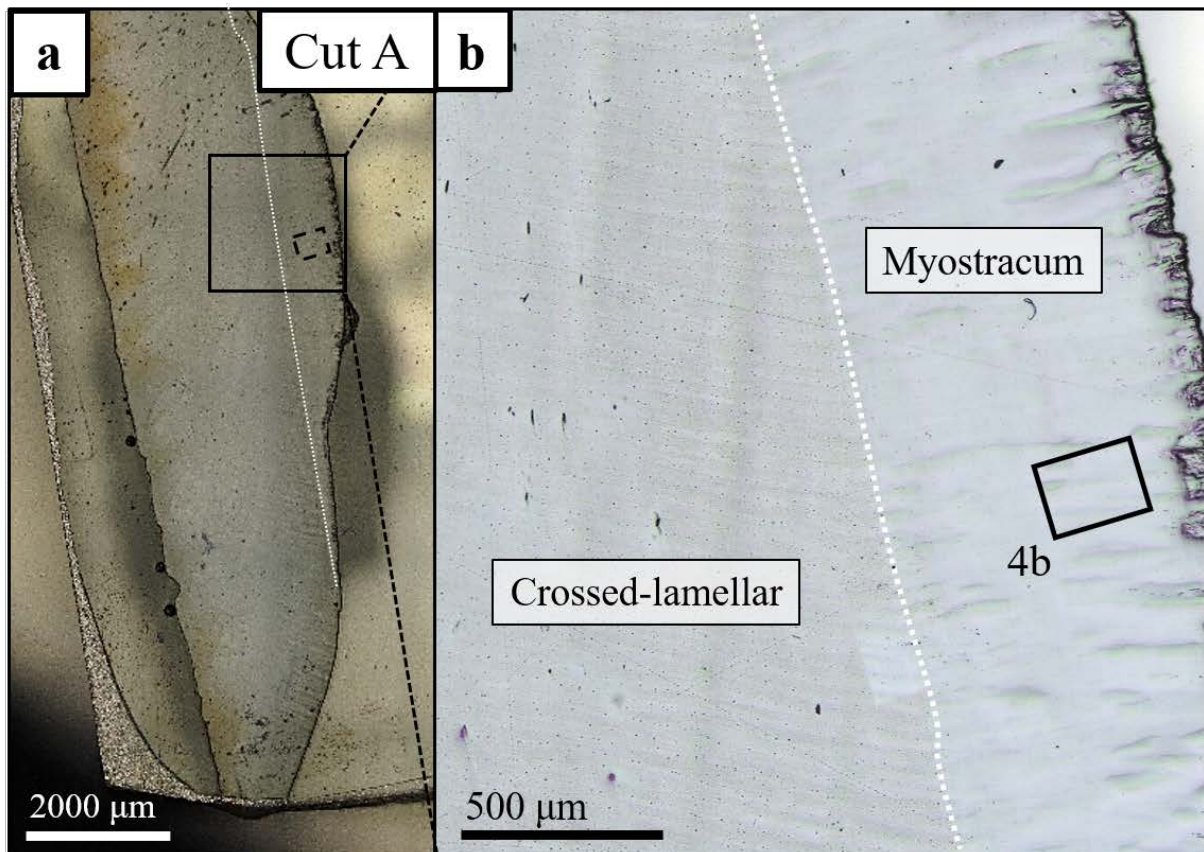


Fig. 2.2-API. Overview indicating the direction and position of the different shell cuts performed on the specimens presented in this article. As highlighted for a shell of *Glycymeris bimaculata* (a, b), the valves were cut to expose the adductor myostraca indicated by dotted lines (c, d). All three cuts are illustrated for a right *Glycymeris* valve (e: modified after Crippa et al., 2020a). The valves were cut transversely through both adductor myostraca (cut A), obliquely, through one adductor myostraca (cut B) or crosswise, exposing the cross-section of the adductor myostraca (cut C).



Glycymeris nummaria measurement positions

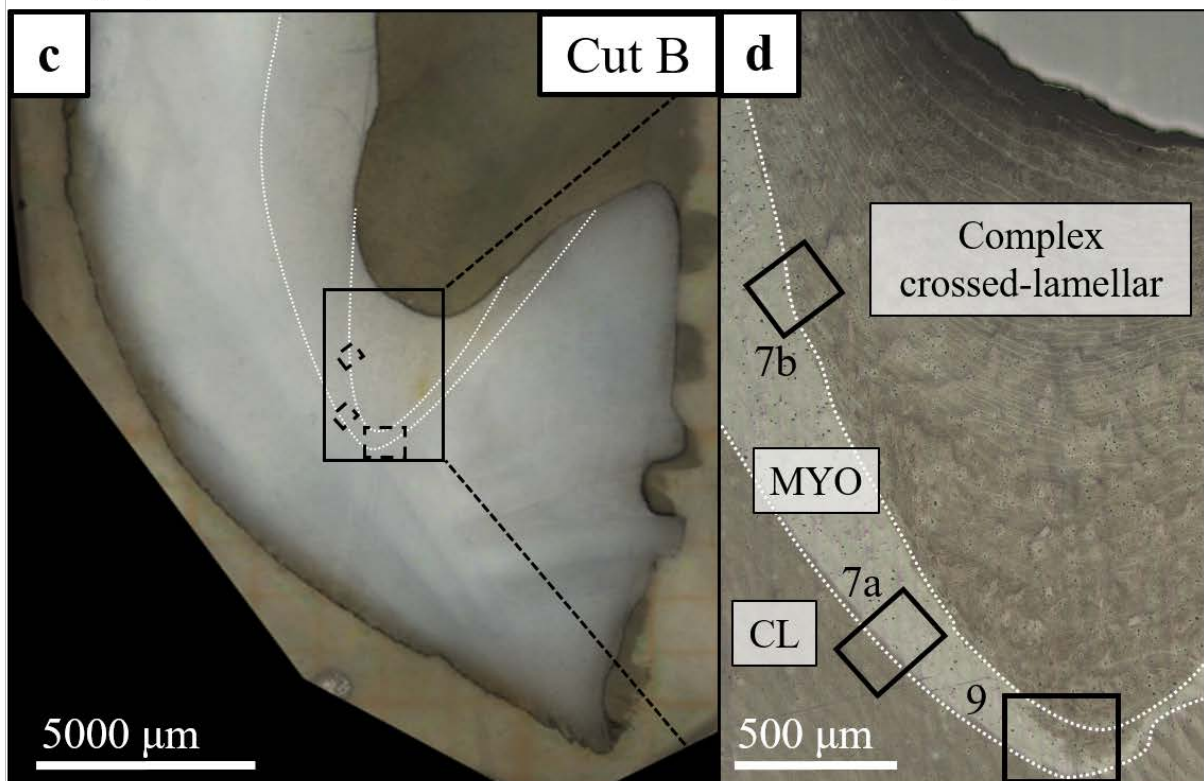
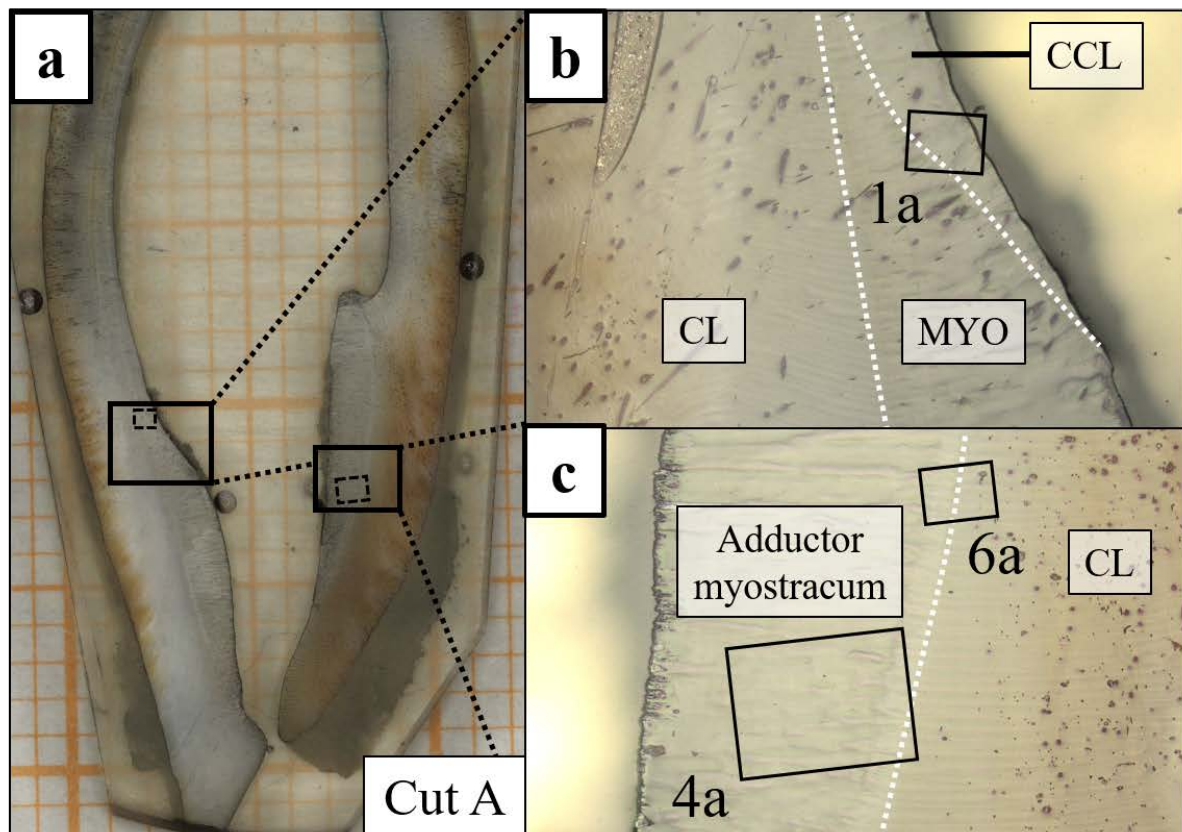


Fig. 2.2-AP2. Laser confocal microscopy image depicting the positions of the most important *Glycymeris nummaria* EBSD scans. (a, b): cut A, (c, d): cut B. The interfaces of the respective layers are highlighted with dashed white lines in the close-up images (b, d). MYO: Myostracum, CL: Crossed-lamellar layer.



Glycymeris bimaculata measurement positions

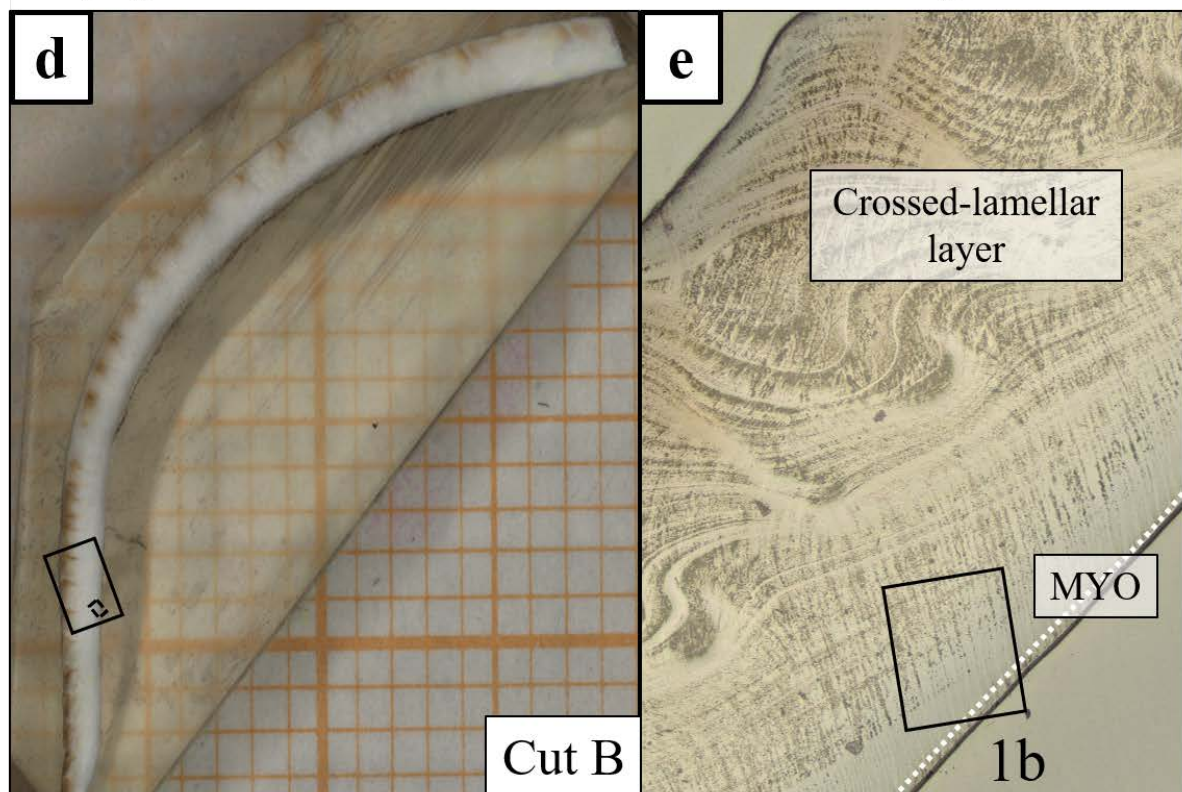


Fig. 2.2-AP3. Laser confocal microscopy image depicting the positions of the most important *Glycymeris bimaculata* EBSD scans. (a, b): cut A, (b, c): cut B. The interfaces of the respective layers are highlighted with dashed white lines in the close-up images (b, c, e). MYO: Myostracum, CL: Crossed-lamellar, CCL: Complex crossed-lamellar.

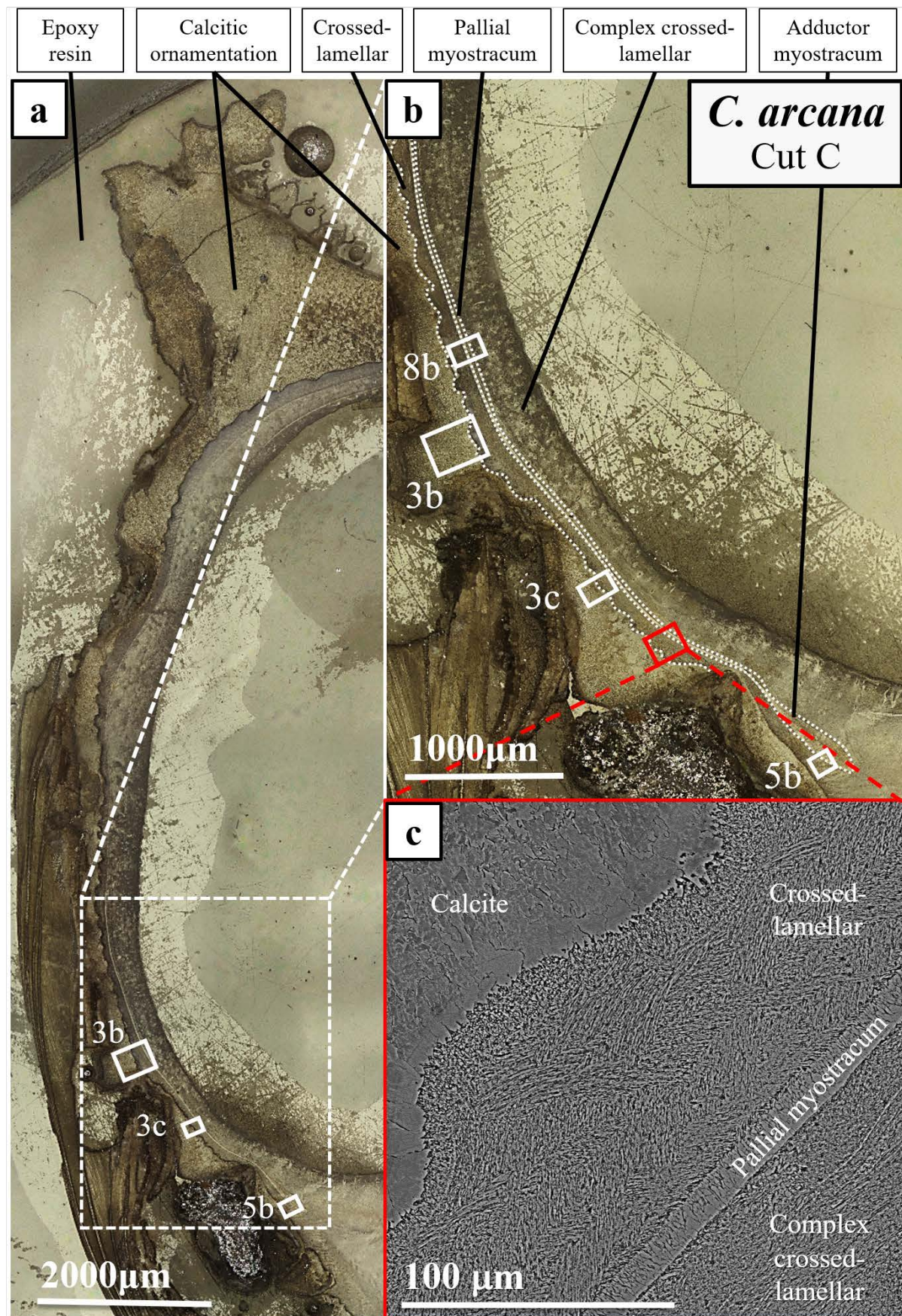


Fig. 2.2-AP4. Laser confocal microscopy images depicting the positions of the most important EBSD scans performed on a *Chama arcana* shell, along cut C (a, b). The interfaces of the respective layers are illustrated with dashed white lines in the close-up image (b). The structure and interfaces of the valve layers are highlighted with an SEM image (c).

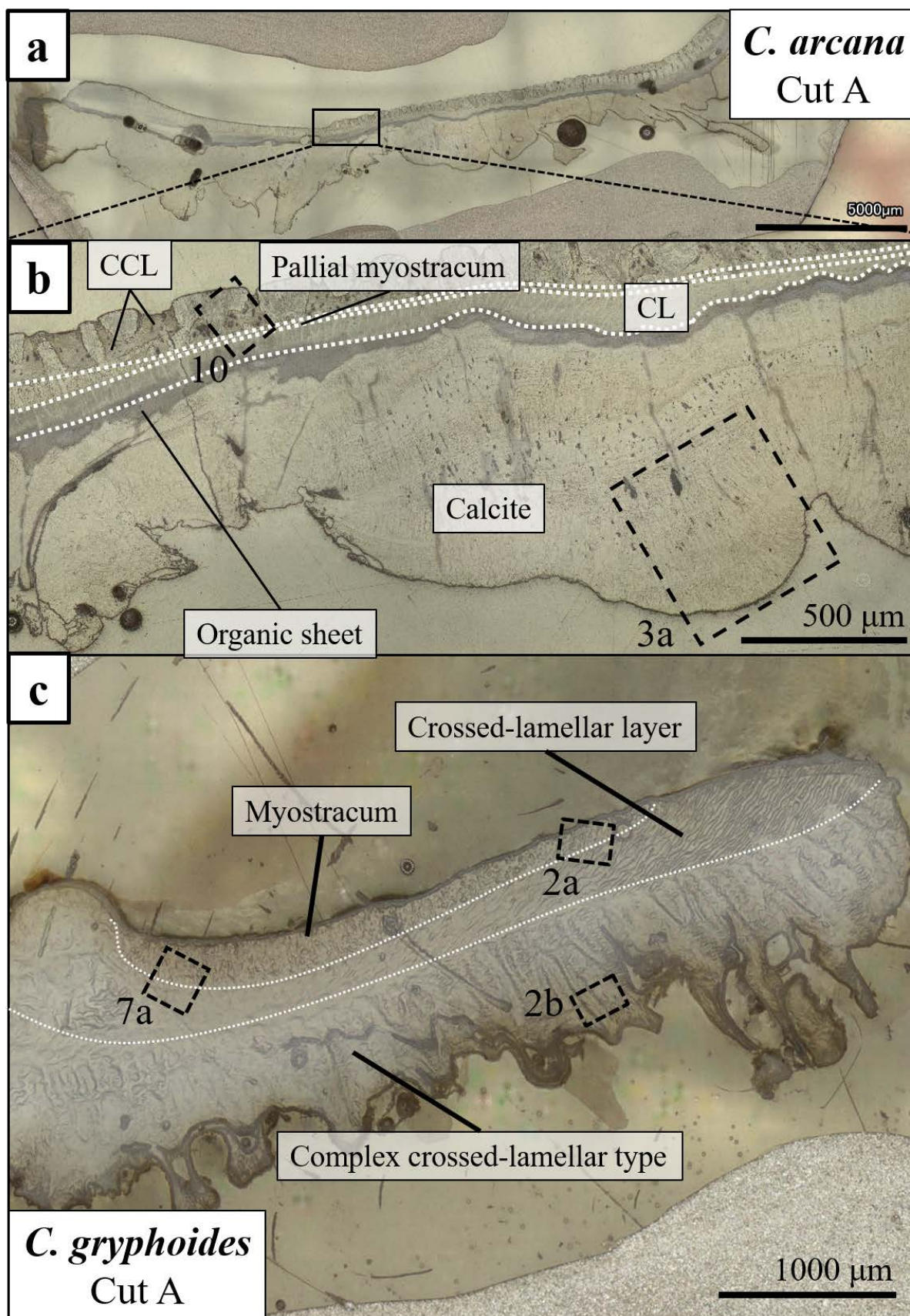


Fig. 2.2-AP5. Laser confocal microscopy image depicting the positions of the most important EBSD scans performed on *Chama gryphoides* shells (a-c). The ornamentation calcite is separated from the aragonitic layers by a thick organic deposit (b). The interfaces of the respective layers are highlighted with dashed white lines (b, c). CCL: Complex crossed-lamellar, CL: Crossed-lamellar.

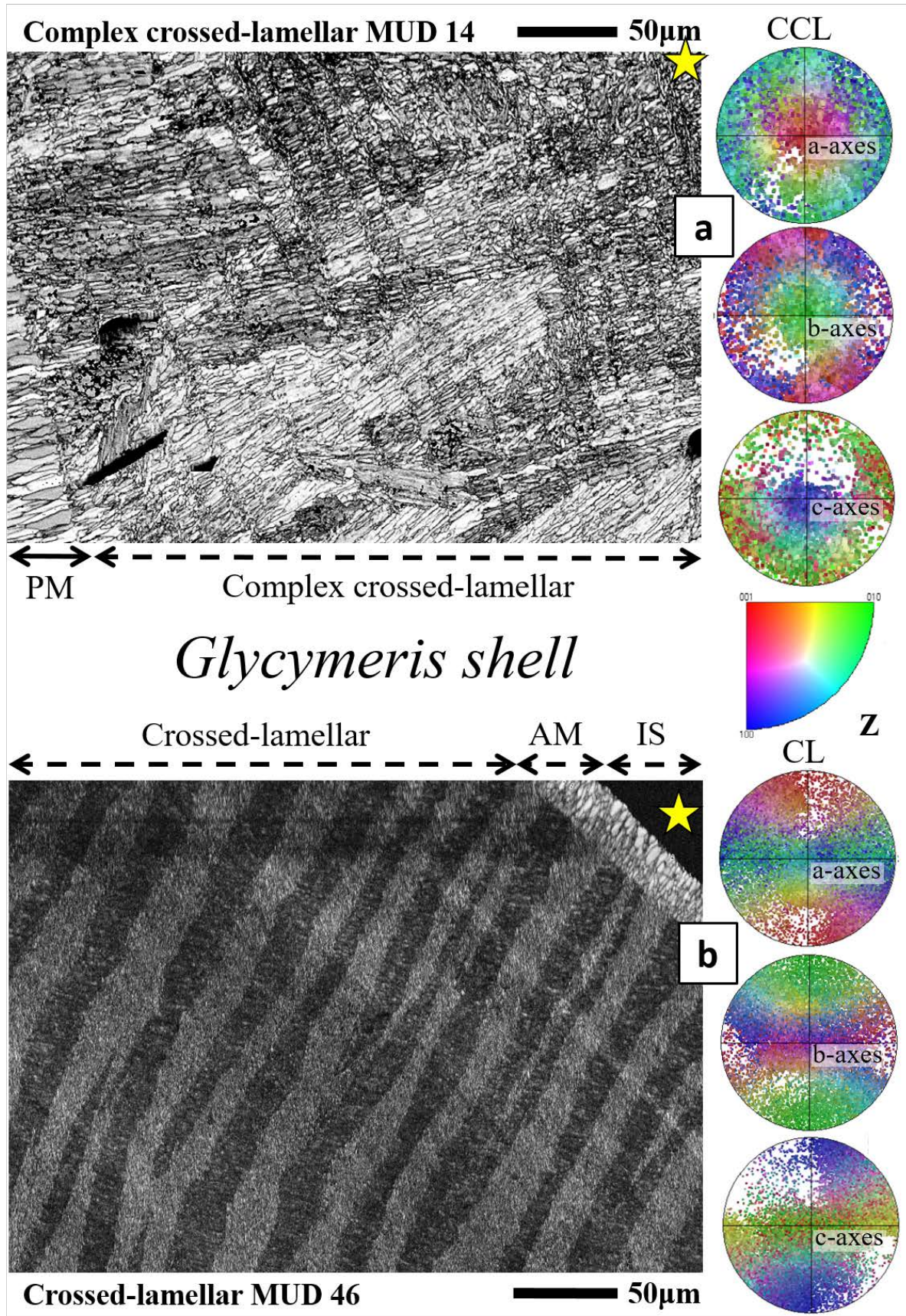


Fig. 2.2-AP6. EBSD band contrast scans of *Glycymeris bimaculata* shells depicting the different structures observed for *Glycymeris*. From the outer shell surface towards the inner shell surface (IS, marked by a yellow star in a, b), the shell comprises a crossed-lamellar, the myostracal (PM: Pallial myostracum, AM: adductor myostracum), and a complex crossed-lamellar layer (CCL, only after the pallial myostracum). The pole figures give crystal orientation data points.

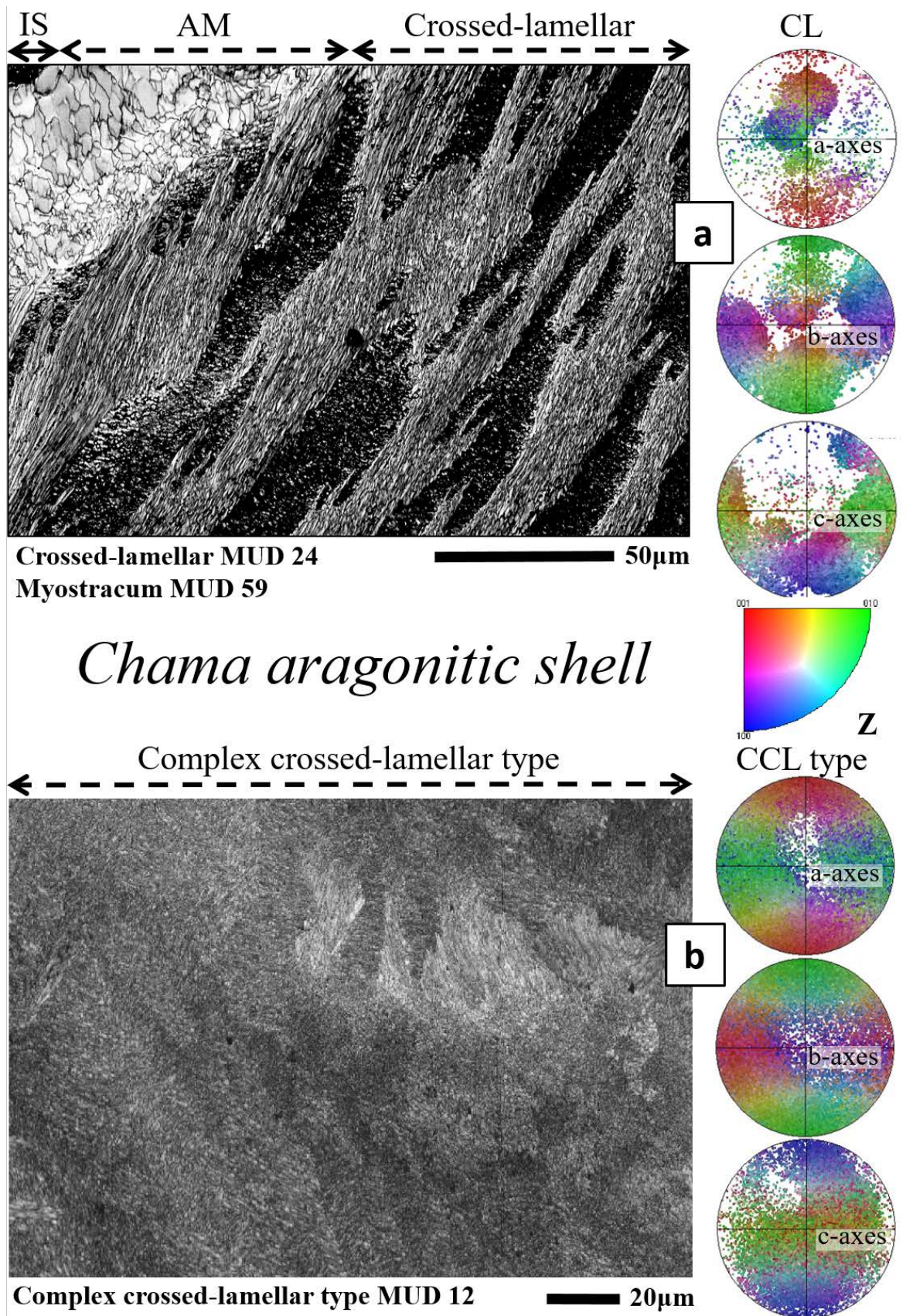


Fig. 2.2-AP7. EBSD band contrast scans depicting the microstructures of different layers of a *Chama gryphoides* shell. The valves comprise a crossed-lamellar (CL) microstructure and an adductor myostracum (AM) along the inner surface (IS) of the shell (a). A complex crossed-lamellar (CCL) type microstructure forms the aragonitic outer shell ornamentations and comprises small crystals arranged in an intricate orientation pattern of first-order lamellae (b). The pole figures give crystal orientation data points.

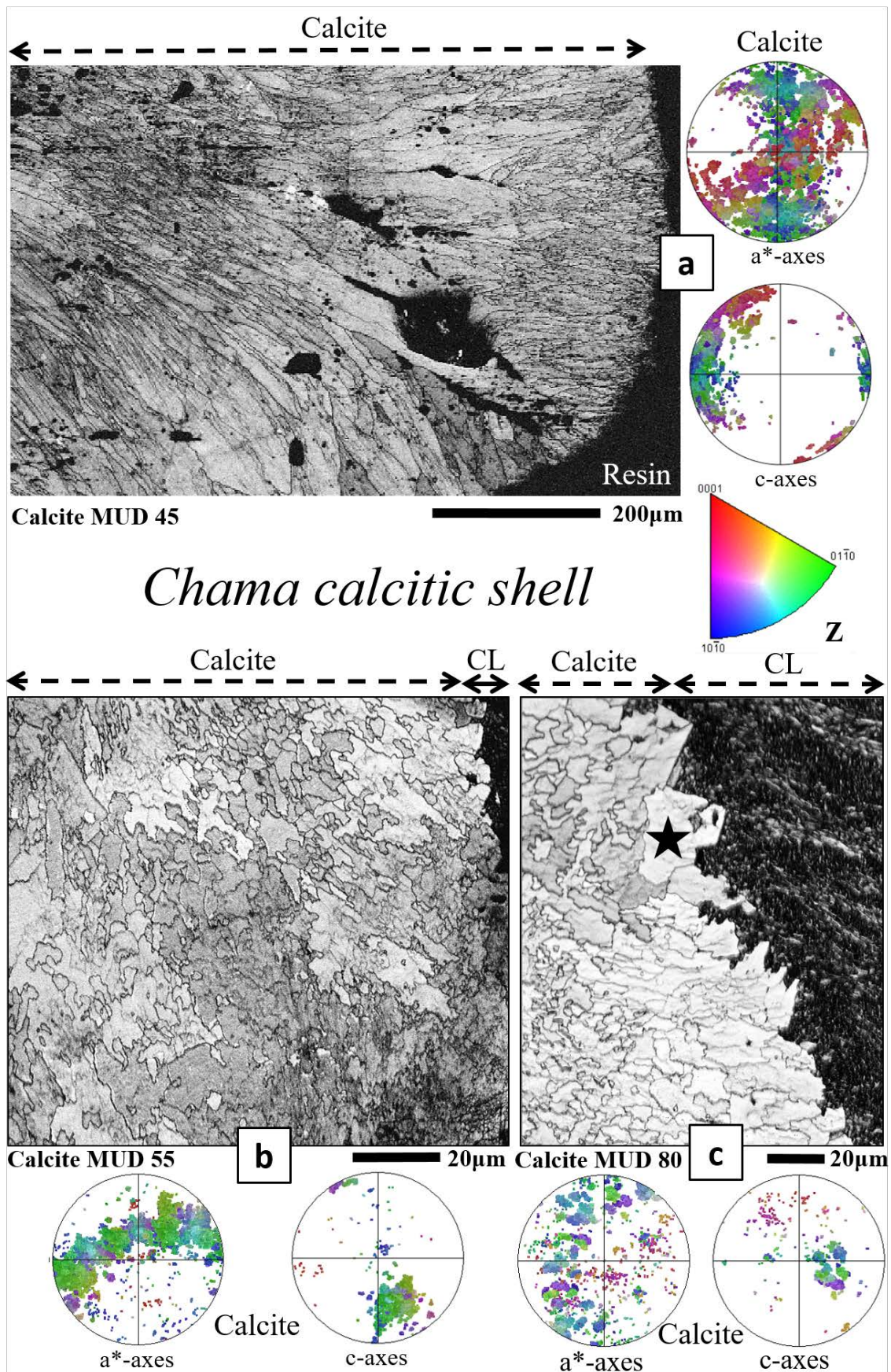


Fig. 2.2-AP8. EBSD band contrast scans depicting the microstructure of the calcitic ornamentation of a *Chama arcana* shell. The pole figures give crystal orientation data points and depict a rotation in c-axes perpendicular to the outer surface of the ornamentations (a). Within the ornamentations, calcitic crystals interdigitate strongly in 3D. The calcitic crystals have very irregular, fractal, morphologies.

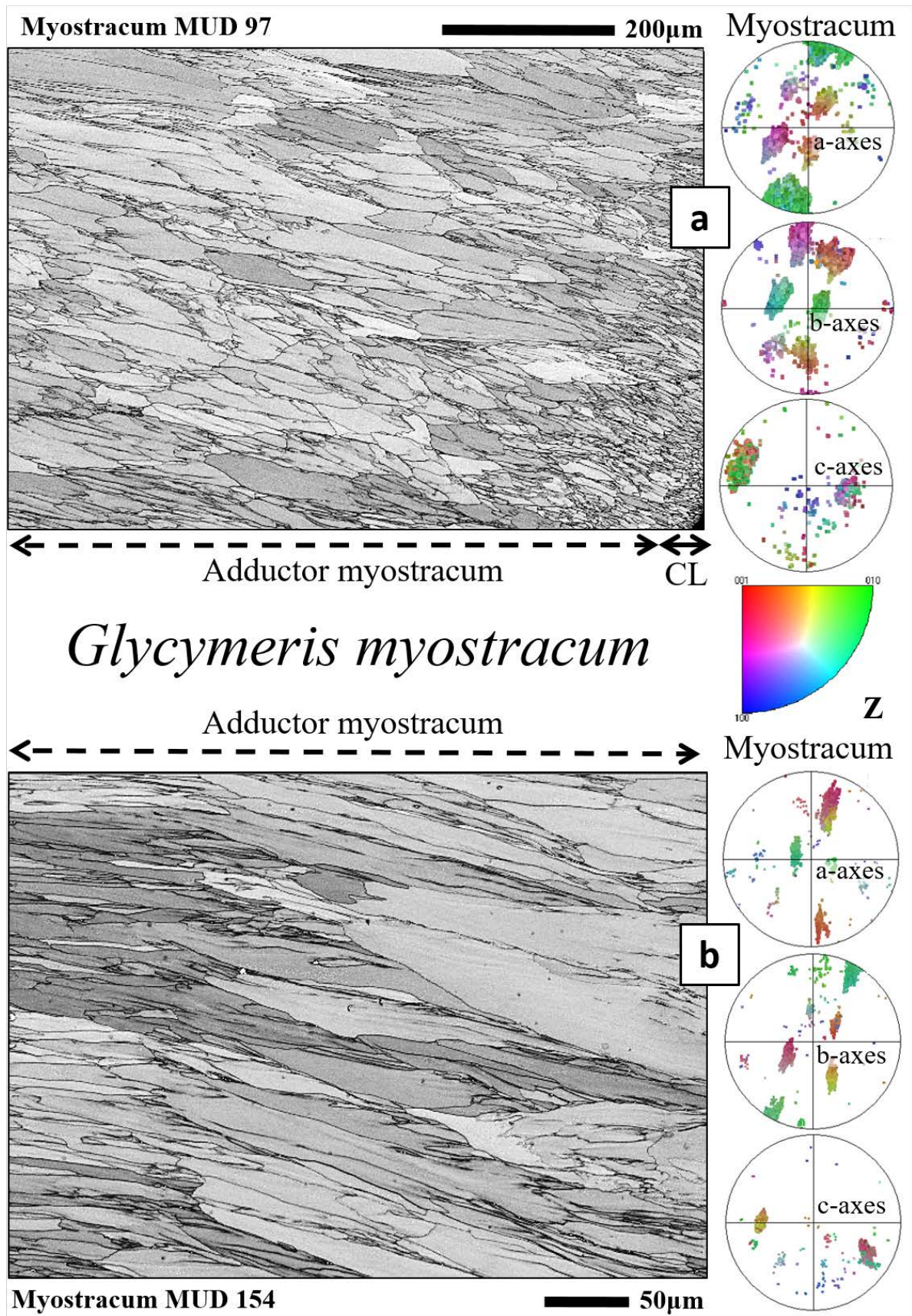


Fig. 2.2-AP9. EBSD band contrast scans depicting the microstructure of the adductor myostracum of *Glycymeris* shells. The increasing grain size towards inner shell surface (a) and successive formation of large prisms (b), away from the crossed-lamellar shell is well visible. The prisms have their c-axes oriented normally to inner shell surface and in the growth direction.

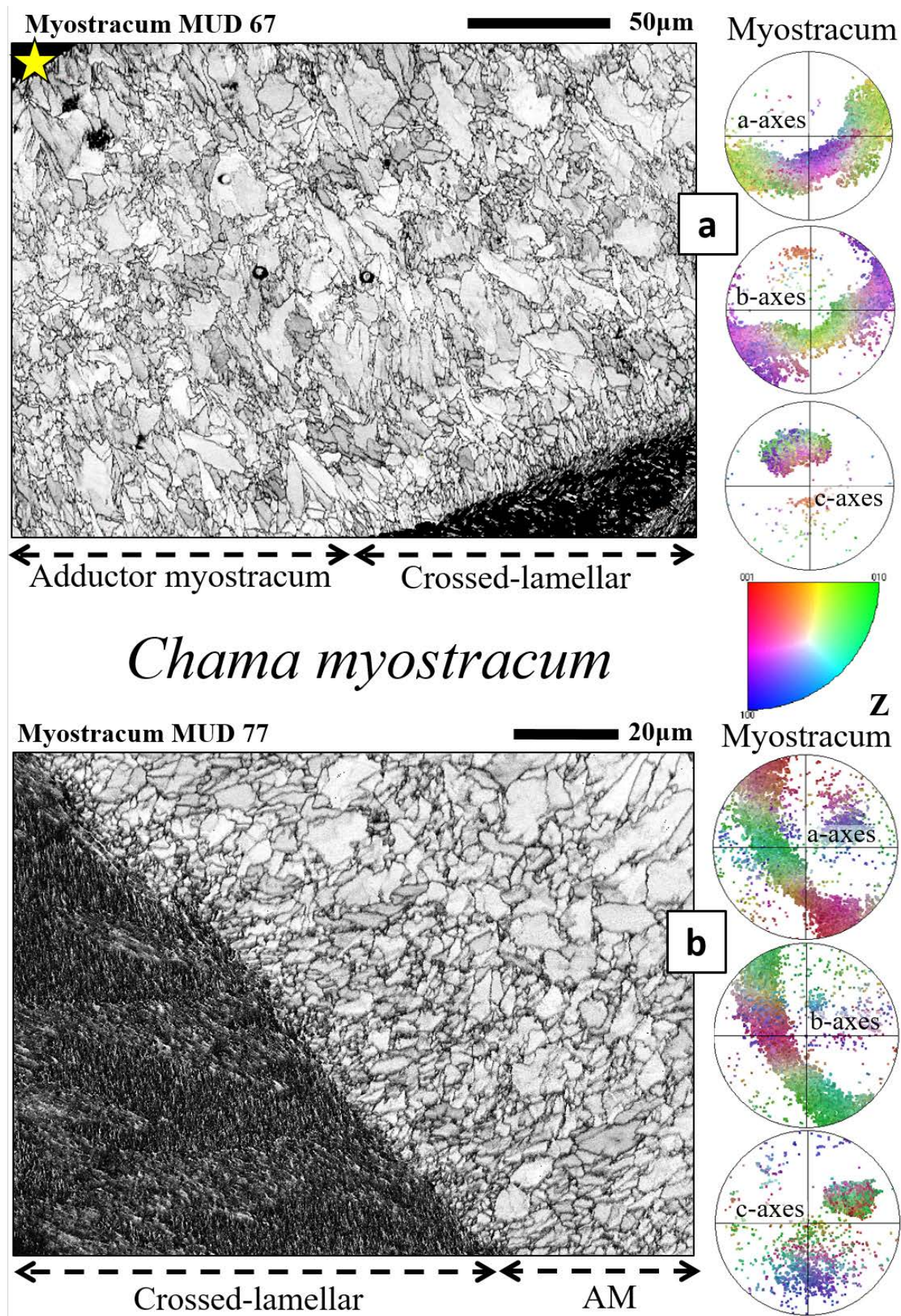


Fig. 2.2-AP10. EBSD scans depicting the microstructures of the adductor myostracum of *Chama* shells. (a): *C. gryphoides*, (b): *C. arcana*. Yellow star in (a): inner surface of the shell. The pole figures give crystal orientation data points.

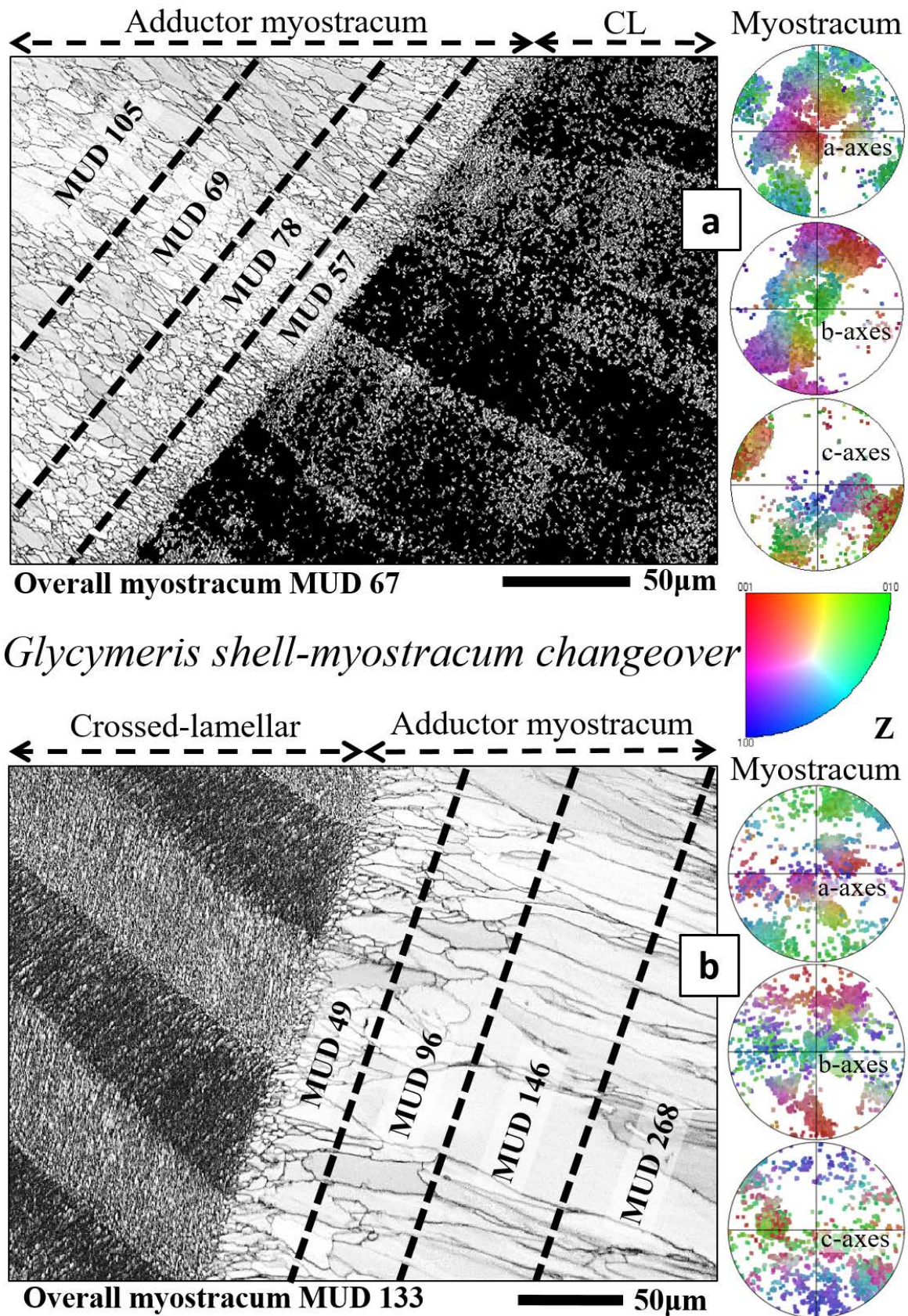


Fig. 2.2-AP11. EBSD scans depicting the changeover from the crossed-lamellar layer to the adductor myostracum in *Glycymeris* shells. (a): *G. nummaria*, (b): *G. pilosa*. The crystals close to the interface between the microstructures are small and isotropic in shape. They increase in size and become prism-shaped towards the inner shell surface (a, b). MUD values of different subsets in the adductor myostracum show that the crystal co-orientation increases with distance from the changeover (a, b). The pole figures give crystal orientation data points of the depicted myostracum regions.

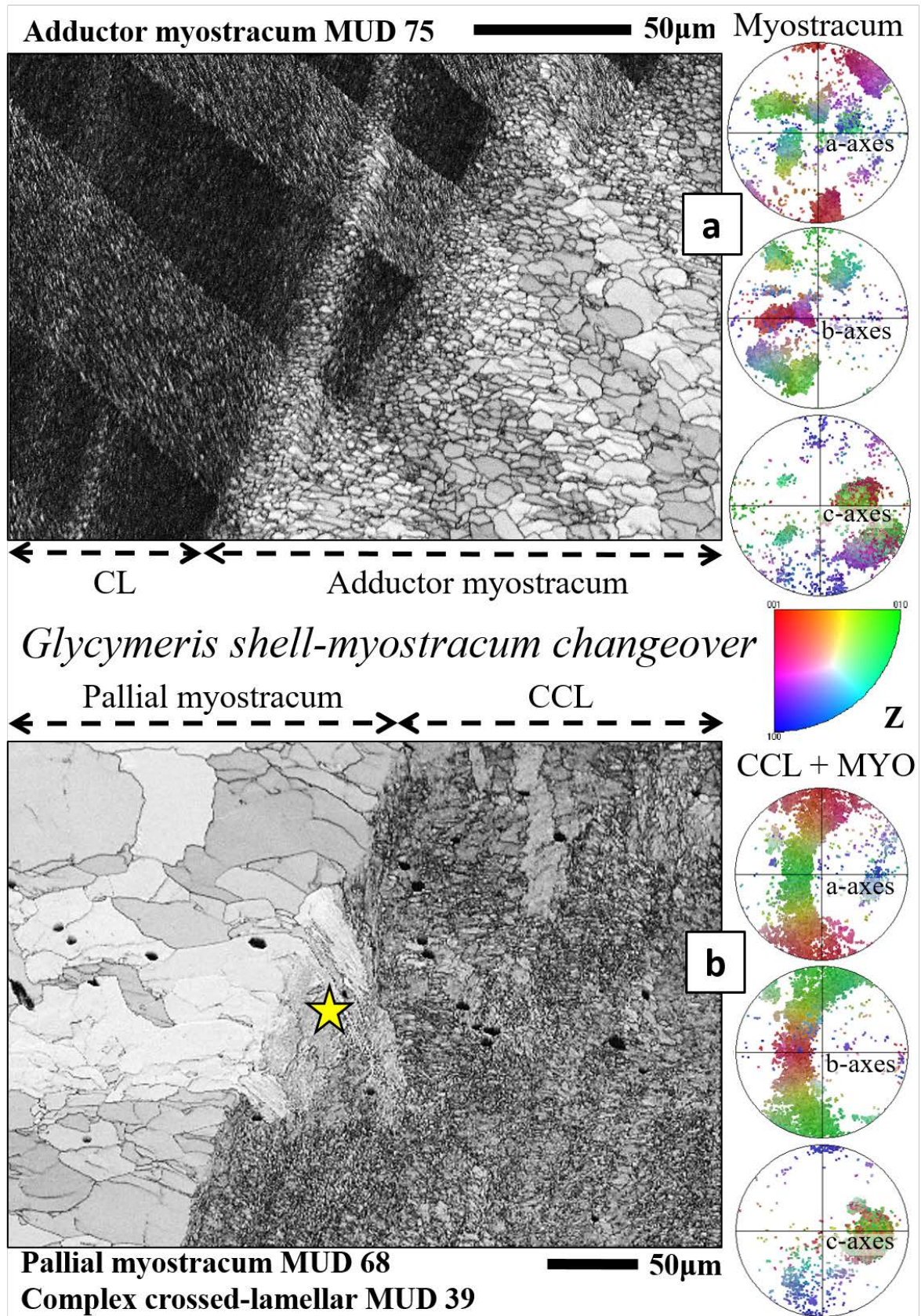


Fig. 2.2-API2. EBSD scans depicting the non-myostracal shell – pallial myostracum changeover in *Glycymeris* shells. (a): change from crossed-lamellar (CL) sets to the pallial myostracum, (b): transition of the pallial myostracum (PM) to the complex crossed-lamellar layer (CCL). (a, b): *G. nummaria*. Large myostracal prisms of the pallial myostracum (yellow star in b) protrude into the complex-crossed lamellar layer. The pole figures give crystal orientation data points.

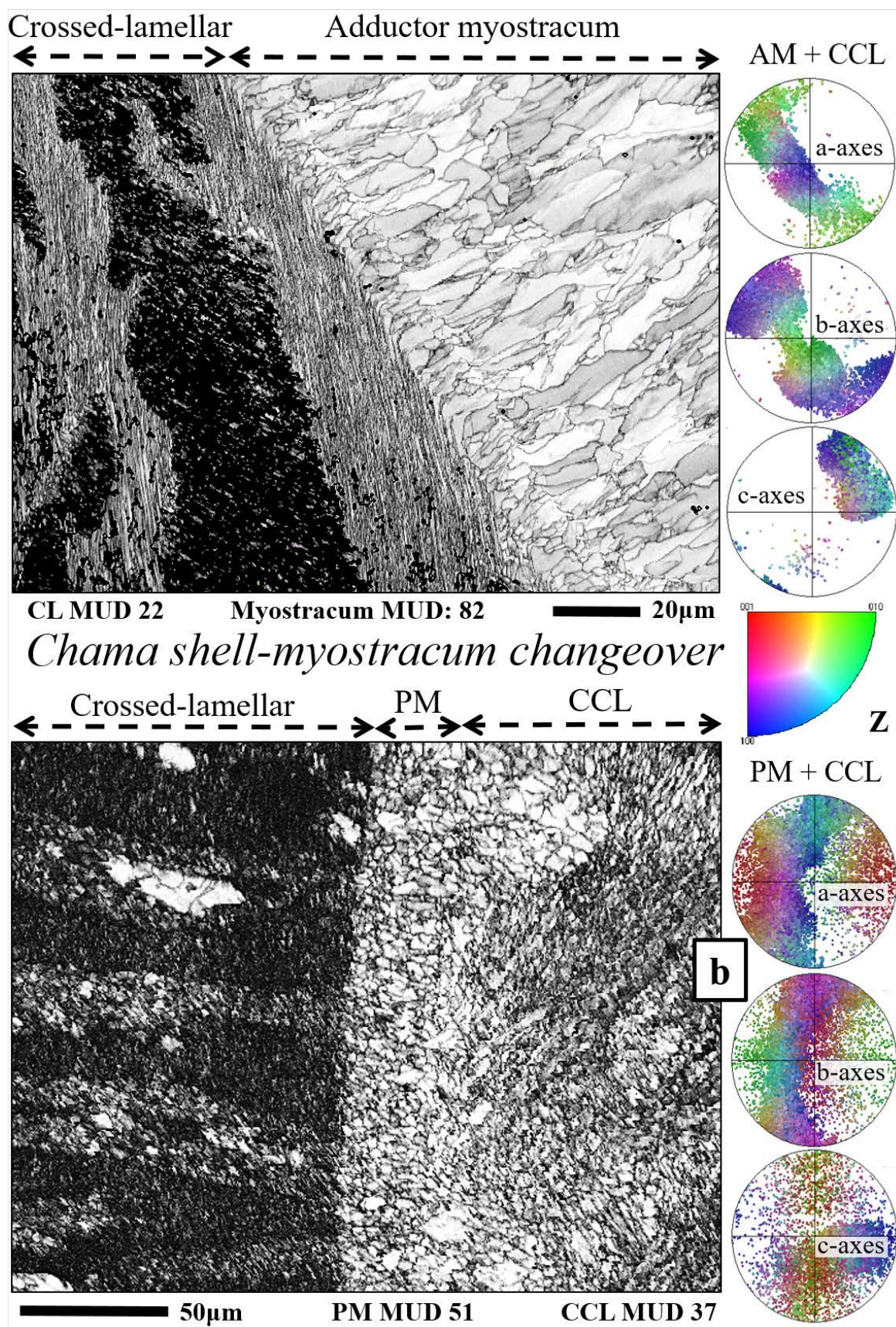


Fig. 2.2-AP13. EBSD scans depicting the interface between non-myostracal and myostracal shell microstructures. (a): *Chama gryphoides* (b): *Chama arcana*. (a): Transition from crossed-lamellar shell to adductor myostracum, (b): changeover from crossed-lamellar shell to pallial myostracum and from pallial myostracum to complex crossed-lamellar shell. The pole figures give crystal orientation data points.

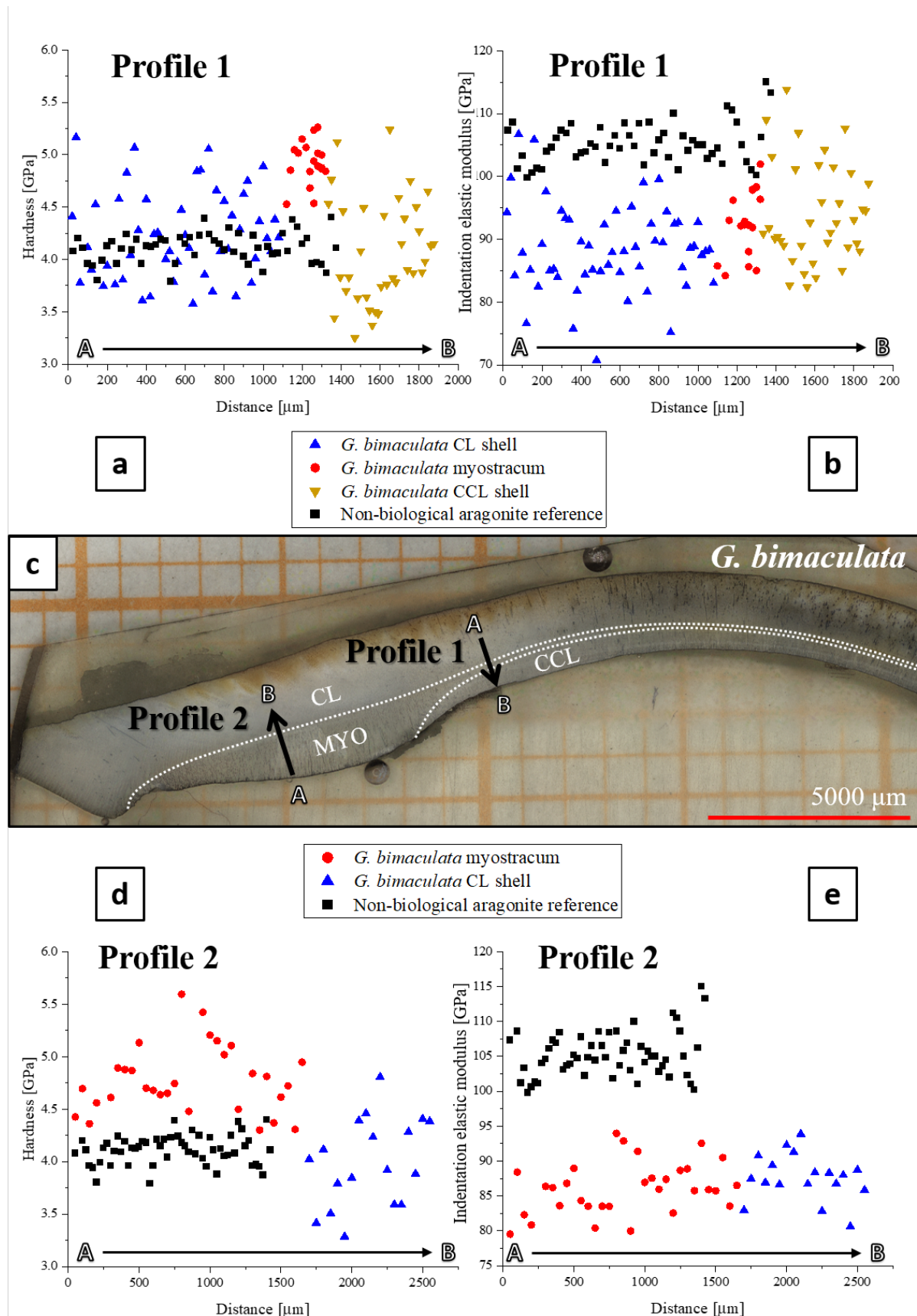


Fig. 2.2-AP14. Nanoindentation results of hardness and indentation elastic modulus for two profiles measured on a transversally sectioned shell of *Glycymeris bimaculata* (a-e). CL: crossed-lamellar, CCL: complex crossed-lamellar, MYO: adductor myostracum. Measurements shown in (a) and (b) were done with an indent spacing of 50 μm , those shown in (c) and (d) with an indent spacing of 20 μm .

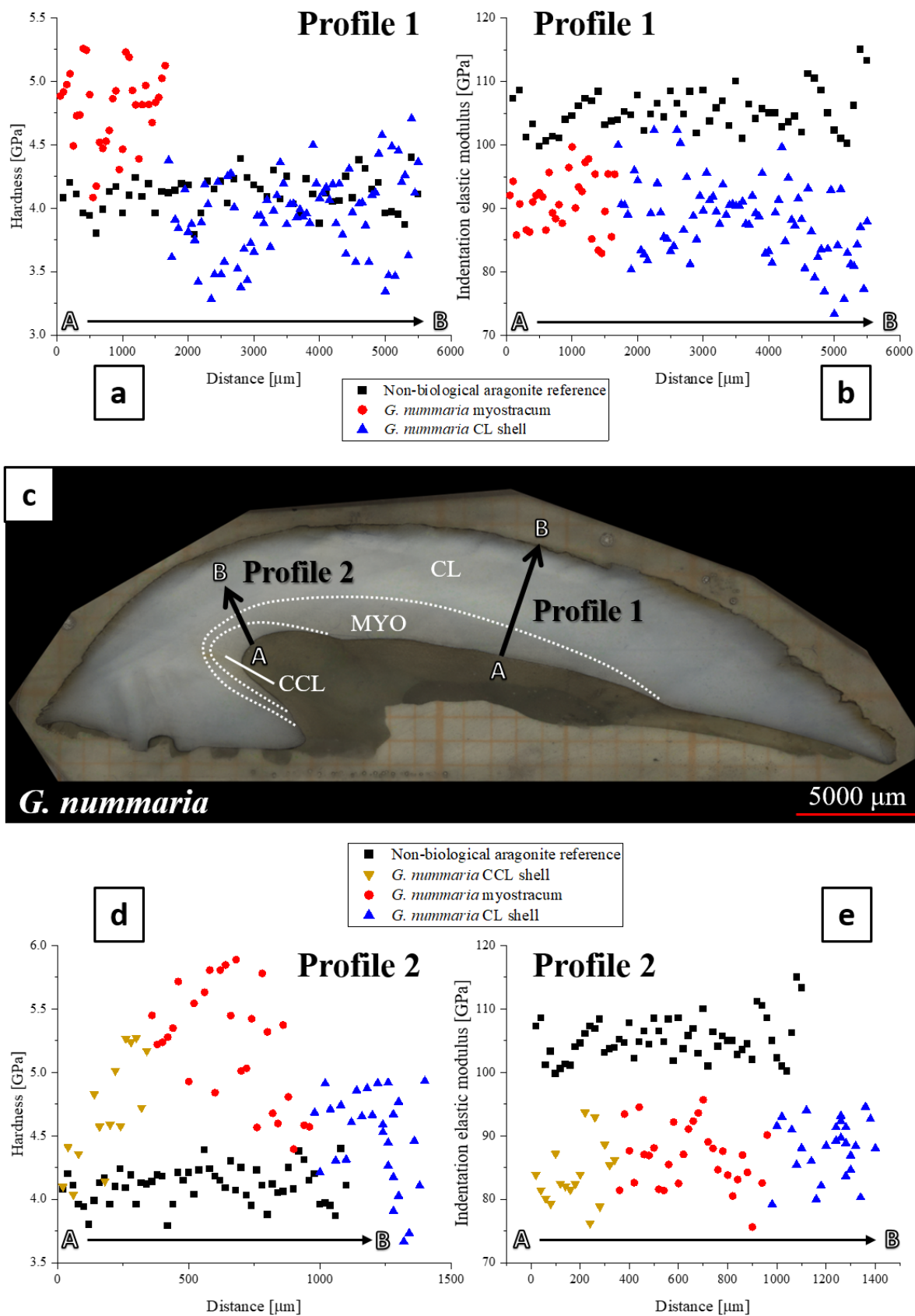


Fig. 2.2-AP15. Nanoindentation results of hardness and indentation elastic modulus for two profiles measured on a transversally sectioned shell of *Glycymeris nummaria* (a-e). CL: crossed-lamellar, CCL: complex crossed-lamellar, MYO: adductor myostracum. Measurements shown in (a) and (b) were done with an indent spacing of 50 μm , those shown in (c) and (d) with an indent spacing of 20 μm .

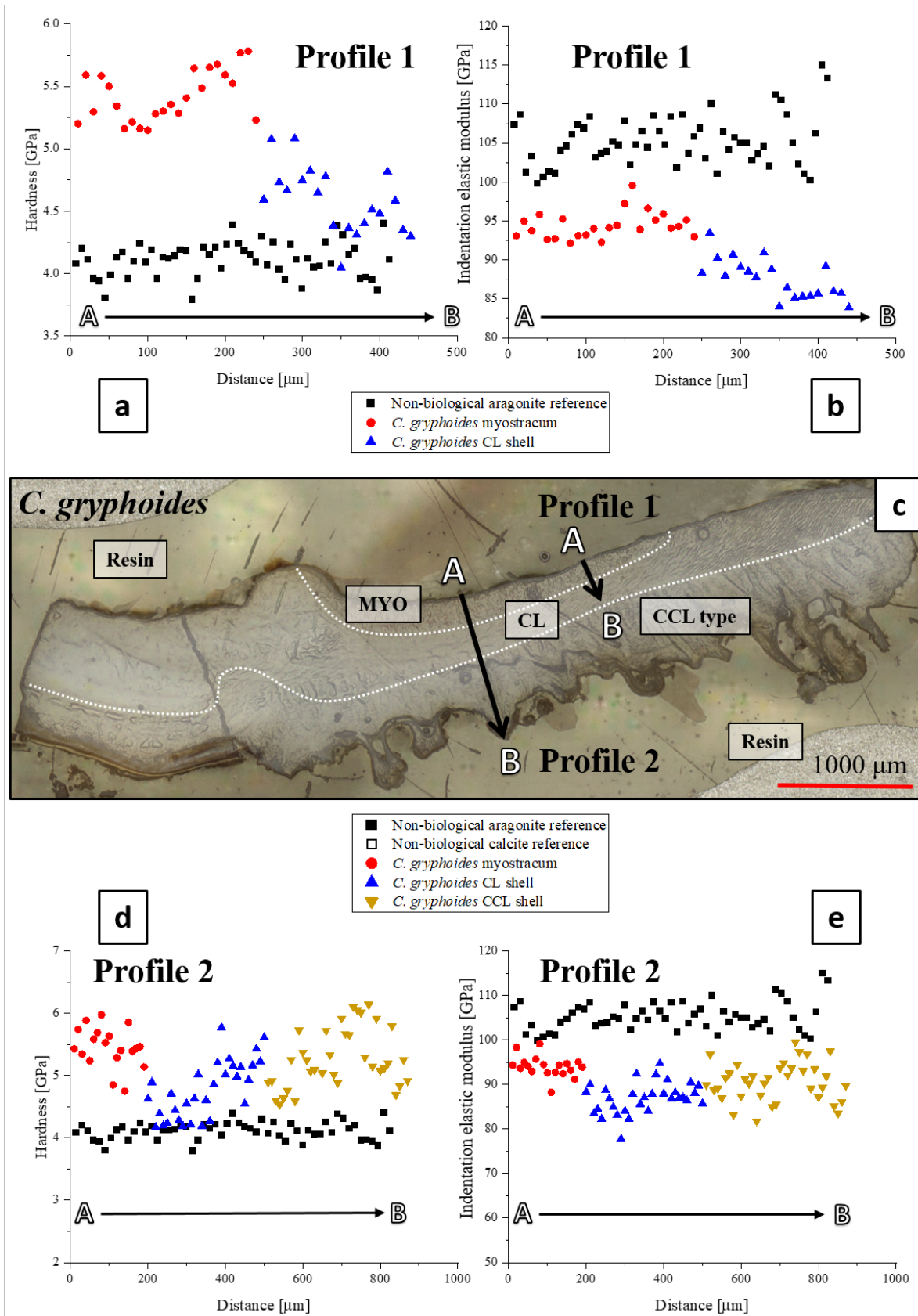


Fig. 2.2-AP16. Nanoindentation results of hardness and indentation elastic modulus for two profiles measured on a transversally sectioned shell of *Chama gryphoides* (a-e). CL: crossed-lamellar, CCL: complex crossed-lamellar, MYO: adductor myostracum. Measurements were conducted with an indent spacing of 10 μm . Due to the small indent spacing multiple parallel rows have been measured and were averaged in the plot to increase the accuracy of the shown values.

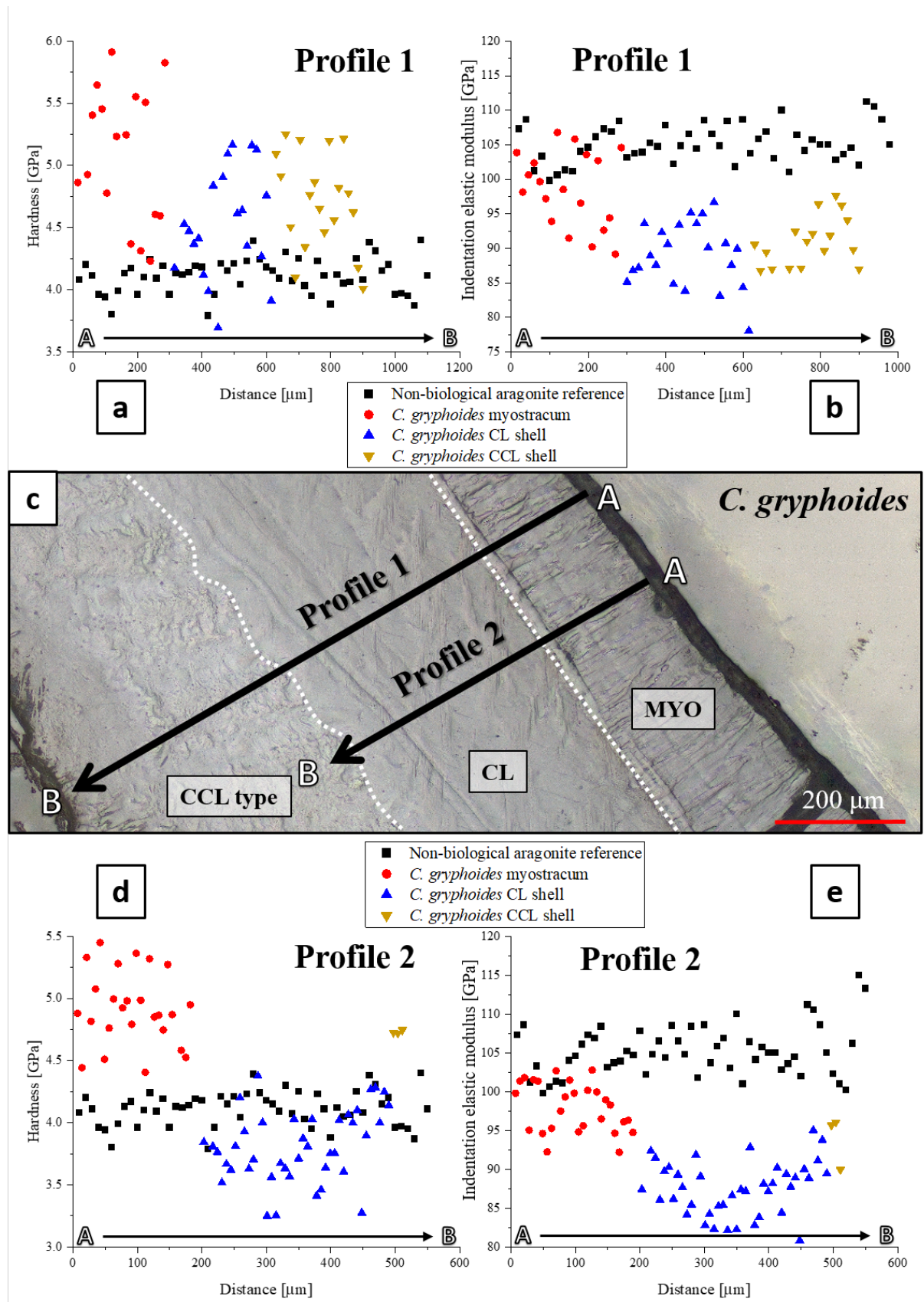


Fig. 2.2-AP17. Nanoindentation results of hardness and indentation elastic modulus for two profiles measured on a transversally sectioned shell of *Chama arcana* (a-e). CL: crossed-lamellar, CCL: complex crossed-lamellar, MYO: adductor myostracum. Measurements shown in (a) and (b) were done with an indent spacing of 15 μm , those shown in (c) and (d) with an indent spacing of 7 μm . Due to the small indent spacing multiple parallel rows have been measured and were averaged in the plot to increase the accuracy of the shown values.

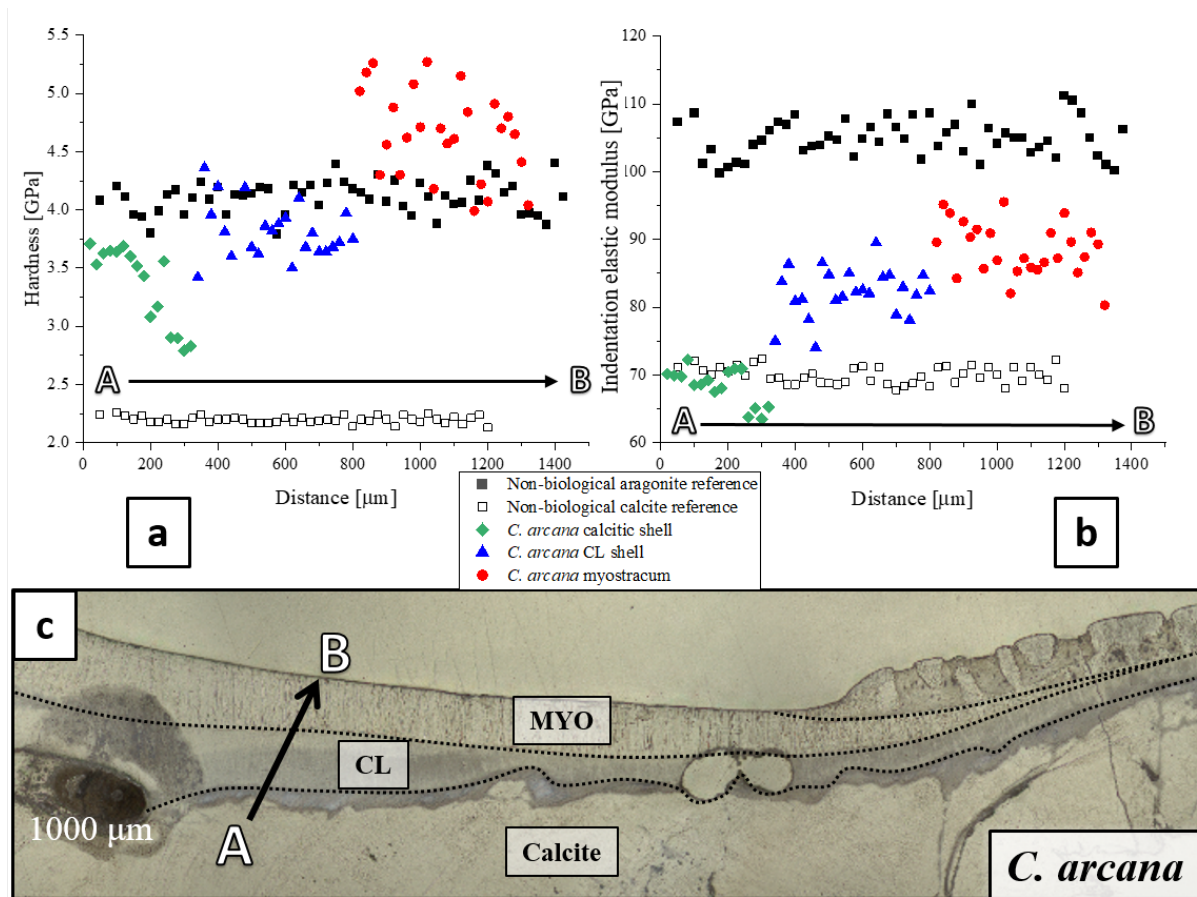


Fig. 2.2-AP18. Nanoindentation results of hardness and indentation elastic modulus for one profile measured on a transversally sectioned shell of *Chama arcana* (a-c). CL: crossed-lamellar, CCL: complex crossed-lamellar, MYO: adductor myostracum. Measurements shown in (a) and (b) were done with an indent spacing of 50 μm. Due to the small indent spacing multiple parallel rows have been measured and averaged. The laser confocal overview image shows the position of the profile on the cross-section of the shell (c).

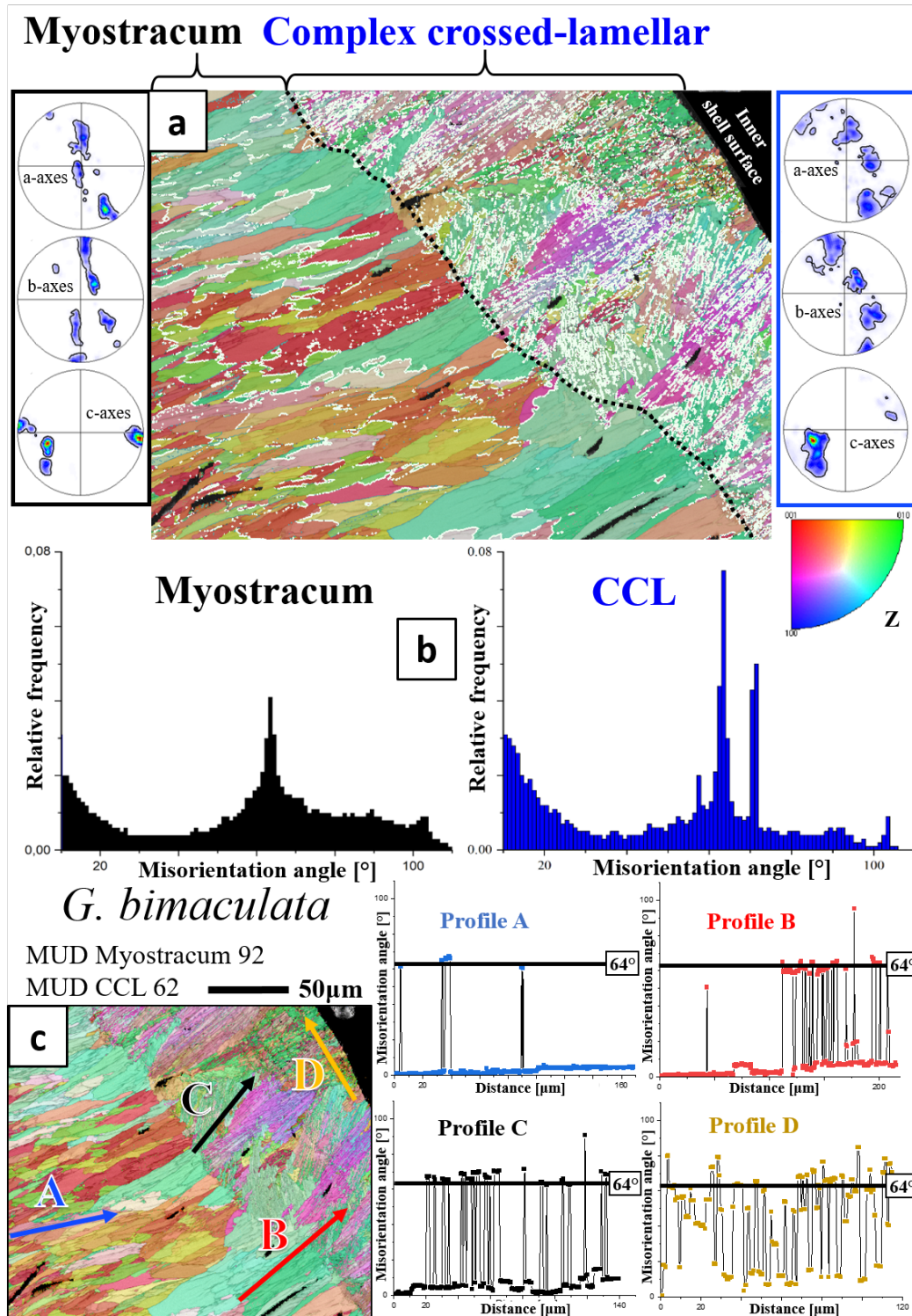


Fig. 2.2-API9. Misorientation angle analysis of different layers in a transversely sectioned *Glycymeris bimaculata* shell. The EBSD map (a) visualizes two types of microstructures: the pallial myostracum and the complex crossed-lamellar, non-myostracal, shell layer (CCL). Grain boundary angles are between 63° and 65°, are highlighted with white points/lines in the EBSD map and indicate aragonitic twinning. Pole figures depicting the orientational probability density distribution for the respective layers (a) visualize, for both layers, a 3D “single-crystal-like” texture. CL: crossed-lamellar, CCL: complex crossed-lamellar. (b): Relative frequency – misorientation angle diagrams for the two shell layers shown in the EBSD map in (a) show that the aragonite of both microstructures is twinned, however, that of the myostracum less, relative to the aragonite of the complex crossed-lamellar shell. Note for the CCL layer we find two misorientation angle peaks, at different degrees of misorientation (b). (c): Misorientation angle – distance diagrams along profiles A to D highlight the strongly twinned nature of the complex crossed-lamellar shell. Profiles A, B in (c): the aragonite within myostracal prisms is little or not twinned. Twinning is present for adjacent prisms.

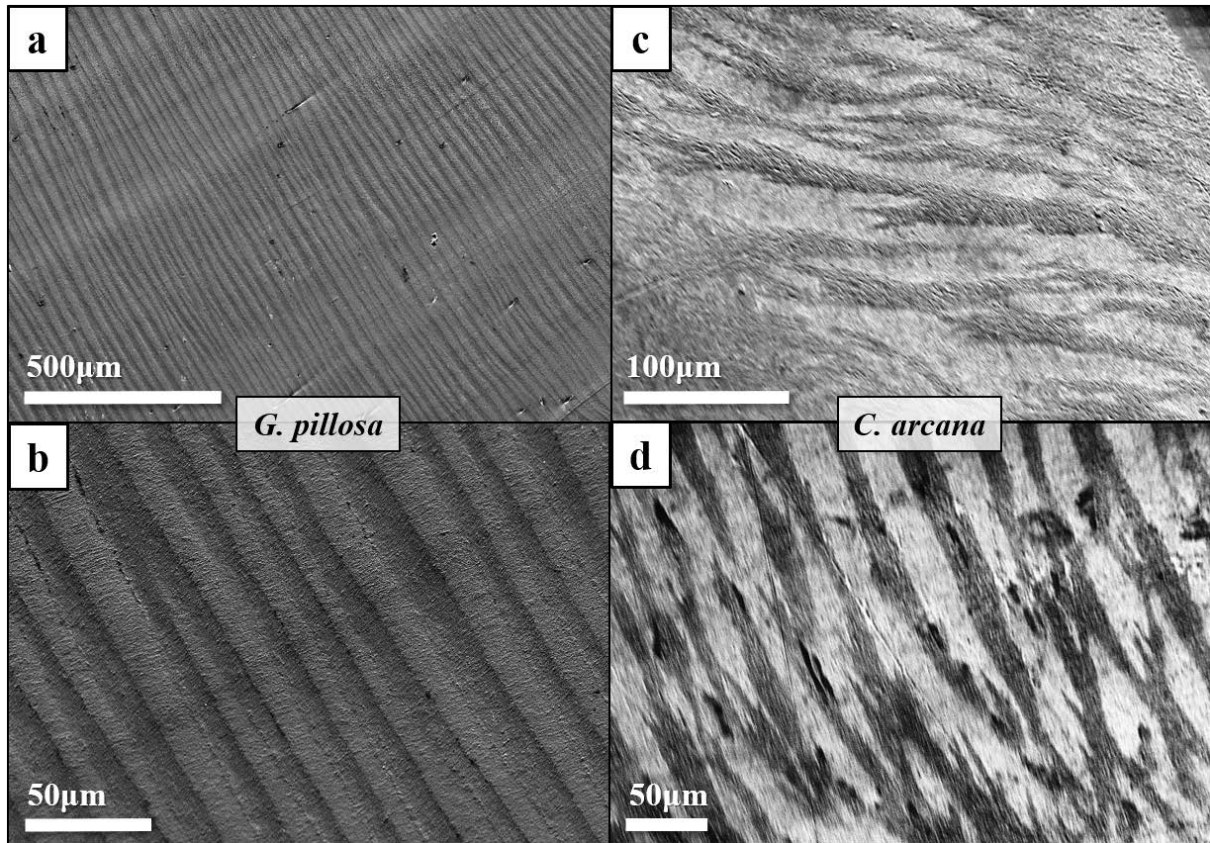


Fig. 2.2-AP20. FE-SEM micrographs depicting the difference in interlacing between the first-order lamellae of *Glycymeris* and *Chama* crossed-lamellar layers. For *G. pillosa* (a, b), the lamellae run, more or less, parallel to each other, there is almost no interlacing between the first-order lamellae. For *C. arcana* (c, d) we find marked interlacing between the first-order lamellae.

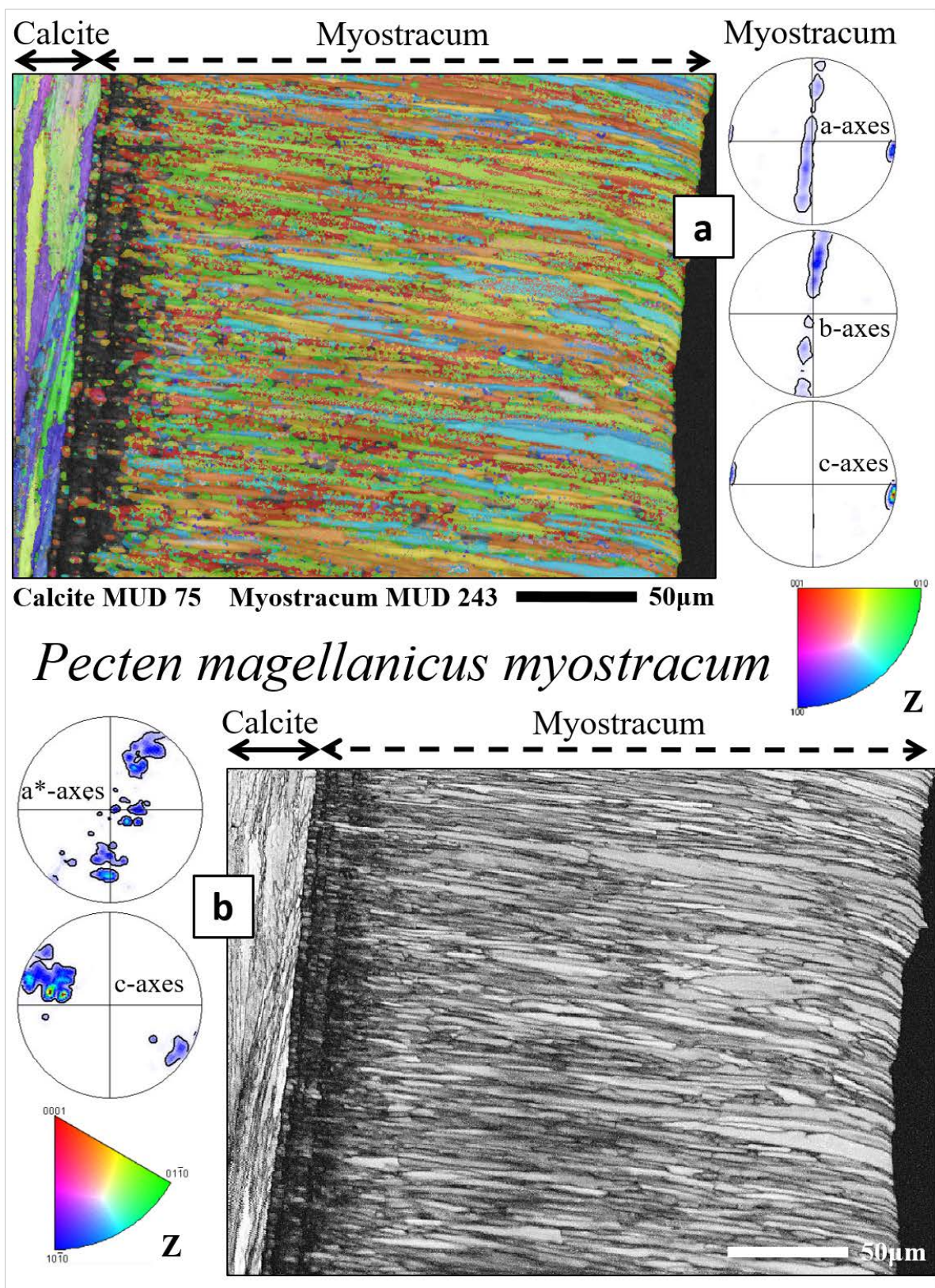


Fig. 2.2-AP21. EBSD scan depicting the microstructure of the foliated, calcitic, shell and the, aragonitic, adductor myostracum of *Placopecten magellanicus*. (a): colour-coded crystal orientation map and pole figures for the aragonite, (b) EBSD band contrast measurement map together with the pole figures of the calcitic shell. In both pole figures we show the orientational probability density distribution. Well observable is the competitive-growth microstructure of the adductor myostracum and the axial (fibre) texture mode of the sheeted calcite and adductor myostracal aragonite.

2.3 CORRELATION BETWEEN NANOMECHANICAL PROPERTIES AND MICROSTRUCTURAL DESIGN CONCEPTS OF BIVALVE MUSCLE ATTACHMENT SITES

S. Hoerl^{1,*}, C. Micheletti², S. Amini², E. Griesshaber¹, K.-U. Hess¹, A. G. Checa^{3,4}, M. Peharda⁵, W. Schmahl¹

1. Department of Geo- and Environmental Sciences, Ludwig-Maximilians-Universität München, Munich, Germany

2. Max Planck Institute of Colloids and Interfaces, Department of Biomaterials, Potsdam, Germany

3. Instituto Andaluz de Ciencias de la Tierra, CSIC-Universidad de Granada, Armilla, Spain

4. Departamento de Estratigrafía y Paleontología, Universidad de Granada, Granada, Spain

5. Institute of Oceanography and Fisheries, Split, Croatia

Materials & Design 2025, 253, 113845.

<https://doi.org/10.1016/j.matdes.2025.113845>

Abstract

Bivalves populate various marine environments and follow diverse lifestyles: attaching to substrates, burrowing into sediments or swimming in water. Their shells play a crucial role in the survival of organisms as they shield the soft tissue from external attacks and facilitate their respective lifestyles. Valve movement is controlled by one or two adductor muscles and the hinge. While the function and structure of adductor muscles can vary, the shell-muscle attachment develops the myostracum, a unique microstructural design. Sectioned parallel and perpendicular to the inner shell surface, we investigated myostracal and non-myostracal microstructures, textures and nanomechanical properties for three bivalve species: The burrowing *Glycymeris pilosa*, the sessile *Chama arcana* and the swimming *Placopecten magellanicus*.

Analyses were conducted using electron backscatter diffraction measurements, laser confocal and backscatter electron imaging, nanoindentation testing and thermogravimetric analysis. We find that the myostracal microstructure is generated mainly through competitive crystal growth determinants, regardless of the bivalve lifestyle and adductor muscle structure. If aragonitic, we show that adjacent shell layers are used as templates for the formation of the myostracal microstructure and highlight how bivalves use the adjacent crystal arrangement to predetermine myostracal microstructure up to inner shell surfaces. Furthermore, this study demonstrates how myostracal layers exceed the hardness of the non-myostracal valves and that of geological aragonite, irrespective of grain size and morphology. Due to the anisotropy of aragonite, we show that aragonite c-axis orientation notably affects the hardness of crystals. The highest hardness is measured when indentation is normal to the shell surface in aragonite c-axes direction.

Keywords

Bivalves; EBSD; nanoindentation; microstructure/texture; myostraca

2.3.1 INTRODUCTION

Mineralised structures generated under biological control are widely recognised in material science as prototypes for advanced materials. These are organic-inorganic composites and show a large variety of structural design concepts. In particular, molluscs developed a large repertoire of shell-forming microstructural design strategies, which are currently used by material scientists as a valuable source of inspiration for the fabrication of innovative synthetic materials.

Within the molluscan phylum, bivalves are the second most species-rich class after the gastropods (Hughes 1986; Mikkelsen 2011; Bieler et al. 2013). Due to their widespread distribution and the lack of major geographical barriers, allopatric isolation is rare in marine environments (Palumbi 1994; Kinlan & Gaines 2003; Norris & Hull 2012). Because of the high gene flow between populations maintained by their mostly planktonic larvae, bivalves are prime examples of the Marine Speciation Paradox (Bierne et al. 2003; Mikkelsen 2011). Throughout their highly successful evolutionary history, they have occupied aquatic habitats worldwide, even inhabiting extreme environments such as the polar seas or abyssal marine regions (Norkko et al. 2005; Krylova et al. 2015; Kamenev et al. 2022; Iglukowska et al. 2023). Through diversification mechanisms, bivalves developed a range of motility strategies, such as byssal attachment to substrate, burrowing into sediments or free swimming (Trueman et al. 1966; Stanley 1970; Stanley 1972; Guderley & Tremblay 2016; Collins et al. 2023; Sharma et al. 2023).

The most prominent and essential adaptation of bivalves is their hard exoskeleton, which protects their soft tissue from predators and external chemical and physical hazards. Nonetheless, this is not the only function of the shells. Bivalve shells are also of great importance for adherence to substrate, stability, locomotion and vision (Eagar 1978; Morton 2001; Kobak 2006; Audino et al. 2020; Sharma et al. 2023; Silva et al. 2023). Bivalve shells are biological composites formed of an organic matrix and a calcium carbonate (CaCO_3) polymorph such as aragonite, calcite or (rarely) vaterite (Taylor et al. 1973; Watabe 1983; De Paula & Silveira 2009). The three polymorphs never mix in a microstructure; however, they may comprise different shell layers (Watabe 1983; Qiao et al. 2008; Spann et al. 2010; Hoerl et al. 2025b). While burrowing and infaunal organisms appear to form predominantly aragonitic shells, bivalves inhabiting other ecological niches are rather bimineralic, with the calcitic layers always being the external shell layers (Taylor et al. 1973; Crame 2000; Iglukowska et al. 2017; Iglukowska et al. 2023; Checa et al. 2025).

Valve movement in bivalved organisms is carried out with the adductor and the pedal muscles that attach to the inner surface of the valves. Nonetheless, the opening and closing of the valves are controlled by an interplay between the adductor and pedal muscles and the ligament (Tremblay et al. 2015). At the attachment sites of muscles to the valves, the myostraca, a specific microstructure, develops within the valves. In bivalve shells, myostracal layers are always aragonitic; even in purely calcitic shells, the myostracum consists of aragonite crystals (Hoerl et al. 2024a; Hoerl et al. 2024b; Checa et al. 2025). It is demonstrated by now that the texture of myostracal crystals is predominantly determined by a competitive crystal growth process (Crippa et al. 2020a; Crippa et al. 2020b; Hoerl et al. 2024a; Hoerl et al. 2024b). While competitive determinants define the microstructure and texture of the myostracum, the organism controls supersaturation and crystal nucleation and the composition of the extracellular polymeric substances. A competitive growth process contrasts with the generation of the other shell layers, which are proactively influenced by biological, chemical and stereochemical determinants (Kennedy et al. 1969; Cuif et al. 2014; Checa 2018). In layers controlled by non-competitive determinants, the biopolymer component is usually organised as a structured matrix; the mineral component fills the structured pattern of voids of the biopolymer matrix (Addadi et al. 2006; Marin et al. 2012). Due to their different growth process, myostracal prisms lack an extracellular organic envelope encasing the prisms. Nonetheless, myostraca are also organic-mineral composites. The organic substance is distributed within the prisms; this is an essential requirement for a strong myostracal prism-muscle attachment (Castro-Claros et al. 2021). The mass fraction of the organic component in most bivalve shells scatters between 0.1-5 wt%, depending on the microstructure of the shell (Lowenstam & Weiner 1989; Weiner & Addadi 1997; Suzuki & Nagasawa 2013). Starting from the periostracum, a primary organic layer that serves as a template for crystal nucleation (Lopes-Lima et al. 2010; Suzuki et al. 2013; Clark et al. 2020), most shell microstructures comprise crystals oriented with their c-axes towards the shell growth surface (Hoerl et al. 2024b).

The focus of the present study is to discuss the interrelation between biomaterial structure designs and nanomechanical properties. Peter et al. (2023) investigated and juxtaposed the latter for a bivalve (*Mytilus galloprovincialis*) and a gastropod (*Haliotis glabra*) shell. This study goes beyond the work of Peter et al. (2023), as we discuss here the connection between material structure and its mechanical properties (i) for microstructures formed by distinct (competitive, biological) growth determinants, however, being present in the same shell and (ii) for the shells of bivalves that follow distinct lifestyles.

The selected bivalves (*Glycymeris pilosa* (Linnaeus, 1767), *Chama arcana* F. R. Bernard, 1976, and *Placopecten magellanicus* (Gmelin, 1791)) form thick but differently-sized shells, live in different habitats and have distinct lifestyles. *G. pilosa* is found along the coastlines of the Mediterranean Sea and forms large (more than 75 mm diameter in shell length) and thick shells with distinct growth patterns (Peharda et al. 2016; Peharda et al. 2019). These characteristics, together with the outstanding longevity

of some Glycymerididae (Peharda et al. 2012; Reynolds et al. 2013), render *Glycymeris* a promising candidate for recording environmental conditions (Brocas et al. 2013; Featherstone et al. 2017; Peharda et al. 2019). *G. pilosa* lacks a functional byssus and secretes solely aragonitic shells adapted for anterior-posterior rocking locomotion during burrowing (Thomas 1978; Legac & Hrs-Brenko 1999). *C. arcana* is found in warm and intertidal environments of the East Pacific, within the upper 30 m of the water column (Bernard 1976). Chamidae are sedentary bivalves that cement to a substrate, leading most species to form differently valved shells (Nicol 1952; Yonge 1967; Allen 1976). Adult organisms need large and elongated adductor muscles to ensure the valves' rapid and prolonged closure in turbid environments (Kennedy et al. 1970). While most *Chama* species form purely aragonitic shells, *C. arcana* shells comprise an ornamentation covering consisting of calcite (Bernard 1976; Hoerl et al. 2024a). Of the three species investigated in this study, *P. magellanicus* is the most mobile and has developed the ability to swim (Manuel & Dadswell 1993; Labrecque & Guderley 2011). Organisms go through different stages of mobility. Veligers are pelagic for 30-50 days, and juveniles attach a byssus to rigid substrates (Pearce et al. 2004; Carey & Stokesbury 2011; Labrecque & Guderley 2011; Stokesbury et al. 2016). As adults, the swimming behaviour of *P. magellanicus* changes with shell size: small scallops (< 30 mm) only swim short distances, while large scallops (> 100 mm) are mostly sedentary (Baird 1958; Caddy 1968; Caddy 1972; Stokesbury & Himmelman 1996; Labrecque & Guderley 2011). Among pectinids, *P. magellanicus* is the fastest swimmer and has the highest hydrodynamic efficiency. Within *P. magellanicus*, adult organisms with medium-sized shells are the most mobile and reach the highest swimming speeds (Dadswell & Weihs 1990). *P. magellanicus* forms thin shells. As adductor muscle movement is essential for its active locomotion (Trueman 1983; Cheng et al. 1996; Labrecque & Guderley 2011), the adductor muscle and its attachment to the shell are very prominent in *P. magellanicus* shells.

Accordingly, our study has the following objectives:

1. We highlight first the microstructure design concept, mineral phase and texture (crystallographic preferred orientation) of myostracal and non-myostracal valve portions for a bivalve species that burrows into the sediment, a species that lives attached to a substrate and a species that can swim fast and intensely through the water.
2. As the valves are opened and closed via muscles that attach to the myostracal valve portions, we place particular interest in understanding the structural and nanomechanical characteristics of myostraca of the selected species following different lifestyles. We highlight the microstructural designs and textures of the shell layers and the adductor myostraca and discuss how these might relate to the mobility and living behaviour of the organisms.
3. A central objective of this study is to present and discuss the selected bivalves' nanomechanical property results for the valves and the myostraca. We examine whether

differences in microstructural designs affect nanomechanical properties, such as indentation elastic modulus and hardness.

Due to the anisotropy of calcite and aragonite crystals (Han et al. 1991; Carter et al. 1993), the crystallographic orientation of crystals can impact nanomechanical property results. Anisotropy is a directional dependence of material properties within crystallographic arrangements (Brookes et al. 1971; Newnham 2004). This behaviour is well-investigated for ceramics, rocks and metals (Bowman et al. 1998; Banabic et al. 2000; Hutchinson 2015); however, anisotropy and its influence on mechanical response or functional performance of structural biomaterials are generally neglected. Investigating the directional variability of nanomechanical properties for biological hard tissues is essential for comparing material properties between different structural biomaterials and optimising specific man-made materials.

4. Accordingly, we investigate for selected biomineralised hard tissues the orientational variability of nanomechanical properties for bivalve myostracal and non-myostracal valve sections. We compare the nanomechanical response of a biomaterial formed mainly through the control of a competitive growth determinant (the myostraca) and a biomaterial formed under biological growth determinants (the non-myostracal shell). We discuss how the anisotropy of aragonite crystals correlates with the measured nanomechanical property results.

Microstructure, texture, and nanomechanical properties were obtained with Electron Backscatter Diffraction (EBSD), field emission scanning electron microscopy (FE-SEM), and depth-sensing nanoindentation. The organic contents of various shell layers were determined using thermogravimetric analysis (TGA). To gain information on the 3D structure and anisotropic behaviour of the shell-forming crystals, measurements were performed in two directions: on perpendicular (cut 1) and parallel (cut 2) sections to the inner shell surface (Fig. 2.3-AP1).

2.3.2 MATERIALS AND METHODS

Materials

We investigated the shells of the three bivalve species *Glycymeris pilosa* (Linnaeus, 1767), *Chama arcana* (F. R. Bernard, 1976) and *Placopecten magellanicus* (Gmelin, 1791). Specimens were live collected, and care was taken to ensure that all investigated specimens were shells of adult organisms. Specimens of *G. pilosa* were sampled in the Pašman channel, Adriatic Sea. Shells of *C. arcana* were sampled near Newport Beach, CA, USA and obtained from collections of the Natural

History Museum (London, UK). Specimens of *P. magellanicus* were collected in deep water off the shore of Nova Scotia, Canada.

Sample preparation for electron backscattered diffraction (EBSD) measurements and nanoindentation testing

All shells were sectioned in two directions (cut 1 and cut 2), and EBSD and nanoindentation measurements were performed on both cuts. Supplementary Figure 2.3-API indicates the cuts through the shells. **Cut 1** is perpendicular to the inner shell surface; EBSD and nanoindentation measurements were performed on a cross-section, distal to proximal, through the shell. Accordingly, the nanoindents were placed parallel to the inner shell surface. **Cut 2** is parallel to the inner shell surface; EBSD and nanoindentation measurements were performed perpendicular to the inner shell surface. Accordingly, the nanoindents were placed perpendicular to the inner shell surface.

For all investigated species, sample surfaces were prepared perpendicular and parallel to the growth direction (Fig. 2.3-APIa, b). Analysing samples along two cuts gives a representative, and three-dimensional overview of the adductor myostraca and adjacent shell layers since EBSD and nanoindentation testing mostly give information about the properties of the exposed sample surface. The valves were cut through the adductor myostraca (Fig. 2.3-APIc-f). The obtained shell pieces were embedded into EPON epoxy resin and were subjected to several mechanical grinding and polishing steps. The final polishing step consisted of etch-polishing with colloidal alumina (particle size $\sim 0.06 \mu\text{m}$) in a vibratory polisher. For cut 1, the shell pieces were polished perpendicular to the inner myostracal surface, exposing a transversal cross-section from the inner to the outer shell surface. For cut 2, the shell pieces were polished parallel to the myostracal layers, exposing only the inner shell surface.

For EBSD measurements, samples were coated with 4–6 nm carbon for FE-SEM imaging with 5 nm Pt/Pd. For laser confocal microscopy imaging and nanoindentation testing, sample surfaces were not coated.

Secondary electron (SE), backscatter electron (BSE) imaging and electron backscattered diffraction (EBSD) measurements

SE, BSE imaging and EBSD measurements were carried out with a Hitachi SU5000 field emission SEM, equipped with an Oxford Instruments Nordlys Nano EBSD detector and an X-Max 80x80 EDS detector. EBSD scans were taken at 20 kV and were performed with a step size of 200 to 450 nm. For indexing the aragonite EBSD patterns the unit cell setting: $a_0 = 4.9614(3) \text{ \AA}$, $b_0 = 7.9671(4) \text{ \AA}$, $c_0 = 5.7404(4) \text{ \AA}$ was used. EBSD data were evaluated with the Oxford Instruments AZtecCrystal 3.0 and HKL Channel 5.0 software.

Nanoindentation testing

Nanoindentation measurements were conducted using a Hysitron Triboindenter TI-950 nanomechanical tester (Bruker, USA) equipped with a 2D standard transducer and a diamond Berkovich tip. A load function of 5s-2s-5s (loading-holding-unloading) with a peak force of 1 mN and a holding time of 2 seconds at maximum load was applied at each measurement. Tip areas were calibrated using standard fused quartz and aluminium samples for the required contact depths. The indentation elastic modulus and the hardness values were determined via the unloading curve according to the Oliver-Pharr method in the Hysitron software (Anstis et al. 1981; Oliver & Pharr 1992). Indents with curves displaying anomalous behaviour or artefacts (e.g., due to the sample or tip moving during indentation) were discarded from indentation elastic modulus and hardness calculations. The indented aragonite and calcite references are from non-biogenic single crystals. Both non-biological references were indented with c-axes misoriented 35-40° to the indentation direction. This c-axis orientation is close to {104}, an orientation that was recently tested to yield average values for hardness and elastic modulus in geological calcite (Deng et al. 2023). For every measured microstructure, we performed maps and/or profiles consisting of at least 60 nanoindents. The instrument was calibrated before each use to guarantee correlation between tip position and optical image.

Thermogravimetric analysis (TGA)

Samples of crossed-lamellar, complex crossed-lamellar and myostracal aragonite, as well as foliated calcite, were drilled utilising a high-precision dental drill from the respective shell portions. Up to 40 mg of powder were obtained for analysis. TGA measurements were performed with a Netzsch STA 449 F1. The samples were heated from room temperature to 600 °C at a constant rate of 10 °C per minute in a static-air atmosphere. Approximately 20 mg of each sample was used for TGA analysis in an open aluminium oxide crucible. Each sample was measured twice, except for one. The error margin for individual measurements is ± 0.05 wt%; however, crossed-lamellar and myostracal layers of *G. pilosa* showed small heterogeneities.

No prior drying of the samples was performed. The weight loss between 25 °C and 100 °C is attributed to adsorbed water. Separate measurements on pure inorganic carbonate samples (calcite and aragonite) under the same conditions showed decarbonisation beginning around 500 °C, with a weight loss of 0.03 wt. % at 540 °C for both samples. Therefore, the study reports mass loss between 100 °C and 540 °C, as detailed in Figure 2.3-AP4.

An in-depth terminology of the structural terms used in this work can be found in Appendix Section A.1 of this thesis.

2.3.3 RESULTS

This study details the correlation between the structural and nanomechanical property characteristics of *Glycymeris pilosa*, *Chama arcana* and *Placopecten magellanicus* shells. The shell of *G. pilosa* consists solely of aragonite, while *C. arcana* and *P. magellanicus* shells are formed of both aragonite and calcite.

The mode of crystal arrangement varies significantly for the different layers of the investigated species. To better interpret the results gained in this study, the shells were sectioned in two directions. cut 1 is perpendicular to the inner shell surface, exposing a cross-section through the shell used for EBSD and nanoindentation measurements. When the shell was sectioned according to cut 1, nanoindents were placed parallel to the inner shell surface. When sectioning according to cut 2, the section was parallel to the inner shell surface; EBSD and nanoindentation measurements were performed perpendicular to the inner shell surface.

The microstructures and textures

Figs. 2.3-1 and 2.3-AP2 show the microstructure and texture of the aragonitic myostraca and the adjacent shell for the investigated bivalve species. Measurements were performed on shell cross-sections (cut 1). The shell of *G. pilosa* consists of crossed-lamellar aragonite (CL), with the first-order lamellae parallel to each other and the growth direction (GD, indicated in Fig. 2.3-1 with a white arrow between the pole figures). The two sets of the first-order lamellae are inclined to each other and consist of small, lath-shaped third-order lamellae. At the changeover to the adductor myostracum, the orientation pattern of the crossed-lamellar shell functions as a nucleation template for the first-formed myostracal crystals (Fig. 2.3-1a). As the myostracal texture is mostly controlled by a competitive crystal growth mechanism (e.g., Crippa et al. 2020a, b; Hoerl et al. 2024a, b), the grain size of prismatic crystals increases drastically towards the inner shell surface (Fig. 2.3-1a). The texture of the *G. pilosa* myostracum is 3D “single-crystal like”. Shells of *P. magellanicus* comprise foliated calcite (FC). This type of microstructure and carbonate polymorph is adjacent to *P. magellanicus* adductor myostraca (Fig. 2.3-1b). The interface between shell calcite and myostracal aragonite is sharp. The first ~10 µm of the myostracum show a high fraction of organic material, indicated by the large number of zero solution pixels observed in this shell region (Fig. 2.3-1b). The *P. magellanicus* myostracum is formed of long (up to 100 µm) and thin (< 5 µm) prisms which are assembled with a strictly axial texture.

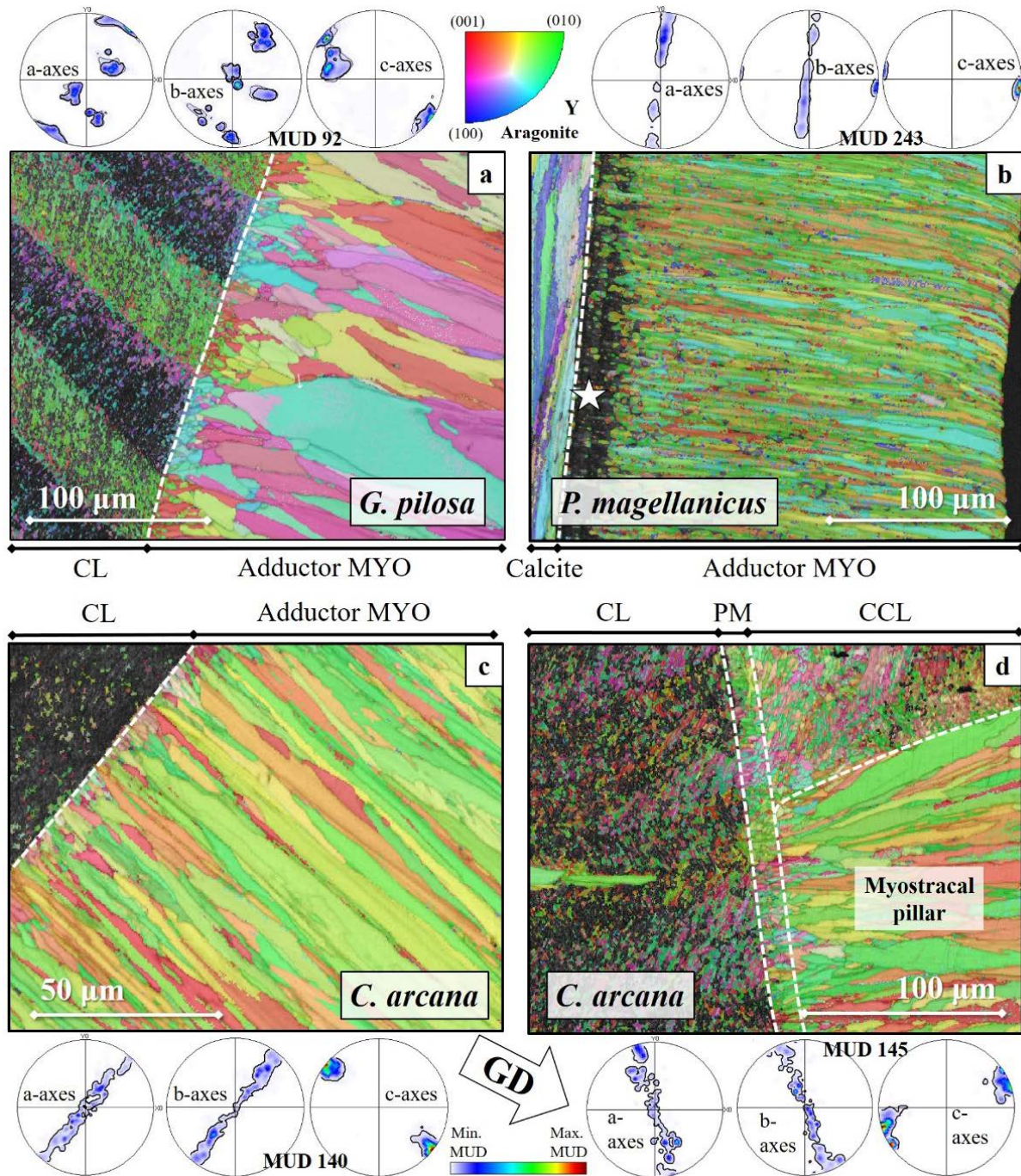


Fig. 2.3-1. Microstructure and texture of myostracal regions sectioned and polished perpendicular to the inner shell surface (cut 1). Colour-coded EBSD maps show the crystal orientation patterns and are complemented by pole figures indicating the orientational probability density distributions of the pure myostraca (a-d). The projection direction and x-y coordinate orientation of the pole figures are equal to the viewing direction and x-y directions (edges) of the corresponding EBSD scan images. The pole figure in *Glycymeris pilosa*, the 3D “single-crystal-like” texture of the crossed-lamellar (CL) layer propagates into the adductor myostracal (MYO) layer (a). The myostracal crystals start as small, isometric grains at the changeover region and become more prismatic and co-oriented as they grow towards the inner shell surface (a). The shell-myostracum interface in *Placopecten magellanicus* is sharp, and an organic-rich layer, visualised by many zero-solution data points, defines the first few μm of the aragonitic layer (white star in b). Towards the inner shell surface, the myostracum comprises long (up to 100 μm), needle-shaped crystals with an axial texture (b). Small, granular crystals initiate the axial adductor myostracum in *Chama arcana* (c) from the changeover with the crossed-lamellar layer. The needle-shaped crystals increase in size and thickness with distance from the changeover. The myostracal pillars in *C. arcana* originate in the pallial myostracum (PM) and have a microstructure similar to the adductor myostracum (d). They have a cone-shaped morphology and grow alongside the complex crossed-lamellar layer (CCL). For all measurements, the approximate growth direction (GD) is indicated by a white arrow.

The shell of *C. arcana* features arrays of calcitic ornamentations at the outermost shell sections. However, the shell between these ornamentations and the adductor myostracum is purely aragonitic. Like the *G. pilosa* myostracum, the *C. arcana* myostracum is also adjacent to crossed-lamellar aragonite towards the outer shell surface. Towards the inner shell surface, *C. arcana* shells consist of complex crossed-lamellar (CCL) aragonite (Fig. 2.3-1c, d). Notable features in *C. arcana* shells are the myostracal pillars that extend towards the inner shell surface and intersect the innermost complex crossed-lamellar shell layer (Fig. 2.3-1d). Myostracal pillars are conical structures that originate from the pallial myostracum (Fig. 2.3-1d) and maintain a myostracal microstructure up to the inner surface of the shell. The prisms of myostracal pillars reach diameters of around 50 μm . The crystals of both adductor myostraca (Fig. 2.3-1c) and myostracal pillars (Fig. 2.3-1d) are elongated and large (up to 200 μm in length). Their axial texture and specific microstructure are typical for a competitive crystal growth process.

Figs. 2.3-2 and 2.3-AP3 depict the microstructure and texture of adductor myostraca and the non-myostracal shell sectioned parallel to the inner shell surface (cut 2) for the three investigated bivalve species. Measurements were taken at the innermost shell surface of the shells of adult organisms. Within the adductor myostraca, we found very irregular prism boundaries and, for the investigated species, a distinct difference in grain/prism size. For *G. pilosa*, grain cross-sections have a diameter of up to 50 μm (Figs. 2.3-2a, 2.3-AP3a). Grain cross-sections of *C. arcana* are smaller than those of *G. pilosa* and have diameters up to 10 μm (Figs. 2.3-2b, 2.3-AP3b). With a size of up to 5 to 6 μm in diameter, we found the smallest grain cross-sections in *P. magellanicus* (Figs. 2.3-2c, 2.3-AP3c). The large prisms in *G. pilosa* and, to a smaller extent, in *C. arcana* and *P. magellanicus* are substructured into multiple, slightly misoriented units (cumulative misorientations up to 5°; e.g., white stars in Fig. 2.3-2a).

Regarding the texture of myostracal aragonite (see the pole figures in Figs. 2.3-2, 2.3-AP3), we found that (i) *G. pilosa* has a different texture relative to *C. arcana* and *P. magellanicus* and (ii) crystallographic texture is more disordered in *C. arcana* myostraca, relative to the crystals that form *P. magellanicus* myostraca (compare the pole figures for *C. arcana* and *P. magellanicus* in Figs. 2.3-2, 2.3-AP3). Therefore, although the *P. magellanicus* myostracum comprises many small prisms (see Figs. 2.3-2, 2.3-AP3), it shows a high degree of crystallographic continuity. The texture of *G. pilosa* adductor myostraca, inherited from the adjacent crossed-lamellar layer, is 3D “single-crystal-like” (well visible from the multiple clustered orientations in the pole figure of Fig. 2.3-AP3a). In contrast, the texture of *C. arcana* and *P. magellanicus* myostraca is axial (see pole figures in Figs. 2.3-2, 2.3-AP3).

When sectioned parallel to the inner shell surface, the microstructure and crystallographic texture of the shell layers adjacent to the adductor myostracum are well visible (Fig. 2.3-3). The contoured pole figures indicate that the crossed-lamellar layer in *G. pilosa* comprises co-oriented first-order lamellae that run mostly parallel to one another (Fig. 2.3-3a). On the other hand, *C. arcana* first-order lamellae are strongly interlaced and show a comparatively low co-orientation strength with a weak

single-crystal-like to axial texture. The foliated calcite layer of *P. magellanicus* has a “turbostratic-like” texture and comprises large (up to 200 μm) substructured units (Fig. 2.3-3c).

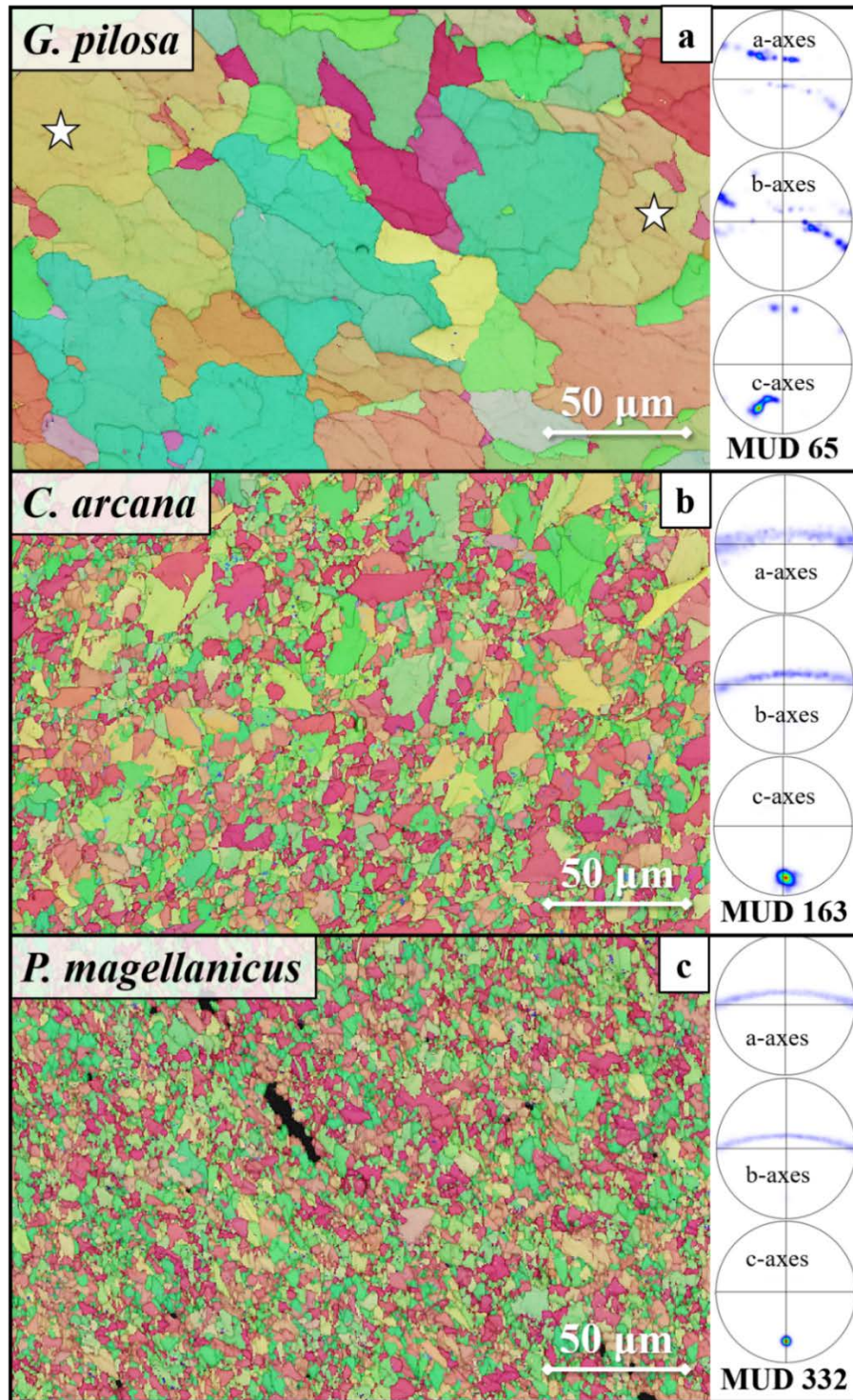


Fig. 2.3-2. Microstructure and crystal orientation patterns of adductor myostraca sectioned and polished parallel to the inner shell surface (cut 2) for the three investigated species. The colour-coded EBSD maps are complemented by pole figures indicating the orientational probability density distributions (a-c). The cross-section of the *Glycymeris pilosa* myostracum comprises large (up to 100 μm diameter) irregular prisms that are internally substructured (white stars in a). The 3D “single-crystal-like” texture and the recurring colour-coded crystal orientations indicate that the crossed-lamellar texture of the changeover region (Fig. 2.3-1a) is still present at the inner shell surface. In *Chama arcana*, the prisms are smaller and neither show a characteristic crystal orientation pattern nor orientation distribution maxima in the axial pole figures (b). *P. magellanicus* shows a texture and microstructure similar to *C. arcana*; however, the grains appear even thinner.

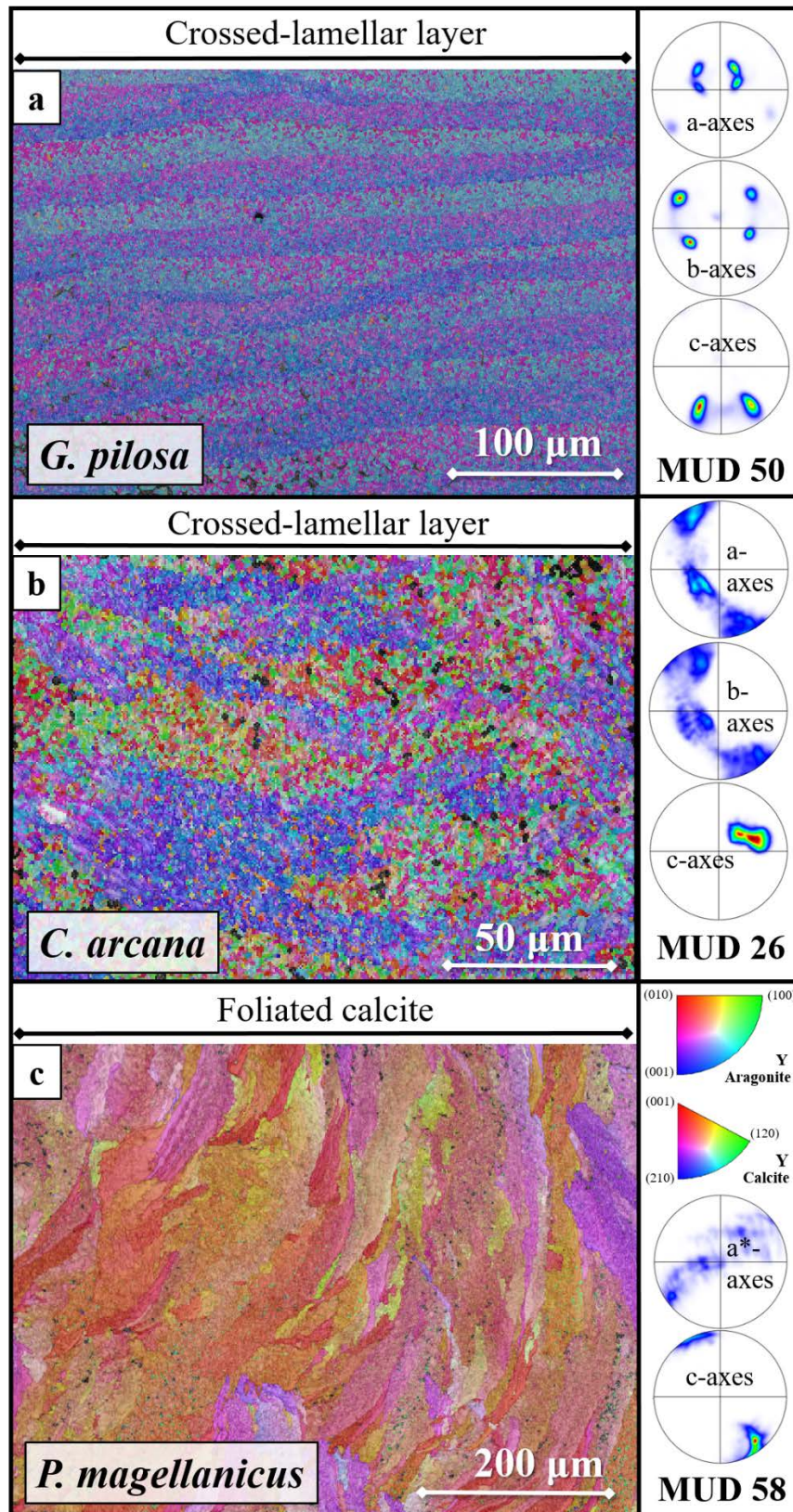


Fig. 2.3-3. Microstructure and texture of shell regions adjacent to myostraca sectioned and polished parallel to the inner shell surface (cut 2). Colour-coded EBSD maps show the microstructure and crystal orientation patterns and are complemented by pole figures indicating the orientational probability density distributions (a-c). In *Glycymeris pilosa*, the crossed-lamellar layer has a 3D “single-crystal-like” texture (a), showing two sets of first-order lamellae that run parallel to the growth direction. In *Chama arcana*, the crossed-lamellar layer is less co-oriented along the a- and b-axes, and the first-order lamellae do not run straight but are intertwined (b). The foliated calcite layer of *P. magellanicus* comprises large (up to 200 μm) substructured units with an axial texture (c).

The nanomechanical properties

Figures 2.3-4, 2.3-5 and Table 2.3-1 present, for the investigated species, hardness and indentation elastic modulus results for myostracal and non-myostracal valve sections, in addition to nanomechanical property results obtained on non-biological calcite and aragonite references.

For *G. pilosa*, the myostracum is the hardest observed layer, exceeding the hardness of the crossed-lamellar valve and the aragonitic reference (Fig. 2.3-4a, b). Depending on the orientation of the myostracal layer towards the loading/unloading direction, the observed nanomechanical properties vary for *G. pilosa*. When indented perpendicular (cut 2), rather than parallel (cut 1), to the inner shell surface, the measured hardness of the adductor myostracum is significantly enhanced (Fig. 2.3-4a, b). The indentation elastic modulus values of the myostracal layer are comparable for both cuts through the shell; nonetheless, the values obtained perpendicular to the inner shell surface are slightly lower. For *G. pilosa*, the lowest average value for the indentation elastic modulus and hardness was observed for the crossed-lamellar layer.

For *P. magellanicus*, the obtained nanoindentation values show similar results: the calcitic reference has the lowest hardness and indentation elastic modulus of the observed materials (Fig. 2.3-4c, d). We found that foliated calcite is significantly harder than geological calcite and also has a slightly increased indentation elastic modulus. For both the parallel and the perpendicular cuts, the myostracum shows the highest hardness (Fig. 2.3-4c, d). The average hardness observed perpendicular to the inner shell surface (cut 2) significantly exceeds the hardness of the myostracum indented parallel to the inner shell layer (cut 1, Fig. 2.3-4c, d). Similar to *G. pilosa*, the obtained mean indentation elastic modulus of the myostracum layer in *P. magellanicus* is slightly decreased when indented perpendicular to the inner shell surface, rather than parallel. For both species, we found that non-biogenic aragonite has a higher indentation elastic modulus than the biological shell layers (Fig. 2.3-4a-d).

Along the inner shell surface of *C. arcana*, we found a variety of microstructures: the adductor myostracum, myostracal pillars and the complex crossed-lamellar shell layer. We indented these microstructures perpendicular (Fig. 2.3-5a, b) and parallel (Fig. 2.3-5c, d) to the inner shell surface. Indentation measurements performed perpendicular to the inner shell surface (cut 1) show similar results for *C. arcana* to what we measured for the other two bivalve species: the adductor myostracum has the highest observed hardness for all shell layers of *C. arcana* and a high nanoindentation elastic modulus, exceeded only by the modulus of the non-biological reference (Fig. 2.3-5a). The hardness of the complex crossed-lamellar aragonite of *C. arcana* exceeds the hardness of the reference and is comparable to the hardness of the myostracal pillars. The observed hardness and elastic modulus for the complex crossed-lamellar layer in *C. arcana* are very similar to the nanoindentation results obtained for the complex crossed-lamellar layer of *Glycymeris* shells, as reported by Hoerl et al. (2024b). We found that despite the similarity in microstructure between myostracal pillars and the adductor myostracum, the hardness

and indentation elastic modulus of myostracal pillars is lower than that of the adductor myostracum (Fig. 2.3-5a, b).

Table 2.3-1. Nanoindentation results for maps indented on *Glycymeris pilosa*, *Chama arcana* and *Placopecten magellanicus* shells. The values are the mean of the indentation measurements reported in this study. The non-biological calcite and aragonite references were tested with c-axes misoriented 35–40° to the indentation direction. (Hoerl et al. 2024b) showed that the complex crossed-lamellar layer in *Glycymeris*, indented parallel to the inner shell surface, is very similar to the complex-crossed-lamellar layer in *Chama*. For the complex crossed-lamellar layer in Glycymerididae, the mean hardness is 4.8 GPa, and the mean indentation elastic modulus is 89.3 GPa (Hoerl et al. 2024b). CL: crossed-lamellar, CCL: complex crossed-lamellar, FC: foliated calcite.

	Species	Hardness [GPa]		Indentation elastic modulus [GPa]	
		Indents to inner shell surface	Indents ⊥ to inner shell surface	Indents to inner shell surface	Indents ⊥ to inner shell surface
Myostracum	<i>G. pilosa</i>	4.6	6.2	97.4	94.4
	<i>C. arcana</i>	5.1	6.1	96.0	93.3
	<i>P. magellanicus</i>	5.2	6.0	97.2	94.0
Myostracal pillar	<i>C. arcana</i>	4.5	5.1	85.7	81.7
Shell	<i>G. pilosa</i> CL	3.4		87.3	
	<i>C. arcana</i> CL	3.7		82.2	
	<i>C. arcana</i> CCL	4.6	1.0	90.2	36.5
	<i>P. magellanicus</i> FC	3.0		72.7	
Geological reference	Aragonite	4.1		105.2	
	Calcite	2.2		70.0	

For indentation measurements performed parallel to the inner shell surface (cut 2) of *C. arcana*, we found similar nanomechanical property relations between the adductor myostracum and the myostracal pillars, both showing enhanced hardness and indentation elastic moduli compared to the aragonite reference. Compared to the myostracal pillars, the adductor myostracum has a significantly higher hardness and indentation elastic modulus (Fig. 2.3-5c, d). While the indentation results for the

myostracal layers of *C. arcana* followed the trend already observed for *G. pilosa* and *P. magellanicus*, the *C. arcana* complex crossed-lamellar layer differed. When indenting the *C. arcana* complex crossed-lamellar layer perpendicular to the inner shell surface, loading and unloading displacement curves show irregular behaviour (Fig. 2.3-AP6). The profiles feature many pop-ins, and the anomalously low values for indentation elastic modulus and hardness are related to these. Thus, the measured hardness values are of limited significance for comparisons (Fig. 2.3-5d, 2.3-AP6).

In essence, when comparing the nanoindentation results between cut 1 and cut 2, we found for cut 2 an increase in hardness of about 37% for *G. pilosa* myostraca, about 20% for *C. arcana* myostraca and about 15% for *P. magellanicus* myostraca (Figs. 2.3-4, 2.3-5, Table 2.3-1). The difference in nanoindentation elastic moduli for the different cuts through the shell is less pronounced. For the adductor myostraca of all three investigated species, it is about 3% (Figs. 2.3-4, 2.3-5, Table 2.3-1). In summary, we found the following trends in nanomechanical properties:

1. For all three investigated species, myostracal aragonite is harder and has a higher indentation elastic modulus relative to the hardness and elastic modulus of the adjacent shell (calcite or aragonite).
2. The complex crossed-lamellar microstructure (CCL) has a higher hardness and a slightly increased indentation elastic modulus relative to the crossed-lamellar (CL) microstructure (for both *C. arcana* and *G. pilosa*).
3. We found a difference in hardness and indentation elastic modulus for measurements performed on the two differently oriented cuts through the shell. The difference is considerable for the hardness; it is present but significantly less notable for indentation elastic modulus results.
4. Of all investigated samples, the hardness and indentation elastic modulus of non-biological calcite is the lowest. The crossed-lamellar (CL) layer shows the lowest hardness and indentation elastic modulus of the investigated aragonitic microstructures. All other aragonitic microstructures surpass the hardness of non-biological aragonite.

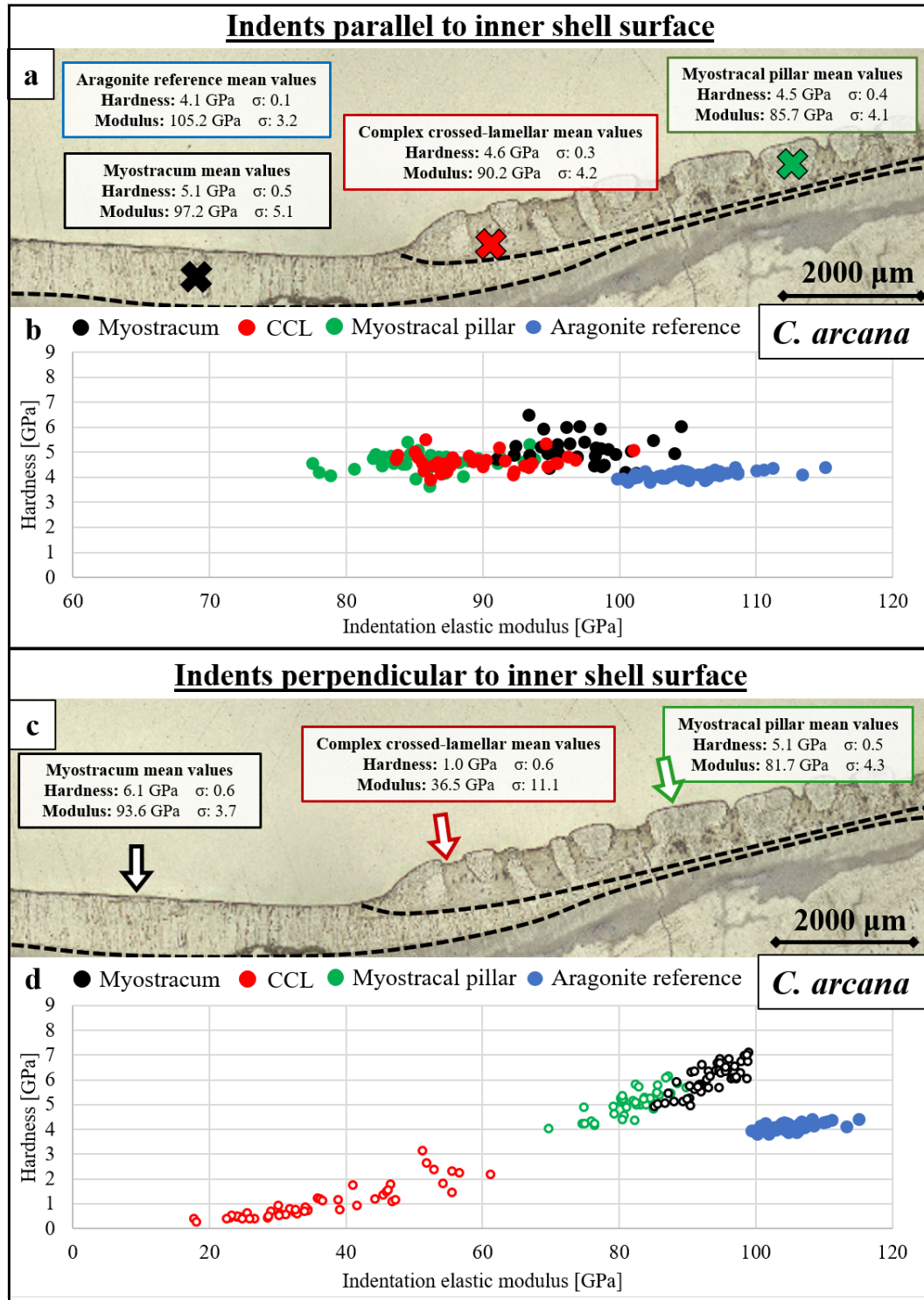


Fig. 2.3-4. The hardness and indentation elastic modulus distribution of different layers and cuts of *Glycymeris pilosa* and *Placopecten magellanicus* samples with a geological aragonite reference. The confocal laser microscopy images (a, c) depict the different shell layers indented for the two species and give the mean values and standard deviations σ for the hardness and elastic indentation moduli. Measurements were performed in the centre of shell layers (for cut 1, roughly indicated by coloured crosses in a and c) or at the inner shell surface (for cut 2, indicated by coloured arrows in a and c). Plot (b) shows that the myostracum layer (black/white) in *G. pilosa* has a distinctly higher hardness than the crossed-lamellar shell (red) and a non-biological aragonite reference (blue). When indented parallel, rather than perpendicular, to the c-axes orientation, the hardness of the myostracum is increased. This is also visible for *P. magellanicus*, where the myostracum is distinctly harder than the foliated calcite (yellow) or the reference (d). For both species, the indentation elastic modulus of the non-myostracal shell is the lowest. However, the myostracal moduli are lower than geological aragonite. In the geological aragonite reference for both profiles and the geological calcite reference, the crystallographic c-axis is misoriented 35–40°, relative to the indentation direction.

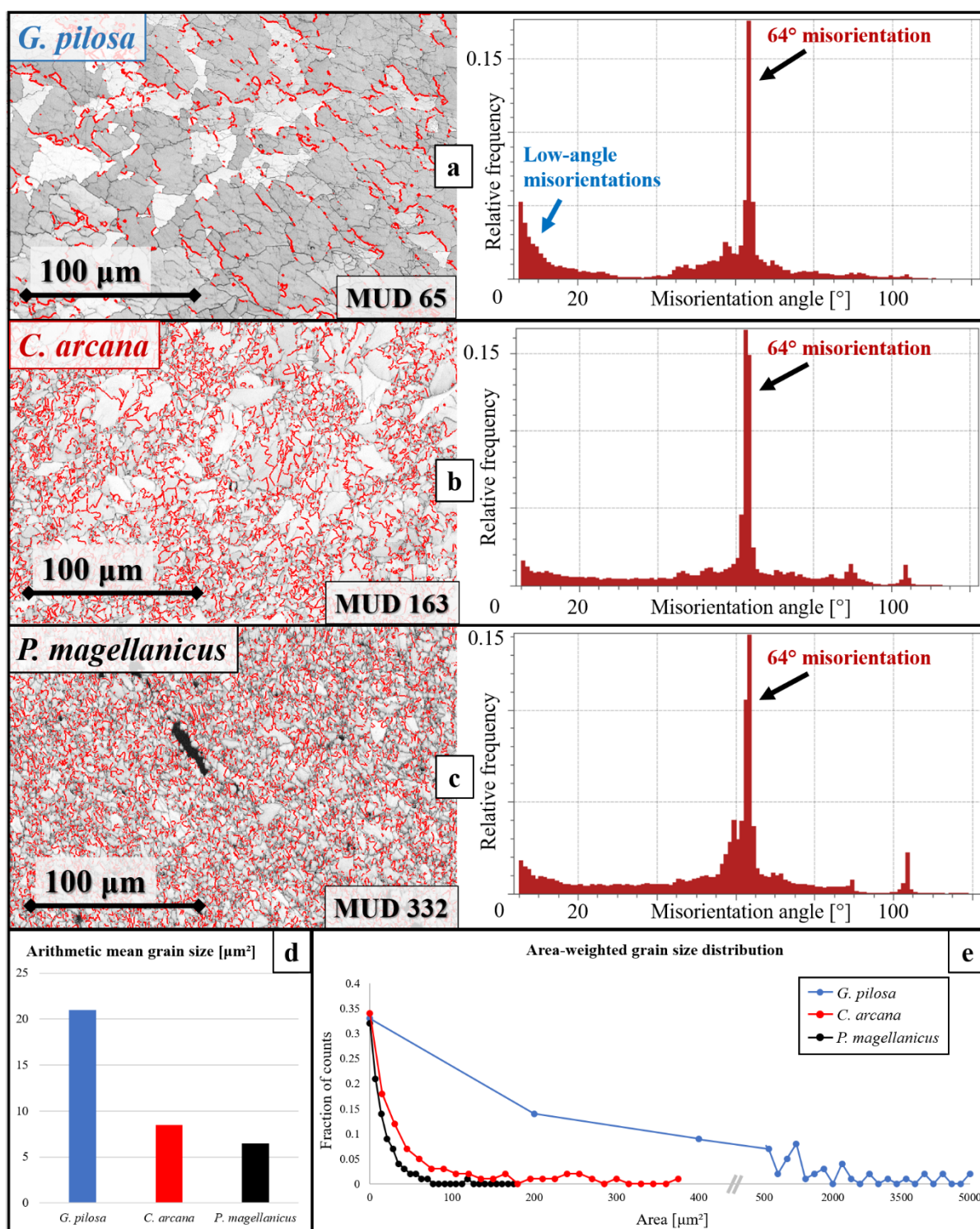


Fig. 2.3-5. The hardness and indentation elastic modulus distribution of different layers and indentation directions of *Chama arcana* shells with a geological aragonite reference. The confocal laser microscopy images (a, c) display the different indentation directions for the two directions and give the mean values and standard deviations σ for the hardness and elastic indentation moduli. Measurements were performed in the centre of shell layers (for cut 1, roughly indicated by coloured crosses in a) or at the inner shell surface (for cut 2, indicated by coloured arrows in c). Plots (b) and (d) show for different indentation directions that the myostracum layer (black) in *G. pilosa* has a higher hardness than the complex crossed-lamellar shell (red), the myostracal pillars (green) and the geological aragonite reference (blue). When indented parallel, rather than perpendicular, to the c-axes-orientation, the hardness of the myostracum and the myostracal pillars increases (d). For both directions, the highest observed indentation elastic modulus is in the reference, followed by the myostracum and the myostracal pillars. When indented parallel to the c-axes orientations, the complex crossed-lamellar layer showed irregular and distorted displacement curves that might not yield reliable results. In the geological aragonite reference for both profiles, the crystallographic c-axis is misoriented $\sim 35^\circ$ to the indentation direction.

2.3.4 DISCUSSION

Previous studies describe that the operation of the bivalve adductor muscle depends on the organism's lifestyle and the interaction between the adductor and pedal muscles and the ligament of the hinge (Tremblay et al. 2015). Muscle fibres consist of actin, myosin, and paramyosin (Chantler 1983) and vary in their organisation, type and degree of structural order (Chantler 1983; Squire 1992). Depending on the lifestyle and environment of bivalved organisms, adductor muscle fibres may vary in thickness, shape and length (Chantler 1983; Dowd & Jimenez 2019).

Up to three muscle parts relate to bivalve valve opening, closure, and locomotion (Hanson & Lowy 1960; Odintsova et al. 2007). The *smooth* muscle fibres perform the 'catch' mechanism of the muscle. This slow and continuous contraction helps to achieve tight and energy-efficient valve closure over long periods (Hanson & Lowy 1960; Rüegg 1971; Funabara et al. 2006). The *obliquely-striated* muscle fibres consist of two overlapping types of muscle filaments that can quickly contract, enabling rapid and strong valve closure. The *cross-striated* muscle fibres in bivalves produce quick contractions. These rapidly squeeze out the water from between the valves and generate a propelling jet of water that can be used for swimming or burrowing (Millman 1967; Guderley & Tremblay 2016). Fast and strong valve movements or prolonged valve closure demand that the adductor muscle fibres and myostracal crystals are strongly interlinked. Bivalves achieve tight connections between muscle fibres and shell crystals via a tendon cell layer secreted by the outer mantle epithelium. This tendon cell layer is positioned between the apical ends of the muscle fibres and the basal surface of the myostracal crystals (Reindl & Haszprunar 1996; Castro-Claros et al. 2021). From focal adhesions of the tendon cell layer, myofilament bundles emerge and penetrate the crystals of the myostraca (Castro-Claros et al. 2021). This leads to one of the strongest known connection mechanisms utilised by invertebrates or vertebrates (Castro-Claros et al. 2021).

While the muscle structure, function, and fibre interconnection are well-investigated for bivalves by now, only a few studies focused on the role and the structural design of the myostracal hard tissue and the changeover from the non-myostracal shell crystals to the prisms of myostraca. In the subsequent sections, we discuss microstructure, texture and nanomechanical property results of myostraca of sessile, burrowing, and swimming bivalves (Figs. 2.3-1 to 2.3-6, 2.3-AP2 to 2.3-AP6). First, we address the determinants of myostracal microstructures and show that the latter are not only determined by the crystal growth process but also influenced by the microstructure and texture of the adjacent, non-myostracal shell. The shells of the chosen organisms are formed of different microstructures (Figs. 2.3-3, 2.3-AP2); accordingly, different microstructures are adjacent to the myostraca of the investigated bivalve species. Subsequently, we will show that even though the growth process affecting myostracal crystal formation appears to be the same for the different species, the structure of myostraca of bivalves leading different lifestyles is not conservative, as stated by other studies (Lowenstam & Weiner 1989; Crippa et al. 2020a; Dong et al. 2022). The competitively generated

myostracal microstructure is modulated by the respective crystal organisation design of the adjacent, non-myostracal shell. Shell crystal organisation is ultimately determined by the shell fabrication requirements imposed on the organism for survival. Second, we discuss the gained nanomechanical property results of myostracal and non-myostracal hard tissue and describe limiting factors for hardness and nanoindentation elastic modulus. Lastly, we discuss for a carbonate biological hard tissue how variation in crystallographic c-axis orientation influences nanomechanical properties of the myostraca and of the non-myostracal hard tissue (Figs. 2.3-7, 2.3-8, 2.3-AP6).

Is the adductor myostracum microstructure the sole result of a competitive growth determinant?

The evolutionary success of bivalves after the end-Permian mass extinction may not necessarily be based only on variation of shell morphology (Fraiser & Bottjer 2007). The global diversity of bivalves we see today can also be related to their ecological success and remarkable ability to invade new environments and quickly adapt to them (Stanley 1972; Vermeij 1977; McLachlan et al. 1995; Bogan 2008).

Within their respective ecological niches, *Glycymeris*, *Chama* and *Placopecten* are very successful, and their shells are well-adapted to the lifestyles they pursue. Glycymerididae have thick (~5 mm), aragonitic shells. With their transverse visceral musculature, *Glycymeris* are perfectly adapted to burrow into the sediment (Ansell & Trueman 1967b; Thomas 1975). The two symmetrical adductor muscles comprise smooth and obliquely-striated fibres and are among the strongest within the group of bivalved organisms (Plateau 1883; Thomas 1975). Organisms belonging to *Chama* are mostly epifaunal and attach their thick (~5 mm) and ornamented shells to a substrate via byssal attachment (Yonge 1967; Crocetta & Russo 2013). Studies have shown that chamid shell morphology is adapted to spatial restrictions imposed by the environment (Pastorino 1991; Hoerl et al. 2024a). Due to their immobility and relatively weak hinge, chamid bivalves developed elongated adductor muscles for rapid valve opening and closure (Yonge 1967; Kennedy et al. 1970). In the Pectinidae, the striated and smooth muscle fibres attach to the shell at a central region and leave a well-visible and large myostracum on the inner surface of the valves (Cragg 1985; Marsh et al. 1992; Andersen et al. 2009). Their thin (2-3 mm) calcitic shells and the interplay between ligament and adductor muscle are decisive for their fast swimming rates (Marsh et al. 1992; Tremblay et al. 2015; Guderley & Tremblay 2016).

Similarities in myostracal structure designs

G. pilosa belongs to the order Arcida, *C. arcana* is a member of Venerida, and *P. magellanicus* belongs to Pectinida. Despite differences in genomics, lifestyle and shell structure, the myostraca of the above-named species show, at first glance, a surprising similarity in myostracal microstructure. It is demonstrated by now that bivalve myostraca are always aragonitic and have a microstructure that varies significantly from the structure of the non-myostracal shells (e.g. Addadi et al. 2006; Checa 2018; Crippa

et al. 2020; Hoerl et al. 2024b). While myostracal crystal growth and microstructure formation appear to be controlled by mainly competitive crystal growth factors, growth of the non-myostracal shell occurs under tighter biological control by the formation of organic membranes confining the morphology of the crystals (e.g. Weiner & Addadi 1997; Checa, Esteban-Delgado & Rodríguez-Navarro 2007; Cuif et al. 2014; Hoerl et al. 2024a). At myostracal formation, the smooth surface of the non-myostracal shell layer adjacent to the myostracum provides the template for the nucleation of the first-formed myostracal crystals. For *Glycymeris* and *Chama*, these nucleate epitaxially onto the non-myostracal shell layer template (Hoerl et al. 2024b). In *P. magellanicus*, the myostracal nucleation is mediated by an organic-rich sheet. The growth of myostracal crystals from the nuclei occurs through a process involving growth competition (Dong et al. 2022; Hoerl et al. 2024a, b), i.e. many crystallites are close to each other and compete for space and ions that are needed for them to grow. The likelihood for a crystallite to grow larger is determined by its crystallographic orientation. The growth rate decreases non-linearly with the deviation of the crystal's fastest growth direction (for carbonate materials, the c-axis) from the orientation normal to the nucleation template. With continuing growth, the less favourably oriented crystals become outperformed and overgrown by the more favourably oriented crystals. As the latter grow in length and diameter, a progressively stronger crystallographic preferred orientation develops along the fastest axis of growth (the c-axis in the present case), while the number of crystals in the microstructure decreases with distance away from the nucleation template (Lee & Choi 2007; Cuif et al. 2023; Hoerl et al. 2024b).

In essence, two distinct processes govern the formation of bivalve myostracal crystals: (i) epitactic nucleation onto a non-myostracal shell layer surface or organic-rich template and (ii) growth of the crystals, driven by the process of growth competition. We find these structural characteristics for the adductor myostraca of the three studied species (Fig. 2.3-1).

A further structural similarity we found for the myostraca of the investigated species, irrespective of differences in myostracal crystal size, is the degree and mode of twinning of the myostracal crystals (Figs. 2.3-6, 2.3-AP5). The common aragonitic twin law, corresponding to a misorientation of 63.8° around [001], is a mirror reflection on the {110} plane, which is mostly the composition plane (Hahn & Klapper 2013). The misorientation angle diagrams for the myostraca of the three investigated species show a relative misorientation maximum around 64° with relative frequencies of about 15% (Figs. 2.3-6, 2.3-AP5). This confirms that crystal twinning is prevalent within the adductor myostraca of the investigated bivalves. The red lines superimposed on the band contrast EBSD maps conducted on the myostraca (Figs. 2.3-6, 2.3-AP5) are 64° grain boundaries. The preferred twinning mode for all investigated myostraca is cyclic twinning following the {110} twin law. Since the twinned surfaces are irregular in the present cases and do not strictly seem to follow the regular {110} plane, we consider them to be penetration twins.

Differences in myostracal structure designs

Despite the two above-mentioned structural similarities for the myostraca of the investigated bivalves, we find strong structural differences between *G. pilosa*, *C. arcana* and *P. magellanicus* myostraca, namely:

- (i) myostracal prism size (EBSD maps in Figs. 2.3-2, 2.3-AP3 and grain size statistics in Figs. 2.3-6d, e, 2.3-AP5),
- (ii) crystal co-orientation strength (MUD values in Figs. 2.3-1 and 2.3-2)
- (iii) myostracal texture (pole figures in Figs. 2.3-2, 2.3-AP3).

The influence of myostracal prism size and crystal co-orientation strength

In contrast to *P. magellanicus* and *C. arcana*, we find for *G. pilosa* myostraca an abrupt increase in prism diameter and length close to the changeover from the non-myostracal valve to the myostracum (Fig. 2.3-1a). As myostracal crystals increase in size with progressive growth due to a growth competition process, we find crystals with very large cross-sections at the *G. pilosa* myostracal inner surface (Figs. 2.3-2a, 2.3-6d, e, 2.3-AP3a). *C. arcana* and *P. magellanicus* do not show such a sudden increase in prism diameter and size close to the changeover from the non-myostracal valve to the myostracum (Fig. 2.3-1b, c). *C. arcana* and particularly *P. magellanicus* myostraca consist of thin and long prisms (up to 5 μm in diameter and 100 μm in length). Accordingly, at the inner myostracal surface, prism cross-sections are rather small (Figs. 2.3-2b, c, 2.3-6d, e, 2.3-AP3b, c).

Contrarily to what was expected from the model of competitive growth, the decrease in prism size from *G. pilosa* via *C. arcana* to *P. magellanicus* along the inner myostracal surfaces (Figs. 2.3-2, 2.3-AP3) is accompanied by an increase in crystal co-orientation strength (see MUD values in Fig. 2.3-5a-c). For the *G. pilosa* myostracum, we find an MUD value of 65, while for the *P. magellanicus* myostracum, we find an MUD value of 332 (Fig. 2.3-6a, c).

At first glance, this is rather surprising as *G. pilosa* features a 3D “single-crystal-like” texture, and *C. arcana* and *P. magellanicus* show an axial texture. Nevertheless, the difference in crystallographic co-orientation statistics of the three myostraca might be caused by the difference in the orientational variation of the c-axes. As the colours for myostracal crystal orientation in Fig. 2.3-1 highlight for *G. pilosa* and, to some extent, for *C. arcana*, myostracal crystal orientations vary significantly between the species. In *G. pilosa*, the misorientation between crystallographic c-axes is inherited from the double maxima of the crossed-lamellar layer. In contrast, for the *P. magellanicus* myostracum, we find a strong crystal coalignment, displayed by the similar colours in the EBSD map (Fig. 2.3-2c). A further reason for the difference in crystal co-orientation strength and, hence, MUD value between the myostraca of the investigated species could be that the large prisms of *G. pilosa* are internally more structured. Thus, they comprise many small misorientations (e.g. white stars in Fig. 2.3-

2a) relative to the degree of internal structuring of the smaller-sized prisms of *C. arcana* and *P. magellanicus*.

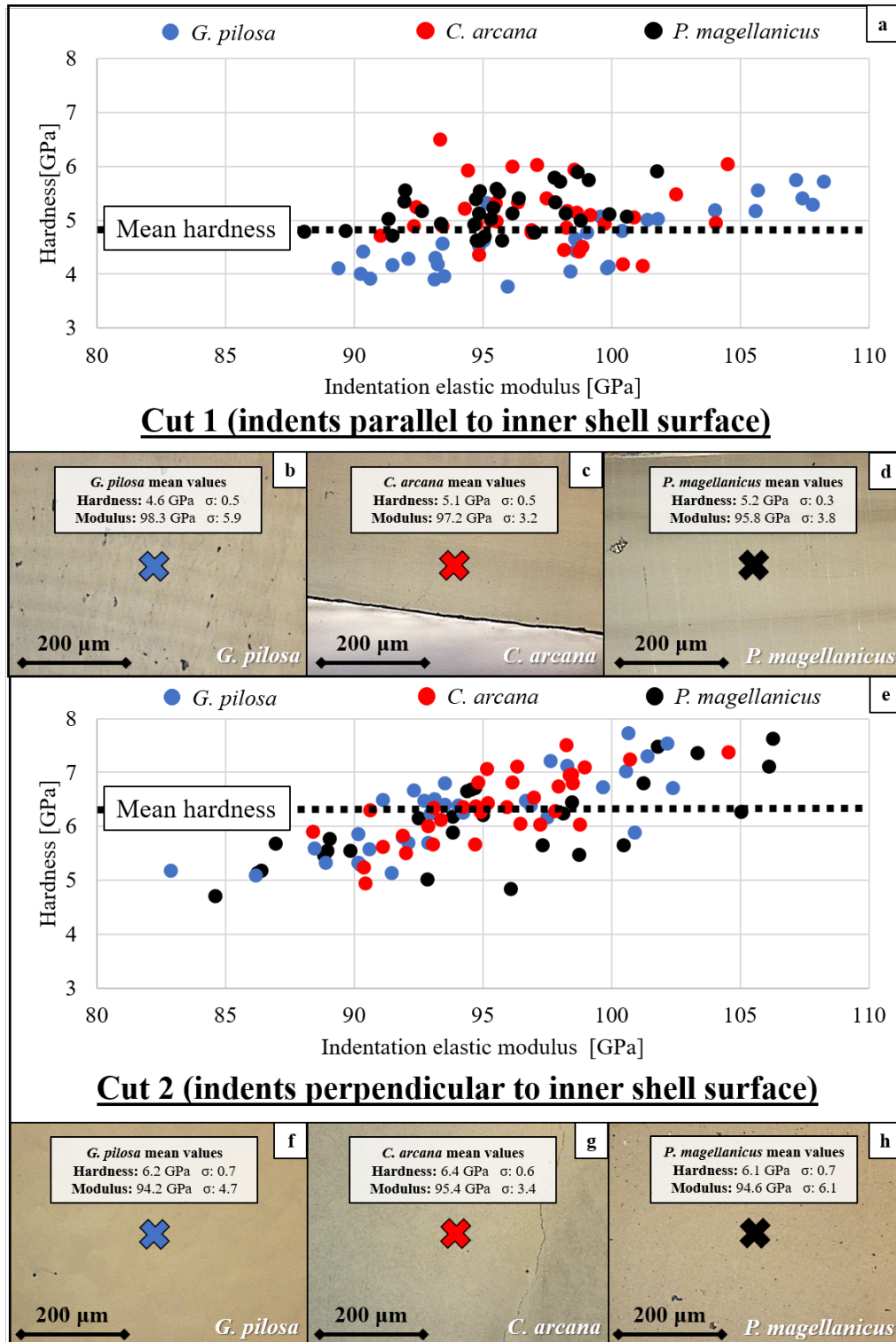


Fig. 2.3-6. Misorientation angle distribution and grain size statistics for adductor myostraca sectioned along cut 2 in *Glycymeris pilosa*, *Chama arcana* and *Placopecten magellanicus*. Irrespective of the texture and microstructure, the myostracal prisms of *G. pilosa* (a), *C. arcana* (b) and *P. magellanicus* (c) predominantly follow a grain misorientation angle of about 64°. This angle corresponds to aragonitic twinning on the (110) and ($\bar{1}\bar{1}0$) planes, constituting more than 15% of all analysed grain boundaries (a-c). The average grain size varies considerably between the three microstructures. When cross-sectioned, *G. pilosa* shows the highest average grain size (d), comprising crystals that may exceed a size of 4000 μ m² (e). *C. arcana* and *P. magellanicus* show similar grain size statistics, however, *C. arcana* crystals appear slightly larger in mean size (d, e).

Myostracal and non-myostracal shell texture

The *G. pilosa* adductor myostracum has a 3D “single-crystal-like” texture inherited from the 3D “single-crystal-like” crystal orientation pattern of the adjacent crossed-lamellar shell (compare pole figures in Fig. 2.3-1a with pole figures in Figs. 2.3-2a, 2.3-3a). A crossed-lamellar microstructure consists of a sequence of first-order lamellae, with the latter being composed of crystals forming two orientational sets, set A and set B (e.g. Fig. 2.3-8c). For *C. arcana* adductor myostracum and myostracal pillars, the crossed-lamellar crystal orientation pattern of the adjacent shell is, at first, also continued within the myostraca. Within the very first few μm of the myostracum, crystals that belong to the set of the first-order lamellae having their c-axes perpendicular to the shell-myostracum changeover surface, outcompete crystals of the other first-order lamellar set. For *C. arcana*, this results in a gradual shift from the 3D “single crystal-like” texture of the non-myostracal crossed-lamellar shell (see the orientation maxima in the pole figures of Fig. 2.3-3b) to an axial texture of the myostracum (see pole figures in Fig. 2.3-2b without distinct a- and b-axes).

The shell of *P. magellanicus* is formed of foliated calcite (Figs. 2.3-3c, 2.3-AP2), while the myostracum comprises competitively grown aragonite (Fig. 2.3-1b). Thus, the *P. magellanicus* myostracal crystals cannot adopt the texture of the adjacent shell layer. Instead, the changeover from the non-myostracal shell to the myostracum features a thin (around 5 μm thick) organic-rich layer (white star in Figs. 2.3-1b, 2.3-AP2c). This organic-rich layer mediates the interconnection between the *P. magellanicus* calcitic shell and the aragonitic myostracum. Similar sheets separating calcitic and aragonitic shell layers have also been observed for other bivalve species, such as *Chama arcana*, *Crassostrea gigas* or *Pinctada margaritifera* (Lee & Choi 2007; Lee et al. 2011; Cuif et al. 2023; Hoerl et al. 2024a). The myostracum of *P. magellanicus* has a marked axial texture with aragonite c-axes oriented towards the direction of growth (Fig. 2.3-1b) and is highly co-oriented (see pole figures in Figs. 2.3-2c, 2.3-AP3c). The texture of the adjacent non-myostracal shell is axial as well; however, it shows a very low degree of crystal co-orientation strength (see pole figures in Figs. 2.3-3c, 2.3-AP2c). As described above, we find very different crystal co-orientation strengths (MUD values) at the innermost myostracal surface of the three investigated species (Fig. 2.3-6a-c). We noted for the investigated species that the longer the texture of the adjacent, non-myostracal shell is continued towards the inner myostracal surface, the lower the myostracal crystal co-orientation strength and the MUD value of the EBSD scan. Of the investigated bivalve species, the *G. pilosa* myostracum adopts, at most, the texture of the adjacent non-myostracal shell; the myostracum has a low crystal co-orientation strength. The *P. magellanicus* myostracum does not adopt the texture of the adjacent non-myostracal shell; its myostracum has the highest crystal co-orientation strength.

Factors that generate modulation of the competitively grown myostracal structure

The crystallography of shell crystals adjacent to the myostracum and their influence on the myostraca

This and previous studies (Crippa et al. 2020a; Crippa et al. 2020b; Hoerl et al. 2024b) highlight that the interface between shell layers, comprising different aragonite microstructures, is not sharp and clear-cut. The transition from one layer to the other is based on the interlinkage of the textures of the adjacent two shell layers.

The three investigated bivalve species have the following shell microstructures adjacent to their myostraca: *G. pilosa* has a crossed-lamellar layer with first-order lamellae running almost perpendicular to the inner shell surface (Fig. 2.3-AP2a). *C. arcana* also has a crossed-lamellar microstructure adjacent to the adductor myostracum; however, in contrast to the first-order lamellae of *G. pilosa*, the morphology of the first-order lamellae is irregular, and the two sets of first-order lamellae are intertwined (Fig. 2.3-3b, 2.3-AP2b and Hoerl et al. (2024a)). The *P. magellanicus* shell adjacent to the adductor myostracum comprises foliated calcite (Fig. 2.3-AP2c). The colour-coded EBSD maps show that at the changeover from the non-myostracal shell to the myostracum, the very first myostracal crystals of *G. pilosa* and *C. arcana* adopt the texture of the adjacent crossed-lamellar layer (Fig. 2.3-1a, d and Hoerl et al. (2024b)). This is due to the topotactic nucleation of myostracal nuclei onto the non-myostracal shell surface, as the orientation pattern of shell crystals continues into the adjacent myostracum. The nucleation stage of myostracum formation is biologically determined. Crystallographic characteristics of myostracal crystal nuclei are determined for *G. pilosa* and *C. arcana* by crystallographic characteristics of crystals of the non-myostracal shell and for *P. magellanicus* by an organic substance secreted by the organism.

The *Glycymeris pilosa* case

Due to the straight morphology of the first-order lamellae in *G. pilosa*, the two sets of first-order lamellae (set A, set B, e.g. Fig. 2.3-8c) are well distinguishable. It is also well observable that the crossed-lamellar crystal orientation pattern of the first-order lamellar shell microstructure is continued into and within the *G. pilosa* myostracum (Fig. 2.3-1a), up to the inner myostracal surface. The two sets of first-order lamellae have crystallographic c-axes orientations tilted relative to each other (Fig. 2.3-3a and Almagro et al. (2016c); Hoerl et al. (2024b)). As myostracal crystal growth is controlled by growth competition, two different crystal growth speeds develop at the formation of the *C. pilosa* myostracum. Depending on aragonite c-axes inclination relative to the nucleation template, the crystals of one set of first-order lamellae grow faster than the crystals of the other set. The crystals of the fast-growing lamella increase, with ongoing growth, quickly in size (Fig. 2.3-1a) and form the very large crystal units that we find at the inner myostracal surface (e.g. Figs. 2.3-2a, 2.3-AP3a), blocking the growth of crystals of the other set of the first-order lamella. Nonetheless, the crystals of the slowly growing set of the first-order lamella are not eliminated entirely, as the two sets of first-order lamellae are, in *G. pilosa*, spatially well

distinguished from each other (Fig. 2.3-3a). They are not intertwined, as is the case for the shell of *C. arcana* (Fig. 2.3-3b).

The *Chama arcana* case

In *C. arcana* shells as well, the non-myostracal shell layer adjacent to the myostracum has a crossed-lamellar microstructure, and the latter microstructure is continued, at least to some extent, into the adjoining myostracum. However, for the *C. arcana* non-myostracal shell, we find an intricate intertwining of the two sets of the first-order lamellae (Fig. 2.3-3b). This causes a tight arrangement of these within the non-myostracal shell as well as at the changeover from the non-myostracal shell to the myostracum. In *C. arcana* shells as well, the two first-order lamellar sets have different c-axis orientations. However, due to the strong intertwining of the two first-order lamellar sets, the set with the crystals having their c-axes oriented precisely perpendicular to the nucleation template fully outcompetes the growth of crystals of the other first-order lamellar set. The result is that crystals of only one crossed-lamellar set remain, and due to their high co-orientation, only one c-axis orientation is kept. This implies that the remaining/kept crystals grow at similar rates and generate the observed *C. arcana* adductor myostracal and myostracal pillar microstructure, formed of similarly-sized, acicular prisms (Fig. 2.3-2c, d). An axial texture develops, as only the c-axes are co-oriented, not necessarily the a- and b-axes.

The *Placopecten magellanicus* case

The shell and myostracum of *P. magellanicus* are a special case. There is a carbonate phase change between the calcite of the non-myostracal shell and the aragonite of the myostracum; thus, structural characteristics are not transmitted from the non-myostracal shell to the adjacent myostracum. Myostracal crystals do not follow a pattern of predetermined orientation inherited from the adjacent valve, as is the case for *G. pilosa* and *C. arcana*. In contrast, *P. magellanicus* myostracal crystals start to grow a few micrometres away from the non-myostracal valve-myostracum interface (Fig. 2.3-1b). They are developed as a sequence of thin, long (several tens of micrometres) acicular crystals with high crystal co-orientation and an axial texture. When the microstructure of the *P. magellanicus* adductor myostracum is compared to that of *G. pilosa* and *C. arcana*, for the adductor myostracum of *P. magellanicus*, the typical structure of a material consisting of competitively grown crystals is least observable (Fig. 2.3-1a-c, compare the image of adductor myostraca of the investigated species). This is also evident from the crystallographic co-orientation strength that does not increase significantly from the nucleation surface to the inner myostracal surface (Fig. 2.3-1b).

Further characteristics influencing adductor myostracum microstructure designs and texture

1. The microstructure at the inner myostracal surface can also be influenced by the thickness of the myostracum layer. The competitive growth mechanism enables the most adequately oriented crystals to outcompete the less adequately oriented crystals and gain in thickness. If the myostracum is thin, the competitive growth mechanism might be interrupted before its final stage, consisting of crystals co-aligned along the fastest-growing axis. Since bivalve muscles change position during shell growth (Castro-Claros et al. 2021), the muscle attachment period defining the myostracal crystal growth differs for each section of the myostracum. In addition, the relative size and thickness of the adductor myostracum, compared to the thickness of the entire shell, vary considerably for different bivalve species (Galtsoff 1964). For most bivalves, the myostracum comprises a substantial part of the shell, constituting up to a third of the shell thickness at muscle attachment sites (Lee & Choi 2007; Lee et al. 2011; Sato & Sasaki 2015). However, some bivalve species show thin (less than 10 μm), stacked myostraca comprising tiny crystals (such as *A. ephippium* or *A. islandica* (le Moine 2022; Hampa 2023)) or a fine, weakly-developed sheet, barely distinguishable from the non-myostracal valve (such as *M. edulis* or *T. planata* (Hoerl 2022; Hampa 2023)). Furthermore, it should be noted that valve activity is not just the result of muscle (adductor, pedal) activity but is rather an integrant within the interplay between the resilience and efficiency of the hinge ligament and the resilience and efficiency of the adductor muscles (Tremblay et al. 2015). Accordingly, definite proof of a clear-cut connection between valve thickness and myostracum microstructure cannot be provided easily.

2. Recent studies report that adductor myostraca contain a significant amount of organic substance (Lee & Choi 2007; Liao et al. 2015). The latter is not developed as organic envelopes encasing the myostracal prisms (Lee & Choi 2007; Liao et al. 2015) but is present as collagen-rich fibrils within the myostracal crystals (Galtsoff 1964; Zhao et al. 2015; Castro-Claros et al. 2021). We conducted TGA measurements for the microstructures encountered in *G. pilosa* and *P. magellanicus* shells (Fig. 2.3-AP4b). TGA results show that myostraca are richest in organic substance relative to the foliated and the crossed-lamellar shell layers. Furthermore, we observe differences in organic content between myostracal and non-myostracal shell layers and significant differences in organic content for the myostracum of *G. pilosa* and that of *P. magellanicus* (Fig. 2.3-AP4). The *P. magellanicus* myostracum consists of an assembly of thin and long prisms (Fig. 2.3-1b), while *G. pilosa* forms the largest part of its myostracum of large-sized prismatic crystals (Fig. 2.3-1a). Bivalve myostraca are organic-inorganic composites. However, due to the competitive crystal growth mechanism, there is no biopolymer extracellular matrix at myostracal shell sections. This contrasts with some non-myostracal shell microstructures that comprise organic matrices filled with minerals. Hence, myostracal prisms are not encased by an organic sheath, and the organic substance is not between but within the prisms. In myostraca, organic matter is present as myofilaments, providing the necessary tight connection for the attaching muscle to the prismatic crystals of the myostracum (Castro-Claros et al. 2021). *G. pilosa*

myostraca are formed of large myostracal prisms; hence, there are few grain interfaces within the *G. pilosa* myostracum. The *G. pilosa* myostracum is most enriched in organic material (Fig. 2.3-AP4), far more than the *P. magellanicus* myostracum, which comprises many thin prisms and, thus, very many prism interfaces. In addition to the above discussion, we take the latter as a further indication that at myostraca, the organic substance is mainly within the prisms. Nonetheless, it could not be determined whether a specific composition of an organic substance or a specific, proactive arrangement of muscle fibres possibly causes organism-related differences in the structural characteristics of myostraca. For gastropods, it has been reported that differences in structure and thickness of the cross-linked adductor muscle bundles can influence myostracal microstructure (Tomba & Watabe 1976).

Nanomechanical properties of myostraca and the non-myostracal shell

The diverse challenges of marine environments for organism survival push biomineralised hard tissues to be as tough and fracture-resistant as possible (Bignardi et al. 2010; Ritchie 2011; Ritchie 2021; Peter et al. 2023). However, in material optimisation, a multi-scale trade-off has to be achieved between adjusting the nanomechanical properties of the hard tissue to meet the requirements needed to generate a lightweight and metabolically cheap structural material. Various factors, such as crystal size, orientation, arrangement, mode of interlinkage, organic substance content, fabric and distribution, influence structural hard tissue's mechanical strength and fracture resistance (Taylor & Layman 1972; Troncoso et al. 2020; Lew et al. 2023; Peter et al. 2023; Hoerl et al. 2024b). Therefore, understanding the effect of crystal orientation and mode of assembly on nanomechanical property results of the structural material is essential, not just for the correct interpretation of the gained results but also to decipher the biomineralisation principles that generate the respective structural biomaterial.

Hardness and indentation elastic modulus

Our study investigated the hardness and indentation elastic modulus of myostracal and non-myostracal valve layers (Figs. 2.3-4, 2.3-5). We juxtaposed the gained results: (i) for each investigated species between the adductor myostracum and the non-myostracal shell and (ii) for the myostraca of the three investigated species for the two performed cuts (cut 1, cut 2) through the shell (Fig. 2.3-7).

Irrespective of the indentation direction, the hardness and indentation elastic modulus of the myostraca exceeds the hardness and indentation elastic modulus of the respective non-myostracal shells. Relative to non-biological aragonite, myostracal hardness is increased; however, myostracal indentation elastic modulus is reduced (Table 2.3-1). Relative to non-biological aragonite, crossed-lamellar (CL) shell hardness is reduced, while complex crossed-lamellar (CCL) shell hardness is increased (Table 2.3-1).

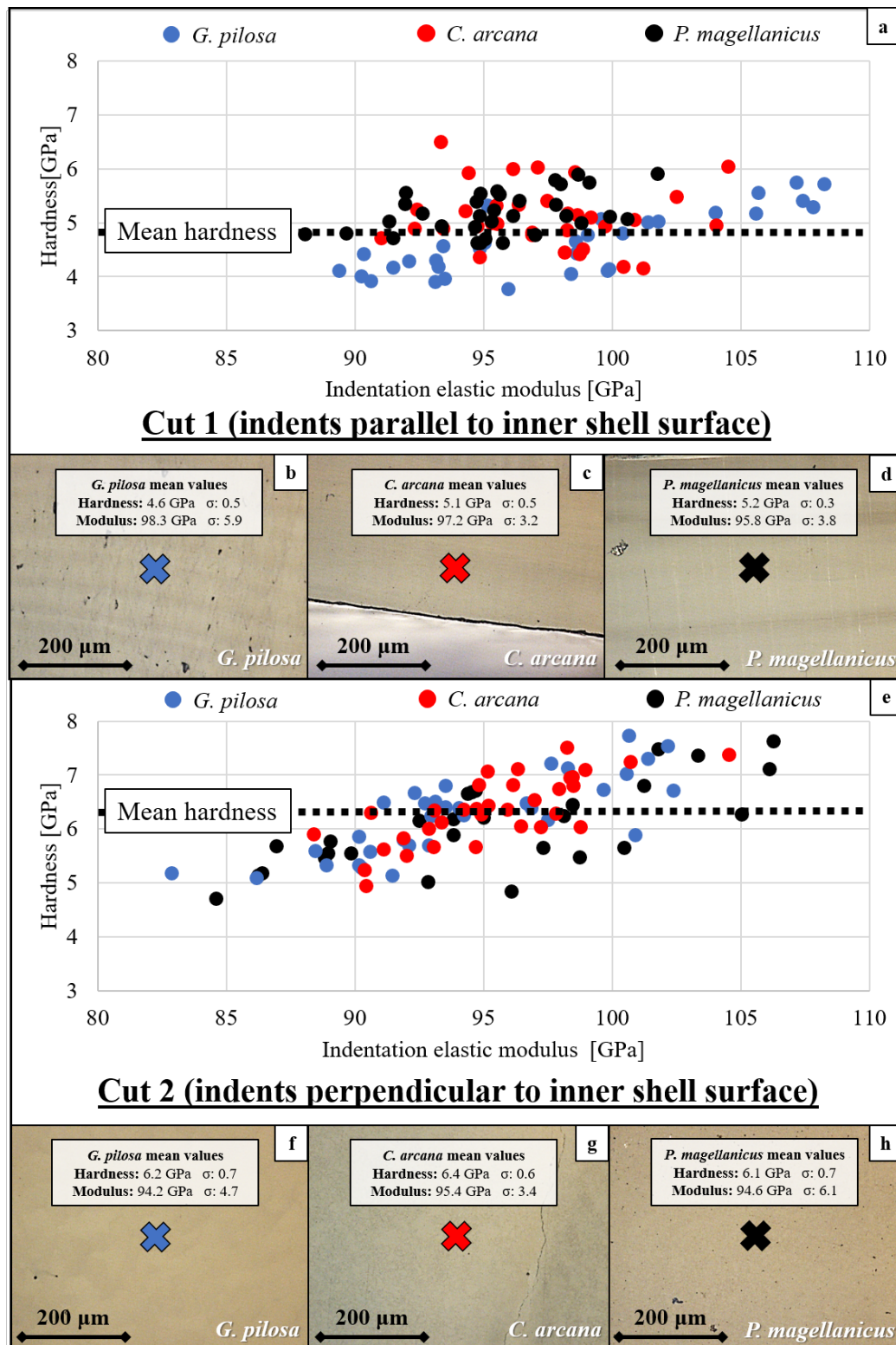



Fig. 2.3-7. The hardness and indentation elastic modulus distribution of adductor myostraca in *Glycymeris pilosa*, *Chama arcana* and *Placopecten magellanicus* for different indentation directions. The plots show the individual data points of the respective myostraca measured perpendicular (a) or parallel (e) to the orientation of the crystallographic c-axes. The confocal laser microscopy images (b-d) and (f-h) display the corresponding microstructures and give the mean values and standard deviations σ for the hardness and elastic indentation moduli. The measurements show that when indented parallel, rather than perpendicular, to the c-axes, the observed myostracal hardness increases by about 1 GPa. Dotted black lines indicate the mean hardness of the three myostraca indented parallel (a) and perpendicular to the inner shell surface (e). For different indentation directions, the indentation elastic moduli of the respective structures do not show significant differences. The adductor myostraca were indented at similar distances from the changeover with the adjacent shell (cut 1) or the inner shell surface (cut 2).

When indented parallel to the inner shell surface (cut 1), the adductor myostraca of the three investigated species show a mean hardness of about 4.9 GPa (Fig. 2.3-7a). Myostracal hardness is lowest (H: 4.6 GPa) for *G. pilosa*, the myostracum that consists of large prisms with a 3D “single-crystal-like” texture inherited from the crossed-lamellar layer (Fig. 2.3-1a). In contrast, myostracal hardness is increased (H: 5.1, 5.2) for the species that form their myostraca of many, rather thin, prisms with an axial texture (Fig. 2.3-1b, c). Table 2.3-2 highlights myostracal mean hardness and indentation elastic modulus values for other bivalve species indented parallel to their inner shell surface. The species are sorted in the table by the increasing influence of the competitive growth mechanism on the myostracal microstructure. *Ostrea stentina* (number 1 in Table 2.3-2) secretes a myostracum, which is strongly distinct in microstructure from the rest of the calcitic shell, via competitive growth without an aragonitic shell template. In contrast, the microstructure of *Tellina planata* (number 7 in Table 2.3-2) myostraca is almost indistinguishable from the microstructure of the rest of the shell layer. Hence, there is little influence of a competitive growth process on myostracal structure formation. The corresponding nanoindentation results indicate that myostraca with a clear-cut competitive growth-derived microstructure character have a higher hardness and elastic indentation modulus relative to those myostraca where the competitive growth-initiated structure is little or almost undeveloped (Table 2.3-2). This effect might explain the slightly lower hardness of the *G. pilosa* myostracum relative to the myostracal hardness of *C. arcana* and *P. magellanicus* (described in greater detail in Chapter 2.4 of this thesis).

Table 2.3-2. Nanoindentation results for indentation maps performed on the adductor myostraca of seven bivalve species. The species were sorted by the influence of the competitive growth process on their respective myostracal layers. *Ostrea stentina* (1.) myostraca have a microstructure characteristic for formation through competitive growth. In contrast, *Tellina planata* (7.) myostraca are very similar in structure to the adjacent granular shell, the latter controlled by biological determinants. The mean values for hardness and indentation modulus for myostraca of the seven bivalves indicate a trend to higher hardness and indentation elastic modulus for those myostraca crystallised predominantly under a competitive growth mechanism, e.g. *O. stentina*, *Peryglypta puerpera*, *Dosinia scalaris* and *Anomia ephippium*. This contrasts species where myostracum formation is little influenced by competitive growth mechanisms. All specimens were sectioned along cut 1, with the indentation direction parallel to the inner shell surface. Myostracal microstructures and an in-depth analysis of the indentation measurements are reported in Chapter 2.4 of this thesis.

Species	Average myostracal hardness [GPa]	Average myostracal modulus [GPa]	 Increase in influence of the competitive growth process
1. <i>Ostrea stentina</i>	5.2	99	
2. <i>Periglypta puerpera</i>	5.1	91	
3. <i>Dosinia scalaris</i>	4.9	97	
4. <i>Anomia ephippium</i>	5.0	94	
5. <i>Mytilus edulis</i>	4.3	84	
6. <i>Arctica islandica</i>	3.3	80	
7. <i>Tellina planata</i>	3.2	71	

Another explanation of the hardness variations includes the size of the myostracal prisms: when the shell is sectioned according to cut 1, the highest hardness is observed for the *P. magellanicus* myostracum, comprising the thinnest and longest prisms of the three investigated myostraca (Fig. 2.3-1b). For artificial materials, the Hall-Petch relation (Hansen 2004; Wang et al. 2008; Callister Jr & Rethwisch 2020; Luo et al. 2023) describes that a decrease in grain size and increase in grain boundary area results in higher yield strength. However, although a similar trend has been reported for biomineralised hard tissues in avian eggshells (Athanasiadou et al. 2018), the Hall-Petch effect is still poorly understood. Accordingly, without additional microstructure-nanomechanical property studies, we cannot unequivocally constrain whether the varying hardness values are a grain size effect. We see a significant difference in myostracal prism thickness between the investigated species (e.g. Fig. 2.3-2); however, the difference in hardness is very small (*G. pilosa*: 4.6 GPa; *C. arcana*: 5.1 GPa; *P. magellanicus*: 5.2 GPa) and only observable in cut 1, when indentation is carried out parallel to the inner shell surface. When indented parallel to the myostracal crystal c-axis (cut 2), the myostracal hardness for the three investigated bivalve species is similar; the mean hardness is 6.2 GPa (Fig. 2.3-7e).

Myostracal indentation elastic modulus is very little affected by the direction of cut through the shell or/and the direction of crystal c-axis orientation (Fig. 2.3-7, Table 2.3-1). Nonetheless, we observe for the indentation elastic modulus as well a distinct difference between the myostraca and the respective shells (Table 2.3-1). The highest indentation modulus we find for non-biological aragonite; the modulus value for the latter is markedly higher than the modulus values of the myostraca and is significantly higher than the modulus values for the respective shells (Table 2.3-1).

Previous studies indicate that indentation elastic modulus results gained on biomaterials depend on the organic matrix within the composite hard tissue (Song et al. 2003; Dietiker 2011; O'Toole-Howes et al. 2019), such that an increased organic content in the structural biomaterial induces a decrease in indentation elastic modulus. In our study, we find that compared to geological aragonite, myostracal and non-myostracal indentation elastic moduli are decreased for all investigated species (Table 2.3-1). The probable reason for the reduced indentation elastic modulus of the different shell layers, relative to non-biological aragonite, is that organic substance is present in all layers of the investigated shells (Fig. 2.3-AP4). Nonetheless, crucial for indentation elastic modulus results of biomaterials is not just the amount of organic substance within a microstructure but also its distribution mode. For example, the crossed-lamellar layer of *G. pilosa* has a low organic content (Fig. 2.3-AP4) but also a distinctly low average indentation elastic modulus (Fig. 2.3-4b and Table 2.3-1). In contrast, the myostracum of *G. pilosa* has a significantly higher organic substance content (Fig. 2.3-AP4) and higher indentation elastic modulus values (Table 2.3-1). This discrepancy can be explained by the different distributions of the organic substances in the *G. pilosa* crossed-lamellar shell and myostracum. In the crossed-lamellar microstructure, the organic substance forms a thin, matrix-like sheath evenly distributed around every lath. In the myostracum, however, collagen-rich fibrils are found within the prisms and lack from the

boundaries of adjacent myostracal prisms. However, it is important to remember that the difference in indentation elastic modulus might also be related to the different microstructures of the adductor myostracum and the respective non-myostracal shell.

We did not measure a significant difference in elastic modulus for the calcite between the inorganic reference and the *P. magellanicus* foliated calcite shell. Of all investigated microstructures, foliated calcite has the least fraction (~1%) of organic matter (Fig. 2.3-AP4). This could explain the small difference in indentation elastic modulus observed between geological and foliated calcite (Table 2.3-1 and Fig. 2.3-4c, d). Furthermore, our study shows that for all investigated species and both cuts through the shell, the adductor myostraca have comparable indentation elastic moduli (Fig. 2.3-7). Hence, myostracal indentation elastic modulus is neither influenced by crystallographic axes orientation of the constituting crystals, nor by their size or mode of assembly.

Difference in nanomechanical properties between C. arcana adductor myostraca and myostracal pillars

Myostracal pillars are, most probably, the result of mantle epithelium attachment and are most common in the Chamacea, where they can occupy a significant fraction of the inner shell layer (Kennedy et al. 1970; Taylor et al. 1973; Doguzhaeva & Mutvei 1986; Hoerl et al. 2024a). They usually arise from the trace of the pallial line and grow towards the inner shell surface, firmly attaching the mantle tissue of the organism to the shell (Kennedy et al. 1970). However, in rare cases, such as in *Cardita variegata*, they can also occupy the marginal section of the outer shell layer (Taylor et al. 1973). The comparison of *C. arcana* adductor myostracum (Fig. 2.3-1c) and myostracal pillar (Fig. 2.3-1d) microstructure does not show major structural differences. Both structures comprise long (up to 100 μm) and relatively thin ($< 5 \mu\text{m}$) prismatic crystals and their growth is guided by the competitive growth mechanism. At the changeover from the crossed-lamellar, non-myostracal valve to the myostracal crystal arrangement, the texture of the crossed-lamellar shell is transmitted to the myostracum. The texture of the non-myostracal valve is more or less axial (see pole figures in Figs. 2.3-3b, 2.3-AP2b); it is in-between a 3D “single-crystal-like” and a fully axial texture). The texture of the adjacent myostraca (adductor myostraca, myostracal prisms) is also axial (Fig. 2.3-1c, d), and the axial texture is maintained until the inner shell surface. However, nanomechanical property measurements give for the adductor myostracum and the myostracal pillars distinct differences in hardness and indentation elastic modulus (Table 2.3-1, Fig. 2.3-5). For both cuts through the shell, we find that the myostracal pillars show a lower hardness relative to the adductor myostracum. When indented parallel to the inner shell surface (cut 1), the hardness between the two layers decreases by 0.6 GPa (Fig. 2.3-5a, b) and when indented perpendicular to the inner shell surface (cut 2), it decreases by 1.0 GPa (Fig. 2.3-5c, d). The mean indentation elastic modulus is reduced for myostracal pillars, relative to myostracal elastic modulus, by more than 10 GPa (Fig. 2.3-5). Due to the rare occurrence of myostracal pillars in bivalve shells, the attachment mechanism between the mantle epithelium and the shell is poorly understood. However, their low indentation elastic modulus values

and microstructure, similar to the myostracum, indicate that the pillars might comprise differences in the distribution of organic matter.

The anisotropic fracture behaviour of the complex crossed-lamellar layer

The complex crossed-lamellar layer is a prominent yet poorly understood microstructure that comprises first-order lamellar blocks with more than two dip directions and an axial texture (Chateigner et al. 2000). The blocks consist of strongly twinned, prismatic aragonite crystals with a relatively small grain size of less than 5 μm (Crippa et al. 2020a; Hoerl et al. 2024b). Although recent studies have shown a “complex crossed-lamellar type” microstructure in the ornamentations of *Chama gryphoides* shells (Hoerl et al. 2024a, b), in general, the complex crossed-lamellar microstructure forms inner shell layers adjacent to the pallial myostracum. Our nanomechanical property results indicate that the complex crossed-lamellar layer’s response to nanoindentation testing strongly depends on the direction of the cut (Fig. 2.3-5, Table 2.3-1). When indented parallel to the inner shell surface (cut 1), the complex crossed-lamellar layer is relatively hard and maintains a relatively low indentation elastic modulus (Fig. 2.3-5a, Table 2.3-1). These nanomechanical property results are particularly astounding when considering the complex crossed-lamellar layer's relatively high organic content compared to other shell layers (Figure 2.3-AP4 and De Noia et al. (2020)).

However, when the complex crossed-lamellar shell layer is indented perpendicular to the inner shell surface (cut 2, Fig. 2.3-5b), the recorded load-displacement curves appear irregular and show multiple pop-in events (Fig. 2.3-AP6). These (nano)failures denote rapid tip displacement under contact load, potentially due to shear-induced cracking (Amini et al. 2015; Kasyap & Senetakis 2021). The localised material failures result in tip sliding and the formation of further penetration/displacement that deteriorates the calculated hardness by including “failure depths”. Thus, we conclude that the low hardness and indentation elastic modulus of the complex crossed-lamellar layer indented parallel to the c-axis orientations (Fig. 2.3-4b, Table 2.3-1) are misleading. This “graceful failure” can be amplified when the material is loaded along crystallographic axes directions, promoting faster chipping and cleavage. It is common in quasi-brittle materials and has previously been observed for crossed-lamellar shells, pointing to their anisotropic mechanical behaviour (Currey & Kohn 1976; Ichim et al. 2007; Meyers et al. 2008). To our knowledge, this is the first study that reports this specific nanomechanical property behaviour for the complex crossed-lamellar microstructure of biological structural materials. Organic material-filled microtubules were observed in the complex crossed-lamellar layer of other molluscs, such as *Neritilia rubida* or *Corbicula fluminea* (Araujo et al. 1994; Kano & Kase 2003). These microchannels might be responsible for the high overall organic content (Fig. 2.3-AP4) and the anisotropic pop-in events along indentation perpendicular to the inner shell surface (Fig. 2.3-AP6).

The effect of c-axis orientation on hardness and indentation elastic modulus

Several studies have shown that the orientation of crystals in bivalve shells is often controlled by biological determinants (Weiner & Addadi 1997; Cuif et al. 2014), even though myostracal crystal texture is guided mainly by competitive growth parameters. In general, crystallographic c-axes appear perpendicular to shelled organisms' inner and outer shell surfaces (Checa et al. 2025). Most likely, the latter is not by chance but is rather a functional property. Thus, testing shell microstructures in a cut parallel to the shell surface is of great interest as it simulates the exposed hard tissue. Previous studies have shown the anisotropic nanomechanical properties of single-crystalline calcite and aragonite (Berman et al. 1993; Pasquini et al. 2015), as well as of biomineralised carbonate microstructures, such as nacre or prismatic calcite (Barthelat & Espinosa 2007; Pasquini et al. 2015; Strag et al. 2020). The single-crystalline calcite and aragonite were tested with c-axes misoriented 35-40° to the indentation direction to compensate for potential anisotropic effects within the non-biological references. Compared to other directions such as {001}, Deng et al. (2023) have recently found that geological calcite shows balanced nanomechanical properties along the {104}-direction, comparable to the reference orientations tested in this study (Fig. 2.3-AP7a, b). To our knowledge, this is the first study that investigates the anisotropic behaviour of aragonite crystals in the exceptionally hard bivalve myostraca and the widespread crossed-lamellar shell. Our results demonstrate that adductor myostraca, indented perpendicular to the inner shell surface (cut 2), have comparable hardness values (Fig. 2.3-7e-h). Averaging more than 6 GPa for all three layers, the mean hardness of cut 2 is significantly higher than the hardness values obtained for cut 1 (Fig. 2.3-7a-d). Interestingly, the indentation elastic modulus values of the three layers are hardly affected by the change in indentation direction (Fig. 2.3-7a, e). This indicates that the difference in myostracal hardness is most likely not caused by a difference in organic content for the investigated shells but rather due to the orientation direction of the crystallographic c-axes.

While the indentation elastic modulus is an inherent material property, the measured hardness of biomineralised materials depends on factors such as architectural packing, crystallinity, porosity, organic content, grain size and grain orientation. While many of these factors can vary in biomineralised hard tissues, they are biologically controlled in the crossed-lamellar layers of *Glycymeris* shells. The first-order lamellae of the latter comprise two sets with very similar crystal size, morphology, organic content and porosity (Figs. 2.3-3a, 2.3-8a in this study and Supplementary Fig. 2.3-S21 in Crippa et al. (2020a)). However, our (Figs. 2.3-3a, 2.3-8) and previous studies (Almagro et al. 2016a; Almagro et al. 2016b; Crippa et al. 2020; Hoerl et al. 2025b) show that the crystals of the two sets (set A, set B) of first-order lamellae differ notably in orientation. This is well visible by the distinct density distribution maxima of contoured pole figures (see the difference in pole figures in Fig. 2.3-8a) displaying the varying c-axis orientations (see arrows within the c-axes pole figures in Fig. 2.3-8a).

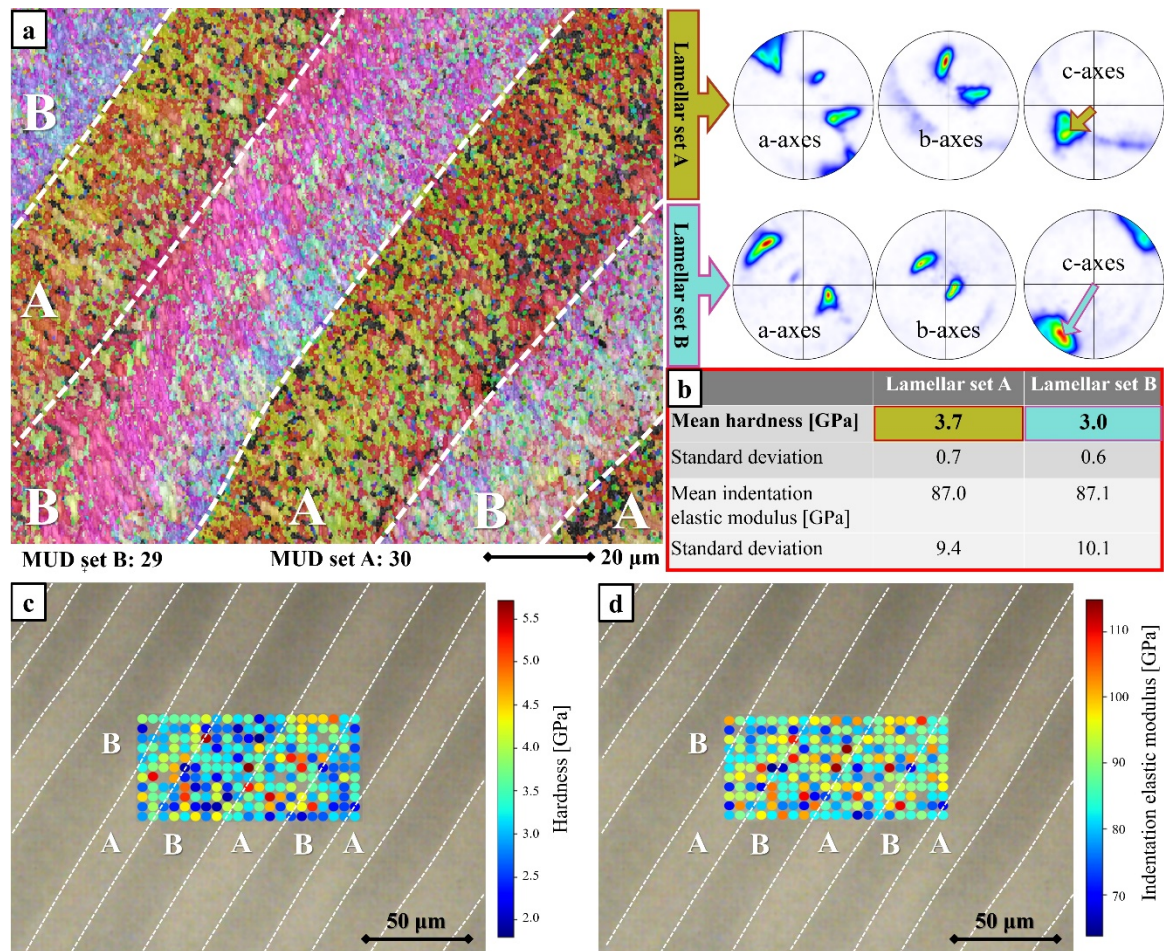


Fig. 2.3-8. Microstructural and nanomechanical analysis of different sets in the crossed-lamellar layer of *Glycymeris pilosa*. A colour-coded EBSD map performed on the shell shows the microstructure and texture of the two sets (a). Both sets are strongly twinned and have a 3D “single-crystal-like” texture, as indicated by the corresponding contoured pole figures (a). Their crystallographic co-orientation is comparable; however, the orientation of the c-axes differs. As indicated by coloured arrows in (a), the crystallographic c-axes of the lamellar set A are slightly tilted towards the indentation direction and the c-axes of set B run perpendicular to the indentation direction. A $100 \times 50 \mu\text{m}^2$ area spanning three first-order lamellae of the crossed-lamellar layer at a comparable position to the EBSD scan was indented (11 x 21 indents at $5 \mu\text{m}$ intervals). Table (b) displays the mean hardness and indentation elastic modulus values for sets A and B and gives the respective standard deviations. Set A shows a higher average hardness than set B; no difference can be observed for the elastic indentation moduli (b). The measured hardness (c) and indentation elastic modulus (d) for each indent are superimposed onto a microscopy image, where the first-order lamellar sets A and B are indicated by lines. Points with anomalous indentation curves were excluded from the plot. The positions of the nanoindentation data points and their assignment to set A or B are depicted in Supplementa Figure AP7.

With the combination of EBSD measurements and indentation testing, we can demonstrate that the obtained hardness values are largely affected by the crystallographic orientation of aragonite c-axes (Fig. 2.3-8b). Nanoindentation measurements were performed across a series of first-order-lamellae (Figs. 2.3-8c, d, 2.3-AP7c) and show that the observed hardness changes notably between the two lamellar sets (for hardness distribution see Fig. 2.3-8c). In contrast, the indentation elastic modulus values do not show a correlation with one or the other set of first-order lamellae. Despite the relatively high standard deviation caused by the heterogeneity of the crossed-lamellar composite layer, the indentation elastic modulus values are, more or less, similar for the two sets (Fig. 2.3-8b, d). The pole figures in Figure 2.3-8a demonstrate that c-axes of crystals of lamellar set A are clustered at an orientation somewhat similar to the indentation direction. In contrast, as the pole figures of Fig. 2.3-8a

show, the c-axes of crystals that form set B are almost perpendicular to the indentation direction. From the nanomechanical property values in Figure 2.3-8b, we observe that within first-order lamellae of *G. pilosa*, the mean hardness of set A is increased by 0.7 GPa, compared to the mean hardness of set B. Therefore, combining EBSD analysis and nanoindentation testing shows that the hardness is increased for the crystals of set A. In this set, we find a co-alignment of crystal c-axis orientations with the indentation direction relative to crystals of the other set (in this case, set B) of the first-order lamellae. Hence, this study indicates that the characteristics of microstructures, such as presetting crystal c-axis orientation, can influence the hardness of the aragonitic biomaterial. Similar or more sophisticated experimental setups in future experiments may help to precisely demonstrate and understand the relation between crystallographic orientation and nanomechanical properties in biomineralised hard tissues.

The present study compared the results of bivalve shell and myostracal microstructures obtained on different cuts through the hierarchical shells. In general, we found a strong correlation between crystal c-axis orientation and the hardness of the biomaterial. For more or less axial microstructures, the effect of azimuthal variability on nanoindentation measurements can be controlled by investigating the crystallographic texture of the indented surface. However, for microstructures that lack crystallographic co-orientation along a single c-axis direction, as is the case for crossed-lamellar structures, azimuthal variability on nanoindentation causes a significant problem regarding the reproducibility and consistency of hardness results. Accordingly, for nanomechanical property studies of biological hard tissues, it is vital to determine the microstructure and crystallographic texture of the investigated material, not only to understand the hard tissue of one particular specimen or/and species but also to enable comparison of nanomechanical property data between specimens and species. Böhm et al. (2016) proposed using conical nanoindentation indenters to analyse biogenic materials and to avoid azimuthal hardness dependence. The latter is not yet widespread for biomineralised materials, and the comparability of results obtained by Berkovich and conical indenters is disputed (Min et al. 2004; Swaddiwudhipong et al. 2006; Sakharova et al. 2009; Moore et al. 2010).

2.3.5 CONCLUSIONS

Bivalved organisms occupy a wide ecological space and can adapt to many lifestyles and environments (Trueman et al. 1966; Millman 1967; Stanley 1970; Stanley 1972; McLachlan et al. 1995; Sharma et al. 2023). This is enabled by developing various microstructure designs, occluding biopolymers into the hard tissue, and generating hierarchical structures. The latter characteristics are the keys to material optimisation, environment adaptation and survival. The valves of bivalve organisms are secreted not only to protect their soft tissue but also to burrow into the sediment, attach to a substrate via cementation, and perform locomotion for swimming. The muscles that control valve activity and the muscle attachment sites to the valves are integral to the organism's success in living a particular lifestyle

and surviving in a specific environment. In the present contribution, we discuss the interlinkage of the non-myostracal and myostracal valve microstructure, texture and nanomechanical properties for bivalves using valve activity to burrow, swim, or be epifaunal and sessile. Combining EBSD measurements with nanoindentation testing on valves sectioned perpendicular and parallel to the inner shell surface, we decipher structural approaches utilised by the investigated organisms to optimise their shell material for leading the above-mentioned lifestyles. We deduce from our results the following conclusions:

1. *G. pilosa* and *C. arcana* influence the microstructure and texture of their myostraca by controlling the structural properties of the non-myostracal shell adjacent to the myostracum, the template used for myostracal crystal nucleation. Even if for different bivalve species, the shell layer adjacent to the myostracum is similar in microstructure (e.g., crossed-lamellar, as is the case for *G. pilosa* and *C. arcana*), minor differences in the pattern of crystal orientation of the non-myostracal shell affect the adjacent myostracal microstructure strongly, since, at similar carbonate phase, the crystallographic texture of the shell is transmitted to the myostracum. For interdigitated and/or thin first-order lamellae (*C. arcana*), the crystals of the transmitted set of first-order lamellae, with their c-axes being perpendicular to the nucleation template and facing towards the growth direction, can quickly outcompete their neighbours. As the remaining co-oriented crystals can no longer gain lateral space, the corresponding myostraca are formed of thin, acicular crystals with an axial texture. For morphologically well-regulated or/and thick first-order lamellae (*G. pilosa*), the progressive elimination of crystals with divergent c-axis orientations to the nucleation template is prolonged. This results in a myostracal microstructure consisting of thick prisms and leading to the 3D “single-crystal-like” texture, extending from the non-myostracal valve to the inner myostracal surface.
2. *P. magellanicus*, *G. pilosa* and *C. arcana* myostraca are aragonitic. If the valve layer adjacent to the myostracum is calcitic, as for *P. magellanicus*, the orientation pattern of the non-myostracal calcite crystals is not transmitted to the adjacent aragonitic myostracum. If the shell layer adjoining the myostracum is aragonitic, as is the case for *G. pilosa* and *C. arcana*, the first-formed myostracal crystals assume the orientation of crystals of the adjacent aragonitic shell.
3. Myostracal microstructure, texture, prism morphology and size do not affect the mode or frequency of twinning of myostracal aragonite. The twinning of myostracal aragonite is extensive, and the extent of twin formation is similar for all investigated species. The twins are cyclic by (110) and ($\bar{1}\bar{1}0$) twin laws and generate a multitude of twin boundaries. These are of main structural importance, as it is shown for manufactured materials that the incorporation of twin boundaries increases the mechanical properties of the material.
4. Nanomechanical results demonstrate that, compared to non-myostracal layers and inorganic aragonite, myostracal aragonite has an increased hardness and indentation elastic modulus.

Myostracal prism size and morphology do not influence the nanomechanical properties of the myostracum.

5. Even if the microstructure and prism size are similar for *C. arcana* adductor myostraca and myostracal pillars, nanomechanical properties differ for the latter structures. The decrease in hardness and indentation elastic modulus of myostracal pillars, relative to the nanomechanical properties of the adductor myostracum, might be due to a different distribution of organic substance within the pillars, in comparison to the distribution of biopolymers within the adductor myostracum.
6. The indentation elastic moduli for the species and shell layers investigated in this study are not only influenced by the sheer amount of organic substance in the different microstructures but, in particular, by the mode of biopolymer distribution within the layer and microstructure.
7. The hardness values obtained for the non-myostracal shell and the myostraca differ significantly, depending on the angle between the indentation direction and crystal c-axis orientation. Layers indented parallel to the crystallographic c-axis orientation show the highest hardness, while crystals indented perpendicular to the c-axis orientation have a reduced hardness. For the indentation elastic modulus, the indentation direction is also influenced by crystal c-axis orientation. However, it is significantly less pronounced than what is observed for the hardness.
8. Furthermore, the anisotropic effect of indentation on hardness is demonstrated in this study for the two sets of a first-order lamella in the crossed-lamellar shell microstructure of *G. pilosa*. In the latter, the average hardness of set A of a first-order lamella (c-axes oriented almost parallel to the indentation direction) is significantly higher than the hardness of set B of the same first-order lamella (c-axes oriented perpendicular to the indentation direction).
9. Nanomechanical properties of the complex crossed-lamellar shell layer vary drastically with indentation direction. When indented parallel to the inner shell surface, the layer appears quite brittle and shows an average hardness similar to myostracal pillars. When indented perpendicular to the inner shell surface, the complex crossed-lamellar layer is subject to many pop-in events, indicating the formation of microcracks and/or lattice dislocations.

In essence, even though the crystal growth mechanism of *G. pilosa*, *C. arcana* and *P. magellanicus* myostraca is similar, we find, for the investigated bivalve species, significant differences in myostracal structural designs as well as in the crystallographic and structural characteristics of myostracal crystals. Our study demonstrates that, in contrast to previous reports (Lowenstam & Weiner 1989; Crippa et al. 2020a; Dong et al. 2022), the structure of bivalve myostraca is not conservative. Differences in myostracal structure are rooted in the fact that myostracal formation combines two processes: crystal nucleation and crystal growth. Myostracal crystal nucleation is influenced by the structural characteristics of the adjacent, non-myostracal shell. In contrast, the formation of the myostracal microstructure is mainly subjected to by growth competition, rather than being controlled by

the formation of organic membranes prior to crystallisation. It is predetermined by structural features transmitted from the biologically controlled non-myostracal shell to the myostraca. In addition, the combination and interplay of different types of fibres forming a muscle affect myostracal structure, as observed in the well-distinguishable muscle fibre imprints of the smooth and striated muscles of *P. magellanicus*.

We conducted an extended study on bivalve myostracal structure, microstructure, and texture (this study; Hoerl 2022; le Moine 2022; Hampa 2023; Rath 2023; Hoerl et al. 2024a, b) and found that the crystallographic characteristics for bivalve myostraca, determined with EBSD, are not family-specific. For example, the myostracal structure and crystallographic characteristics we found for *P. magellanicus* (Pectinidae) were also detected for the myostracum of *Ostrea stentina* (Ostreidae). Likewise, the myostracal structure and crystallographic characteristics of *G. pilosa* (Glycymerididae) are also observable in the shells of *Dosinia scalaris* (Veneridae) and *Anadara polii* (Arcidae). Myostracal structural features of *C. arcana* (Chamidae) are also present in the shells of *Acanthocardia tuberculata* (Cardiidae), *Periglypta puerpera* (Veneridae) and *Lampsilis cardium* (Unionidae). Keeping in mind the highly specialised shell structures that bivalves developed to maximise their chances of survival (such as different microstructural motifs (Boggild 1930; Taylor et al. 1969; Carter et al. 2012; Checa et al. 2025) or ornamentations (Kennedy et al. 1970; Ubukata 2005; Ye et al. 2023)), it is remarkable that the myostracal structure, microstructure, texture and formation mechanism is comparable across bivalve families. While myostracal microstructure and texture are also influenced by other requirements, e.g. environmental characteristics, their design is largely predetermined by biologically controlled and proactive templates, such as adjacent aragonitic shell layers or organic-rich sheets.

Acknowledgements

We thank Prof. N. Lagos Suárez, Centro de Investigación e Innovación para el Cambio Climático – CIICC, Universidad Santo Tomas, Santiago, Chile, Prof. E.M. Harper, Department of Earth Sciences, University of Cambridge, Downing Street, Cambridge CB2 3EQ, U.K. and Prof. C. Salas and Prof. S. Gofas, Departamento de Biología Animal, Facultad de Ciencias, Universidad de Málaga, Málaga, Spain for the samples.

Author contributions

Conceptualisation, S.H., E.G.; Formal analysis, S.A., A.G.C., W.W.S.; Investigation, S.H., E.G., C.M., S.A., K.U.H.; Methodology, S.H., E.G., M.P.; Supervision, S.A., E.G., W.W.S.; Validation, A.G.C., W.W.S.; Visualization, S.H., E.G.; Writing – original draft, S.H., E.G.; Writing – review & editing, C.M., S.A., E.G., K.U.H., A.G.C., M.P., W.W.S.

2.3.6 SUPPLEMENTARY INFORMATION

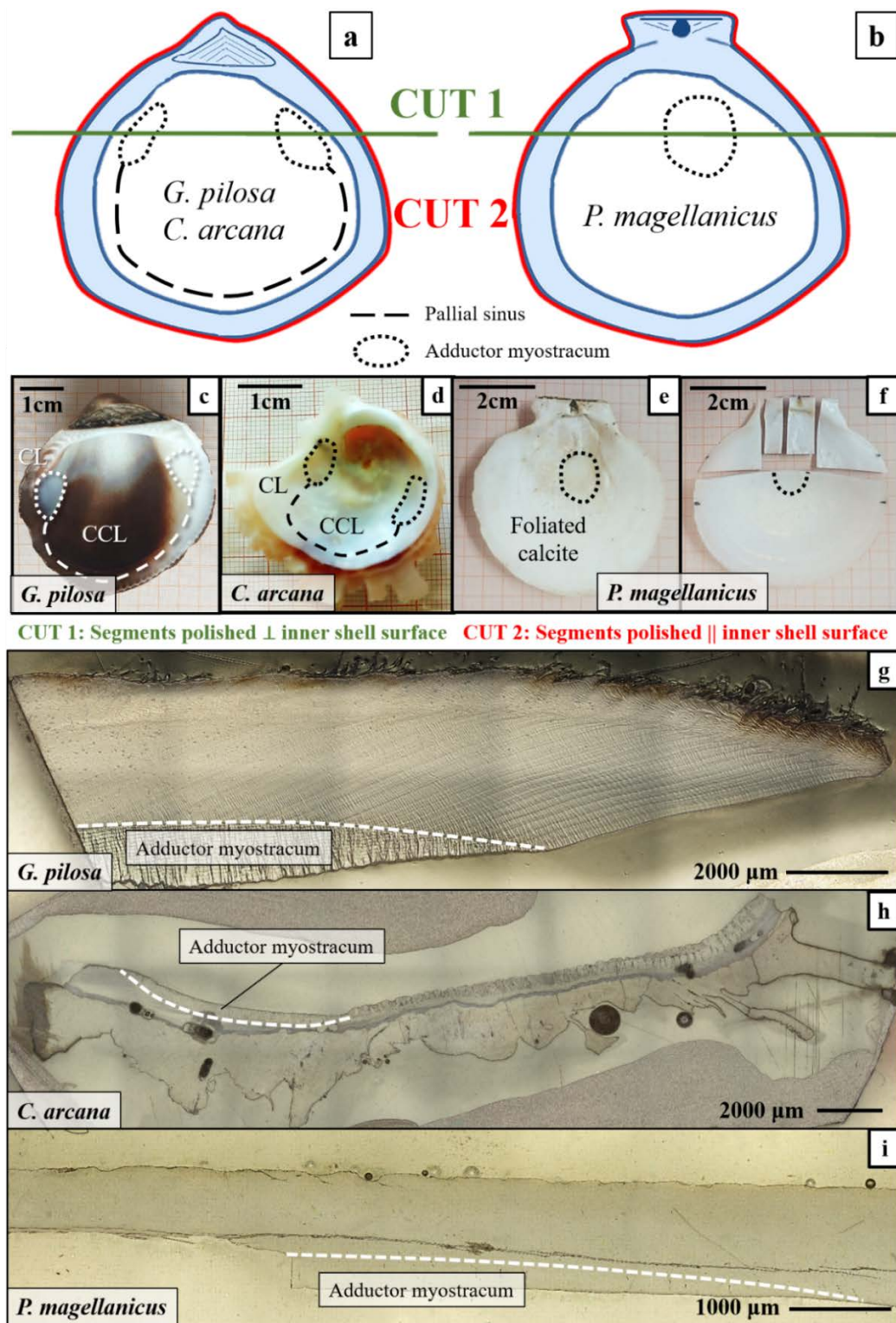


Fig. 2.3-API. Overviews indicating the direction and position of the different shell cuts performed on the specimens presented in this article. The two cuts are illustrated for a valve featuring two adductor muscle scars, such as *Chama arcana* and *Glycymeris pilosa* (a: modified after Crippa et al. (2020a)), and a valve featuring one adductor muscle scar, such as *Placopecten magellanicus* (b). The valves were cut and polished to expose the adductor myostraca indicated by dotted lines (a-i). For all three species (c-f), cut 1's segments were polished perpendicular to the inner shell surface. Cut 2's segments were polished parallel to the inner shell surface. Laser confocal microscopy images show the overview over the cross-sectional cuts perpendicular to the inner shell surface (cut 1) for the three investigated species: *G. pilosa* (g), *C. arcana* (h) and *P. magellanicus* (i).

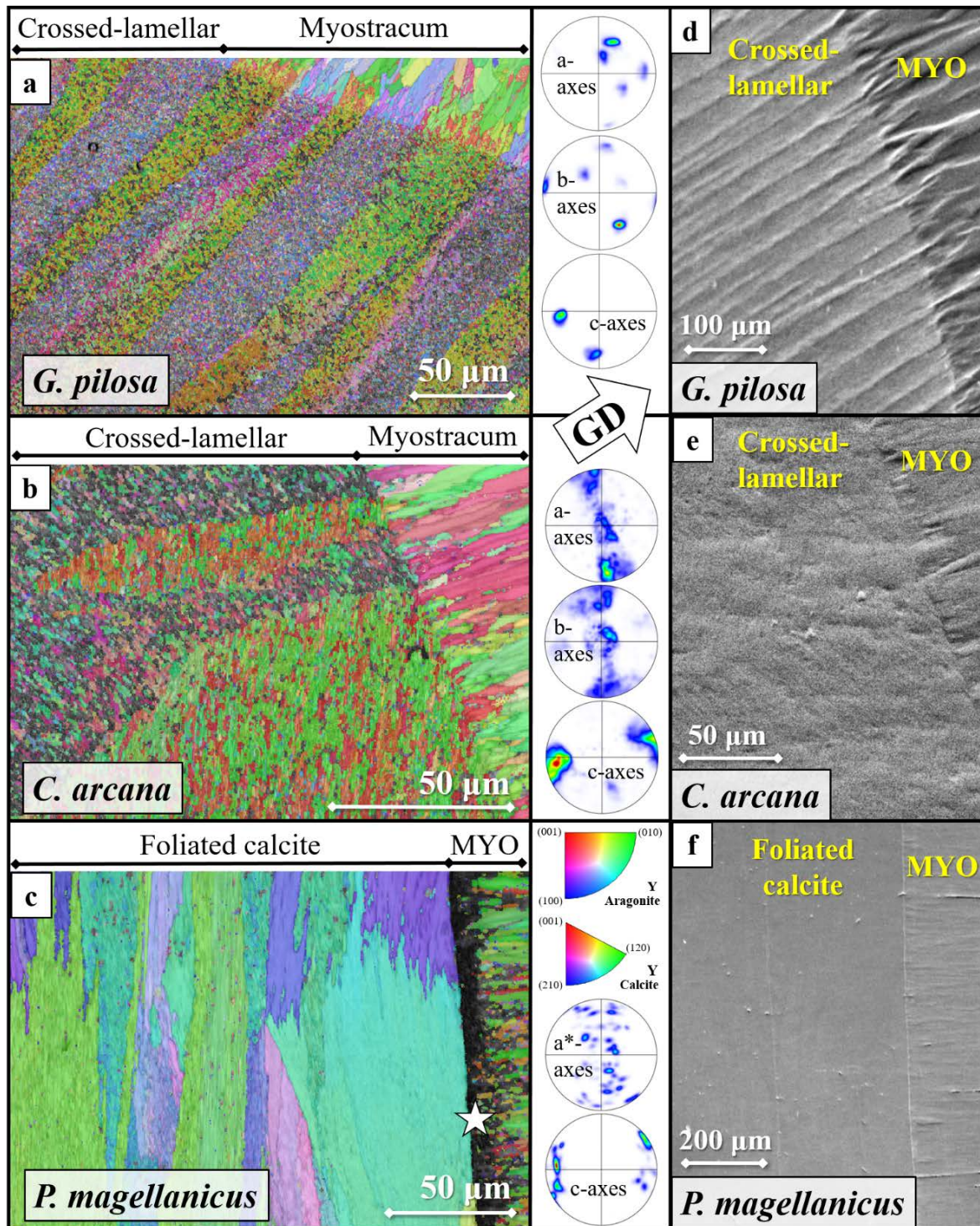


Fig. 2.3-AP2. Microstructure and texture of shell regions adjacent to myostraca sectioned and polished perpendicular to the inner shell surface (cut 1). Colour-coded EBSD maps show the microstructure and crystal orientation patterns and are complemented by pole figures indicating the orientational probability density distributions (a-c). In *Glycymeris pilosa*, the crossed-lamellar layer has a 3D “single-crystal-like” texture (a) and shows two sets of first-order lamellae that run parallel to the growth direction (GD). In *Chama arcana*, the crossed-lamellar layer is less co-oriented along the a- and b-axes, and the first-order lamellae do not run straight but are intertwined (b). Adjacent to the aragonitic myostracum, *Placopecten magellanicus* comprises a foliated calcite layer with a poorly co-oriented axial texture (c). An organic-rich sheet (white star in c) is visible at the sharp interface between foliated calcite and aragonitic adductor myostracum. Towards the inner shell surface, the myostracum consists of long (up to 100 μm) needle-shaped crystals with an axial texture (b). The microstructures are further highlighted by FE-SEM images that show the changeover between shell and myostraca for the three species *G. pilosa* (d), *C. arcana* (e) and *P. magellanicus* (f).

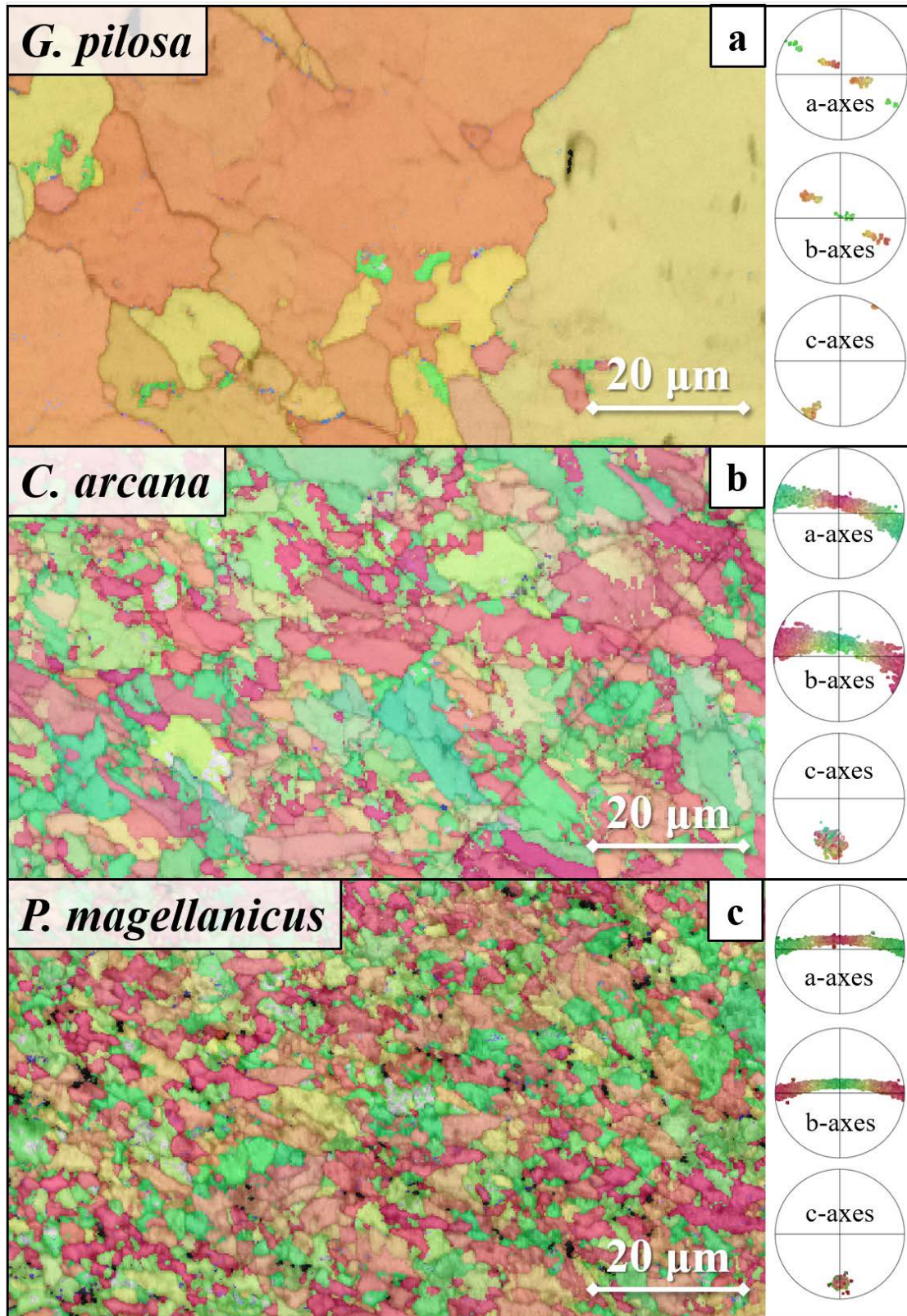


Fig. 2.3-AP3. Microstructure and crystal orientation patterns of adductor myostraca polished parallel to the inner shell surface (cut 2) for the three investigated species. The colour-coded EBSD maps are complemented by pole figures indicating the orientational probability density distributions (a-c). The cross-section of the *Glycymeris pilosa* myostracum comprises large (up to 100 μm diameter), irregular prisms (a). The 3D “single-crystal-like” texture and the recurring colour-coded crystal orientations indicate that the crossed-lamellar texture of the changeover region (Figs. 2.3-1a, 2.3-AP2b) is still present at the inner shell surface. In *Chama arcana*, the prisms are smaller and neither show a characteristic crystal orientation pattern nor orientation distribution maxima in the axial pole figures (b). *Placopecten magellanicus* shows a texture and microstructure similar to *C. arcana*, however, the strongly co-oriented grains appear thinner (c).

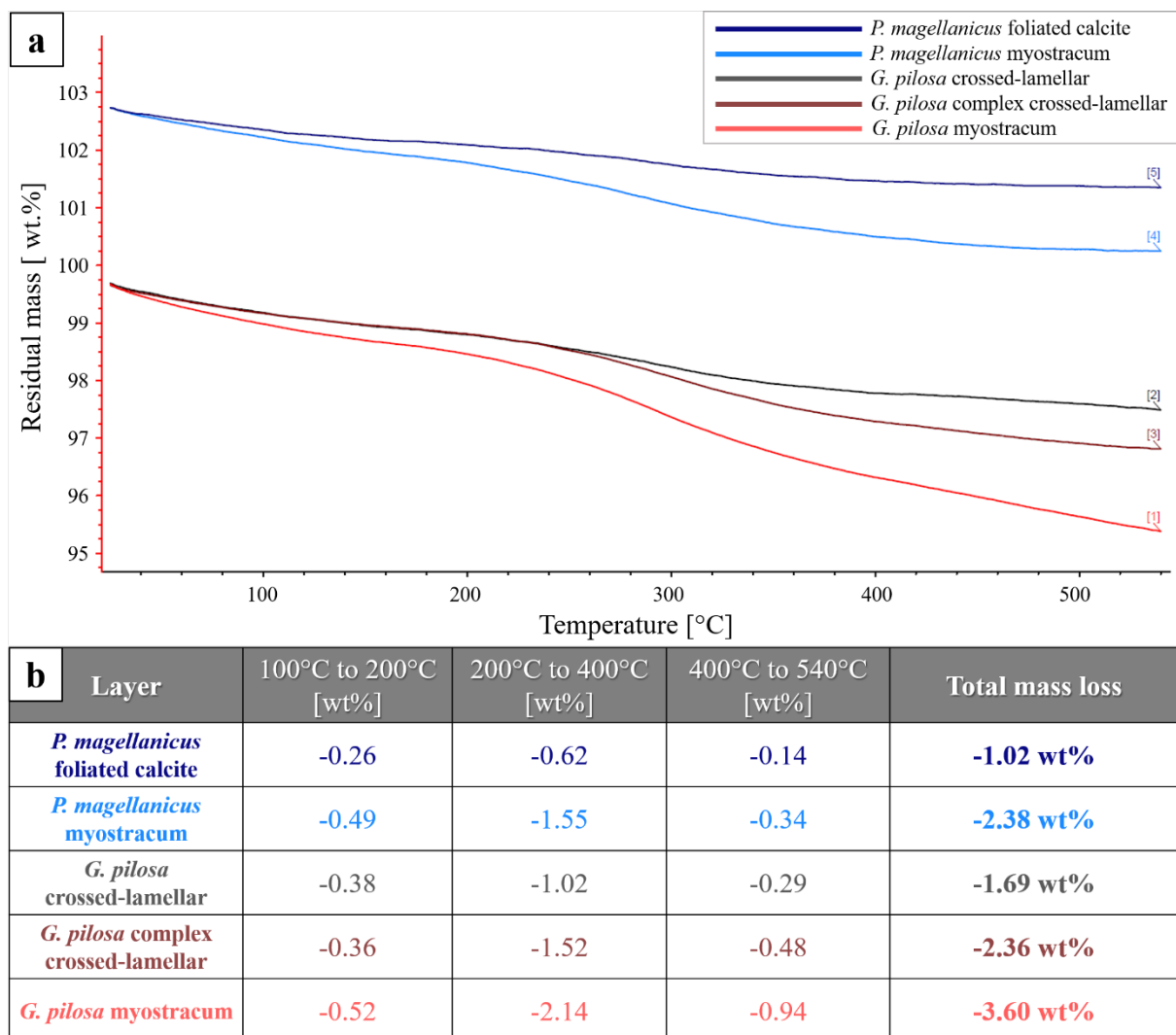


Fig. 2.3-AP4. Thermogravimetric analysis plots of the foliated calcite layer and the adductor myostracum in *Placopecten magellanicus* as well as the crossed-lamellar layer, crossed-lamellar layer and myostracum in *Glycymeris pilosa*. The samples were measured from room temperature to 600°C in steps of 10°C per minute. To minimise the influence of carbonatic transitions and enclosed water on the total mass loss, only the section between 100°C and 540°C was regarded for its calculation. The plots display the weight loss with increased temperature; the two curves for *P. magellanicus* have been shifted for better visibility (a). The table (b) shows the weight loss fraction in selected temperature segments and the total mass loss from 100°C to 540°C.

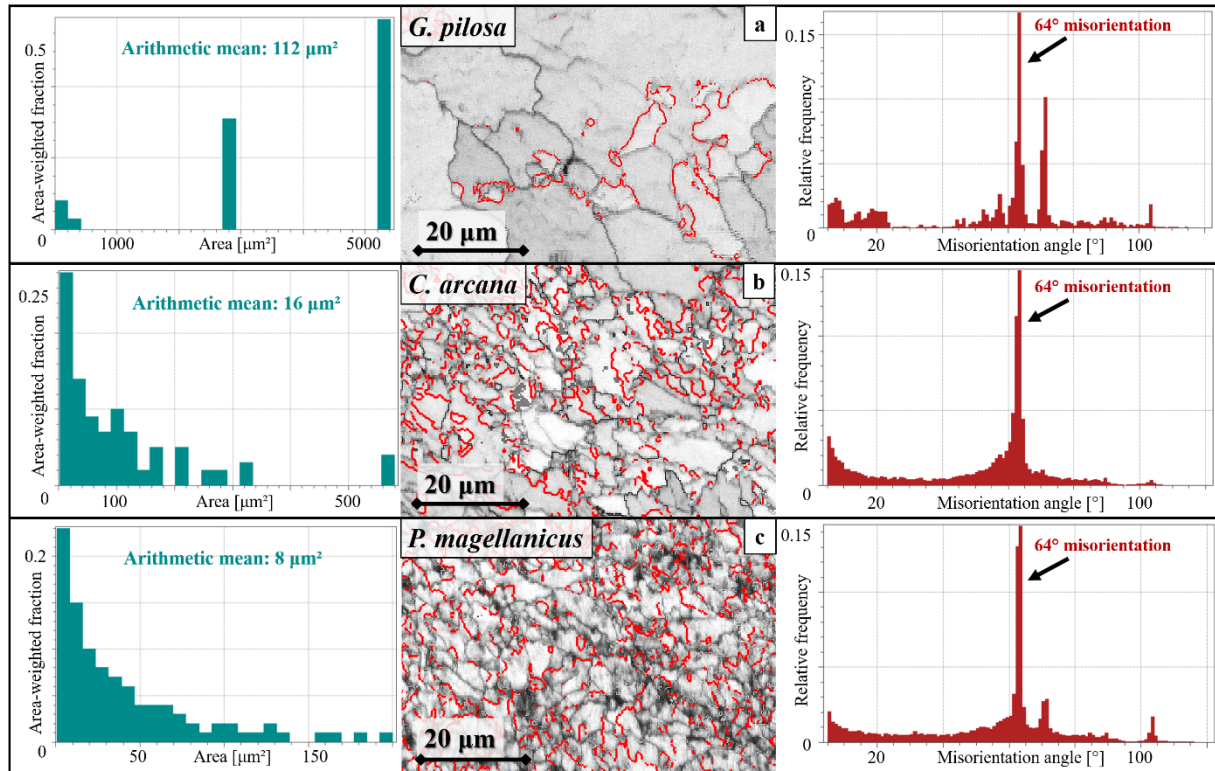


Fig. 2.3-AP5. Misorientation angle distribution and grain size statistics for adductor myostraca sectioned along cut 2 in *Glycymeris pilosa*, *Chama arcana* and *Placopecten magellanicus*. Irrespective of the texture and microstructure, the myostracal prisms of *G. pilosa* (a), *C. arcana* (b) and *P. magellanicus* (c) predominantly follow a grain misorientation angle of about 64°. This angle corresponds to aragonitic twinning on the (110) and ($\bar{1}\bar{1}$ 0) planes, constituting more than 15% of all analysed grain boundaries (a-c). The average grain size varies considerably between the three microstructures. When cross-sectioned, *G. pilosa* shows the highest mean grain size with about 112 μm^2 (d), comprising crystals that may exceed a size of 4000 μm^2 (e). *C. arcana* and *P. magellanicus* show similar grain size statistics, however, *C. arcana* crystals appear to be slightly larger in mean size (d, e).

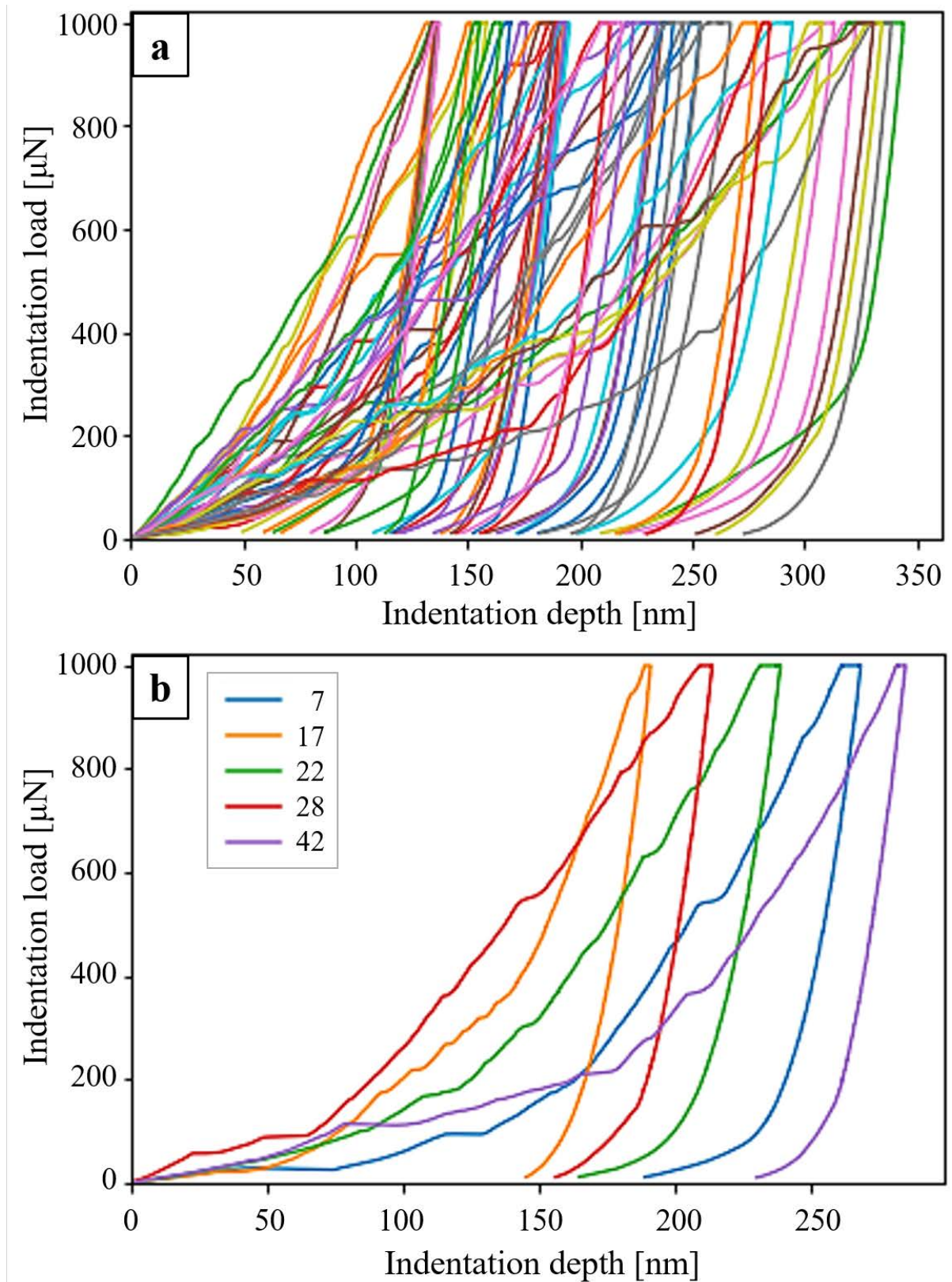


Fig. 2.3-AP6. Indentation curves of the complex crossed-lamellar layer in *Chama arcana*, indented perpendicular to the inner shell surface. Most indented points show pop-in events, i.e., sudden and irregular displacement bursts during loading, leading to a broad spectrum of peak indentation depths (a). The influence of pop-in events on the indentation depth curves can be seen from five randomly selected data points plotted in (b).

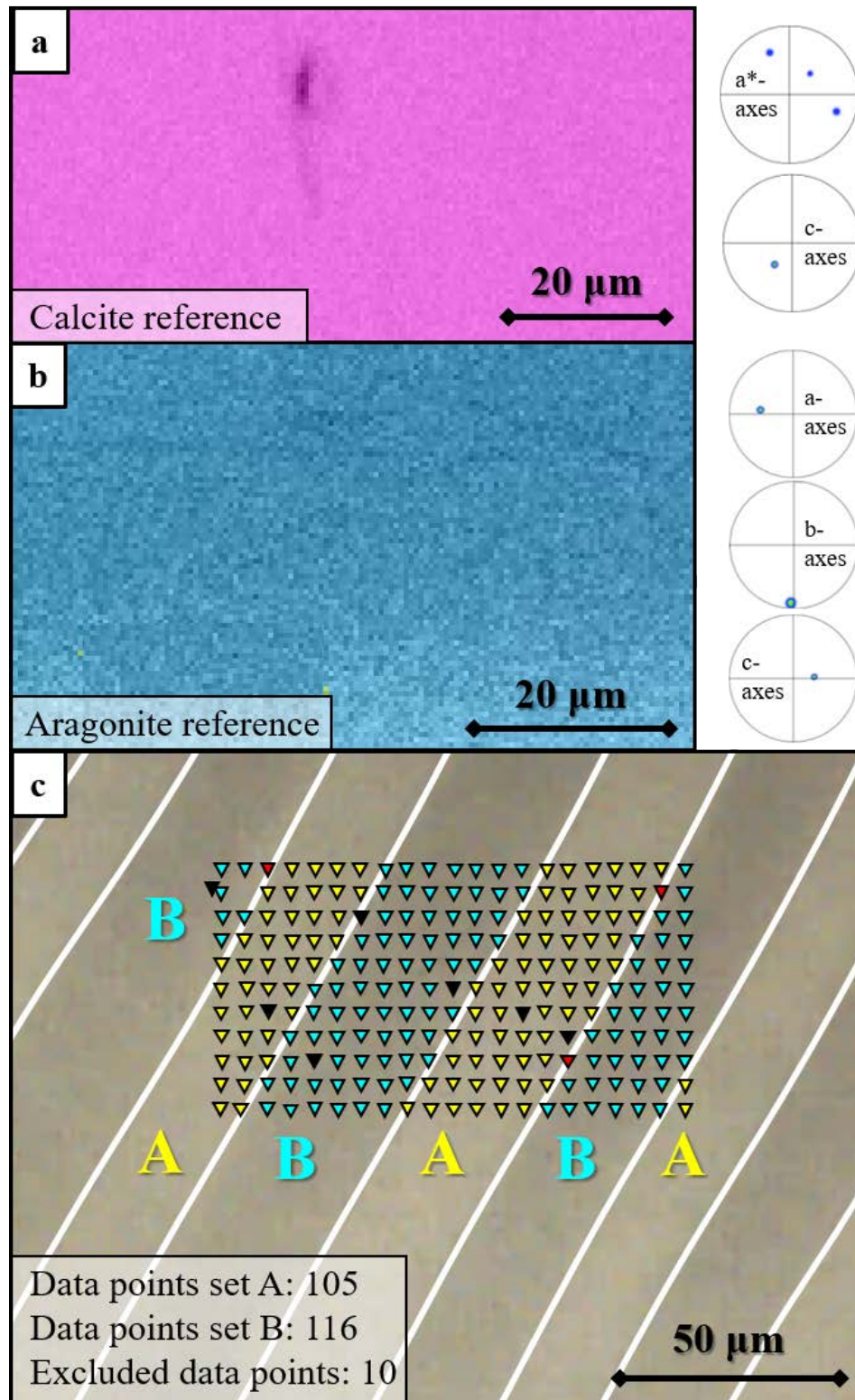


Fig. 2.3-AP7. Textures of the non-biological single crystals used as nanoindentation references (a, b) and indentation positions of nanoindentation data points used for compiling the nanomechanical properties of the *Glycymeris pilosa* crossed-lamellar layer in Fig. 2.3-8. EBSD measurements of the single-crystalline samples used as reference in Table 2.3-1 and Figs. 2.3-4, 2.3-5 and 2.3-7 show the crystallographic orientation (a, b). Both the calcite (a) and the aragonite (b) references have the crystallographic c-axis misoriented 35-40° to the indentation direction, comparable to the {104} direction. Of the 231 total data points tested in the crossed-lamellar layer (see Fig. 2.3-8), 105 were attributed to set A (yellow triangles in c), and 116 were attributed to set B (blue triangles in c). Seven points were excluded because of anomalous loading-unloading curves or erroneous positions (black triangles in c), and three additional points were excluded from the calculations as they could not be assigned to one first-order lamella but rather to the interface between two inclined lamellae (red triangles in c). The instrument was calibrated to guarantee the correlation between the tip position and the optical image.

2.4 MICROSTRUCTURE, TEXTURE AND NANOMECHANICAL PROPERTIES OF CONSERVATIVE AND NON-CONSERVATIVE BIVALVE MYOSTRACA

With an estimated 8,000 to 20,000 species, bivalves are not only the second most diverse class of molluscs (Morton & Machado 2019), but they also were, are and will play an important role in the anthropological diet (Aru et al. 2018; eds. Smaal et al. 2019). The first archeological documentation of consumption, cultivation and usage of molluscs for dietary purposes stems from prehistoric times, with bivalves becoming important organisms for human populations living near rivers or seas (Voultsiadou et al. 2010; Morand 2020). Although more and more bivalve farmers realise the benefits of hatching diverse bivalve species, much of the modern research on bivalves and bivalve shells has been limited to commercially valuable species (Duthie 2012; Santhanam 2018).

It is well-known that bivalves can occupy a wide range of marine environments, spanning saltwater and, in some cases, freshwater environments across the entire globe (Flessa & Jablonski 1995; Lopes-Lima et al. 2018; Huang et al. 2023). However, many bivalves and, in particular, the microstructure and hierarchy of their biomineralised shell are not yet described in great detail. A microstructure that is particularly neglected is the myostracum, also known as the adductor muscle scar. Despite its outstanding nanomechanical properties (Chapters 2.1 and 2.3 of this thesis), the myostracum is often simply described as a prismatic aragonite layer (Lowenstam & Weiner 1989; Dong et al. 2022).

This section highlights in great detail the microstructure and material properties of seven bivalve shells belonging to different families and occupying different ecological habitats. The characterisation is focused on the myostracal layers and the adjacent, non-myostracal shell. The investigated species are *Ostrea stentina* (Payraudeau, 1826), *Peryglypta puerpera* (Linne, 1758), *Dosinia scalaris* (Menke, 1843), *Anomia ephippium* (Linnaeus, 1758), *Mytilus edulis* (Linnaeus, 1758), *Arctica islandica* (Linnaeus, 1758) and *Tellina planata* (Linnaeus, 1758). By combining high-resolution EBSD measurements with nanoindentation testing, the crystal texture, shell structure and hard tissue material properties of the shells of these species are illustrated, discussed and juxtaposed.

2.4.1 METHODS

The selected bivalve shells were sectioned transversely through the adductor myostraca, analogous to cut A described for *Chama* and *Glycymeris* in Chapter 2.2.2 of this thesis (see also Fig. 2.2-API). To minimise statistical deviations caused by the azimuthal hardness variability of aragonite and calcite, only one cut was investigated for these seven shells. The sections were embedded in EPON epoxy resin and subjected to several mechanical grinding and polishing steps. The polished samples were imaged with FE-SEM and laser confocal imaging and analysed with EBSD analysis and

nanoindentation testing. For EBSD analysis, samples were coated with 4–6 nm of carbon for EBSD analysis, with 5 nm Pt/Pd for SEM imaging. For laser confocal imaging and nanoindentation testing, sample surfaces were not coated. The detailed experimental protocols can be found in Appendix sections A.1, B.2 and B.4 of this thesis.

For each species, I prepared multiple samples of adult organisms. To relate microstructure and nanomechanical properties, the EBSD and nanoindentation measurements reported in this section were performed on the same samples and at similar locations. Shells of *D. scalaris*, sampled from the Tasman Sea near the North Island, New Zealand, and *P. puerpera*, sampled from Olango island, Philippines, were obtained from the Bavarian State Collection of Zoology. Shells of *M. edulis* were collected from Naples harbour, Italy, and *A. islandica* was sampled near Dundas Islands, BC, Canada. Shells of the remaining three species, *O. stentina*, *T. planata* and *A. ephippium*, have all been collected near Benalmádena, Spain.

2.4.2 RESULTS AND DISCUSSION

Conservative myostraca

In this section, I introduce the terms “conservative myostraca” and “non-conservative myostraca”. The majority of recent bivalve shells form rather conservative myostraca with a microstructure that is largely influenced by a competitive crystal growth mechanism. Non-conservative myostraca may feature crystal morphologies or textures that are indistinct and resemble the microstructure of the adjacent, non-myostracal shell layers. It is worth noting that these two models are not entirely distinguishable from one another. Instead, they comprise a wide spectrum of myostracal microstructures, which are displayed in this section. Of the seven bivalve myostraca presented in this section, three show microstructures that are distinct from the non-myostracal shell and are strongly influenced by competitive growth parameters. The “hybrid myostraca” comprise two species showing elements of a competitively grown microstructure but merge with the adjacent non-myostracal shell. The other two myostraca resemble, to a large extent, the morphology and crystallographic texture of the neighbouring, non-myostracal shell portions.

Of the broad range of myostraca analysed in this and other studies (e.g., Hampa, 2023; Le Moine, 2022; Rathi, 2023), the myostraca directly adjacent to a calcitic shell portion, for example that in the shell of *O. stentina*, can be considered to be the prototype for a conservative myostracum (Fig. 2.4-1). Due to the difference in structural-crystallographic characteristics of the foliated calcite layer and of the adjacent aragonitic myostracum, there is no epitaxial growth of the initial myostracum crystal on top of the adjacent template. Instead, small and isotropic aragonite crystals with an axial texture comprise the first few μm of the adductor myostracum (Fig. 2.4-1a). Towards the inner shell surface, crystals increase in size and form a microstructure of prismatic crystals with irregular grain boundaries. Throughout the adductor myostracum, the texture remains strictly axial, with the aragonite c-axes

oriented perpendicular to the inner shell surface. A continuous crystal orientation pattern is not visible from the colour-coded EBSD measurement (Fig. 2.4-1a). Despite the apparent lack of crystallographic continuity between the foliated calcite layer and the adductor myostracum, the c-axes poles of the two layers appear to be oriented similarly. This is due to the “turbostratic-like” texture of the foliated calcite in oyster shells, as described by Griesshaber et al. (2025). In this layer, one {106} plane of the calcite crystals is oriented perpendicular to the inner shell surface, leaving the c-axes to form a circular distribution relative to this plane direction. The resulting ring is indicated from the graded rotation of a*- and c-axes in the pole figures (Fig. 2.4-1a); the complete texture is visible from measurements comprising a larger section of the foliated calcite layer (e.g., Fig. 1.3-2).

As expected from their different microstructure and crystal crystallographic characteristics, the nanomechanical properties of *O. stentina* foliated and myostracal layers diverge strongly. Compared to a non-biogenic calcite reference, the foliated layer shows a mean hardness that is improved by more than 40% (Fig. 2.4-1b, c). The elastic indentation modules of the two calcite layers are comparably low, and scatter in a range of 70-75 GPa. The aragonitic adductor myostracum of *O. stentina* has the highest hardness of the four structures, reaching a mean value of 5.2 GPa. Compared to the geological aragonite reference, the elastic indentation modulus is slightly decreased. Thus, the biomineralised *O. stentina* shell and myostraca show improved nanomechanical properties compared to their non-biological counterparts (Fig. 2.4-1b, c). In the foliated shell, this is achieved by the highly controlled crystal organization and texture.

The purely aragonitic bivalve *P. puerpera* features a bimodal-like myostracum (Fig. 2.4-2). Adjacent to a prismatic aragonite layer with an axial texture, the first ~50 µm show a crystal morphology that varies to the subsequent section of the adductor myostracum. Since the initial myostracum crystals seem to epitaxially adapt the texture of the prismatic layer, the changeover is rather smooth (Fig. 2.4-2a). The initial myostracum crystals are significantly larger (mean size 10 µm) than the small crystals in the prismatic layer (mean size 3 µm) and have very sharp, irregular grain boundaries. A possible explanation for this bimodal-like myostracum is that the initial section serves as a transitional layer between the prismatic layer with its small, isotropic crystals, and the conservative myostracum of *P. puerpera* that grows large, anisotropic crystals towards the inner shell surface (Fig. 2.4-2a). As reported by Le Moine (2022), the myostracal layer of *P. puerpera* can reach a total thickness of more than 2 mm.

Despite the different crystal morphology of the transitional myostracum section, the crystallographic texture and nanomechanical properties are equal to the adjacent myostracum section. Hence, they are not differentiated in the graph displaying hardness and elastic indentation modulus (Fig. 2.4-2b). Both the prismatic layer and the adductor myostracum display improved nanomechanical properties in comparison to a geological reference. On average, their elastic moduli are decreased by about 15 GPa (Fig. 2.4-2c). Despite the rather large standard deviations (Fig. 2.4-2b, c), it is well-visible

that the adductor myostracum has the highest average hardness (5.1 GPa), followed by the prismatic aragonite (4.6 GPa) and surpassing the average hardness of the aragonitic reference (4.1 GPa).

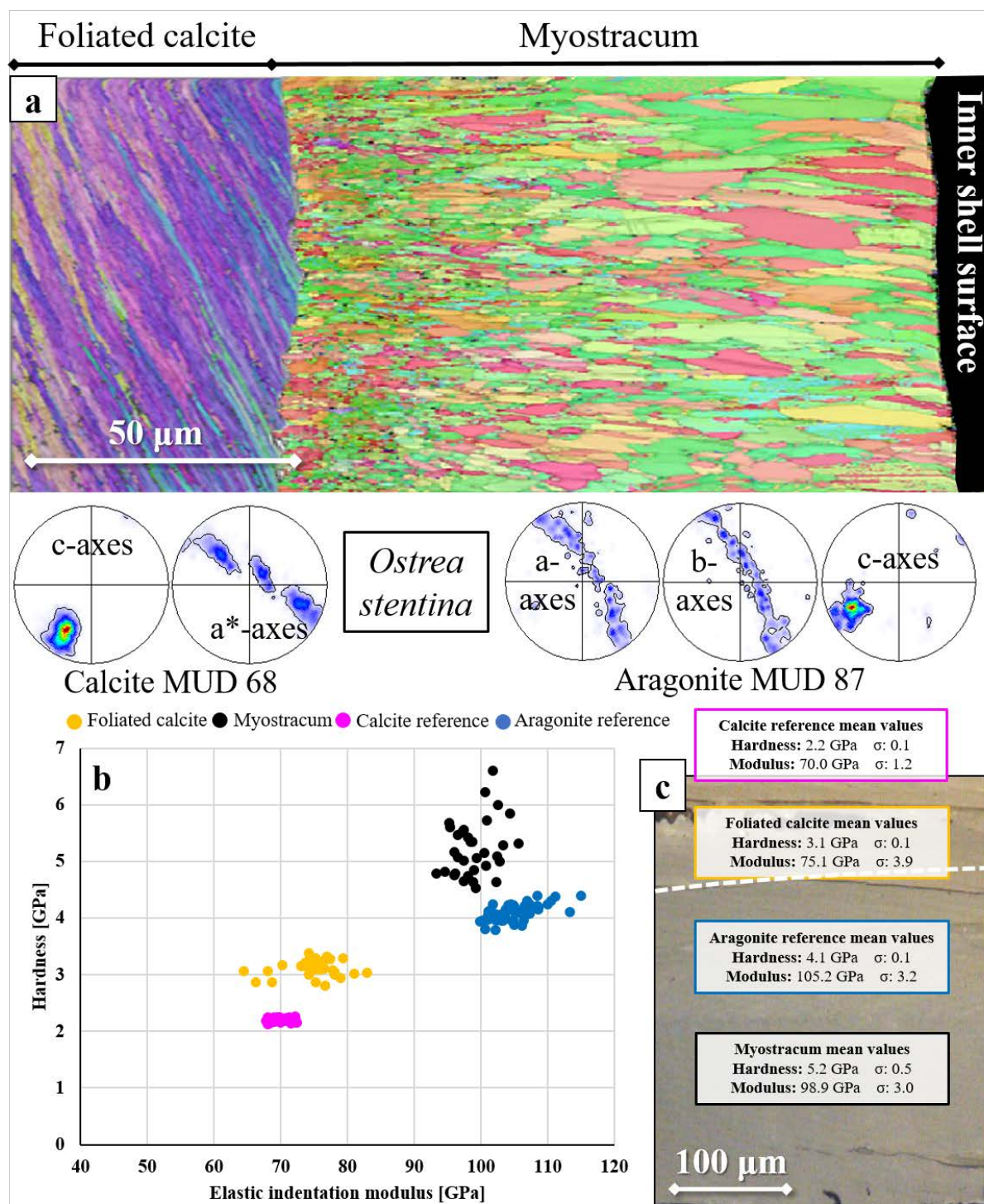


Figure 2.4-1. The microstructure and nanomechanical properties of different layers of an *Ostrea stentina* shell compared to non-biogenic references. The foliated layer comprises thin (< 5 µm), regularly interlocked sheets of calcite (a). The “turbostratic-like” texture, shown by Griesshaber et al. (2025) for the foliated layer in *O. stentina*, is indicated by the gradual axes shift in the calcitic pole figures (a). The aragonitic adductor myostracum exhibits an axial texture and a microstructure, indicating predominantly competitive growth determinants (a). Towards the inner shell surface, crystals increase in size, aspect ratio and crystallographic co-orientation (a). The hardness and elastic indentation modulus distribution (b) and mean values (c) show the improved nanomechanical properties of the foliated calcite layer and myostracum compared to the non-biogenic references.

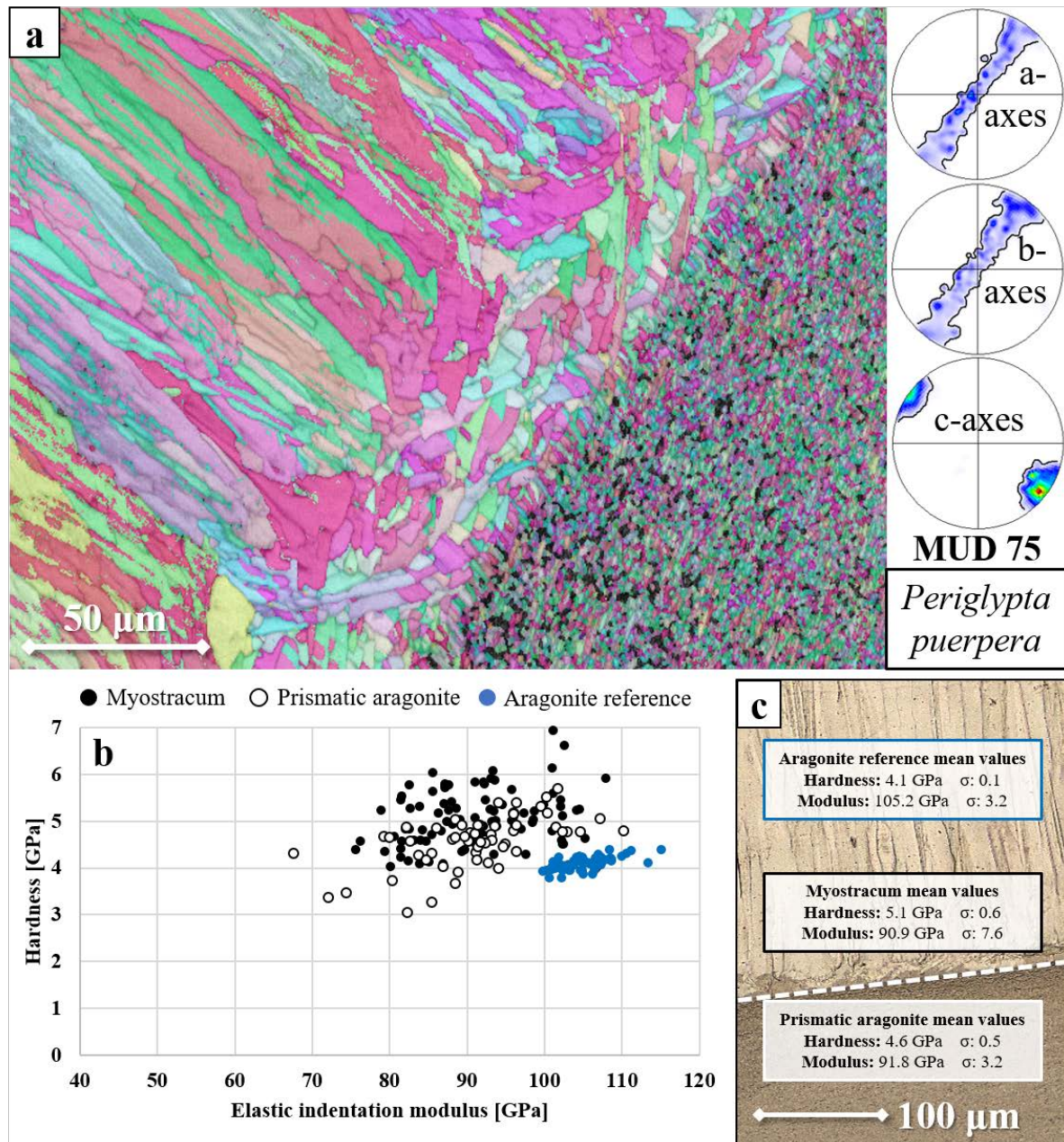


Figure 2.4-2. The microstructure and nanomechanical properties of the *Periglypta puerpera* myostraca and the adjacent prismatic aragonite layer. The axial texture with c-axis orientations perpendicular to the inner shell surface is transmitted from the prismatic layer to myostracum and continued in the latter (a). For the first 50 µm of the myostracum, prisms are rather small and broad; however, they get longer and co-aligned towards the inner shell surface (a). The prismatic and the myostracal aragonite in *P. puerpera* show higher hardness and slightly reduced elastic indentation modulus compared to the geological reference (b). With an average hardness of 5.1 GPa when indented parallel to the inner shell surface, the myostracum is slightly harder than the prismatic layer (b, c).

While *D. scalaris* myostraca show a crystallographic texture that very much resembles that of the adjacent crossed-lamellar shell, the crystal morphologies of the two layers vary strongly (Fig. 2.4-3). Since many elements of crystal growth by growth competition are visible, the adductor myostracum can, thus, be considered to be a conservative myostracum, albeit its resemblance to the crossed-lamellar orientation pattern (Fig. 2.4-3a). The texture of the myostracum is 3D “single-crystal-like” with two maxima for the aragonitic c-axes, corresponding to each set of lamellae (described in more detail in Chapter 2.2 of this thesis). From the changeover with the outermost crossed-lamellar layer to the

changeover with the innermost complex crossed-lamellar layer, the texture of the adductor myostracum only changes slightly (Fig. 2.4-3a). While the colour-coded EBSD map depicts an increase in crystal size and aspect ratio towards the inner shell surface, the characteristics of a competitive growth process are not as well developed as it is the case for *O. stentina* or *P. puerpera* shells. Polycyclic twinning is visible in both, the myostracal prisms and the complex crossed-lamellar layer (yellow star in Fig. 2.4-3a) of *D. scalaris* shells.

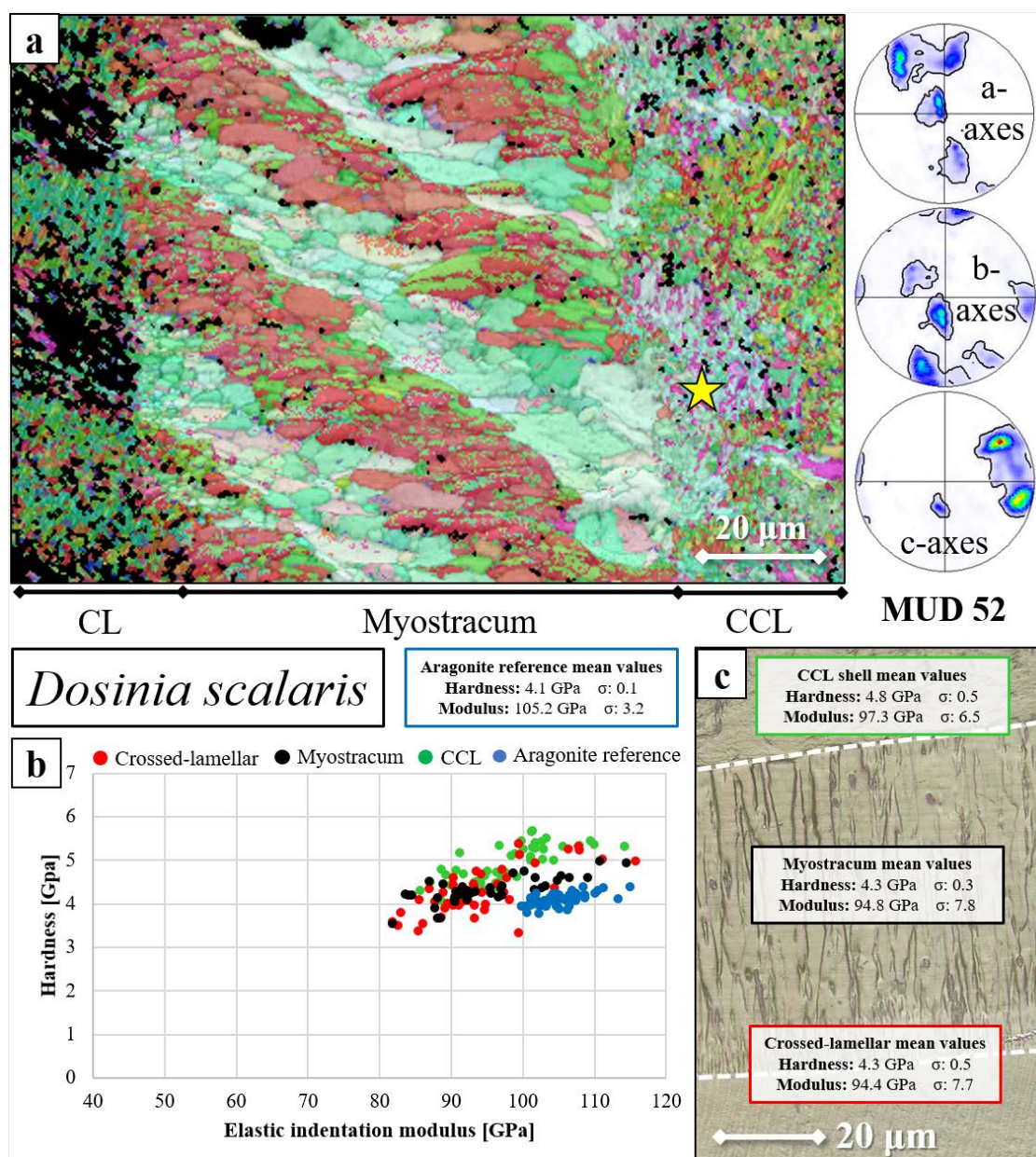


Figure 2.4-3. The microstructure and nanomechanical properties of the *Dosinia scalaris* myostraca and the adjacent crossed-lamellar aragonite layers. The 3D “single-crystal-like” texture of the outer crossed-lamellar shell (CL) is the template for myostracal prism growth and mostly continues throughout the pallial myostracum (a). At the interface with the complex crossed-lamellar layer (CCL), myostracal crystal orientations are transmitted to the initial complex crossed-lamellar blocks (yellow star in a). However, similar to *Glycymeris* shells (Chapter 2.1.4 of this thesis), this texture is not actively continued in the complex crossed-lamellar shell and, thus, is lost after ~20 μ m of the CCL shell (a). Indented parallel to the inner shell surface, the crossed-lamellar and myostracal layers in *D. scalaris* show similar nanomechanical properties that exceed the hardness of the reference while having lower average values for the elastic indentation modulus (b, c). The highest hardness in *D. scalaris* shells was observed in the complex crossed-lamellar layer with an average hardness of 4.8 GPa (b, c).

Compared to the nanomechanical properties of *O. stentina* and *P. puerpera* shells, the adductor myostracum of *D. scalaris* is significantly softer. As visible from Fig. 2.4-3b, c, the mean hardness values of the *D. scalaris* crossed-lamellar (4.3 GPa) and complex crossed-lamellar (4.8 GPa) shells are higher or match the myostracum (4.3 GPa). All three shell layers show comparatively low elastic indentation moduli, ranging from 94.4 to 97.3 GPa, with the complex crossed-lamellar layer displaying the highest mean modulus. The increased hardness and low elastic indentation modulus of the crossed-lamellar and complex crossed-lamellar shells can be explained by their relatively low organic content, as shown for *Glycymeris* shells (Fig. 2.3-AP4). While the myostracal hardness in *D. scalaris* is slightly higher than that of the geological reference, it is well below the hardness of other bivalves that have a conservative myostracum (e.g., Chapters 2.2 and 2.3 of this thesis, Le Moine (2022)). Chapter 2.3.4 discusses that the myostracal microstructure in aragonitic bivalves is a result of epitaxial nucleation and the competitive growth process. Since the developing microstructure is mostly determined by competitive growth constraints rather than biological factors, the texture of the initial myostracum layer at the changeover largely influences the microstructure of the adjacent crystals. Thus, it is possible that the similarity of the myostracum and crossed-lamellar layer at the changeover prevents the formation of a well-developed and distinctive adductor myostracum with corresponding and distinctive nanomechanical properties.

Hybrid myostraca

Hybrid myostraca show distinct features of the adjacent, non-myostracal shell, as well as to elements of a microstructure generated by a competitive growth mechanism. Although their myostracal microstructures are different from one another, *Anomia ephippium* and *Mytilus edulis* are prime examples of hybrid myostraca. Adjacent to the adductor myostracum, *A. ephippium* shells feature a crossed-lamellar layer. Compared to other shells with crossed-lamellar layers, e.g., *D. scalaris* (Fig. 2.4-3), the crystallographic orientations of the two first-order lamellar sets are poorly distinguishable, as visible from the colour-coded map. Rather than having a single-crystal-like texture, the crossed-lamellar layer of *A. ephippium* is axial, with the c-axes of both sets being, more or less, clustered perpendicular to the inner shell surface (Fig. 2.4-4a). The adductor myostracum of *A. ephippium* follows the texture of the crossed-lamellar layer, with a very smooth changeover between the microstructures (Fig. 2.4-4a). Indeed, the two layers are only distinguishable from their grain morphologies. While the crossed-lamellar crystals are small (< 5 µm) and lath-shaped, myostracal crystals are long (up to 20 µm) and needle-shaped (Fig. 2.4-4a). However, the most peculiar characteristic of the *A. ephippium* adductor muscle scars when sectioning the shell along the applied cut is the alternating layers of “myostracum-like” and crossed-lamellar sheets with varying thicknesses (Fig. 2.4-4a).

The inner shell surface of *A. ephippium* features three muscle scars, with the smaller adductor myostracum surrounded by two larger scars generated by the attachment of the byssal retractor muscles

(Tebble 1976). Therefore, this particular periodic microstructure of *A. ehippium* adductor muscle scars is most probably caused by a temporary attachment of byssal retractor muscles to the shell. As described in more detail in Section 2.1 of this work, muscle attachment causes the secretion of crystals with an assembly pattern resembling a competitively-grown microstructure. However, as the muscles detach from the shell, the organism continues the secretion of the purely biologically controlled layer, which in this case is the crossed-lamellar shell.

Although grown shells of *A. ehippium* can reach large diameters of up to 7cm (Studencka 2018), their average total thickness is only a few mm. Through the limited space, both the adductor myostracum and the “myostracum-like” sheets caused by byssal muscle attachment are relatively thin. As indicated in Section 2.3 of this Thesis, a low thickness of the myostracal layer may impede certain elements of a competitively-grown microstructure, such as the development of a sharp axial texture or grain sizes strongly increasing away from the nucleation template. Even when the alternating layers of “myostracal-like” and non-myostracal sheets are disregarded, the adductor myostracum in *A. ehippium* shells can be considered to be a hybrid myostracum due to its microstructural resemblance to the adjacent shell portion.

Compared to the geological aragonite reference, both the myostracum and the crossed-lamellar layer of *A. ehippium* show decreased elastic moduli, surpassing the tested hardness of the geological reference by about 1 GPa (Fig. 2.4-4b, c). Notably, similar to the results obtained for *D. scalaris* shells, the adductor myostracum in *A. ehippium*, more or less, maintains the texture of the crossed-lamellar layer. Furthermore, the nanomechanical hardness and elastic indentation modulus of the two aragonitic microstructures in *A. ehippium* also show relatively similar mean values to one another (Fig. 2.4-4b, c). This supports the suggestion that, besides a high degree of mineralisation, the key factor for high nanomechanical hardness values is the crystallographic texture, namely, the orientation pattern of the crystals. Accordingly, morphological factors, such as the size and shape of the grains, appear to influence the nanomechanical properties of the Ca-carbonate biomaterial only to a lesser degree.

Comprising an even less distinct adductor myostracum, another example of a hybrid adductor myostracum can be found in the shells of the well-investigated *M. edulis*. Similar to *A. ehippium*, the shells of *M. edulis* have a thick outer layer of calcite that is separated from the myostracum by an aragonitic layer, in this case, nacre (Fig. 2.4-5a). While the outer prismatic calcite layer has a single-crystal-like texture with slightly graded a^* -axes, the nacre tablets show an axial texture. This texture is adopted by the adductor myostracum, a thin layer of individual aragonite crystals (Fig. 2.4-5a).

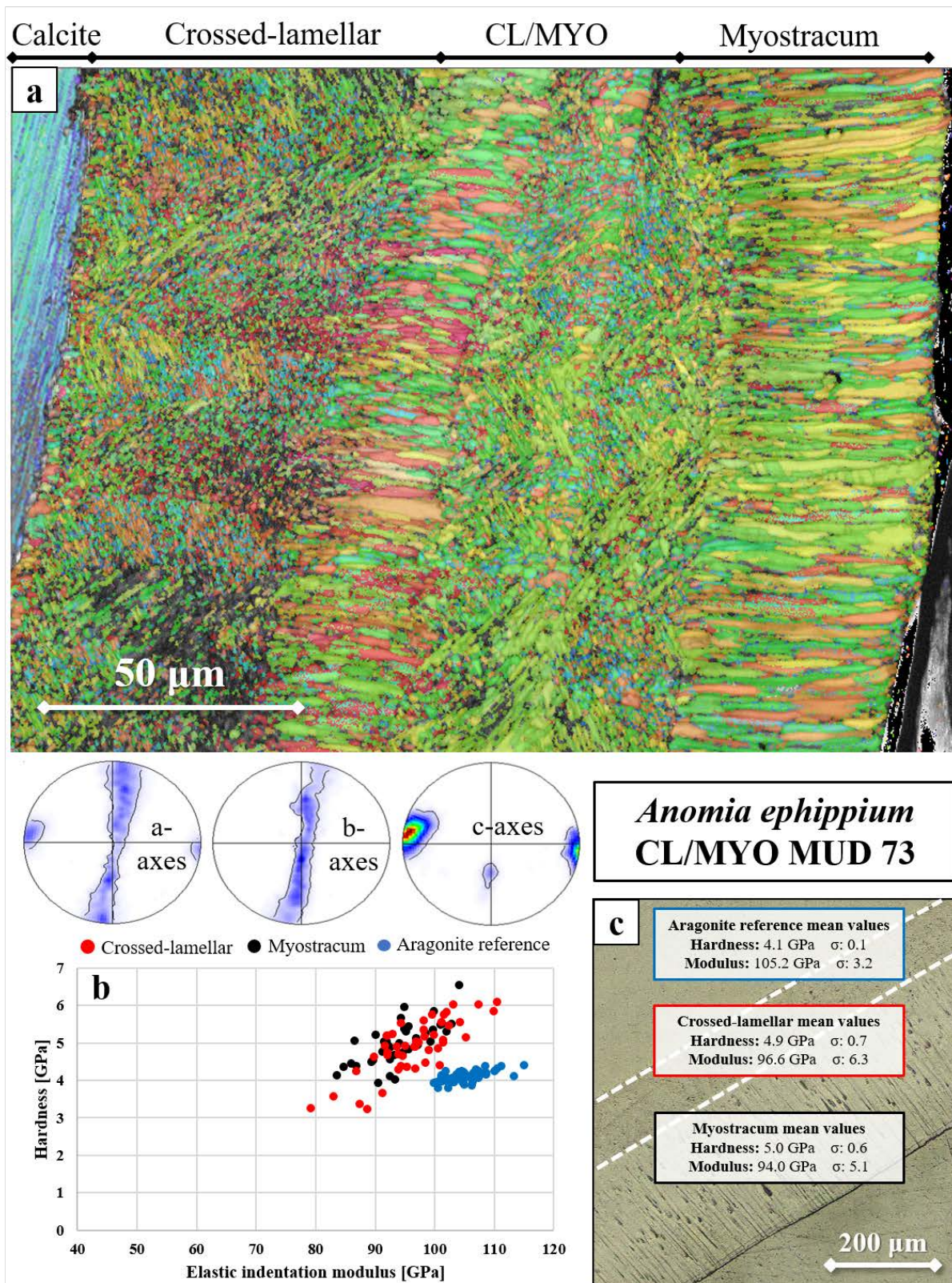


Figure 2.4-4. The microstructure and nanomechanical properties of the *Anomia ephippium* myostraca and the adjacent crossed-lamellar aragonite layer. The crossed-lamellar layer (CL) in *A. ephippium* does not comprise rigorous first-order lamellae with a 3D “single-crystal-like” texture but appears poorly organised with an axial texture (a). Particularly for *A. ephippium* shells is that the adjacent myostracum (MYO), inheriting and continuing the crossed-lamellar texture, is not always a singular secluded layer but can appear and disappear periodically (a). In the thicker regions of the myostracum, prisms are needle-shaped, thin (< 5 µm thickness) and have an axial texture (a). When indented parallel to the inner shell surface, the nanomechanical properties of crossed-lamellar and myostracal layers in *A. ephippium* appear quite similar and are optimised compared to the geological reference (b, c).

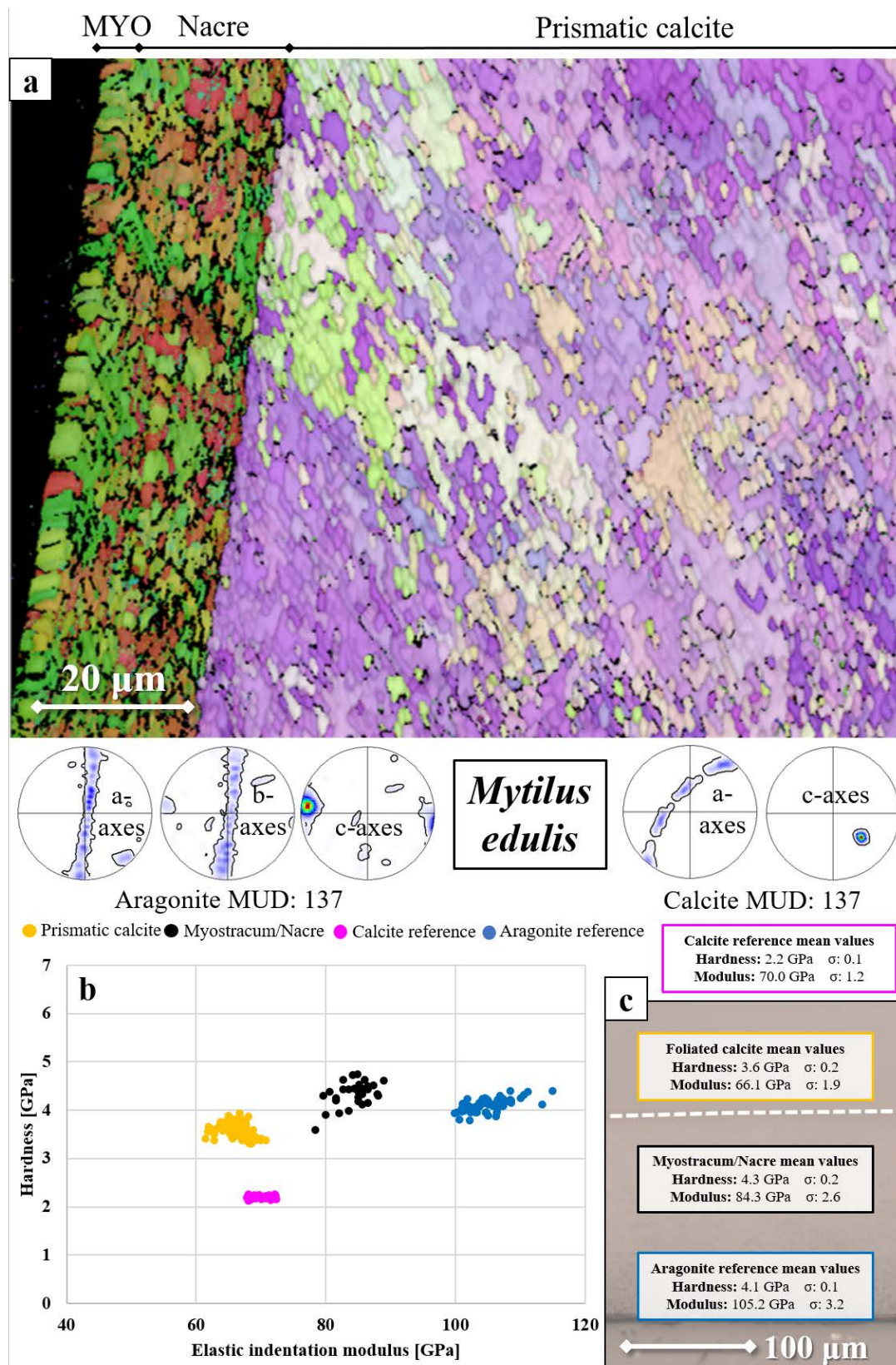


Figure 2.4-5. The microstructure and nanomechanical properties of the *Mytilus edulis* myostraca and the adjacent prismatic calcite and nacreous aragonite layers. The adductor myostracum in *M. edulis* shells is a thin sheet ($< 5 \mu\text{m}$) of stacked prisms that assume the texture of the adjacent nacre. Despite the slightly larger crystals, it is barely distinguishable from the nacreous layer and shows similar nanomechanical properties, thus, the two microstructures were combined for (b) and (c). The myostracum and nacre in *M. edulis* are slightly harder than the geological reference, and the indentation elastic modulus is decreased by about 20 GPa (b, c). For the prismatic calcite, the modulus is slightly lower, and hardness is significantly enlarged compared to the geological calcite reference (b, c). Indentation was performed parallel to the inner shell surface.

Compared to the nacre tablets, the *M. edulis* myostracal crystals are slightly longer and larger ($\sim 5 \mu\text{m}$), however, the overall thickness of the myostracum is significantly smaller than that of all the other species described in the previous chapters of this thesis. Despite the microstructural similarities to the adjacent, non-myostracal layer, the *M. edulis* myostracum is undoubtedly distinguishable from the nacre and can, therefore be classified as a hybrid myostracum.

As described in a previous study (Hoerl 2022) and validated with indentation measurements (Fig. 2.4-5b), the nanomechanical properties of the *M. edulis* adductor myostracum and nacre are virtually identical. Due to this fact and the small thickness of the adductor myostracum layer, the two microstructures have been combined in Fig. 2.4.5b, c. The two aragonitic layers have a slightly increased hardness of 4.3 GPa (compared to 4.1 GPa for the geological aragonite reference), while the elastic indentation modulus is decreased by more than 20 GPa to about 84.3 GPa. Compared to a geological calcite reference, the outer prismatic calcite layer also shows enhanced nanomechanical properties, with a significantly increased hardness (3.6 GPa vs. 2.2 GPa) and a slightly decreased elastic indentation modulus (70 GPa vs. 66.1 GPa).

Non-conservative myostraca

As the name suggests, non-conservative myostraca do not follow a distinct microstructural motif but may come in many different characteristics and structures, many of which are not known yet. The two non-conservative myostraca described in this work were observed in shells of *Arctica islandica* and *Tellina planata*, two bivalve species that occupy different ecological niches. Shells of *A. islandica* can be found in great depths and are frequently used in sclerochronological studies due to the longevity of the organisms (Stott et al. 2010; Helama et al. 2014; Conti et al. 2024). They comprise a thick layer of granular aragonite along the outer shell surface and feature a heterogeneous myostracum at the adductor muscle scars (Fig. 2.4-6a). Rather than forming a distinct layer, the myostracum actually comprises multiple sheets of varying thickness (5-50 μm). The sheets comprise aragonitic crystals that range from small granular crystals (a few μm) to larger, prismatic crystals (up to 20 μm) and are separated by thin, organic-rich layers (see Fig. 2.4-6a and Le Moine (2022)). Both the adjacent granular shell layer and the adductor myostracum have an axial texture with an MUD value of 25. Additionally, the broad c-axes maximum in the contoured pole figure also indicates a relatively low crystallographic co-orientation (Fig. 2.4-6a). The adductor myostracum shows no characteristics of typical microstructures generated by competitive crystal growth parameters, such as increasing grain size and crystallographic co-orientation with distance from the nucleation surface. In contrast, it rather resembles the adjacent granular shell layer in both its microstructure and crystal texture.

Both the myostracum and, especially, the granular layer of *A. islandica* exhibit low values for the tested elastic indentation modulus (Fig. 2.4-6b, c). The non-myostracal granular layer found in *A. islandica* shells is surprisingly soft, albeit comprising aragonite crystals. With an average hardness of 1.8 GPa, it is significantly softer than the adjacent myostracum as well as non-biogenic aragonite and

even calcite (Fig. 2.4-6b, c). Even the myostracum, a layer that usually stands out for its exceptional nanomechanical properties, exhibits a comparatively low mean hardness of 3.3 GPa, which is markedly lower than that of the aragonite reference (4.1 GPa). Although most biomineralised hard tissues exhibit a relatively broad standard deviation when measuring their nanomechanical properties, the spread of hardness data points in the *A. islandica* myostracum is notable (Fig. 2.4-6b, c). Correlating the nanomechanical measurements with the observed microstructure, however, it appears that the spread in hardness may be due to the microstructural heterogeneity of the *A. islandica* shells (Fig. 2.4-6). Another possible explanation for the low hardness and high standard deviation is the non-conservative microstructure formation mechanism, compared to competitively-generated myostraca.

The microstructure with the least distinct and conservative myostracum of all bivalves observed in this study was found in *Tellina planata* shells. Similar to *A. islandica*, *T. planata* forms a granular shell layer adjacent to the adductor myostracum. However, the granular layer in *T. planata* is not only characterised by exceptionally small grains (few μm) but also by a single-crystal-like texture (Fig. 2.4-7a). In contrast to the aragonitic crossed-lamellar layer, which is frequently observed in bivalve shells, this texture is characterised by a single probability density maximum of the c-axes and only two major maxima for the a- and b-axes. This factor, along with the tight clustering of c-axis orientations along the texture direction, results in a well-co-oriented structure with a high MUD value of 178 (Fig. 2.4-7a). The microstructure of the adjacent myostracum is almost indistinguishable from that of the granular shell, featuring minute grains with homogeneous size and texture (Fig. 2.4-7a). The adductor myostracum in *T. planata* shells, therefore, shows no characteristics of competitive crystal growth determinants influencing its microstructure.

Regarding the nanomechanical properties observed for the different layers of *T. planata* shells, the trend of comparatively soft myostracal layers in non-conservative myostraca continues: the *T. planata* myostracum is not only markedly softer than the adjacent granular shell layer but also the geological aragonite reference (Fig. 2.4-7b, c). Notably, it is not only the hardness but also, in particular, the elastic indentation modulus that is decreased for the adductor myostracum (71.1 GPa), compared to the granular shell (90.7 GPa) and the reference (105.2 GPa). The nanomechanical characterisation of conservative myostracal layers for several species has usually shown a significant decrease in elastic indentation modulus compared to the reference. However, the degree of reduction observed for *T. planata* myostraca is unprecedented for bivalve myostraca and, once more, proves the distinctiveness of this microstructure.

Although the standard deviations of hardness and elastic indentation modulus for both *T. planata* layers are comparably large (Fig. 2.4-7b, c), their data sets are well distinguishable and do not appear to be associated. This contradicts the microstructural similarities that were observed via EBSD analysis. A reason for this discrepancy could be the combination of granular microstructural features with an enlarged content in intragranular organic material, similar to conservative myostraca (See Fig. 2.3-AP4).

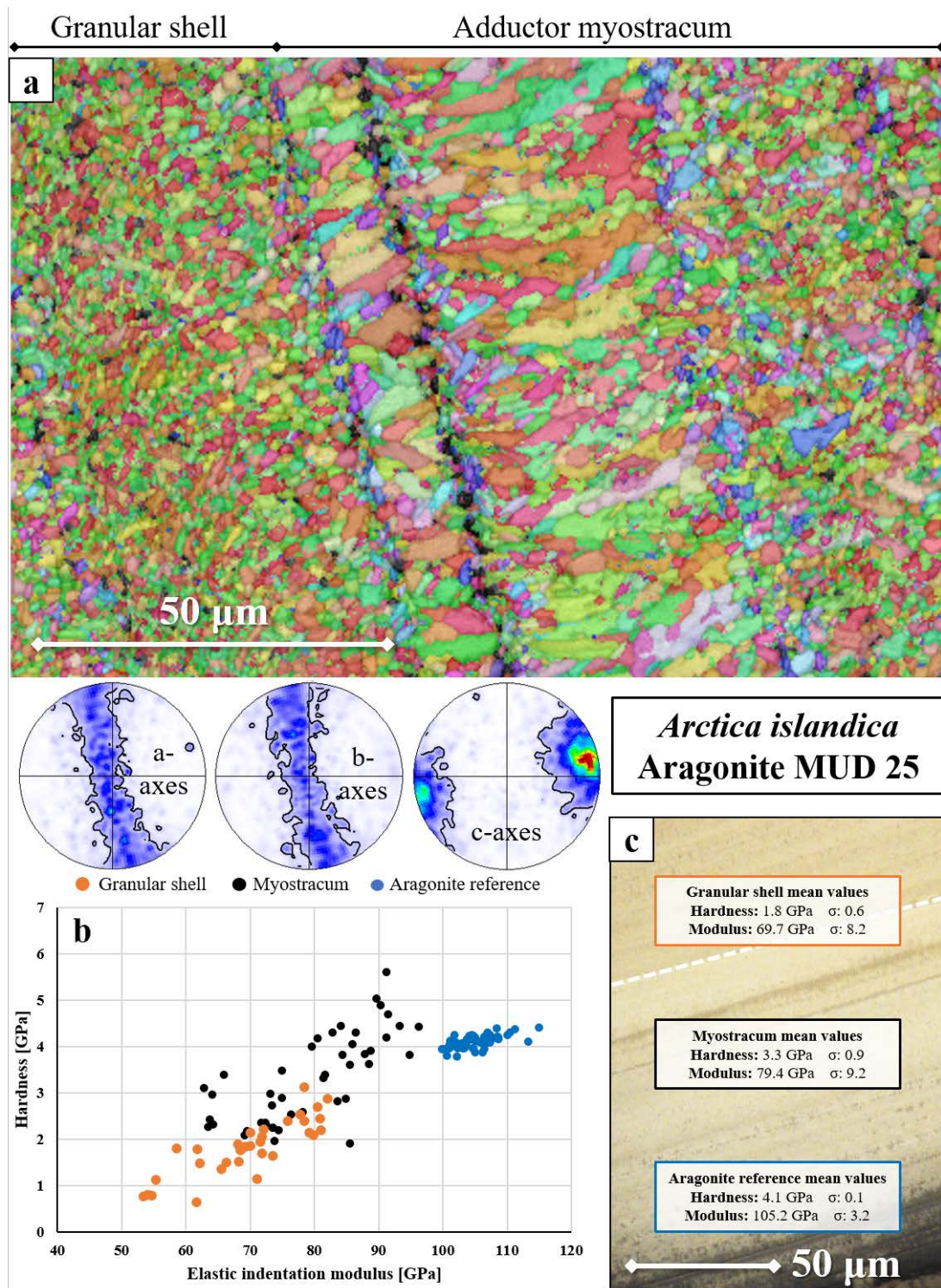


Figure 2.4-6. The microstructure and nanomechanical properties of the *Arctica islandica* myostraca and the adjacent granular layer. The adductor myostracum in *A. islandica* shells comprises multiple sheets of granular to prismatic grains with variable sizes. The myostracal sheets are separated by a thin sheet rich in organic material (red stars in a) or a sudden change in prism size (white star in a). The axial texture of the myostracum is assumed from the granular layer, and the myostracum lacks typical characteristics of competitive growth determinants, such as increasing crystal co-orientation or size towards the inner shell surface. The granular shell of *A. islandica* shows a very low hardness and indentation elastic modulus when indented parallel to the inner shell surface (b, c). Although slightly harder, the hardness and elastic indentation modulus of the *A. islandica* myostracum are also significantly lower than those of non-biological aragonite (b, c).

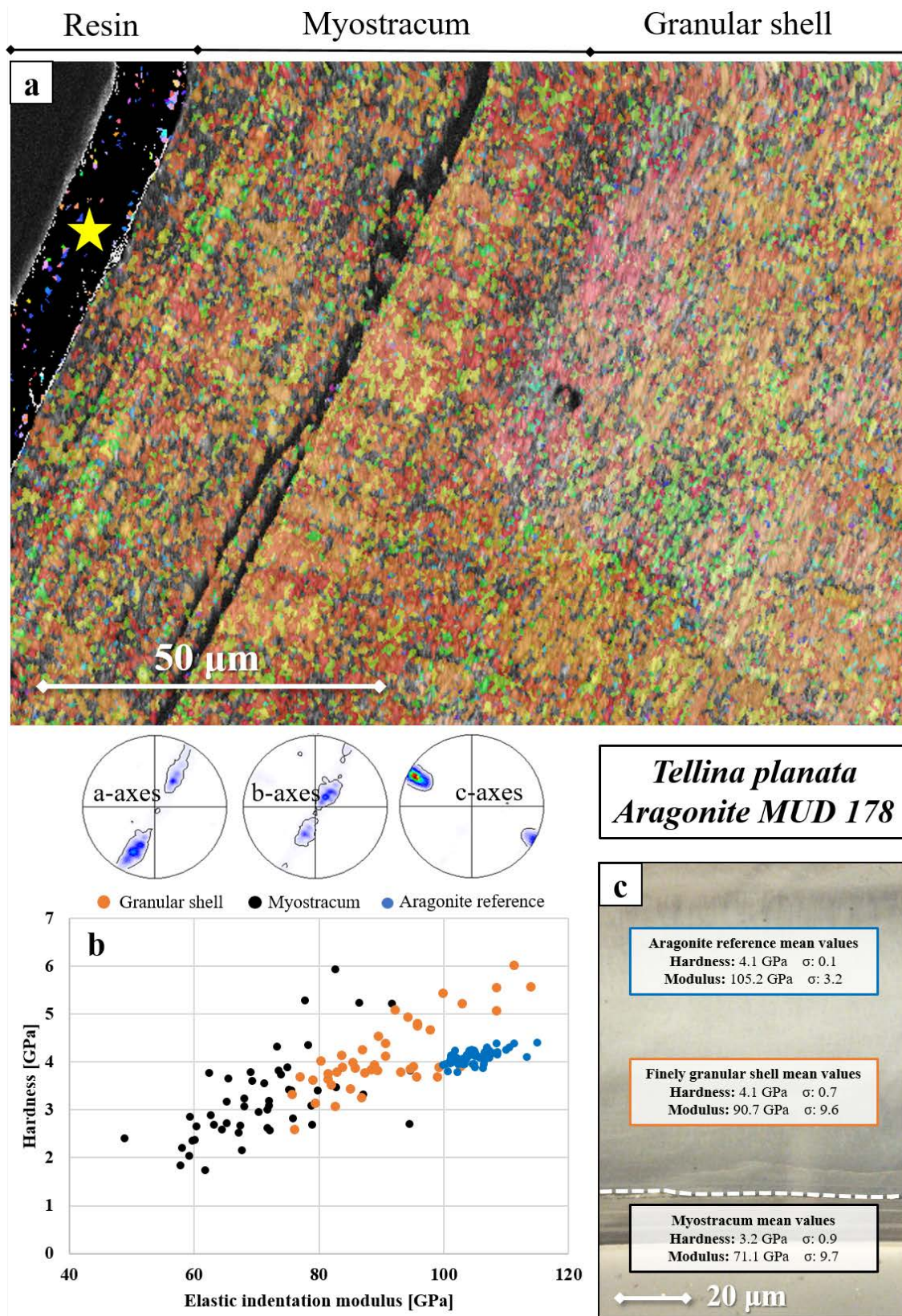


Figure 2.4-7. The microstructure and nanomechanical properties of the *Tellina planata* myostraca and the adjacent finely granular layer. The crystal size, morphology and texture of the myostracum layer are barely distinguishable from the finely granular shell and do not show any characteristics of a competitive crystal growth mechanism (a). The white star in (a) indicates a gap between the resin and shell, which is a result of sample preparation and is not part of the myostracum. The hardness and elastic indentation modulus of the *T. planata* myostracum, when indented parallel to the inner shell surface, are lower than the values observed for finely granular or geological aragonite (b, c). The finely granular shell has a similar hardness to the reference; however, the observed elastic indentation modulus is significantly decreased to an average value of 90.7 GPa.

The interrelation between competitive growth features and nanomechanical properties

In addition to previous work (Chapters 2.1 to 2.3 of this thesis), this section highlighted the microstructures and nanomechanical properties of myostracal and non-myostracal layers in seven additional bivalve species. The combination of nanomechanical testing and high-resolution EBSD analysis shows a clear trend between myostracal material properties and the influence of competitive growth parameters on microstructure generation. As summarised in Table 2.4-1, those myostraca that follow a microstructure generated predominantly through competitive growth determinants tend to have a higher hardness and elastic indentation modulus than the non-conservative myostraca. It is essential to consider the impact of the adjacent shell layer on the development and properties of the myostracum. Myostraca that are directly adjacent to a calcitic shell layer, such as the foliated calcite in *O. stentina* shells, tend to have a microstructure comprising a strictly axial texture that exhibits distinct features of a competitive growth mechanism and is not influenced by the prior layer. All investigated myostraca adjacent to an aragonitic layer initially adopt the texture from the previous microstructure. If the adductor myostracum grows conservatively under a large influence of competitive growth parameters, this texture will gradually vanish with distance from the adjacent layer: Crystals that have their crystallographic c-axis (the fastest-growing axis in aragonite) oriented parallel to the growth direction can outcompete misaligned crystals, and the initial texture is gradually converted to an axial texture. Since this conversion process occurs on a large scale (tens to hundreds of μm), myostraca adjacent to aragonitic layers may sometimes exhibit a less pronounced degree of competitive growth features and, instead, resemble the adjacent shell layer. This may explain the slightly lower hardness and elastic indentation modulus observed for these myostraca (Table 2.4-1).

The non-conservative myostraca (e.g., in *A. islandica* and *T. planata*) do not, or only to a limited extent, exhibit features of microstructure generation through competitive growth parameters (Figs. 2.4-6, 2.4-7). The non-conservative myostraca investigated in this section show the lowest average values for both hardness and elastic indentation modulus. This leads to the conclusion that certain characteristics of conservative microstructure generation through competitive growth parameters can enhance the hardness of biomineralised hard tissues, such as myostraca. The most probable reason for this, as suggested by Castro-Claros et al. (2021), is that the organic material in conservative myostraca is distributed differently than in the other shell layers. In contrast to non-myostracal layers, where organic matter is mostly found along grain boundaries, most of the organic material in myostracal layers is located within the grains, e.g., as bundles of collagen-rich fibres penetrating the large prisms (Castro-Claros et al. 2021). This may yield advantages in the propagation of small cracks, thereby improving the nanomechanical properties.

Table 2.4-1. Nanoindentation results for indentation maps performed on the adductor myostraca of the seven bivalve species. The species are sorted by the influence of the competitive growth process on their respective myostracal layers. The mean values for hardness and indentation modulus of the seven bivalves indicate a trend towards higher hardness and indentation elastic modulus for those myostraca that crystallised predominantly under competitive growth determinants. This contrasts species where myostracum formation is little influenced by competitive growth determinants. All specimens were measured with the indentation direction parallel to the inner shell surface.

Species	Layer preceding myostracum	Average myostracal hardness [GPa]	Average myostracal modulus [GPa]
<i>Ostrea stentina</i>	Foliated calcite	5.2	99
<i>Periglypta puerpera</i>	Prismatic aragonite	5.1	91
<i>Dosinia scalaris</i>	Crossed-lamellar aragonite	4.9	97
<i>Anomia ephippium</i>	Crossed-lamellar aragonite	5.0	94
<i>Mytilus edulis</i>	Nacreous aragonite	4.3	84
<i>Arctica islandica</i>	Granular aragonite	3.3	80
<i>Tellina planata</i>	Finely granular aragonite	3.2	71

↑
Increase in influence of the competitive growth process

The mechanism causing the presence or absence of competitive growth processes in bivalve shells is not yet fully understood. While conservative myostraca bear tremendous contract force (Castro-Claros et al. 2021) and show an exceptional hardness that surpasses that of non-biological aragonite, non-conservative myostraca have an outstandingly low elastic indentation modulus, i.e. the layer is less stiff. Therefore, it is possible that, depending on the lifestyle and environment of the bivalve, generating a distinct myostracum with large, rigid grains may be less favourable than hybrid or non-conservative myostraca. It also seems possible that the different degrees of competitive growth parameters can arise from structural differences in the adductor muscles or be predetermined by the type of microstructure adjacent to the myostracum. However, the latter has not yet been investigated and requires the in-depth characterisation of the shell and, in particular, myostraca of several more bivalve species.

2.4.3 CONCLUSIONS

In contrast to most other microstructures found in bivalve shells, the texture and grain morphology of the myostracum can vary significantly, both within a single layer and across multiple species. In contrast to some previous studies, which classified the myostracum as a well-defined shell structure that is conservative across most molluscan classes and genera (Lowenstam & Weiner 1989; Dong et al. 2022), the results of this study show that their microstructure is more complex than anticipated. Through the combination of high-resolution EBSD measurements and nanoindentation testing, the following conclusions can be deduced:

1. While most bivalve species form myostraca with microstructures determined predominantly by competitive crystal growth parameters, some species form hybrid or non-conservative myostraca that resemble, to varying degrees, the microstructure of the adjacent non-myostracal shell.

2. Myostraca adjacent to outer aragonitic shell layers initially assume the texture of the adjacent shell microstructure and generally show a smooth interface with the latter.
If the myostracum grows conservatively under a large influence of competitive growth parameters, the initial texture gradually vanishes into an axial texture with the crystallographic c-axes oriented parallel to the growth direction.
If the myostracum grows non-conservatively, the texture and microstructure of the adjacent shell are continued into the myostracum.
3. Myostraca being not adjacent to outer aragonitic layers but neighbouring, e.g., a calcitic microstructure, always grow conservatively. Rather than showing a smooth changeover with the adjacent layer, the interface is sharp, and the texture is not transmitted onto the myostracum. Although the initial crystals are often small (a few μm) and isotropic, towards the inner shell surface, the microstructure develops into large (up to 50 μm) prismatic crystals with a distinct axial texture.
4. Due to its heterogeneity at different growth stages, the myostracal microstructure is influenced not only by competitive growth parameters but also by the total thickness of the myostracal layer. Myostracal layers can be thin, comprising only a single layer of small crystals (5 μm), or reach a remarkable thickness of up to 2 mm.
5. Despite the relatively similar axial texture of most myostraca, their nanomechanical properties can vary significantly, directly depending on the development of competitive growth characteristics. Non-conservative myostraca generally exhibit low hardness and a low elastic indentation modulus, whereas conservative myostraca have high hardness and a medium elastic indentation modulus.
6. If the shell layer adjacent to the myostracum is aragonitic, the nanomechanical properties of the non-myostracal shell portions show large similarities to the myostracal layer: For the soft non-conservative myostraca, the granular aragonite layers were also soft. For the hard conservative myostraca, the crossed-lamellar or prismatic layers were also hard.

2.5 CRYSTAL ORGANISATION AT MUSCLE ATTACHMENT SITES OF BIVALVED MARINE ORGANISMS: A JUXTAPOSITION BETWEEN BRACHIOPOD AND BIVALVE SHELLS

S. Hoerl^{1,*}, E. Griesshaber¹, D. Weller¹, S. Amini², V. Häussermann³, M. A. Bitner⁴, K. Achterhold⁵, F. Pfeiffer⁵, W. W. Schmahl¹

1. Department of Earth and Environmental Sciences, Ludwig-Maximilians-Universität München, Munich, Germany

2. Department of Biomaterials, Max Planck Institute of Colloids and Interfaces, Potsdam, Germany

3. Escuela de Ciencias del Mar, Facultad de Recursos Naturales, Pontificia Universidad Católica de Valparaíso, Valparaíso, Chile

4. Institute of Paleobiology, Polish Academy of Sciences, Warsaw, Poland

5. Department of Physics, TUM School of Natural Sciences, Technische Universität München, Garching, Germany

Crystals 2025, 15(7), 649

<https://doi.org/10.3390/cryst15070649>

Abstract

The movement of valves of bivalved invertebrates is enabled through the action of muscles and the interplay between the muscles and the hinge ligament. The muscles that move the valves attach to their internal surface. To promote the structural integrity at the mechanically mismatched interfaces, a specific crystal microstructure and texture are present at the muscle attachment sites. These are different from the crystal microstructure and texture of the rest of the valves. We present here for modern two- and three-layered brachiopod shells (*Magellania venosa*, *Liothyrella neozelanica* and *Gryphus vitreus*) the mode of crystal organisation at sites of adductor and diductor muscle attachments, (i) relative to the microstructure and texture that forms the other sections of the valves and (ii) relative to crystal organisation of muscle attachment sites of bivalved invertebrates of other phyla, namely, species of the class Bivalvia. We discuss similarities/differences in Ca-carbonate phase, microstructure and texture between rhynchonellate brachiopods and bivalves, and discuss whether the Ca-carbonate crystal organisation of muscle attachment sites is convergent for bivalved marine organisms. We show significant differences in muscle attachment site architecture and highlight the different structural solutions developed by nature for shells of marine organisms that serve the same purpose.

Keywords

EBSD; biominerals; muscle attachment; brachiopods; microstructure/texture; layered bioceramics

2.5.1 INTRODUCTION

The ability to initiate valve movement and to maintain gape is of fundamental importance for bivalved invertebrates, such as bivalves or brachiopods. The latter organisms are filter feeders, and opening their valves and keeping them open for a prolonged period enables the circulation of nutrient-loaded waters between the valves and guarantees their survival (Angiolini et al. 2019; Hirose & Endo 2021; Vinn et al. 2024). It is equally important to close the valves quickly and keep them tightly shut in the face of an external threat to protect the soft tissue and the organs (Bengtson 2005; Peel 2015). Valve movement requires the action of muscles. Brachiopods use their adductor and diductor muscles to control valve opening and closure, and use their (pedicle) adjustor muscles to orient the shell as a whole, relative to the substrate (e.g., LaBarbera 1978; James et al. 1992; Alexander 2001; Hoel 2008; Hirose & Endo 2021). For valve activities, bivalves always utilise their adductor and pedal muscles in combination with their hinge ligament (e.g., Yonge 1973; Kahler et al. 1976; Tremblay et al. 2015; Ponder et al. 2019).

Invertebrate hard tissue secretion is performed by epithelial mantle cells that line the inner valve surface (Simkiss & Wilbur 1989; eds. Rowley et al. 2022). The invertebrate epithelial cell layer comprises different types of secreting cells (Simkiss 1988; Simkiss & Wilbur 1989; Ponder et al. 2019; Simonet Roda et al. 2019b; Checa et al. 2025). Specialised epithelial cells differ in ultrastructure from those that secrete the crystals of the rest of the shell (Castro-Claros et al. 2021). It has been shown for bivalves that the morphology and arrangement of crystals of those valve sections where the muscles attach differ significantly from the morphology and organisation of crystals that form the other sections of the shell (Lee et al. 2011; Dong et al. 2022; Hoerl et al. 2025b).

Crystal shape, microstructure, and texture of bivalve muscle attachment sites, the myostraca, have been extensively investigated (Dong et al. 2022; Hoerl et al. 2024b; Hoerl et al. 2025b), and profound knowledge has been accumulated on myostracal crystal formation, morphology and organisation. It has been shown that bivalve myostraca are always aragonitic, even when the shell consists of calcite (Hoerl et al. 2024b; Hoerl et al. 2025b) and have, in general, but not exclusively (see Chapter 2.4 of this thesis), a very specific microstructure and texture (Hoerl et al. 2024b; Hoerl et al. 2025b). The outstanding microstructure and texture of bivalve muscle scars are largely the result of the crystal growth process that governs the growth of the myostracal crystals, namely, crystal growth through growth competition. When crystals form through growth competition, in biogenic as well as inorganic environments, due to high supersaturation, many crystallites form at nucleation and, at growth, compete for space (Stevens et al. 2017; Crippa et al. 2020a). With ongoing growth, only crystals with their growth vector normal to the orientation of the nucleation template grow to large entities (Sanchez-Navas et al. 2013; Stevens et al. 2017; Crippa et al. 2020a). The effect of the competitive growth process is that, with progressive growth, there is a strong decrease in the number of crystals, accompanied by a strong increase in crystal size. Furthermore, for bivalves, myostracal

aragonite c-axes become aligned in parallel and oriented normal to the inner shell surface and parallel to the orientation of organic filaments that connect the muscle fibres to the crystals of the myostraca (Nakahara & Bevelander 1970; Nakahara & Bevelander 1971; Crippa et al. 2020a; Le Moine 2022; Rath 2023; Hoerl et al. 2024b).

The assembly of competitive-growth-generated myostracal crystals has been observed for species of many bivalve genera (Taylor et al. 1969; Taylor et al. 1973; Dong et al. 2022) and, accordingly, it has been suggested that bivalve myostracal microstructure is conservative (Dong et al. 2022). This is not entirely the case, as: 1. The myostracal crystal organisation of more than 30 bivalve species from 11 bivalve orders was observed and, even though many species secreted their myostraca with a competitive growth induced crystal organisation, for some species, the myostracal crystal microstructure did not imply that the crystals grew through growth competition (Chapter 2.4 of this thesis). 2. Recent work demonstrated that the competitive growth-generated bivalve myostracal microstructure is inconsistent (Hoerl et al. 2024b; Hoerl et al. 2025b). Influencing factors for the modulation of the bivalve myostracal microstructure and texture were (i) the microstructure and texture of the template, of the shell layer where the myostracal crystals nucleate, and (ii) adaptation of shell microstructure and texture for survival in different environments (Hoerl et al. 2024b; Hoerl et al. 2025b; Chapter 2.4 of this thesis). Hence, when investigated in great detail, even though comparable, myostracal microstructure and texture cannot be considered conservative across the Bivalvia.

Organisms of the class Rhynchonellata (phylum Brachiopoda) are sessile, filter-feeding and form calcitic shells (Williams et al. 1965; Cusack & Williams 2001; Garbelli et al. 2017). They are widespread in many marine environments (Williams et al. 1965; Peck et al. 1997; Williams et al. 2000; Harper et al. 2004; Peck & Harper 2010; Harper et al. 2017; Cross et al. 2018; Ye et al. 2019; Bitner 2021). Like bivalves, brachiopods need to open and close their valves quickly and maintain them in an open or closed position for extended periods (Richardson 1986; Robinson 2014). Furthermore, cell ultrastructural studies have shown that the connection of muscle fibres to the muscle attachment sites and the ultrastructure of the muscle attachment site secreting cells are similar for rhynchonellate brachiopods and bivalves (MacKinnon 1977; James et al. 1992; Paniagua et al. 1996; Ponder et al. 2019; Castro-Claros et al. 2021). Accordingly, the following questions led to the present study: 1. As brachiopods are also bivalved marine organisms that depend upon valve opening and closure, but are not closely related (Helmkamp et al. 2008), do we see similarity in carbonate phase, crystal morphology and crystal organisation between brachiopod and bivalve muscle attachment sites? 2. Does the brachiopod muscle attachment site also have a competitive growth-related microstructure and texture? 3. Brachiopod, bivalve and gastropod muscle attachment site crystals are secreted by specialised cells. The attachment of the muscle fibres to the crystals of the muscle scar is comparable for brachiopods, bivalves and gastropods (Nakahara & Bevelander 1970; Tompa & Watabe 1976; MacKinnon 1977).

Thus, is the structure and crystallography of the muscle attachment section of the valves convergent across the phyla of Brachiopoda and Mollusca?

In this contribution, we highlight and discuss the crystal organisation of muscle attachment sites for two and three-layered modern rhynchonellate brachiopod shells, namely, for *Magellania venosa* (Dixon, 1789; two-layered shell), *Gryphus vitreus* (Born, 1778; three-layered shell) and *Liothyrella neozelanica* Thomson, 1918 (three-layered shell). Rhynchonellate brachiopod shells consist of a maximum of three layers (e.g., Simonet Roda et al. (2022) and references therein). All rhynchonellate brachiopod shells have a primary and a fibrous shell layer. The primary layer forms the outer shell layer, and the fibrous layer forms the inner shell layer. *G. vitreus* and *L. neozelanica* form their shell of three layers: a primary, a fibrous, and an innermost columnar layer (Simonet Roda et al. 2022; Crippa et al. 2025). For the *G. vitreus* shell, we found that the three shell layers are positioned next to each other; for the *L. neozelanica* shell, we observed a sequential alternation between the fibrous and the columnar microstructure at the inner part of the shell (Goetz et al. 2009; Simonet Roda et al. 2022). In addition to the questions above, this study examines a possible difference or similarity of the crystal organisation at muscle attachment sites between two-layered and three-layered shells, i.e., when the muscles attach to fibres or columns.

Although there are very many similarities between lifestyle, living environment, the biomineralisation system, valve action and utilisation of muscle types for valve movement between Bivalvia and Rhynchonellata, we found that the muscle attachment sites as a whole, their structural characteristics and imprint appearance differ significantly. However, we found that the microstructure of the muscle attachment site is changed for species of both invertebrate classes (Rhynchonellata and Bivalvia), relative to the microstructure of those shell sections where muscles do not attach. A possible reason for the latter could be that specialised, cuboidal cells secrete the muscle attachment site crystals for species of both invertebrate classes. In contrast, the remainder of the shell is secreted mainly by columnar epithelial cells (Bubel 1984; James et al. 1992).

We found similar structural characteristics of muscle attachment sites between Rhynchonellata and Bivalvia in crystal texture and carbonate crystal c-axis orientation, irrespective of the developed Ca-carbonate phase (calcite or aragonite) of the muscle attachment site crystals. The latter appears to be an important requirement for a tight and strong connection between the muscle strands and the crystals (Castro-Claros et al. 2021). For species of both invertebrate classes, the strength of the muscle strand-crystal attachment is achieved with the insertion of collagen fibrils, derived from the apical microvilli of the tendon cells, into the crystals. Interestingly, this fundamental process, namely the insertion of polymer fibrils into the muscle attachment site crystals and their morphological orientation, is present for both rhynchonellate and bivalve species. However, it is unclear whether the two classes developed this trait independently (Weiner & Dove 2003; Dove 2018; Gilbert et al. 2022a; Wernström et al. 2022).

2.5.2 MATERIALS AND METHODS

Materials

We investigated the occurrence and the distribution of muscles and the structure, microstructure and texture of their attachment sites to the valves for the modern brachiopods *Magellania venosa* (Dixon, 1789), *Liothyrella neozelanica* Thomson, 1918, and *Gryphus vitreus* (Born, 1778). *M. venosa* was sampled at Comau Fjord, southern Chile, *L. neozelanica* at Doubtful Sound, New Zealand, and *G. vitreus* near Montecristo, Italy. Samples were collected alive from different depths, and care was taken not to damage the soft tissue upon collection. We investigated ten specimens of *M. venosa*, six specimens of *G. vitreus* and three specimens of *L. neozelanica*. Only those shells were examined where the valves were fully and tightly shut. This ensured that, at very careful opening of the valves, the muscles were still attached in their original position to the calcite of the valves.

Sample preparation

The shells were air-dried and, subsequently, the valves were opened. First, the lophophore and the lophophore support were removed. Then, the coelomic epithelium, the epithelial cover that shields the brachiopod musculature, was removed. For removal of the latter, only tweezers were used; we did not use any chemicals or water to expose the muscles.

The shells were cut dry for electron backscatter diffraction (EBSD) preparation, and the saw blade was not cooled with water. This ensured that, upon embedding into EPON epoxy resin, the muscle fibres were still at/adjacent to the calcite of the valves. The latter also enabled us to discriminate between valve sections where the striated and/or smooth adductor muscle fibres attach. The valves, hinge and muscles were cut perpendicular to the mirror plane of the shell (Fig. 2.5-S1A), and shell/muscle slices were embedded into epoxy resin. We also investigated cross-sections through the anterior part of the valves; here, muscles are not present. All shell muscles of Rhynchonelliformea are concentrated within the posterior part of the shell (Fig. 2.5-S1A). The embedded shell and muscle samples were subjected to several mechanical grinding and polishing steps. The grinding and polishing agents were not water-based, but oil-based. The final preparation consisted of etch-polishing in a vibratory polisher, performed for 15 minutes. For measurements, the samples were coated with 4-6 nm of carbon.

Methods

First, we identified the shell regions where the different muscles attached to the valves. This occurred via micro-computed tomography (Phoenix V|tome|x S 240; GE HealthCare, USA), as visible in Supplementary Video S1. Subsequently, the valves were imaged with the different types of muscles still in place with a Digital Microscope (VHX-7000, Keyence Japan), a Confocal Laser Scanning Microscope (VK-X1000, Keyence, Japan), a Field Emission Scanning Electron Microscope (FE-SEM;

SU5000, Hitachi, Japan) and an Environmental Scanning Microscope (Quattro S, Thermofisher Scientific, USA). EBSD measurements were carried out with a Hitachi SU5000 FE-SEM, equipped with an Oxford Instruments Nordlys Nano EBSD detector. EBSD scans were taken at 20 kV and were performed with a step size of 300 to 800 nm. EBSD data were evaluated with the Oxford Instruments AZtecCrystal 3.0 and HKL Channel 5.0 softwares. For indexing the calcitic EBSD patterns, we used the unit cell setting: $a = b = 4.99 \text{ \AA}$ and $c = 17.07 \text{ \AA}$. Rather than providing the crystallographic texture for the bulk sample, data obtained via EBSD measurements does not exceed $50 \mu\text{m} \times 50 \mu\text{m} \times 10 \text{ nm}$. However, in contrast to X-ray diffraction or neutron diffraction, the texture is not only shown by pole figures for the bulk sample, but can be determined for small regions or layers. For shells of each species, the crystallographic texture is generally consistent, as indicated by additional unpublished measurements and Supplementary Figures 2.5-S5 to 2.5-S7. The EBSD pole figure coordinate system is indicated in Fig. 2.5-7 and applies to all measurements shown in this study.

In almost all figures, we show a sketch of the topological relationship between the muscles and their attachment to the dorsal and ventral valves. The sketch was inspired by Figure 22 of James et al. (1992), but redrawn and modified to highlight the specific muscles shown in the figure. An in-depth terminology of the biological and structural terms used in this work can be found in Appendix Section A.1 of this thesis.

2.5.3 RESULTS

In this study, we investigated the structural organisation and crystallography of the crystals at the attachments of valve-moving muscles to the valves. First, we describe the different muscles that move brachiopod valves. Subsequently, we describe the crystals to which the muscles attach. *M. venosa* is the largest modern rhynchonellate brachiopod; it secretes the thickest shell and is the largest of the three investigated species. Accordingly, it forms large-sized muscles, relative to the muscles of *L. neozelanica* or *G. vitreus* (Fig. 2.5-1) or other modern rhynchonellate species. As the large-sized muscles were easier to localise, we concentrated our ultrastructural description of the muscles on the muscles of *M. venosa*, complemented, however, with findings on *L. neozelanica* and *G. vitreus*. When describing the different muscles in Figs. 2.5-1 to 2.5-6, 2.5-S2 to 2.5-S4, a modified sketch of James et al. (1992) was added to illustrate the arrangement of the different muscles relative to each other, highlighting their attachment positions onto the valves. We investigated the attachments of all three brachiopod muscles to the valves and examined the latter for both valves.

Figures 2.5-1 to 2.5-6 and 2.5-S2 to 2.5-S4 highlight ultrastructural characteristics of the muscles used by modern rhynchonellate brachiopods for valve and shell movement. The adductor muscles close the valves, the diductor muscles open them, the (pedicle) adjustor muscles move the shells as a whole for orienting them appropriately to, e.g., currents and/or light (McCammon 1971; Ackerly

1991; James et al. 1992; Ackerly 1993). Figures 2.5-7 to 2.5-12 visualise the crystal organisation in those valve sections where the muscles attach. This study focuses on the morphological, arrangement, and crystallographic characteristics of valve crystals at attachments of adductor muscles, whose function – the closure of the valves – induces higher stresses at these attachment sites. This study analysed the crystallographic microstructure, carbonate phase, crystal texture, and co-orientation strength. The investigated shells were sectioned in one direction, perpendicular to the mirror plane through the shell (Fig. 2.5-S1A). Cross-sections were obtained through the valves and the muscles. When investigating the crystals at muscle attachments, we scanned with EBSD those valve portions where the attaching muscles could still be seen in SE micrographs (e.g., Figs. 2.5-9E, 2.5-10B, SE micrographs of Fig. 2.5-12B, C). This ensured that the EBSD measurements were performed at valve sections where the muscle bundle was attached. Nonetheless, for each investigated species, we scanned with EBSD also valve portions that were distant from the muscle attachment sites (e.g., Figs. 2.5-7A, 2.5-10A, 2.5-12A). These scans were used as a reference for shell microstructure and texture, which is intrinsic to the hard tissue of a particular brachiopod species.

The shell of modern rhynchonellate brachiopods consists of a maximum of three shell layers. Most species only form an outer primary and inner fibrous shell layer; however, some species secrete a third shell layer of prism-to-column-shaped crystals (Simonet Roda et al. 2022). We investigated the crystals at adductor muscle attachment sites of *Magellania venosa*, *Liothyrella neozelanica* and *Gryphus vitreus*. The shell of *M. venosa* consists of two layers and two microstructures, namely, an outer primary and an inner fibrous shell layer (this study and Simonet Roda et al. (2022)). The shells of *L. neozelanica* and *G. vitreus* consist of three shell layers and three different microstructures. Both have an outer primary layer followed inward by a fibrous and a columnar shell layer (this study and Simonet Roda et al. (2022)). However, we found an alternation between the fibrous and the columnar microstructures in *L. neozelanica* shell cross-sections (Figs. 5D, 6 in Goetz et al. (2009)). This feature is not observed for the shell of *G. vitreus*. For *G. vitreus*, the primary layer, fibrous and columnar microstructures are next to each other and do not form sequential alternations, as is the case for *L. neozelanica* (this study and Simonet Roda et al. (2022)).

The muscles of *M. venosa*, *L. neozelanica* and *G. vitreus* assemble within the posterior part of the shell cavity, generated by the hinged ventral and dorsal valves (Figs. 2.5-3A, 2.5-5A, 2.5-6A). As a mirror plane runs through rhynchonellate brachiopod valves (Fig. 2.5-S1A), the adductor, diductor and adjustor muscles are developed in pairs (Figs. 2.5-1, 2.5-S1B). As illustrated in Supplementary Figure 2.5-S1B, a pair of adductor muscles attaching to the dorsal valve can be divided into two branches, the striated and smooth adductor muscles (Fig. 2.5-S1C). Here, the combination of one striated and one smooth adductor muscle branch is termed an adductor muscle segment (Fig. 2.5-S1B, C).

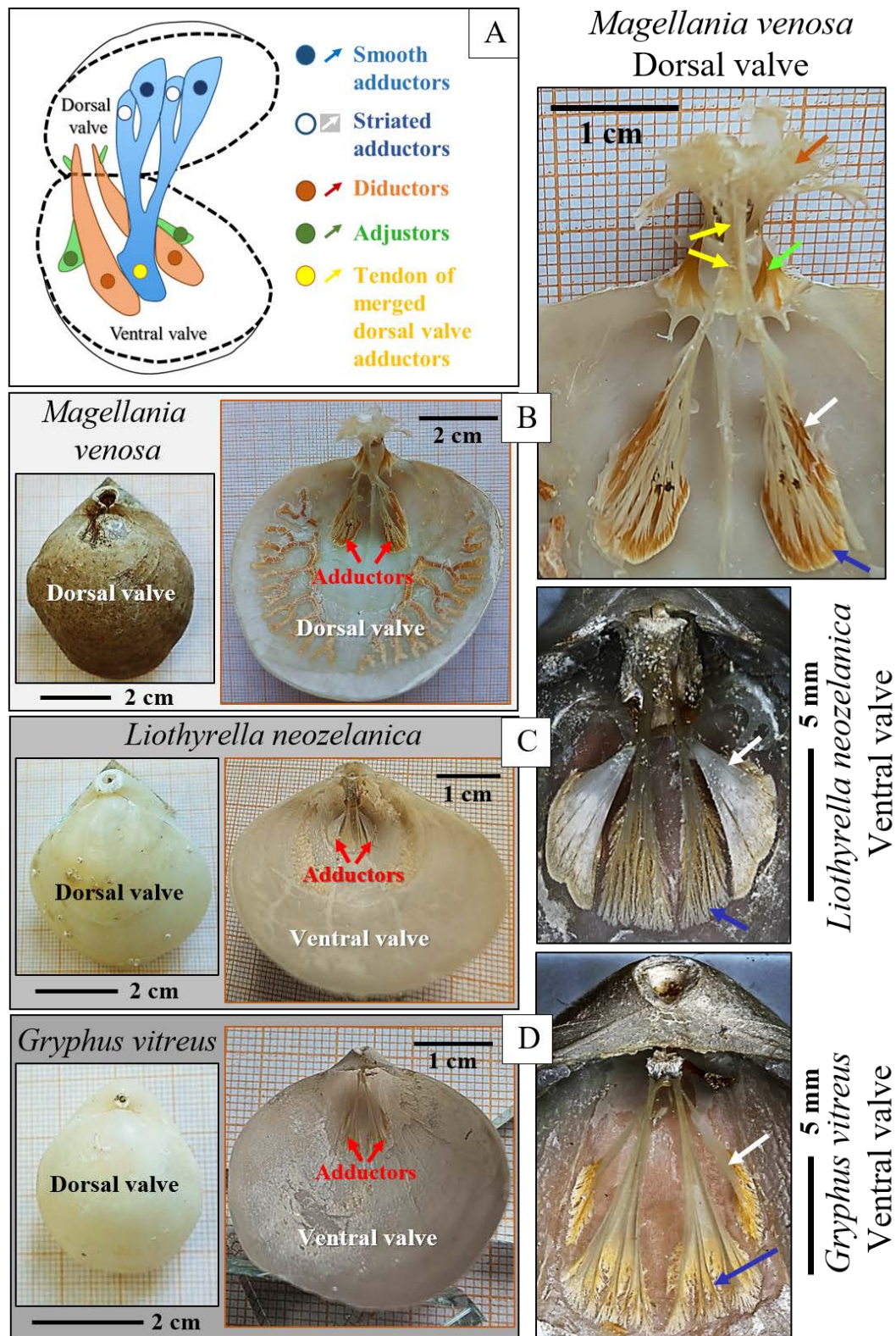


Figure 2.5-1. The shell, valves and different muscles of the brachiopod species investigated in this study: *Magellania venosa* (B), *Liothyrella neozelanica* (C) and *Gryphus vitreus* (D). A: Sketch, modified after (James et al. 1992), depicting the two brachiopod valves and indicating the structure and attachment positions of adductor, diductor and adjustor muscles to the valves as well as the attachment location of the tendon of merged the dorsal valve adductor striated and smooth muscles. The valve-moving muscles of rhynchonellate brachiopods develop in pairs. Thus, within the shell cavity, there is always a pair of adductors (red arrows in B to D), a diductor and an adjustor muscle bundle. In addition, each adductor muscle of the pair of adductors consists of two branches (white and blue arrows in B to D). For all three investigated species, the pair of adductor muscles branches is well visible, positioned left and right of the hinge (blue and white arrows in B to D) and consisting of the smooth and the striated adductor muscle fibres (shown in Figs. 2.5-6, 2.5-S2).

Magellania venosa dorsal valve

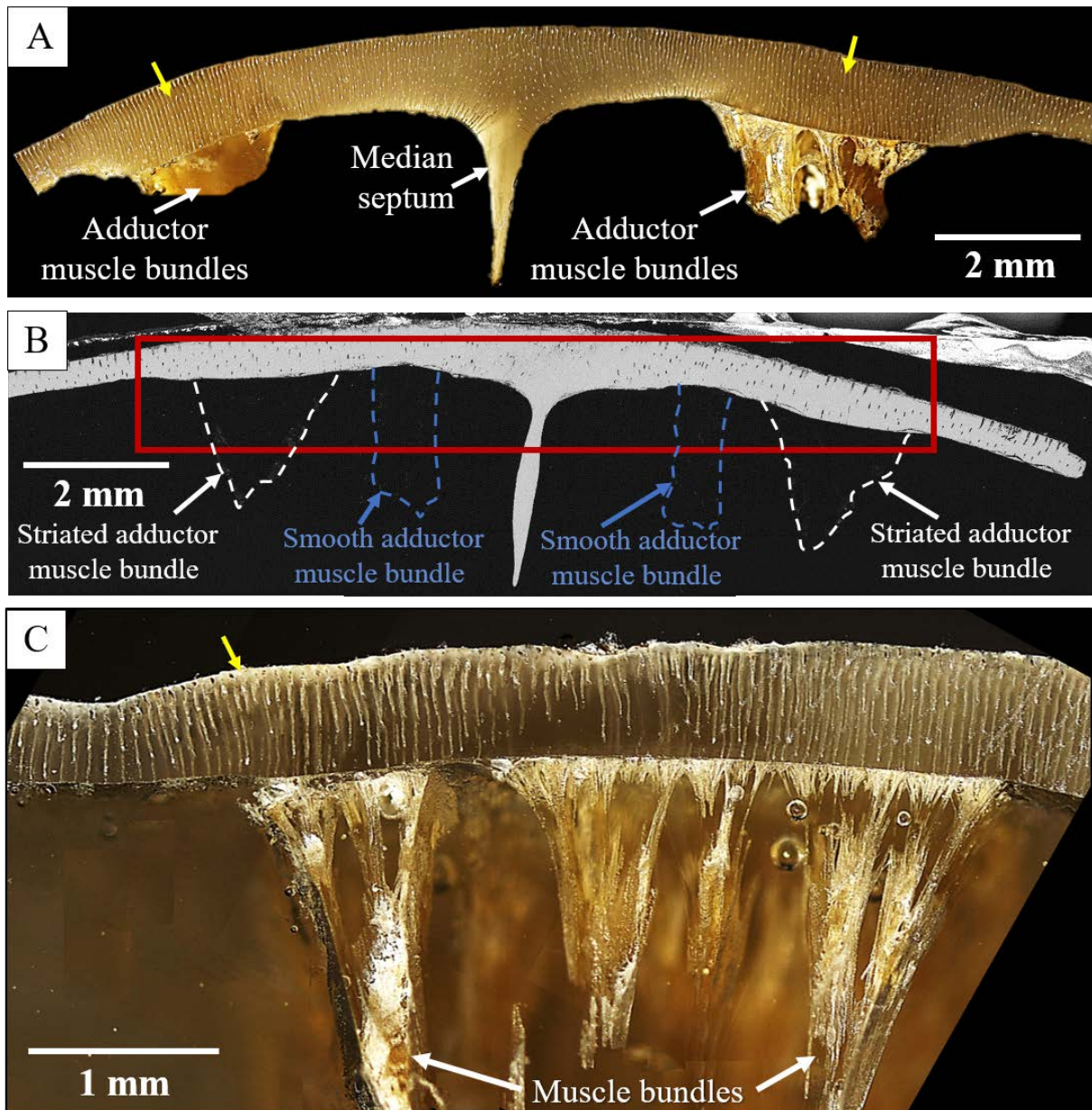


Figure 2.5-2. Bundles of adductor muscle fibres that attach to the dorsal valve of *Magellania venosa*. The thickening of the dorsal valve at the attachment sites of the muscles and the hinge is well observable from the micrograph (yellow arrows in A) and backscattered electron images (B). However, for the investigated species, we observed specifically thickened valve sections not just at the muscle attachment sites, as is the case for the muscle scars of bivalves (Fig. 2.5-13A and Hoerl et al. (2024b)), but also near the hinge (red box in B). White arrows in the micrograph C point to bundles of striated adductor fibres.

A pair of diductor and a pair of adjustor muscles attach their base to the ventral and the dorsal valves (Figs. 2.5-3 to 2.5-5). At the dorsal valve, a pair of specific adductor muscles is attached (Figs. 2.5-1, 3). These merge and form one tendon, which attaches to the ventral valve (Figs. 2.5-3, 2.5-5). For all three investigated species, the pair of adductor muscle that attaches to the ventral valve has a segment attaching to the left and another to the right of the median septum of the hinge (Figs. 2.5-1, 2.5-2). Each adductor muscle segment consists of two branches. This is well-observable for all three investigated species (Fig. 2.5-1). The two adductor branches are positioned next to each other, nonetheless, are delimited spatially from each other, as one adductor branch attaches to the valve behind the other

adductor branch (Figs. 2.5-1, 2.5-S2). Accordingly, for all three investigated species, we observed different attachment positions for the two adductor branches. Based on muscle ultrastructure, our study shows that the two branches of the dorsal valve adductor muscles consist of different types of muscles. One branch is formed of smooth, the other of striated muscles (Figs. 2.5-6, 2.5-S2).

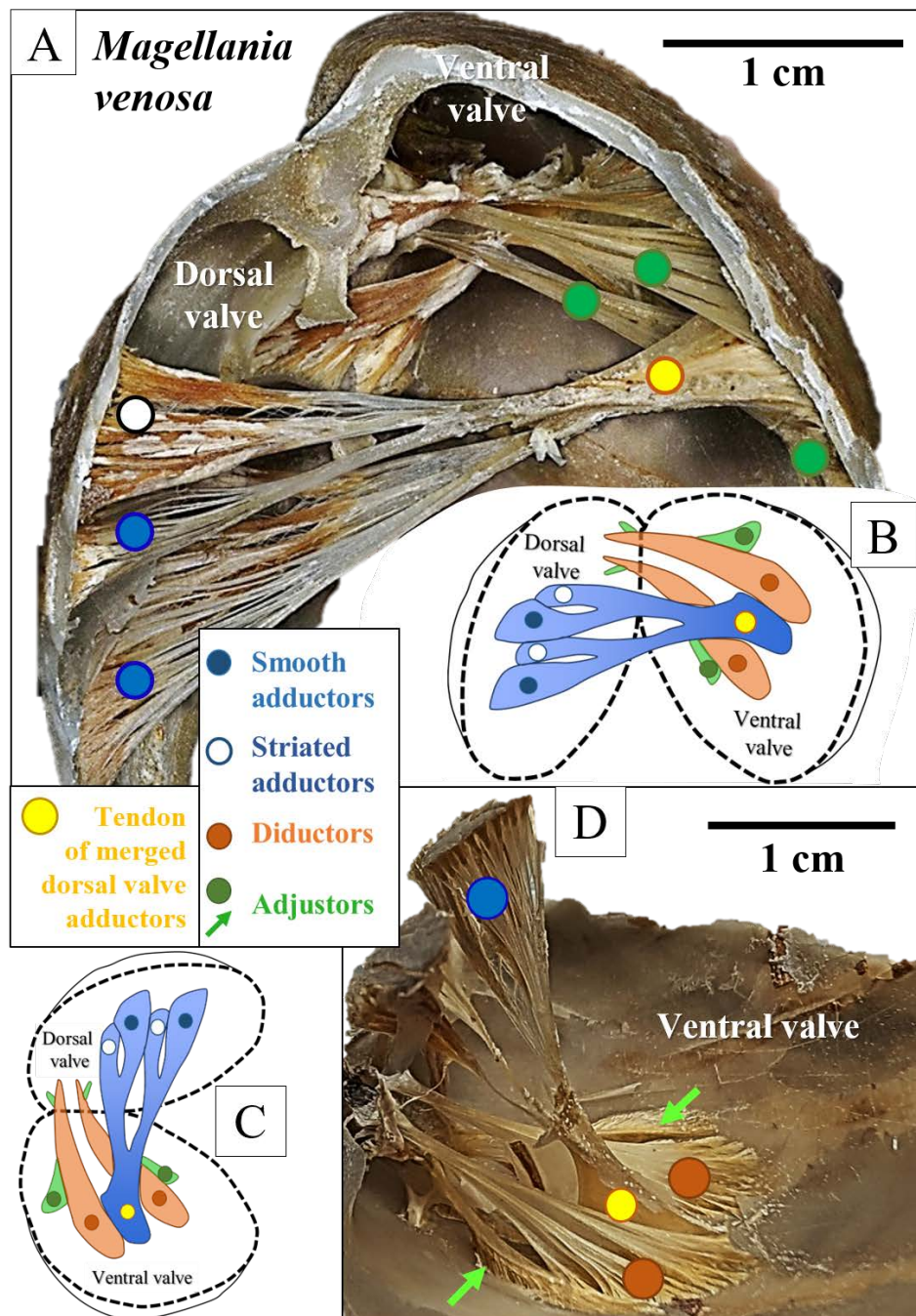


Figure 2.5-3. A: 3D image visualising the adductor and adjustor muscle pairs of a *Magellania venosa* shell, their arrangements within the shell cavity and their attachment positions to the valves. Note that the muscles are positioned in the posterior part of the shell cavity, generated by the hinged dorsal and ventral valves. See the two branches for one of the adductor pairs (blue and white circles in A), attached to the dorsal valve and well separated. The branches and two pairs of adductor muscles converge into a tendon that attaches to the ventral valve (yellow circle in A). B, C: Sketch indicating the different muscles and visualising their position on the inner surface of the ventral and dorsal valve. D: The course of the pairs of the diductor and adjustor muscles, attaching to the ventral valve of a *M. venosa* shell. The difference in muscle size and attachment position to the valve is well observable. Note the position of the tendon (yellow circles in B, D) that originates from the confluence of the ventral valve adductors and their branches.

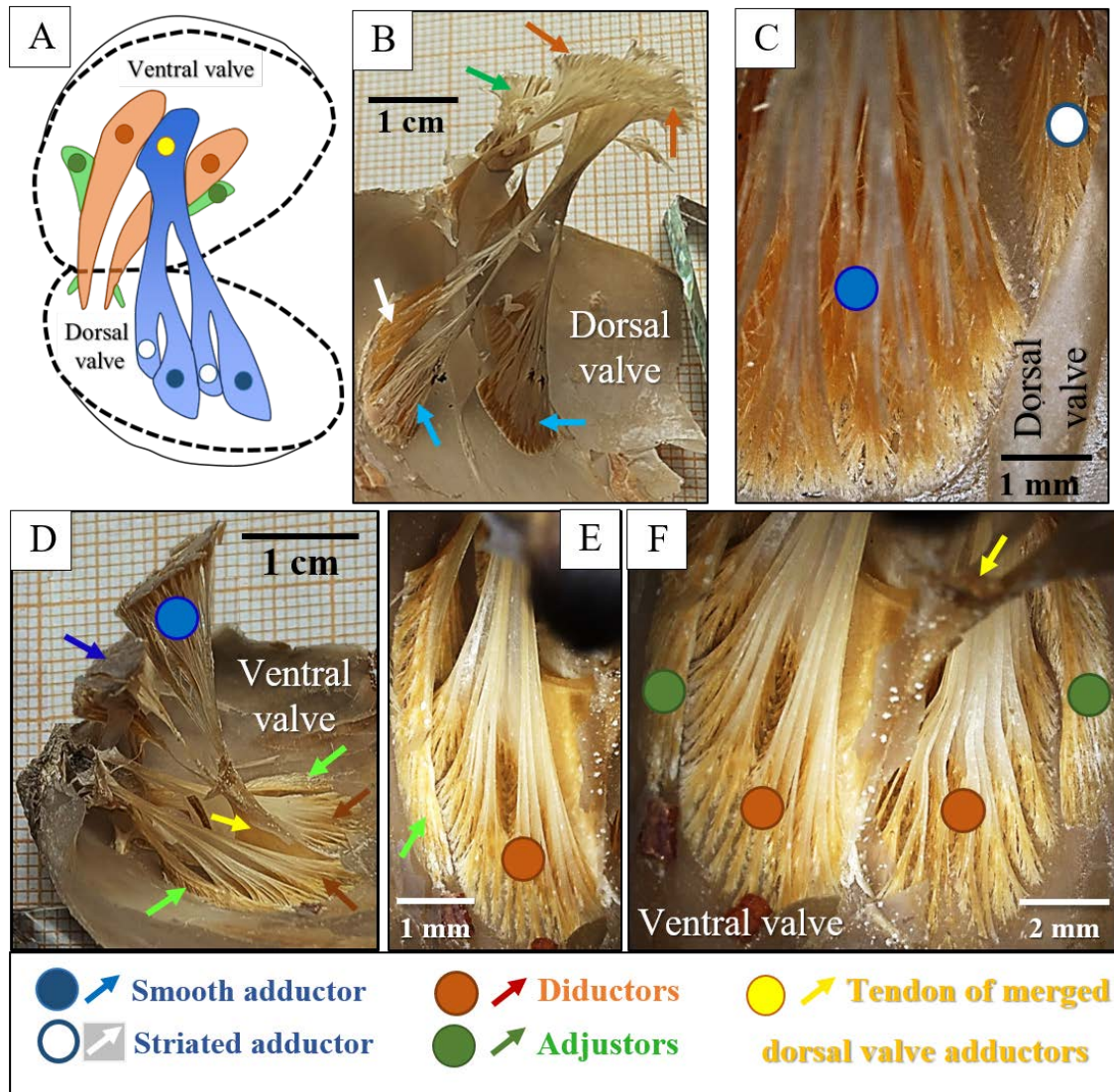


Figure 2.5-4. A: sketch visualising the different types of muscles that initiate movement of the *Magellania venosa* ventral and dorsal valves. B: view onto the pairs of adductor, diductor and adjustor muscle bundles. C to F: view onto the diductor and adjustor muscle bundles and fibres.

Following the adductor muscles, the diductors are the next largest, valve-moving, rhynchonellate muscles (Figs. 2.5-3B, 2.5-4, 2.5-5). Their attachment site to the dorsal valve is minute, unlike their attachment site to the ventral valve. We found large diductor muscle attachment sites onto the ventral valves, positioned left and right to the adductor tendon (Figs. 2.5-3D, 2.5-5C, F). When the diductor muscle bases are viewed from above, a pair of slightly overlapping diductors are visible, attaching to the ventral valve (Fig. 2.5-5C, F). Of the three valve/shell-moving muscles, the smallest muscle is the adjustor muscle (Fig. 2.5-5E). As is the case for the diductor muscles, the attachment sites of the adjustor muscles onto the dorsal valve are also minute. However, when attaching to the ventral valve, the adjustor attachments increase considerably in size and curve around the attachment of the diductor muscle (Fig. 2.5-3D). The adjustor muscles run partly behind the diductor muscles (Figs. 2.5-3D, 2.5-5E). Thus, when viewed from above, we found in a row, however, in a stepped arrangement, the attachment of the adductor tendon, that of the diductors and, close to the valve margin, that of the adjustors.

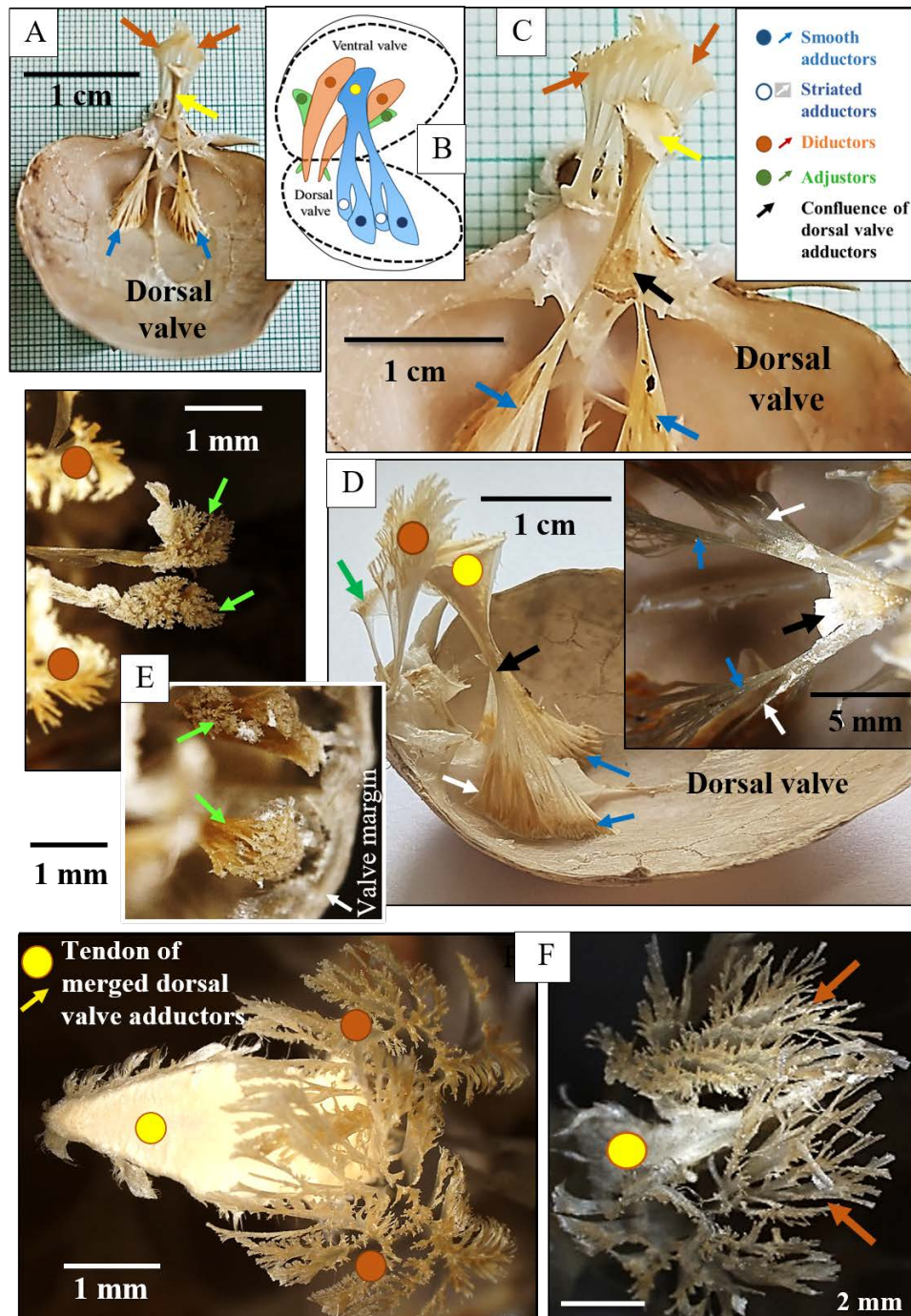


Figure 2.5-5. A to E: Top and side views of the different muscles of *Magellania venosa*. B: Sketch, visualising the positions and attachments of the muscles to the internal surface of the ventral and dorsal valves. D: Side and top view of the confluence of the dorsal valve adductors into a single tendon (black arrows in D). E: Top view of the adjustor muscle bundles (highlighted by green arrows). F: Top view of the diductor muscle bundles. Note that these slightly overlap. C, F: See the surface of the tendon, formed of the dorsal valve adductors (yellow circle in F). See the tendon being positioned between the diductors and that the diductors are slightly offset to the tendon. Note that the adjustors are behind the tendons and the diductors and are closest to the valve (insert in E, F). Hence, the tendon, diductor and adjustor muscles are positioned close to each other in a row, even slightly overlapping.

It is interesting to find that, for the investigated species, all three muscles have, on one end, a small, on the other a large thickness (e.g., sketched in Fig. 2.5-1A). Furthermore, it should be noted that the large base of the adductors and the small bases of the diductors and adjustors attach to the dorsal valve. In contrast, the large bases of the diductors and adjustors attach to the ventral valve. At the same

time, the extent of the attachment site of the adductor tendon is rather small when compared to the attachment size of the adductors onto the dorsal valve. Hence, we found a structured distribution of muscle attachments on the two brachiopod valves for the investigated species and the investigated muscles.

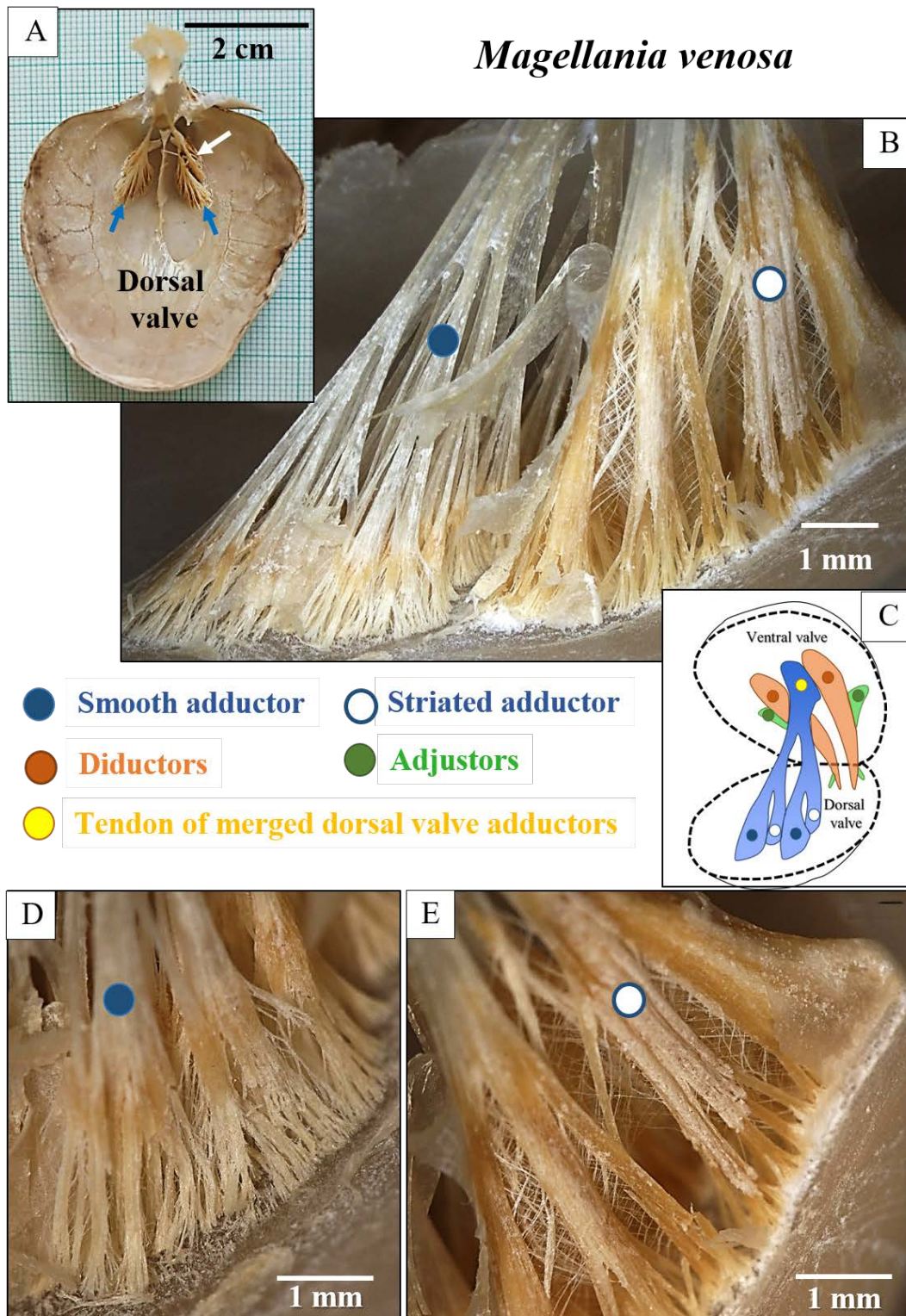


Figure 2.5-6. A, B, D and E: The branches of one *Magellania venosa* dorsal valve adductors. See the difference in structure between the smooth and striated adductor branch; see also Fig. 2.5-S2. C: Sketch visualising the muscles that move the valves of modern rhynchonellate brachiopods.

Magellania venosa

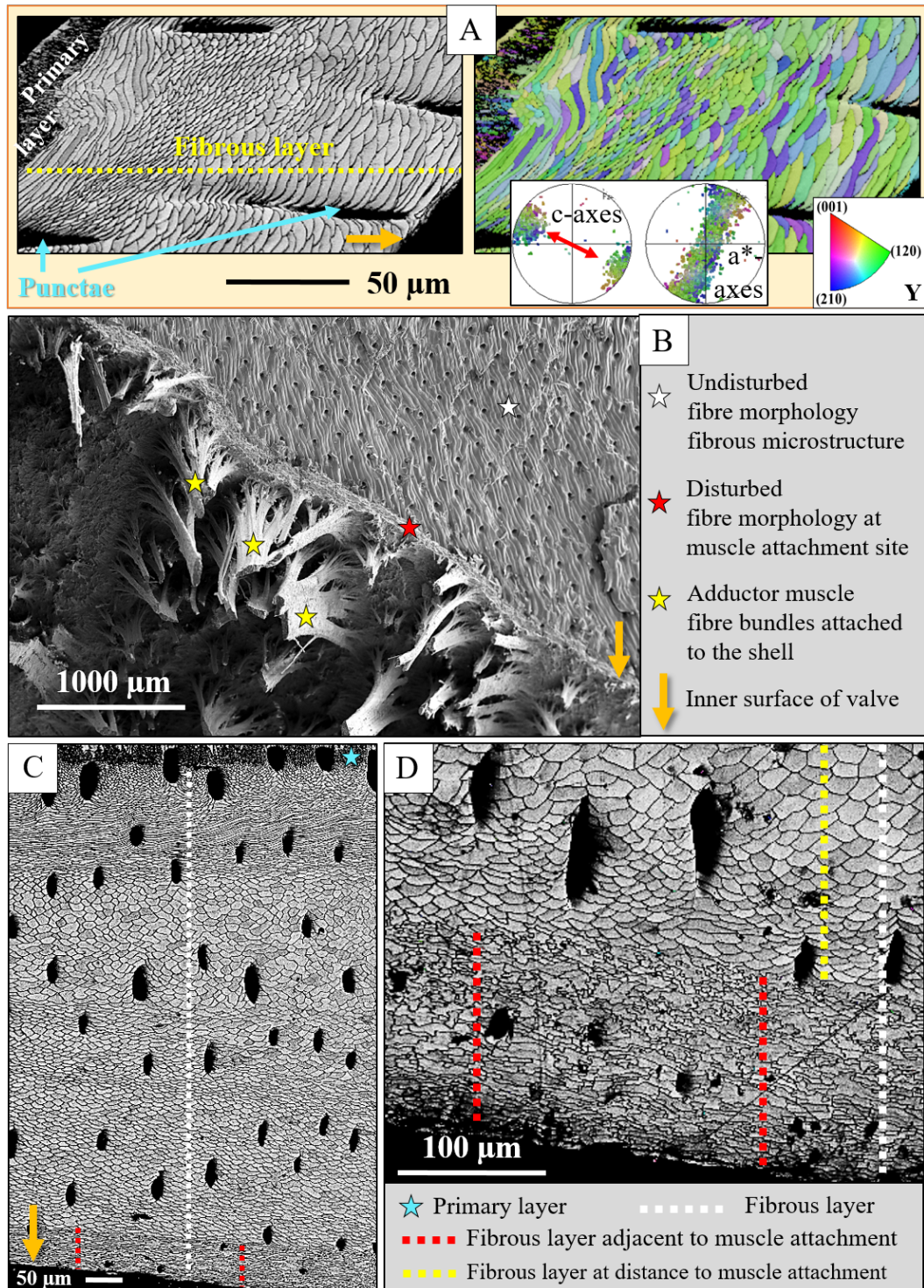


Figure 2.5-7. A to D: Structure, microstructure and texture of calcite fibre arrays of the two-layered shell of *Magellania venosa* shells cut transversely and longitudinally. B to D: The structure and microstructure of the fibrous shell layer adjacent to the attachment of the muscle bundles and distant to the attachment of the muscles to the valves. The orange arrows in A to D point to the inner valve surfaces. A thin, 120 to 150 µm thick layer of calcite, significantly different in structure to the fibrous microstructure of the rest of the shell, is visible where the muscle bundles attach to the valves (red star in B, red dashed lines in C, D). Within the valve section next to the attachment of the muscles, the typical morphology of brachiopod fibres is not observable (D); the crystals (fibres) are strongly distorted in morphology. A: EBSD scan, given as band contrast measurement image (left in A) and colour-coded for crystal orientation (right in A, modified after Simonet Roda et al. (2022)). The fibres are well aligned in the stack and show an axial crystal texture that is more or less parallel to the growth direction (see red arrow in pole figure in A). A, C, D: EBSD band contrast or crystal orientation images. B: FE-SEM micrograph, SE contrast. The EBSD coordinate system (indicated for the c-axes pole figure in A) is maintained for all measurements reported in this study.

Where the adductor muscles attach to the valves, a valve section is thickened (Figs. 2.5-2A, 2.5-S1D). However, valve thickening is not limited to the sole attachment of individual muscle bundles; the thickened valve region extends over a larger portion of the valve (Figs. 2.5-2A, 2.5-S1D). As for the rest of the shell, the thickened valve region consists of calcite (Figs. 2.5-9B, 2.5-10E, 2.5-12B). This thickened valve section might be addressed as an additional shell layer (Figs. 2.5-7B, 2.5-8), as it is distinct in microstructure, relative to the rest of the shell (Figs. 2.5-7 to 2.5-12). We found that for all three investigated species, irrespective of whether the inner layers of the shell are formed of fibres or columns, the innermost layer comprises a particular microstructure at the thickened valve sections. This is a specific microstructure with a strongly irregular appearance and features crystals with fractal-like morphologies (Figs. 2.5-7D, 2.5-8A, 2.5-9F, 2.5-10F, 2.5-11A, B, 2.5-12B, C). The latter crystal morphology and microstructure are distinct from those of the crystals that form the other parts (the absolute majority) of the shell (Figs. 2.5-7A, 2.5-10A, 2.5-12A). Subsequently, this microstructure formed of the fractal-like crystals is termed ‘distorted’. The valve layer with the distorted microstructure is intimately connected to valve sections that are formed of the conventional and, for brachiopod shells, typical fibrous and columnar microstructures (Figs. 2.5-7D, 2.5-9C, F, 2.5-10F, 2.5-11A, B). The distorted microstructure, which forms the innermost layer of the thickened shell sections, appears to evolve from the fibrous and/or columnar microstructures (e.g., Figs. 2.5-9A, F, 2.5-11B). Despite the difference in microstructure (described above), it is very interesting to observe that crystal texture does not change. It is axial for shell layers formed of crystals with undisturbed but also with disturbed crystal morphologies (see pole figures in Figs. 2.5-9C, D, 2.5-10F, 2.5-12B, C).

The crystals with fractal-like morphologies can be addressed neither as fibres nor columns. Nonetheless, their c-axis orientations are perpendicular to the inner shell surface. In one rare case, we observed for the two-layered shell of *M. venosa*, fibre-shaped crystals within the “distorted-microstructure-layer”, adjacent to the attachment of muscle fibres (Fig. 2.5-8). We found that the calcitic c-axis orientations are parallel to the morphological orientation of the muscle fibre bundle. When crystal morphologies, irrespective of whether for fibres or columns, between undistorted and distorted shell sections are compared, we observed for all investigated species that crystal morphologies at innermost thickened valve sections are serrated and fractal-like and that these crystals interdigitate strongly (Figs. 2.5-8A, 2.5-10C, 2.5-12B, C). This is not the case for fibres and columns that form the other parts of the shell, where the “conventional” brachiopod microstructure prevails (Figs. 2.5-7A, 2.5-10A, 2.5-12A).

As mentioned above, the thickened shell layer, comprising the layer with the distorted microstructure at its innermost surface, is not just strictly connected to the sites where the muscle bundles attach. This specific layer is thickest at the muscle bundle attachments (e.g., Figs. 2.5-10, 2.5-11). However, it also covers valve inner surfaces that surround the regions of the muscle attachments. Nonetheless, with distance away from the muscle attachment sites, the layer with the distorted microstructure thins out (Figs. 2.5-9H, 2.5-11C).

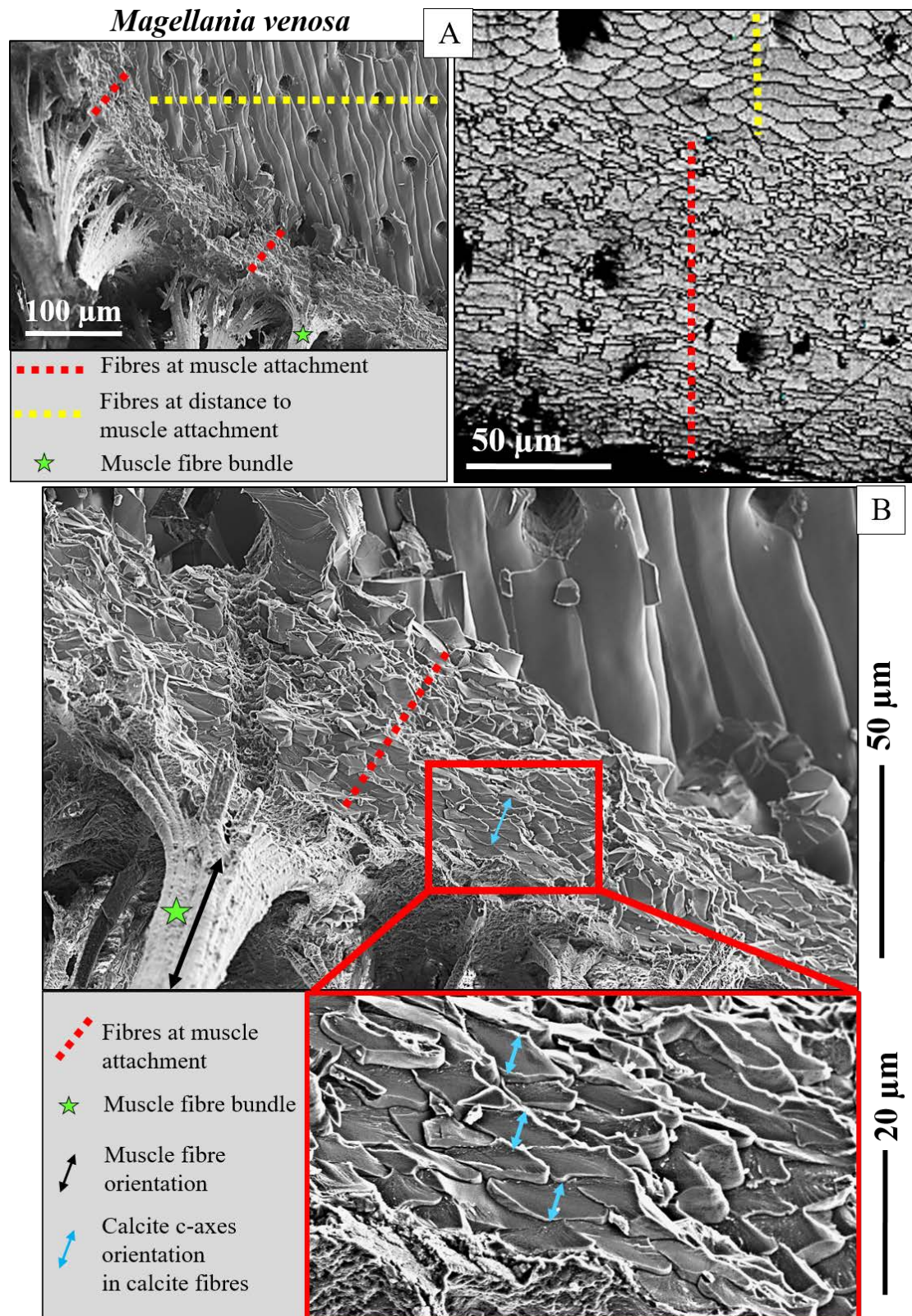


Figure 2.5-8. A, B: Shell fibre structure at muscle attachment sites directly adjacent to muscle fibre bundles that attach to the inner surface of *Magellania venosa* shells. Left in A and B: FE-SEM micrographs, SE contrast. Right in A: EBSD band contrast measurement image. Well visible is the generally distorted morphology of the fibres that form the shell adjacent to the muscle attachment sites. Nonetheless, outlines of undistorted brachiopod fibres are occasionally visible (e.g., red square in B). For these, we can deduce the morphological axis of the fibre and, accordingly, even in SE micrographs, the orientation of calcite crystals that form the fibres. Schmahl et al. (2012b) have shown that the calcite c-axis orientation directions are perpendicular to the morphological long axis of brachiopod fibres. The latter implies that the fibre calcite c-axis orientation direction of valve sections at muscle attachment sites is parallel to the morphological orientation of the muscle fibre and bundle.

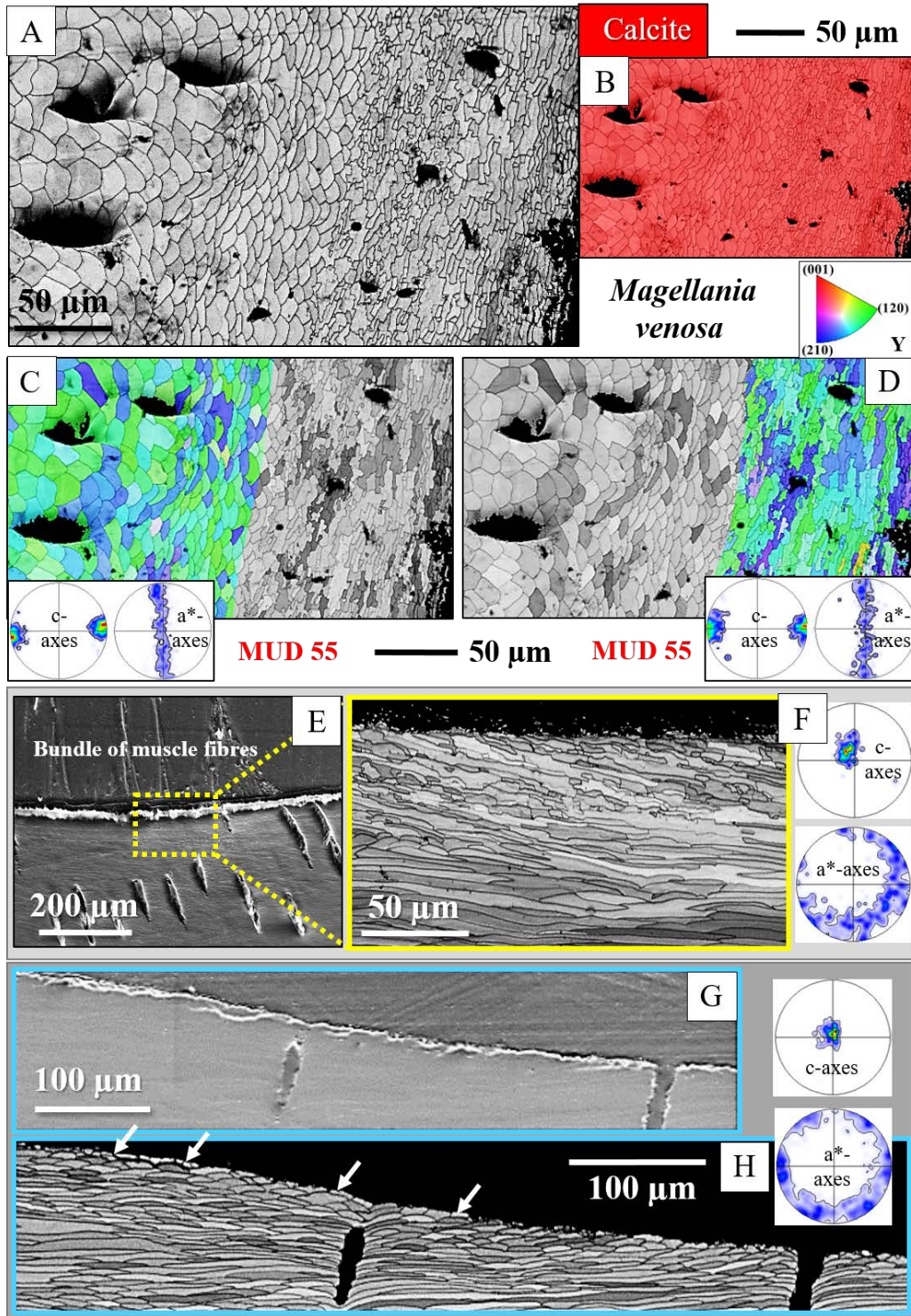


Figure 2.5-9. EBSD scans showing the microstructure, texture, and carbonate phase of the fibrous *Magellania venosa* valve section where muscles attach to the valves. A, F, and H are EBSD band contrast measurement images. C and D show EBSD band contrast (in grey) overlain with crystal orientation (in colour). E, G: FE-SEM images, SE contrast. The muscle attachment sites of modern rhynchonellate shells consist of calcite (B). Irrespective of fibre morphological axis orientation, for both transversely (A, C) and longitudinally (F) cut fibres, fibre morphology at the valve section where the muscles attach is strongly distorted. The layer with distorted fibre morphology forms a lining at the inner shell surface (Fig. 7B, C) that thins out with distance from the shell portion where the muscle bundles attach (H). White arrows in H point to the very thin (few μm) seam of fibres with distorted morphology that line the inner surface of the valve. With distance from the muscle attachment sites, the inner valve surface microstructure consists of undistorted rhynchonellate brachiopod fibres. Pole figures in C, D, F, and H demonstrate the axial nature of the calcite texture, irrespective of whether the EBSD scan was taken at a muscle attachment site or away from the latter. C, D: there is no difference in crystal co-orientation strength (MUD value) between valve sections at muscle attachments and those away from muscle attachments.

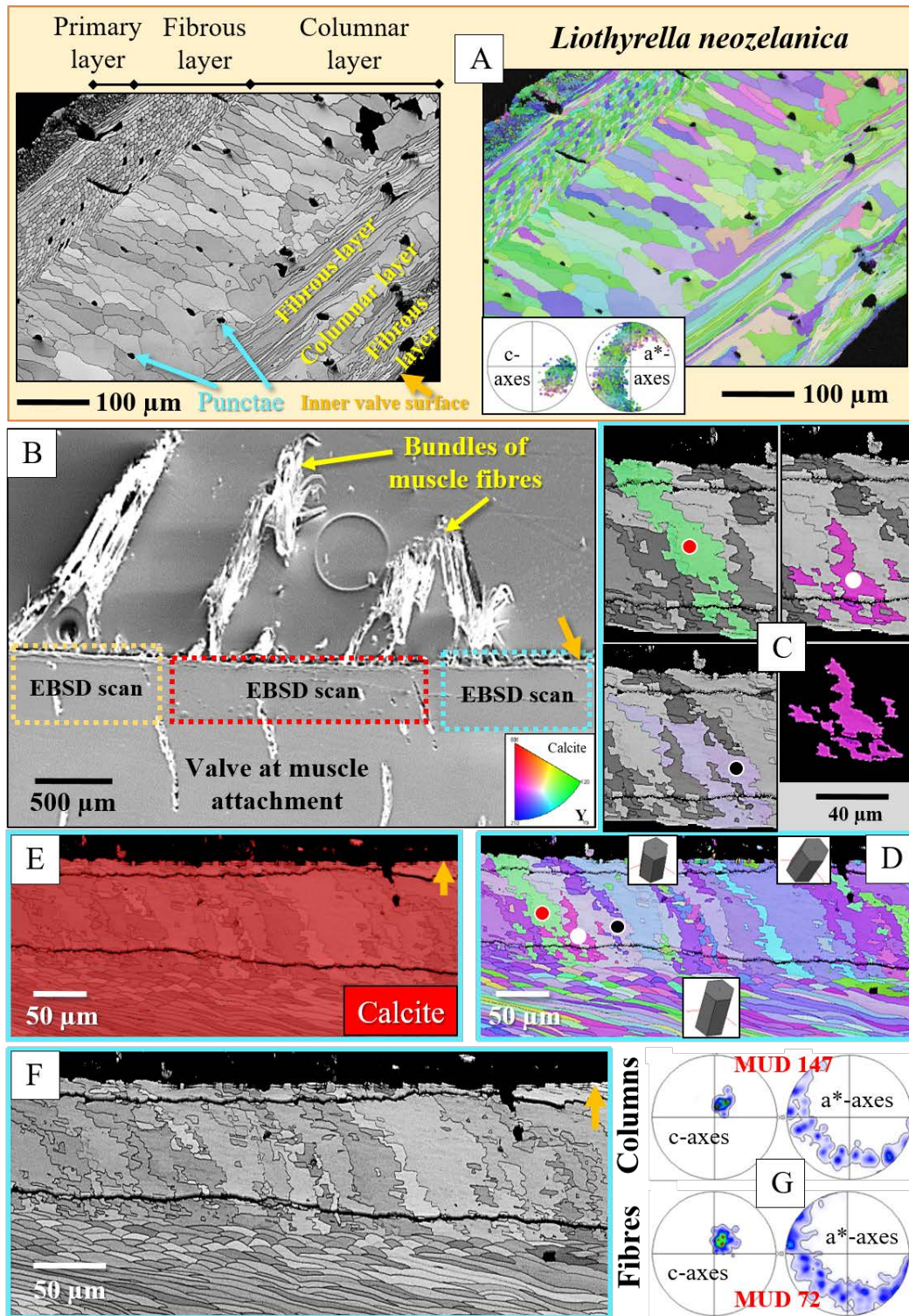


Figure 2.5-10. Microstructure, texture and carbonate phase of the three-layered shell of *Liothyrella neozelanica* at muscle attachment sites (B to G) and away from these shell sections (A). Left in A and F: band contrast image of EBSD measurement. Right in A and D: Colour-coded EBSD map showing calcite crystal orientations. EBSD measurement images in A are modified after Simonet Roda et al. (2022). C: Colour-coded maps of individual attachment site crystals highlight their complex morphologies. B: FE-SEM micrograph, SE contrast. We show three EBSD scans for *L. neozelanica*, their position indicated in B with blue, red, and yellow rectangles. One EBSD scan is given in D to F; the others are given in Fig. 2.5-11A, B. All three EBSD scans scan the valve adjacent to muscle bundles and cover the crystals adjacent and distant to the muscle attachments. Muscle attachment valve sections of *L. neozelanica* consist of calcite (E). For *L. neozelanica*, the calcite of the valves at muscle attachments is formed of elongated crystals that faintly resemble columns (D, F). These interdigitate (C) and have strongly irregular outer morphologies (D, F). For both the fibres and the elongated crystals at muscle attachment sites, we found an axial texture (G) and high crystal co-orientation strengths (MUD values in G).

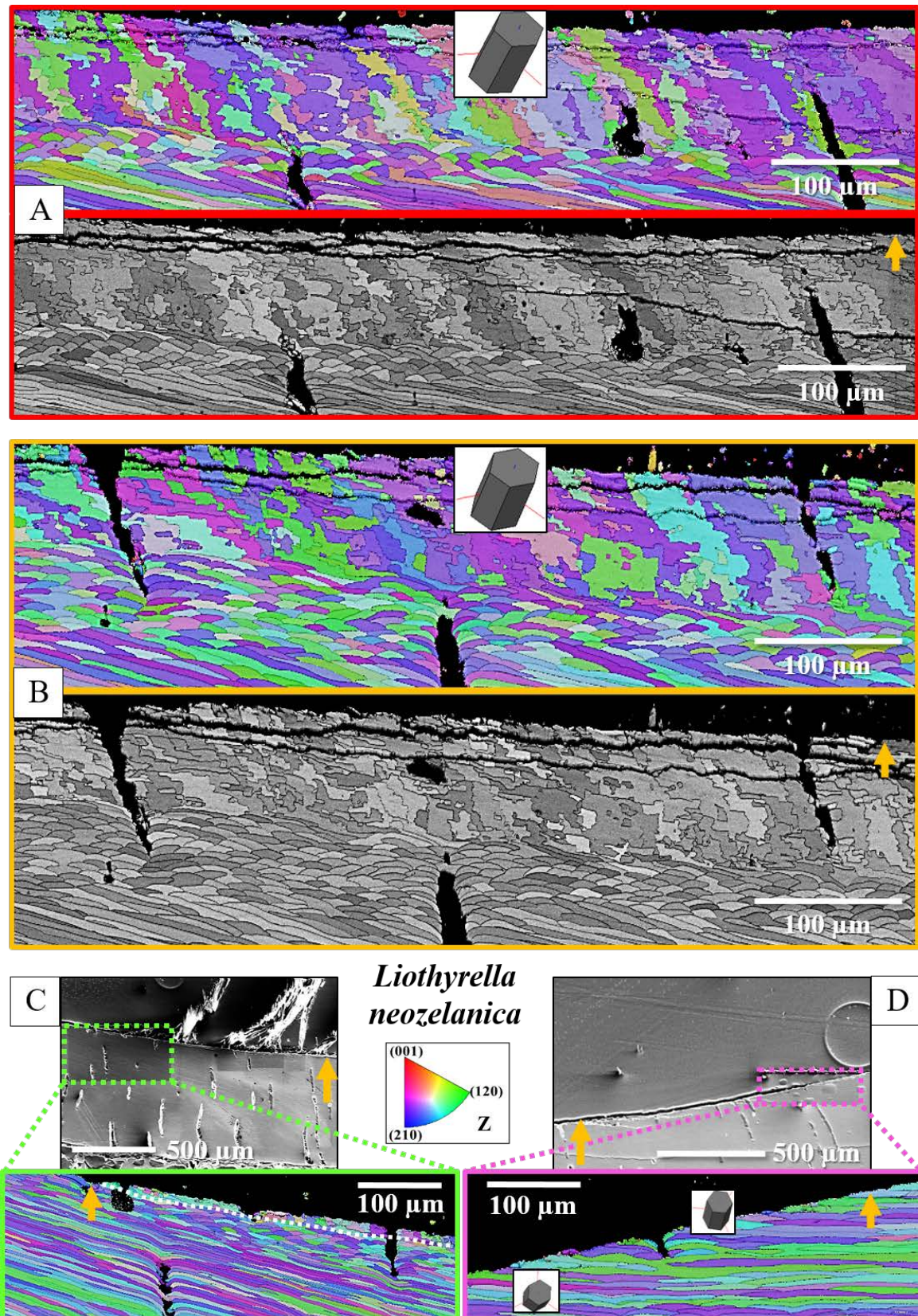


Figure 2.5-11. EBSD scans taken on the valves of *Liothyrella neozelanica* at muscle attachments (A, B) demonstrate the changed microstructure of shell calcite adjacent to muscle attachments relative to the columns and/or fibres in other valve sections (e.g., Figs. 2.5-10A, 2.5-11D). In these scans, we also observed a seam of elongated crystal units at the inner shell surface, which have a strongly irregular morphology and interdigitate with neighbouring elongated units. As for the two-layered *M. venosa*, the specific layer developed at muscle attachments to the shell becomes thinner with distance from the muscle attachment sites (C) and, at some point, disappears completely (D). Crystal orientation is indicated with sketched crystals in A, B and D, and the growth direction up to the inner shell surface is indicated by orange arrows.

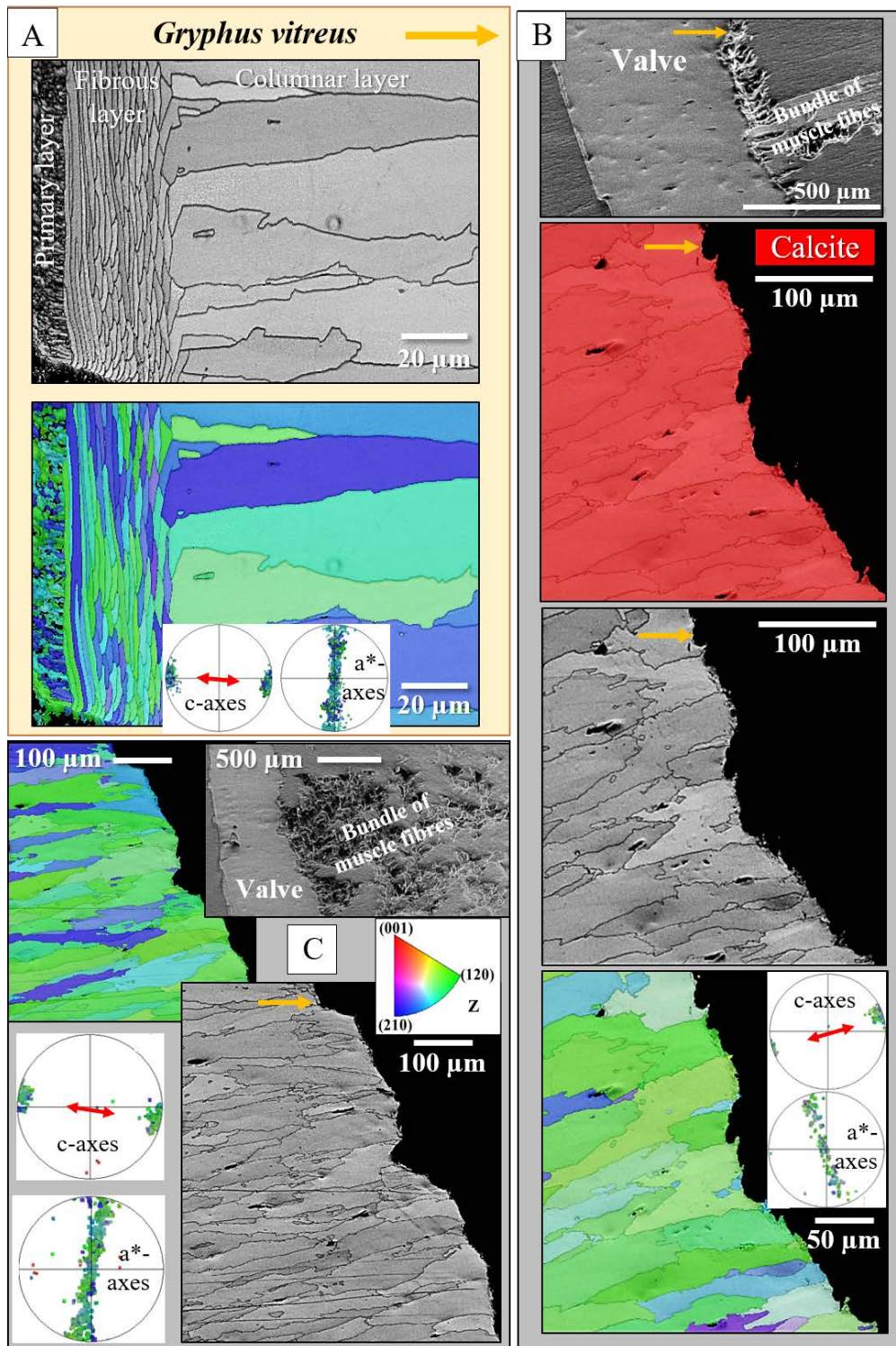


Figure 2.5-12. Microstructure, texture and carbonate phase of valve sections at muscle attachment sites for the three-layered shell of *Gryphus vitreus*. *G. vitreus* shells comprise a primary, a fibrous and a columnar shell layer (A). However, unlike *Liothyrella neozelanica*, there is no sequential alternation of the fibrous and the columnar microstructure in *G. vitreus* shells. Thus, at the inner surface, the shell consists always of an array of columns (A). EBSD measurement images in A are modified after (Simonet Roda et al. 2022). In general, in *G. vitreus* shells, the columns are large entities and have regular morphologies. Shell crystals are assembled with an axial microstructure with c-axes parallel to the growth direction (red arrows in pole figure A). At muscle attachments (B, C), we also observed arrays of columns. Nonetheless, the morphology of the columns becomes slightly irregular (B, C), and the columns interdigitate in 3D. The columns at muscle attachment sites also comprise calcite and have an axial texture (see pole figures in B and C). The top micrograph in B and the insert in C are FE-SEM images, SE contrast. The map coloured in red in B shows that the carbonate phase of the crystals at muscle attachment sites is calcite. Grey-scaled in A to C are EBSD band contrast maps, complemented with coloured EBSD maps visualising crystal orientation.

2.5.4 DISCUSSION

Rhynchonellata (Brachiopoda) and Bivalvia (Mollusca) belong to different phyla. Rhynchonellate brachiopods and most bivalve molluscs are filter-feeding, marine organisms with species of many taxa being sessile and/or cementing to the substrate. Both have a global distribution and are adapted to many, partly comparable, habitats (Ponder et al. 2019; Checa et al. 2025) and references therein).

The species of both invertebrate classes secrete mineralised shells, consisting of two valves and a hinge. For species of both classes, shell secretion is performed by the cells of a mantle epithelium, which lines the inner surface of the shell and encloses the soft body and the pallial cavity. The mantle epithelium consists of an outer and inner layer, separated from each other by connective tissue. For species of both classes, the outer epithelium, which performs shell secretion, is single-layered and comprises cuboidal and specialised cells, while the inner epithelium mainly comprises columnar cells (Watabe 1983; Bubel 1984; Lemaire-Gony & Boudou 1997). Although representing different phyla, the biomineralisation system of the Brachiopoda and Mollusca is comparable (Checa et al. 2025), such that before secretion of the mineralised shell layers, an organic periostracum is deposited (Fraiser & Bottjer (2007); Simonet Roda et al. (2022); Checa et al. (2025) and references therein). Shell growth occurs for both the Rhynchonellata and the Bivalvia across a thin extrapallial space (Nakahara & Bevelander 1970; Nakahara & Bevelander 1971; Simonet Roda et al. 2019b). The latter is a few tens of nm thick and is located between the proximal surface of the mineralised shell inner surface and the secreting outer epithelial mantle cells (Checa et al. 2014; Audino et al. 2015).

The muscles and their attachment to the attachment site crystals

Brachiopods and bivalves protect their soft tissue and organs with the structural hard tissue of the two valves, hinged together at the posterior end of the shell. The motion of the valves is accomplished via the muscles. Species of both invertebrate classes are capable of: (i) fast and slow valve opening and closure, as well as of (ii) valve opening and closure for short and prolonged periods (Rudwick 1961; Thayer 1975; Chantler 1983; James et al. 1992; Ackerly 1993; Ponder et al. 2019; Hamaya et al. 2025). Valve movement is achieved via adductor and diductor muscles in the case of brachiopods. Bivalves utilise their adductor and pedal muscles as well as their hinge ligament for valve action. Rhynchonellata and Bivalvia can move their valves at different speeds. This requires using various types of muscles, either one particular muscle or a combination of different types of muscles (Chantler 1983). We observed both circumstances for species of Rhynchonellata and Bivalvia. This involves the use of both smooth and striated muscles (MacKinnon 1977; Chantler 1983). One main difference between smooth and striated muscles is that, in the case of smooth muscles, no banding pattern is observable when the

muscle is imaged with SEM. In contrast, a banding pattern is well visible for striated muscles, where striation arises from the filament structure of the muscle (Chantler 1983; Paniagua et al. 1996). Brachiopods and bivalves utilise striated muscle fibres for phasic catch contractions and achieve quick valve opening and closure. Smooth muscle fibres exert tonic forces and are used for slow but prolonged valve opening and closure (Rudwick 1961; Wilkens 1978; Eshleman et al. 1982; Chantler 1983; Ponder et al. 2019).

The connection of muscle fibres to the muscle attachment site crystals is similar for shelled invertebrates (Nakahara & Bevelander 1970; Tompa & Watabe 1976; MacKinnon 1977). The muscles of brachiopods, bivalves and gastropods do not connect directly to the crystals that form the muscle attachment sites. A series of structures is linearly arranged between the apical base of the muscle fibres and the proximal surface of the attachment site crystals (Nakahara & Bevelander 1970; Tompa & Watabe 1976; MacKinnon 1977; Bubel 1984; Ponder et al. 2019; Castro-Claros et al. 2021). At muscle attachment sites of shelled invertebrates, the secreting mantle epithelium consists of specialised epithelial cells, the tendon cells (MacKinnon 1977; Bubel 1984; Ponder et al. 2019). These are located between the muscle bases and the proximal surface of the muscle site crystals (Nakahara & Bevelander 1970; Tompa & Watabe 1976; MacKinnon 1977) and are distinct in ultrastructure from the columnar epithelial cells, which secrete the crystals of the rest of the valves. Tendon cells contain bundles of tonofilaments, which extend throughout their length. The apical and basal surface of tendon cells is dotted with hemidesmosomes (Nakahara & Bevelander 1970; Tompa & Watabe 1976; MacKinnon 1977). In addition to the hemidesmosomes, the apical surface of the tendon cells is densely seamed with knob-shaped microvilli. However, the tendon cells do not attach their microvilli directly to the muscle attachment site crystals. A layer of organic fibrils lies between the apical surface of the tendon cells and the proximal surface of the attachment site crystals. These fibrils fill the extrapallial space and become incorporated into the attachment site crystals at shell crystal secretion by the tendon cells (Nakahara & Bevelander 1971; Tompa & Watabe 1976; MacKinnon 1977; Bubel 1984; Castro-Claros et al. 2021). The basal membrane of the tendon cells is strongly infolded and seamed with hemidesmosomes. The basal ends of the muscle fibres terminate close to the basal membrane of the tendon cells and anchor, also with hemidesmosomes, to the hemidesmosomes of the basal membrane of the tendon cells (Nakahara & Bevelander 1971; Tompa & Watabe 1976; Bubel 1984). The above detailed mode of attachment of the muscles to the muscle attachment site crystals is similar for shelled invertebrates; thus, it is similar for brachiopods and molluscs.

The attachment of the muscles of bivalved organisms to the inner shell surface belongs to one of the strongest connections in the biological realm (Chantler 1983). This is due to: (i) the high muscular strength of invertebrate muscles; the latter is the force that muscles can exert against resistance in a single effort (Chantler 1983), and (ii) the mode of connection between the muscles and the crystals, to which the muscles attach (Castro-Claros et al. 2021). At the muscle attachment site, the tendon cell

fibrils associated with their apical microvilli anchor within the crystals. It is well-known that the connection of very different materials, such as inorganic-organic composites, can be prone to interface failure (Chang et al. 2022; Sun et al. 2022; Niemiec & Kim 2024; Ullah et al. 2024). However, even though very dissimilar materials join at the muscle-crystal interface, due to the anchoring of the fibrils within the attachment site crystals, very little stress accumulates at the biopolymer fibril-crystal junction, and the connection between the muscle strands and the attachment site crystals becomes strongly increased in strength (Castro-Claros et al. 2021).

As visualised in this study, each trunk of the pair of brachiopod adductor muscle (Fig. 2.5-S1B) consists of two branches (Figs. 2.5-3A, 2.5-6, 2.5-S1B, E). These branches attach to the inner surface of the dorsal valve, have different appearances, and their attachment site is spatially well-differentiated from each other (Fig. 2.5-S1C, E). The two branches of the brachiopod adductor muscle consist of different types of muscles. The adductor branch closer to the median septum of the hinge is formed of smooth muscles; the branch further away from the median septum consists of striated muscles. The different types of muscles and their arrangement in the shell cavity are also well investigated for bivalves (Hanson & Lowy 1960; Seilacher 1979; Nunzi & Franzini-Armstrong 1981; Cragg 1985; Funabara et al. 2006; Guderley & Tremblay 2016; Ponder et al. 2019; Wu et al. 2022; Vyatchin & Dyachuk 2025). However, such a clear-cut spatial distinction (e.g., Fig. 2.5-13B) between a smooth and a striated muscle component of a specific type of muscle has not yet been observed. Figures 2.5-13C, D, 2.5-S5 to 2.5-S7 show the microstructure and texture of crystals where the smooth and the striated adductor muscle branches of *Magellania venosa* attach to the inner surface of the dorsal valve. The morphology of attachment site crystals is highly fractal, and the microstructure of the inner valve section is distorted (white stars in Fig. 2.5-13C, D) and is distinct from those shell regions that are distant from the muscle attachment sites (yellow stars in Fig. 2.5-13C, D). We found no structural differences in the crystal morphology and microstructure of muscle attachment sites for smooth and/or striated muscle bundles (Fig. 2.5-13A to D). This is not surprising, as, for both smooth and striated muscle bundles, the muscle attachment site crystals are secreted similarly and by similar types of cells, namely the tendon cells.

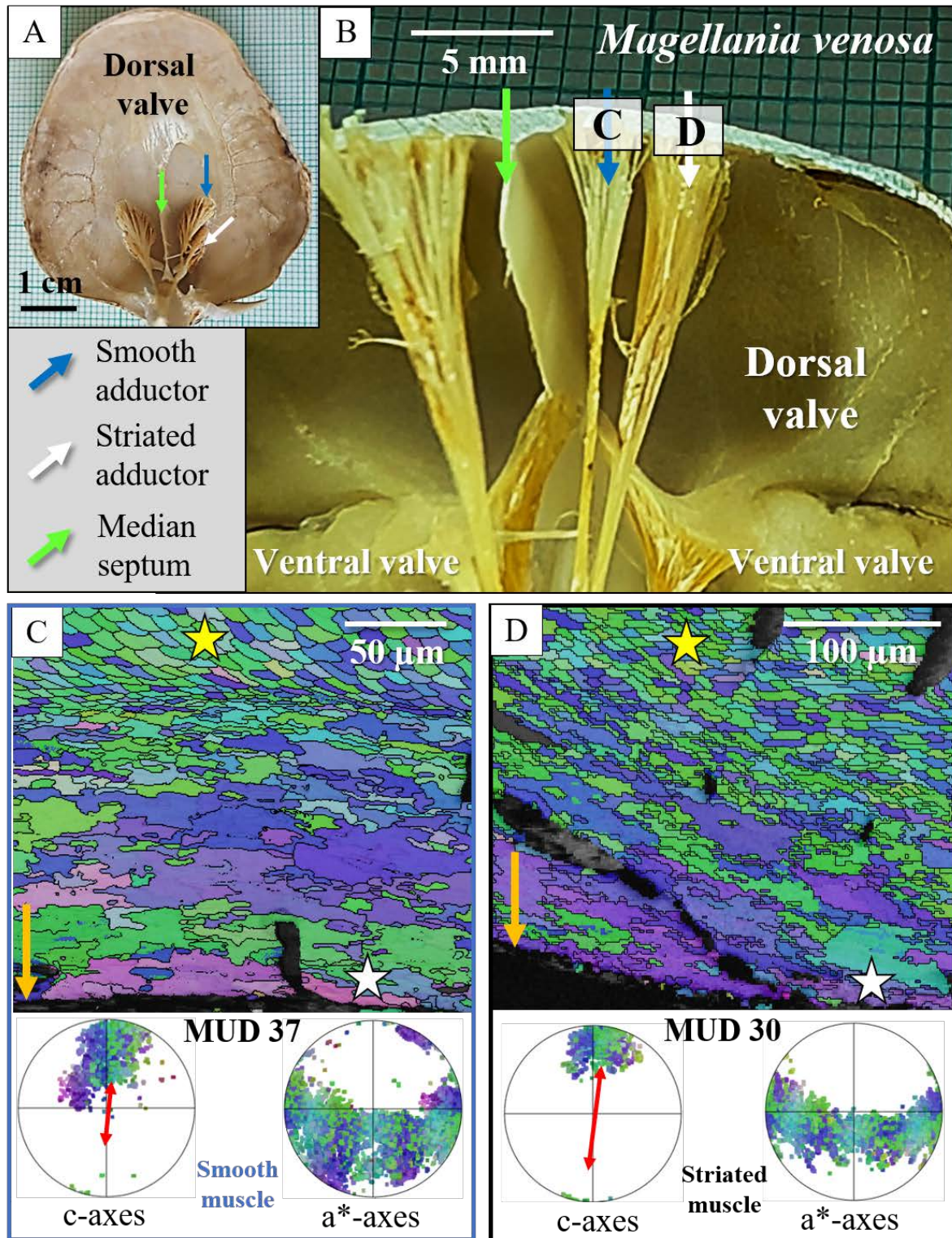


Figure 2.5-13. Comparison of the striated and smooth adductor muscle bundles and attachment site microstructures in *Magellania venosa*. Smooth (blue arrows in A, B) and striated muscles (white arrows in A, B) are spatially separated in a linear arrangement next to the hinge (green arrows in A, B). Colour-coded EBSD maps of smooth (C) and striated (D) valve sections at muscle attachment sites of *M. venosa* show comparable microstructures and textures. While the fibrous calcitic shell (indicated by yellow stars in C, D) is organised, the muscle attachment site crystals appear irregular and interdigitate in 3D (indicated by white stars in C, D). The texture and crystal co-orientation strength of the two sections are similar, with rather low MUD values and c-axes (red arrows in C, D) oriented parallel to the growth direction (orange arrows in C, D).

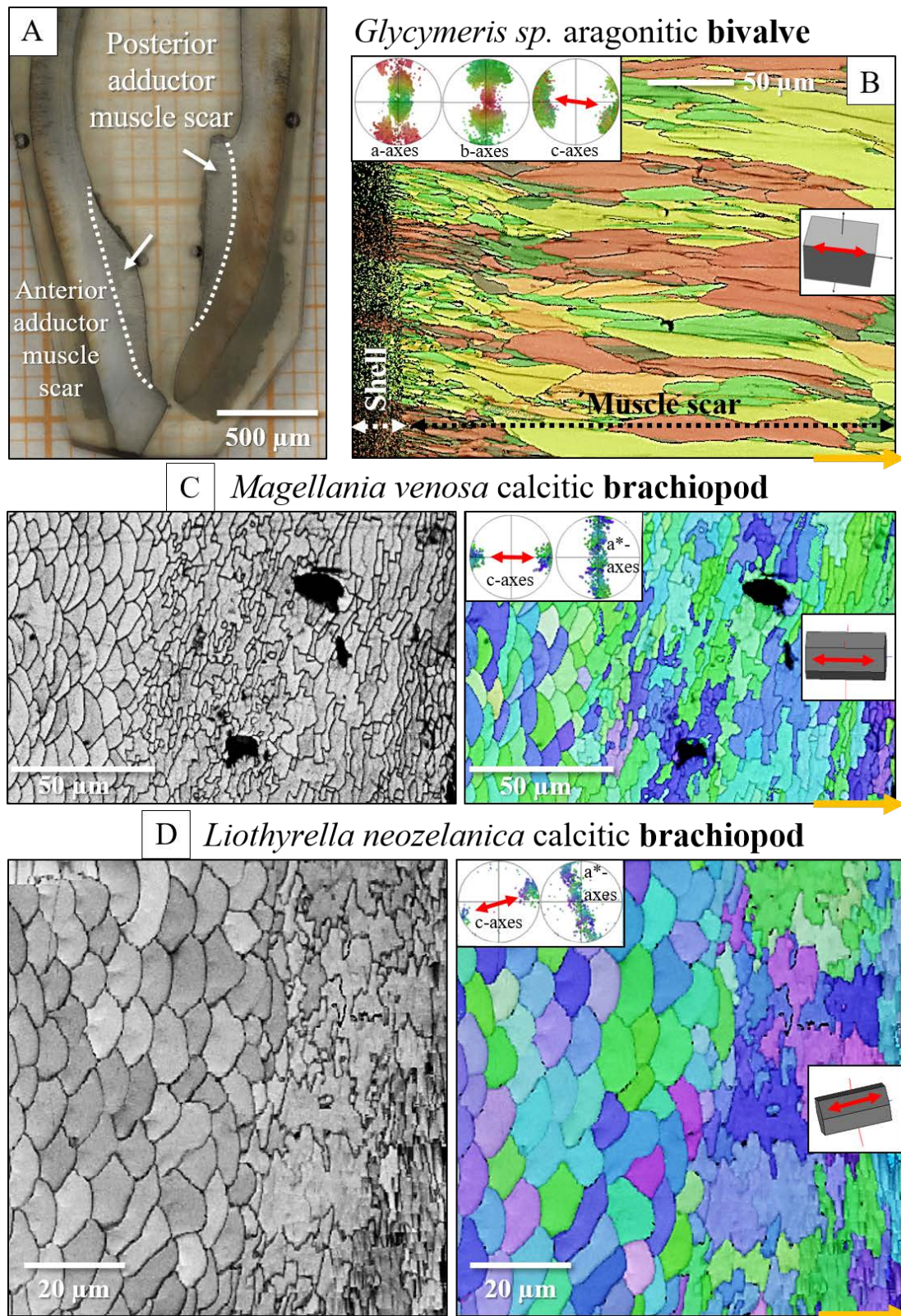


Figure 2.5-14. Juxtaposition of valve/shell microstructure between the muscle scar of a bivalve (here *Glycymeris* sp. (A, B)) and the muscle attachment sites of two-layered and three-layered brachiopod shells (C, D). The EBSD measurement in B is modified after Crippa et al. (2020a). The orange arrows in B to D point towards the inner shell surface, and the red arrows in B to D indicate calcite c-axis orientation directions. A: Confocal laser microscopy overview of a cross-section through *Glycymeris* valves and myostraca, the muscle attachment sites. Bivalve adductor myostraca are macroscopically well visible (white arrows in A). Generally, bivalve adductor myostraca are quite thick and aragonitic, and they have a specific microstructure and texture due to their growth process (Hoerl et al. 2024b; Hoerl et al. 2025b). Although also different in microstructure to the rest of the shell, brachiopod muscle attachment sites are not as prominent as in bivalve myostraca.

Are the muscle attachment sites of Rhynchonellata and Bivalvia convergent in structure?

In the previous section, we described general attributes shared by rhynchonellates and bivalve species. Thus, is the structure, microstructure, and texture of rhynchonellate brachiopod and bivalve muscle attachment site crystals also comparable? Rhynchonellata and Bivalvia overlap in living environment, lifestyle, comparability of the hard tissue mineralisation system, the generation of a hinged valved shell, the movement of the valves via muscles, and the use of similar types of muscles. However, our study shows that the muscle attachment site crystals differ significantly for the investigated species of rhynchonellates and bivalves (Chapters 2.1 to 2.5 of this thesis and Kennedy et al. (1969)). Nonetheless, it should be noted that the crystallographic texture of the muscle attachment site portions of the investigated species is similar. The assembly of the muscle attachment site crystals has an axial texture, with calcite and aragonite c-axis oriented perpendicular to the inner shell surface (Figs. 2.5-9D, E, 2.5-11G, 2.5-12B, C and Chapters 2.1 to 2.4 of this thesis), for both the investigated species of Rhynchonellata and Bivalvia.

When comparing structural-crystallographic attributes of rhynchonellate and bivalve muscle attachment sites, we found that:

1. The muscle scar of bivalves is a prominent, protruding structure (Fig. 2.5-14A), limited in extent to only those valve sections where the muscle bundles directly attach to the valves. For rhynchonellate brachiopods, we observed extensive thickening of the valve portions at and near muscle attachment sites (see Fig. 2.5-2 for dorsal valves). However, the latter is not only present at the sites of muscle attachments but also extends to regions that surround those valve portions where the brachiopod muscles attach to (Fig. 2.5-2A, red rectangle in Fig. 2.5-2B). The innermost layer of the thickened shell portion shows a disturbed microstructure of fractal-like crystals. With distance from the muscle attachment, the layer with the disturbed microstructure thins out and disappears (white arrows in Figs. 2.5-9H, 2.5-11C).
2. One of the most distinctive characteristics is that, in contrast to rhynchonellate brachiopods, the muscle scars of bivalves have a competitive growth-derived microstructure (Fig. 2.5-14B and Hoerl et al. (2025b)). These myostraca consist of prisms with irregular morphologies, assembled in a very specific way that depends upon the microstructure of the adjacent shell layer. This was not observed for the investigated rhynchonellate brachiopod species. As detailed in this contribution, the microstructures of muscle attachment crystals of brachiopod shells are also distinct from the rest of the shell. However, muscle scar crystal formation of brachiopod shells is not generated by competitive growth; the muscle scar crystals have highly irregular morphologies and a very disturbed microstructure (Figs. 2.5-7, 2.5-8, 2.5-14). Irrespective of whether muscle attachment crystals originate from fibres

or columns (Figs. 11A, B, 2.5-12B, C, 2.5-13C, D), their morphologies are fractal-like (Figs. 2.5-10C, 2.5-12C, 2.5-14C, D) and the crystals interdigitate in 2.5-3D,

3. The carbonate phase of brachiopod muscle attachment sites is always calcite, while bivalve muscle scars always consist of aragonite, even when the adjacent shell layer is formed of calcite (Hoerl et al. 2025b). While the reasons for this are not yet fully understood, it might be due to historical restrictions. The earliest bivalve shells were presumably purely aragonitic, and the ability to secrete calcite microstructures may have developed later in bivalves (Wang et al. 2014).
4. The texture pattern of the brachiopod muscle attachment site crystals is similar to that of the adjacent shell layer, and it is not changed with progressive attachment site crystal growth. At first, bivalves also adopt the texture pattern of the adjacent section of the valves if it contains the same calcium carbonate phase (Hoerl et al. 2025b). However, with progressive attachment site crystal growth, the texture of bivalve muscle scar crystals changes slightly (Crippa et al. 2020a; Hoerl et al. 2024b; Hoerl et al. 2025b).

Nonetheless, one characteristic is similar between rhynchonellate brachiopods and bivalves for the muscle attachment site crystals. For species of both invertebrate classes, the carbonate crystal c-axis orientation is perpendicular to the inner shell surface and parallel to the morphological axis of the muscle fibre bundle (Figs. 2.5-8B, 2.5-9D, 2.5-10D, 2.5-11A, B, 2.5-12B, C, 2.5-14B, C, and Chapters 2.1 to 2.4 of this thesis). The analogy of muscle attachment site crystal c-axis orientation for brachiopods and bivalves, relative to the inner shell surface, is rooted in the mode of attachment of the muscle bundles to the attachment site crystals via the tendon cells. It might be required to generate a strong muscle bundle-attachment site crystal connection. The secretion of muscle attachment site crystals by the tendon cells and the orientation of their crystallographic c-axes, relative to the inner shell surface, is a biological convergence trait (for definition see Methods Section 2.5.2) and was most likely developed independently by bivalved species of two invertebrate phyla. Nonetheless, it should be kept in mind that brachiopods and bivalves have a partly comparable habitat preference and lifestyle (MacKinnon 1977; Ponder et al. 2019).

Combining the microstructure and texture results of this study on brachiopod shells with the results gained for bivalve shells (Chapters 2.1 to 2.4 of this thesis), we can state that the microstructure and calcium carbonate phase of bivalve and rhynchonellate brachiopod muscle attachment sites are not convergent. Two main reasons account for the latter:

1. Brachiopods and bivalves are species of different phyla, and varying strategies of Ca-carbonate structural biomaterial formation may have been developed for muscle scar generation.

2. However, the main reason is probably that brachiopods and bivalves apply different solutions for valve opening and closure (Yonge 1967; Wainwright 1982; Shadwick & Gosline 1983; Carlson 1989; Carriker 1996; Tremblay et al. 2015; Guderley & Tremblay 2016).

(i) The bivalve shell comprises two valves, connected along one edge by a flexible hinge ligament (Yonge 1973; Kahler et al. 1976). The bivalve ligament has two parts, an inner and an outer layer (Yonge 1967; Carriker 1996). The bivalve adductor muscle pulls the valves together and closes them, stretching the outer layer of the ligament and compressing its inner portion (Wainwright 1982; Shadwick & Gosline 1983). At the release of the adductor muscle contraction, the elastic recoil of the inner ligament layer opens the two valves (Wainwright 1982; Shadwick & Gosline 1983).

(ii) The brachiopod shell does not have a hinge ligament. Brachiopods have a toothed hinge with a pair of teeth and a pair of sockets (James et al. 1992). Brachiopods use only their muscle system for closing and opening their valves, the adductor muscles for closing, and the diductor muscles for opening them (James et al. 1992). In contrast to bivalves, brachiopod valve closure is a two-stage process, consisting of a rapid and a slow but prolonged valve movement. As described in this study, each trunk of the pair of adductors has two branches, a striated and a smooth adductor branch (Figs. 2.5-6, 2.5-S2). And, as also shown in this study, the two adductor branches attach adjacent, however, to different sites to the dorsal valve (e.g., Fig. 2.5-1B). The striated adductor branch is the quick, the smooth adductor branch is the catch muscle. The quick muscle initiates a rapid valve closure, while the catch muscle induces the complete closure of the valves and holds these shut for a long period (Rudwick 1961; Thayer 1975; Ackerly 1993). The latter phenomenon is not observed for bivalves.

Hence, even though secreted by similar mantle epithelial cells and utilising similar types of muscles, the muscle imprints generated at attachment to the inner valve surface are not and cannot be identical for rhynchonellate brachiopods and bivalves, as different valve opening and closing mechanisms are developed. Accordingly, with the study of rhynchonellate and bivalve muscle attachment sites, we showcase that the mechanism of generating specific sections for attaching valve-operating muscles is similar in both classes. However, the distantly related classes Bivalvia and Rhynchonellata approach the structural formation of shell microstructures at valve-muscle attachment sites differently.

2.5.5 CONCLUSIONS

Morphological analogies, overlapping habitats and similarity in lifestyle between rhynchonellate brachiopods and bivalved molluscs invite comparisons of the physiology of organisms that form these two invertebrate classes (Rudwick 1961; Wilkens 1978). Like bivalves, brachiopods open and close their shells with muscles that exhibit phasic and tonic contractions. These enable fast

and sustained valve opening and closing. However, unlike bivalves, the valves of brachiopods are located dorsally and ventrally to the soft tissue body. Furthermore, unlike bivalves, the valves of rhynchonellate brachiopods are opened with a pair of diductor muscles and lack the involvement of an elastic hinge ligament, as developed by bivalves ((Wilkins 1978) and references therein).

Distinct imprints mark the sites of attachment of brachiopod and bivalve muscle bases on the inner surfaces of their shells. The imprints result from modifications of the ultrastructure and secretory behaviour of epithelial cells that perform the secretion of the shell. Our study aimed to visualise the structure of rhynchonellate brachiopod adductor, diductor and adjustor muscles, to visualise the adductor muscle imprints on the valves and, in particular, to investigate structural characteristics of brachiopod muscle attachment site crystals and of their assemblies. In a wider perspective, an important aim of our study was to discuss the notion of convergence for the microstructure and texture of muscle attachment sites of the Rhynchonellata and the Bivalvia.

We deduce the following conclusions from the results of this study:

1. In rhynchonellate brachiopods, the adductor and diductor muscle bases attach to calcite fibres and to calcite columns.
2. The attachment site crystals have very irregular, fractal morphologies. Adjacent attachment site crystals interdigitate markedly in 3D. The attachment site portion of the valves is intimately connected to the non-attachment site sections of the shell.
3. There is a marked difference in microstructure between the inner shell surface of the attachment site and the non-attachment site valve sections. The texture of the attachment site and non-attachment site calcite is similar. We found an axial texture for both.
4. The difference in microstructure between attachment site and non-attachment site valve sections results from the difference in the ultrastructure and secretory behaviour of the secreting cells. A layer of cuboidal, tendon cells secretes the muscle attachment site crystals, while the crystals of the rest of the shell are mainly secreted by columnar cells.
5. Attachment site calcite c-axis orientations are perpendicular to the inner shell surface and parallel to the morphological axis of the muscle bundles. This is a finding we observed for species of Rhynchonellata and Bivalvia and is, most probably, necessary for a strong muscle base-tendon cell polymer fibril-crystal attachment.
6. Regarding the structural convergence for muscle attachment sites of rhynchonellate brachiopods and bivalves, we could find some structural characteristics of muscle attachment sites that are similar for species of the investigated invertebrate classes. For both invertebrate classes, the texture of the adjacent shell layer continues in the microstructure of the muscle attachment layer. This may derive

from the determinants of the similar secreting epithelial cells underlying the muscle attachment sites. However, it should be kept in mind that valve actions are realised differently by rhynchonellate brachiopods and bivalves. Bivalve valve movement is not only the result of muscle action, but also the involvement of the hinge ligament. In contrast, rhynchonellate brachiopods do not involve a ligament in valve motion, but solely utilise their muscles. Thus, different constraints operate on muscle involvement when opening and closing the valves for rhynchonellate brachiopods and bivalves and are a determining factor in the generation of the structural differences that were observed between rhynchonellate and bivalve muscle attachment sites.

7. The action of opening and closing the valves is realised differently by rhynchonellate brachiopods and bivalves. Bivalve valve movement not only results from muscle action, but also involves hinge ligament action. In contrast, rhynchonellate brachiopods do not involve a ligament in valve motion; they solely employ muscles. Thus, different constraints operate on muscle involvement at opening and closing the valves for rhynchonellate brachiopods and bivalves. These might be determining factors in the formation of the differences that were observed between rhynchonellate and bivalve muscle attachment sites.

Acknowledgments

We thank Tingting Zhu, Max Planck Institute of Colloids and Interfaces, Department of Biomaterials, Potsdam, Germany, and Chiara Micheletti, Max Planck Institute of Colloids and Interfaces, Department of Biomaterials, Potsdam, Germany and Chalmers University of Technology, Gothenburg, Sweden, for their help with imaging on the Thermo Scientific Quattro ESEM. We thank Antonio G. Checa, University of Granada, Spain, and Sandra J. Carlson, University of California, Davis, United States, for their valuable comments discussing the data.

W.W.S., E.G., and S.H. were funded by the German Research Council Programmes GR 9/1234, SCHM 930/11-2.

Author contributions

Conceptualisation, S.H., E.G.; Formal analysis, V.H., M.A.B., W.W.S.; Investigation, S.H., E.G., D.W., S.A.; Methodology, S.H., E.G., D.W., S.A., K.A., F.P.; Supervision, E.G., S.A., W.W.S.; Validation, V.H., M.A.B; Visualization, S.H., E.G; Writing – original draft, S.H., E.G; Writing – review & editing, D.W., S.A., V.H., M.A.B, K.A., F.P..

2.5.6 SUPPLEMENTARY INFORMATION

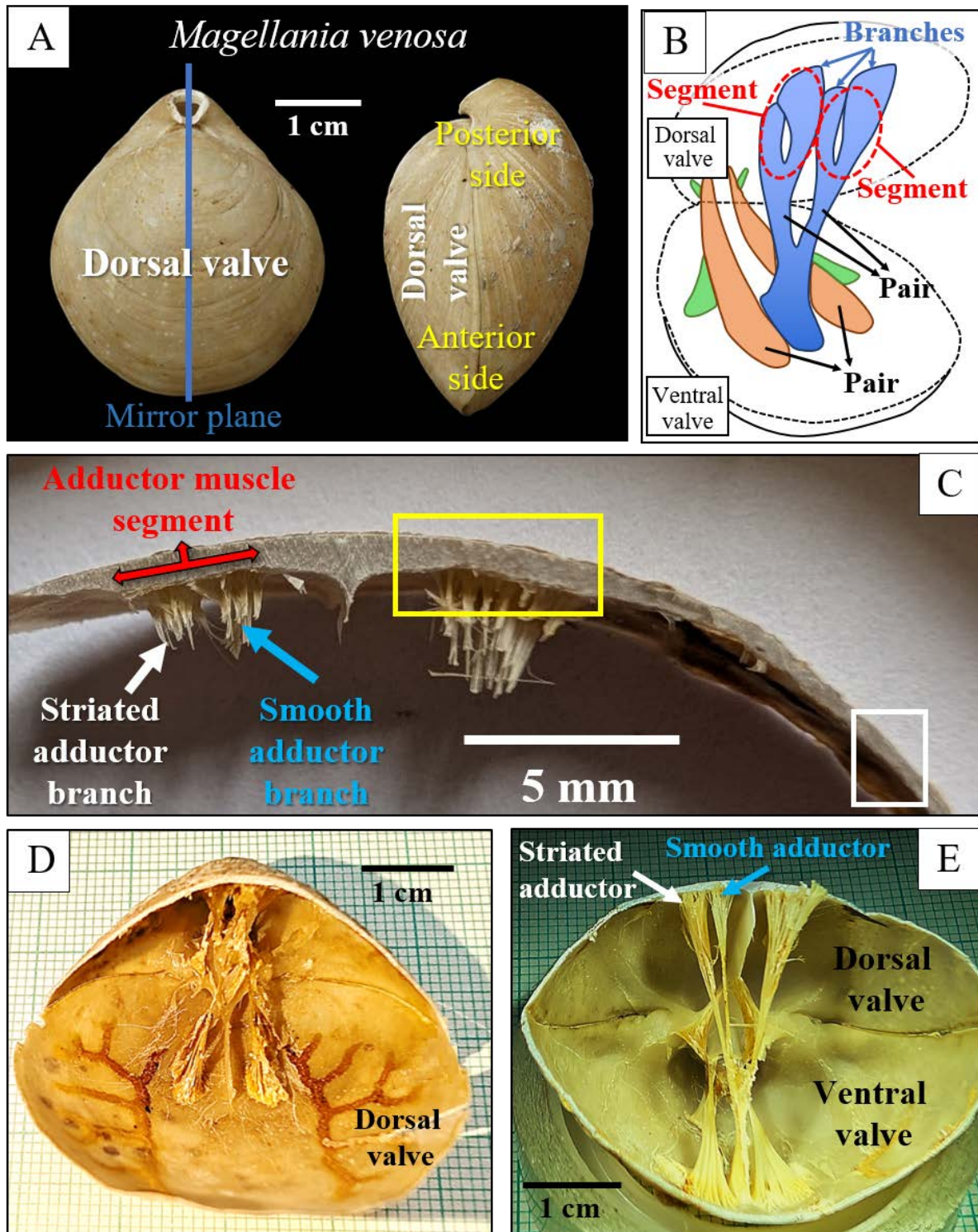


Figure 2.5-S1. A: The ventral and dorsal valves of modern rhynchonellate brachiopod shells, i.e., *Magellania venosa*. The image shows the course of the mirror plane through the valves and the definition of the shell's posterior and anterior shell portions. B: Schematic illustration of a brachiopod shell defining brachiopod muscle branches, segments and pairs. C: A typical shell cross-section through the valve and the attaching muscle bundle before embedding. The adductor muscles are in position, relative to the adjacent shell. The topological distinction between smooth and striated adductors within an adductor muscle segment is well visible. Compared to the rest of the shell (white box in C), the thickness of the shell is enhanced at the regions of adductor muscle attachment, as well as the hinge (yellow box in C). D, E: light micrographs of *M. venosa* indicate the muscle structure and distribution within the valves.

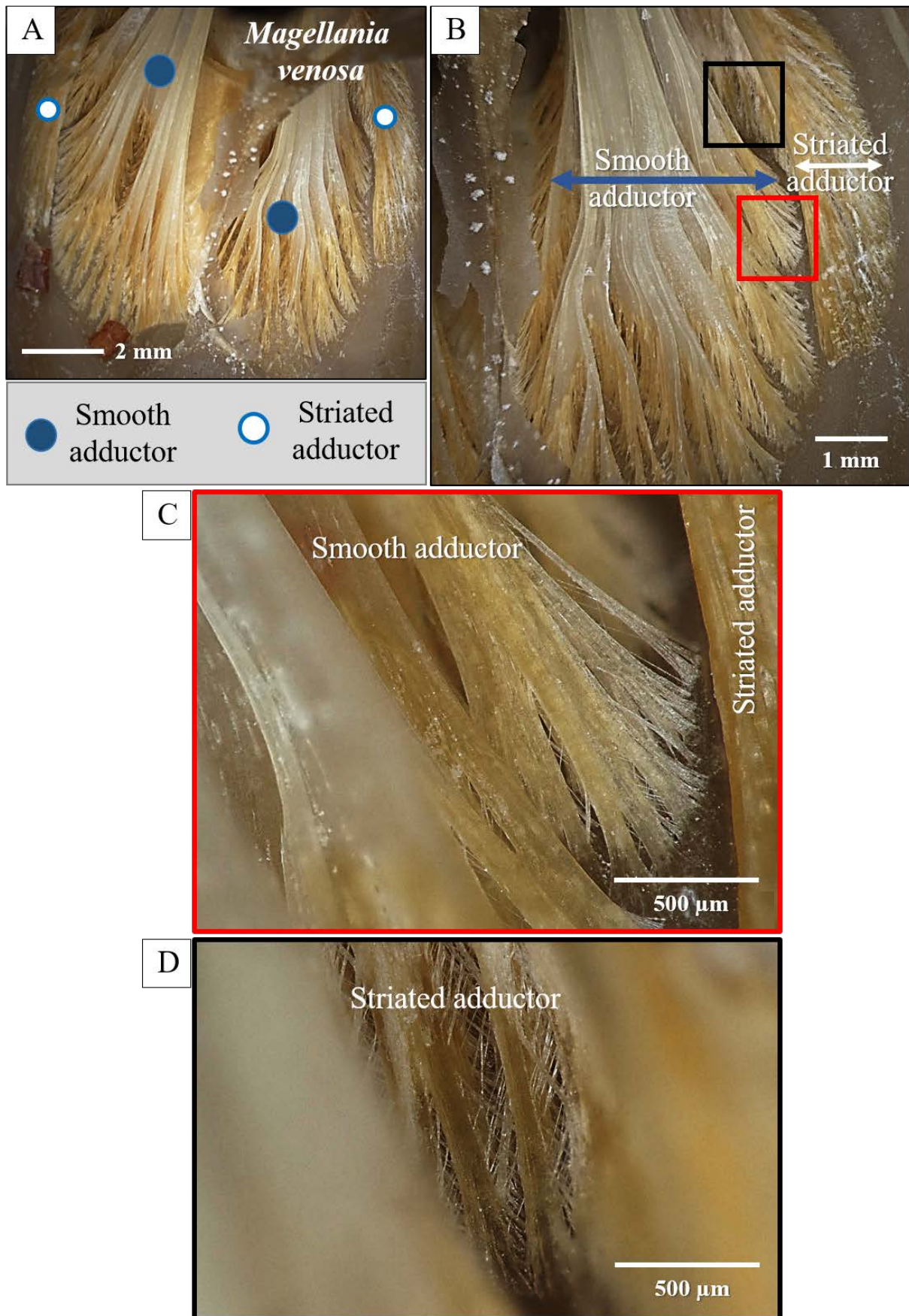


Figure 2.5-S2. A to D: Digital micrographs show the difference in the internal structure of *Magellania venosa* smooth and striated adductor muscle bundles. C, D: Close-up images highlighting the distribution and interconnection of the smooth (red box) and striated (black box) adductor muscles.



Figure 2.5-S3. Digital micrographs of *Liothyrella neozelanica* smooth and striated adductors (B) and the tendon (side view: C; top view: D) generated from the merged dorsal valve adductors. A: Sketch, visualising the distribution and attachments of modern rhynchonellate muscles to the shell valves.

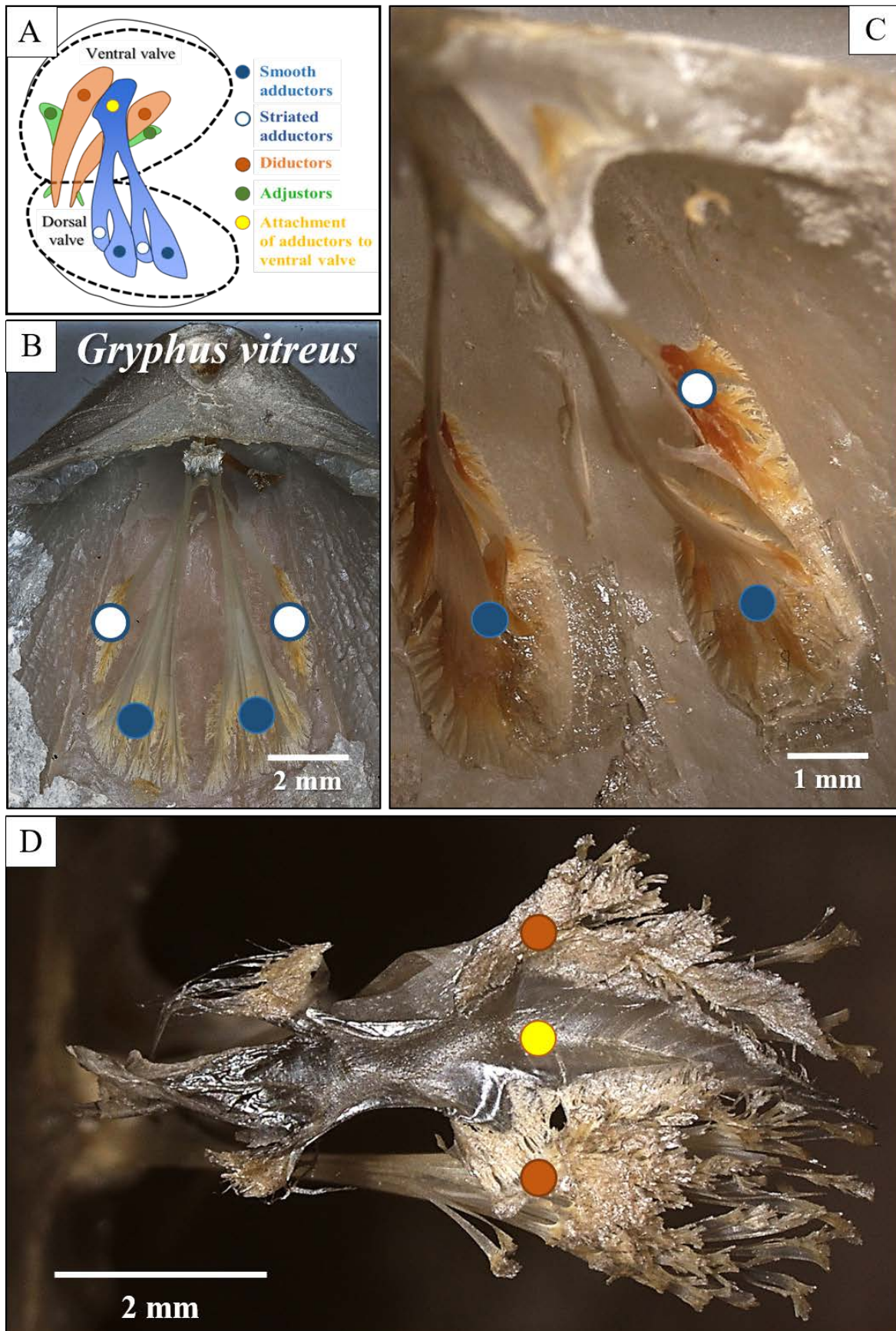


Figure 2.5-S4. Visualisation of *Gryphus vitreus* shell and muscle features. A: Sketch visualising the valve-moving muscles of modern rhynchonellate brachiopod shells. B to D: Digital micrographs of the shell of *G. vitreus*. Well visible is the topological distinction between the smooth and striated adductors (B, C). D: Top view onto the tendon, formed of merged dorsal valve adductors, between the overlapping diductors.

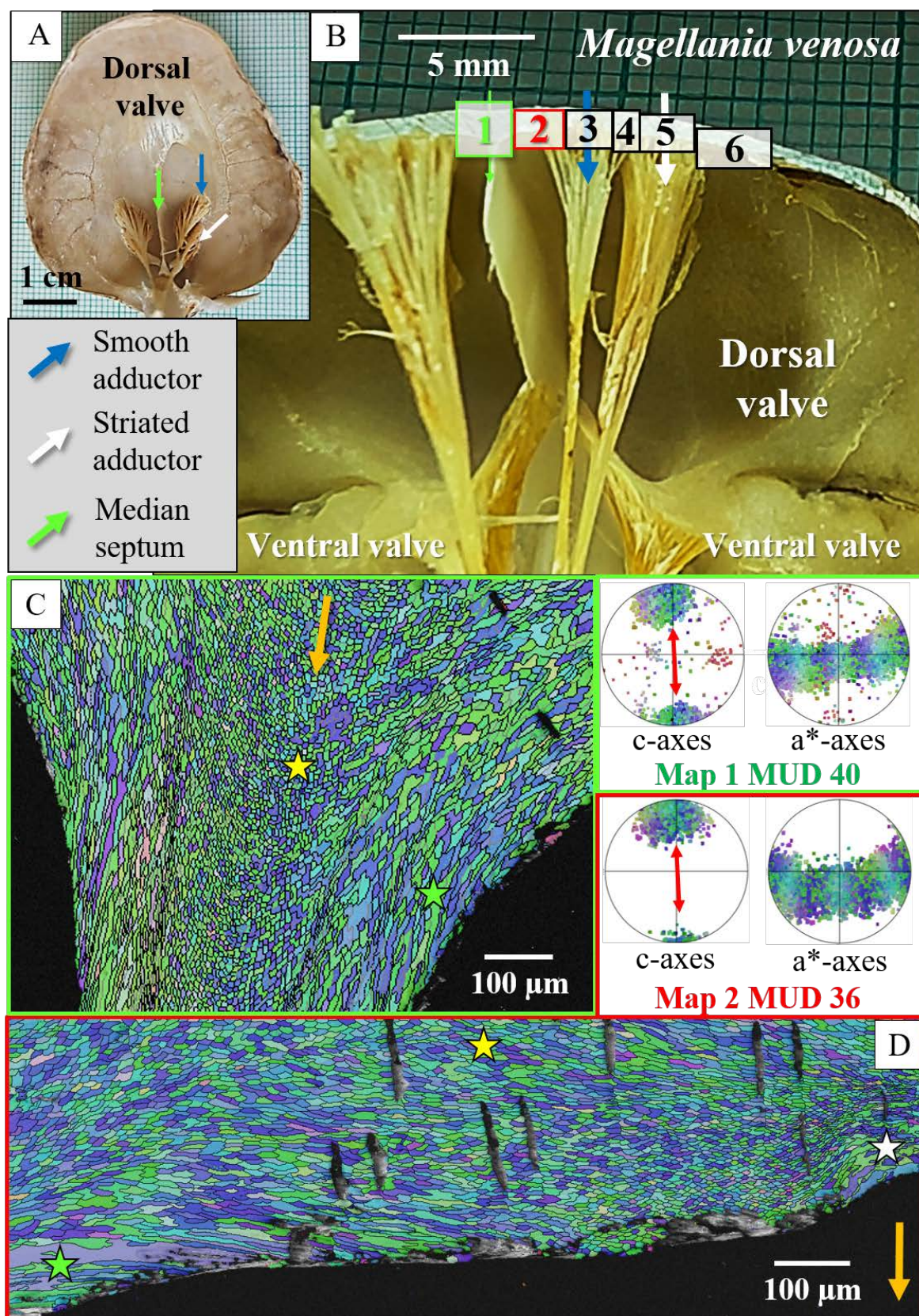


Figure 2.5-S5. Microstructure near the hinge (green arrows in A, B) in *Magellania venosa* shells. The positions of the EBSD maps are indicated in B. Colour-coded EBSD maps show that the hinge comprises organised fibres in the centre of the shell (yellow stars in C, D) and elongated fibres at the inner hinge surface (green stars in C, D). Towards the smooth adductor muscle site, the crystals show disturbed morphologies and interdigitate in 3D (white star in D). The hinge (C) and the valve section near the hinge (D) show axial textures with the c-axes (indicated by red arrows in the pole figures in C, D) oriented parallel to the growth direction (indicated by orange arrows in C, D).

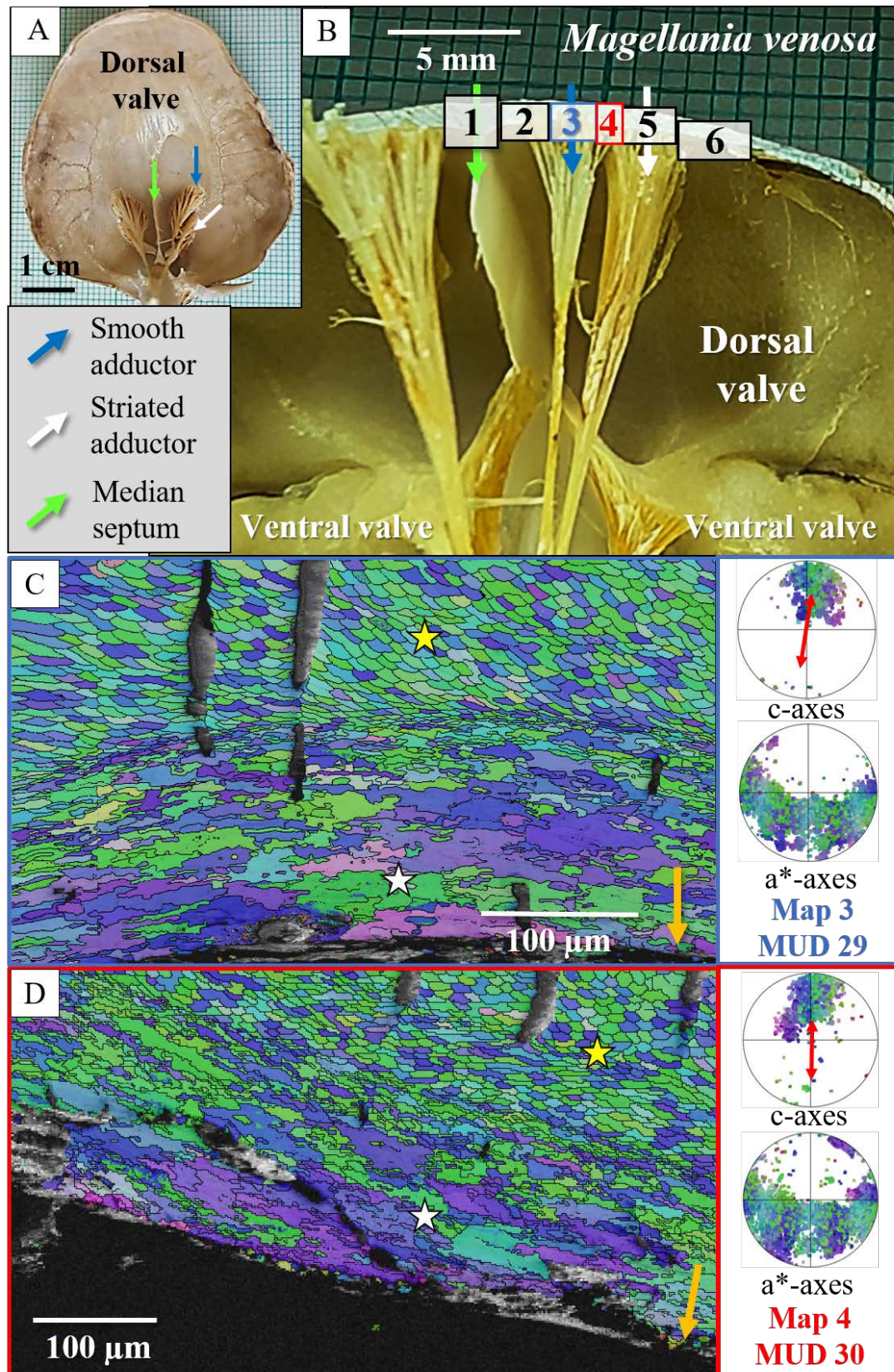


Figure 2.5-S6. Microstructure near the smooth adductor muscle bundle (blue arrows in A, B) in *Magellania venosa* shells. The positions of the EBSD maps are indicated in B. Colour-coded EBSD maps show that the smooth adductor muscle site comprises organised fibres in the centre of the shell (yellow stars in C, D) and interdigitating, disturbed crystal morphologies at the inner shell surface (white stars in C, D). The valve section between the smooth and the striated adductor muscle sites is indistinct in microstructure from the muscle attachment sites (D). Both measurements show axial textures with the c-axes (indicated by red arrows in the pole figures in C, D) oriented parallel to the growth direction (indicated by orange arrows in C, D).

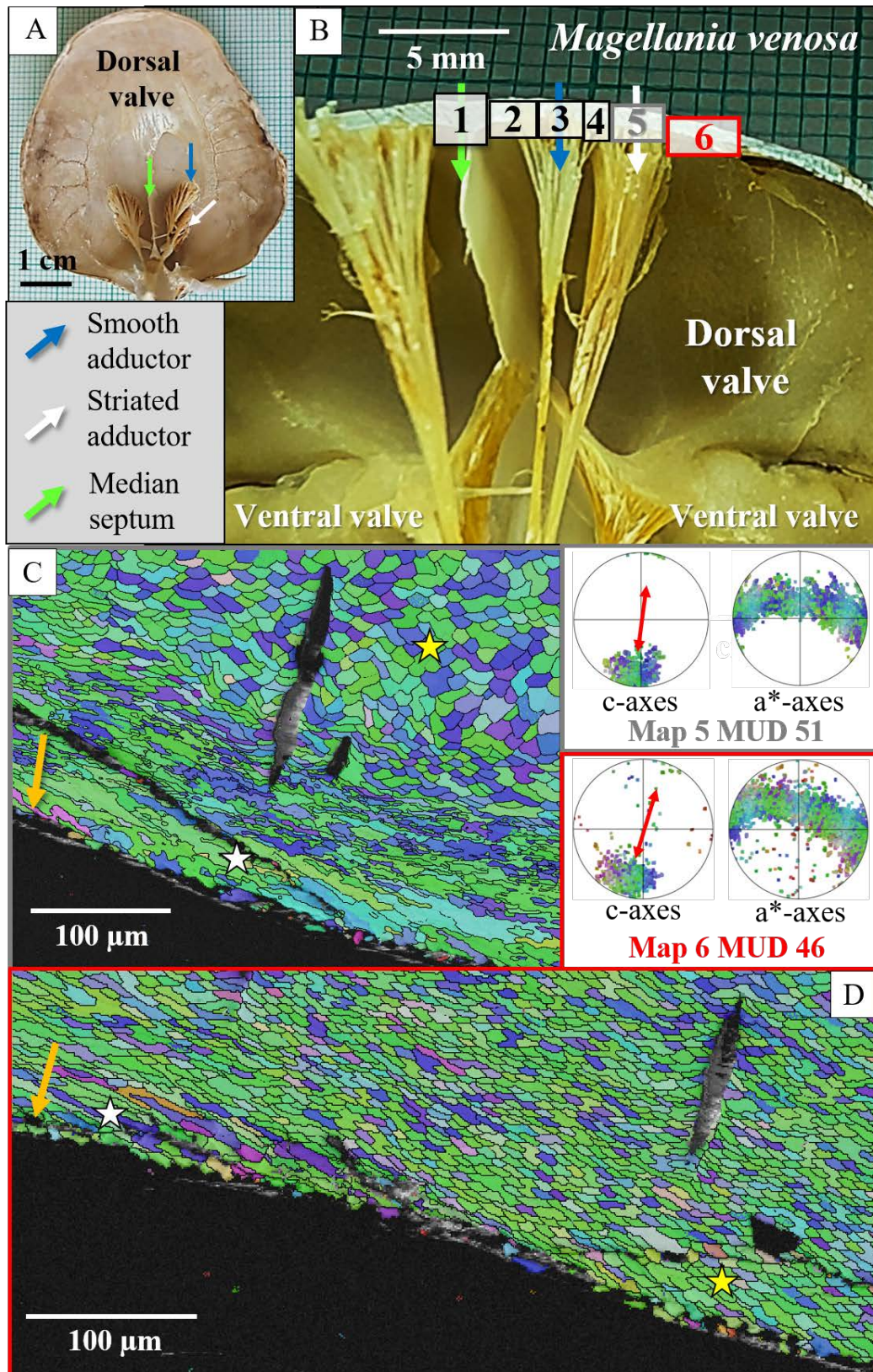


Figure 2.5-S7. Microstructure near the striated adductor muscle bundle (white arrows in A, B) in *Magellania venosa* shells. The positions of the EBSD maps are indicated in B. Colour-coded EBSD maps show that the striated adductor muscle site comprises organised fibres in the centre of the shell (yellow star in C) and interdigitating, disturbed crystal morphologies at the inner shell surface (white star in C). With distance from the muscle attachment sites, the irregular microstructure (white star in D) gradually thins out into the organised fibre crystal morphology (yellow star in D). Both measurements show axial textures with the c-axes (indicated by red arrows in the pole figures in C, D) oriented parallel to the growth direction (indicated by orange arrows in C, D).

2.6 EVALUATING THE SINGLE CRYSTALLINITY OF SEA URCHIN CALCITE

Sebastian Hoerl^{1,*}, Erika Griesshaber¹, Antonio G. Checa², Aimo Winkelmann³, Frank Förster^{1,4},
Osama Alsheikha^{1,5}, Felix Hidalgo⁶, Elena Sturm¹, Sandro Jahn¹, Wolfgang W. Schmahl¹

¹ Department für Geo- und Umweltwissenschaften, Ludwig-Maximilians-Universität München, 80333 Munich, Germany

² Departamento de Estratigrafía y Paleontología, Universidad de Granada, 18071 Granada, Spain

³ Academic Centre for Materials and Nanotechnology (ACMiN), AGH University of Krakow, 30-059 Krakow, Poland

⁴ Department of Earth Sciences, University of Geneva, 1205 Geneva, Switzerland

⁵ Faculty of Biology, Chemistry & Earth Sciences, University of Bayreuth, 95447 Bayreuth, Germany

⁶ Departamento de Zoología, Universidad de Granada, 18071 Granada, Spain

Acta Biomaterialia 2025, 198, 334-355.

<https://doi.org/10.1016/j.actbio.2025.03.044>

Abstract

Recent advancements in electron backscatter diffraction (EBSD) data evaluation enable the determination of misorientation between crystals below 0.1°, while with conventional EBSD data evaluation, the smallest misorientation precision between crystals scatters between 0.5°-1°. Sea urchin tests and spines are lightweight biomaterials with a serrated microstructure comprising interlinked calcite crystals. We investigated the microstructure and crystallographic texture of *Cidaris cidaris* and *Paracentrotus lividus* test and spine calcite with advanced EBSD measurement and data evaluation. In particular, we re-evaluated the widely accepted single-crystallinity of sea urchin calcite. We found that the test and the spines comprise calcite crystals with different fabrics and a significant variation in crystal co-orientation strength. Even the highly co-oriented calcite of *C. cidaris* and *P. lividus* is not perfectly single-crystalline. We found test and spine portions that feature significant internal misorientations (1-3°). Test c-axis orientation in *C. cidaris* is tangential to the outer test surface, while in the spines, it is parallel to the morphological axis of the spine. Primary and secondary spines feature a bimodal crystal texture comprising co-oriented calcite surrounded by a cortex of misoriented crystals. Crystal misorientation in the spine cortex seems to result mainly from competitive growth determinants. Deciphering the degree of crystallinity and mode of crystal organisation of biological hard tissues is vital for understanding their exceptional control of structure, material architecture and material properties.

Keywords

EBSD; biomineralisation; sea urchins; EBSD matching; microstructure/texture

2.6.1 INTRODUCTION

Echinoids are among the many organisms that secrete Ca-carbonate skeletons, which serve various functions, including locomotion and protecting their soft tissue and major organs from environmental hazards (Strathmann 1981; Domenici et al. 2003). In contrast to molluscs, brachiopods and bryozoans that use an epithelial system for hard tissue mineralisation, echinoderms use a syncytium for mineral formation (Simkiss & Wilbur 1989). The epithelial system of biomineralisation involves the transfer of ions, secretes proteinaceous substances and minerals and generates rather compact layers of a composite material, which, in general, consists of a structured biopolymer matrix filled with small-sized crystals (Simkiss & Wilbur 1989). At biomineralisation via syncytia, the cells generate large three-dimensional mineral units with a perforated pattern (Simkiss & Wilbur 1989). Forming sizable skeletal elements of large fenestrated crystals enables the fabrication of structures that are lightweight and, at the same time, rigid and resistant (Wainwright 1982; Simkiss & Wilbur 1989). Indeed, many studies demonstrate how echinoderms profit from their lightweight skeletons having exquisite mechanical properties (Hasenpusch 2000; Lai et al. 2007; Nickel et al. 2009; Yang et al. 2022a; Yang et al. 2022b; Perricone et al. 2023). Echinoids form their skeleton and skeletal elements of high-Mg calcite (Weber 1969). The calcite comprises the test (composed of many large crystal plates with a stereom architecture), the spines (anchored by muscles entwined around the struts of the test tubercles), the pedicellariae (stalked appendages containing skeletal supports protruding from the surface of the test) and the chewing apparatus (consisting of the jaw bone that surrounds the five teeth). The latter is present in many, but not in all echinoids (Weber 1969; Wang et al. 1997; Dubois & Ameye 2001). Nonetheless, even though the test covers the soft tissue of the organism, the echinoid test is regarded to be a mesodermal internal skeleton, with the test encasing the major organs of the animal. The outer surfaces of the test and spines, however, are coated by a thin layer of skin and muscles.

The crystallography of echinoderm calcite crystals is well-investigated by now (Raup 1960; Raup 1962a; Magdans & Gies 2004). Each echinoid skeletal element has a specific crystallographic pattern that, in general, is consistent within sea urchin species, genera, families, and even orders (Bodenbender 1997). The crystal texture of echinoid tests shows two modes of crystallographic calcite axes orientation: The c-axes are oriented either (1) perpendicular to the test plate surfaces or (2) tangential to the curvature of the test in the aboral direction (Raup 1959). In the case of the spines, the orientation of the calcite crystallite c-axes follows the orientation of the morphological long axes of the spines (Su et al. 2000).

Nonetheless, even though sea urchin calcite crystal orientation patterns are well determined by now, the crystallinity of the calcite is still controversial and under debate. The question that is not resolved yet is whether the crystals or crystallites of the test and the spines are single crystals, mesocrystals, or even little textured polycrystals. Hence, assessing the degree of misorientation between adjacent crystals/crystallites is of main scientific importance. X-ray diffraction studies of Su et al.

(2000), Moureaux et al. (2010), Nissen (1969) and Donnay & Pawson (1969), and results of the etching protocols of Okazaki et al. (1981) suggest that sea urchin spines are large single crystals, while the studies of Seto et al. (2012), Aizenberg et al. (1997) and Cölfen et al. (2022) define the calcite of sea urchin spines as meso- or mosaic crystals.

The development of high-resolution crystallographic analysis techniques, particularly electron backscatter diffraction (EBSD), allows us to refine our knowledge of the crystallography of individual crystals obtained from transmission electron microscopy (TEM) imaging and texture determination with X-ray diffraction (XRD) measurements and Rietveld data analysis. In contrast to XRD or TEM, EBSD measurements provide spatially resolved information and have a significantly larger field of view. This renders the EBSD technique as a powerful technique for material science, in particular, for the analysis of structural hard tissues, biologically secreted or man-made. However, a key factor for high-resolution EBSD measurements is its angular precision. The main factors influencing and determining the angular precision of EBSD scans are the method used for identifying and locating the EBSD pattern and the selected pattern indexing technique. With conventional Hough-based indexing techniques, EBSD can perform minimal misorientation determination with an angular orientation precision between 0.5° and 1° (Zaefferer 2011). Recently, new approaches to EBSD pattern indexing have been developed, which are based on the direct correlation between experimentally determined and simulated EBSD patterns (Nolze et al. 2017; Lenthe et al. 2019; Winkelmann et al. 2020; Trimby et al. 2024). This results in a marked improvement in angular precision and allows the determination of misorientation between adjacent crystals below 0.1° . Accordingly, the above described advanced EBSD pattern indexing technique (subsequently named EBSD pattern matching) enables the determination of minute misorientations in a crystalline material. Sea urchin calcite is ideal for investigating misorientations and, particularly, minute misorientations in a structural material, as it was, up to now, often regarded to be a single-crystalline biomaterial (Magdans & Gies 2004; Ma et al. 2008).

In this study, we investigate in great detail the test and spine calcite of the sea urchin *Cidaris cidaris* (Linnaeus, 1758). We complement our results with measurements gained on the test and spine of *Paracentrotus lividus* (Lamarck, 1816). The class Echinoidea consists of two sub-classes, Perischoechinoidea and Euechinoidea. For comparative reasons, we chose to investigate the calcite of a species belonging to Perischoechinoidea (*C. cidaris*) and of a species belonging to the Euechinoidea (*P. lividus*). Both species live in comparable marine environments, in waters of the eastern Atlantic and of the Mediterranean Sea (Colombero et al. 1977), are epibenthic and dwell on all types of surfaces of the shelf region (Mortensen 1927; Tyler & Gage 1984). While *P. lividus* inhabits shallower and more highly energetic habitats, *C. cidaris* is mostly found in quieter environments and deeper waters (Boudouresque & Verlaque 2020; ed. Lawrence 2020). For protection and locomotion, *C. cidaris* uses its test but also its long and, from each other, widely separated primary and the smaller, on the test densely distributed, secondary spines (Strathmann 1981). In *C. cidaris*, each interambulacral plate features one primary

spine. The latter is surrounded by multiple secondary spines which protect the primary muscle attachment zones together with the pedicellariae (Coppard et al. 2012; ed. Lawrence 2020; Hebert et al. 2024). For *P. lividus*, the protective test is very densely covered with the long and sharply pointed primary spines as well as with the small secondary spines. This study is part of a larger project aiming to understand the microstructure and crystallographic texture of echinoid skeletal elements, investigating, in particular, the nature of the misorientations between the calcite crystallites (Battas 2023).

Using high-resolution EBSD for our microstructural analysis, we report both EBSD measurements and maps evaluated with conventional and electron backscatter pattern matching modes. First, we give an overview of the crystallographic architecture of the test, the tubercles as well as the primary and secondary spines. We highlight the misorientations found in the above-mentioned sea urchin skeletal elements. These were, previously, reported to be single-crystalline (Magdans & Gies 2004). We show the misorientation angle distribution gained from conventional EBSD data evaluation as well as refined by the EBSD pattern matching method and highlight the range of misorientations in the calcite of the investigated sea urchin species. For *P. lividus* and *C. cidaris*, we detected a wide range of crystal co- and misorientation. Some stereom sections comprise crystals that have a single crystal-like co-orientation. However, we also detected stereom sections with small-angle misorientations ($< 2^\circ$) and, strikingly, stereom regions that feature a polycrystalline microstructure with large-angle misorientations ranging up to a few tens of degrees. We show with our study how EBSD analysis combined with the pattern matching method can be used to refine the microstructural and crystallographic information obtained for echinoid skeletal elements. To our knowledge, this is the first study applying the pattern matching method to biomineralised hard tissues. It is a technique that might also be useful to understand in greater detail the microstructure of further complex hard tissues, such as bones, teeth and enamel.

Accordingly, based on the misorientation between crystals, we detected that the calcite of the investigated sea urchin species is structured. It can be highly co-oriented; however, it can also be almost untextured with a low crystallographic co-orientation. This is a very surprising finding and demonstrates that sea urchin calcite is not as single-crystalline as previously suggested by many studies (Su et al. 2000; Ma et al. 2008).

2.6.2 MATERIALS AND METHODS

Materials

The study was performed on two species of sea urchins in the class of echinoids, namely *Cidaris cidaris* (Linnaeus, 1758) and *Paracentrotus lividus* (Lamarck, 1816). The sampling area for the

specimens is five nautical miles south of Isola d'Elba (Italy) in the central-northern part of the Mediterranean Sea (approx. 42°39' N 10°17' E). The species were collected in May 2014 in the sublittoral zone at 80 – 100 m depth as by-catch from a bottom set net. The sampled seabed consists mainly of coralline algae pebbles (maerl), a typical Mediterranean underwater substrate at dim light conditions (Ballesteros 2006). The sea urchins had been air-dried when used for sample preparation.

Sample preparation for electron backscatter diffraction

Four *C. cidaris* and four *P. lividus* specimens were dissected to investigate the large primary and shorter secondary spines, as well as the test. The present study examined two primary spines, three secondary spines, and two tests for each species. The spines and the tests were embedded into EPON epoxy resin and were subjected to several mechanical grinding and polishing steps. The final polishing step involved etch-polishing with colloidal alumina (particle size $\sim 0.06 \mu\text{m}$) in a vibratory polisher. Samples were coated with 4–6 nm of carbon for EBSD analysis, with 5 nm Pt/Pd for SEM imaging. For laser confocal imaging, sample surfaces were not coated.

Secondary electron (SE), backscatter electron (BSE) imaging and electron backscatter diffraction (EBSD) measurements

SE, BSE imaging and EBSD measurements were carried out with a Hitachi SU5000 field emission SEM equipped with an Oxford Instruments NordlysNano EBSD detector and an X-Max 80x80 EDS detector. EBSD scans were taken at 20 kV and were performed with a step size of 300 to 450 nm. EBSD data were evaluated using the Oxford Instruments AZtecCrystal 3.0 and HKL Channel 5.0 conventional software as well as the Oxford Instruments AZtecCrystal MapSweeper software. For MapSweeper, the orientation of the EBSD patterns was refined by calcite simulations with the lattice parameters $a=4.99 \text{ \AA}$, $b=4.99 \text{ \AA}$ and $c=17.07 \text{ \AA}$. The latter implements an efficient pattern matching method for EBSD data evaluation and significantly improves angular precision (Trimby et al. 2024).

Misorientation diagrams report the cumulative misorientation along profiles, i.e. the misorientation compared to the starting point of the profile that functions as a fixed reference. Misorientation values are averaged over five pixels width to enhance data comparability and minimize statistical errors. For the pattern-matched Kernel average misorientation maps, we displayed a range in misorientation between 0° and 2° , with a Kernel filter size of 9×9 . For the pattern-matched map in Fig. 2.6-2e, the data points display the misorientation to the measurement's average crystallographic orientation. The map, generated with the latter texture component, allows us to see the global influence of structures, such as growth increments, but impedes to visualize local misorientations. Our study is based on 74 EBSD measurements.

An in-depth terminology of the structural terms used in this work can be found in Appendix Section A.1 of this thesis.

2.6.3 RESULTS

This study highlights the microstructure and texture of the *C. cidaris* (Perischoechinoidea) test as well as primary and secondary spines (Figs. 2.6-1 to 2.6-10, 2.6-AP1 to 2.6-AP5). We complement the structural results gained on *C. cidaris* calcite with microstructure and texture measurements made on *P. lividus* (Euechinoidea) tests and spines (Figs. 2.6-11, 2.6-12). For both species, EBSD data were evaluated using conventional Hough transformation-based indexing and EBSD pattern matching. To better understand crystal orientation patterns, both species' test and spines were sectioned in two directions (Figs. 2.6-1c, 2.6-AP3). Laser confocal microscopy images depict overviews of the surfaces scanned with EBSD and show the site of EBSD scans. The microstructures are visualised with EBSD maps featuring the inverse pole figure (IPF) colouring method with reference direction X (e.g., Fig. 2.6-1a). The crystallographic texture is given with pole figures that display the density distribution of the crystallographic c- and a*-axes poles. The crystallographic-structural and biological terminology is defined in the Terminology Section A.1 and is illustrated in Supplementary Figure 2.6-AP3.

Figure 2.6-1 gives an overview of EBSD measurements performed on the two cuts through the test of *C. cidaris*. The first cut traverses the entire test from the oral to the aboral side, exposing a circular cross-section of the shell (Fig. 2.6-1a, c). The direction of the second cut is perpendicular to the first cut, traversing the interambulacral area of the test from the mouth to the anus of the animal (Fig. 2.6-1b, c). The sites of the conducted EBSD scans are displayed on confocal microscopy overview images (Fig. 2.6-1a, b). For each EBSD scan, the orientation of calcite crystals is indicated using sketched crystals and pole figures. Many pole figures show multiple density distribution maxima (Fig. 2.6-1a), demonstrating that the test comprises different crystallographic units, termed crystal plates. These crystals and/or crystal plates are large, mm-sized, units. In both cuts, adjacent crystal plates vary in orientation and gradually shift in c- and a*-axes orientation (see pole figures in Figs. 2.6-1a, b). Calcite c-axes are oriented parallel to the outer test surface and rotate with the outer surface of the test (Figs. 2.6-1a, b). Because cut 1 is off-centre from the anal and oral areas, the bottom and top plates appear to be oriented perpendicular, rather than parallel, to the outer test surface (Fig. 2.6-1a, b, the corresponding sketched crystals are marked with a red star).

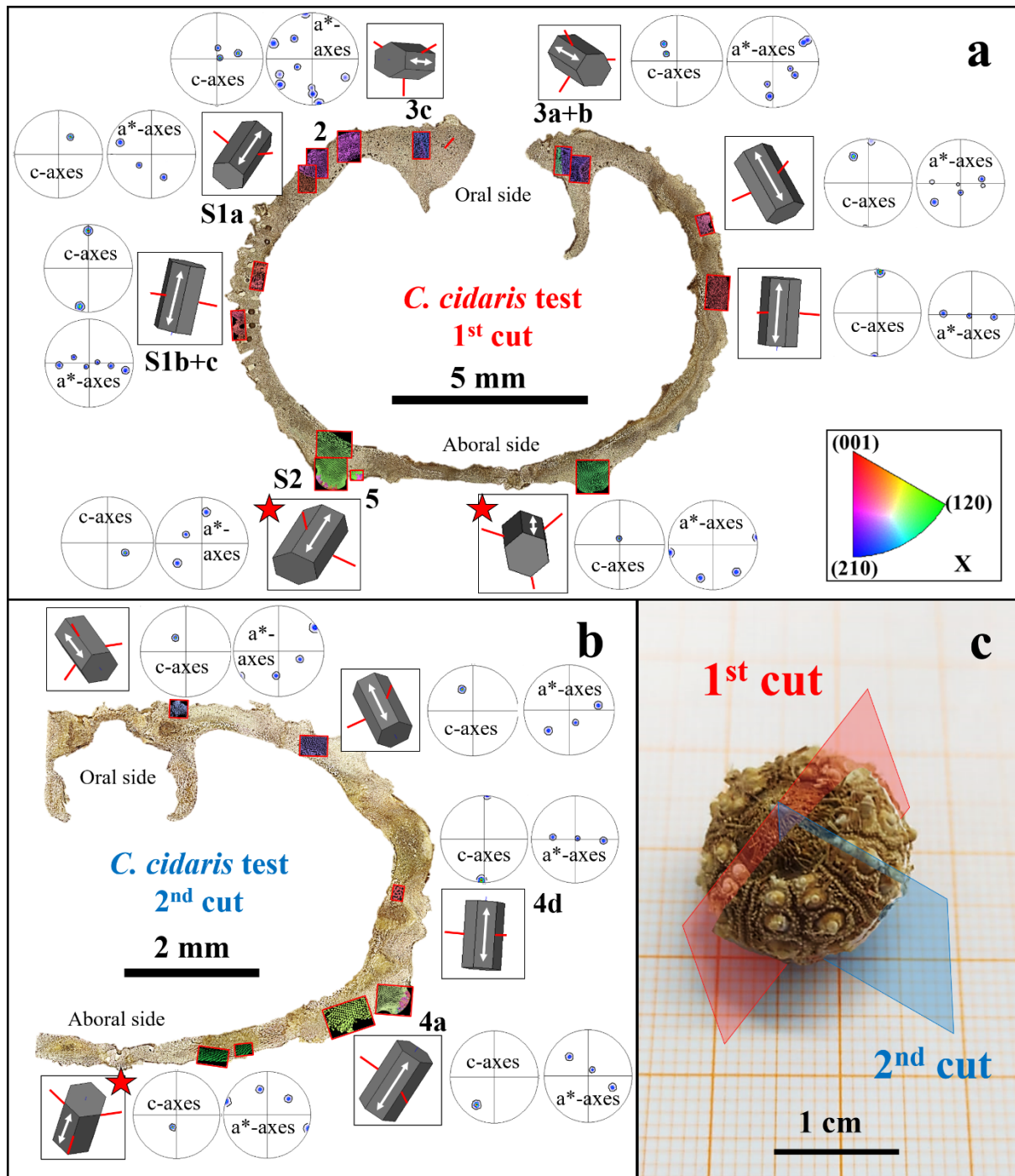


Figure 2.6-1. The texture, calcite c-axis orientation and position of EBSD measurements for two *Cidaris cidaris* tests (a, b), cut in two directions (1st cut, 2nd cut, c). Confocal laser microscopy images depict the positions of the performed EBSD scans on the first (a) and on the second cut specimen (b). Density distribution pole figures for c- and a*-axes for selected EBSD measurements show the preferred crystallographic orientation of the plates (a, b). Measurements covering adjacent plates show multiple c-axes orientation maxima in the pole figures; see also Figures 2.6-3 and 2.6-API1. Sketched crystals visualise the orientation of a*-axes (red lines) and c-axes (white arrows) and demonstrate that the c-axes are oriented parallel to test outer surface. Planes through the *C. cidaris* test indicate the positions of the first (red) and of the second (blue) cut (c). Red stars in (a) and (b) point to those measurements where calcite c-axis orientation does not appear to be parallel to outer test surface. The latter is due to the cut-effect explained in the Results section.

Figure 2.6-2a, b shows a plate; the latter covers the entire thickness of the test cross-section (Fig. 2.6-2c). The EBSD scan (Fig. 2.6-2a, b) was evaluated with conventional Hough transformation-based data evaluation. We observed the strong mineralisation of the stereom and a high crystal co-orientation strength. We found a uniform orientation in the map and an MUD value of 697 for the entire measurement (Fig. 2.6-2b, d). A large area has been scanned (about 1 mm x 600 μ m); nonetheless, the strong uniformity in colour (Fig. 2.6-2b) indicates only one crystal orientation, i.e. the single crystallinity of the calcite in that stereom portion. Hence, based on conventional EBSD data evaluation, we found a 3D “single-crystal-like” long-range order for that stereom section (see pole figures in Fig. 2.6-2d). When the EBSD data set is evaluated with the pattern matching procedure, misorientations within the trabecular growth lines become visible (Fig. 2.6-2e). In addition, we observed small-angle misorientations within the stereom; in the map (yellow arrows in Fig. 2.6-2e) and in the misorientation diagrams (Fig. 2.6-2f). We found misorientations up to about 2° (Fig. 2.6-2f). These are, in general, concentrated at trabecular intersections, the junctions where trabeculae meet (indicated with yellow arrows in Fig. 2.6-2e). Nonetheless, as the profile C-D in the misorientation diagram of Fig. 2.6-2g demonstrates, the calcite within the trabeculae does not seem to be significantly misoriented, even when EBSD data are evaluated with the EBSD pattern matching method (Fig. 2.6-2g). This indicates that intratrabecular calcite of *C. cidaris* is well co-oriented.

Figure 2.6-3 and Supplementary Figure 2.6-AP1 visualise the conjunction of crystal plates within the test and their interlaced connection. The colour-coded EBSD maps demonstrate that the interface between the crystal plates has no rectilinear course and that the plates are intricately interlinked. Adjacent stereom crystals are entangled in three dimensions in a complex way, well visible from the intertwining of crystalline trabeculae (Fig. 2.6-3a-c). We also found a marked misorientation between adjacent crystals/crystal plates (see misorientation-distance diagrams of Figs. 2.6-3c, 2.6-AP1). Although the pole figures show comparable calcite c-axis orientation for neighbouring crystal plates, the misorientation angle-distance diagrams demonstrate a misorientation between adjacent crystal plates of up to 40° (Figs. 2.6-3c, 2.6-AP1a). We investigated the degree of misorientation between adjacent crystal plates for the entire circumference of the test. For the circumference through the plates, we found no systematics in misorientation between the crystal plates, e.g., no gradation in misorientation. The misorientation angle between adjacent crystal plates varied arbitrarily between 5° and 40°.

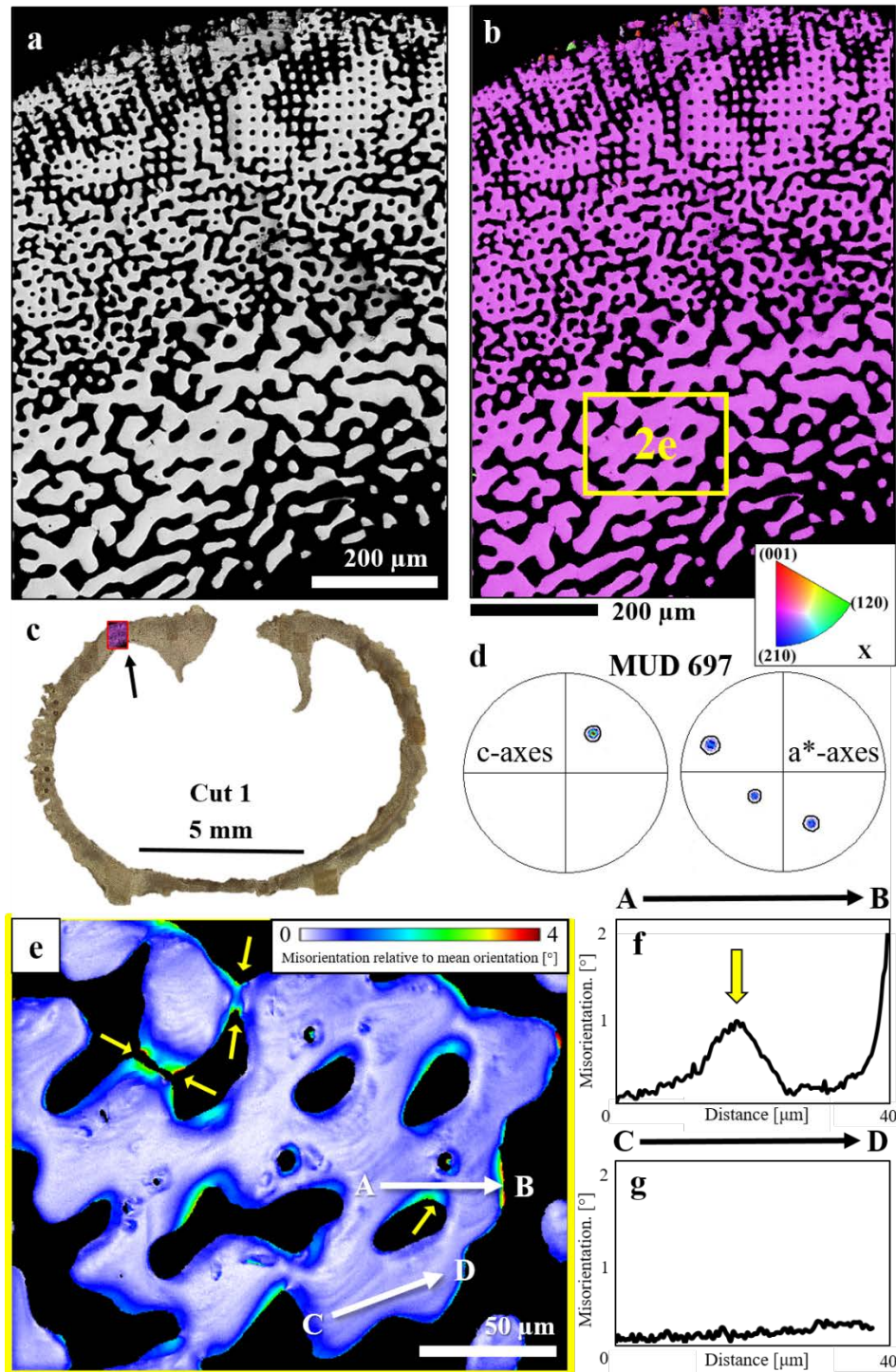


Figure 2.6-2. Microstructure and texture of a *Cidaris cidaris* test plate, covering the entire cross-section of the test (a, b). The measurement was performed close to the oral region of the test sectioned according to the first cut. The EBSD band contrast measurement image (a) and the colour-coded crystal orientation map (b) show two stereom/trabeculae architectures, rectilinear at outer (top of maps) and labyrinthine at inner test layers/sections (bottom of maps). EBSD measurement position is indicated in the laser confocal image (c). The contoured pole figures show a 3D “single-crystal-like” long-range order and a high MUD value of 697 (d). While the measurement shown in (b) was evaluated with conventional EBSD data evaluation, the measurement given in (e) was evaluated with pattern matching. The position of the EBSD scan shown in (e) is indicated by a yellow rectangle in (b). Applying EBSD pattern matching and displaying the texture differences relative to the mean crystallographic orientation of the stereom, we show small-angle misorientations (up to 2°) within the stereom fabric (e). Strikingly, intratrabecular growth increments in the stereom show tiny misorientations that are not observable with conventional EBSD or Kernel average misorientation maps (e). Two misorientation-distance profiles traversing the hard tissue indicate well-observable misorientation maxima along trabecular junctions (yellow arrows in e, f), as well as the high co-orientation of intratrabecular calcite (g).

Even though the calcite is highly co-oriented within the plate trabeculae and, thus, in many parts of the test stereom, the calcite of the tubercular terminal knob is polycrystalline. A tubercle is part of a ball-and-socket joint (Figs. 2.6-4a, 2.6-AP2a), consisting of a knob-like protuberance where the primary spines are connected to a ring of muscles entwined around the trabeculae of the labyrinthic test stereom (Fig. 2.6-4a). The tubercle consists of densely space-filling calcite; within the tubercles, the trabeculae form a dense microperforate stereom network. Towards the interior of the test, the tubercle comprises the terminal knob and the basal boss (Fig. 2.6-4a); the latter leads into the stereom of a test plate (Fig. 2.6-4a). For the basal boss and the terminal knob, we observed differences in stereom space-filling density and crystal co-orientation strength. Nonetheless, we found a perfectly smooth transition between the different tubercle sections (Figs. 2.6-4a, b, 2.6-AP2a, b). The stereom of the tubercle has a less regular fabric than the fabric of the stereom of the adjacent test (Figs. 2.6-4a, b, 2.6-AP2a, b). The crystals at the terminal knob have an irregular morphology and show a high misorientation between each other (Figs. 2.6-4a, b, 2.6-AP2a, b, EBSD map and corresponding pole figures). For the crystals that form the stereom of the basal boss, we found small-angle misorientations (yellow star in Figs. 2.6-4b, 2.6-AP2b). These are observed only when EBSD data are evaluated with the pattern matching technique and displayed in a Kernel average misorientation map (Figs. 2.6-4c, 2.6-AP2c-e). These small-angle misorientations are frequent along the trabecular intersections of the microperforate boss and by far surpass the misorientations found in the labyrinthic test plate (Fig. 2.6-4d). As the amount of pores in the microperforate tubercle is still very high, the calcite of the tubercle comprises many trabecular junctions and, hence, many small-angle misorientations (Fig. 2.6-4c). While the intratrabecular stereom of the test plates shows a 3D “single-crystal-like” texture with the c-axes oriented parallel to the outer surface of the test, the polycrystalline terminations of the knobs have an axial texture with calcite c-axes oriented roughly perpendicular to the outer surface of the tubercular terminal knob (see the pole figures in Figs. 2.6-4a, b, 2.6-AP2a, b). We found an MUD of 700 for the test plate (Fig. 2.6-4d), an MUD of 665-685 for the tubercular basal boss and an MUD of 79 to 87 for the polycrystalline tubercular terminal knob (Figs. 2.6-4, 2.6-AP2).

A similar microstructure to the polycrystalline knob, comprising a polycrystalline as well as a 3D “single-crystal-like” part and termed parapet (Durham & Melville 1966), can be found at the outer shell surface right next to the primary tubercle (Figs. 2.6-5a, b). This convex structure encases the tubercle to lock in with the base of the primary spine (Fig. 2.6-5b). The polycrystalline parapet has a low degree of crystallographic co-orientation (red star in Figs. 2.6-5c-f) and an axial texture that comprises c-axes oriented perpendicular to the outer parapet surface. In contrast, the adjacent 3D “single-crystal-like” stereom is oriented perpendicular to the parapet (orange star in Figs. 2.6-5c-e, g). As shown by the pattern-matched misorientation map, apart from a few positions at trabecular junctions, the test is, more or less, free from internal misorientations (Fig. 2.6-5e). On the other hand, the polycrystalline parapet shows misorientation streaks (white arrows in Fig. 2.6-5e) that run alongside the pores of the microperforate stereom, close to the outer parapet surface.

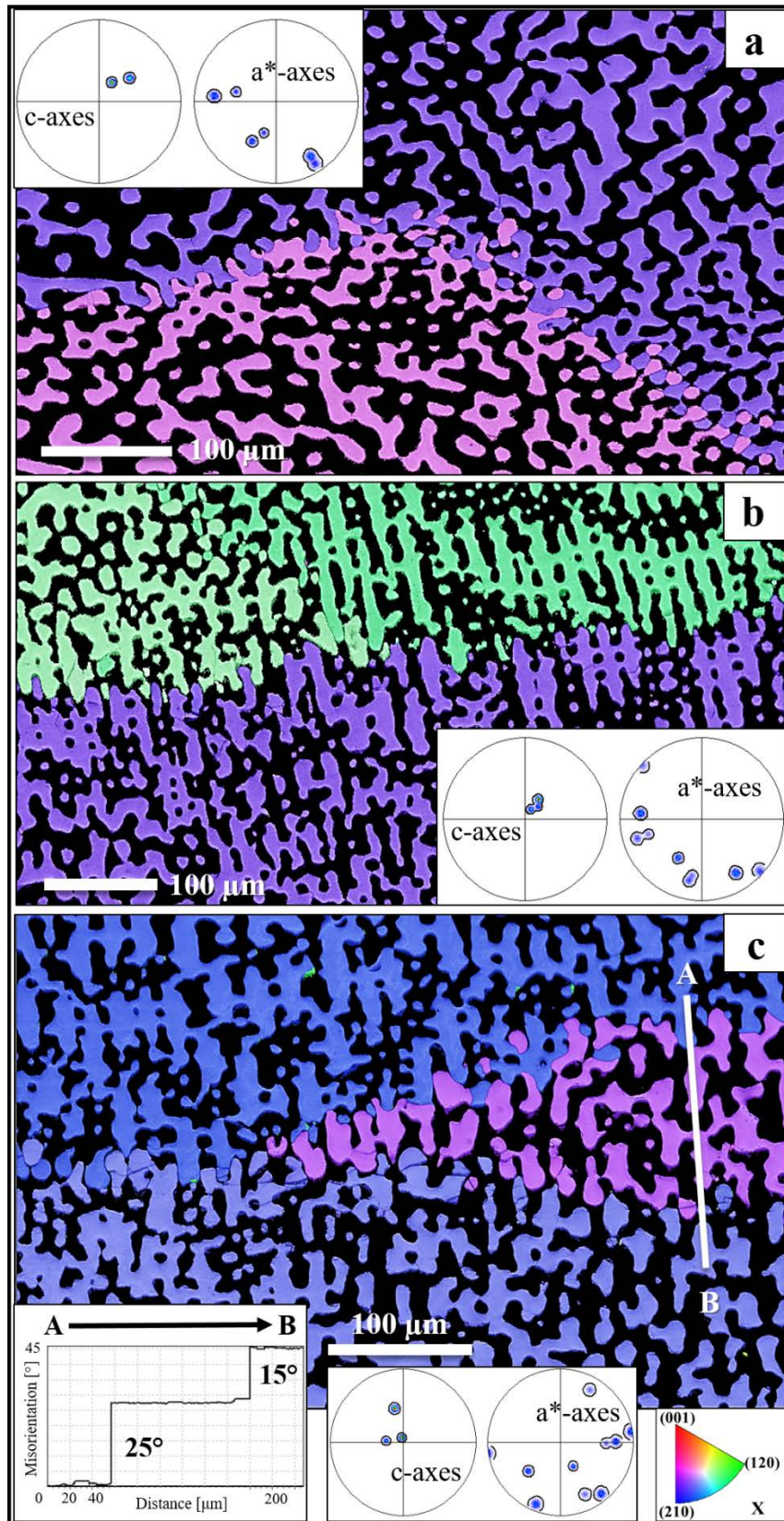


Figure 2.6-3. EBSD scans visualizing the stereom of different test plates of the *Cidaris cidaris* test as well as their interlinkage (a-c). The test was sectioned according to the first cut. The colour-coded EBSD maps are complemented with the corresponding contoured pole figures. The latter display a 3D “single-crystal-like” texture for individual plates. Test plates interconnect along undulated interfaces (a-c). Adjacent test plates are significantly misoriented, at some instances up to 40°; see misorientation versus distance plot in (c). The measurements were evaluated with conventional EBSD data evaluation. The positions of the scans are indicated in the overview of the test in Fig. 2.6-1a.

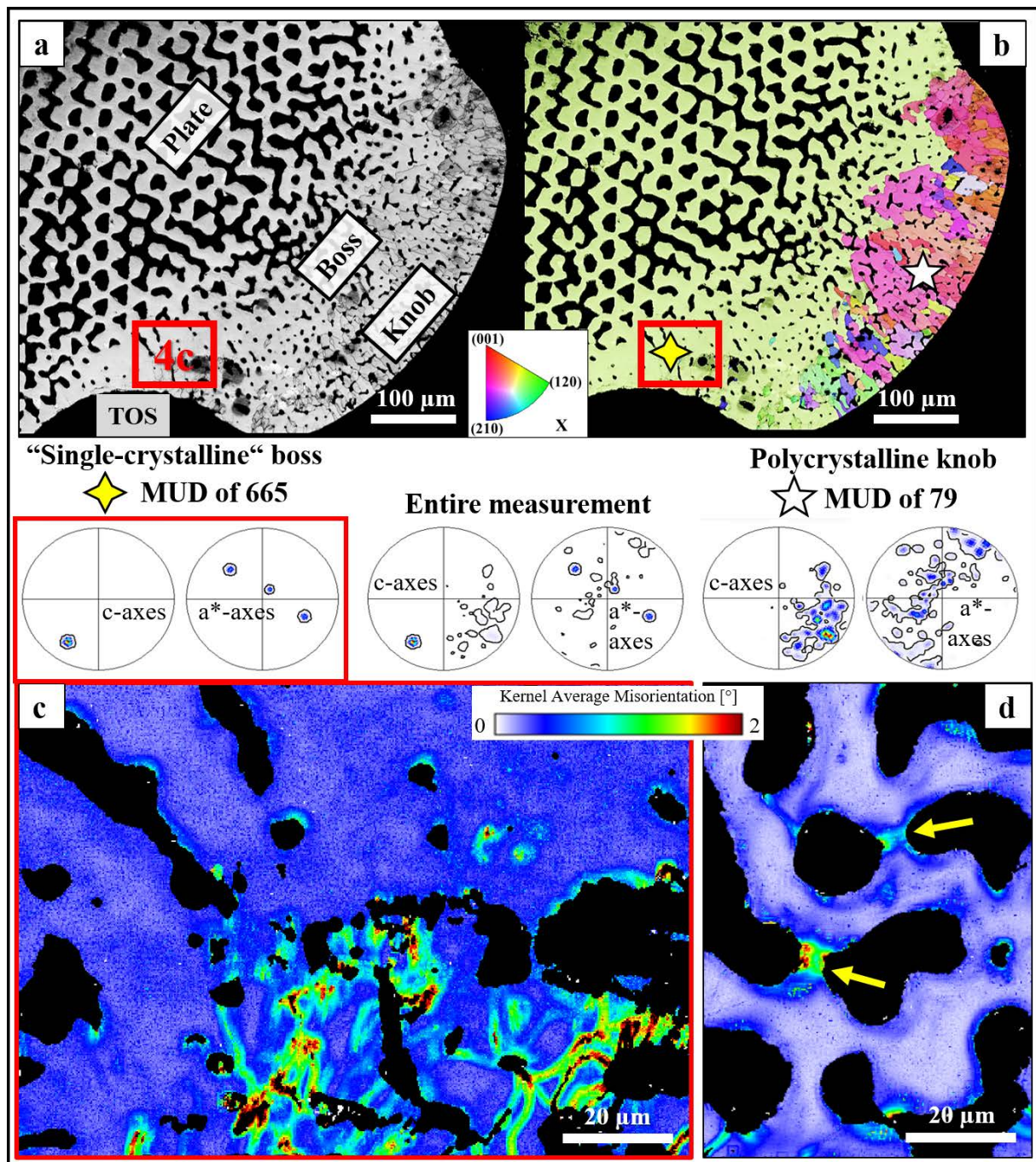


Figure 2.6-4. Crystal assembly architecture and the bimodal texture of tubercular calcite at the aboral region of the test of a *Cidaris cidaris* specimen. As visible from the band contrast measurement (a) and the colour-coded orientation maps (b), the tubercle comprises a co-oriented section (yellow star in b) and a strongly misoriented, polycrystalline region, the latter being along the tubercle outer surface (TOS, white star in b). The contoured pole figures show the texture for the boss and knob of the tubercle as well as for the entire measurement (a, b). The orthogonality in calcite c-axis orientation between the stereom of the boss and the plate and the tubercle knob is well visible. The measurement shown in (a, b) was evaluated with conventional EBSD data evaluation. Pattern matching EBSD data evaluation applied to a subset of the tubercle (c) reveals the presence of many small-angle misorientations (1° to 2°) within the boss, and near the terminal knob (c). At trabecular intersections of a measurement located in the core of the plate (yellow arrows in d), misorientations can reach 2° to 3° . Misorientations for the trabeculae near the terminal knob are higher than in the core of the plate (d). The positions of the EBSD scans can be retraced from Fig. 2.6-1b; the area of the close-up map (c) is marked with a red rectangle in (a, b).

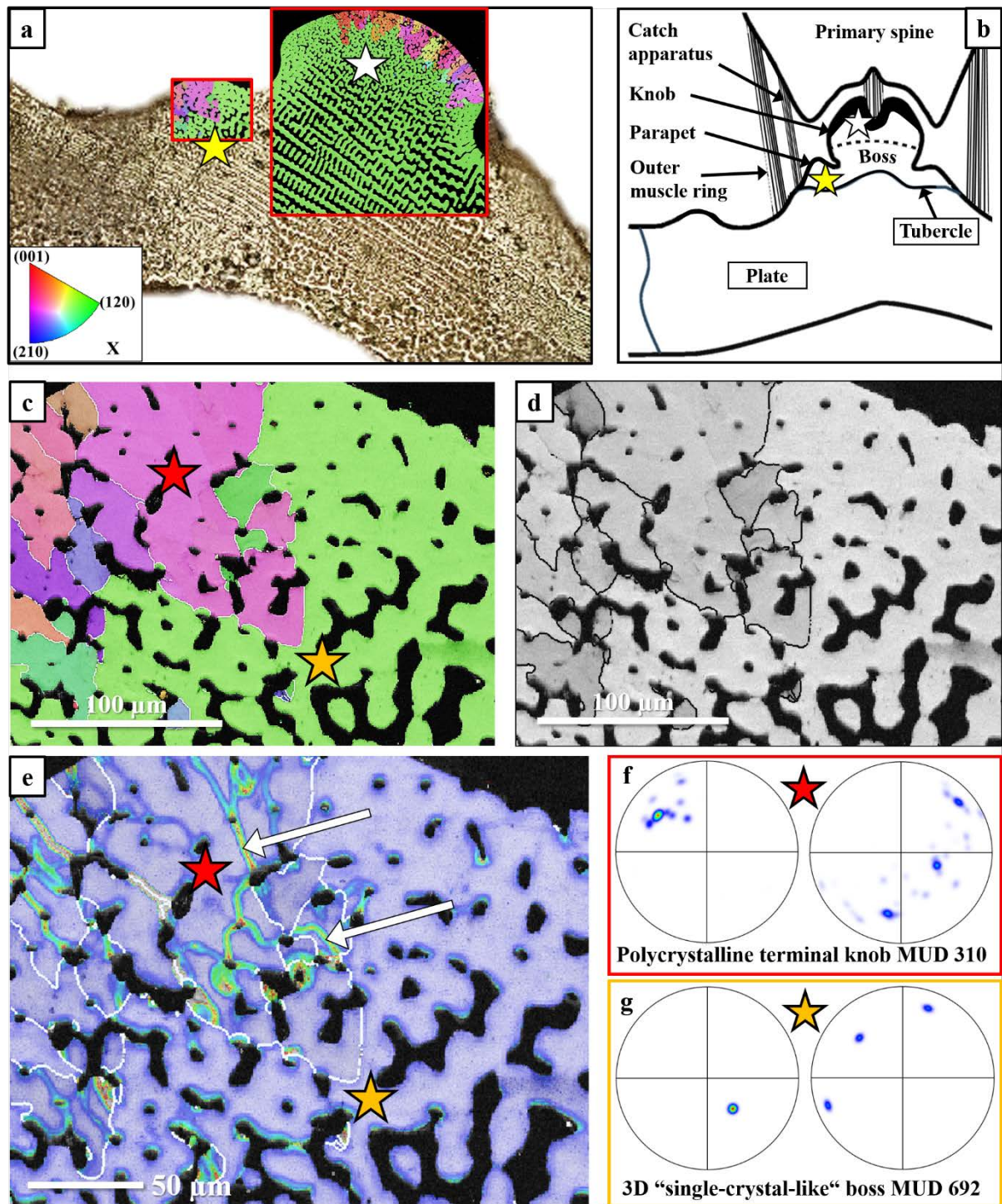


Figure 2.6-5. Microstructure and internal misorientations of a parapet located next to a primary tubercle, where the muscle ring attaches to the *Cidaris cidaris* test (a, b). Terminology and spine attachment are depicted in a schematic illustration (b). EBSD data were evaluated with conventional EBSD data evaluation (c, d) and pattern matching (e). Analogous to Fig. 2.6-4c, d, the pattern-matched measurement is displayed as a Kernel average misorientation map between 0° - 2° (e). Pole figures show colour-coded data points of the two subsets (f, g). Similar to the terminal knob of primary tubercles (Figs. 2.6-4c-e, A2), the microstructure of the parapet stereom (red star in c) differs from the labyrinthic stereom of the inner test plate (orange star in c). The trabeculae follow a tighter meshwork that leaves smaller pores and is formed of an assembly of polycrystals (a, b). Aside from the grain boundaries, the stereom comprises many internal misorientations that are particularly frequent at trabecular junctions and can well be detected by EBSD pattern matching (c). The polycrystalline parapet has an axial texture with the c-axes clustered in an orientation perpendicular to the outer parapet surface (d), while the calcite of the test plate is co-oriented and can be considered to be 3D “single-crystal-like” (e). Misorientation streaks are frequent in the polycrystalline parapet (white arrows in e).

Most sea urchins form two series of spines: the primary (long) and the secondary (short) spines. For *C. cidaris*, both spines comprise a medulla, the central portion of the spine, and a cortex surrounding the medulla along a large part of the shaft until the tip (Figs. 2.6-6, 2.6-7, 2.6-AP3). The longer primary and the shorter secondary spines show pronounced differences in the microstructure of their base. The outer base surface of the primary spines has a 3D single-crystal-like long-range order that extends through the co-oriented trabeculae (Fig. 2.6-6a). Despite the consistent IPF colouring throughout the basal part of the primary spine, the MUD value scatters at about 670, and the pole figures reveal angular deviations (Fig. 2.6-6a). This indicates that primary spine stereom calcite is highly co-oriented, nonetheless, as it comprises low angle misorientations, it cannot be addressed as single-crystalline. However, up to now, there is no agreement from which value of mosaic-spread a single crystal should no longer be termed a single crystal but a polycrystalline entity. For secondary spines, the basal part is not strictly co-oriented and features large (~100 μm diameter) outer surface regions of polycrystalline material (Fig. 2.6-6b-d). Data refinement by EBSD pattern matching revealed many internal small-angle boundaries in the crystals along the microperforate outer spine layer. These form misorientations between 0.5-1.5° (Fig. 2.6-6d). Towards the highly co-oriented, labyrinthic stereom of the medulla, intratrabecular misorientations are significantly decreased (Fig. 2.6-6d).

In *C. cidaris*, the cortical layer of the primary spine has a rough surface. We found aggregations of crystals forming spiky longitudinal crests along the outermost cortex surface (Fig. 2.6-7a, b). The cortex surface of secondary spine tips is rather smooth and significantly less structured than the surface of primary spines (Fig. 2.6-7a, b). At the outer edge of the primary/secondary spine shaft, the connection between the medulla and the cortex becomes visible (Fig. 2.6-7a, b). Their interface is uneven; multiple thin series of pores continue from the medulla into the cortex (Fig. 2.6-7b). The crystallographic c-axes in the 3D “single-crystal-like” medulla (yellow star in Fig. 2.6-7b) are parallel to the direction of the shaft. The polycrystalline cortex (white star in Fig. 2.6-7b) has an axial texture with calcite c-axes being aligned more or less perpendicular to the c-axes of the medulla (Fig. 2.6-7b). Towards the tip of the spine; the outer spine surface becomes increasingly serrated (Fig. 2.6-7a, b).

We obtained similar structural-crystallographic characteristics for *C. cidaris* secondary spines (Fig. 2.6-7c, d). The highly co-oriented medulla (red star in Fig. 2.6-7d) interlocks in a complex way with the weakly axially textured polycrystalline cortex (white star in Fig. 2.6-7d). It appears that *C. cidaris* secondary spines have a smoother outer surface when compared to the outer tip surface of the primary spines (Figs. 2.6-7, 2.6-AP4). The stereom of both the primary and the secondary spine medullae is galleried (for definition, see Terminology Section A.1) with large, interconnected pores (Fig. 2.6-7a-d) that appear to continue into the adjacent cortex (e.g., Fig. 2.6-7b). Nonetheless, the outermost 50 μm of both types of spines is rather formed of microperforate (for definition see Terminology Section A.1) calcite.

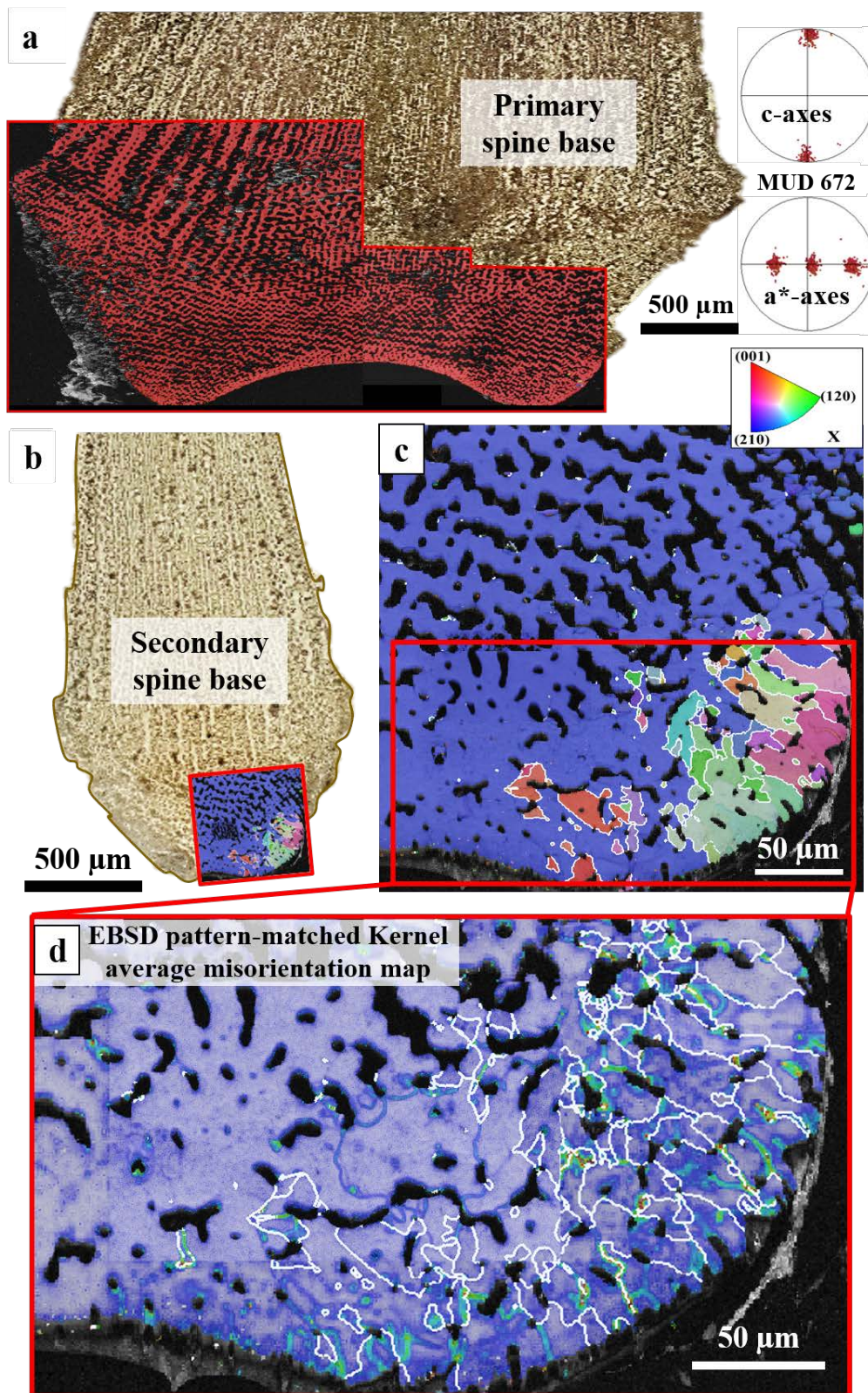


Figure 2.6-6. Microstructure and texture of the basal portion of *Cidaris cidaris* primary and secondary spines visualised with laser confocal images (a, b) and EBSD maps (a, c, d), with conventionally evaluated EBSD data (a, c), and with EBSD data evaluated with pattern matching (d). Analogous to Fig. 2.6-4c, d, the pattern-matched measurement is displayed as a Kernel average misorientation map between 0° - 2° (d). For primary spines, the calcite of the entire basal stereom is co-oriented (a). The stereom architecture changes from microporofate along the outer spine surface to galleried in the medulla (a). At the basal outer surface of secondary spines, where the muscle ring attaches to the basal section of the spine, we found a spine portion formed of irregularly shaped and misoriented crystals (c). EBSD pattern matching revealed many small-angle misorientations within the crystals as well as in the microporofate stereom along basal spine outer surface.

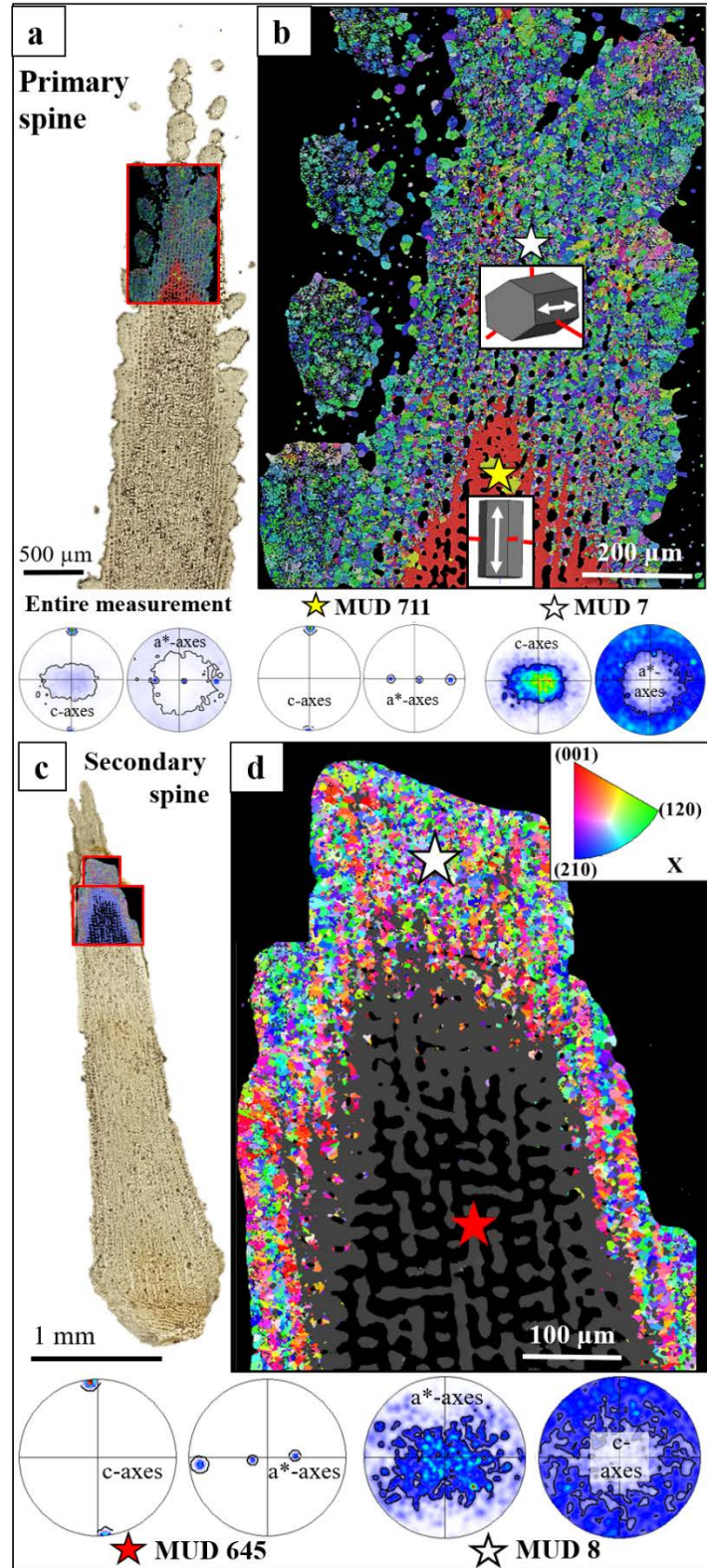


Figure 2.6-7. Microstructure and texture at the tip of *Cidarid cidaris* primary and secondary spines (a-d). EBSD measurement positions are indicated with the confocal laser microscopy images (a, c), EBSD data were evaluated with conventional EBSD data evaluation. For the primary spine (b), the colour-coded EBSD map and the corresponding pole figures indicate a single-crystal-like microstructure and texture for the medulla for the spine (yellow star in b), while for the cortex (white star in b) we observed a polycrystalline microstructure and texture. As shown with the sketched crystals in (b) and well visible from the given pole figures, crystal orientations of the cortex are perpendicular to that of the stereom. Secondary spine tips have comparable microstructure and texture, as observed for primary spine tips (b, d). We found, for both primary and secondary spines, an immense difference in MUD value and, hence, crystal co-orientation strength for the medulla (MUD: 711, 645) and the cortex (MUD: 7, 8) of the spine.

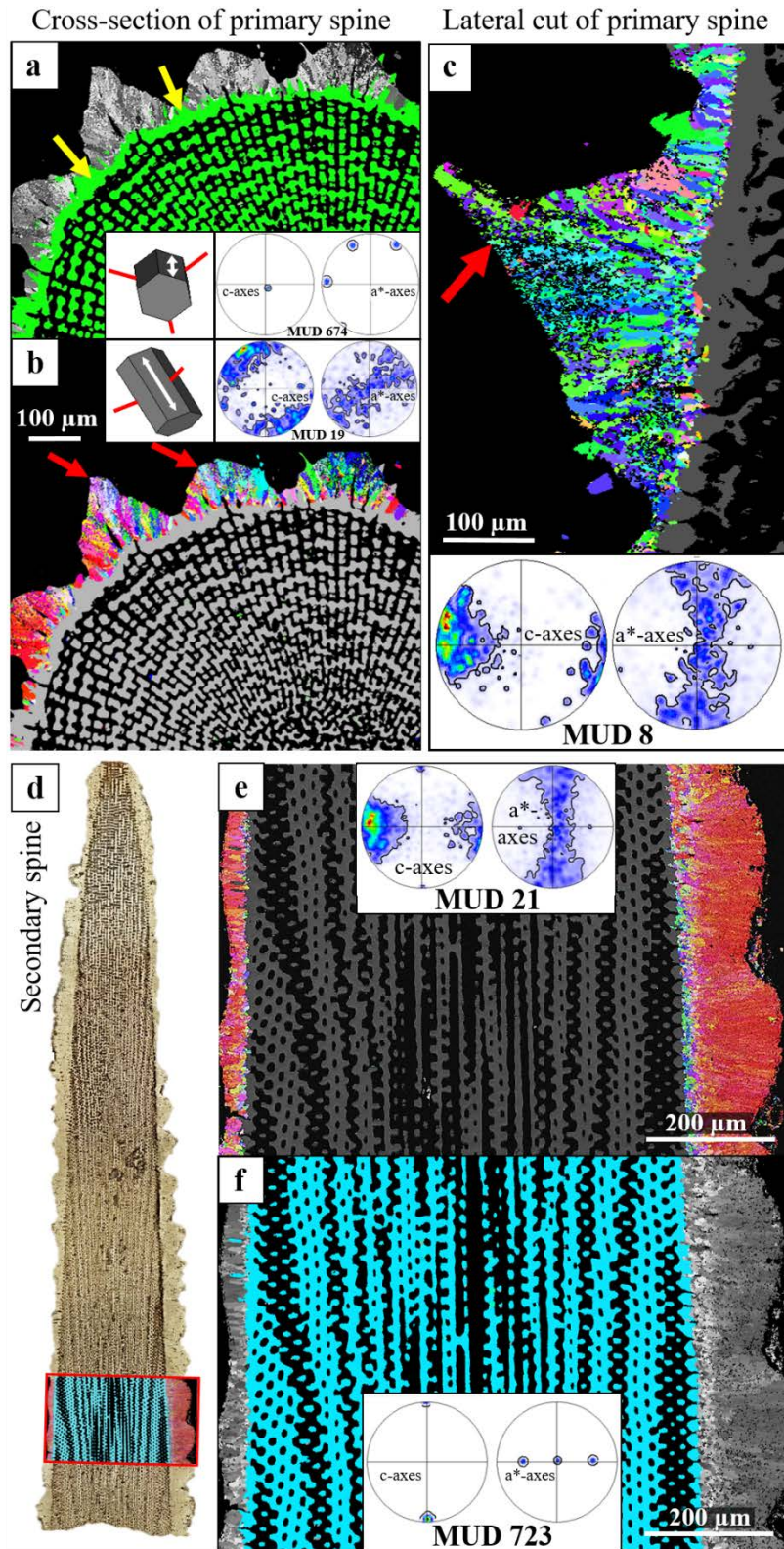


Figure 2.6-8. Microstructure and texture of *Cidaris cidaris* spine medulla and cortex along the shaft of the spine (a-f), for a primary (a-c) and secondary (d-f) spine and cross (a, b) and lateral (c-f) sections through the spine. EBSD data were evaluated with conventional EBSD data evaluation. The stereom of the medulla is galleryed. A three-dimensionally imperforate tube of calcite is present at the interface of the stereom of the medulla with the adjacent cortex (yellow arrows in a). Along the cross-sectional (b) and the lateral cut (c) through primary spines, the cortex forms longitudinal crests (red arrows in b, c). Despite their polycrystalline microstructure, the calcite of the longitudinal crests has an axial texture with the c-axes being oriented perpendicular to the c-axis of the medulla (sketched crystals in a, b). In secondary spines (d), the microstructure of the cortex gradually shifts from low to high crystal co-orientation. In contrast, the central part of the secondary spine has a single-crystal-like long-range order (f).

Figure 2.6-8 highlights two spines sectioned in different cuts close to their base. A primary spine was sectioned perpendicular (Fig. 2.6-8a, b) and parallel to its morphological long axis (Fig. 2.6-8c), and a secondary spine was cut parallel to its morphological long axis (Fig. 2.6-8d-e). The distinctness in microstructure and texture between the medulla and the cortex is well visible. The stereom of the medulla comprises trabeculae arranged in radial lines (Fig. 2.6-8a, b) and with calcite c-axes oriented parallel to the direction of the shaft (sketched crystal and pole figure in Fig. 2.6-8a). Directly adjacent to the cortex, the crystal network of the medulla is continuous and imperforate (yellow arrows in Fig. 2.6-8a). Sectioned perpendicular to the long axis of the spine, the crystals of the cortex are elongated (Fig. 2.6-8c). Rather than forming a sheath with a constant extent that surrounds the stereom of the medulla, the crystals of the cortex are grouped into longitudinal crests (red arrows in Fig. 2.6-8b, c). However, these do not cover the entire outer stereom surface evenly. High-spatial resolution EBSD scans visualise the complex internal structure of a primary spine longitudinal crest (Fig. 2.6-8c). In secondary spines, the texture and microstructure of the shaft appear similar (Fig. 2.6-8d-f). The cortex has an axial texture with crystallographic c-axes preferentially oriented perpendicular to the outer spine surface (Fig. 2.6-8e). In contrast, the medulla is formed of a galleried, highly co-oriented calcite stereom that is mostly imperforate along the interface with the cortical layer. Thus, for all investigated spine specimens of *C. cidaris*, the crystallographic texture of the cortex is perpendicular to that of the medulla (Fig. 2.6-8b, c, e).

2.6.4 DISCUSSION

Test and spine stereom architecture

In cidaroid tests and spines, various stereom architectures are developed, depending on the species and the region in the skeletal element (Grossmann 2010; Nebelsick et al. 2015). We found rectilinear, galleried, microperforate and labyrinthic stereom architectures (for the definition of the fabrics, see Terminology Section A.1). For *C. cidaris*, the distribution of different stereom fabrics in the test is less homogenous than described by Smith (Smith 1980). Instead, the distribution of the above-named stereom fabrics is localised to certain regions of the test and/or the spines.

The internal section of the ambulacral and interambulacral test plates with the attached tubercles comprises an irregular pattern of large pore channels, and trabeculae called the labyrinthic stereom fabric (Pearse & Pearse 1975; Smith 1980). This stereom fabric is abundant in sea urchin plates; Wainwright et al. (Wainwright 1982) described the labyrinthic stereom as the main architectural design element of sea urchin tests and spines. At central regions of the ambulacral and interambulacral plates, the stereom is streaked with extensive trabeculae; elongated pore channels tend to form one-directional galleries with perpendicular struts. Reaching the tubercle, the ordered stereom fabric of the test decreases in porosity and pore size. The large pore channels are replaced by very small and irregularly arranged

pores, and a microperforate dense fabric forms the stereom of the tubercles. A rectilinear stereom architecture, creating the basal boss of the tubercle, as suggested by Smith (Smith 1980), could neither be seen with FE-SEM, nor confocal laser microscopy imaging. However, a rectilinear stereom was observed along the outer section and surface of the test plate. Galleried stereom occurs in the test near the tubercles, however, it is far less abundant in the test of the investigated *C. cidaris* species than reported by Smith (Smith 1980).

The spines of *C. cidaris* have varying stereom fabrics at their base, shaft, and tip. The spine shaft can be subdivided into the medulla and cortex, each with a distinct pore architecture. In the shaft, the stereom in the medulla is microperforated along the outer spine surface and rather galleried and lamellar on the inside. The linearity and co-orientation of the pore channels seem to increase towards the cortex. In the basal region of the spine, the microstructure of the medulla is primarily labyrinthic, and the pore channels continue into the outer base surface. An identical internal architecture was observed for the cidaroid *Prionocidaris baculosa* (Fig. 1 in Dery et al. (2018)). For this species, the stereom fabric is predominantly labyrinthic at the base of the spines. However, along the outer base surface of the spines of *P. baculosa*, the stereom fabric seems to be less perforate than in the core region of the spine.

Smith (Smith 1978; Smith 1980) suggested that the change in stereom architecture in the test and the spines might be closely related to functional aspects. The above-described anisotropic arrangement of trabeculae and pore canals increases the test plate's resistance to bending stress (Ji et al. 2022). Grossmann & Nebelsick (2013a) experimentally confirmed structural implications for the stereom differentiation. According to Grossmann & Nebelsick (2013b), the chaotic distribution of struts in the stereom also impedes crack propagation. Stress-transfer capacity was reported by Tsafnat et al. (2012) using micro-computed tomography. Through simulations, high-stress concentrations occurred at specific points in the test and spine's architecture, where brittle cracking would most likely happen (Tsafnat et al. 2012). Connective tissue within the porous microstructure of the stereom, enhanced by orientation and gradation of the pores in interplay with organic and possibly amorphous interfaces, would lessen stress concentration and enable a more even stress distribution (Trotter et al. 2000; Nickel et al. 2017; Ji et al. 2022).

Crystallographic arrangement of calcite in the test and the spines

The primary and secondary spines

The calcite of *C. cidaris* spines is formed with two crystal textures. The medulla of the base and the shaft have a 3D single-crystal-like long-range order. In contrast, the cortex at the outer tip of the spine is a polycrystalline aggregate with a low preferred crystallographic orientation. The c-axes of the medullar trabeculae are oriented parallel to the morphological long axis of the spine (Donnay & Pawson 1969; Berman et al. 1990), while the c-axes of the cortex crystallites are oriented perpendicular to that

of the longitudinal medullar trabeculae. The texture difference between the spine cortex and the medulla results from different mineralisation processes. The texture of the medulla is mainly controlled by biological factors predetermining its microstructure and texture. In contrast, the growth process of the cortex is largely influenced by competitive growth determinants evoking the formation of the axial texture of the cortex crystals. The lack of crystallographic continuity and the compactness of the micro-perforated cortex stereom are interpreted as important factors in enhancing the structural stability of the spine (Dery et al. 2018). The cortex comprises sub- μm sized crystallites with a varying degree of crystal co-alignment.

The changeover from the highly co-oriented medulla to the polycrystalline cortex is intricate. As visible from the subset analysis for the tip of two secondary spines (Fig. 2.6-9), the single-crystal-like framework of the medulla continues into the cortex (Fig. 2.6-9a). Exposing thin lines of tiny trabeculae (white star in Fig. 2.6-9a) that run parallel to the morphological long axis of the spine, subsets of the EBSD measurement in Fig. 2.6-9a show the extension of the medulla up to the outer surface of the spine tip. It should be noted that the cross-sections of the extended medullar trabeculae are significantly smaller in the spine tip than the cross-sections observed in the monophasic medulla. The medullar/trabecular extension maintains the crystal orientation of the highly co-oriented medulla, and the medullar/trabecular lines run parallel to the morphological long axis of the spine, irrespective of their position in the spine (Fig. 2.6-9a).

The extensions of the medulla play a significant role in the crystallisation of the cortex. The polycrystalline cortex is subdivided into two subsets with similar crystal orientation patterns (Fig. 2.6-9b, c). Each subset has its crystallographic c-axes oriented perpendicular to the medulla as well as to one another (see sketched crystals in Fig. 2.6-9a-c). Rather than being randomly distributed within the cortex, the subset maps of the cortex show that the two sets of crystal orientation (set 1 and set 2) align in strict lines (Fig. 2.6-9b, c) and that these run parallel to the lines of the medullar extension (Fig. 2.6-9a). Therefore, the microperforate tip of the cortex has a 3D microstructure with a clear-cut and ordered crystal orientation pattern and the arrangement of the crystallites that form the very tip of the cortex is not random. The tip of the cortex comprises thin parallel entities where the medullar extensions (Fig. 2.6-9a), the first orientational set of crystals (set 1, Fig. 2.6-9b) and the second orientational set of crystals (set 2, Fig. 2.6-9c) alternate in a lamellar fashion. Based on the linear and ordered arrangement of the medullar/trabecular extensions and on the two ordered sets of crystals inherent to the cortex, it can be assumed that the extended medullar stereom functions as a nucleation substrate for the small cortex crystals. The trabeculae of the medulla that extend into the cortex and function as nucleation surfaces have a morphology resembling spheres. Thus, the cortex crystals that nucleate on these surfaces grow in all directions perpendicular to the trabecular morphological long axis (see the large scatter of data in the pole figures in Fig. 2.6-9a, b). This explains the lack of crystallographic co-orientation within the two sets of crystals, despite their axial texture (Fig. 2.6-9b, c).

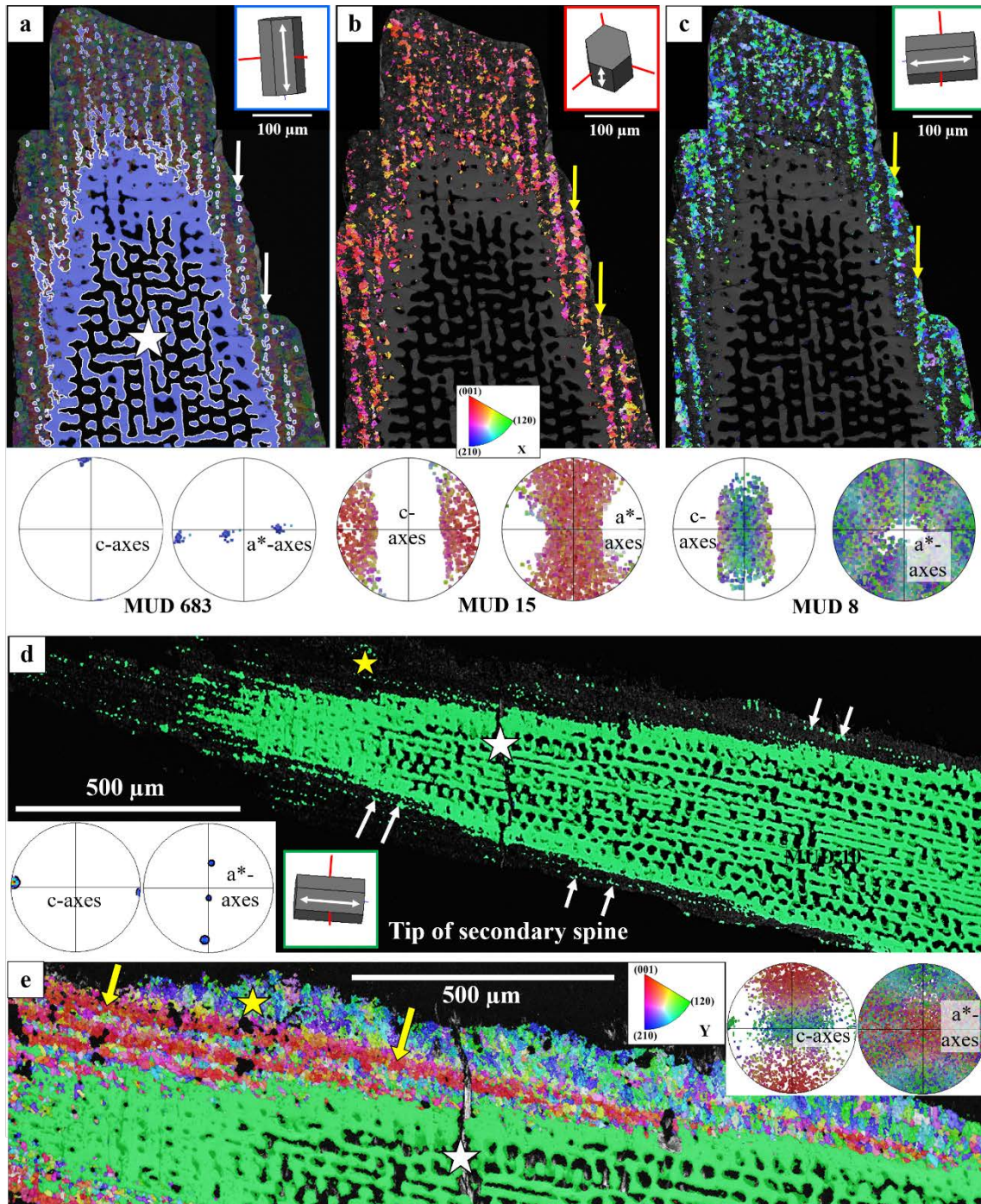


Figure 2.6-9. Microstructure and crystallographic texture of *Cidaris cidaris* spine medulla and medullar extensions (white stars arrows in a, d) and of the first-formed cortex crystals at the very tip of the spine (yellow arrows in b, c, e). EBSD data were evaluated with conventional EBSD data evaluation. The competitive growth microstructure of the cortex shaft is already well observable close to the tip of the spine (yellow stars in d, e). At its very tip, the spine cortex consists of medullar extensions (white arrows in a, d) and two sets of first-formed crystals (yellow arrows in b, c, e). Set 1 and set 2 cortex crystals are differentiated from each other by their orientations, both of which are orthogonal to the orientation of the medullar trabeculae as well as to each other. This is indicated by sketched crystals (a, b, c) and/or the colours of the set 1 and set 2 crystals (red and blue; coding for orientation (yellow arrows in b, c, e)). The medulla consists of a galleried stereom, formed of co-oriented calcite (white star in a, d, e). Small trabeculae (medullar extensions) are organised in parallel series (white arrows in a) with similar crystallographic orientation as the calcite of the medulla (white arrows and pole figure in d). The extending trabeculae (white arrows in a, d) are significantly thinner than the trabeculae of the galleried stereom of the medulla (white star in a, d, e). Polycrystalline sheets of granular crystals (b, c) enclose the medullar extensions, and form the cortical crystals. The latter crystals have an axial texture and a low co-orientation strength. The c-axis orientation of the set 1 and set 2 crystals is always perpendicular to the axes of the medullar extensions; the two sets of crystals are ordered in parallel lines (yellow arrows in b, c, e).

A similar pattern can be observed for a further secondary spine tip that also shows a clear-cut relationship between the medullar/trabecular extensions and the crystallographic orientation pattern of set 1 and set 2 of the cortex (Fig. 2.6-9d, e). Similar to previous measurements, the medulla has a 3D single-crystal-like long-range order (Fig. 2.6-9d). The medullar/trabecular extensions forming a framework of thin, parallel lines (Fig. 2.6-9d) function as the nucleation surface for cortex crystal growth (Fig. 2.6-9e). Thus, the cortex appears to feature multiple crystal entities with similar orientations that stretch parallel to the morphological long axis of the spine, up to its outer tip surface (Fig. 2.6-9e). The c-axes orientation of cortex crystals scatters broadly perpendicular to the medullar orientation. It can be concluded that the microstructure and crystallographic texture of the cortex crystals are determined by the surface configuration of the extended trabeculae of the medulla; their growth process is largely influenced by competitive growth determinants (Checa 2018).

Considering that a competitive growth process determines the microstructure of the cortex layer crystals, it is fascinating to find that this process can lead to the complex serrated and undulating outer spine surfaces observed for *C. cidaris* (e.g., Figs. 2.6-7, 2.6-8). Our results indicate that the outer surface of the medulla is rarely perfectly smooth and conical. As overview measurements suggest, the medulla rather forms longitudinal crests with angular outlines (Fig. 2.6-AP4). Indeed, the thin trabecular extensions of the medulla can predetermine the thickness, morphology and outer surface of the entire cortex layer. Even when considering that their small thickness partly appears from the cut that sections them more and more tangentially, the trabecular extensions still vary from the microstructure of the inner medullar stereom. Observable at regular distances along the cross-section of a primary spine (Fig. 2.6-AP5a), the medullar extensions form fan-like extensions (white arrows in Fig. 2.6-AP5b, c). Similar to the tip of the spine, this framework of fan-like extrusions is filled with fine-grained crystals, oriented perpendicular to the extension of the medulla (see pole figures in Fig. 2.6-AP5b, c). This specific microstructural arrangement in the upper shaft and tip of the spine and within the longitudinal crests may be a unique way for the organism to optimise two aspects of the outer spine surface:

- (i) Generating a porous framework that functions as a nucleation template for the cortex and allows the organism to crystallise sophisticated spine morphologies, such as the longitudinal crests, at low metabolic cost.
- (ii) Compared to the relatively weak stereom that can promote crack development (Moureaux et al. 2010), the thin encasing cortex can better dissipate cracks in its polycrystalline microstructure, thus optimising the spine's toughness without losing the energy absorption properties of the stereom (Yang et al. 2022b). For the latter, two microstructural characteristics are important: (1) the small size of most cortex crystals leads to many grain boundaries. These can block dislocation and crack development in biological as well as man-made materials (Shin et al. 2016). (2) The c-axes orientations of the cortex crystals are generally oriented orthogonal to the outer spine surface.

Previous studies investigating the azimuthal variability of mechanical properties in biomineralised tissues showed that the hardness increased when measurements were performed on materials with crystal c-axes perpendicular to the tested surface (Berman et al. 1993; Hoerl et al. 2025b). Accordingly, even though the microstructure of the cortex crystals appears to be driven to a large extent by a competitive growth mechanism, the previously described specific texture is also relatable to material function, i.e. to some degree it is biologically determined.

The competitive growth mechanism that influences the texture and microstructure of the cortex is also obvious from the spine shaft, where the nucleation surface provided by the trabeculae of the medulla is smooth (Figs. 2.6-8d-f, 2.6-10). The texture of the first-formed cortex crystals at the spine shaft is broadly axial; however, their co-orientation strength is low, as indicated by MUD values between 50 and 70. Towards the outer spine shaft cortex surfaces, crystal sizes (from $\sim 20 \mu\text{m}^2$ to around $200 \mu\text{m}^2$; see Fig. 2.6-AP5a-c) and crystal co-orientation strength (see MUD values in Fig. 2.6-10) increase, and crystal orientation becomes more and more coherent with distance away from the medulla. These structural characteristics point to a microstructure determined by growth competition. At crystal formation through growth competition, many crystals nucleate close to each other and, at growth, compete for space. Due to the anisotropic growth kinetics of calcite, the likelihood for a small crystal to grow into a large entity and to outcompete its neighbours depends on its crystallographic orientation. It is inversely related to the deviation of the crystal's growth direction (c-axis) from an orientation normal to the nucleation template. The growth competition process results in a substantial decrease in the number of crystals, an increase in crystal size and the generation of a progressively stronger crystallographic preferred orientation as one moves away from the nucleation substrate (Fig. 2.6-10b, c). Calcite c-axes in the outer cortex shaft of *C. cidaris* are almost parallel to each other, and the texture reaches MUD values up to 220 (Fig. 2.6-10). Nonetheless, the crystals at the outer cortex are still significantly more misoriented than the crystals that form the highly co-oriented medulla, where we found MUD values of about 660 to 700. We conclude that since the medulla or its trabecular extensions function as nucleation surfaces for the growth of the cortex, the smoothness of the outer medullar surface defines the arrangement and crystallographic texture of the cortex crystals.

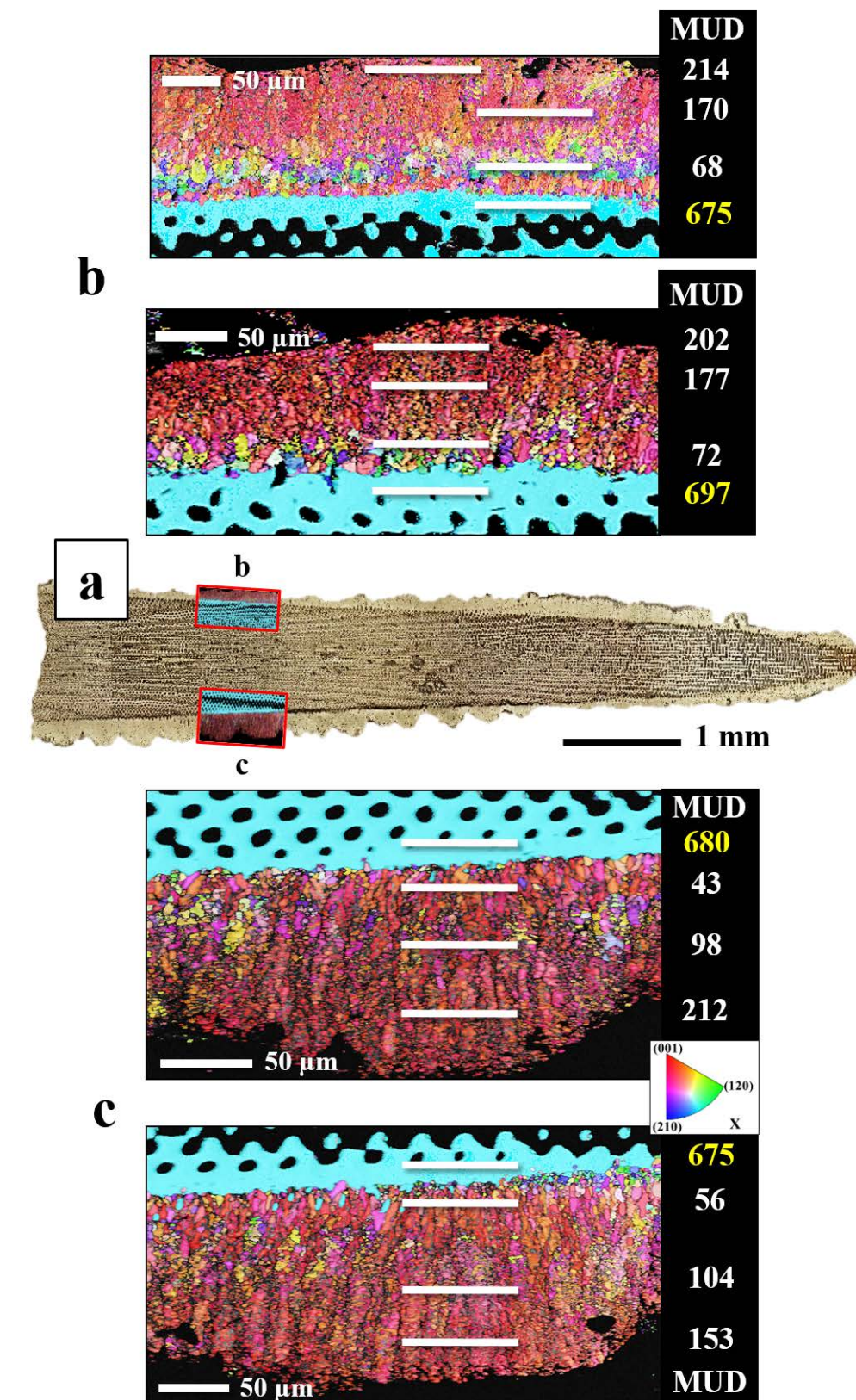


Figure 2.6-10. Calcite crystal co-orientation strength, expressed with MUD values, for the medulla and for the cortex along the shaft of a *Cidaris cidaris* secondary spine (a-c). The position of EBSD scans is given with a confocal micrograph (a); measurements were performed on opposing sides of the outer spine surface. The calcite of the stereom of the medulla is co-oriented, showing MUD values between 675 and 700 (b, c). The calcite of the first-formed cortex crystals is significantly less co-oriented ($43 < \text{MUD} < 72$), however, their co-orientation strength increases towards the outer spine surface ($153 < \text{MUD} < 214$) (b, c). EBSD data were evaluated with conventional EBSD data evaluation.

Since trabecular extensions run parallel to the morphological long axis of the spine, they are most apparent at the tip of the spine where their close spacing is best visible (Fig. 2.6-9). The cortex crystals nucleating from the trabecular/medullar extension framework, therefore, spatially restrict themselves in three dimensions (Figs. 2.6-7, 2.6-9, 2.6-AP5d-f). This impedes the growth of large crystals and generates the particular microstructure and irregular crystal morphologies that we observed for the cortex at spine tips. In contrast, the cortical layers along the shaft of the spines show lack of trabecular/medullar extensions. This generates a rather smooth outer nucleation surface for the growth of cortex crystals, although the topography of the inner stereom, per se, is very intricate. Due to the lack of trabecular extensions blocking the crystallisation pathway away from the medulla, the cortex crystals at the shaft can grow competitively, increasing in size and crystallographic co-orientation. For secondary spines, we found that the cortex occupies only for the upper third of the entire spine's outer surface (Fig. 2.6-AP6a). The onset of the cortex is directed by a ring-shaped medullar bump that follows the orientation of the trabeculae (yellow star in Fig. 2.6-AP6b). It is imperforate and has a thickness of up to 50 μm , comparable with the thickness of the adjacent cortex (Fig. 2.6-AP6b). Below this bump, the outer surface of the secondary spines is defined by a co-oriented microstructure that resembles the microstructure of the medulla (Fig. 2.6-AP6c). However, rather than forming a galleried stereom, the pore size decreases towards the outer spine surface; this outermost hard tissue is usually imperforate (Fig. 2.6-AP6c). We conclude that even though the microstructures of the spine cortex differ significantly for the tip and shaft of the spine, the crystal growth process is consistent throughout the entire cortex. With the cortex of the spine, we observed, for the first time for a carbonate biological hard tissue, two different configurations of the competitive growth process: (1) an initial and (2) an advanced growth configuration, predetermined by the surface structure of the nucleation template and facilitated by the available space for the growth of crystals.

The test

The *c*-axis orientation of the calcite plates in the test is tangential to the outer test surface, as reported by Raup (1959), who identified the crystallographic orientation in coronal plates of *C. cidaris* using optical light microscopy. The results of the EBSD measurements in this study agree with the relation between the crystallographic orientation of this echinoderm calcite and its test morphology, as shown by Raup (1959). The *c*-axes of the calcite crystals within the test plates follow the curvature of the outer test surface in the aboral side's direction (Fig. 2.6-1). Several hypotheses have been proposed to explain why some sea urchin tests show this characteristic; however, its functional significance is still unknown. Raup (1959; 1960; 1965) assumed that the preferred crystallographic orientation of the *c*-axes might be related to environmental adaptations. According to this theory, light-sensitive echinoids could utilise the anisotropic transmission properties of calcite to adapt to shallow, sunlit environments and block unwanted sunlight. However, no correlation could be found between the crystallographic organisation of the test and the habitat (Raup 1962a). It is more likely that the preferred *c*-axes

orientation is important for plate curvature and, thus, controlled by the secreting epithelium (Raup 1962a; Raup 1962b) or results from developmental constraints during growth (Bodenbender 1997).

The test plates feature single-crystal-like stereom frameworks slightly tilted to each other along the test profile. The axial co-orientation strength within the test plate varies between MUD values of 661 and 716. As a reference, synthetically grown calcite single crystals have an MUD value of 712 (Griesshaber et al. 2017) and 725 (Nindiyasari et al. 2015). Strikingly, the highest abundance of individual test plates was detected on the oral side near the masticatory apparatus. Each section is structurally locked by interconnecting trabecular extensions as described by Seilacher (Seilacher 1979), Hidaka and Takahashi (1983) and Smith et al. (1991). Misorientation angles between neighbouring sections vary between 15° and 45°.

Exceptional for both cuts through the shell and both investigated sea urchin species is the polycrystalline rim of the primary tubercles (along the terminal knob) at the aboral side (Figs. 2.6-4, 2.6-11). The tubercle rim resembles a polycrystalline aggregate with an axial texture. The longitudinal axes of the tubercle crystals are oriented perpendicular to the single-crystal-like plate and the outer tubercle surface. The crystallites are limited to the denser microperforate stereom fabric (Figs. 2.6-4a, b, 2.6-AP2a, b). The 3D “single crystal-like” plate contrasts with the polycrystalline boss, which lacks crystal orientation continuity. While this bimodal-like texture pattern could also be found in the base of secondary spines (Fig. 2.6-7b-d), it was not observed for the base of the primary spines (Fig. 2.6-7a). Okazaki et al. (1981) reported a similar polycrystalline microstructure using crystal etching and decoration. Their study showed no correspondence between the c-axes of the tubercle and the c-axes of the spine base, indicating that the two structures develop independently from each other. Donnay and Pawson (1969) mention that the rotating spine on the tubercle tip, connected by a ball-and-socket joint, has a grinding action. The mechanical stress breaks off small bits of skeletal material, which will fuse to a polycrystalline structure during growth (Towe 1967; Okazaki et al. 1981). Our results indicate that for both the tubercle, the parapet and the secondary spines (Fig. 2.6-5), the polycrystalline regions do not disrupt the porous architecture of the stereom but rather continue it up to the outer shell surface (Figs. 2.6-5, 2.6-6, 2.6-AP2). Similar to the cortical layer in primary and secondary spines, the axial texture of the polycrystalline knob runs perpendicular to the single-crystal-like plate. This shows that the tubercle crystals are not randomly oriented. Their orientation follows a directed growth process that might result from growth competition.

In summary, our study shows the interesting properties of calcite microstructure and texture at the sea urchin terminal knob of tubercles, parapets and along the outer sections of the spine base. These sections consist of calcitic trabeculae, their growth and organisation is strongly biologically determined. Nonetheless, calcite microstructure and texture are distinct from the rest of the test or spine. We found large crystals (mean area: 800 μm^2) with dendritic morphologies and calcite c-axes oriented perpendicular to the skeletal element and orthogonal to the calcite orientation of the adjacent test or

spine. These skeletal portions, the terminal knob of the tubercle, the parapet and the surface of the base of the spine, are located near muscle attachment sites (Figs. 2.6-5, 2.6-AP3). Valved marine organisms develop a specific crystal microstructure and crystal texture at the sites where the muscles attach to the valves. As shown for other shelled organisms, e.g. for bivalves (Hoerl et al. 2024a, b) and brachiopods (Hoerl et al. 2025a), it appears that at muscle attachment sites of echinoids as well the crystals adjacent to the tendon cell layer of the attaching muscles often feature large entities. These crystals generally have their c-axes oriented perpendicular to the surface of the skeletal element (this study and (Hoerl et al. 2024a, b) and, most probably, for a strong attachment, parallel to the collagen-rich fibrils that leave the focal adhesions of the muscle cells. Although the shell-muscle attachment varies between echinoderms and bivalves or brachiopods, it is interesting to observe that across different phyla, the presence and attachment of muscles seems to influence and manipulate the microstructure of biological hard tissues.

Comparison of calcite microstructure and texture for sea urchin species living in the same habitat

C. cidaris is a specimen representing the Cidaroidea, a subclass of the Echinoidea. First EBSD measurements on the *C. cidaris* test and skeletal elements were reported by Förster (2020). A different subclass of Echinoidea is the Euechinoidea; this subclass includes most sea urchin species living today. First EBSD measurements are reported by Alsheikha (2020) for the test and the spines of the euechinoidean sea urchin *Paracentrotus lividus*. *P. lividus* is a well-studied organism (Politi et al. 2004; Moureaux et al. 2010; Goetz et al. 2014; Varkoulis et al. 2020) and lives in shallow waters in the Mediterranean Sea. *C. cidaris* and *P. lividus* often coexist; however, they occupy different subareas of the same habitat.

In contrast to the crystallographic pattern of the test of *C. cidaris* (Fig. 2.6-11a), *P. lividus* exhibits c-axes orientation perpendicular to the test plate's outer surface (Fig. 2.6-11b). Test plates in *P. lividus* mainly comprise a single-crystalline-like labyrinthic stereom fabric. The microstructure of the boss varies significantly, with galleries running perpendicular to the test surface (Fig. 2.6-11b). The terminal knob of the tubercle comprises a polycrystalline aggregate that is not limited to the tubercle rim, as it is the case for the tubercle of *C. cidaris*. This might indicate differences in the muscle-tubercle attachment configuration for the two investigated sea urchin species.

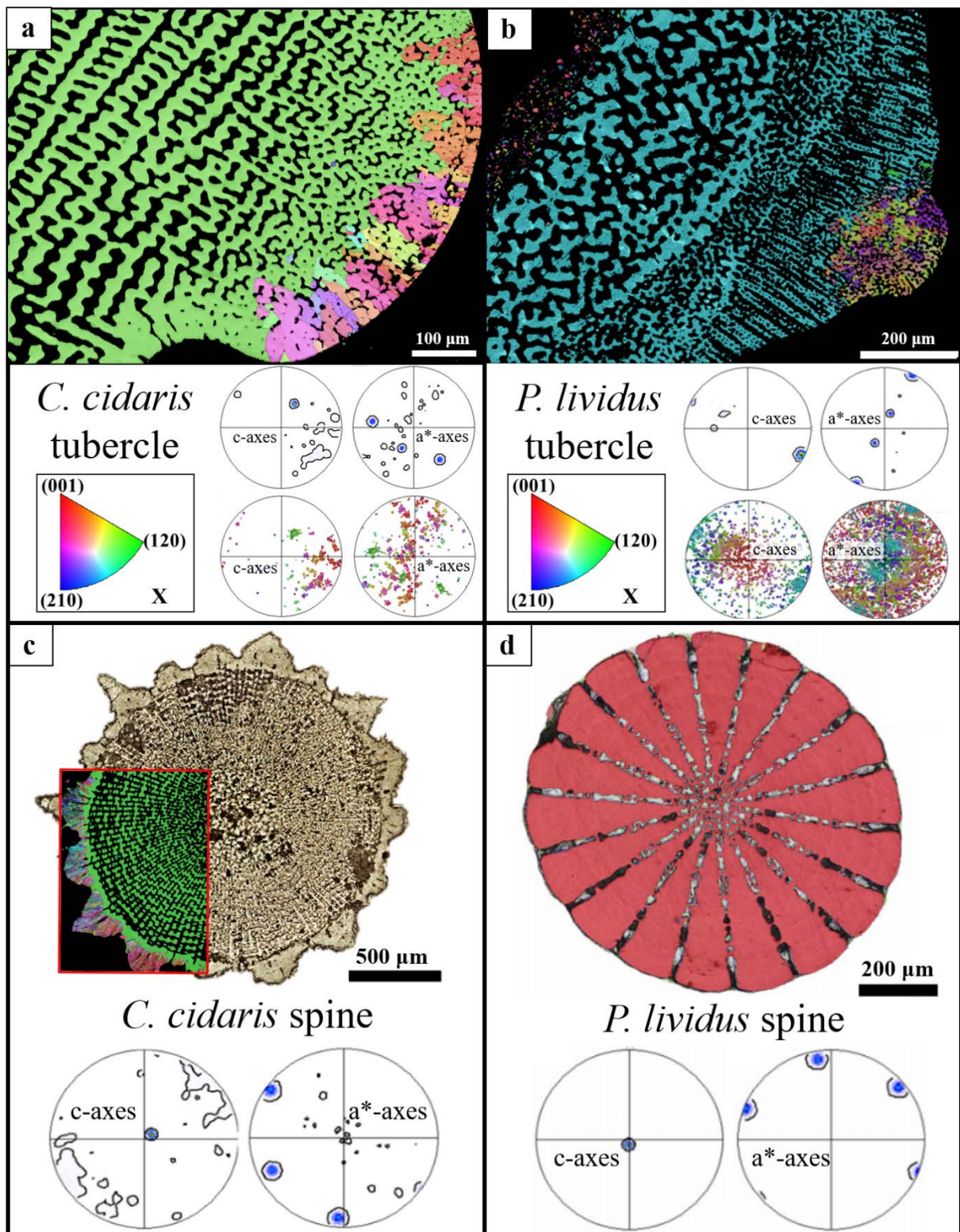


Figure 2.6-11. Comparison of microstructure and texture characteristics between *Cidaris cidaris* and *Paracentrotus lividus* tubercle (a, b) and spines (c, d). EBSD data were evaluated with conventional EBSD data evaluation. The colour-coded EBSD maps of *C. cidaris* (a) and *P. lividus* (b) visualize the interlinkage between the highly co-oriented calcite of the plate and that of the polycrystalline knob of primary tubercles. The polycrystalline terminal knobs keep the porous stereom structure of the plate, however, differ strongly in their crystallographic texture (a, b). EBSD scans were performed on the cross-sections of *C. cidaris* (c) and *P. lividus* (d) primary spines. *C. cidaris* spines feature a polycrystalline cortex surrounding the single-crystalline medulla (c). *P. lividus* spines do not have a cortex; instead, they are formed of co-oriented stereom calcite at the spine base that merges into radially arranged, dense wedges (d).

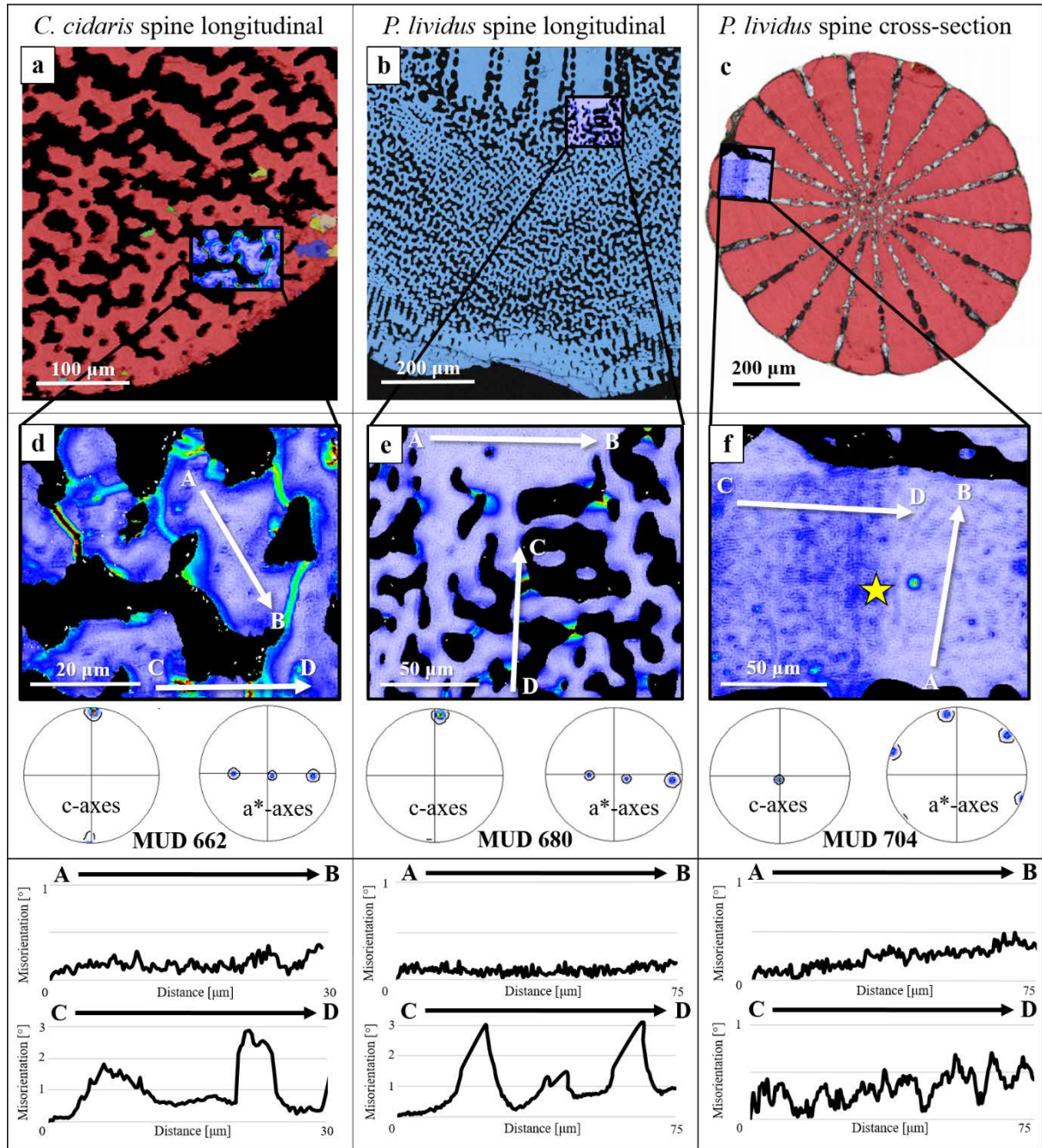


Figure 2.6-12. Comparison of internal misorientations between *Cidaris cidaris* and *Paracentrotus lividus* spines. EBSD data were evaluated with conventional EBSD data evaluation (a-c) and evaluation using pattern matching (d-f). Colour-coded EBSD overview maps (a-c) show the spine microstructure and the position of the maps that were evaluated with pattern matching (d-f). Analogous to Fig. 2.6-4c, d, the pattern-matched measurements are displayed as Kernel average misorientation maps between 0°-2° (d-f). The pattern-matched EBSD maps are complemented with contoured pole figures and misorientation versus distance profiles (d-f). In the stereom of *C. cidaris* and the basal spine part of *P. lividus*, misorientations in the trabeculae are low (< 1°). High misorientations, up to 3°, are present at the connecting bridges between the trabeculae (d, e). The dense wedges of *P. lividus* are highly co-oriented and only show small misorientations up to 0.5° (f). The yellow star in (f) highlights a region with increased misorientation frequency that runs laterally to the spine septa of the *P. lividus* spine cross-section.

The studies of Alsheikha (2020) and Varkoulis et al. (2020) reveal a compact microstructure of the spine shaft and tip of *P. lividus* that strongly contrasts the perforate stereom of *C. cidaris* spines (Fig. 2.6-11c, d). The spines of *P. lividus* comprise tightly spaced wedges, the septa, which increase in thickness towards the outer spine surface feature a 3D single-crystal-like long-range order (Fig. 2.6-

11d). The porous zone between the wedges is narrow in cross-section and appears uniformly thick. Longitudinal cuts through the two species' primary spines highlight differences in microstructure of the spine basal area. The primary spines of *C. cidaris* comprise a labyrinthic medulla with many small-angle misorientations, particularly along the trabecular junctions (Fig. 2.6-12a, d). In contrast, the basal part of *P. lividus* spines comprises a galleried, single-crystal-like stereom on the inside of the spine and a microperforate stereom along the spine's outer surface (Fig. 2.6-12b, e). The spine base, shaft and tip show crystallographic texture continuity, and the microstructural changeover between the basal stereom and the imperforate septa is smooth in *P. lividus* spines. The crystallographic orientation of the *c*-axes follows the orientation of the long axis of the spine (Fig. 2.6-12c, f). In contrast to *C. cidaris*, the spines of *P. lividus* lack a polycrystalline, weakly co-oriented cortex.

Hence, although living in the same habitat, *C. cidaris* and *P. lividus* exhibit differences in texture and microstructure of both the test and the spines. The presence of a cortex and the highly porous microstructure in *C. cidaris* spines, compared to those of *P. lividus*, are striking features and might yield advantages in resilience to, e.g., stress distribution, hard tissue regeneration and other structural attributes.

The single crystalline character of the sea urchin test and spine

The 3D “single crystal-like” stereom of the plates and the medulla of the spines of *C. cidaris* show a strong axial co-orientation strength with MUD values ranging from 662 to 723. As mentioned in Section 2.2, laboratory-grown calcite single crystals have MUD values between 712 (Griesshaber et al. 2017) and 725 (Nindiyasari et al. 2015).

Authors who used conventional EBSD measurement and data evaluation report that sea urchin spines are single crystals (Moureaux et al. 2010). However, as demonstrated in this study, small misorientations are not detected with conventional EBSD measurement and data evaluation. An exception to the latter is formed by the study of Goetz et al. (2010). Based on high-resolution EBSD measurements and, in particular, a specific EBSD data evaluation, the authors could show minor orientation differences of up to 0.1° within the septa of the sea urchin *Amblypneustes pachistus* (Goetz et al. 2010). While the polycrystalline nature of sea urchin skeletal elements has previously been suggested by other authors, such as Seto et al. (2012), Cölfen et al. (2022), and Goetz et al. (2014), the combination of high-precision EBSD and the pattern matching method used in the presented study shows for the first time the presence and distribution of small-angle misorientations. Rather than using an image transform, the latter method tests for each point in the measured EBSD map dynamical pattern simulation with precise calibration parameters (Trimby et al. 2024). Through EBSD pattern matching, we detected that the orientation precision of EBSD measurements for biological carbonate hard tissues becomes significantly improved to an angular precision of less than 0.1° compared to the 0.5° to 1°

angular precision with the standard Hough-transformation-based EBSD data evaluation method (Engler et al. 2023).

The small-angle misorientations in the *C. cidaris* test

High-resolution misorientation maps and profiles show that *C. cidaris* shells comprise considerable misorientations in both test plates and spines (e.g., Figs. 2.6-2e-g, 2.6-4c, d, 2.6-5d, 2.6-6d, 2.6-12d and 2.6-AP2c-e). We observed large-angle misorientations (more than 5°) in the polycrystalline parts and small-angle misorientations (up to 3-5°) in the single-crystal-like sea urchin calcite (see Terminology Section A.1). In the plates, the inner trabeculae usually have a high crystallographic co-orientation (MUD values > 700). This is indicated by whitish colours in the high-resolution EBSD maps (e.g., see arrow visualizing the trajectory location of profile C-D in Fig. 2.6-2e) and with the cumulative misorientation profiles (e.g., Figs. 2.6-2e, g, 2.6-4d). We consider the inner trabeculae to be more or less single-crystalline.

Due to the perforate character of the stereom framework, the test plates have a large interior surface. Angular misorientations predominantly appear along the trabecular junctions, reaching misorientation angles up to 2° (Fig. 2.6-2e, f, 2.6-4d). Our study shows that the regions with low-angle misorientations between crystals are not evenly distributed along the skeletal element surface; they are particularly frequent for pore cross-sections with strong curvatures (yellow arrows in Fig. 2.6-4d). Since the labyrinthic stereom comprises many trabeculae that simultaneously grow in different directions, it is common that trabeculae converge and interconnect. However, strongly curved interconnection surfaces may interfere with the stereom organisation, which is responsible for the advanced mechanical properties observed for the sea urchin hard tissue (Ji et al. 2022). Thus, the misoriented areas might result from the organism's attempt to counteract structural instabilities that result from the generation of the labyrinthic stereom framework. This behaviour has been recently suggested for the echinoderm stereom in the starfish *Protoreaster nodosus*, regarding the misorientations as a by-product of the complex skeletal formation process that strives for the optimisation of the hard tissue mechanical performance (Hyde & Meldrum 2022; Yang et al. 2022a).

Our high-resolution EBSD measurements indicate that the crystallographic co-orientation of the different stereom fabrics is not similar. For example, differences in the misorientation angle distribution become visible when comparing the microperforate stereom near the tubercular boss (Fig. 2.6-4c, 2.6-AP2c-e) with the labyrinthic stereom located in the centre of the same test plate (Fig. 2.6-4d). The latter shows, in general, small misorientation angles for intratrabecular regions or the trabecular connections (Fig. 2.6-4d). However, in the microperforate section near the outer shell surface, the Kernel average misorientation is significantly higher. This is particularly well observable in the central part of the trabeculae, where the microperforate stereom has an average local misorientation of ~0.5° versus ~0.1° in the labyrinthic stereom (Fig. 2.6-4c, d). The microperforate stereom near the tubercle features streak-

like regions of internal misorientations ($1-2^\circ$) that appear to connect the pores and traverse the stereom (Fig. 2.6-4c). These frequently occurring misorientation streaks could result from deformations caused by high stresses acting on the tubercle due to muscular activity. However, the exact origin of this feature, which also occurs in the muscle attachment region of primary spines (see Fig. 2.6-12a, d) is not yet understood and needs to be analysed in more detail.

Comparison of the single-crystallinity of C. cidaris and P. lividus spines

Angular misorientations near sharp pore surfaces of a 3D “single-crystal-like” stereom are not limited to the plates of the test; they are also frequent in the spines of *C. cidaris*. Near the base, the primary spines of *C. cidaris* form a labyrinthic stereom of co-orientated trabeculae; here, we find significant misorientations along the trabecular junction surfaces (Fig. 2.6-12a, d). The misorientation profiles in the pattern-matched EBSD measurements (Fig. 2.6-12d) indicate that the intratrabecular spine sections are well co-oriented with a cumulative misorientation angle below 0.5° . Even though, the spines cannot be considered to be single-crystalline due to the high misorientation angles of up to 3° towards the trabecular surfaces and intersections (profile C-D in Fig. 2.6-12d). The lack of orientational continuity is, furthermore, apparent from the rather low MUD value of 662 of the spine (Fig. 2.6-12d).

In contrast to *C. cidaris*, the stereom in *P. lividus* primary spines does not extend from the base to the tip but gradually shifts into septa starting upwards from the shaft. In the basal areas of *P. lividus* spines, the stereom appears to be galleried, with the channels somewhat aligned longitudinally to the growth axis of the spine (Fig. 2.6-12b). While in *P. lividus* crystallographic misorientations within trabeculae and the dense septa are very low ($< 0.3^\circ$), the stereom also features scattered areas with high misorientations (up to 3° , Fig. 2.6-12e). Nonetheless, these are far less widespread in *P. lividus* spines, compared to *C. cidaris* spines. Two misorientation profiles traversing the septa both longitudinally and perpendicularly show that the misorientation distribution differs within the cross-section of the spine (Fig. 2.6-12c, f). Perpendicularly (profile A to B in Fig. 2.6-12f), misorientations appear regular and have a cumulative misorientation angle below 0.5° . Longitudinally, from the outer spine surface towards the medulla (Profile C-D in Fig. 12f), cumulative misorientations fluctuate periodically; the point-to-point misorientations are significantly higher than the ones for the lateral profile. Differentiated regions of enhanced misorientation lateral to the growth direction of the septa (yellow star in Fig. 2.6-12f) and the periodic misorientations crossing the septa indicate different growth spurts from the inner to the outer spine surface. Thus, the hard tissue crystallised in the same growth spur is highly co-oriented; however, the hard tissue that crystallised at different growth spurs comprises considerable misorientations. Our results not only demonstrate the polycrystallinity of sea urchin calcite, but also show that the degree of internal misorientation varies depending on the stereom fabric and thickness of the respective trabeculae. A similar effect has recently been observed with SAXS and WAXS studies on different stereom fabrics in *Cidaris rugosa*: The authors report a polycrystalline structure with a

varying degree of internal co-orientation that might be caused by differences in trabecular order (Jessop et al. 2024).

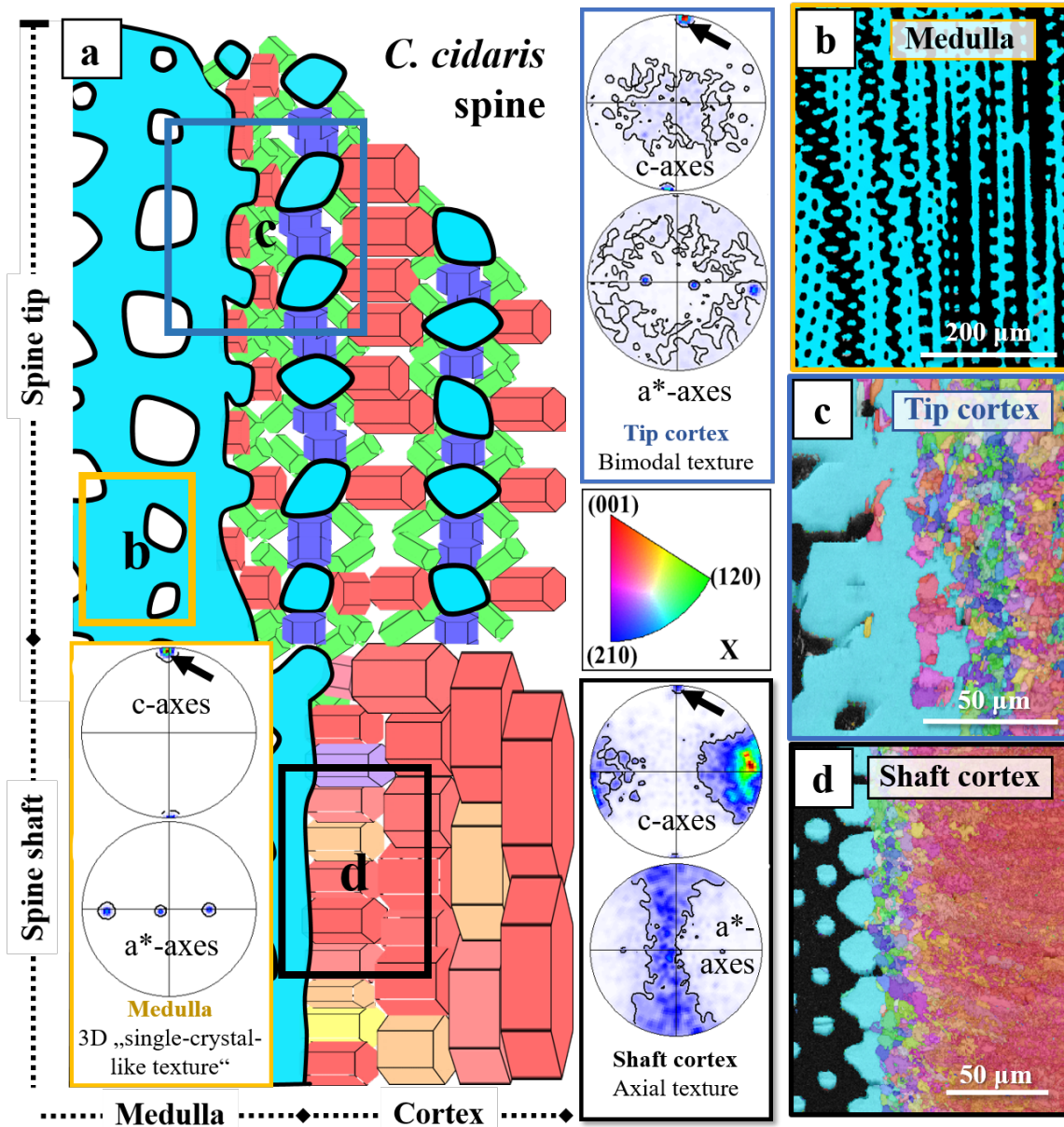


Figure 2.6-13. Schematic illustration (a) depicting crystal arrangement of spine medulla (b), at cortex tip (c) and at cortex shaft (d) for *Cidaridaris cidaris*. For substantiation of the suggested crystal growth model in (a) we include the microstructure and texture of spine calcite at the medulla (b), the cortex tip (c) and the cortex shaft (d) gained from EBSD scans. Measurements were evaluated with conventional EBSD data evaluation. The sizes of the sketched hexagonal crystals in (a) illustrate the evolution of grain sizes following the competitive growth model. The shaft and tip of the spines comprise two main fabrics. The medulla is formed by highly co-oriented trabeculae organised in a galleried to rectilinear stereom (b). At growth, a series of thin parallel trabecular extensions form first. This trabecular framework functions as a substrate for the growth of the cortex crystals. At the spine tip, where a high frequency of trabecular extensions was observed, the cortex crystals spatially restrict one another in three dimensions (c). Due to the periodic arrangement of trabecular extensions, a linear pattern of small and irregular crystals becomes visible when applying an IPF colour-coded map to the measurement (c). As the series of trabecular extensions run parallel to the morphological long axis of the spine, only a small number of them perforate the shaft cortex, leaving a rather smooth nucleation template for the cortical layer (d). Thus, the crystals can competitively grow away from the medulla, generating a microstructure of increasingly large and co-oriented crystals towards the outer spine surface (d).

Applying misorientation profiles or texture component maps to pattern-matched EBSD maps allows us to see long-range changes in crystallographic orientation compared to a reference point. Both the *C. cidaris* and the *P. lividus* stereom show gradual rotations of the crystallographic axes. This becomes obvious from cumulative misorientation profiles (white arrows in Figure 2.6-12d, e, f) and is also observable in greater detail in texture component maps (Figs. 2.6-AP7, 2.6-AP8). For a *C. cidaris* tubercle (Fig. 2.6-AP7) and a *P. lividus* spine (Fig. 2.6-AP8), the texture component maps yield cumulative misorientations up to 2°. For the microperforate boss in *C. cidaris*, some trabeculae even have an orientational divergence of 4° compared to the mean orientation value of the measurement (Fig. 2.6-AP7). It should be noted that, surprisingly, these gradual misorientations seem to accumulate towards a specific direction in the structural element. For the tubercle, the number of misorientations increases towards the outer knob surface (Fig. 2.6-AP7), and for the spine, it increases parallel to the morphological long axis of the spine (Fig. 2.6-AP8).

In essence, the EBSD pattern matching method allows us to detect minute misorientations within biomineralised tissues with great orientational precision. The measurements performed for the test plate, tubercle, and the primary spines of *C. cidaris* and *P. lividus* show a consistent pattern between stereom organisation and small-angle misorientations.

- (i) The highest degree of crystallographic co-orientation was observed for the dense, imperforate septa of *P. lividus* (Fig. 2.6-12e, f). These structures can be considered single-crystalline. Local misorientations of more than 0.1° are uncommon, as there is a lack of major pores in the network, i.e., there is an absence of trabecular junctions within the biomineralised tissue.
- (ii) For the perforate stereom fabrics such as the galleried or the labyrinthic stereom (Figs. 2.6-2e, 2.6-4d), the crystallographic co-orientation depends on the distribution and interconnection of the trabeculae. The inner trabecular hard tissue is highly co-oriented; however, trabecular intersections creating sharp curves might cause significant misorientations. The latter may arise from the organism attempting to interconnect the differently aligned trabeculae and to smoothen pore surfaces for structural stability.
- (iii) The highest degree of misorientation was observed in the dense and microperforate stereom fabrics near the outer surfaces of the test and of the primary spines (Figs. 2.6-4, 12d). Due to decreased ordering and size of the pores, as discussed in the first Discussion section of the , the biomineralised tissue is traversed by many misorientation streaks that reduce the strength of co-orientation (indicated by the MUD value) of the calcite. These streaks are not yet well-understood. They may either stem from internal or/and external stresses exerted on the outer shell surfaces of the test and of the spines. They also might be due to the increased amount of small-sized pores, relative to the inner plate of the test.

- (iv) Our study shows that the test plates and spines in *C. cidaris* are not perfectly single-crystalline. Not only do they have polycrystalline calcite assemblies at the tubercles, parapets, spine base and cortex of the spines, but the 3D “single-crystal-like” biomineralised tissue of these skeletal elements comprises, in addition, cumulative misorientations features of up to 3° or even more.

2.6.5 CONCLUSIONS

The echinoid species *C. cidaris* forms a high-Mg calcite skeleton, with the mineralised parts consisting of a test, primary and secondary spines and the chewing apparatus. The test comprises an assembly of crystal plates and their tubercles (Figs. 2.6-1, 2.6-4). The test microstructure is a 3D meshwork of thin bands or columns, the trabeculae, which interconnect at junctions. The microstructure of the spines comprises a central medulla, formed of a network of trabeculae, and a cortex, composed of a polycrystalline assembly of small crystals that encase most of the spine shaft up to the tip (Figs. 2.6-13, 2.6-AP4).

This contribution highlights and discusses the crystallography, microstructure, and texture of the *C. cidaris* test and spines. Results are based on high-resolution EBSD measurements and sophisticated EBSD data evaluation using the pattern matching method. For the first time, for biological hard tissues, we show how this method can be used to obtain precise microstructural and textural information for biomineralised materials such as echinoid skeletal elements. Of central interest for the presented study is the assessment of misorientations within the crystals that form the stereom of the test, the tubercles and the spines for disclosing the degree of crystallinity of *C. cidaris* calcite. Even though this study focuses on the calcite of *C. cidaris*, we complement the obtained results on *C. cidaris* with measurements and observations on the calcite of *P. lividus* for comparison and a better understanding. With the latter, we investigate the structural hard tissue of sea urchin species of two echinoderm subclasses, the Cidaroidea and the Euechinoidea. We conclude the following for the calcitic hard tissue of *C. cidaris* and *P. lividus*.

The test:

1. Stereom trabeculae and pore arrangement in *C. cidaris* calcite develop with two main architectures. At outer test regions and surfaces, the stereom fabric is rectilinear and the pore organisation is microperforate; at inner test regions and surfaces, the stereom trabecular arrangement is labyrinthic and the pore organisation is irregular. We follow the stereom and pore nomenclature of Smith (1980).
2. The test consists of calcite plates. In *C. cidaris*, these interlock intricately along the serrated edges of plates. Adjacent plates are misoriented to each other through large angle

misorientations by a few tens of degrees. As EBSD data evaluation based on pattern matching demonstrates, individual test plates cannot be considered single crystals. Their calcite is rather misoriented at trabecular junctions through small-angle misorientations. Misorientations at trabecular junctions range up to 3° . Additionally, for a single crystal, MUD values should be well above 700 when calculated with a half-width of 5° and a cluster size of 3. For individual test plates, we found MUD values between 670 and 700 (half-width of 5° and cluster size 3). The decrease in MUD value for individual plates is caused mostly by low-angle misorientations at trabecular junctions. The abundance of trabecular junctions depends on the architecture of the test stereom.

3. Stereom calcite between the trabecular junctions, the intratrabecular calcite, is more or less single-crystalline. Misorientations (evaluated with EBSD pattern matching) are generally below 0.5° . MUD values are well above 700 (half-width of 5° and cluster size 3).

The tubercles:

4. The primary tubercles, the joints where the spines connect to the test plates, comprise a microstructure that differs from the stereom of the test plates. In the basal boss of the tubercle, the calcite is microperforate, formed of a dense stereom consisting of calcitic trabeculae. In the terminal knob of the tubercle, the stereom architecture is similar to that of the basal boss; however, the calcite is polycrystalline with a low crystal co-orientation strength. MUD values of the terminal knob are below 80 (half-width of 5° and cluster size 3). The basal boss is defined by a very high abundance of low-angle misorientations and, thus, a decreased MUD that scatters between 600 and 650.
5. Many crystallographic-structural aspects of tubercular calcite differ from those of the adjacent test calcite. The tubercular polycrystals have an axial texture; calcite c-axis orientations are mostly perpendicular to the outer tubercle surface. The adjacent test plates have a 3D “single-crystal-like” long-range order, with calcite c-axis orientations parallel to the surface of the test. Thus, calcite c-axis orientations of the test and of the adjacent tubercle are orthogonal.

The spines:

6. Stereom architecture, microstructure and texture of *C. cidaris* primary and secondary spines vary drastically, depending on the position within the spine. For both primary and secondary spines, we found a central galleried medulla encased by a polycrystalline cortex. For primary spines, the cortex extends over the entire shaft of the spine; for secondary spines, only about half of the spine shaft is enclosed by a cortical layer. The beginning of the cortex is determined by bumps encircling the outer surface of the medulla. For both types of spines, the cortex is thickest at the spine tip.

7. The outer surface of the medulla functions as a template for the nucleation of the cortex crystals, however, no epitaxy is evident. Along the shaft of the spine, the galleried medulla structure forms in 2D a *smooth outer surface of topologically adjacent and connected medullar galleries*. At the tip of the spine, we found a 3D, *closely-spaced network of thin galleried medullar extensions*. Cortex crystals nucleate normal to all surfaces of the outer trabeculae, with their c-axis always oriented normally to the c-axis of the medulla. Even though the outer surface of the cortex at the spine tip has a smoothness different from that of the cortex along the shaft of the spine, their growth processes are similar. The microstructure of cortex crystals is determined by growth competition.
8. The difference in cortex microstructure between the tip and the shaft of the spine is relatable to the 3D configuration of the medullar template surface (smooth or rough) and the availability of space for crystal growth. A network of round-shaped and closely-spaced medullar extensions intricately interconnected in 3D governs the tip of the spine. From the surface of these templates, crystals grow in all directions. However, due to space restrictions given by the closely-spaced medullar extensions, the growth progress is inhibited in 3D, and the 'standard competitive growth microstructure' cannot develop. We observed with the microstructure of the cortex at the very tip of the spine only the start of the competitive growth process. In contrast, along the spine shaft, towards its base, the medullar template surface is only restricted in 2D; hence, there is space for the crystals to grow away from the medulla and the competitive growth microstructure develops to advanced growth stages.
9. Since the microstructure of cortex crystals is mainly controlled by growth competition, the constitution of the medullar template and space for the growth of crystals predetermines the microstructure of cortex crystals. In contrast, the microstructure of medullar and test stereom calcite is only influenced by organism-related, biological determinants.
10. Neither *C. cidaris* nor *P. lividus* test plates, tubercles, parapets and spines should be addressed as single crystals. EBSD results show single-crystal-like, highly co-oriented sections, such as intratrabecular calcite between trabecular junctions. However, individual test plates and the medulla of the spines comprise many trabecular junctions. At all of these junctions, we observed misorientations up to 3°. Between adjacent test plates, we observed high-angle misorientations (5° to 40°). For the strongly misoriented calcite along the terminal knob and in the spines, we found also high-angle misorientations (10° to 50°).

Acknowledgements

We thank Moritz Zenkert, Ludwig-Maximilians-Universität München, Munich, Germany, for his help with sample preparation. We thank Shahrouz Amini, Max Planck Institute of Colloids and Interfaces, Potsdam, Germany, for his help with interpreting the data.

Author contributions

Conceptualisation, S.H., E.G.; Formal analysis, A.G.C., A.W., W.W.S.; Investigation, S.H., E.G., F.F., O.A.; Methodology, S.H., E.G., A.W.; Supervision, E.G., W.W.S.; Validation, A.G.C., F.H., W.W.S.; Visualization, S.H., E.G.; Writing – original draft, S.H., E.G., F.F.; Writing – review & editing, A.G.C., A.W., O.A., F.H., E.S., S.J., W.W.S.

2.6.6 SUPPLEMENTARY INFORMATION

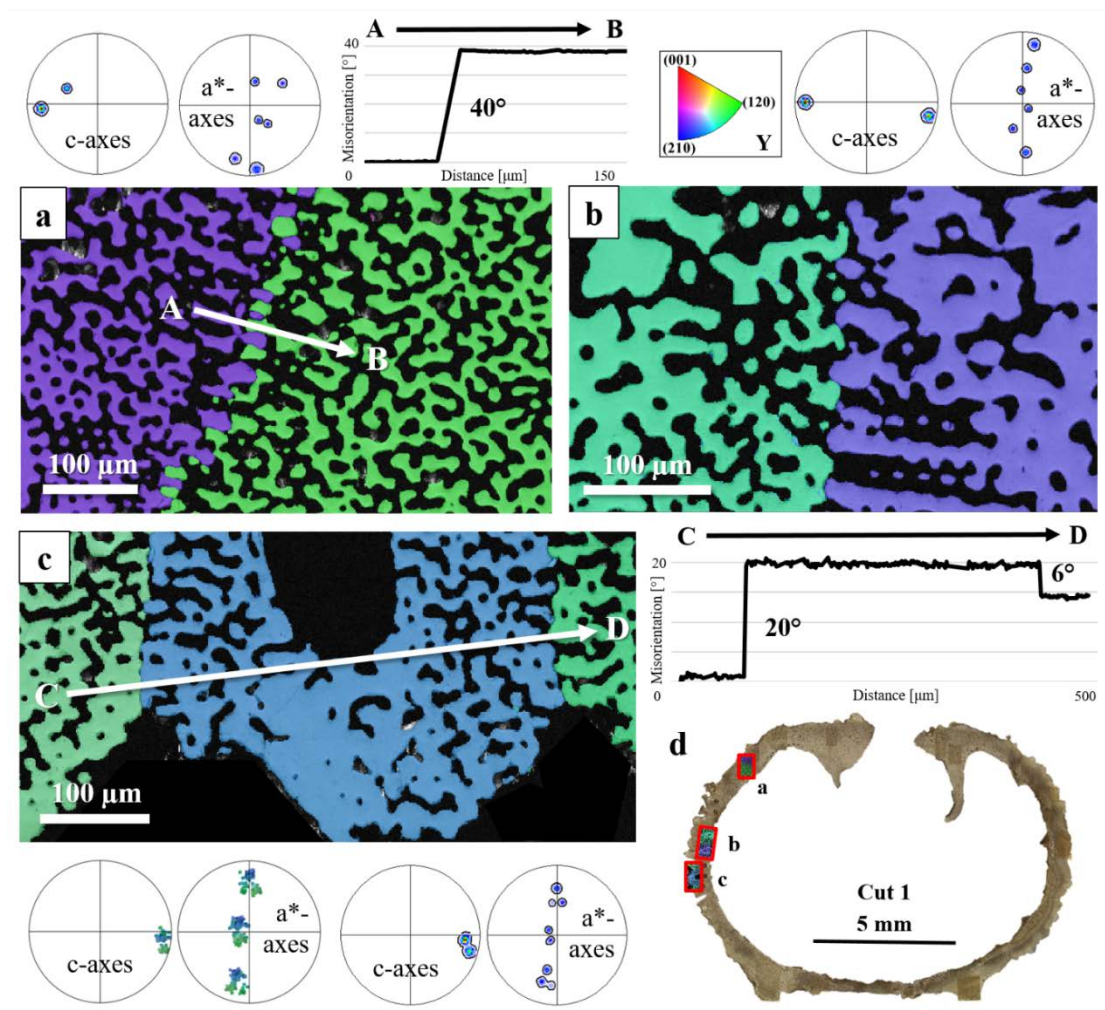


Figure 2.6-AP1. EBSD maps depicting the interlocking of adjacent test plates, the microstructure and texture of individual plates and the degree of misorientation between the plates of *Cidaridiscidaris*. EBSD data were evaluated using conventional EBSD data evaluation. The first cut was applied to section the test. The similarity in colour indicates the strong co-orientation of the calcite within the plates (a-c). Misorientation profiles A-B and C-D (a, c) show the presence of large angle misorientations (e.g. 20°, 40°) between adjacent plates. The laser confocal overview image depicts the measurement positions on the test (d).

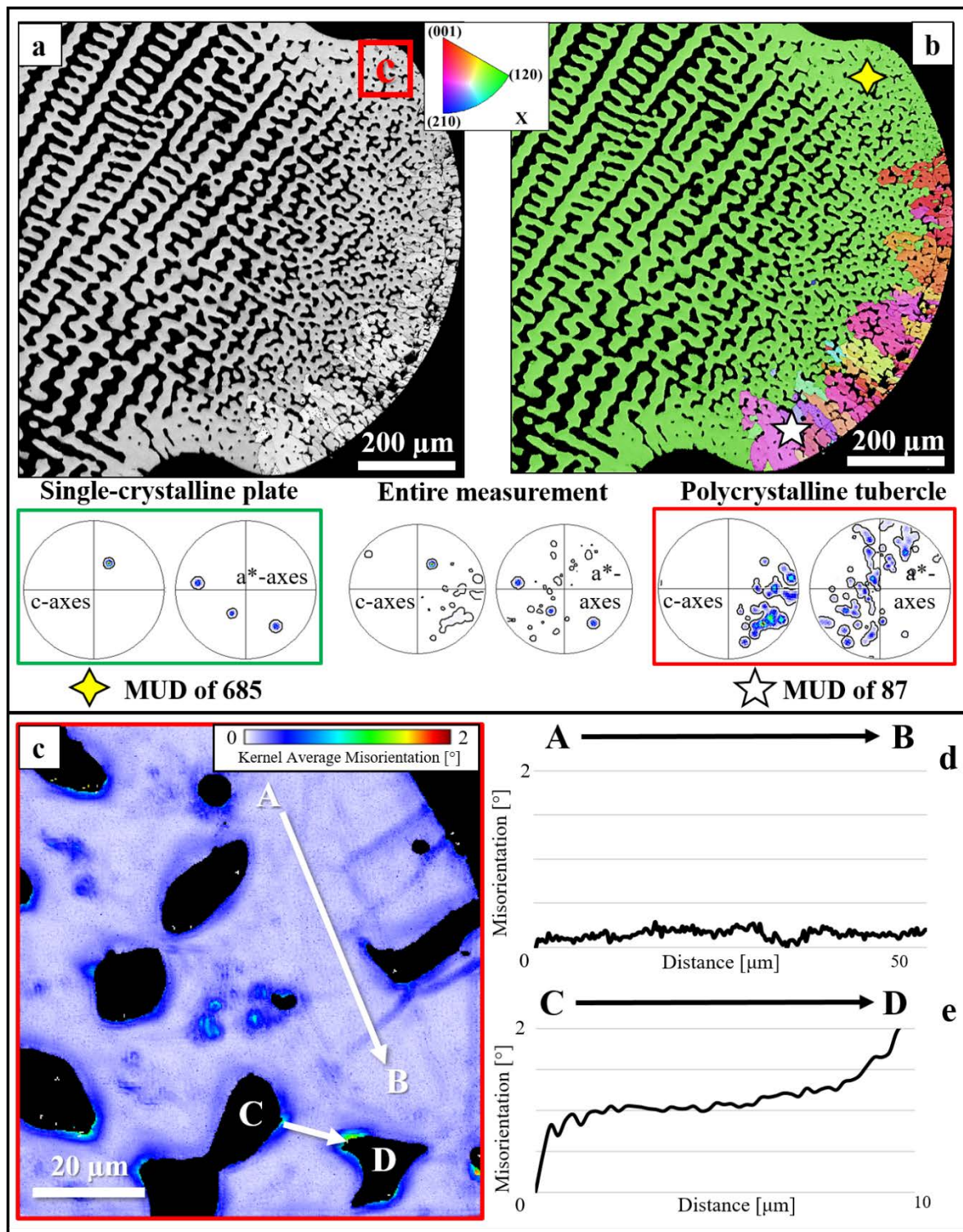


Figure 2.6-AP2. The second cut was applied to the EBSD map of the tubercle at the aboral region of the test of *Cidaris cidaris*. EBSD data were evaluated with conventional EBSD data evaluation (a, b) and pattern matching (c). The band contrast measurement (a) and colour-coded EBSD maps (b) show the bimodal microstructure and texture of the tubercles. Contoured pole figures highlight the 3D "single-crystal-like" long-range order of calcite in the plate, the axial texture of the tubercle and the orthogonal arrangement of calcite orientation between the stereom of the plate and that of the tubercle. The pattern-matched EBSD measurement shows internal misorientations within the plate and close to the tubercle (c). Misorientation versus distance profiles show a high degree of co-orientation within intratrabecular calcite (d). At trabecular junctions, misorientations can be 2° and even higher (e).

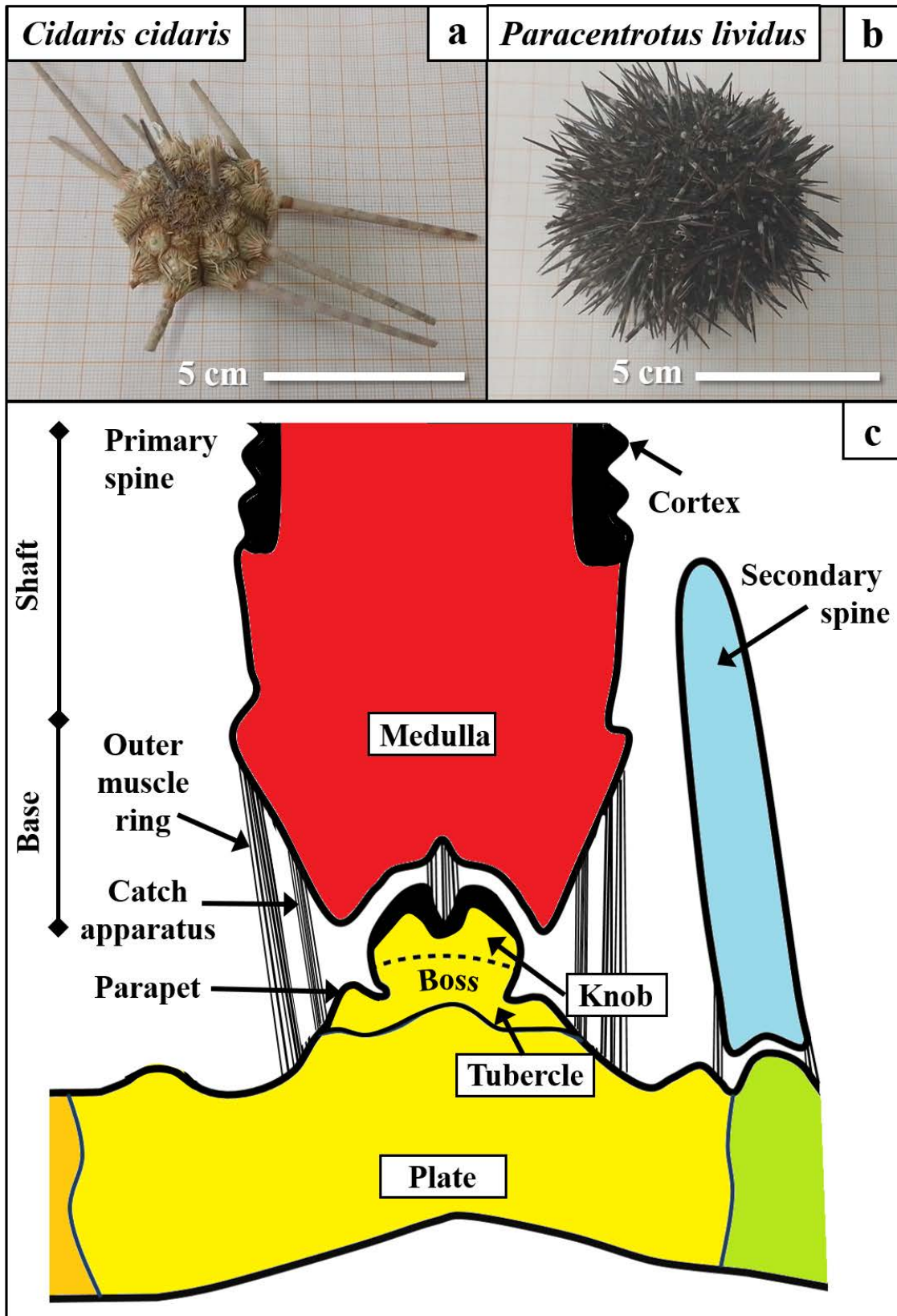


Figure 2.6-AP3. Micrographs of *Cidaris cidaris* and *Paracentrotus lividus* test and spines (a, b). Sketch showing sea urchin spines attaching to the test (c). While the long primary and shorter secondary spines in *C. cidaris* have distinctly different morphologies and sizes (a), the spines of *P. lividus* are less distinct in morphology and size (b). The terminology and mode of primary and secondary spine attachment to the test are illustrated in the schematic drawing (c). The drawing shows how spines are connected to the test via a muscle ring surrounding the basal part of the spine. At the tubercle, a ball-and-socket joint anchors the spine to the trabecular framework at the terminal knob of the tubercle and the test plate, allowing for both flexible spine movement and a strong connection.

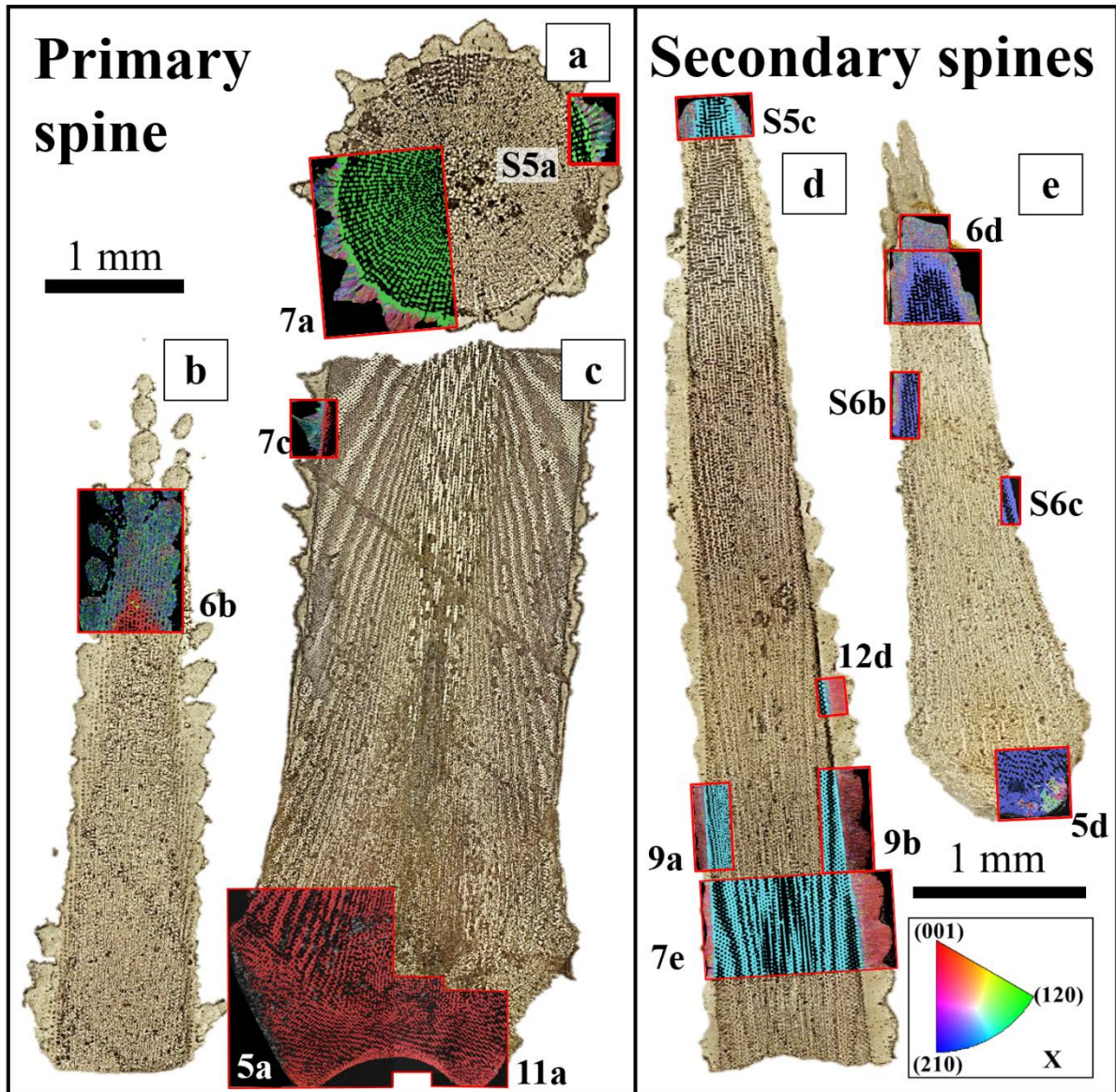


Figure 2.6-AP4. Confocal laser microscopy overviews of the investigated spines of *Cidaris cidaris* indicating the positions of EBSD scans. The specimen shown in (a) is a cross-section cut through a primary spine. Other primary spines were cut laterally through the tip (b) or base of the spine (c). The specimens shown in (d) and (e) are secondary spines cut along the lateral direction.

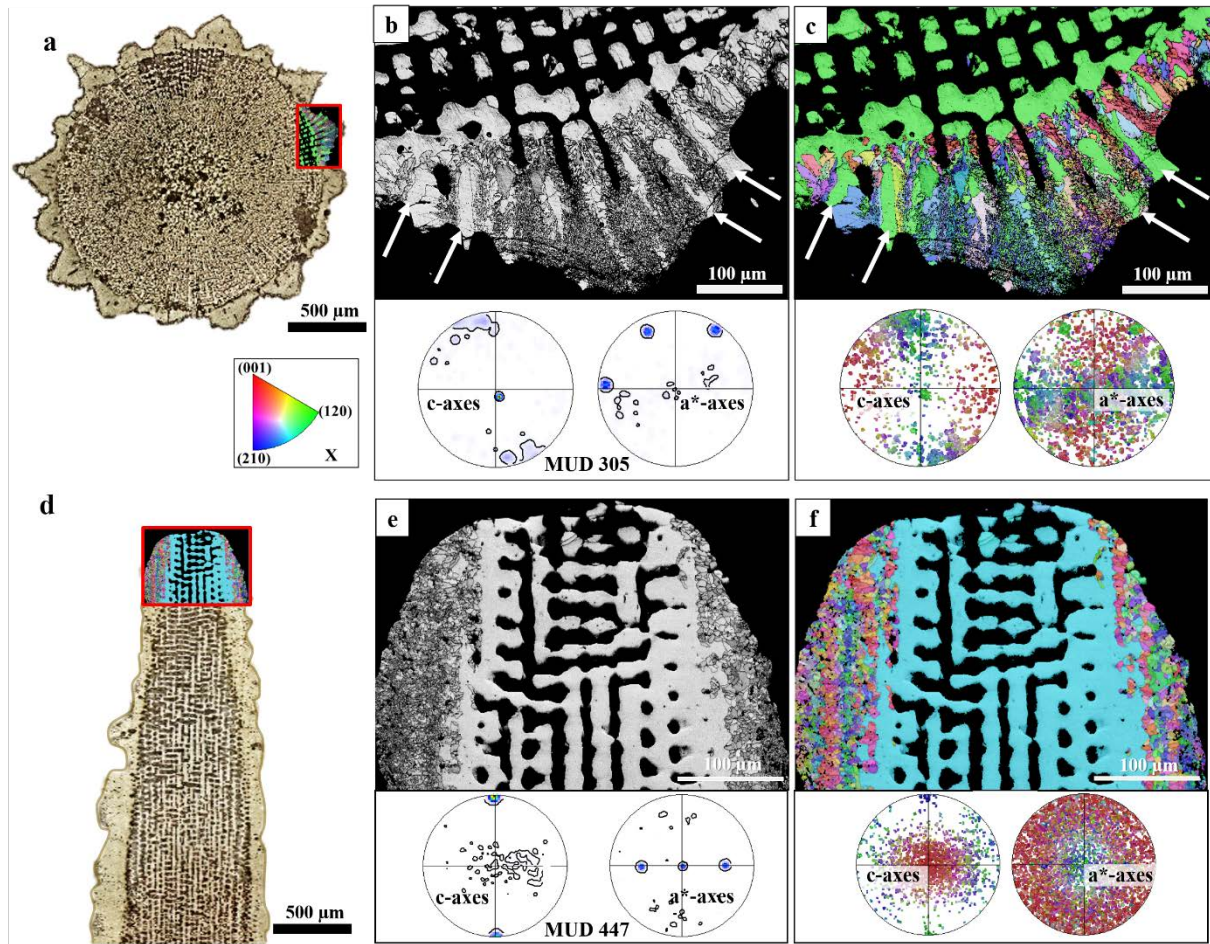


Figure 2.6-AP5. EBSD maps highlighting the microstructure and texture of a *Cidaris cidaris* primary spine medulla and cortex. Spines were cross-sectioned (a-c) or sectioned laterally (d-f). EBSD data were evaluated using conventional EBSD data evaluation. The measurement positions are indicated on the laser confocal overview images (a, d). The trabeculae of the 3D “single-crystal-like” medulla in the primary spines continue into the cortex (b, c). In the latter, the fan-like trabecular extensions (white arrows in b, c) form a template for the growth of small, irregularly shaped crystals oriented perpendicularly to the medulla (b, c, e, f). These crystals fill the space within the framework of medullar extensions and generate complex cortical structures such as longitudinal crests or barbs (a, d). The crystal growth mechanism of primary (a-c) and secondary spines (d-f) is similar.

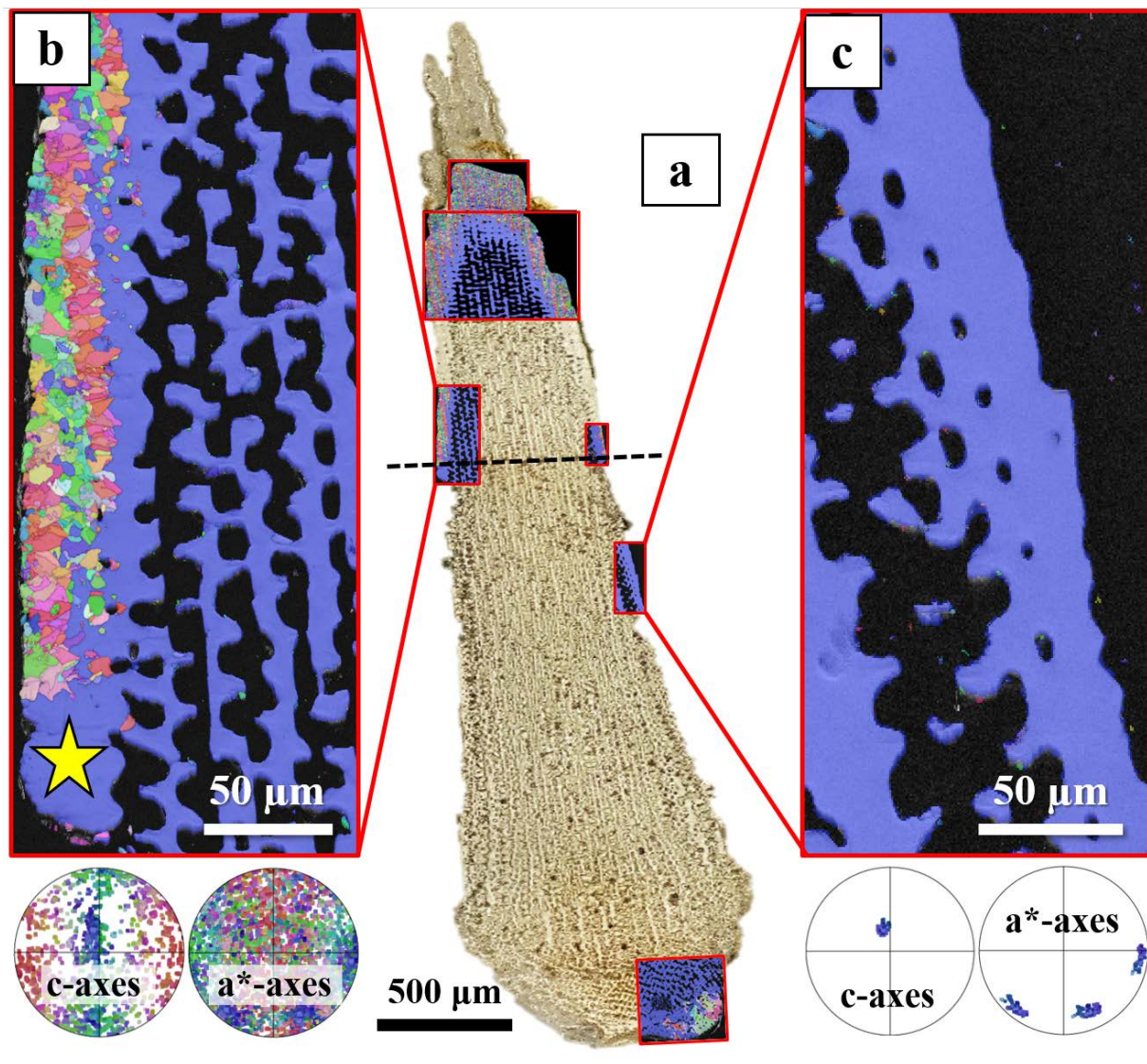


Figure 2.6-AP6. EBSD maps highlighting the outer shaft surface of a secondary and laterally sectioned *Cidaris cidaris* spine. EBSD data were evaluated using conventional EBSD data evaluation. The structure and extent of the cortex are shown with the laser confocal microscopy image (a); the EBSD maps visualise the crystallographic texture and microstructure at different spine positions (a). Besides the polycrystalline arrangement of calcite at the base of the spine, where the muscle ring attaches to the outer spine surface, most of the base and the shaft comprise a stereom formed of co-oriented calcite. The upper third of the spine medulla is surrounded by a cortex that includes multiple parallel series of small, irregularly shaped crystals (b). Interestingly, the beginning of the cortex seems to be spatially mediated by a large bump (~20 μm , yellow star in b) that spans the entire thickness of the cortex layer (b). Both the bump and the cortical layer are micro- to imperforate; strongly contrasting the large pores in the galleried stereom of the medulla (b). This feature can also be observed at the outer shaft surface of the spine, where the cortex is not yet present, and the outer trabeculae form a dense, imperforate network (c).

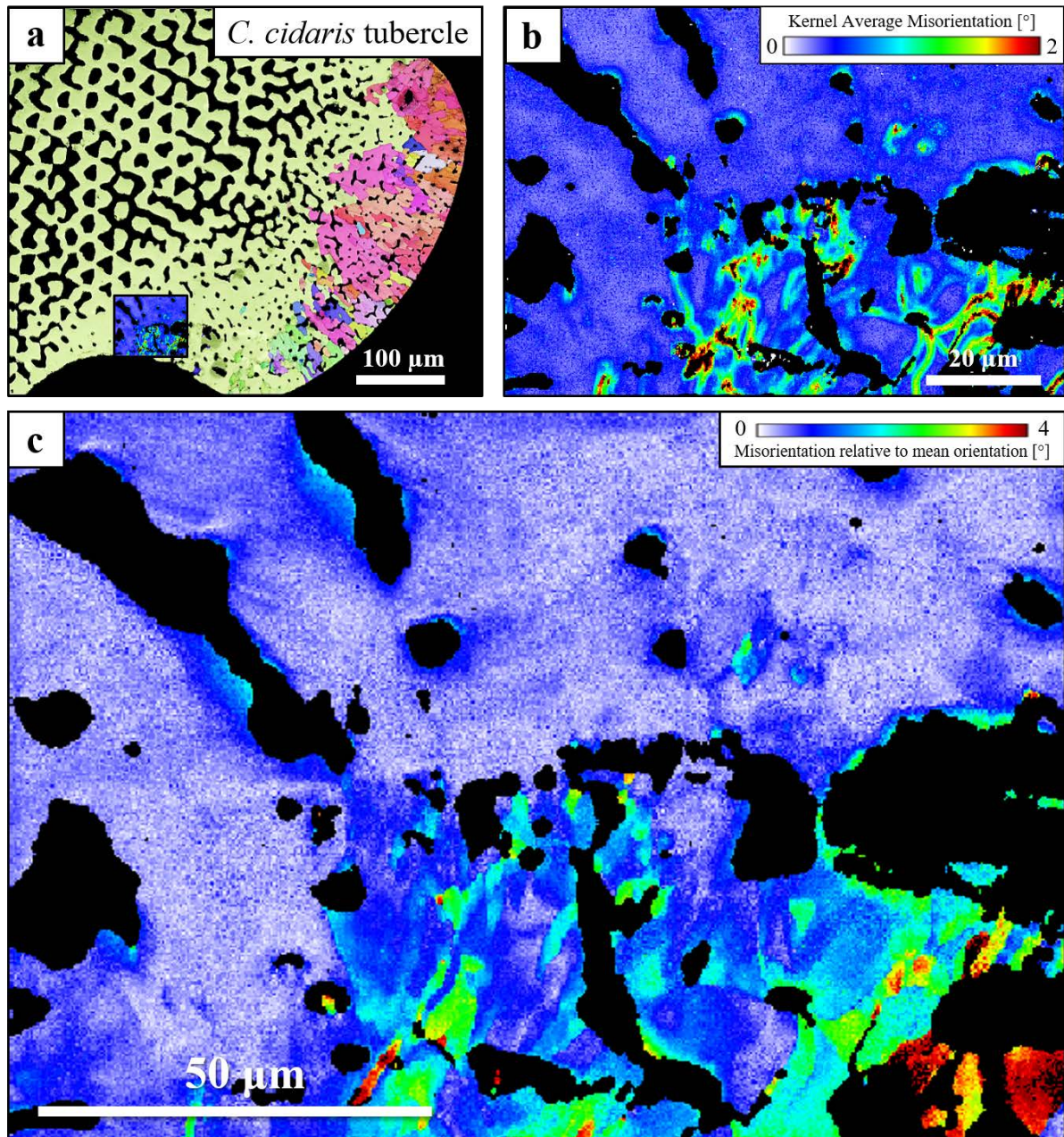


Figure 2.6-AP7. Short- and long-range misorientation distribution near a *Cidaris cidaris* primary tubercle. The measurement is located at the transition from labyrinthic to microperforate stereom near the outer boss surface (a). The high-resolution EBSD measurement displayed in (b) and (c) was refined with EBSD pattern matching. The kernel average misorientation map, depicting short-range misorientations within a kernel size of 5x5, shows a higher misorientation frequency near the outer boss surface, especially as small-angle misorientation streaks between pores (b). In contrast, the texture components map highlights long-range misorientations by comparing the data point orientation with the mean orientation of the trabecular framework (c). It shows that the cumulative crystallographic misorientation in the stereom increases up to 4° towards the terminal knob of the tubercle (c).

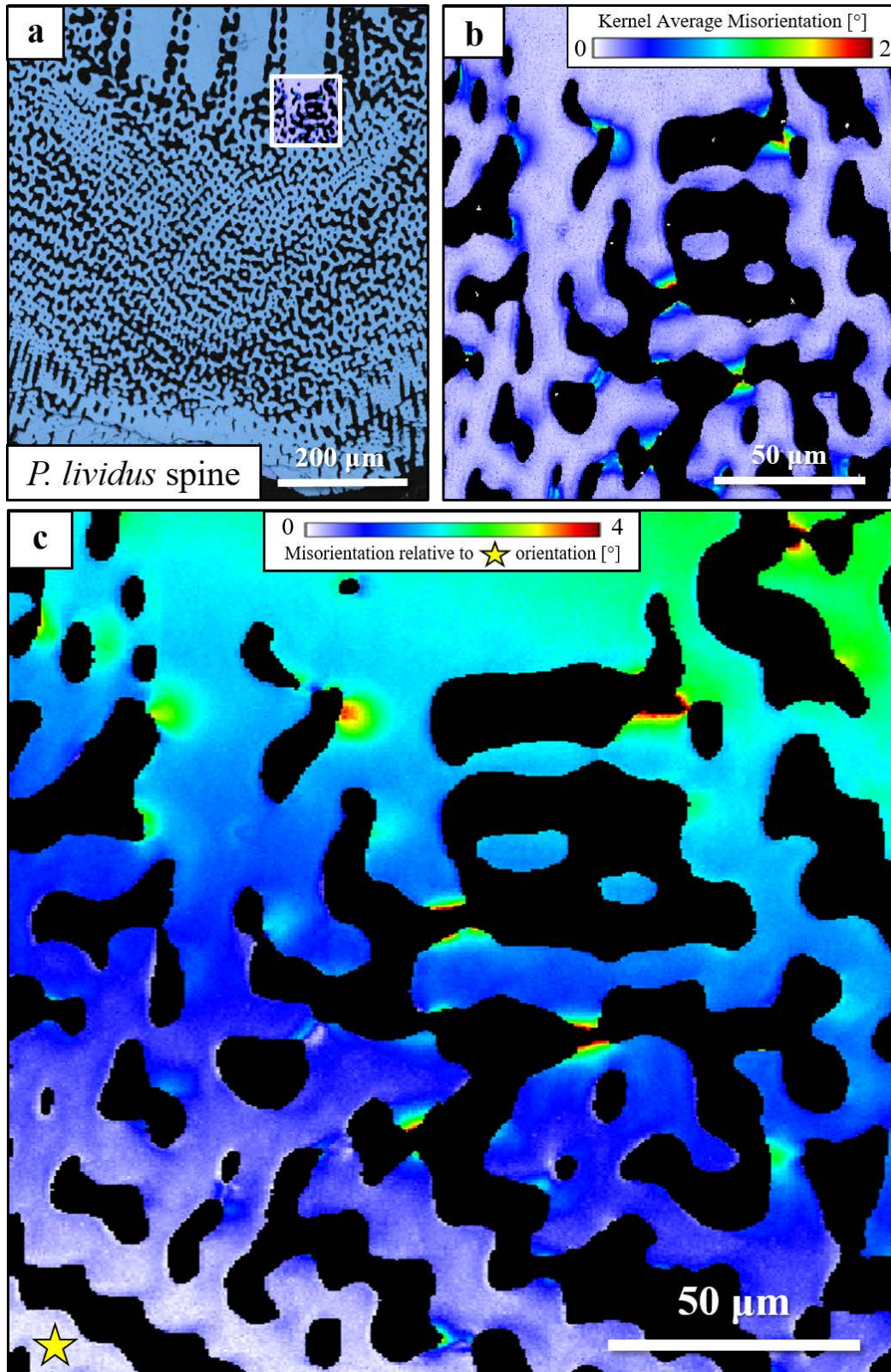


Figure 2.6-AP8. Short- and long-range misorientation distribution at the medulla of a *Paracentrotus lividus* spine. The measurement is located at the transition from labyrinthine stereom to the spine wedges (a). The high-resolution EBSD measurement displayed in (b) and (c) was refined with EBSD pattern matching. The kernel average misorientation map, depicting short-range misorientation within a kernel size of 5x5, shows a high degree of co-orientation within the stereom, with the exceptions of a few trabecular junctions that show misorientations (b). In contrast, the texture components map highlights long-range misorientations by comparing the data point orientation with the orientation of the trabecula at the bottom left of the map (indicated with a yellow star in c). It shows that the cumulative crystallographic misorientation in the stereom increases up to 4° towards the imperforate wedges of the spine (c).

2.7 EBSD PATTERN MATCHING FOR CHARACTERISATION OF BIOMATERIAL TEXTURE AND MICROSTRUCTURE

When trying to comprehend and retrace the crystal growth mechanism of biological hard tissues, a key factor is the transmission and continuation of the crystallographic texture. When analysing biomineralised microstructures with EBSD and evaluating the datasets with conventional, Hough-based indexing techniques, even modern EBSD systems and detectors produce an angular precision of around 0.5° (Zaefferer 2011). Electron backscatter pattern matching, a novel technique that reindexes and refines all stored Kikuchi patterns using a simulation, is a new approach to significantly improve the angular precision of EBSD measurements (Nolze et al. 2017; Lenthe et al. 2019; Winkelmann et al. 2020; Trimby et al. 2024). As described in Chapter 2.6 of this thesis, pattern matching can improve the precision to 0.1° , exposing detailed microstructural features that are almost invisible with conventional EBSD measurements.

This section illustrates the application and research potential of the EBSD pattern matching technique for different biomineralised hard tissues. Here, pattern-matched measurements show in great detail the misorientation distribution within and between grains, as well as unprecedented microstructural features that are only visible when achieving good angular precision. Comparing conventionally analysed and pattern-matched datasets of four aragonitic and calcitic microstructures, this section evaluates, discusses and compares the crystal co-orientation statistics of different species.

2.7.1 METHODS

Four different types of microstructures were sectioned and prepared for high-resolution EBSD analysis. The sections were embedded in EPON epoxy resin and subjected to several mechanical grinding and polishing steps. The polished samples were coated with 4–6 nm of carbon for EBSD analysis and with 5 nm Pt/Pd for SEM imaging. The EBSD datasets have been evaluated using both the conventional Hough-based indexing technique and electron backscatter pattern matching. The detailed experimental protocols are presented in Appendix Section B.1.

For each species, I prepared multiple samples along different cuts that are displayed in Supplementary Fig. 2.7-AP1. Shells of *Pinna nobilis* were sampled from the Almería coast, Spain; shells of *Atrina vexillum* were sampled from Pandanan Island, Philippines; Shells of *Atrina serrata* were sampled from Sambel Island, FL, and shells of *Pteria penguin* were sampled in the Philippines. The shells of *Anadara gibbosa* were sampled from the Málaga coast, Spain, and *Glycymeris pilosa* shells were sampled in the Pašman channel, Adriatic Sea. Samples of the sea urchin *Cidaris cidaris* were collected near Elba Island, Italy.

2.7.2 RESULTS AND DISCUSSION

Internal small-angle misorientations of calcitic columns in different bivalves

The calcitic columnar prismatic microstructure is a common microstructure observable across many bivalve families, including ostreids, pinnids, and mytilids (Ubukata 1994; Checa et al. 2005). Not only do calcitic columnar prismatic layers show exceptional nanomechanical properties (Taylor & Layman 1972; Checa et al. 2005), but they also follow a particular texture and crystal arrangement: Typical calcitic columnar prismatic microstructures comprise large crystal columns (up to 1 mm) separated by thick organic envelopes and following an axial texture with c-axes oriented perpendicular to the inner shell surface (Checa et al. 2005; Nalepka et al. 2020). These columns are considered single-crystalline; however, the crystallographic orientation has been evaluated so far only with conventional EBSD methods (Nalepka et al. 2020). Through the utilisation of modern techniques such as electron backscatter pattern (EBSP) matching, the angular precision of EBSD data can be enhanced greatly (see Chapter 2.6 of this thesis). The evaluation of high-resolution measurements of the four bivalve species *Pinna nobilis*, *Atrina serrata*, *Atrina vexillum*, and *Pteria penguin* using the EBSP matching method enables the in-depth characterisation of the calcitic columnar prismatic layer and the misorientation distribution. As described in the Methods Section 2.7.1, samples were sectioned both perpendicular (cut 1) and parallel (cut 2) to the inner shell surface.

To get a general overview of the calcitic columnar prismatic layer in the different bivalves, conventional measurements are sufficient, as their significantly smaller data files are faster and easier to evaluate. Measurements performed on samples cut perpendicular to the inner shell surface (cut 1) show the columns sectioned parallel to their morphological long axis, exposing the long calcitic prisms (Fig. 2.7-AP2). The grain boundaries appear even, and the pole figures confirm the axial texture of the columns, with the c-axes being co-oriented perpendicular to the inner shell surface (Fig. 2.7-AP2a). Shells cut parallel to the inner shell surface (cut 2) expose the cross-sections of the columns. The scan shows how thick organic envelopes separate the irregularly shaped prisms. Surprisingly, the pole figures of the cross-sectioned prisms reveal some degree of misorientation between the c-axes of the individual columns (Fig. 2.7-AP2b): While they are more or less co-aligned in an “axial-like” texture perpendicular to the inner shell surface, the misorientation angle between the c-axes of the neighbouring columns can reach up to 20°. As described by Nalepka et al. (2020), the directional dependence of c-axial coalignment on the cut may be attributed to the special growth mechanism of the calcitic columnar prismatic layer, where the crystallographic c-axes of the basic units are oriented parallel to the morphological long axis of the columns and the growth direction. Since the grains appear to mostly preserve their initial orientation, axial misorientations caused by the natural shell curvature can continue until the inner shell surface (Nalepka et al. 2020). This forms a laminated arrangement of column orientations in the calcitic columnar prismatic layer (see Fig. 2 in Nalepka et al. (2020)), causing neighbouring grains to appear either co-aligned or slightly misaligned, depending on the position and direction of the cut.

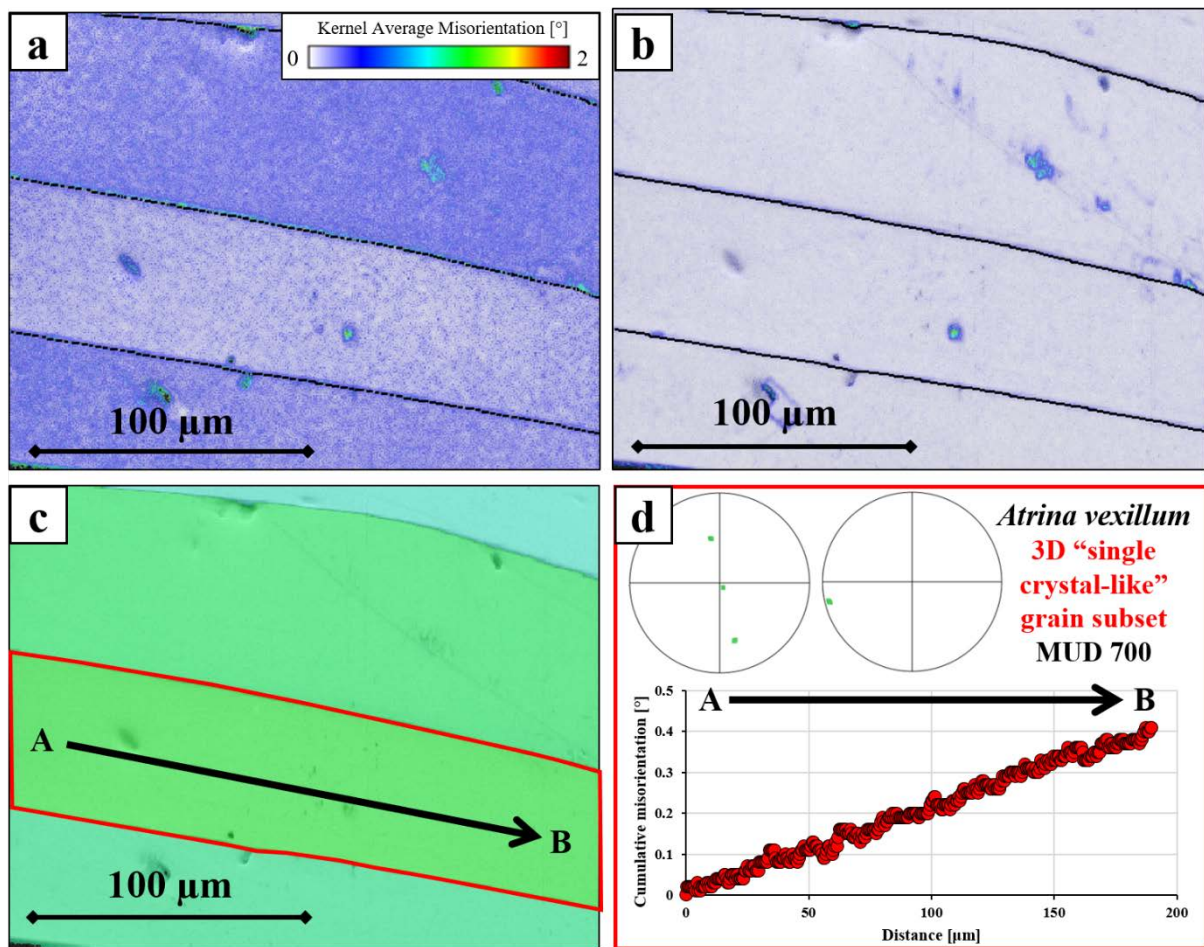


Figure 2.7-1. Microstructure and internal co-orientation of *Atrina vexillum* columns sectioned parallel to the column long axes. The standard EBSD measurement without pattern matching (a) reveals scattered internal misorientations of approximately 0.5° within the columns. EBSD pattern matching reveals that the columns comprise very low misorientations aside from a few holes or scratches that most likely result from sample preparation (b). A misorientation profile along a 3D "single-crystal-like" column (marked with a red outline in c) reveals a very small cumulative misorientation of less than 0.5° from one column edge to the other (d). The high crystal co-orientation strength and the small degree of misorientation indicate that *A. vexillum* prisms can be considered single-crystalline.

When the individual crystals of the calcitic columnar prismatic layer are analysed in more detail, the advantages and superiority of the EBSD matching method, compared to conventional Hough-based indexing techniques, quickly become obvious. A conventionally evaluated map of the axial calcitic columnar prismatic layer sectioned along cut 1 in *Atrina vexillum* exhibits a relatively low angular precision of $\sim 0.5^\circ$. This causes Kernel average misorientation maps to be noisy and imprecise (Fig. 2.7-1a). If the measurement is pattern-matched, the angular precision is increased to $\sim 0.1^\circ$ (see Section 2.6). This allows a more precise and truthful representation of the crystallographic co-orientation within the columns: Rather than featuring evenly distributed low-angle misorientations across the columns, as suggested by the map evaluated with conventional methods (Fig. 2.7-1a), individual columns are highly co-oriented (Fig. 2.7-1b). As indicated by the cumulative misorientation angle profile across a single column (Fig. 2.7-1c, d), a fine, gradual rotation can be detected parallel to the morphological long axis of the prism. Nonetheless, the large MUD value of 700 and the exiguity

of this internal misorientation demonstrate the high co-orientation within calcitic columns of the calcitic columnar prismatic layer in *A. vexillum* along cut 1.

From a measurement of *Atrina serrata* columns sectioned perpendicular to the inner shell surface (cut 1), similar conclusions can be drawn. Without sophisticated data evaluation and refinement, the map wrongfully features evenly distributed misorientations of around 0.5° (Fig. 2.7-2a). After refinement by EBSD matching, the angular precision is enhanced, and the pole figures and Kernel average misorientation map reveal a high degree of co-orientation within the columns (Fig. 2.7-2b, c). As suggested by cumulative misorientation angle profiles, neighbouring columns can be misoriented by up to 50° (Fig. 2.7-2d), while the misorientation within a single columnar prism is below 0.5° (Fig. 2.7-2e). Isolated areas of enhanced misorientations (yellow stars in Fig. 2.7-2c) can be attributed to cutting effects that are not structural features but rather result from sample preparation.

Similar to the measurements evaluated exclusively with Hough-based indexing methods, pattern-matched measurements of calcitic columnar prismatic layers sectioned parallel to the inner shell surface (cut 2) reveal some degree of misorientations within and between the columns. For example, the calcite columns in *Pteropoda penguin* shells show not only dendritic-like misorientation streaks but also gradual rotations across the prisms (Fig. 2.7-3a). This rotation is visible from a gradual shift in IPF colour (yellow stars in Fig. 2.7-3b) as well as cumulative misorientation profiles (Fig. 2.7-3c, d). From one end of the column to the other, misorientation angles can reach up to 10° (Fig. 2.7-3c, d). Despite the high angular precision of below 0.1° in this measurement, the internal point-to-point misorientations within the cross-sectioned prisms range from 0.1° up to 0.4° (Fig. 2.7-3e). This is almost the same as the cumulative misorientations measured across columns sectioned parallel to the morphological long axis (See Figs. 2.7-1d, 2.7-2e)

Furthermore, when sectioned along cut 2, the crystallographic c-axes across the entire measurement are distinctly less co-oriented than for columns sectioned along cut 1 (for comparison, see the similarity in colour-coding and, thus, co-orientation of columns in Fig. 2.7-3c). As indicated by the low MUD value and the broad scattering of c-axes in the axial-like microstructure, the calcite columnar prismatic layer has a lower degree of misorientation than suggested by scans along cut 2. Once again, this is most likely due to the sheet-like arrangement of calcite columns and depends on the chosen scale of observation. Individual sheets appear to have a relatively high crystallographic co-orientation. When considering columns across the entire valve, however, the crystallographic c-axes appear misoriented as they follow the curvature of the shell surface.

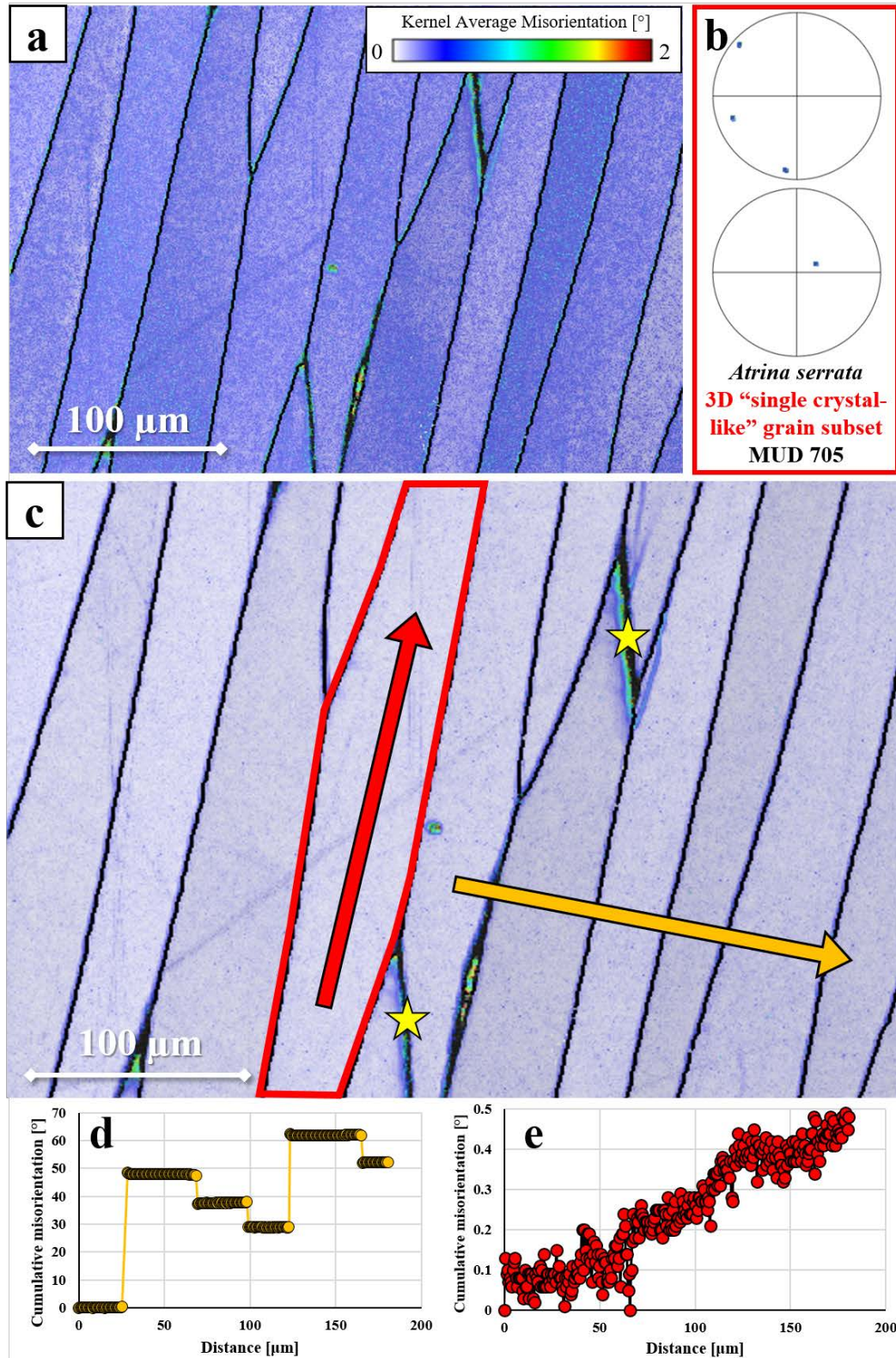


Figure 2.7-2. Microstructure and internal co-orientation of *Atrina serrata* columns sectioned parallel to the column long axes. The standard EBSD measurement without pattern matching (a) reveals randomly scattered internal misorientations of approximately 0.5° within the columns. However, the high crystal co-orientation strength of individual columns (b) and small kernel average misorientation in the pattern-matched measurement (c) reveal the 3D "single-crystal-like" character of most columns. Some columns appear to have misorientations along their upper boundaries (indicated by yellow stars in c). However, this can be attributed to cut effects during sample preparation. Cumulative misorientation profiles across columns reveal that column boundaries exhibit misorientation angles of up to 50° and do not appear to follow a periodic pattern (d). The small cumulative misorientation angle of 0.5° across $200\ \mu\text{m}$ in the highlighted column (red frame in c) further indicates a 3D "single-crystal-like" character (e).

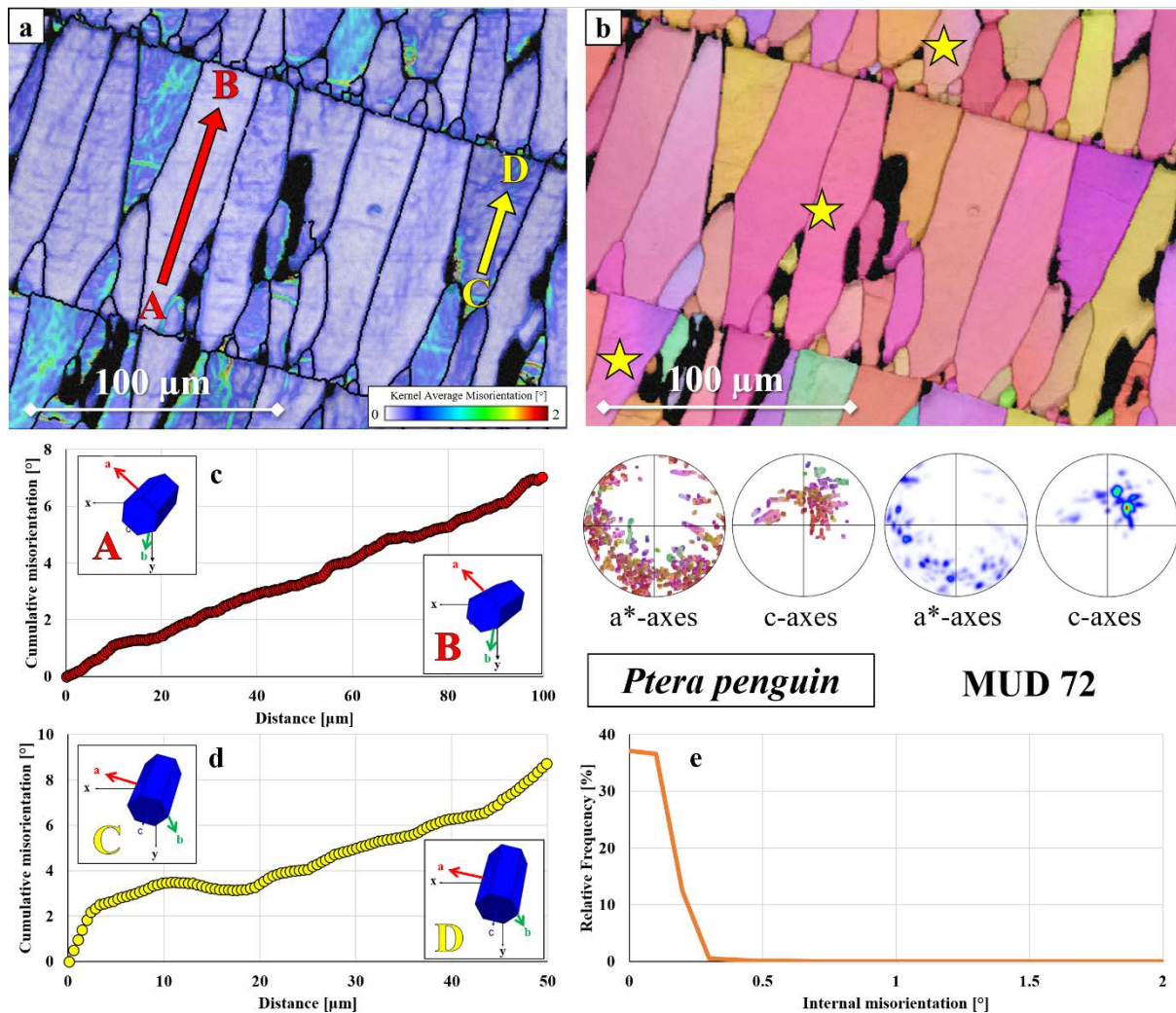


Figure 2.7-3. Microstructure and internal co-orientation of *Ptera penguin* column sections cut perpendicular to the column's long axes. The shells of *P. penguin* comprise multiple sheets of poorly co-oriented columns that extend more than 100 μm (a, b). The pattern-matched EBSD measurement reveals a heterogeneous misorientation distribution across the columns: While most columns show a low kernel average misorientation, some show streaks of high ($> 1^\circ$) misorientations traversing the entire grains (a). While these streaks might be a remnant of stresses during sample preparation, misorientation profiles reveal graded rotations of the unit cell axes across the column edges (c, d). Cumulative misorientation angles between the points (A-B, and C-D) may reach up to 10° (c, d) and can also be recognised from the gradual colour shift in some columns of the colour-coded EBSD map (yellow stars in b). The misorientation angle distribution across the entire measurement (e) reveals that the majority of misorientations are small-angle misorientations within the columns.

Internal small-angle misorientations of the calcitic stereom in sea urchins

The microstructure and crystallographic co-orientation of sea urchin skeletal elements, such as the test and spines, have been debated in numerous studies (e.g., Nissen 1969; Aizenberg et al. 1997; Su et al. 2000; Moureaux et al. 2010; Seto et al. 2012; Cölfen et al. 2022). Implementing the EBSD pattern matching method for the first time for biomineralised hard tissues, the results of Chapter 2.6 of this thesis indicated that the question about single-crystallinity in sea urchin calcite is not straightforward and depends on the chosen scale of observation. While intratrabecular portions of the stereom have a high crystallographic co-orientation and can be considered single-crystalline, some stereom fabrics

show significant misorientation boundaries along trabecular junctions. As Chapter 2.6 of this thesis has only considered a limited amount of stereom architectures and sea urchin species, this section focuses on understanding the texture and microstructure of different sea urchins in even greater detail.

The crystallographic texture of a certain microstructure can be illustrated and quantified using different approaches. For more information on the MUD value, see the Terminology Section A.1.1 of this work.

- (i) The first and most simple approach is the multiple of uniform distribution (MUD) of the measurement's pole figures. In principle, the analysis software measures the density of the crystallographic orientations of all data points and how much they deviate from a random texture. If all orientations cluster densely along a specific orientation, the MUD value is large, indicating high crystallographic co-orientation. In contrast, broadly distributed orientations with a low density generate a lower MUD value, indicating lower crystallographic co-orientation. As the entire information of all data points is comprised of a single number, this method enables the quick and easy comparison of various measurements and subsets. However, its simplicity is also its biggest downside, as the sheer MUD value is influenced by dataset size and quality, magnification and grain size distribution. Additionally, the MUD value gives no indication of the orientation distribution.
- (ii) Another option to measure the crystallographic co-orientation is the implementation of three Euler angles. In this method, the spatial orientation of every data point is described by three orthogonal orientations. By quantifying the full width at half maximum of the peaks or calculating the standard deviation of the Euler angles, the latter can be used to analyse the degree of crystallographic co-orientation. This method is not as simple and straightforward as comparing the MUD values. However, it is more precise and expressive. Euler angle analysis is suitable for microstructures with a low degree of crystallographic co-orientation. For well-cooriented microstructures, however, the quantification and interpretation of the peaks can be challenging.
- (iii) A third option for comparing the crystallographic co-orientations of microstructures is the texture component analysis. In principle, it works by defining a reference orientation (such as the average orientation of the indexed data points) and quantifying the misorientation of every pixel to this orientation. Texture component analysis can be displayed both as an EBSD map and as a plot, displaying the angular misorientation frequency in comparison to the reference orientation. If the indexed orientations have a small angular deviation from the mean orientation, the microstructure is highly co-oriented, whereas untextured-like microstructures will frequently show large-angle deviations. Due to its precision and flexibility of the chosen range, texture component analysis is well-suitable for microstructures with a high crystallographic co-orientation.

Overall, as shown in this section for measurements on single-crystal-like *C. cidaris* stereom, each method of quantifying the crystallographic co-orientation has its benefits and drawbacks. While they complement each other very well, the “best” method often depends on the individual measurement and the research objectives.

In sea urchin calcite, the trabeculae of the labyrinthic stereom fabric (i.e., found in the test of *C. cidaris*) often show a very coarse and open pore structure with relatively thin trabeculae (Smith 1980). When evaluated with conventional EBSD analysis techniques, such as Hough-based indexing, this can lead to a slight misindexation of specific sample areas, such as the interfaces between resin and outer trabecular surface (Fig. 2.7-4a). Alongside the comparatively low angular precision of conventional indexing, this constitutes a significant error margin for investigating the fine structure and crystallographic texture of stereom fabrics. Through EBSD pattern matching and refining, the angular precision is enhanced greatly, allowing the precise characterisation of the crystallographic texture (Fig. 2.7-4b) and misorientation distribution within the labyrinthic fabric (Fig. 2.7-4c). Analysing the distribution and standard deviation of the three Euler angles in the pattern-matched dataset (Fig. 2.7-4b), it becomes obvious that the microstructure is actually well co-oriented. While all three Euler plots feature a single, sharp peak with the standard angular deviations being well under 1° , the labyrinthic stereom calcite is not perfectly co-oriented (Fig. 2.7-4b). This is not only visible from the Euler angles but also from the MUD value of 678 (as a reference, synthetically grown calcite single crystals have an MUD value; see Chapter 2.6 of this thesis) but also from the Kernel average misorientation map that exposes misorientations around 1° located at trabecular junctions (yellow arrows in Fig. 2.7-4c).

The influence of trabecular junctions on the crystallographic texture of the sea urchin calcite is also shown in another measurement performed on a *C. cidaris* spine with a fascicular stereom fabric (Fig. 2.7-5). In this microstructure, trabecular rods interconnect not only by branching but also by small struts that run perpendicular to the rods, creating a dense and irregular array (Smith 1980). While this arrangement looks fairly co-oriented in a regular, IPF-coloured map (Fig. 2.7-5a), the texture component maps show the substructuring in this stereom fabric (Fig. 2.7-5b, c). In comparison to the conventionally indexed dataset, EBSD pattern matching and refinement enhances the angular precision. Nonetheless, as visible from the crystal co-orientation statistics, the co-orientation actually decreases after pattern matching. This is indicated not only by the texture component maps with the MUD value decreasing from 521 to 479 (Fig. 2.7-5b, c) but also by the Euler angle distribution (Fig. 2.7-5d) and the texture component statistics (Fig. 2.7-5e). Compared to a highly co-oriented microstructure such as the labyrinthic stereom in the *C. cidaris* test (Fig. 2.7-4), the fascicular stereom has a relatively broad orientational distribution (Fig. 2.7-5e), which emphasises that sea urchin calcite should not universally be considered single-crystalline.

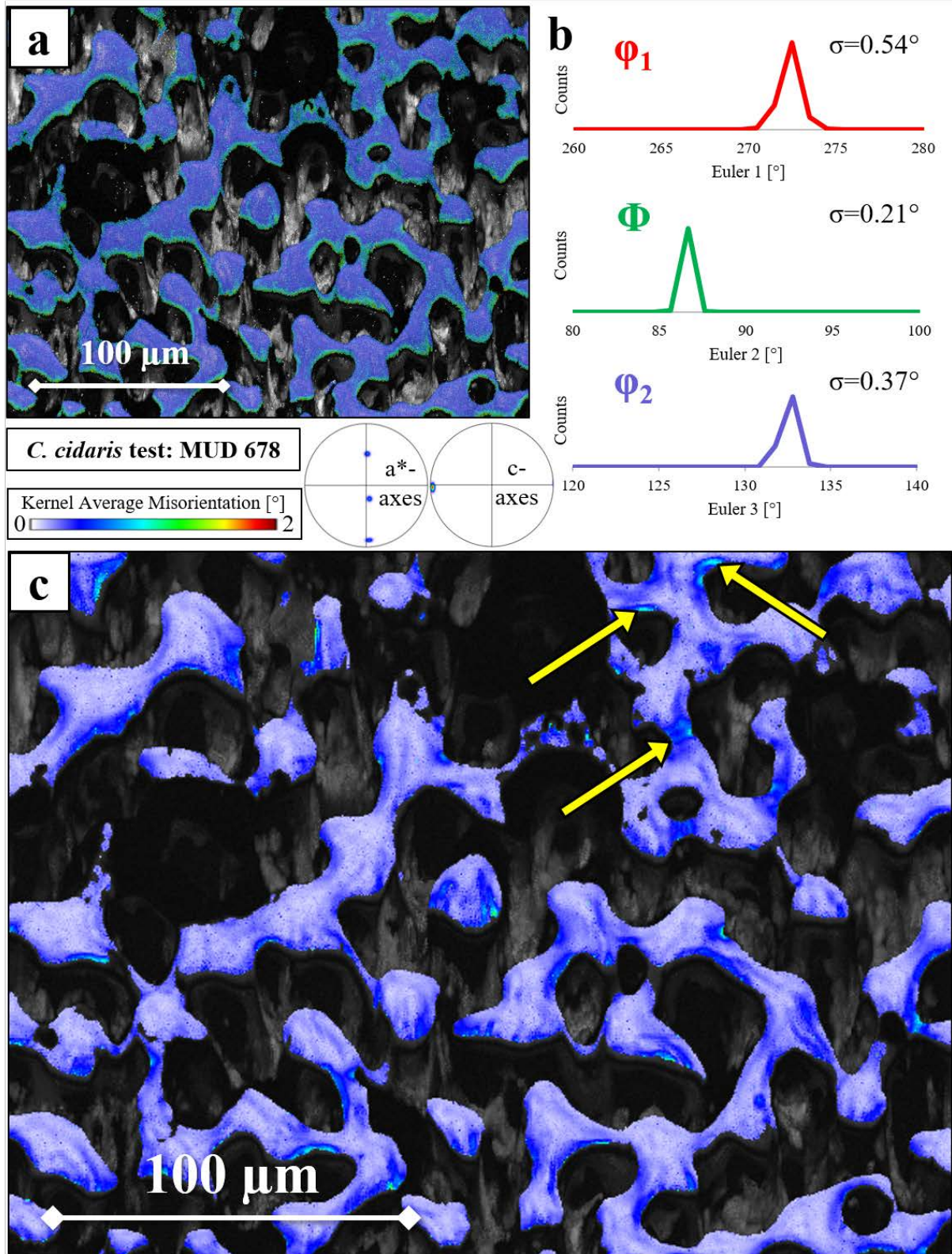


Figure 2.7-4. Microstructure and internal co-orientation of the labyrinthine stereom in the *C. cidaris* test. Using conventional EBSD data evaluation, small-angle-misorientations cannot be properly displayed due to the poor orientation precision of 0.5–1° (a). Refinement through EBSD matching reveals that the majority of misorientation angles are well below 1° (b), and the kernel average misorientations of a 9×9 square around the data points are mostly below 0.5° (c). Despite the frequent distribution of large pores (up to 50 μm) within the calcitic network, the biomineralised trabeculae are thus highly co-oriented. Occasional regions of misorientations exceeding 1° can be found along outer trabecular surfaces (yellow arrows in c), predominantly at trabecular junctions. These small impurities in crystal co-orientation cause the MUD value of the measurement (678, see b) to be slightly lower than that of single crystals grown artificially in the laboratory (700–720).

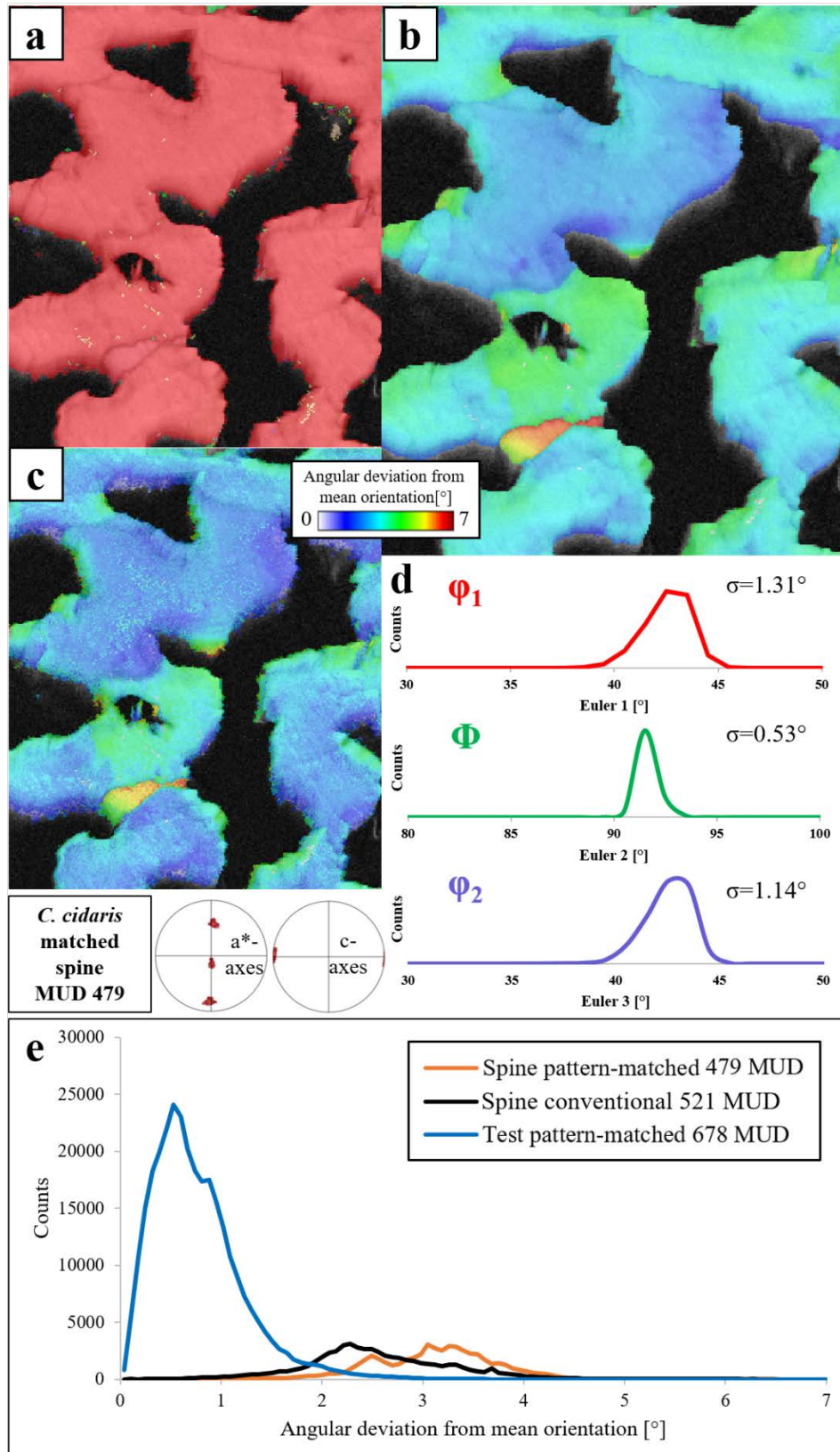


Figure 2.7-5. Crystal co-orientation analysis of the fascicular stereom fabric in a *C. cidaris* spine. As indicated by an IPF coloured map (a) and texture component maps (b, c), the stereom is substructured and comprises frequent misorientations up to 5°. The texture component maps are color-coded by misorientations up to 7° from the average misorientation for a conventionally evaluated (b) and a pattern-matched dataset (c). The relatively low MUD value, the high angular variation of Euler angles (d) and the quantitative texture component plot indicate a lower crystal co-orientation than labyrinthine test stereom (Fig. 2.7-4). While the latter shows an average angular deviation from the mean orientation between 0-2°, the texture component analysis for fascicular stereom is 2-3° (conventional evaluation) or even more than 3° (pattern-matched).

Analysing datasets with high angular precision not only allows a better understanding and characterisation of biomineralised microstructures but also enables the comparison of different methods used to quantify and compare the crystallographic co-orientation. Although all three crystal co-orientation statistic methods used in this section are unique and yield advantages and disadvantages, they have all proved to be valuable sources of information. Despite compressing the complex data into a single number, the MUD value is the most simple but effective method to truthfully quantify and compare the crystal co-orientation of different microstructures. Comparing the highest observed MUD values of the skeletal elements in nine different echinoid species analysed in this study, a clear trend can be observed (Table 2.7.1). Irrespective of the measurement location (test or spine), all investigated species show a relatively high crystallographic co-orientation. Although the MUD values range from 658 up to 723, there seems to be no common relation between the type of skeletal element or the echinoid order and the single crystallinity (Table 2.7.1). However, as Chapter 2.6 of this thesis and this section show, the frequency and dimension of small-angle misorientations seem to be affected by the type of stereom fabric, which can vary considerably within a single test plate (Smith 1980; Yamaguchi & Kanazawa 2009; Förster 2020). Further research that applies the EBSD pattern-matching method to different stereom fabrics is crucial to characterise the general misorientation distribution and, thus, the single-crystallinity of different sea urchin species and skeletal elements.

Table 2.7-1 Summary table of the investigated echinoid species and the highest recorded MUD value for the respective skeletal element. Only the 3D single-crystal-like plates/medulla were considered for the generation of the MUD value.

Echinoid species	Location	MUD value
<i>Heterocentrotus mamillatus</i>	Test	713
	Spine	708
<i>Arbacia lixula</i>	Test	706
	Spine	658
<i>Coelopleurus maillardi</i>	Test	671
	Spine	701
<i>Echinocardium cordatum</i>	Test	691
<i>Clypeaster reticulatus</i>	Test	719
<i>Arachnoides placenta</i>	Spine	703
<i>Echinotrix diadema</i>	Spine	691
<i>Cidaris cidaris</i>	Test	697
	Spine	723
<i>Paracentrotus lividus</i>	Test	680
	Spine	704

Internal small-angle misorientations of porous calcite in quail eggshells

The biomineralised hard tissue and eggshells of *Coturnix japonica* are valuable for research as these quails are of small size, grow quickly and have an ageing process that is similar to other birds and mammals (Holmes & Ottinger 2003; Skic et al. 2024). To understand the hierarchical structure of the calcitic eggshell and optimise the farming and transport of quail eggshells for the food industry, different studies have investigated the chemistry and mechanical properties of *C. japonica* shells (Genchev 2012; Narinc et al. 2015; Tatara et al. 2015; Skic et al. 2024). Nonetheless, the exact mechanisms behind the texture generation, porosity and grain morphology are still far from being understood. Here, the microstructure and texture of fresh *C. japonica* eggshells, sectioned perpendicular (cut 1) and parallel (cut 2) to the inner shell surface (Fig. 2.7-AP1b, c), were investigated in great detail, applying the novel EBSD matching method. This subsection is a collaboration with Shahrouz Amini and Jingxiao Zhong from the Max-Planck Institute of Colloids and Interfaces, Potsdam.

The first measurement was performed close to the outer shell on a sample sectioned along cut 1. The grains have rough, uneven morphologies and interlock with each other (Fig. 2.7-6). This fractal-like morphology is most likely the result of intermingling of the organic network with the calcite crystals, as described by Silyn-Roberts & Sharp (1986) Using conventional EBSD indexing techniques, Kernel average misorientation maps display a low angular precision of about 0.5° (Fig. 2.7-6a). When refining the measurement via EBSD matching, the angular precision is enhanced, and the quality of the measurement increases drastically, exposing the porous calcite grains and the intricate interlocking mechanism along their boundaries (Fig. 2.7-6b). The measurement illustrates how the small pores (sub- μm) create minuscule sources of intragranular misorientations. Similar to the microperforate stereom of *C. cidaris* tubercles (see Figs. 2.6-4c, 2.6-5e), dendritic-like misorientation streaks traverse some grains (yellow star in Fig. 2.7-6b). Irrespective of the latter small-angle misorientations within the grains, the overall internal co-orientation of the *C. japonica* eggshell grains is relatively high. This is indicated not only by the low Kernel average misorientations in the pattern-matched map but also by a cumulative misorientation profile. This profile traverses a grain (highlighted by the red outline in Fig. 2.7-6b) and reaches a maximum cumulative misorientation below 1° (Fig. 2.7-6c). The pole figures indicate that the overall texture of the eggshell microstructure near the outer shell surface appears untextured-like, with the crystallographic a^* - and c -axes scattering on a great circle. However, other measurements comprising a larger scan area indicate a weak axial-like texture with c -axes somewhat co-oriented perpendicular to the outer shell surface (Fig. 2.7-AP3).

A close-up measurement performed with a magnification of 2000x shows in more detail the distribution and morphology of the pores, as well as their influence on the texture of the biomineralised hard tissue (Figs. 2.7-7 and 2.7-8). Using conventional evaluation tools, Kernel average misorientation maps fail to properly depict the pore structure due to the low angular precision (Fig. 2.7-7a). In pattern-matched maps, however, the distribution and size of the porous areas are well-visible from their

misorientations compared to the smooth, exposed shell (Fig. 2.7-7b). Obviously, due to the concave pore surface, data points located on exposed pores are likely to index unreliable orientations. However, investigating the grain areas that are located right next to the pores enables conclusions about whether and how the pores influence the intragranular co-orientation in *C. japonica* eggshells.

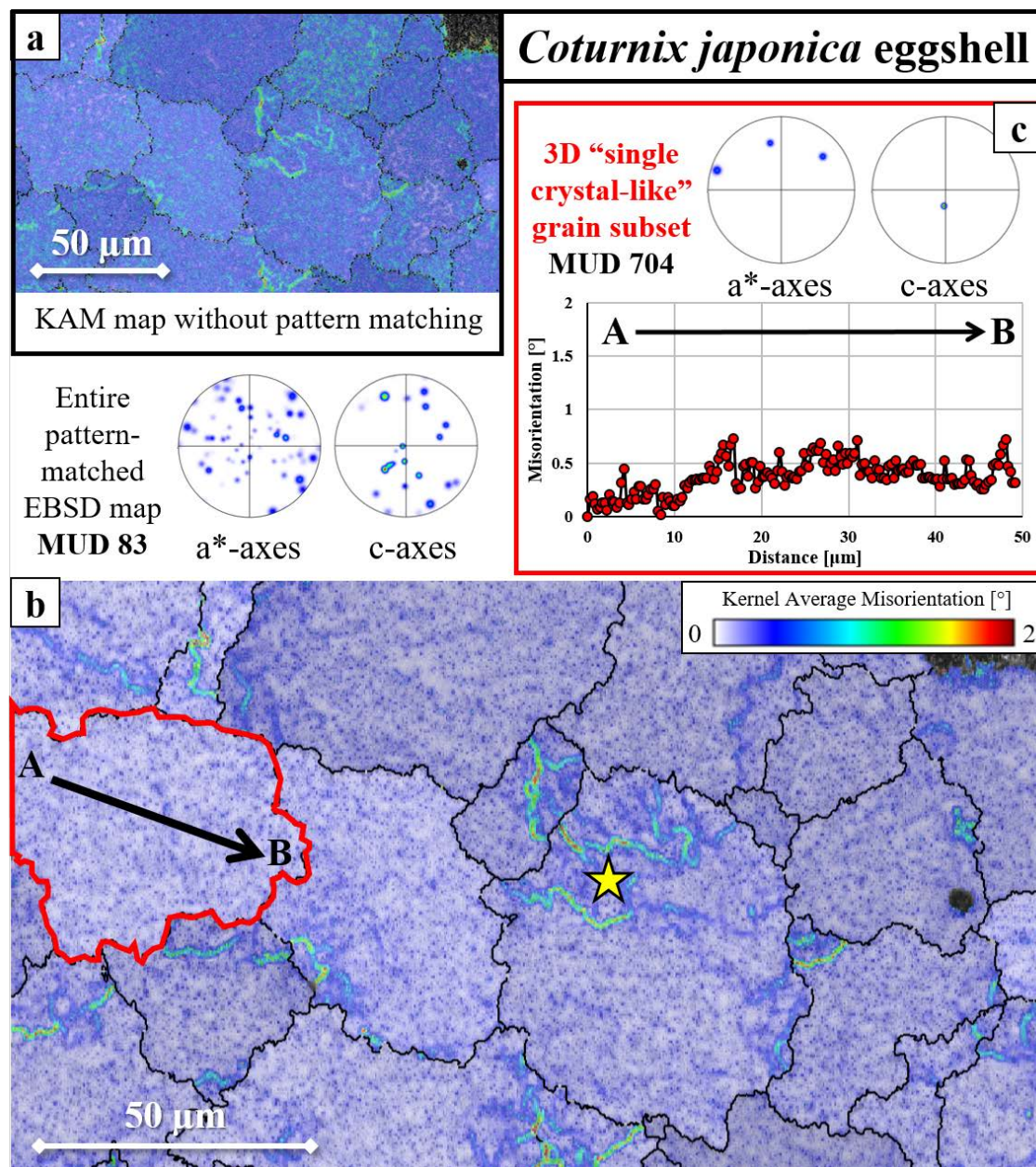


Figure 2.7-6. Microstructure and internal co-orientations of the calcite grains in a *Coturnix japonica* eggshell sectioned along cut 1. The measurement reveals irregular grain sizes, orientations, boundaries and morphologies (a, b) that are commonly observed in quail eggshells (Mohd Norsham et al. 2020). The kernel average misorientation distribution in standard EBSD maps without pattern matching lacks resolution and shows misorientations of around 0.5° scattered across the measured area (a). The precise EBSD pattern-matching method reveals a pattern of co- and misorientation in the calcite grains. Similar to bivalve columns and sea urchin calcite (see Chapters 2.7.1 and 2.7.2 of this thesis), some grains exhibit a distinct pattern of misorientation streaks (e.g., the yellow star in b), which may result from sample preparation. However, the pattern-matched EBSD map also reveals tiny, small-angle misorientation points scattered across all grains (b). They can be attributed to dispersed macropores. In addition to the pores, *C. japonica* grains (e.g., highlighted by the red frame in b) are well-co-oriented and exhibit low cumulative misorientations across a profile that runs perpendicular to the outer shell surface (c). With an average MUD value of around 700, most grains can thus be considered single-crystalline despite the small angular deviations resulting from internal pores.

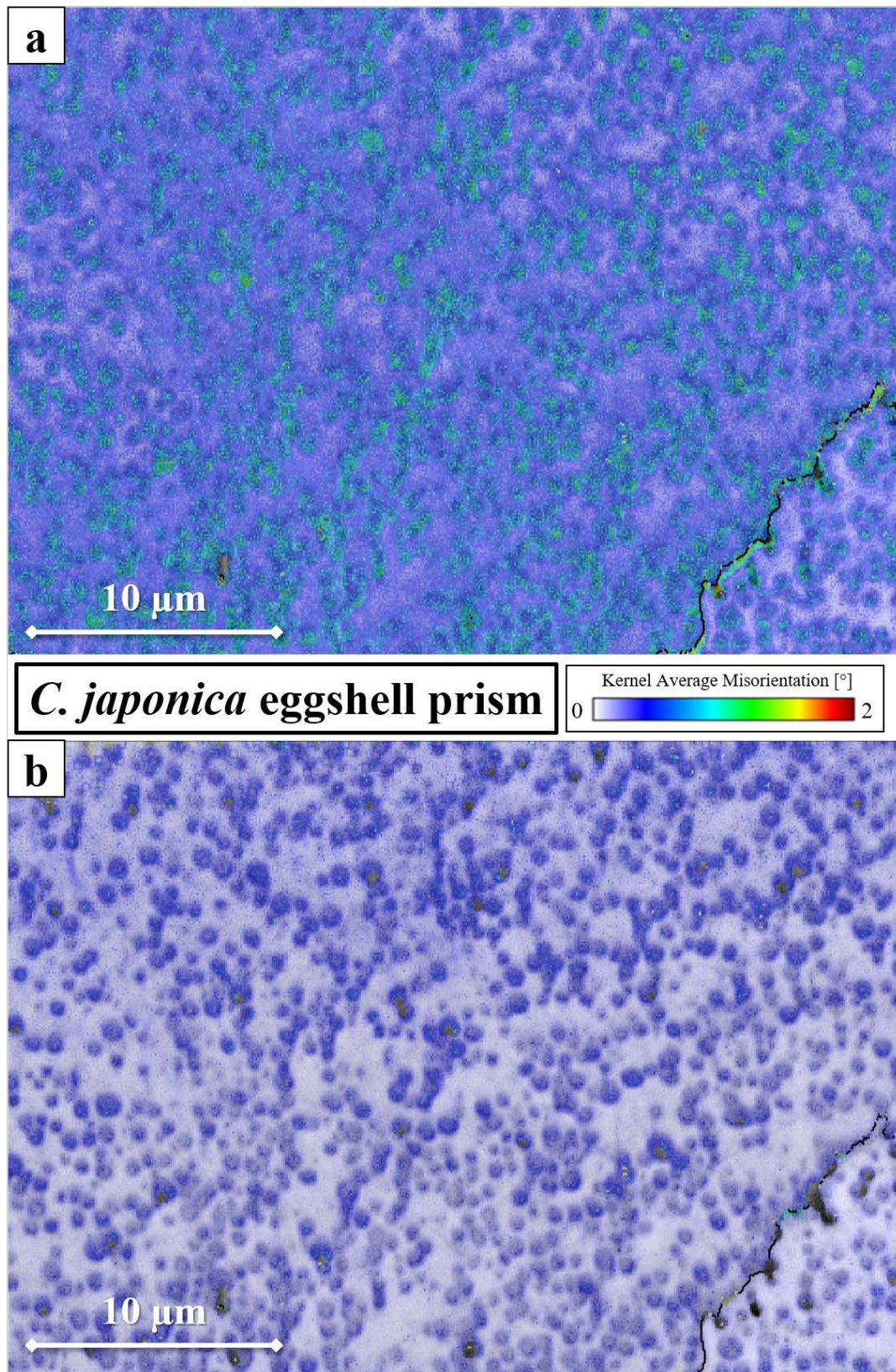


Figure 2.7-7. High-resolution EBSD scan (magnification x2000) of a *C. japonica* eggshell sectioned along cut 1 revealing the internal pore distribution and co-orientation of two eggshell grains. From the unprocessed EBSD measurement (a), the pore distribution and its effect on internal crystal co-orientation are not visible due to the relatively poor orientation precision. The EBSD pattern matching method reveals very low kernel average misorientations in the imperforate hard tissue, whereas points within pores may deviate up to 0.5° (b). The scan confirms that the macropores do not seem to impact the misorientations of the imperforate hard tissue and are never interconnected but always separated by hard tissue. Pores do not seem to follow an obvious distribution pattern (b).

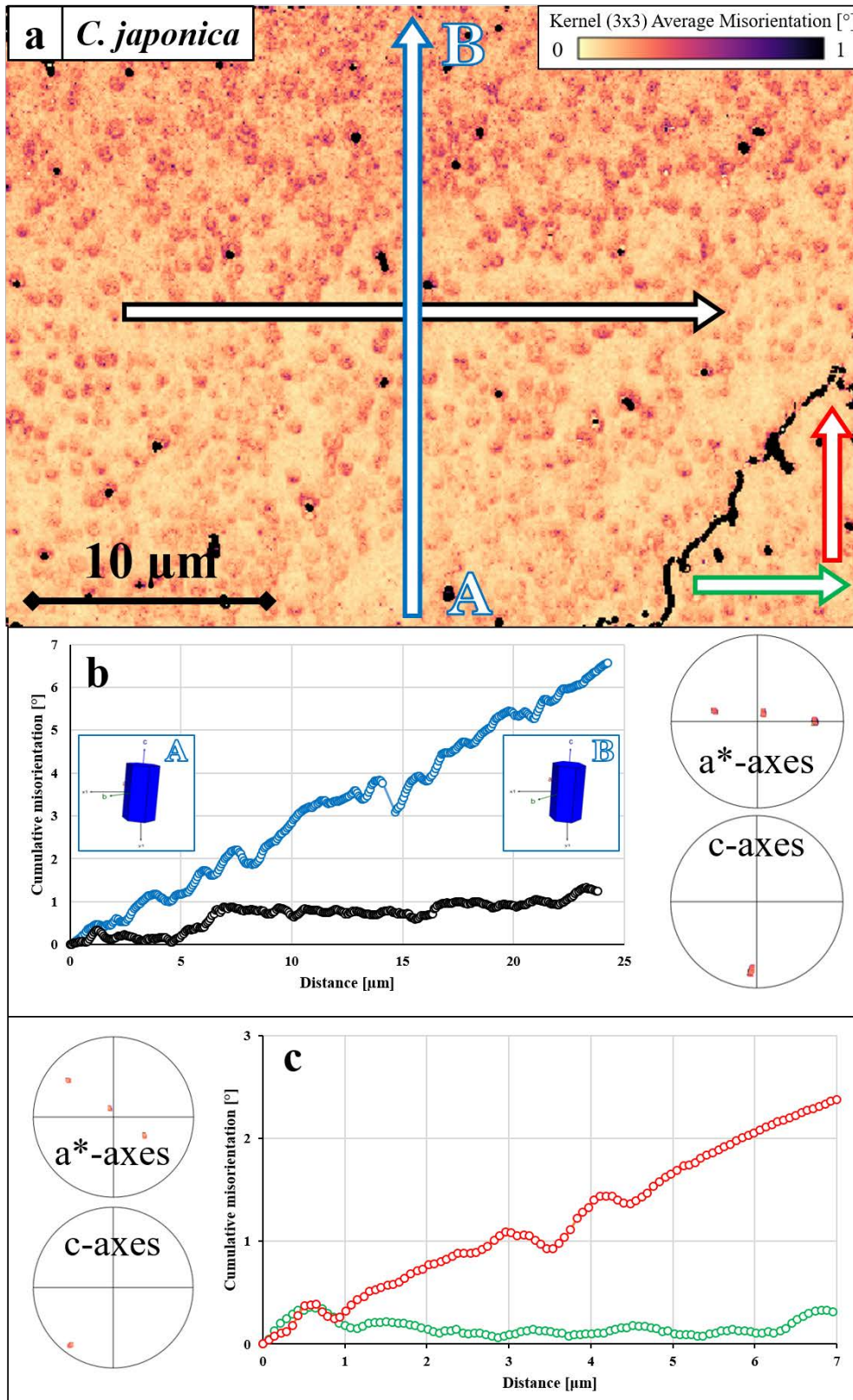


Figure 2.7-8. Texture and internal misorientations of the high-resolution EBSD scan (magnification x2000) of a *C. japonica* eggshell. Rather than using a kernel width of 5x5 (as used in all other kernel average misorientation maps reported in this study), the kernel width for map (a) was decreased to a minimum of 3x3 to visualise only the local misorientations. The map shows a change in kernel average misorientation angle from the bottom ($< 0.1^\circ$ in imperforate shell sections) to the top (up to 0.5° in imperforate shell sections). No such trend can be observed along the horizontal direction for the two grains. Vertical (parallel to the outer shell surface) and horizontal (perpendicular to the outer shell surface) profiles along the larger grain (b) and smaller grain (c) reveal the cumulative misorientation angles between the measurement edges.

Due to the high angular precision of pattern-matched maps, as well as the minuteness of angular misorientations and the high magnification of this scan, it is beneficial to manipulate the Kernel average misorientation map parameters that were used for all other measurements in this section: setting the upper angular limit of the Kernel average misorientation map to 1° and changing the Kernel size to 3×3 not only enhances the visibility of the colour-coded orientations but also allows the angular comparison with only the immediate neighbours (Fig. 2.7-8a). This is needed because of the high magnification of the scan that results in a higher amount of pixels scanned per μm of the sample. A higher Kernel size may distort the misorientation distribution. The map shows that the areas that are directly adjacent to outer pore surfaces do not show enhanced misorientations (Fig. 2.7-8a). Therefore, it can be concluded that the pores do not disrupt the microstructure of the biomineralised hard tissue.

Additionally, cumulative misorientation profiles indicate that, although the grains in *C. japonica* eggshells have a high local co-orientation (on a sub- μm scale), orientations can change from one side of a grain to the other. For both the large grain (Fig. 2.7-8b) and the smaller grain on the bottom right (Fig. 2.7-8c), this continuous lattice rotation has an azimuthal dependence: If the profile runs vertically (perpendicular to the outer shell surface) the cumulative misorientation is larger than for horizontal profiles (parallel to the outer shell surface). Although, as indicated by sketched unit cells in the misorientation profiles (Fig. 2.7-8b), this rotation is not major, it is structural and also visible from gradual rotations of Kikuchi bands in the detected EBSD signals between points A and B.

Internal small-angle misorientations of aragonitic prisms in bivalve myostraca

The previous sections of this thesis, such as Chapters 2.1 to 2.4, have highlighted in great detail the formation mechanism, crystallographic texture and nanomechanical properties of various bivalve myostraca. Since these chapters have focused mostly on the microstructure of the entire myostracum and only to a lesser extent on the properties of the individual aragonite crystals, the results were evaluated with conventional, Hough-based indexing techniques. Here, for the first time for an aragonitic biomineralised hard tissue, the microstructure of the myostracum is evaluated with EBSP matching. Highlighting small-angle misorientations within myostracal crystals, this technique was applied for high-resolution measurements of the bivalves *Anadara gibbosa* and *Glycymeris pilosa*. The measurements not only prove the advantages of pattern-matching methods for the EBSD data evaluation of aragonitic materials but also, for the first time, give insights into the fine structure of conservative bivalve myostraca.

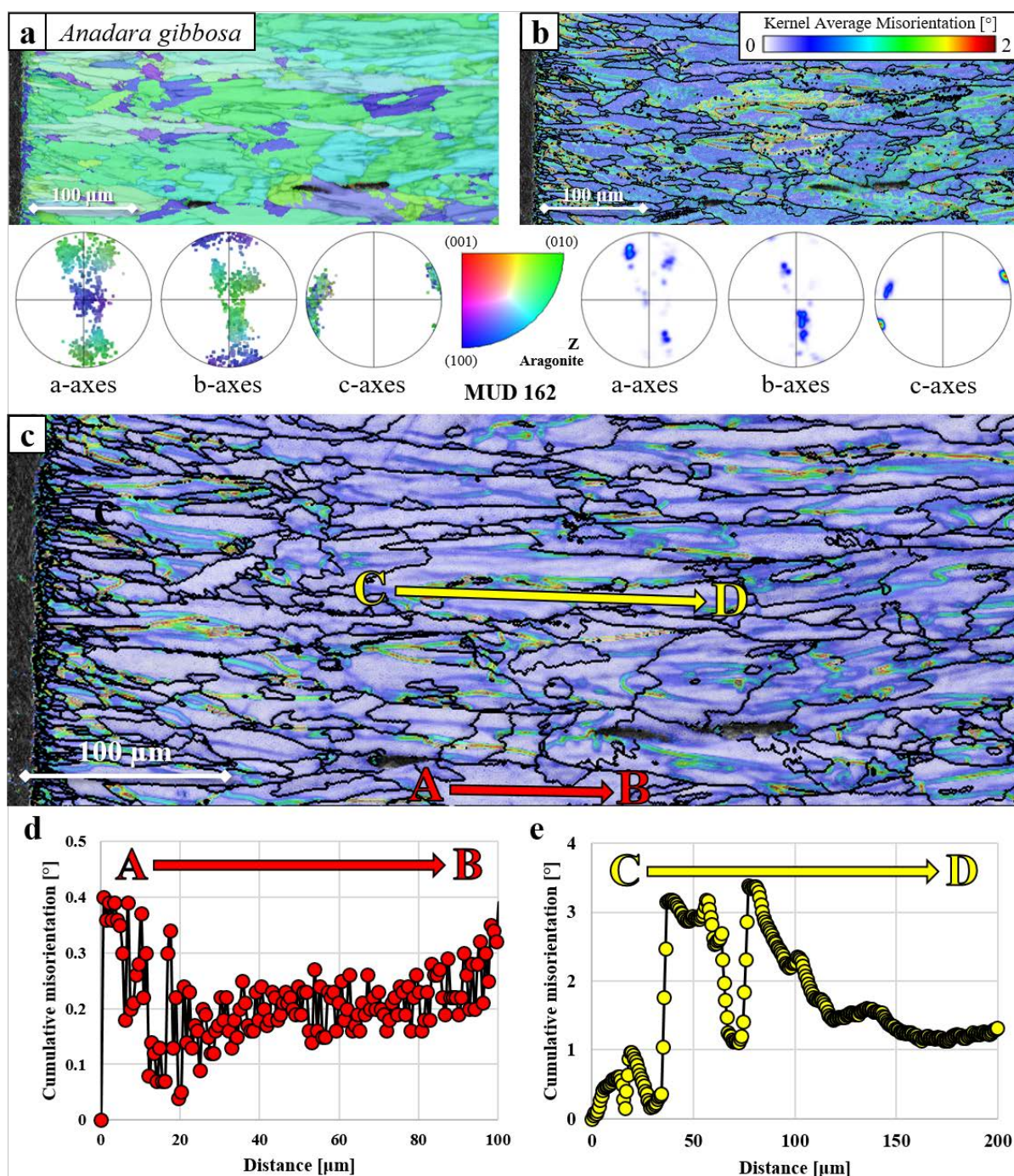


Figure 2.7-9. Pattern-matched EBSD scan revealing the microstructure and internal misorientations of an aragonitic *Anadara gibbosa* myostracum typical for competitive crystal growth. The colour-coded scan and the pole figures indicate an axial texture and a high degree of co-orientation (a). Due to the low orientation precision of conventional EBSD scanning, understanding small-angle misorientations within the aragonitic prisms is rather challenging (b). Applying the pattern matching method significantly improves the orientation precision and unravels advanced patterns in the kernel average misorientation map (c). The refined scan and misorientation profiles indicate that aragonitic prisms generally appear highly cooriented (c, d). However, some prisms comprise misorientation streaks that run predominantly in the growth direction and may lead to internal misorientations of more than 3° (c, e). Since they appear similar to the streaks described for calcite in previous chapters of this study, they may result from the specific sample preparation necessary for EBSD measurements.

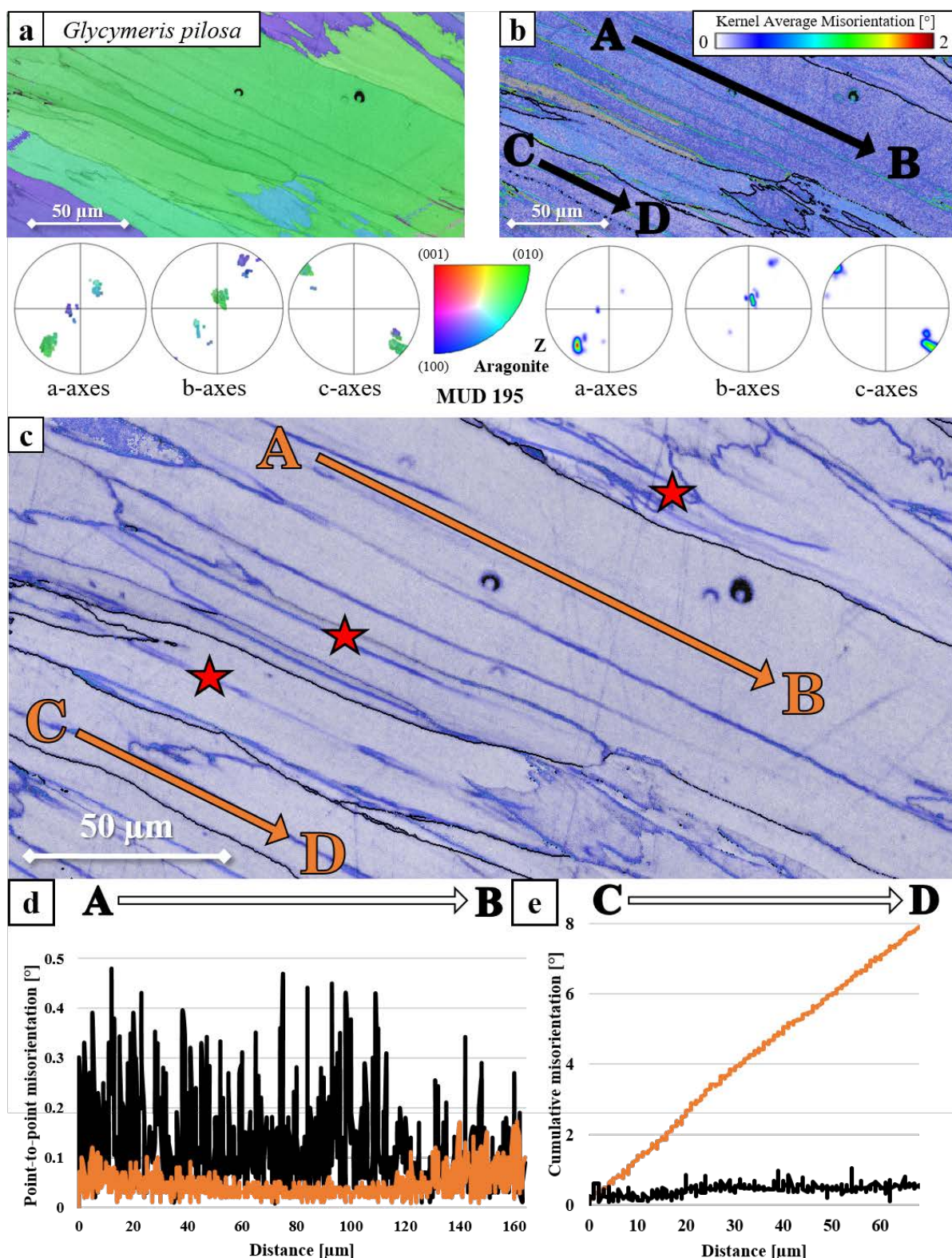


Figure 2.7-10. Pattern-matched EBSD scan revealing the microstructure and internal misorientations of an aragonitic *Glycymeris pilosa* myostracum typical for competitive crystal growth. The myostracum of *G. pilosa* has a 3D "single-crystal-like" texture and a high degree of crystallographic co-orientation (a). Compared to a conventionally evaluated map (b), electron backscatter matching improves angular precision (c). In contrast to conventional maps, structural features such as the subunits within myostracal prisms (indicated by red stars in c) are displayed with a better resolution. Point-to-point misorientation profiles show that pattern matching can decrease the standard deviation from about 0.5° to 0.1° (d). Cumulative misorientation profiles reveal a long-range rotation of the crystallographic orientations within *G. pilosa* myostracal prisms (e).

The myostracum of *A. gibbosa* starts with small, isotropic crystals that quickly increase in size towards the inner shell surface. With distance from the interface, a microstructure typical for a competitive growth mechanism is generated (Fig. 2.7-9a). When using the conventional EBSD analysis software, the low angular precision makes it difficult to recognise the presence and distribution of misoriented areas within the myostracal prisms (Fig. 2.7-9b). However, applying pattern matching to the dataset improves the angular precision, thus revealing areas with enhanced misorientations and well co-oriented regions (Fig. 2.7-9c). Parallel to the growth direction, most of the crystals are permeated by thin, dendritic-like streaks of misorientations that show similarities to measurements of sea urchin tubercles (Fig. 2.6-4 to 2.6-6) and *C. japonica* eggshells (Fig. 2.7-6). Whether these streaks are a structural feature of certain biomineralised materials or arise during sample preparation is uncertain. While most of the aragonitic prisms show a high crystallographic co-orientation with a low cumulative misorientation angle (Fig. 2.7-9d), prisms with misorientation streaks can feature sudden misorientation maxima of up to 3° (Fig. 2.7-9e).

Since the relatively small length and diameter of the *A. gibbosa* myostracal crystals make it difficult to fully understand the texture and small-angle misorientations of the myostracal crystals, the investigated area of the *G. pilosa* myostracum is located close to the inner shell surface. Prisms can reach up to 500 µm in length and have c-axes well co-oriented perpendicular to the inner shell surface (Fig. 2.7-10a). When comparing the conventionally evaluated map (Fig. 2.7-12b) with the pattern-matched map (Fig. 2.7-10c), the latter has higher angular precision and shows more details about the substructuring of myostracal prisms. All myostracal prisms in *G. pilosa* seem divided by low-angle (~0.5°) boundaries that run parallel to the growth direction (indicated by red stars in Fig. 2.7-10c). This substructuring appears to be more frequent in *G. pilosa* than in *A. gibbosa*, possibly because of the larger grain size.

Two misorientation angle profiles that traverse the conventionally evaluated and pattern-matched maps through the identical points in the measurement (A-B and C-D) allow the qualitative analysis of the two evaluation methods. The first profile measures point-to-point misorientations along a long profile spanning 160 µm through a single *G. pilosa* prism (Fig. 2.7-10d). The conventionally evaluated map (black graph in Fig. 2.7-10d) indicates frequent and disorganised misorientations up to 0.5°. In contrast, refining the data set via EBSP matching reveals that the point-to-point misorientation is very low (below 0.1°) along the entire prism. When considering the cumulative misorientation from point C, the two evaluation methods once again yield very different results: The conventional Hough-based indexing method only shows minor misorientation fluctuations up to 1° and indicates that the crystallographic orientation is more or less consistent throughout the entire prism (Fig. 2.7-10e). In contrast, the pattern-matched measurement reveals a continuous rotation up to 8° within the myostracal prism. Comparing the Kikuchi bands of two data points on the edge of myostracal prisms confirms that this gradual rotation is a structural feature and not due to misindexing. In essence, electron backscatter

matching can not only decrease the standard deviation of the indexed crystallographic orientations in aragonitic biomaterials. Still, it may also enable the detection and characterisation of structural features that are hidden when using conventional analysis methods.

2.7.3 CONCLUSIONS

By improving the angular precision of EBSD maps of biomineralised hard tissues from 0.5° to 0.1° , the EBSD pattern matching and refinement method has opened many new research possibilities. Characterising four different types of microstructures and comparing the results with conventional pattern indexing techniques showed the potential of this new technique and yielded interesting and new information unprecedented with conventional EBSD analysis. Based on microstructure and texture characterisation of pattern-matched EBSD data, the following conclusions can be deduced for the different biomineralised hard tissues:

The calcitic columns of bivalve shells:

1. Analysed parallel to the columnar, morphological long axes, the prisms of the calcitic columnar prismatic layer have a high crystallographic co-orientation and do not show significant internal misorientations. The texture of the microstructure is axial, with crystallographic c-axes oriented perpendicular to the inner shell surface.
2. Analysed perpendicular to the columnar, morphological long axis, considerable misorientations are visible within and between the columns. Within a column, the orientation gradually rotates by up to 10° . Neighbouring columns can be misoriented up to 50° with c-axes distributed in an “axial-like” texture.

The calcite of sea urchin tests and spines:

3. The internal co-orientation of the biomineralised calcite in the skeletal elements of sea urchin tests and spines, such as *C. cidaris*, depends on the stereom architecture. Many trabecular junctions create many small-angle misorientation boundaries; these decrease the crystallographic co-orientation between the crystallites. As indicated by different texture-related statistic methods (such as the MUD value, Euler angle analysis and texture component analysis), the sea urchin calcite of *C. cidaris* cannot be generally considered single-crystalline.
4. In contrast to conventional EBSD analysis, the EBSD pattern matching method can detect minute internal misorientations in *C. cidaris* stereom calcite with high accuracy. Although this refinement improves the angular precision of the measurement, the average angular deviation from a reference orientation is often higher than in conventionally analysed datasets.

5. The degree of crystallographic co-orientation is comparable between different echinoid species and different skeletal elements. Most EBSD measurements show MUD values ranging between 658 and 723, indicating microstructures with well co-oriented calcite crystallites, however, with a varying distribution of low-angle misorientations.

The calcitic quail eggshells:

6. The microstructure near the outer shell surface of *C. japonica* eggshells has an intricate structure with large (up to 100 μm), irregularly-shaped grains and is poorly co-oriented. The texture is little textured, ranging from untextured to an axial-like texture, with a broad clustering of crystallographic c-axes perpendicular to the outer shell surface.
7. The grains are traversed by small, disconnected pores ($< 1 \mu\text{m}$) that are more or less homogeneously distributed. Data points directly adjacent to the outer pore surfaces do not show enhanced misorientations, indicating that the pores do not disrupt the microstructure of the *C. japonica* eggshell hard tissue.
8. Within *C. japonica* eggshell grains, the crystallographic orientation gradually changes depending on the direction of misorientation profiles. Perpendicular to the outer shell surface the rotation of crystallographic axes is significantly higher than parallel to the outer shell surface.

The aragonitic prisms of conservative bivalve myostraca:

9. More or less parallel to the growth direction, bivalve myostracal prisms show a strong substructuring that causes small-angle misorientations. The degree of substructuring may depend on the size of the myostracal prisms and is frequent in shells with large aragonitic prisms, such as *G. pilosa*.
10. Along the morphological long axis of the prisms, a gradual rotation of the crystallographic orientation can be observed. This rotation is only visible from minute deviations in Kikuchi pattern position and orientation or through EBSD data evaluation with pattern matching. Across a single grain, the rotation can be as high as 8° .

2.7.4 SUPPLEMENTARY INFORMATION

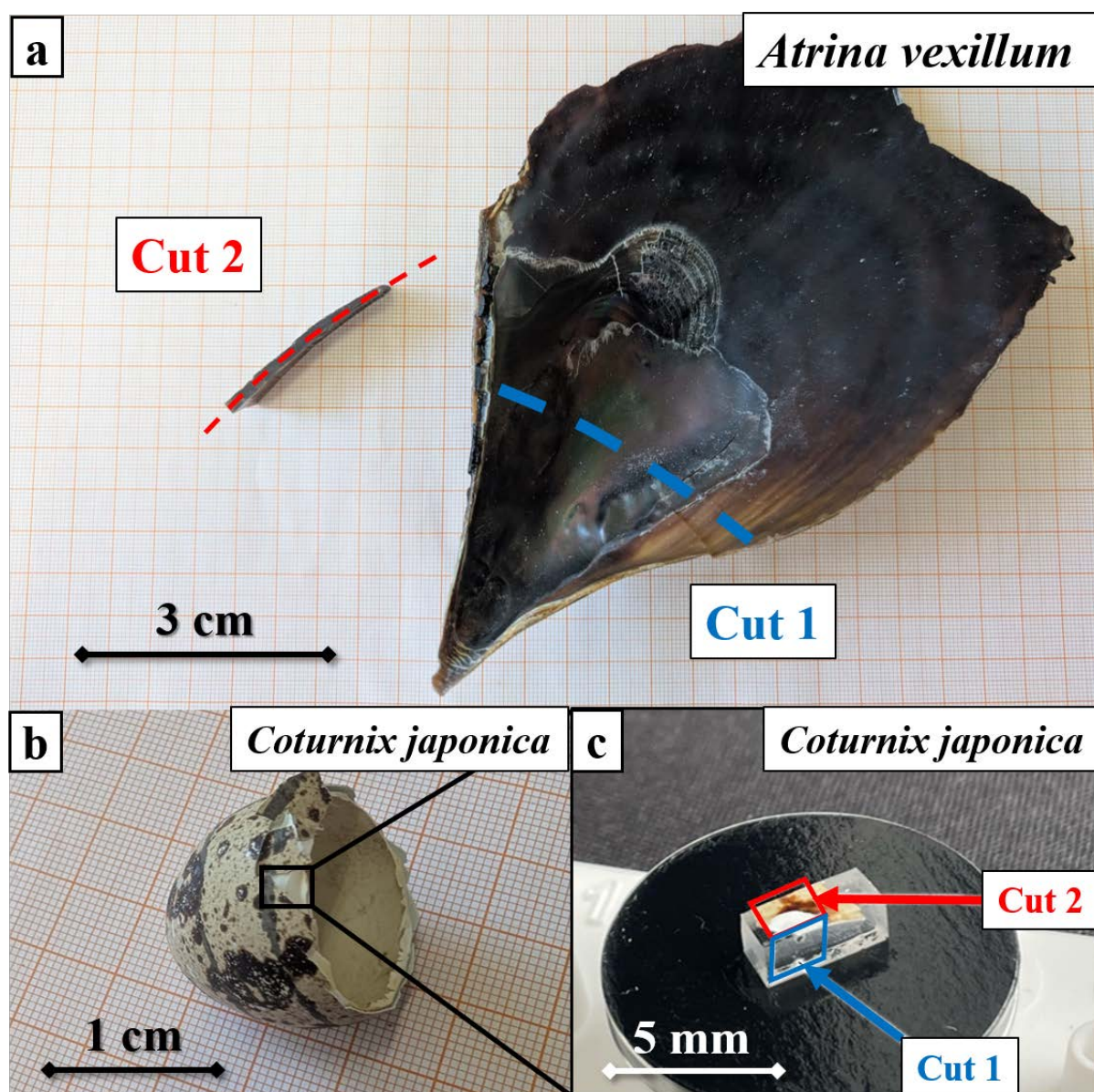


Figure 2.7-AP1. Photographs depicting the different applied cuts for the investigated bivalve shells and quail eggshells. Bivalve shells were sectioned perpendicular to (cut 1) and parallel to (cut 2) the inner shell surface, as depicted in (a) for a valve of *Atrina vexillum*. Quail eggshells of *Coturnix japonica* were sectioned transversely (b) and polished along two perpendicular directions (c): Perpendicular to the inner shell surface (cut 1) and parallel to the inner shell surface (cut 2). The applied cutting directions for the *Cidaris cidaris* sea urchin test are visible in Fig. 2.6-1 of this thesis.

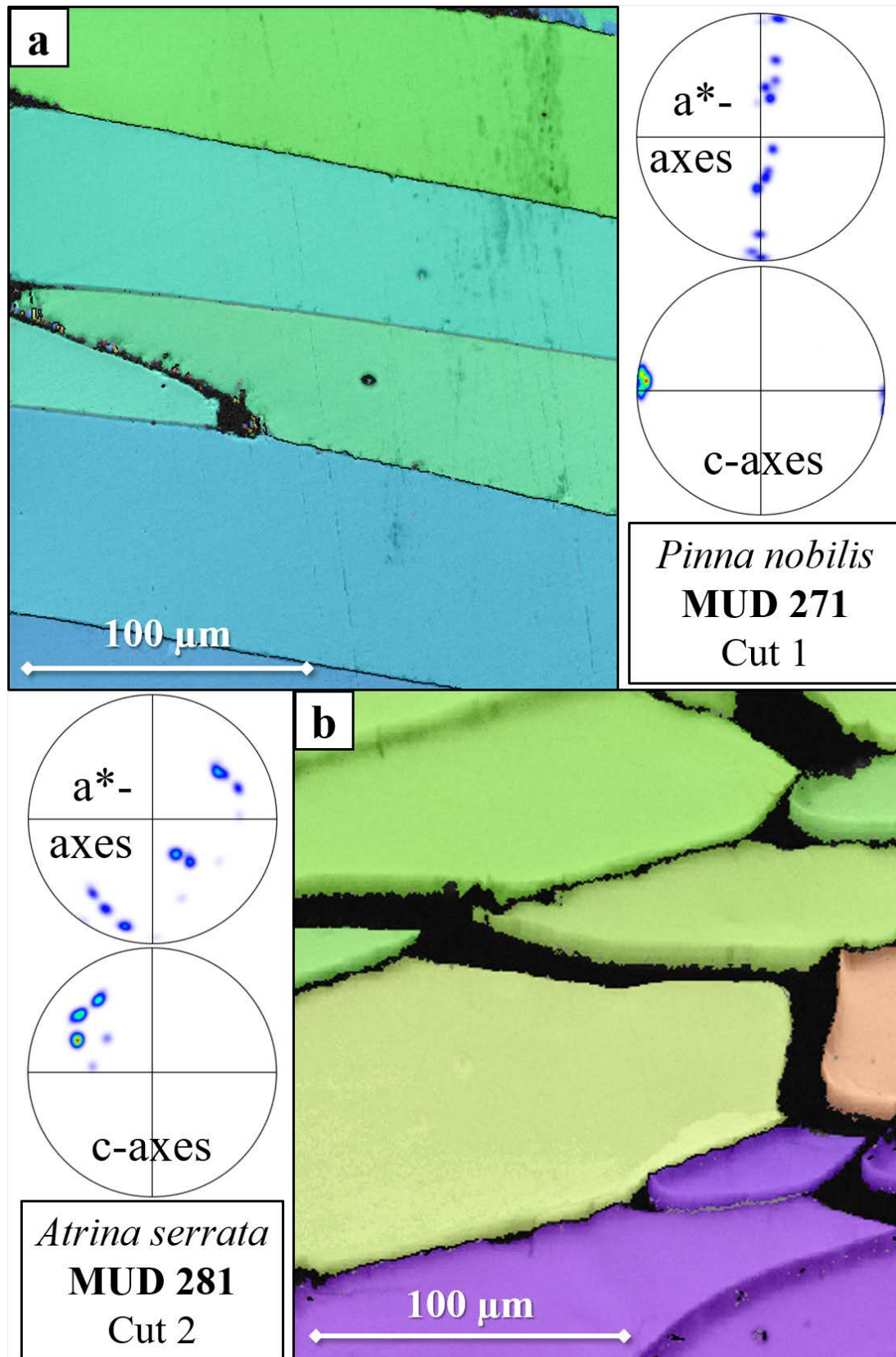


Figure 2.7-AP2. The microstructure and texture of calcitic bivalve columns sectioned along two cuts. The EBSD measurements were evaluated with the common AZtecCrystal software without pattern matching. The *Pinna nobilis* sample was cut parallel to the prisms and shows an axial texture, with a- and b-axes varying slightly (a). In *Atrina serrata*, columns were sectioned perpendicular to their long axis. The pole figures display a graded texture, with the c-axes gradually rotating across the prisms and the a- and b-axes shifting accordingly (b). Despite the different orientational density distributions, the MUD values of the two measurements are similar, displaying rather high crystal co-orientation strengths (a, b).

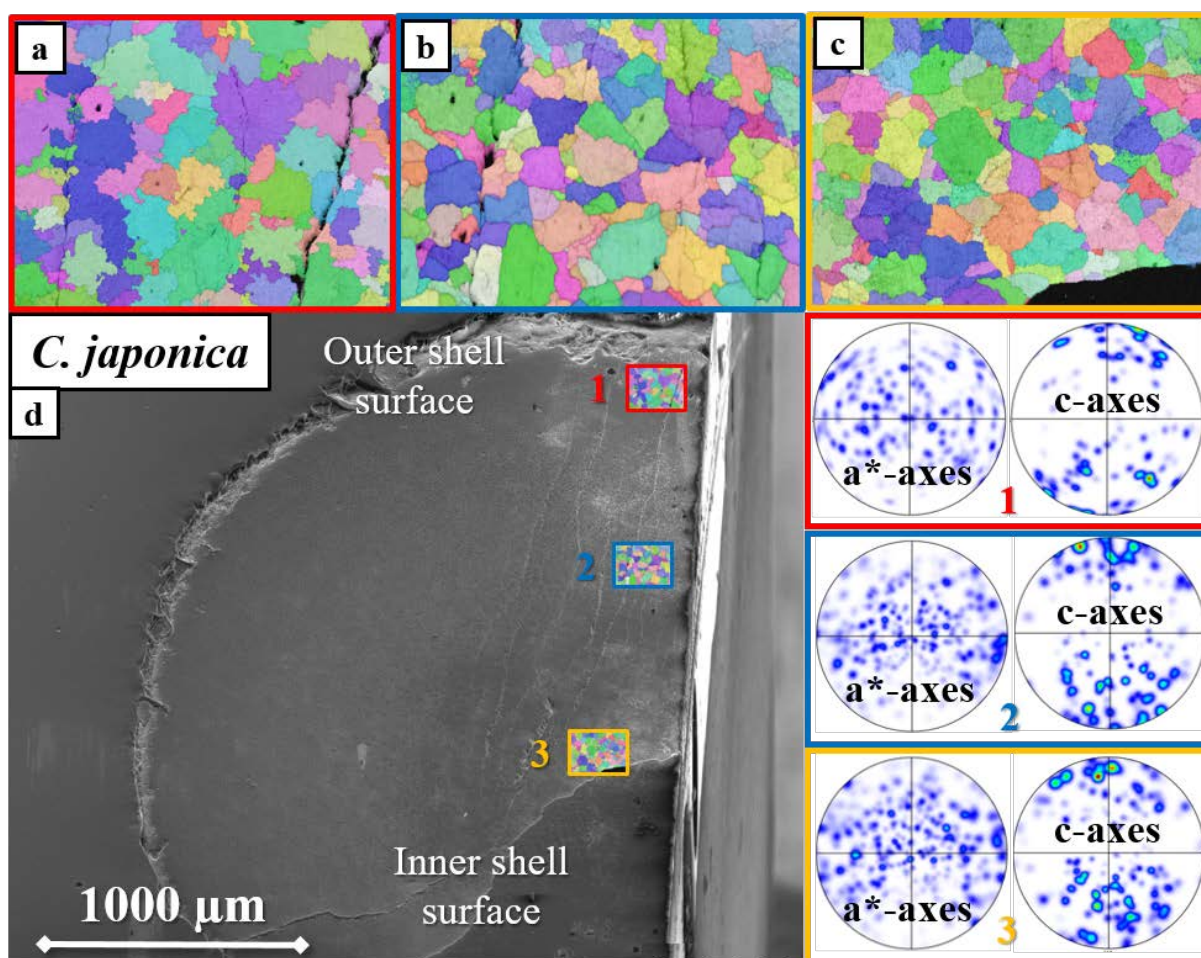


Figure 2.7-AP3. *Coturnix japonica* eggshell microstructure and texture at different regions of a shell sectioned along cut 2. Close to the outer shell surface (Position 1), the grain boundaries appear uneven and rough (a). With distance from the outer shell surface (Position 2 and 3), the grain boundaries become smoother, with the average grain size decreasing slightly (b, c). Irrespective of the measurement position, the microstructure has an axial-like texture with c-axes oriented somewhat perpendicular to the outer shell surface (d). The measurement positions are indicated on an FE-SEM image of the eggshell sample (d).

3 CONCLUSIONS AND OUTLOOK

3.1 CONCLUSIONS

Biomaterialised materials are hybrid composites formed of organic matrices and inorganic minerals. Although most biomaterialised hard tissues comprise calcium carbonate minerals, there is a huge biodiversity regarding mineral morphologies and microstructures (e.g., Wilt 2005; Deng et al. 2022; Jia et al. 2022). This variety can be attributed to the functional demands of biomaterialised hard tissues, enabling the organisms to pursue a certain lifestyle and, thus, ensuring their survival. Through millions of years of evolution and adaptation to the ecological constraints of different environments, modern-day organisms can form biomaterials with excellent material properties, such as high mechanical strength and flexibility, while maintaining a low weight (e.g., Nudelman & Sommerdijk 2012; Yao et al. 2017; Yu & Zhu 2024). Thus, understanding the biomaterialisation principles of highly functional and elaborate biocomposite materials not only allows environmental and evolutionary insights but is also of key importance for fabricating advanced biomimetic materials.

The present dissertation focuses on the detailed analysis of microstructure, crystal texture and material properties of various Calcium carbonate biomaterialised hard tissues. This thesis is divided into two parts:

The first and main part of this thesis is devoted to an in-depth understanding of the hierarchical structure of invertebrate bivalve shells, focusing, in particular, on the unique and outstanding microstructures that form at those valve sections where the valve-moving muscles attach to the valves. The shells of bivalved invertebrates are secreted by the cells of a single-layered mantle epithelium. At adductor muscle attachment, the muscle attachment sites are formed through specialised tendon cells. Since exerting control over valve activity is crucial for the survival of bivalved invertebrate organisms, the adductor muscle attachment site crystals form via particular growth mechanisms, enabling a tight and strong connection to the muscle fibres. This growth mechanism generally involves two processes: (i) the epitaxial nucleation onto an adjacent shell layer with a highly controlled microstructure and texture, and (ii) the growth of large (micrometre-sized), irregularly-shaped crystals. For bivalves, the growth of these is driven by a competitive growth mechanism.

The second part of this thesis discusses crystal growth mechanisms, microstructures and crystal textures of sea urchin skeletal elements. In contrast to molluscs and brachiopods, the biomaterialisation of sea urchin skeletal elements supposedly also include intracellular nucleation processes (Gilbert & Wilt 2011). The microstructures and textures of sea urchin tests and spines is generated through biological as well as competitive growth mechanisms. Calcite crystallites of sea urchin tests and spines are very co-oriented. A further aim of the second part of this thesis was to apply an advanced EBSD data evaluation method, the pattern matching EBSD data evaluation technique. With the use of the latter

minute misorientations are revealed for the sea urchin hard tissue that are not detected with conventional EBSD data evaluation. Subsequently, a short summary will be given of the results and scientific gains of the different sections that form this thesis.

Section 2.1 highlights in great detail the different microstructures and textures of bivalves of the bivalve genus *Chama*. Shells of chamids show a great diversity in microstructures and crystal morphologies, forming up to five different microstructures and comprising both aragonite and calcite within a single shell. High-resolution EBSD measurements have shown intricate hierarchical structures in the shells of both the purely aragonitic *Chama gryphoides* as well as for *Chama arcana*, which forms its shell of aragonite and shell ornamentations of calcite. Our EBSD data analysis revealed the transmission of crystallographic texture at the changeover between adjacent shell layers and explores the biomineralisation principles used by the organism to create functional biocomposite shells. We found key differences in the crystal morphology and microstructure of analogous layers in separate *Chama* species and discuss possible reasons for these anomalies.

Based on the large microstructural diversity observed for chamid shells, Section 2.2 compares the microstructure and texture of myostracal and non-myostracal shell layers of bivalves of different orders. Although *Chama* (order Venerida) and *Glycymeris* (order Arcida) follow different lifestyles and occupy distinct environments, the shells of these two bivalve genera comprise similar microstructural motifs (Taylor et al. 1969; Taylor et al. 1973). Investigating the biomineralised tissues and, in particular, the myostraca, with in-depth EBSD analysis and nanomechanical testing, our measurements indicated minor differences between the genera: in all layers of the burrowing *Glycymeris* shells we observed higher co-orientation and a more regulated and ordered arrangement of crystals and first-order lamellae, as compared to the intricate crystal morphologies found in *Chama*. The nanomechanical testing yielded similar results for the aragonitic microstructures of all investigated shells, with the highest hardness observed in the competitively grown myostraca (increased by up to 20% compared to the non-myostracal valve). In both *Glycymeris* and *Chama* shells, the crystallographic texture is always initially transmitted between adjacent shell layers of the same mineral phase; however, each microstructure may develop an independent texture with distance from the changeover of shell layers to myostraca. Different modes of aragonitic twinning around [001] were identified for the different shell layers; however, twinning was prevalent in all investigated aragonitic microstructures. The calcitic ornamentations of *Chama* shells are not twinned.

Section 2.3 covers in more detail the microstructural design principles of bivalve myostraca, and discusses whether they can be related to morphological functions due to different lifestyles that the organisms pursue. We compared the valve and myostraca of the burrowing *Glycymeris pilosa*, the sessile *Chama arcana* and the swimming *Placopecten magellanicus*. Our structural results indicate that, in contrast to crystals of the rest of the valves, the aragonitic myostracal microstructure is not as actively controlled by the organism, despite its relatively high organic content. Myostracal crystals are secreted

by specialised cells, the tendon cells, that are not in direct connection with the forming myostracal hard tissue (Tomba & Watabe 1976; Castro-Claros et al. 2021). Accordingly, bivalve myostracal crystal growth microstructure and texture is largely determined by a competitive growth mechanism. However, bivalve myostracal microstructure can be influenced by controlling the texture and calcium carbonate phase of the valve template, i.e., the shell layer that is directly adjacent to the myostracum. If this template is aragonitic, the first-formed myostracum crystals assume the orientation of the adjacent, non-myostracal crystals. Our results show that the grain size, texture and grain morphology of myostracal crystals develop differently for different nucleation templates. If the nucleation template is morphologically well-regulated, e.g., the first-order lamellae in *G. pilosa*, we observed thick, irregular prisms with a single-crystal-like texture. If the nucleation template consists of thin, interdigitated first-order lamellae, such as in *C. arcana*, we observed smaller prisms with an axial texture. If the nucleation template is calcitic, such as in *P. magellanicus*, the texture of the valve template is not transmitted to the myostracum and the myostracum is formed of very thin, regular prisms and a highly axial texture, with c-axes co-oriented perpendicular to the inner shell surface. For the myostraca of all investigated bivalve species, the grain boundaries of the investigated myostraca show a high frequency of cyclic twinning around [001], irrespective of the adjacent layer.

As described in Section 2.3, the observed nanomechanical hardness and indentation elastic modulus of the three myostraca are similar. Yet, we observed marked differences when changing the indentation direction, relative to the crystallographic c-axes. When the samples were indented perpendicular to the inner shell surface, myostracal hardness was increased by 15-37% compared to the same shells indented parallel to the inner shell surface. Moreover, we could show a difference in average hardness in the two sets of *G. pilosa* crossed-lamellar first-order lamellae, which showed a deviation in c-axis orientations. The hardness was significantly increased for the lamellar set with c-axes pointing parallel to the indentation direction. This observation is in correlation with studies on inorganic calcium carbonates (Berman et al. 1993; Pasquini et al. 2015; Deng et al. 2023), indicating that the crystallographic orientation and, in particular, the orientation of c-axes, can distort the results of nanomechanical testing in biomineralised hard tissues.

Sections 2.1 to 2.3 focused on microstructure, hierarchical growth and nanomechanical properties of competitively grown myostracum layers. Previous studies describe this microstructure as a characteristic layer of prismatic aragonite crystals that is conservative in structure for the different bivalve species (Kennedy et al. 1969; Dong et al. 2022). However, as shown in [Section 2.4](#) of this dissertation, this is not valid for all bivalve adductor myostraca. The high-resolution EBSD analysis of shells of more than 30 bivalve species, investigated in this study (Table A.2-1), rather suggests the classification of myostraca into three categories: the conservative myostraca, the hybrid myostraca and the non-conservative myostraca.

- (i) Conservative myostraca are observed for most of the investigated bivalve species. Their distinct microstructure is characterised by mostly large and long prisms that have irregular grain boundaries and form an axial texture. The crystallographic c-axes are oriented more or less perpendicular to inner shell surfaces, as a competitive growth mechanism determines myostracal microstructure generation.
- (ii) The hybrid myostraca show characteristics of conservative myostraca (such as enlarged grains or a clear-cut interface boundary with the adjacent shell layer); however, their microstructures are less distinct than those of the conservative myostraca. This is represented by usually thin myostraca comprising a single layer of aragonite crystals or a sequential myostracum that blends in with the adjacent shell microstructure.
- (iii) In some cases, the myostracum layer is barely distinguishable from the microstructure of the adjacent shell layer. Those myostraca are considered non-conservative, as they show no elements of microstructure generation through a competitive growth mechanism.

Irrespective of the influence of the competitive growth process, I observed for all investigated bivalve myostraca with aragonitic microstructures that the crystallographic texture of the nucleation template is always transmitted to the crystals of the myostracum. The microstructure of the layer preceding the myostracum might influence the development of a competitively-grown myostracum, as for some layers (e.g., crossed-lamellar, prismatic aragonite) I always found conservative myostraca and for other layers (e.g., granular aragonite) I mostly observed non-conservative myostraca. Nanomechanical testing indicates that an increase in the influence of a competitive growth process correlates with the observed nanomechanical properties: Distinct conservative myostraca show the highest hardness and elastic indentation moduli, while the hybrid and, in particular, the non-conservative myostraca are softer and show significantly lower elastic indentation moduli (Table 2.4-1).

The data obtained on the microstructure, texture and nanomechanical properties of bivalve myostracal and non-myostracal shell layers demonstrates the complex growth mechanism that is utilised by bivalve molluscs to form hierarchical, sophisticated biocomposite shells that protect them from environmental threats. However, bivalves are not the only marine invertebrates forming two-valved calcium carbonate shells that are opened or closed, depending on the ecological constraints. Thus, Section 2.5 investigated the calcitic shells, particularly the muscle attachment sites, of rhynchonellate brachiopods. These belong to the phylum Brachiopoda, while bivalves belong to the phylum Mollusca.

While the two invertebrate classes share, to some extent, similar lifestyles, habitats and biomineralisation systems, the muscle attachment sites of brachiopods and bivalves are quite different. The calcitic rhynchonellates form a different calcium carbonate phase for generating the muscle attachment sites, compared to the bivalves. The muscle attachment sites of rhynchonellate brachiopods are calcitic; the myostraca of bivalves are always aragonitic. Regarding the microstructure, rhynchonellate muscle attachment site crystals have a fractal-like morphology and comprise strongly

interdigitating blocks of crystals. Although an increased thickness compared to other rhynchonellate valve portions is observable, the muscle attachment site is not as thick and prominent as that of the conservative bivalve myostraca. Nonetheless, probably initiated by the similar determinants of the secreting epithelial cells underlying muscle attachment sites, the tendon cells, we also found some microstructural similarities for the muscle attachment sites of rhynchonellate brachiopods and bivalves. For example, for both invertebrate classes, the adjacent shell layer transmits its crystallographic texture onto muscle attachment site crystals, if the latter comprises the same calcium carbonate phase. Furthermore, crystallographic c-axes are always oriented parallel to the muscle fibres, and both bivalves and rhynchonellate brachiopod muscle attachment site crystals form large units that are distinct in microstructure from the other shell layers. Thus, despite some convergent traits between the muscle attachment sites of species of the bivalved invertebrate classes, representing two different phyla, we show that some structural characteristics evolved independently in a similar way, e.g., the attachments of the muscles via tendon cells to the valves. Other attributes, such as muscle attachment site crystal growth, carbonate phase and microstructure is entirely different for the investigated species of the different invertebrate classes and phyla.

In rhynchonellate brachiopods and bivalve molluscs, the investigated biomineralised tissues are formed extracellularly via epithelial mantle cells that, at muscle attachment sites, are specialised (Simonet Roda et al. 2019b; Castro-Claros et al. 2021). However, other marine invertebrates, such as echinoids, also use muscles to control their biomineralised skeletons and skeletal elements and to protect their soft tissue from predators (Stauber & Märkel 1988; Ziegler et al. 2012). Biomineralising their skeletal elements within syncytial sclerocytes (Simkiss & Wilbur 1989; Vidavsky et al. 2016), echinoids can form complex, yet highly co-oriented microstructures of high-magnesium calcite. [Section 2.6](#) of this dissertation describes the crystallographic texture and microstructure of tests and spines in two echinoid species, namely *Cidaris cidaris* and *Paracentrotus lividus*. For different parts of the test plates and spines, we found that the calcite trabeculae are arranged in different stereom architectures. Within a spine and within a test plate, the crystallographic textures resemble more or less single crystals. However, at the primary test tubercles, the attachment sites where the muscles attach to and interconnect the plate and the spine, a distinct, polycrystalline microstructure was observed. This microstructure comprises small, fractal-like crystals with the calcite c-axes oriented perpendicular to the outer shell surface with an axial texture. Interestingly, a similar microstructure was observed at the basal outer spine surface of the sea urchin spines, opposing the tubercles of the test. For both primary and secondary spines of *C. cidaris*, we also observed a polycrystalline cortex that encapsulates the medulla from the shaft to the tip of the spines. The outer surface of the medulla functions as a template for cortex nucleation, with crystallographic calcite c-axes of the cortex crystals oriented more or less perpendicular to the outer medulla surface. At the tip of the spines, this creates an intricate growth pattern due to nucleation within the intertrabecular pores. Along the shaft of the spines, however, where the nucleation template is rather smooth, the cortex crystals exhibit a competitive growth mechanism, generating, at

progressive growth, a microstructure of co-oriented crystals with distance away from the nucleation surface.

Furthermore, this study evaluated the single-crystallinity within echinoid skeletal elements by employing the EBSD pattern-matching method for the first time for biomineralised calcium carbonate hard tissues. This method improves the angular precision of high-resolution EBSD scans from 0.5° to less than 0.1° . Thus, this evaluation method allows us to precisely determine minute misorientations within the sea urchin hard tissues. EBSD analysis with pattern matching revealed small-angle ($< 2^\circ$) misorientations within the single-crystal-like trabeculae. As these misorientations appear frequently at trabecular junctions, the stereom architecture defines the degree of single-crystallinity in the respective portion of the spine or the test. For spatially ordered stereom sections without pores or with few trabecular junctions, crystallographic co-orientation is highest. In essence, our microstructural characterisation suggests that neither *C. cidaris* nor *P. lividus* skeletal elements should be addressed as single crystals. The presence of polycrystalline areas and small-angle misorientations in sea urchin calcite does not confirm the claim of X-ray diffraction studies (Donnay & Pawson 1969; Nissen 1969; Su et al. 2000; Moureaux et al. 2010) that suggested that the calcite of sea urchin spine is single crystalline.

The successful application of the EBSD pattern matching method for the biomineralised tissues of sea urchin test and spines has inspired the investigation of further biomaterials with the pattern matching EBSD data evaluation method, as described in [Section 2.7](#). The latter chapter examined small-angle misorientations and the evolution of the crystallographic texture for four different microstructures: (i) For the calcitic columnar prismatic layer of various bivalves, analysed parallel and perpendicular to the inner shell surfaces, pattern matching reveals gradual rotations of up to 10° perpendicular to the morphological long axis of individual prisms. Parallel to the morphological long axis of the prisms, the crystallographic axes only show minute rotations below 0.5° . (ii) Further analysis of sea urchin skeletal elements of *C. cidaris* reveals differences in precision of conventional data evaluation versus pattern matching and discusses whether and how single-crystallinity can be quantified and compared. Measurements performed on *C. cidaris* test and spines are juxtaposed with eight other sea urchin species from different orders. (iii) Calcitic eggshells of *Coturnix japonica* comprise fractal-like prisms that are highly porous. Pattern matching demonstrated that the small pores ($< 1 \mu\text{m}$) do not seem to disrupt the crystallographic texture of the eggshell layer. However, a gradual rotation of crystallographic axes was detected; the rotation is highest on profiles perpendicular to the outer shell surface. (iv) Within the aragonitic prisms of bivalve myostraca, pattern matching revealed the structure and distribution of small-angle misorientation streaks and the minute rotation of the crystallographic axes along the morphological long axis of the prisms.

3.2 OUTLOOK

The design principles, biomineralisation mechanisms and their correlation with material properties, such as hardness and elasticity, are intricate and still far from fully understood. Investigating in great detail the texture and microstructure of archetypical biological hard tissues for species of various classes and phyla can provide answers to a limited section of this vast scientific field. However, as we continue to understand some biomineralisation processes, many new questions arise, and possibilities for further research open up.

New research perspective, the hyives could cover the following points:

1. A complete understanding of the microstructure generation mechanisms in conservative and non-conservative bivalve myostraca

This work investigated for the first time the microstructure, texture and nanomechanical properties of non-conservative myostraca present at bivalve muscle scars, which do not exhibit the traditional microstructure generated through competitive growth parameters. Instead, these non-conservative myostraca show great similarities in texture, grain morphology and hardness compared to the adjacent, non-myostracal shell layers. The preliminary results of these characterisations indicate that the microstructure, particularly the crystallographic phase and texture, may greatly influence or even support the generation of hybrid or non-conservative myostraca over the conservative myostraca.

To confirm or contradict this theory and understand the biomineralisation principles that trigger the growth of these atypical myostraca, future work may involve a methodical sample selection approach based on the structural results gained through this study. Investigating the changeover and growth of myostraca adjacent to various microstructures will be of key importance for recognising the biomineralisation principles of conservative and non-conservative myostraca. This demands investigating and characterising other bivalve species not covered in this work. Furthermore, future studies could consider morphological constraints, such as shell size or adductor muscle thickness, and environmental constraints, such as temperature or salinity during shell growth.

Finally, there is one other potential factor that might play a role in the microstructure generation of the myostracum: the ligament. While it is shown that the hinge ligament in bivalves plays a significant role for various valve activities, in particular for valve opening, (Yonge 1973; Kahler et al. 1976; Tremblay et al. 2015; Ponder et al. 2019), it is not yet fully understood if and how this influences the myostracal microstructure. Keeping in mind the different microstructures at the adductor muscle sites of rhynchonellate brachiopods (which do not have a hinge ligament) and bivalves, it is feasible that the hinge is generally of main importance for the adductor muscle structure, and thus, for the development of the myostracum.

2. The investigation of the distribution of the organic substance within the shell and myostracal crystals

Compared to bones or tooth dentin (Gong et al. 1964; Driessens 1980; Elliott 2002; Teruel et al. 2015; Foley et al. 2020), the weight percentage of organic materials in bivalved invertebrate shells or sea urchin skeletal elements is low (Ameye et al. 2001; Mann 2001; Mann et al. 2008; Copper 2018). Nonetheless, the organic components, e.g., generating the extracellular organic matrix, play a significant role in forming biomineralised tissues. While the composition of the organic matrix material in bivalves and rhynchonellates starts to be understood, little work has been done on the distribution patterns of organic substances within the shell. Future work could aim to localise, distinguish and quantify the different biopolymers present in the shell using, for example, selective etching techniques. It would be of great interest to compare the biomineralised hard tissues of various phyla, species, and microstructures to reveal the different biopolymers' functionality and role.

Furthermore, the studies presented here have shown how thermogravimetric analysis techniques can quantify the organic content in different shell layers and correlate the latter to the material properties of the hard tissue layers. This is particularly interesting for bivalve myostraca, where we observed a high organic content, yet the distribution and structure of the latter are still far from clear. The adductor muscle-shell attachment of bivalves is one of the strongest connections of invertebrates (Chantler 1983). Thus, understanding the topological relation and mechanism of this connection in detail would be of great value for generating man-made biocomposite materials.

3. The correlation of different biomineralised microstructures and the crystallographic orientations of the crystals with mechanical properties

It is very interesting to observe that biomineralised hard tissues can form tough composite structures of inorganic crystals and an organic matrix, which are both inferior in nanomechanical hardness. While the mechanisms and preconditions for tough materials are, more or less, understood for simple and inorganic materials (e.g., Sakai & Bradt 1993; Kobayashi 2004; Brostow et al. 2015), the nanomechanical analysis of biocomposite hard tissues still raises some questions, e.g., how the arrangement of grains and organic matrix affects the hardness or whether the Hall-Petch effect is valid for biomineralised materials.

It has repeatedly been shown in this thesis that myostraca with a conservative structural design show exceptional nanomechanical properties. Therefore, of particular interest could be highlighting what makes the myostracum so nanomechanically hard, compared to other biomineralised shell layers. Opposed to most bivalve shells, the biomineralised muscle attachment site in rhynchonellate brachiopods does not feature long, prismatic aragonite crystals but comprises irregular and interdigitated calcite units. Nonetheless, the muscle attachment mechanism and the determinants for shell generation are similar for species of these two invertebrate classes. Thus, future studies could explore whether the

mechanical properties of rhynchonellate muscle attachment sites are also enhanced in hardness, compared to other shell portions.

This work has shown that, for biomineralised hard tissues, the measured hardness depends not only on the microstructure but also on the crystallographic orientation of grains. Further experiments should be designed to thoroughly examine and understand this azimuthal variability for designing experiments that allow a better comparability between the mechanical properties of different biomaterials. This could include (i) the application of new techniques, such as micromechanical testing, (ii) employing different nanoindentation tips, such as conical tips, or (iii) indenting a material along different directions and different crystallographic planes. Moreover, it would be interesting to compare azimuthal differences in differently mineralised materials, e.g., for aragonite forming non-myostracal prisms, myostracal prisms or inorganic crystals grown in solution or hydrogels.

4. The application of advanced EBSD tools for the in-depth structural analysis of biomaterials

We applied for the first time for biomineralised calcium carbonate hard tissues the novel method of EBSD pattern matching to a limited number of materials. Our structural results show great potential from this technique, as it increases the angular precision from around 0.5° to below 0.1° . This not only removes noisy data points but can also reveal the presence and distribution of small-angle misorientations within biomineralised grains, e.g., of biological aragonite and calcite, as well as in other crystals. In particular, for microstructures that are formed of large grains, e.g., the calcite columnar prismatic layer of bivalves, the pattern matching analysis method allows the accurate characterisation of the crystal texture, revealing a minute yet gradual rotation within the calcitic columnar prismatic units. An in-depth characterisation of layers, formed solely of columns or prisms, for the shells of different species will be of great interest to gain information on the crystal growth mechanism of this unique microstructure, as it shows both a high organic content and a high tensile, compressive and bending strength.

However, the pattern matching method will be useful to locate misorientations and precisely quantify the degree of single-crystallinity and crystallographic co-orientation in a given material. Comparing different biomineralised hard tissues that show single-crystalline long-range orders, such as the sea urchin stereom, hydrogel-grown crystals, or the aragonitic sclerites of molluscs, can answer the question of whether there is something like a biomineralised single-crystalline material. Furthermore, while this work has shown that the MUD-value can well approximate the degree of co-orientation within a material, it has also pointed out the limits of the latter, especially when comparing highly co-oriented microstructures. The elaboration of a more sophisticated and reliable method, e.g., utilising texture components or Euler angles, could be of great interest not only for describing biomineralised hard tissue, but also for inorganic or man-made materials characterised by EBSD analysis.

Somewhat complementary to data evaluation with EBSD pattern-matching methods, the novel 3D-EBSD technique combines the conventional 2D-EBSD with the slice-and-view method. In the latter, a focused ion beam is used to cut thin layers of the sample surface in sequential series with EBSD scans. The retrospective stitching of these scans into a 3D model allows for the measurement and analysis of the evolution of the crystallographic texture and microstructure of certain regions of interest. These may include the changeover from non-myostracal valve into the myostracum of bivalves or into the adductor muscle scar in brachiopods, both of which feature intricate crystal morphologies and textures that are difficult to interpret with two-dimensional EBSD maps. A further interesting application of 3D-EBSD could be in sea urchins, reproducing the three-dimensional trabecular structure of various stereom fabrics and analysing via pattern-matching the distribution of minute misorientations within the trabeculae.

5. The utilisation of computational modelling to understand critical parameters for the generation of competitively-grown microstructures

Due to their functionality, most biomineralised materials have a microstructure and texture highly controlled by the organism. However, microstructure generation occurs mainly through competitive crystal growth parameters in some invertebrates. Despite their similar growth mechanisms, the competitively grown microstructures in the argonaut prismatic layer (Checa et al. 2021), the dorsal shield in cuttlefish (Griesshaber et al. 2023), the sea urchin cortex or bivalve myostraca (this work) all vary significantly in grain size and morphology as well as in crystallographic co-orientation. To determine whether these characteristics are predetermined solely by certain physical parameters, or might be controlled/influenced by the biomineralising cells or the organic substances/layers present within the competitively-grown microstructures, computational modelling might be of great use.

Comparing simulations of different nucleation scenarios, such as smooth (e.g., prismatic layer in *Argonauta*) versus complex nucleation surfaces (e.g., dorsal shield in *Sepia* or spine cortex in *Cidaris*) or a predefined (e.g., *Glycymeris* myostraca) versus an unrestricted initial texture (e.g., in *Placopecten* myostraca or the prismatic layer in *Argonauta*) will help to understand the influence of the specific parameters. Moreover, it will be interesting to compare the simulated competitive growth microstructures with the ones we find in nature, as analysing the differences between the two might give unprecedented insights into crystal growth kinetics in those microstructures.

4 BIBLIOGRAPHY

- Ackerly, S.C., 1991, 'Hydrodynamics of rapid shell closure in articulate brachiopods', *Journal of Experimental Biology*, 156(1), 287–314.
- Ackerly, S.C., 1993, 'Mechanical couplings in the shell closing mechanism of articulate brachiopods: Implications for the evolution of skeleto-muscular architecture', *Paleobiology*, 19(4), 420–432.
- Addadi, L., Joester, D., Nudelman, F. & Weiner, S., 2006, 'Mollusk shell formation: A source of new concepts for understanding biomineralization processes', *Chemistry – A European Journal*, 12(4), 980–987.
- Addadi, L., Raz, S. & Weiner, S., 2003, 'Taking advantage of disorder: Amorphous calcium carbonate and its roles in biomineralization', *Advanced Materials*, 15(12), 959–970.
- Addadi, L. & Weiner, S., 2014, 'Biomineralization: Mineral formation by organisms', *Physica Scripta*, 89(9), 098003.
- Agbaje, O.B.A., Wirth, R., Morales, L.F.G., Shirai, K., Kosnik, M., Watanabe, T. & Jacob, D.E., 2017, 'Architecture of crossed-lamellar bivalve shells: The southern giant clam (*Tridacna derasa*, Röding, 1798)', *Royal Society Open Science*, 4(9), 170622.
- Ahamed, M.K., Wang, H. & Hazell, P.J., 2022, 'From biology to biomimicry: Using nature to build better structures – A review', *Construction and Building Materials*, 320, 126195.
- Aidley, D.J. & Stanfield, P.R., 2000, *Ion channels: Molecules in action*, Reprinted, Cambridge Univ. Press, Cambridge.
- Aizenberg, J., Hanson, J., Koetzle, T.F., Weiner, S. & Addadi, L., 1997, 'Control of macromolecule distribution within synthetic and biogenic single calcite crystals', *Journal of the American Chemical Society*, 119(5), 881–886.
- Aizenberg, J., Lambert, G., Weiner, S. & Addadi, L., 2002, 'Factors involved in the formation of amorphous and crystalline calcium carbonate: A study of an ascidian skeleton', *Journal of the American Chemical Society*, 124(1), 32–39.
- Albéric, M., Caspi, E.N., Bennet, M., Ajili, W., Nassif, N., Azaïs, T., Berner, A., Fratzl, P., Zolotoyabko, E., Bertinetti, L. & Politi, Y., 2018, 'Interplay between calcite, amorphous calcium carbonate, and intracrystalline organics in sea urchin skeletal elements', *Crystal Growth & Design*, 18(4), 2189–2201.
- Albéric, M., Stiffler, C.A., Zou, Z., Sun, C.-Y., Killian, C.E., Valencia, S., Mawass, M.-A., Bertinetti, L., Gilbert, P.U.P.A. & Politi, Y., 2019, 'Growth and regrowth of adult sea urchin spines involve hydrated and anhydrous amorphous calcium carbonate precursors', *Journal of Structural Biology: X*, 1, 100004.
- Alexander, R.R., 2001, 'Functional morphology and biomechanics of articulate brachiopod shells', *The Paleontological Society Papers*, 7, 145–170.
- Alexander, R.R., Stanton Jr, R.J. & Dodd, J.R., 1993, 'Influence of sediment grain size on the burrowing of bivalves: Correlation with distribution and stratigraphic persistence of selected neogene clams', *Palaaios*, 289–303.
- Allen, J., 1976, 'On the biology and functional morphology of *Chama gryphoides* Linne (Bivalvia; Chamidae).', *Vie et Milieu*, 26, 243–260.
- Aller, R.C., 1974, 'Prefabrication of shell ornamentation in the bivalve *Laternula*', *Lethaia*, 7(1), 43–56.
- Almagro, Í., Drzymala, P., Berent, K., Sainz-Díaz, C.I., Willinger, M.G., Bonarski, J. & Checa, A.G., 2016a, 'New crystallographic relationships in biogenic aragonite: The crossed-lamellar microstructures of mollusks', *Crystal Growth & Design*, 16(4), 2083–2093.

- Almagro, Í., Drzymała, P., Rodríguez-Navarro, A.B., Sainz-Díaz, C.I., Willinger, M.G., Bonarski, J. & Checa, A.G., 2016b, 'Crystallography and textural aspects of crossed lamellar layers in Arcidae (Bivalvia, Mollusca) shells', *Key Engineering Materials*, 672, 60–70.
- Alsheikha, O., 2020, *Microstructure crystallography and chemical characterisation of synthetic and biological calcium carbonates.*, Master thesis, Ludwig-Maximilians-Universität, München.
- Alves, N.M., Leonor, I.B., Azevedo, H.S., Reis, R.L. & Mano, J.F., 2010, 'Designing biomaterials based on biomineralization of bone', *Journal of Materials Chemistry*, 20(15), 2911.
- Ameye, L., De Becker, G., Killian, C., Wilt, F., Kemps, R., Kuypers, S. & Dubois, P., 2001, 'Proteins and saccharides of the sea urchin organic matrix of mineralization: Characterization and localization in the spine skeleton', *Journal of Structural Biology*, 134(1), 56–66.
- Ameye, L., Hermann, R., Killian, C., Wilt, F. & Dubois, P., 1999, 'Ultrastructural localization of proteins involved in sea urchin biomineralization', *Journal of Histochemistry & Cytochemistry*, 47(9), 1189–1200.
- Amini, S., Masic, A., Bertinetti, L., Teguh, J.S., Herrin, J.S., Zhu, X., Su, H. & Miserez, A., 2014, 'Textured fluorapatite bonded to calcium sulphate strengthen stomatopod raptorial appendages', *Nature Communications*, 5(1), 3187.
- Amini, S., Tadayon, M., Idapalapati, S. & Miserez, A., 2015, 'The role of quasi-plasticity in the extreme contact damage tolerance of the stomatopod dactyl club', *Nature Materials*, 14(9), 943–950.
- Andersen, Ø., Torgersen, J.S., Pagander, H.H., Magnesen, T. & Johnston, I.A., 2009, 'Gene expression analyses of essential catch factors in the smooth and striated adductor muscles of larval, juvenile and adult great scallop (*Pecten maximus*)', *Journal of Muscle Research and Cell Motility*, 30(5–6), 233–242.
- Andreassen, J.-P. & Lewis, A.E., 2017, 'Classical and nonclassical theories of crystal growth', in A.E.S. Van Driessche, M. Kellermeier, L.G. Benning & D. Gebauer (eds.), *New Perspectives on Mineral Nucleation and Growth*, pp. 137–154, Springer International Publishing, Cham.
- Angiolini, L., Crippa, G., Azmy, K., Capitani, G., Confalonieri, G., Della Porta, G., Griesshaber, E., Harper, D.A.T., Leng, M.J., Nolan, L., Orlandi, M., Posenato, R., Schmahl, W.W., Banks, V.J. & Stephenson, M.H., 2019, 'The giants of the phylum Brachiopoda: A matter of diet?', G. Sevastopulo (ed.), *Palaeontology*, 62(6), 889–917.
- Ansell, A.D. & Trueman, E.R., 1967a, 'Burrowing in *Mercenaria mercenaria* (L.) (Bivalvia, Veneridae)', *Journal of Experimental Biology*, 46(1), 105–115.
- Ansell, A.D. & Trueman, E.R., 1967b, 'Observations on burrowing in *Glycymeris glycymeris* (L.) (Bivalvia, Arcacea)', *Journal of Experimental Marine Biology and Ecology*, 1(1), 65–75.
- Anstis, G.R., Chantikul, P., Lawn, B.R. & Marshall, D.B., 1981, 'A critical evaluation of indentation techniques for measuring fracture toughness: I, Direct crack measurements', *Journal of the American Ceramic Society*, 64(9), 533–538.
- Araujo, R., Ramos, M.A. & Bedoya, J., 1994, 'Microtubules in the shell of the invasive bivalve *Corbicula fluminea* (Muller, 1774)(Bivalvia: Heterodonta)', *Journal of Molluscan Studies*, 60(4), 406–413.
- Aru, V., Khakimov, B., Sørensen, K.M. & Engelsens, S.B., 2018, 'The foodome of bivalve molluscs: From hedonic eating to healthy diet', *Journal of Food Composition and Analysis*, 69, 13–19.
- Athanasiadou, D., Jiang, W., Goldbaum, D., Saleem, A., Basu, K., Pacella, M.S., Böhm, C.F., Chromik, R.R., Hincke, M.T., Rodríguez-Navarro, A.B., Vali, H., Wolf, S.E., Gray, J.J., Bui, K.H. & McKee, M.D., 2018, 'Nanostructure, osteopontin, and mechanical properties of calcitic avian eggshell', *Science Advances*, 4(3), eaar3219.
- Audino, J.A., Marian, J.E.A.R., Wanninger, A. & Lopes, S.G.B.C., 2015, 'Mantle margin morphogenesis in *Nodipecten nodosus* (Mollusca: Bivalvia): New insights into the development and the roles of bivalve pallial folds', *BMC Developmental Biology*, 15(1), 22.

- Audino, J.A., Serb, J.M. & Marian, J.E.A.R., 2020, 'Hard to get, easy to lose: Evolution of mantle photoreceptor organs in bivalves (Bivalvia, Pteriomorphia)', *Evolution*, 74(9), 2105–2120.
- Avery, R. & Etter, R.J., 2006, 'Microstructural differences in the reinforcement of a gastropod shell against predation', *Marine Ecology Progress Series*, 323, 159–170.
- Baird, R.H., 1958, 'On the swimming behaviour of scallops (*Pecten maximus* L.)', *Journal of Molluscan Studies*, 33(2), 67–71.
- Ballesteros, E., 2006, 'Mediterranean coralligenous assemblages: A synthesis of present knowledge', in R.N. Gibson, R.J.A. Atkinson & J.D.M. Gordon (eds.), *Oceanography and Marine Biology*, 0 edn., pp. 135–208, CRC Press.
- Banabic, D., Bunge, H.-J., Pöhlndt, K. & Tekkaya, A.E., 2000, *Formability of metallic materials: Plastic anisotropy, formability testing, forming limits*, Springer Berlin Heidelberg, Berlin, Heidelberg.
- Barthelat, F. & Espinosa, H., 2007, 'An experimental investigation of deformation and fracture of nacre—mother of pearl', *Experimental mechanics*, 47, 311–324.
- Battas, A., 2023, *The symmetry and crystal arrangement of biologically formed carbonate materials*, Master thesis, Ludwig-Maximilians-Universität, München.
- Becker, A., Ziegler, A. & Eppe, M., 2005, 'The mineral phase in the cuticles of two species of Crustacea consists of magnesium calcite, amorphous calcium carbonate, and amorphous calcium phosphate', *Dalton Transactions*, (10), 1814.
- Becker, R. & Döring, W., 1935, 'Kinetische Behandlung der Keimbildung in übersättigten Dämpfen', *Annalen der physik*, 416(8), 719–752.
- Bengtson, S., 2005, 'Mineralized skeletons and early animal evolution', in A. Seilacher (ed.), *Evolving form and function: Fossils and development*, pp. 101–124, Peabody Museum of Natural History, Yale University, New Haven, CT.
- Beniash, E., 2011, 'Biomaterials—hierarchical nanocomposites: The example of bone', *WIREs Nanomedicine and Nanobiotechnology*, 3(1), 47–69.
- Beniash, E., Aizenberg, J., Addadi, L. & Weiner, S., 1997, 'Amorphous calcium carbonate transforms into calcite during sea urchin larval spicule growth', *Proceedings of the Royal Society of London. Series B: Biological Sciences*, 264(1380), 461–465.
- Beratis, I., 2019, 'Interpretation of the Miocene fossils in the Strymon basin in Northern Greece to determine their habitat', *Acta Scientifica Naturalis*, 6(2), 130–144.
- Berent, K., Gajewska, M. & Checa, A.G., 2023, 'Organization and formation of the crossed-foliated biomineral microstructure of limpet shells', *ACS Biomaterials Science & Engineering*, 9(12), 6658–6669.
- Berezovsky, A.A., 2021, 'Redescription of *Chama clavaticostata* Klushnikov (Bivalvia) from the Middle Eocene of Ukraine', *Paleontological Journal*, 55(3), 272–276.
- Berman, A., Addadi, L., Kvick, Å., Leiserowitz, L., Nelson, M. & Weiner, S., 1990, 'Intercalation of sea urchin proteins in calcite: Study of a crystalline composite material', *Science*, 250(4981), 664–667.
- Berman, A., Hanson, J., Leiserowitz, L., Koetzle, T.F., Weiner, S. & Addadi, L., 1993, 'Biological control of crystal texture: A widespread strategy for adapting crystal properties to function', *Science*, 259(5096), 776–779.
- Bernard, F.R., 1976, 'Living Chamidae of the Eastern Pacific (Bivalve: Heterdonta)', *Contributions in science*, 278, 1–43.
- Bieler, R., Mikkelsen, P.M. & Giribet, G., 2013, 'Bivalvia—A discussion of known unknowns*', *American Malacological Bulletin*, 31(1), 123–133.

- Bierne, N., Bonhomme, F. & David, P., 2003, 'Habitat preference and the marine-speciation paradox', *Proceedings of the Royal Society of London. Series B: Biological Sciences*, 270(1522), 1399–1406.
- Bignardi, C., Petraroli, M. & Pugno, N.M., 2010, 'Nanoindentations on conch shells of gastropoda and bivalvia molluscs reveal anisotropic evolution against external attacks', *Journal of Nanoscience and Nanotechnology*, 10(10), 6453–6460.
- Bitner, M.A., 2021, 'Lower Eocene (Middle Ilerdian) brachiopods from the Campo region, Central Pyrenees, north-eastern Spain', *Spanish Journal of Palaeontology*, 15(2), 117–128.
- Blamart, D., Rollion-Bard, C., Meibom, A., Cuif, J.-P., Juillet-Leclerc, A. & Dauphin, Y., 2007, 'Correlation of boron isotopic composition with ultrastructure in the deep-sea coral *Lophelia pertusa* : Implications for biomineralization and paleo-pH: Boron isotopic composition in coral', *Geochemistry, Geophysics, Geosystems*, 8(12), Q12001.
- Bodenbender, B.E., 1997, 'Echinoderm skeletal crystallography and paleobiological applications', *The Paleontological Society Papers*, 3, 191–204.
- Boehm-Courjault, E., Gonzales, F., Jacot, A., Kohler, F., Mariaux, A., Niederberger, C., Salgado-Ordorica, M.A. & Rappaz, M., 2009, 'EBSD: A powerful microstructure analysis technique in the field of solidification', *Journal of Microscopy*, 233(1), 160–169.
- Bogan, A.E., 2008, 'Global diversity of freshwater mussels (Mollusca, Bivalvia) in freshwater', *Hydrobiologia*, 595(1), 139–147.
- Boggild, O.B., 1930, 'The shell structure of the mollusks', *Det Kongelige Danske Videnskabernes Selskabs Skrifter. Naturvidenskabelig og Mathematisk Afdeling, Raekke 9, 2*, 231–326.
- Böhm, C.F., Demmert, B., Harris, J., Fey, T., Marin, F. & Wolf, S.E., 2016, 'Structural commonalities and deviations in the hierarchical organization of crossed-lamellar shells: A case study on the shell of the bivalve *Glycymeris glycymeris*', *Journal of Materials Research*, 31(5), 536–546.
- Boudouresque, C.F. & Verlaque, M., 2020, '*Paracentrotus lividus*', *Developments in Aquaculture and Fisheries Science*, vol. 43, pp. 447–485, Elsevier.
- Bowden, J., 1958, 'The structure and innervation of lamellibranch muscle', *International Review of Cytology*, vol. 7, pp. 295–335, Elsevier.
- Bowman, K.J., Moon, R., Drewry, E., Wan, S., Tortorici, P. & Dayananda, M.A., 1998, 'Anisotropic properties in textured ceramics', *Materials Science Forum*, 273–275, 587–594.
- Branson, O. & De Nooijer, L.J., 2025, 'Calcium carbonate biomineralisation: Insights from trace elements', *Elements*, 21(2), 105–111.
- Braun, F., 1897, 'Ueber ein Verfahren zur Demonstration und zum Studium des zeitlichen Verlaufes variabler Ströme', *Annalen der Physik*, 296(3), 552–559.
- Britton, T.B., Jiang, J., Guo, Y., Vilalta-Clemente, A., Wallis, D., Hansen, L.N., Winkelmann, A. & Wilkinson, A.J., 2016, 'Tutorial: Crystal orientations and EBSD — Or which way is up?', *Materials Characterization*, 117, 113–126.
- Brocas, W.M., Reynolds, D.J., Butler, P.G., Richardson, C.A., Scourse, J.D., Ridgway, I.D. & Ramsay, K., 2013, 'The dog cockle, *Glycymeris glycymeris* (L.), a new annually-resolved sclerochronological archive for the Irish Sea', *Palaeogeography, Palaeoclimatology, Palaeoecology*, 373, 133–140.
- Brom, K.R. & Szopa, K., 2016, 'Morphological diversity of microstructures occurring in selected recent bivalve shells and their ecological implications', *Contemporary Trends in Geoscience*, 5(2), 104–112.
- Brookes, C.A., O'Neill, J.B. & Redfern, B.A.W., 1971, 'Anisotropy in the hardness of single crystals', *Proceedings of the Royal Society of London. A. Mathematical and Physical Sciences*, 322(1548), 73–88.

- Brostow, W., Hagg Lobland, H.E. & Khoja, S., 2015, 'Brittleness and toughness of polymers and other materials', *Materials Letters*, 159, 478–480.
- Bubel, A., 1984, 'Epidermal cells', in J. Bereiter-Hahn, A.G. Matoltsy & K.S. Richards (eds.), *Biology of the Integument*, pp. 400–447, Springer Berlin Heidelberg, Berlin, Heidelberg.
- Busch, H., 1926, 'Calculation of the channel of the cathode rays in axial symmetric electromagnetic fields', *Annalen Der Physik*, 81(25), 974–993.
- Caddy, J.F., 1968, 'Underwater observations on scallop (*Placopecten magellanicus*) behaviour and drag efficiency', *Journal of the Fisheries Research Board of Canada*, 25(10), 2123–2141.
- Caddy, J.F., 1972, 'Progressive loss of byssus attachment with size in the sea scallop, *Placopecten magellanicus* (Gmelin)', *Journal of Experimental Marine Biology and Ecology*, 9(2), 179–190.
- Cairns, S.D. & Macintyre, I.G., 1992, 'Phylogenetic implications of calcium carbonate mineralogy in the Stylasteridae (Cnidaria: Hydrozoa)', *PALAIOS*, 7(1), 96.
- Callister Jr, W.D. & Rethwisch, D.G., 2020, *Materials science and engineering: An introduction*, 10th edn., John Wiley & Sons, Hoboken.
- Carey, J.D. & Stokesbury, K.D.E., 2011, 'An assessment of juvenile and adult sea scallop, *Placopecten magellanicus*, distribution in the Northwest Atlantic using high-resolution still imagery', *Journal of Shellfish Research*, 30(3), 569–582.
- Carlson, S.J., 1989, 'The articulate brachiopod hinge mechanism: Morphological and functional variation', *Paleobiology*, 15(4), 364–386.
- Carriker, M., 1996, 'The shell and ligament', in V.S. Kennedy & R.I.E. Newell (eds.), *The eastern oyster Crassostrea virginica*, pp. 76–168, Maryland Sea Grant College, College Park, Md.
- Carter, G.M., Henshall, J.L. & Wakeman, R.J., 1993, 'Knoop hardness and fracture anisotropy of calcite', *Journal of Materials Science Letters*, 12(6), 407–410.
- Carter, J., Harries, P., Malchus, N., Sartori, A., Anderson, L., Bieler, R., Bogan, A., Eugene Coan, E., Cope, J. & Cragg, S., 2012, 'Treatise online, part N', *Illustrated glossary of the Bivalvia*, 48., vol. 1, p. 209, University of Kansas Paleontological Institute, Lawrence.
- Carter, J.G., 1990, *Skeletal Biomineralization: Patterns, Processes and Evolutionary Trends: Volume I*, Springer.
- Carter, M.C., 2008, '*Glycymeris glycymeris* Dog cockle', *Marine life information network: Biology and sensitivity key information reviews*, Marine Biological Association of the United Kingdom., Plymouth.
- Casella, L.A., Griesshaber, E., Simonet Roda, M., Ziegler, A., Mavromatis, V., Henkel, D., Laudien, J., Häussermann, V., Neuser, R.D., Angiolini, L., Dietzel, M., Eisenhauer, A., Immenhauser, A., Brand, U. & Schmahl, W.W., 2018, 'Micro- and nanostructures reflect the degree of diagenetic alteration in modern and fossil brachiopod shell calcite: A multi-analytical screening approach (CL, FE-SEM, AFM, EBSD)', *Palaeogeography, Palaeoclimatology, Palaeoecology*, 502, 13–30.
- Casella, L.A., Griesshaber, E., Yin, X., Ziegler, A., Mavromatis, V., Müller, D., Ritter, A.-C., Hippler, D., Harper, E.M., Dietzel, M., Immenhauser, A., Schöne, B.R., Angiolini, L. & Schmahl, W.W., 2017, 'Experimental diagenesis: Insights into aragonite to calcite transformation of *Arctica islandica* shells by hydrothermal treatment', *Biogeosciences*, 14(6), 1461–1492.
- Castro-Claros, J.D., Checa, A., Lucena, C., Pearson, J.R. & Salas, C., 2021, 'Shell-adductor muscle attachment and Ca²⁺ transport in the bivalves *Ostrea stentina* and *Anomia ephippium*', *Acta Biomaterialia*, 120, 249–262.
- Chan, X.Y., Chua, C., Tan, S. & Le Ferrand, H., 2022, 'Energy dissipation in composites with hybrid nacre-like helicoidal microstructures', *Composites Part B: Engineering*, 232, 109608.

- Chang, J., Gong, X., Zhang, Y., Sun, Z., Xia, N., Zhang, H., Wang, J. & Zhang, X., 2022, 'Simulation analysis of organic–inorganic interface failure of scallop under ultra-high pressure', *Coatings*, 12(7), 963.
- Chantler, P., 1983, 'Biochemical and structural aspects of molluscan muscle', in K.M. Wilbur & A.S.M. Saleuddin (eds.), *The mollusca.*, vol. 4, pp. 77–154, Academic Press, New York.
- Chateigner, D., Hedegaard, C. & Wenk, H.-R., 2000, 'Mollusc shell microstructures and crystallographic textures', *Journal of Structural Geology*, 22(11–12), 1723–1735.
- Checa, A.G., 2018, 'Physical and biological determinants of the fabrication of molluscan shell microstructures', *Frontiers in Marine Science*, 5, 353.
- Checa, A.G., Esteban-Delgado, F.J. & Rodríguez-Navarro, A.B., 2007, 'Crystallographic structure of the foliated calcite of bivalves', *Journal of Structural Biology*, 157(2), 393–402.
- Checa, A.G., González-Segura, A., Rodríguez-Navarro, A.B. & Lagos, N.A., 2020, 'Microstructure and crystallography of the wall plates of the giant barnacle *Austromegabalanus psittacus*: A material organized by crystal growth', *Journal of The Royal Society Interface*, 17(164), 20190743.
- Checa, A.G., Griesshaber, E., Salas, C., Angiolini, L. & Schmahl, W.W., 2025, 'Mollusc and brachiopod carbonate biomineralization', in P. Fratzl, L.M. Liz-Marzán & N.A. Kotov (eds.), *Biomineralization and Bioinspired Composites*.
- Checa, A.G., Linares, F., Grenier, C., Griesshaber, E., Rodríguez-Navarro, A.B. & Schmahl, W.W., 2021, 'The argonaut constructs its shell via physical self-organization and coordinated cell sensorial activity', *Iscience*, 24(11), 103288.
- Checa, A.G., Rodríguez-Navarro, A.B. & Esteban-Delgado, F.J., 2005, 'The nature and formation of calcitic columnar prismatic shell layers in pteriomorphian bivalves', *Biomaterials*, 26(32), 6404–6414.
- Checa, A.G., Salas, C., Harper, E.M. & Bueno-Pérez, J. de D., 2014, 'Early stage biomineralization in the periostracum of the “living fossil” bivalve *Neotrigonia*', *PLoS One*, 9(2), e90033.
- Chen, C.-P. & Lawrence, J.M., 1987, 'The role of carbonic anhydrase in facilitating the transport of CO₂ in the tooth of *Lytechinus variegatus* (Echinodermata: Echinoidea)', *Comparative Biochemistry and Physiology Part A: Physiology*, 87(2), 327–331.
- Chen, P.-Y., McKittrick, J. & Meyers, M.A., 2012, 'Biological materials: Functional adaptations and bioinspired designs', *Progress in Materials Science*, 57(8), 1492–1704.
- Chen, Y., Feng, Y., Deveau, J.G., Masoud, M.A., Chandra, F.S., Chen, H., Zhang, D. & Feng, L., 2019, 'Biomineralization forming process and bio-inspired nanomaterials for biomedical application: A review', *Minerals*, 9(2), 68.
- Cheng, J.-Y., Davison, I.G. & Demont, M.E., 1996, 'Dynamics and energetics of scallop locomotion', *Journal of Experimental Biology*, 199(9), 1931–1946.
- Cheng, L., Shahin, M.A. & Cord-Ruwisch, R., 2014, 'Bio-cementation of sandy soil using microbially induced carbonate precipitation for marine environments', *Géotechnique*, 64(12), 1010–1013.
- Chevillotte, L., 2022, *Mineral and biopolymer organization patterns in bacterial EPS-hydrogel-calcite composite aggregates*, Master thesis, Ludwig-Maximilians-Universität, München.
- Clark, M.S., Peck, L.S., Arivalagan, J., Backeljau, T., Berland, S., Cardoso, J.C.R., Caurcel, C., Chapelle, G., De Noia, M., Dupont, S., & et al., 2020, 'Deciphering mollusc shell production: the roles of genetic mechanisms through to ecology, aquaculture and biomimetics', *Biological Reviews*, 95(6), 1812–1837.
- Cölfen, H., 2010, 'A crystal-clear view', *Nature materials*, 9(12), 960–961.
- Cölfen, H., Bürgi, H.-B., Chernyshov, D., Stekiel, M., Chumakova, A., Bosak, A., Wehinger, B. & Winkler, B., 2022, 'Mesocrystalline structure and mechanical properties of biogenic calcite from sea urchin spine',

- Acta Crystallographica Section B Structural Science, Crystal Engineering and Materials*, 78(3), 356–358.
- Collins, K.S., Edie, S.M. & Jablonski, D., 2023, 'Convergence and contingency in the evolution of a specialized mode of life: Multiple origins and high disparity of rock-boring bivalves', *Proceedings of the Royal Society B: Biological Sciences*, 290(1992), 20221907.
- Colombera, D., Vitturi, R. & Zanirato, L., 1977, 'Chromosome number of *Cidaris cidaris* (Cidaridae, Echinoidea)', *Acta Zoologica*, 58(4), 185–186.
- Commings, P., Karothu, D.P. & Naumov, P., 2019, 'Is a bent crystal still a single crystal?', *Angewandte Chemie International Edition*, 58(30), 10052–10060.
- Conci, N., Vargas, S. & Wörheide, G., 2021, 'The biology and evolution of calcite and aragonite mineralization in Octocorallia', *Frontiers in Ecology and Evolution*, 9, 623774.
- Conti, M.L.G., Butler, P.G., Reynolds, D.J., Trofimova, T., Scourse, J.D. & Penkman, K.E.H., 2024, 'A new method for amino acid geochronology of the shell of the bivalve mollusc *Arctica islandica*', *Geochronology*, 6(2), 175–198.
- Coppard, S.E., Kroh, A. & Smith, A.B., 2012, 'The evolution of pedicellariae in echinoids: An arms race against pests and parasites', *Acta Zoologica*, 93(2), 125–148.
- Copper, P., 2018, *Brachiopods*, 1st edn., CRC Press, London.
- Coronado, I., Pérez-Huerta, A. & Rodríguez, S., 2015, 'Crystallographic orientations of structural elements in skeletons of Syringoporidae (tabulate corals, Carboniferous): Implications for biomineralization processes in Palaeozoic corals', *Palaeontology*, 58(1), 111–132.
- Cragg, S.M., 1985, 'The adductor and retractor muscles of the veliger of *Pecten maximus* (L.)(Bivalvia)', *Journal of Molluscan Studies*, 51, 276–283.
- Crame, J.A., 2000, 'Intrinsic and extrinsic controls on the diversification of the Bivalvia', in S.J. Culver & P.F. Rawson (eds.), *Biotic Response to Global Change*, 1st edn., pp. 135–148, Cambridge University Press.
- Crippa, G., Griesshaber, E., Checa, A.G., Harper, E.M., Roda, M.S. & Schmahl, W.W., 2020a, 'Orientation patterns of aragonitic crossed-lamellar, fibrous prismatic and myostracal microstructures of modern *Glycymeris* shells', *Journal of Structural Biology*, 212(3).
- Crippa, G., Griesshaber, E., Checa, A.G., Harper, E.M., Simonet Roda, M. & Schmahl, W.W., 2020b, 'SEM, EBSD, laser confocal microscopy and FE-SEM data from modern *Glycymeris* shell layers', *Data in Brief*, 33, 106547.
- Crippa, G., Jurikova, H., Leng, M.J., Zanchi, M., Harper, E.M., Rae, J.W.B., Savickaite, K., Viaretti, M. & Angiolini, L., 2025, 'Brachiopods as archives of intrannual, annual, and interannual environmental variations', *Limnology and Oceanography Letters*, 10(3), 390–402.
- Crocetta, F. & Russo, P., 2013, 'The alien spreading of *Chama pacifica* Broderip, 1835 (Mollusca: Bivalvia: Chamidae) in the Mediterranean Sea', *Turkish Journal of Zoology*, 37(1), 92–96.
- Cross, E.L., Harper, E.M. & Peck, L.S., 2018, 'A 120-year record of resilience to environmental change in brachiopods', *Global Change Biology*, 24(6), 2262–2271.
- Cubillas, P., Köhler, S., Prieto, M., Chaïrat, C. & Oelkers, E.H., 2005, 'Experimental determination of the dissolution rates of calcite, aragonite, and bivalves', *Chemical Geology*, 216(1–2), 59–77.
- Cuif, J.-P., Burghammer, M., Chamard, V., Dauphin, Y., Godard, P., Moullac, G., Nehrke, G. & Perez-Huerta, A., 2014, 'Evidence of a biological control over origin, growth and end of the calcite prisms in the shells of *Pinctada margaritifera* (Pelecypod, Pterioidea)', *Minerals*, 4(4), 815–834.

- Cuif, J.-P., Lo, C. & Dauphin, Y., 2023, 'Evidence of a scheduled end for prism growth in the shell of *Pinctada margaritifera*: Closure of the calcite biomineralization area by a specific organic membrane', *Minerals*, 14(1), 20.
- Currey, J.D., 1977, 'Mechanical properties of mother of pearl in tension', *Proceedings of the Royal Society of London. Series B. Biological Sciences*, 196(1125), 443–463.
- Currey, J.D., 1988, 'Shell form and strength', in K.M. Wilbur (ed.), *The mollusca*, Form and function., vol. 11, Academic Press, Plymouth.
- Currey, J.D., 2002, *Bones: Structure and mechanics*, 2. ed., Princeton University Press, Princeton, NJ.
- Currey, J.D. & Kohn, A.J., 1976, 'Fracture in the crossed-lamellar structure of *Conus* shells', *Journal of Materials Science*, 11(9), 1615–1623.
- Currey, J.D. & Taylor, J.D., 1974, 'The mechanical behaviour of some molluscan hard tissues', *Journal of Zoology*, 173(3), 395–406.
- Cusack, M., Pérez-Huerta, A., Janousch, M. & Finch, A.A., 2008, 'Magnesium in the lattice of calcite-shelled brachiopods', *Chemical Geology*, 257(1–2), 59–64.
- Cusack, M. & Williams, A., 2001, 'Chemico-structural differentiation of the organocalcitic shells of rhynchonellate brachiopods', *Brachiopods*, pp. 31–41, CRC Press.
- Dadswell, M.J. & Weihs, D., 1990, 'Size-related hydrodynamic characteristics of the giant scallop, *Placopecten magellanicus* (Bivalvia: Pectinidae)', *Canadian Journal of Zoology*, 68(4), 778–785.
- De Broglie, L., 1924, 'Recherches sur la théorie des quanta', *Ann. de Phys.*, 10(3).
- De Noia, M., Telesca, L., Vendrami, D.L.J., Gokalp, H.K., Charrier, G., Harper, E.M. & Hoffman, J.I., 2020, 'Population genetic structure is unrelated to shell shape, thickness and organic content in European populations of the soft-shell clam *Mya arenaria*', *Genes*, 11(3), 298.
- De Paula, S.M. & Silveira, M., 2009, 'Studies on molluscan shells: Contributions from microscopic and analytical methods', *Micron*, 40(7), 669–690.
- De Yoreo, J.J., Gilbert, P.U.P.A., Sommerdijk, N.A.J.M., Penn, R.L., Whitlam, S., Joester, D., Zhang, H., Rimer, J.D., Navrotsky, A., Banfield, J.F., Wallace, A.F., Michel, F.M., Meldrum, F.C., Cölfen, H. & Dove, P.M., 2015, 'Crystallization by particle attachment in synthetic, biogenic, and geologic environments', *Science*, 349(6247), aaa6760.
- Debenedetti, P.G., 1997, *Metastable liquids: Concepts and principles*, Princeton University Press, Princeton.
- Demichelis, R., Schuitemaker, A., Garcia, N.A., Koziara, K.B., De La Pierre, M., Raiteri, P. & Gale, J.D., 2018, 'Simulation of crystallization of biominerals', *Annual Review of Materials Research*, 48(1), 327–352.
- Deng, Z., Chen, L. & Li, L., 2023, 'Comparative nanoindentation study of biogenic and geological calcite', *Journal of the Mechanical Behavior of Biomedical Materials*, 137, 105538.
- Deng, Z., Jia, Z. & Li, L., 2022, 'Biomineralized materials as model systems for structural composites: Intracrystalline structural features and their strengthening and toughening mechanisms', *Advanced Science*, 2103524.
- Dery, A., Tran, P.D., Compère, P. & Dubois, P., 2018, 'Cidaroids spines facing ocean acidification', *Marine Environmental Research*, 138, 9–18.
- Dickson, J.A.D., 2004, 'Echinoderm skeletal preservation: Calcite-aragonite seas and the Mg/Ca ratio of Phanerozoic oceans', *Journal of Sedimentary Research*, 74(3), 355–365.
- Dietiker, M., 2011, *Nanoindentation of gold nanostructures and nacre-like nanocomposites: Size effects and limits of strength* – PhD thesis, ETH Zurich.

- Ding, M., Wang, T., Maerz, B., Robertson, S., Sun, Z., Fan, L., Shi, Y. & Wu, H., 2019, 'Formation of twins in AlON material and its effects on the Vickers hardness and fracture toughness', *Ceramics International*, 45(17), 21127–21135.
- Doguzhaeva, L. & Mutvei, H., 1986, 'Functional interpretation of inner shell layers in Triassic ceratid ammonites', *Lethaia*, 19(3), 195–209.
- Domenici, P., González-Calderón, D. & Ferrari, R.S., 2003, 'Locomotor performance in the sea urchin *Paracentrotus lividus*', *Journal of the Marine Biological Association of the United Kingdom*, 83(2), 285–292.
- Donald, I. & McMillan, P., 1976, 'Ceramic-matrix composites', *Journal of materials Science*, 11, 949–972.
- Dong, W., Huang, J., Liu, C., Wang, H., Zhang, G., Xie, L. & Zhang, R., 2022, 'Characterization of the myostracum layers in molluscs reveals a conservative shell structure', *Frontiers in Marine Science*, 9, 862929.
- Donnay, G. & Pawson, D.L., 1969, 'X-ray diffraction studies of echinoderm plates', *Science*, 166(3909), 1147–1150.
- Dove, P.M., 2018, *Biom mineralization*, 1st ed, Walter de Gruyter GmbH, Boston.
- Dowd, W.W. & Jimenez, A.G., 2019, 'High-shore mussels, *Mytilus californianus*, have larger muscle fibers with lower aerobic capacities than low-shore conspecifics', *Marine Biology*, 166(2), 22.
- Driessens, F.C.M., 1980, 'The mineral in bone, dentin and tooth enamel', *Bulletin des Sociétés Chimiques Belges*, 89(8), 663–689.
- Du, J.S., Bae, Y. & De Yoreo, J.J., 2024, 'Non-classical crystallization in soft and organic materials', *Nature Reviews Materials*, 9(4), 229–248.
- Dubois, P. & Ameye, L., 2001, 'Regeneration of spines and pedicellariae in echinoderms: A review', *Microscopy Research and Technique*, 55(6), 427–437.
- Durham, J.W. & Melville, R.V., 1966, 'Part U: Echinodermata 3. Skeletal morphology', in H. Exline, G. Regnéll, D.L. Pawson, C.D. Wagner, R.C. Moore, A.G. Fischer, P.M. Kier, G. Ubaghs, K.E. Caster, R.V. Kesling, D.L. Frizzell, H.B. Fell, C.W. Wright & W.K. Spencer (eds.), *Treatise on invertebrate paleontology*, vol. 1, The Geological Society of America, Kansas.
- Duthie, I., 2012, 'Global perspective of bivalve hatchery processes', *Shellfish production aquaculture technology*, Nuffield Australia, Project No 1017.
- Eagar, R.M.C., 1978, 'Shape and function of the shell: A comparison of some living and fossil bivalve molluscs', *Biological Reviews*, 53(2), 169–210.
- Ebert, T.A., 2007, 'Growth and survival of postsettlement sea urchins', *Developments in Aquaculture and Fisheries Science*, vol. 37, pp. 95–134, Elsevier.
- Eckold, G., 1994, *Design and manufacture of composite structures*, Woodhead publishing.
- Ellers, O., Johnson, A.S. & Moberg, P.E., 1998, 'Structural strengthening of urchin skeletons by collagenous sutural ligaments', *The Biological Bulletin*, 195(2), 136–144.
- Elliott, J.C., 2002, 'Calcium phosphate biominerals', *Reviews in Mineralogy and Geochemistry*, 48(1), 427–453.
- Emig, C.C., 2017, *Atlas of Antarctic and sub-Antarctic Brachiopoda*, 3rd edn., Carnets de Géologie, Madrid.
- Engler, O., Zaefferer, S. & Randle, V., 2023, *Introduction to texture analysis: Macrot texture, micro texture, and orientation mapping*, 3rd edn., CRC Press, Boca Raton.

- Eshleman, W.P., Wilkens, J.L. & Cavey, M.J., 1982, 'Electrophoretic and electron microscopic examination of the adductor and diductor muscles of an articulate brachiopod, *Terebratalia transversa*', *Canadian Journal of Zoology*, 60(4), 550–559.
- Fabritius, H.-O., Sachs, C., Raabe, D., Nikolov, S., Friák, M. & Neugebauer, J., 2011, 'Chitin in the exoskeletons of Arthropoda: From ancient design to novel materials science', in N.S. Gupta (ed.), *Chitin*, Topics in Geobiology., vol. 34, pp. 35–60, Springer Netherlands, Dordrecht.
- Fabritius, H.-O., Sachs, C., Triguero, P.R. & Raabe, D., 2009, 'Influence of structural principles on the mechanics of a biological fiber-based composite material with hierarchical organization: The exoskeleton of the lobster *Homarus americanus*', *Advanced Materials*, 21(4), 391–400.
- Falini, G., Fermani, S., Vanzo, S., Miletic, M. & Zaffino, G., 2005, 'Influence on the formation of aragonite or vaterite by otolith macromolecules', *European Journal of Inorganic Chemistry*, 2005(1), 162–167.
- Fay, A.M. & Smith, A.M., 2021, 'In a pinch: Skeletal carbonate mineralogy of crabs (Arthropoda: Crustacea: Decapoda)', *Palaeogeography, Palaeoclimatology, Palaeoecology*, 565, 110219.
- Featherstone, A.M., Butler, P.G., Peharda, M., Chauvaud, L. & Thébault, J., 2017, 'Influence of riverine input on the growth of *Glycymeris glycymeris* in the Bay of Brest, North-West France', J.M. Dias (ed.), *PLOS ONE*, 12(12), e0189782.
- Feng, Q.L., Li, H.B., Cui, F.Z., Kim, T.N., & others, 1999, 'Crystal orientation domains found in the single lamina in nacre of the *Mytilus edulis* shell', *Journal of materials science letters*, 18(19), 1547–1549.
- Feng, W., Chen, Z. & Sun, W., 2003, 'Diversification of skeletal microstructures of organisms through the interval from the latest Precambrian to the Early Cambrian', *Science in China Series D: Earth Sciences*, 46(10), 977–985.
- Fischer-Cripps, A.C. & Nicholson, D.W., 2004, 'Nanoindentation. Mechanical engineering series', *Applied Mechanics Reviews*, 57(2), B12–B12.
- Flessa, K.W. & Jablonski, D., 1995, 'Biogeography of recent marine bivalve molluscs and its implications for paleobiogeography and the geography of extinction: A progress report', *Historical Biology*, 10(1), 25–47.
- Foley, B., Greiner, M., McGlynn, G. & Schmahl, W.W., 2020, 'Anatomical variation of human bone bioapatite crystallography', *Crystals*, 10(10), 859.
- Förster, F., 2020, *Crystallographic characterization of sea urchin skeletal elements*, Master thesis, Ludwig-Maximilians-Universität, München.
- Fraiser, M.L. & Bottjer, D.J., 2007, 'When bivalves took over the world', *Paleobiology*, 33(3), 397–413.
- Fransen, M.J., Overwijk, M.H.F. & Kruit, P., 1999, 'Brightness measurements of a ZrO/W Schottky electron emitter in a transmission electron microscope', *Applied Surface Science*, 146(1–4), 357–362.
- Frenzel, M. & Harper, E.M., 2011, 'Micro-structure and chemical composition of vateritic deformities occurring in the bivalve *Corbicula fluminea* (Müller, 1774)', *Journal of structural biology*, 174(2), 321–332.
- Fu, X., Wang, X.-D., Zhao, B., Zhang, Q., Sun, S., Wang, J.-J., Zhang, W., Gu, L., Zhang, Y., Zhang, W.-Z., Wen, W., Zhang, Z., Chen, L., Yu, Q. & Ma, E., 2022, 'Atomic-scale observation of non-classical nucleation-mediated phase transformation in a titanium alloy', *Nature Materials*, 21(3), 290–296.
- Funabara, D., Kanoh, S., Siegman, M.J., Butler, T.M., Hartshorne, D.J. & Watabe, S., 2006, 'Twitchin as a regulator of catch contraction in molluscan smooth muscle', *Journal of Muscle Research and Cell Motility*, 26(6–8), 455–460.
- Gabriel, J., 1981, 'Differing resistance of various mollusc shell materials to simulated whelk attack', *Journal of Zoology*, 194(3), 363–369.

- Gal, A., Sorrentino, A., Kahil, K., Pereiro, E., Faivre, D. & Scheffel, A., 2018, 'Native-state imaging of calcifying and noncalcifying microalgae reveals similarities in their calcium storage organelles', *Proceedings of the National Academy of Sciences*, 115(43), 11000–11005.
- Galtsoff, P.S., 1964, *The American oyster, Crassostrea virginica gmelin*, vol. 64, US Government Printing Office, Washington, D.C.
- Garbelli, C., Angiolini, L. & Shen, S., 2017, 'Biomineralization and global change: A new perspective for understanding the end-Permian extinction', *Geology*, 45(1), 19–22.
- Gauldie, R.W., Sharma, S.K. & Volk, E., 1997, 'Micro-Raman spectral study of vaterite and aragonite otoliths of the coho salmon, *Oncorhynchus kisutch*', *Comparative Biochemistry and Physiology Part A: Physiology*, 118(3), 753–757.
- Gayathri, S., Lakshminarayanan, R., Weaver, J.C., Morse, D.E., Kini, R.M. & Valiyaveetil, S., 2007, 'In vitro study of magnesium-calcite biomineralization in the skeletal materials of the seastar *Pisaster giganteus*', *Chemistry – A European Journal*, 13(11), 3262–3268.
- Gebauer, D. & Cölfen, H., 2011, 'Prenucleation clusters and non-classical nucleation', *Nano Today*, 6(6), 564–584.
- Gebauer, D., Gale, J.D. & Cölfen, H., 2022, 'Crystal nucleation and growth of inorganic ionic materials from aqueous solution: Selected recent developments, and implications', *Small*, 18(28), 2107735.
- Gebauer, D., Raiteri, P., Gale, J.D. & Cölfen, H., 2018, 'On classical and non-classical views on nucleation', *American Journal of Science*, 318(9), 969–988.
- Genchev, A., 2012, 'Quality and composition of Japanese quail eggs (*Coturnix japonica*).', *Trakia journal of sciences*, 10(2), 91.
- Gibbs, J.W., 1878, 'On the equilibrium of heterogeneous substances', *American Journal of Science*, s3-16(96), 441–458.
- Gilbert, P.U.P.A., Bergmann, K.D., Boekelheide, N., Tambutté, S., Mass, T., Marin, F., Adkins, J.F., Erez, J., Gilbert, B., Knutson, V., Cantine, M., Hernández, J.O. & Knoll, A.H., 2022a, 'Biomineralization: Integrating mechanism and evolutionary history', *Science Advances*, 8(10), eabl9653.
- Gilbert, P.U.P.A., Lew, A., Stiffler, C., Tits, A., Schmidt, C., Luffey, E., Scholl, A., Cantamessa, A., Muller, L. & Delaunois, Y., 2022b, 'Convergent, slightly misoriented crystals toughen corals and seashells'.
- Gilbert, P.U.P.A., Porter, S.M., Sun, C.-Y., Xiao, S., Gibson, B.M., Shenkar, N. & Knoll, A.H., 2019, 'Biomineralization by particle attachment in early animals', *Proceedings of the National Academy of Sciences*, 116(36), 17659–17665.
- Gilbert, P.U.P.A. & Wilt, F.H., 2011, 'Molecular aspects of biomineralization of the echinoderm endoskeleton', in W. Müller (ed.), *Progress in Molecular and Subcellular Biology*, vol. 52, pp. 199–223, Springer, Berlin, Heidelberg.
- Goetz, A.J., Griesshaber, E., Abel, R., Fehr, T., Ruthensteiner, B. & Schmahl, W.W., 2014, 'Tailored order: The mesocrystalline nature of sea urchin teeth', *Acta Biomaterialia*, 10(9), 3885–3898.
- Goetz, A.J., Griesshaber, E., Neuser, R.D., Lüter, C., Hühner, M., Harper, E. & Schmahl, W.W., 2009, 'Calcite morphology, texture and hardness in the distinct layers of rhynchonelliform brachiopod shells', *European Journal of Mineralogy*, 21(2), 303–315.
- Goetz, A.J., Griesshaber, E. & Schmahl, W.W., 2010, 'An easy approach to increase the precision of EBSD analysis – Examples from a sea urchin calcite study', *Solid State Phenomena*, 160, 229–234.
- Goetz, A.J., Steinmetz, D.R., Griesshaber, E., Zaefferer, S., Raabe, D., Kelm, K., Irsen, S., Sehrbrock, A. & Schmahl, W.W., 2011, 'Interdigitating biocalcite dendrites form a 3-D jigsaw structure in brachiopod shells', *Acta Biomaterialia*, 7(5), 2237–2243.

- Gong, J.K., Arnold, J.S. & Cohn, S.H., 1964, 'Composition of trabecular and cortical bone', *The Anatomical Record*, 149(3), 325–331.
- Gorzelak, P., 2021, *Functional micromorphology of the echinoderm skeleton*, 1st edn., Cambridge University Press.
- Gránásy, L., Rátkai, L., Zlotnikov, I. & Pusztai, T., 2024, 'Physical phenomena governing mineral morphogenesis in molluscan nacre', *Small*, 20(5), 2304183.
- Grant, S.W., 1990, 'Shell structure and distribution of *Cloudina*, a potential index fossil for the terminal Proterozoic', *American Journal of Science*, 290-A, 261–294.
- Griesshaber, E., Checa, A.G., Salas, C., Hoffmann, R., Yin, X., Neuser, R., Rupp, U. & Schmahl, W.W., 2023, 'Biological light-weight materials: The endoskeletons of cephalopod mollusks', *Journal of Structural Biology*, 215(3), 107988.
- Griesshaber, E., Neuser, R.D. & Schmahl, W.W., 2010, 'The application of EBSD analysis to biomaterials: Microstructural and crystallographic texture variations in marine carbonate shells', *Semin. Soc. Esp. Mineral*, 7, 22–34.
- Griesshaber, E., Sancho Vaquer, A., Checa, A.G., Salas, C., Harper, E.M. & Schmahl, W.W., 2025, 'The textural motif of foliated calcite in Ostreoida (Mollusca)', *Crystals*, 15(3), 244.
- Griesshaber, E., Schmahl, W.W., Neuser, R., Pettke, T., Blum, M., Mutterlose, J. & Brand, U., 2007, 'Crystallographic texture and microstructure of terebratulide brachiopod shell calcite: An optimized materials design with hierarchical architecture', *American Mineralogist*, 92(5–6), 722–734.
- Griesshaber, E., Schmahl, W.W., Ubhi, H.S., Huber, J., Nindiyasari, F., Maier, B. & Ziegler, A., 2013, 'Homoepitaxial meso- and microscale crystal co-orientation and organic matrix network structure in *Mytilus edulis* nacre and calcite', *Acta Biomaterialia*, 9(12), 9492–9502.
- Griesshaber, E., Yin, X., Ziegler, A., Kelm, K., Checa, A., Eisenhauer, A. & Schmahl, W.W., 2017, 'Patterns of mineral organization in carbonate biological hard materials', in S. Heuss-Aßbichler, G. Amthauer & M. John (eds.), *Highlights in Applied Mineralogy*, pp. 245–272, De Gruyter.
- Grossmann, J.N., 2010, *Stereom differentiation in sea urchin spines under special consideration as a model for a new impact protective system* – PhD thesis, Universität Tübingen .
- Grossmann, J.N. & Nebelsick, J.H., 2013, 'Comparative morphological and structural analysis of selected cidaroid and camarodont sea urchin spines', *Zoomorphology*, 132(3), 301–315.
- Grotzinger, J.P., Watters, W.A. & Knoll, A.H., 2000, 'Calcified metazoans in thrombolite-stromatolite reefs of the terminal Proterozoic Nama Group, Namibia', *Paleobiology*, 26(3), 334–359.
- Guderley, H.E. & Tremblay, I., 2016, 'Swimming in scallops', *Developments in Aquaculture and Fisheries Science*, vol. 40, pp. 535–566, Elsevier.
- Guo, C., Xin, R., Wu, G., Liu, F., Hu, G. & Liu, Q., 2019, 'Observation of twin transmission process in Mg alloys by in situ EBSD', *Advanced Engineering Materials*, 21(7), 1801340.
- Guo, X., Li, C., Wang, H. & Xu, Z., 2018, 'Diversity and evolution of living oysters', *Journal of Shellfish Research*, 37(4), 755–771.
- Hahn, S., Rodolfo-Metalpa, R., Griesshaber, E., Schmahl, W.W., Buhl, D., Hall-Spencer, J.M., Baggini, C., Fehr, K.T. & Immenhauser, A., 2012, 'Marine bivalve shell geochemistry and ultrastructure from modern low pH environments: Environmental effect versus experimental bias', *Biogeosciences*, 9(5), 1897–1914.
- Hahn, T. & Klapper, H., 2013, 'Twinning of crystals', *International Tables for Crystallography*, pp. 413–483, John Wiley & Sons, Ltd.

- Hamaya, A., Fujisaki, K., Sasagawa, K. & Miura, K., 2025, 'A novel method for *Mytilus galloprovincialis* adductor muscle activity measurement during and after physical stimulation', *Journal of Biomechanics*, 187, 112754.
- Hampa, F.H., 2023, *Crystal assembly patterns of biocarbonate materials*, Master thesis, Ludwig-Maximilians-Universität, München.
- Han, Y.H., Li, H., Wong, T.Y. & Bradt, R.C., 1991, 'Knoop microhardness anisotropy of single-crystal aragonite', *Journal of the American Ceramic Society*, 74(12), 3129–3132.
- Hansen, N., 2004, 'Hall–Petch relation and boundary strengthening', *Scripta materialia*, 51(8), 801–806.
- Hanson, J. & Lowy, J., 1960, 'Structure and function of the contractile apparatus in the muscles of invertebrate animals', *Structure and function of muscle*, vol. 1, pp. 265–335, Academic Press New York.
- Harayashiki, C.A.Y., Márquez, F., Cariou, E. & Castro, Í.B., 2020, 'Mollusk shell alterations resulting from coastal contamination and other environmental factors', *Environmental Pollution*, 265, 114881.
- Harper, D.A.T., Cocks, L.R.M., Popov, L.E., Sheehan, P.M., Bassett, M.G., Copper, P., Holmer, L.E., Jin, J. & Jia-yu, R., 2004, 'Brachiopods', in B.D. Webby, F. Paris, M.L. Droser & I.G. Percival (eds.), *The Great Ordovician Biodiversification Event*, pp. 157–178, Columbia University Press.
- Harper, D.A.T., Popov, L.E. & Holmer, L.E., 2017, 'Brachiopods: Origin and early history', A. Smith (ed.), *Palaeontology*, 60(5), 609–631.
- Harper, E.M., 1998, 'Calcite in chamid bivalves', *Journal of Molluscan Studies*, 64(3), 391–399.
- Harper, E.M., 2000, 'Are calcitic layers an effective adaptation against shell dissolution in the Bivalvia?', *Journal of Zoology*, 251(2), 179–186.
- Harper, E.M., 2016, 'Unanswered questions in the evolution of biomineralisation', in G. Grupe & G.C. McGlynn (eds.), *Isotopic landscapes in bioarchaeology*, pp. 1–13, Springer Berlin Heidelberg, Berlin, Heidelberg.
- Harper, E.M. & Checa, A., 2017, 'Physiological versus biological control in bivalve calcite prisms: Comparison of Euheterodonts and Pteriomorphs', *The Biological Bulletin*, 232(1), 19–29.
- Hasenpusch, W., 2000, 'Die Stachel der Griffelseeigel', *Mikrokosmos*, 89(1), 23–27.
- He, L., Mo, S., Sun, L., Luo, W., Wang, J., Tian, N., He, J., Zou, Z. & Long, F., 2023, 'Nonclassical and classical crystallization: The formation of spindle-shaped CaCO₃ covered with abundant nanoscale rhombic calcites ubunits', *Crystal Growth & Design*, 23(6), 4105–4114.
- Hebert, E., Silvia, M. & Wessel, G.M., 2024, 'Structural and molecular distinctions of primary and secondary spines in the sea urchin *Lytechinus variegatus*', *Scientific Reports*, 14(1), 28525.
- Helama, S., Nielsen, J.K., Nielsen, J.K., Hanken, N.-M. & Evison, K., 2014, 'Preboreal oscillations inferred from *Arctica islandica* sclerochronology', *Geobios*, 47(5), 305–313.
- Helmkamp, M., Bruchhaus, I. & Hausdorf, B., 2008, 'Phylogenomic analyses of lophophorates (brachiopods, phoronids and bryozoans) confirm the Lophotrochozoa concept', *Proceedings of the Royal Society B: Biological Sciences*, 275(1645), 1927–1933.
- Henrich, R. & Wefer, G., 1986, 'Dissolution of biogenic carbonates: Effects of skeletal structure', *Marine Geology*, 71(3–4), 341–362.
- Henzler, K., Fetisov, E.O., Galib, M., Baer, M.D., Legg, B.A., Borca, C., Xto, J.M., Pin, S., Fulton, J.L., Schenter, G.K., Govind, N., Siepmann, J.I., Mundy, C.J., Huthwelker, T. & De Yoreo, J.J., 2018, 'Supersaturated calcium carbonate solutions are classical', *Science Advances*, 4(1), eaao6283.

- Hidaka, M. & Takahashi, K., 1983, 'Fine structure and mechanical properties of the catch apparatus of the sea-urchin spine, a collagenous connective tissue with muscle-like holding capacity', *Journal of Experimental Biology*, 103(1), 1–14.
- Hild, S., Marti, O. & Ziegler, A., 2008, 'Spatial distribution of calcite and amorphous calcium carbonate in the cuticle of the terrestrial crustaceans *Porcellio scaber* and *Armadillidium vulgare*', *Journal of Structural Biology*, 163(1), 100–108.
- Hirose, M. & Endo, K., 2021, 'Phylum Brachiopoda', *Invertebrate zoology: A tree of life approach*, pp. 329–340, CRC Press.
- Hoel, O.A., 2008, 'Evidence for muscular control of the apical pedicle in a Silurian Leptaenine brachiopod from Gotland, Sweden, and its life position', in D.A.T. Harper, S.L. Long & C. Nielsen (eds.), *Fossils and Strata*, vol. 54, pp. 53–58, Wiley-Blackwell.
- Hoerl, S., 2022, *Dependency between crystal organization and material properties in bivalve shells* – PhD thesis, Ludwig-Maximilians-Universität, München .
- Hoerl, S., Griesshaber, E., Checa, A.G. & Schmahl, W.W., 2024a, 'The biological crystals in chomid bivalve shells: Diversity in morphology and crystal arrangement pattern', *Crystals*, 14(7), 649.
- Hoerl, S., Griesshaber, E., Weller, D., Amini, S., Häussermann, V., Bitner, M.A., Achterhold, K., Pfeiffer, F. & Schmahl, W.W., 2025a, 'Crystal organisation at muscle attachment sites of bivalved marine organisms: A juxtaposition between brachiopod and bivalve shells', *Crystals*, 15(7), 649.
- Hoerl, S., Le Moine, T., Peter, N.J., Amini, S., Griesshaber, E., Wang, J., Harper, E.M., Salas, C., Checa, A.G., Schwaiger, R. & Schmahl, W.W., 2024b, 'Crystal organisation and material properties of *Chama* and *Glycymeris myostraca* and shells', *Materialia*, 36, 102149.
- Hoerl, S., Micheletti, C., Amini, S., Griesshaber, E., Hess, K.-U., Checa, A.G., Peharda, M. & Schmahl, W.W., 2025b, 'Correlation between nanomechanical properties and microstructural design concepts of bivalve muscle attachment sites', *Materials & Design*, 113845.
- Holmes, D.J. & Ottinger, M.A., 2003, 'Birds as long-lived animal models for the study of aging', *Experimental Gerontology*, 38(11–12), 1365–1375.
- Huang, J., Lin, F., Liu, C. & Luo, M., 2024, 'Oxidation and cross-link of tyrosine-rich proteins are involved in the periostracum formation of the green mussel *Perna viridis* (Linnaeus)', *Journal of Proteomics*, 296, 105112.
- Huang, Q., Yu, D., Xu, B., Hu, W., Ma, Y., Wang, Y., Zhao, Z., Wen, B., He, J., Liu, Z. & Tian, Y., 2014, 'Nanotwinned diamond with unprecedented hardness and stability', *Nature*, 510(7504), 250–253.
- Huang, S., Edie, S.M., Collins, K.S., Crouch, N.M.A., Roy, K. & Jablonski, D., 2023, 'Diversity, distribution and intrinsic extinction vulnerability of exploited marine bivalves', *Nature Communications*, 14(1), 4639.
- Huang, Z., Pan, Z., Li, H., Wei, Q. & Li, X., 2014, 'Hidden energy dissipation mechanism in nacre', *Journal of Materials Research*, 29(14), 1573–1578.
- Hubendick, B., 1957, 'On the molluscan adhesive epithelium', *Arkiv för Zoologi*, 11(6), 31–36.
- Huber, J., Griesshaber, E., Nindiyasari, F., Schmahl, W.W. & Ziegler, A., 2015, 'Functionalization of biomineral reinforcement in crustacean cuticle: Calcite orientation in the partes incisivae of the mandibles of *Porcellio scaber* and the supralittoral species *Tylos europaeus* (Oniscidea, Isopoda)', *Journal of Structural Biology*, 190(2), 173–191.
- Hudson, J., 1968, 'The microstructure and mineralogy of the shell of a Jurassic mytilid (Bivalvia)', *Palaeontology*, 11(2).
- Hughes, R.N., 1986, *A functional biology of marine gastropods*, Johns Hopkins Univ. Pr, Baltimore, Md.

- Hutchinson, B., 2015, 'Critical assessment 16: Anisotropy in metals', *Materials Science and Technology*, 31(12), 1393–1401.
- Hyde, S.T. & Meldrum, F.C., 2022, 'Starfish grow extraordinary crystals', *Science*, 375(6581), 615–616.
- Ichim, I., Li, Q., Li, W., Swain, M.V. & Kieser, J., 2007, 'Modelling of fracture behaviour in biomaterials', *Biomaterials*, 28(7), 1317–1326.
- Iglikowska, A., Beldowski, J., Chelchowski, M., Chierici, M., Kędra, M., Przytarska, J., Sowa, A. & Kukliński, P., 2017, 'Chemical composition of two mineralogically contrasting Arctic bivalves' shells and their relationships to environmental variables', *Marine Pollution Bulletin*, 114(2), 903–916.
- Iglikowska, A., Przytarska, J., Humphreys-Williams, E., Najorka, J., Chelchowski, M., Sowa, A., Hop, H., Włodarska-Kowalczyk, M. & Kukliński, P., 2023, 'Shell mineralogy and chemistry – Arctic bivalves in a global context', *Marine Pollution Bulletin*, 189, 114759–114759.
- Isaji, S., Kase, T., Tanabe, K. & Uchiyama, K., 2002, 'Ultrastructure of muscle-shell attachment in *Nautilus pompilius* Linnaeus (Mollusca : Cephalopoda)', *The Veliger*, 45, 316–330.
- Jackson, D.J., McDougall, C., Woodcroft, B., Moase, P., Rose, R.A., Kube, M., Reinhardt, R., Rokhsar, D.S., Montagnani, C., Joubert, C., & others, 2010, 'Parallel evolution of nacre building gene sets in molluscs', *Molecular biology and evolution*, 27(3), 591–608.
- James, M.A., Ansell, A.D., Collins, M.J., Curry, G.B., Peck, L.S. & Rhodes, M.C., 1992, 'Biology of living brachiopods', *Advances in Marine Biology*, vol. 28, pp. 175–387, Elsevier.
- James, N.P. & Klappa, C.F., 1983, 'Petrogenesis of Early Cambrian reef limestones, Labrador, Canada', *SEPM Journal of Sedimentary Research*, Vol. 53(4), 1051–1096.
- Jessop, A.-L., Millstead, A.J., Kirkensgaard, J.J.K., Shaw, J., Clode, P.L. & Schröder-Turk, G.E., 2024, 'Composite material in the sea urchin *Cidaris rugosa*: Ordered and disordered micrometre-scale bicontinuous geometries', *Journal of The Royal Society Interface*, 21(212), 20230597.
- Ji, H.M., Qi, Q.J., Liang, S.M., Yu, H. & Li, X.W., 2022, 'Ordered stereom structure in sea urchin tubercles: High capability for energy dissipation', *Acta Biomaterialia*, 150, 310–323.
- Jia, Z., Deng, Z. & Li, L., 2022, 'Biomaterialized materials as model systems for structural composites: 3D architecture', *Advanced Materials*, 34(20), 2106259.
- Johnson, E.H., 2020, 'Experimental tests of bivalve shell shape reveal potential tradeoffs between mechanical and behavioral defenses', *Scientific Reports*, 10(1), 19425.
- Jørgensen, S.E. & Fath, B.D., 2008, *Encyclopedia of ecology*, Elsevier, Amsterdam, Netherlands.
- Joshi, D.R., 1993, 'Hardness anisotropy of rhombohedral crystals of calcite. Variation of hardness with orientation', *Crystal Research and Technology*, 28(1), 111–117.
- Kahil, K., Weiner, S., Addadi, L. & Gal, A., 2021, 'Ion pathways in biomineralization: Perspectives on uptake, transport, and deposition of calcium, carbonate, and phosphate', *Journal of the American Chemical Society*, 143(50), 21100–21112.
- Kahler, G.A., Fisher Jr, F.M. & Sass, R.L., 1976, 'The chemical composition and mechanical properties of the hinge ligament in bivalve molluscs', *The Biological Bulletin*, 151(1), 161–181.
- Kamat, S., Kessler, H., Ballarini, R., Nassirou, M. & Heuer, Arthur.H., 2004, 'Fracture mechanisms of the *Strombus gigas* conch shell: II-micromechanics analyses of multiple cracking and large-scale crack bridging', *Acta Materialia*, 52(8), 2395–2406.
- Kamenev, G.M., Mordukhovich, V.V., Alalykina, I.L., Chernyshev, A.V. & Maiorova, A.S., 2022, 'Macrofauna and nematode abundance in the Aayssal and hadal zones of interconnected deep-sea ecosystems in the

- Kuril Basin (Sea of Okhotsk) and the Kuril-Kamchatka Trench (Pacific Ocean)', *Frontiers in Marine Science*, 9, 812464.
- Kano, Y. & Kase, T., 2003, 'Systematics of the *Neritilia rubida* complex (Gastropoda: Neritiliidae): Three amphidromous species with overlapping distributions in the Indo-Pacific.', *Journal of Molluscan Studies*, 69(3), 273–284.
- Kashchiev, D., 2000, *Nucleation: basic theory with applications*, Butterworth-Heinemann, Oxford.
- Kashchiev, D. & Van Rosmalen, G.M., 2003, 'Review: Nucleation in solutions revisited', *Crystal Research and Technology*, 38(7–8), 555–574.
- Kasyap, S.S. & Senetakis, K., 2021, 'Application of nanoindentation in the characterization of a porous material with a clastic texture', *Materials*, 14(16), 4579.
- Kauffman, E.G., 1969, 'Form, function, and evolution', *Mollusca 8 Bivalvia*, 1(3), N130–N205.
- Kennedy, J.W., Morris, N.J. & Taylor, J.D., 1970, 'The shell structure, mineralogy and relationships of the Chamacea (Bivalvia)', *Paleontology*, 13(3), 379–413.
- Kennedy, W.J., Taylor, J.D. & Hall, A., 1969, 'Environmental and biological controls on bivalve shell mineralogy.', *Biological Reviews*, 44(4), 499–530.
- Kier, W.M., 1988, 'The arrangement and function of molluscan muscle', *Form and Function*, pp. 211–252, Elsevier.
- Kinlan, B.P. & Gaines, S.D., 2003, 'Propagule dispersal in marine and terrestrial environments: A community perspective', *Ecology*, 84(8), 2007–2020.
- Kirner, F. & Sturm, E.V., 2021, 'Advances of nonclassical crystallization toward self-purification of precious metal nanoparticle mixtures', *Crystal Growth & Design*, 21(9), 5192–5197.
- Kirschvink, J. & Hagadorn, J., 2000, '10 A Grand Unified Theory of Biomineralization', *The Biomineralisation of Nano- and Micro-Structures*.
- Klompaker, A.A. & Kelley, P.H., 2015, 'Shell ornamentation as a likely exaptation: Evidence from predatory drilling on Cenozoic bivalves', *Paleobiology*, 41(1), 187–201.
- Kobak, J., 2006, 'Factors influencing the attachment strength of *Dreissena polymorpha* (Bivalvia)', *Biofouling*, 22(3), 141–150.
- Kobayashi, I., 1991, 'Evolutionary trends of shell microstructure in bivalve molluscs', *Mechanisms and Phylogeny of Mineralization in Biological Systems*, pp. 415–419, Springer Japan, Tokyo.
- Kobayashi, I. & Samata, T., 2006, 'Bivalve shell structure and organic matrix', *Materials Science and Engineering: C*, 26(4), 692–698.
- Kobayashi, T., 2004, *Strength and toughness of materials*, Springer Japan, Tokyo.
- Kogure, T., Suzuki, M., Kim, H., Mukai, H., Checa, A.G., Sasaki, T. & Nagasawa, H., 2014, 'Twin density of aragonite in molluscan shells characterized using X-ray diffraction and transmission electron microscopy', *Journal of Crystal Growth*, 397, 39–46.
- Kokorin, A.I., Mirantsev, G.V. & Rozhnov, S.V., 2014, 'General features of echinoderm skeleton formation', *Paleontological Journal*, 48(14), 1532–1539.
- Koller-Hodac, A., Germann, D.P., Gilgen, A., Dietrich, K., Hadorn, M., Schatz, W. & Hotz, P.E., 2010, *Actuated bivalve robot study of the burrowing locomotion in sediment*, 2010 IEEE International Conference on Robotics and Automation, 1209–1214, IEEE.

- Krieger Lassen, N., Juul Jensen, D. & Conradsen, K., 1992, 'Image processing procedures for analysis of electron back scattering patterns', *Scanning Microscopy*, 6(1), 7.
- Krylova, E., 2006, 'Bivalves of seamounts of the north-eastern Atlantic', *Biogeography of the North Atlantic Seamounts*, pp. 76–95, KMK Scientific Press, Ltd. Moscow.
- Krylova, E.M., Kamenev, G.M., Vladychenskaya, I.P. & Petrov, N.B., 2015, 'Vesicomyninae (Bivalvia: Vesicomysidae) of the Kuril–Kamchatka Trench and adjacent abyssal regions', *Deep Sea Research Part II: Topical Studies in Oceanography*, 111, 198–209.
- LaBarbera, M., 1978, 'Brachiopod orientation to water movement: Functional morphology', *Lethaia*, 11(1), 67–79.
- Labrecque, A. & Guderley, H., 2011, 'Size, muscle metabolic capacities and escape response behaviour in the giant scallop', *Aquatic Biology*, 13(1), 51–64.
- Lafuste, J., 1970, 'Lames ultra-minces à faces polies. Procédé et application à la microstructure des Madréporaires fossiles', *Comptes Rendus de l'Académie des Sciences de Paris (Série D)*, 270(1970), 679–681.
- Lai, M., Kulak, A.N., Law, D., Zhang, Z., Meldrum, F.C. & Riley, D.J., 2007, 'Profiting from nature: macroporous copper with superior mechanical properties', *Chemical Communications*, (34), 3547.
- Lai-Fook, J., 1967, 'The structure of developing muscle insertions in insects', *Journal of Morphology*, 123(4), 503–527.
- Lambert, G. & Lambert, C.C., 1996, 'Spicule formation in the New Zealand ascidian *Pyura pachydermatina* (Chordata, Ascidiacea)', *Connective Tissue Research*, 34(4), 263–269.
- Lastam, J., Griesshaber, E., Yin, X., Rupp, U., Sánchez-Almazo, I., Heß, M., Walther, P., Checa, A. & Schmahl, W.W., 2023a, 'The unique fibrillar to platy nano- and microstructure of twinned roaliid foraminiferal shell calcite', *Scientific Reports*, 13(1), 2189.
- Lastam, J., Griesshaber, E., Yin, X., Rupp, U., Sánchez-Almazo, I., Heß, M., Walther, P., Checa, A. & Schmahl, W.W., 2023b, 'Patterns of crystal organization and calcite twin formation in planktonic, roaliid, foraminifera shells and spines', *Journal of Structural Biology*, 215(1), 107898.
- Lauer, C., Haußmann, S., Schmidt, P., Fischer, C., Rapp, D., Berthold, C. & Nickel, K.G., 2020, 'On the relation of amorphous calcium carbonate and the macromechanical properties of sea urchin spines', *Advanced Engineering Materials*, 22(4), 1900922.
- Lauer, C., Sillmann, K., Haußmann, S. & Nickel, K.G., 2018, 'Strength, elasticity and the limits of energy dissipation in two related sea urchin spines with biomimetic potential', *Bioinspiration & Biomimetics*, 14(1), 016018.
- Launey, M.E. & Ritchie, R.O., 2009, 'On the fracture toughness of advanced materials', *Advanced Materials*, 21(20), 2103–2110.
- Lawrence, J.M. (ed.), 2020, *Sea urchins: Biology and ecology*, Fourth edition, Academic Press, an imprint of Elsevier, London, United Kingdom ; San Diego, CA.
- Le Moine, T., 2022, *Characterization of the microstructure and the texture of calcium carbonate crystals in bivalve shells*, Master thesis, Ludwig-Maximilians-Universität, München.
- Leadbeater, B.S.C. & Riding, R., 1986, *Biom mineralization in lower plants and animals: Proceedings of an international symposium held at the University of Birmingham, April 1985*, Published for the Systematics Association by the Clarendon Press; Oxford University Press, Oxford.
- Lee, S.W. & Choi, C.S., 2007, 'The correlation between organic matrices and biominerals (myostracal prism and folia) of the adult oyster shell, *Crassostrea gigas*', *Micron*, 38(1), 58–64.

- Lee, S.-W., Jang, Y.-N. & Kim, J.-C., 2011, 'Characteristics of the Aragonitic Layer in Adult Oyster Shells, *Crassostrea gigas*: Structural Study of Myostracum including the Adductor Muscle Scar', *Evidence-Based Complementary and Alternative Medicine*, 2011, 1–10.
- Legac, M. & Hrs-Brenko, M., 1999, 'A review of bivalve species in the eastern Adriatic Sea. III. Pteriomorpha (Glycymerididae)', *Natura Croatica: Periodicum Musei Historiae Naturalis Croatici*, 8(1), 9–25.
- LeGeros, R.Z., Pan, C.-M., Suga, S. & Watabe, N., 1985, 'Crystallo-chemical properties of apatite in atremate brachiopod shells', *Calcified Tissue International*, 37(1), 98–100.
- Lemaire-Gony, S. & Boudou, A., 1997, 'Mantle and gill fine structure in the freshwater Asiatic clam, *Corbicula fluminea* (Müller)', *Annales de Limnologie - International Journal of Limnology*, 33(3), 163–178.
- Lenthe, W.C., Singh, S. & Graef, M.D., 2019, 'A spherical harmonic transform approach to the indexing of electron back-scattered diffraction patterns', *Ultramicroscopy*, 207, 112841.
- Levi-Kalisman, Y., Raz, S., Weiner, S., Addadi, L. & Sagi, I., 2002, 'Structural differences between biogenic amorphous calcium carbonate phases using X-ray absorption spectroscopy', *Advanced Functional Materials*, 12(1), 43.
- Lew, A.J., Stiffler, C.A., Tits, A., Schmidt, C.A., Scholl, A., Cantamessa, A., Müller, L., Delaunois, Y., Compère, P., Ruffoni, D., Buehler, M.J. & Gilbert, P.U.P.A., 2023, 'A molecular-scale understanding of misorientation toughening in corals and seashells', *Advanced Materials*, 35(28), 2300373.
- Leyva-Porras, C., Cruz-Alcantar, P., Espinosa-Solís, V., Martínez-Guerra, E., Piñón-Balderrama, C.I., Compean Martínez, I. & Saavedra-Leos, M.Z., 2019, 'Application of Differential Scanning Calorimetry (DSC) and Modulated Differential Scanning Calorimetry (MDSC) in Food and Drug Industries', *Polymers*, 12(1), 5.
- Li, C., Kou, Q., Zhang, Z., Hu, L., Huang, W., Cui, Z., Liu, Y., Ma, P. & Wang, H., 2021, 'Reconstruction of the evolutionary biogeography reveal the origins and diversification of oysters (Bivalvia: Ostreidae)', *Molecular Phylogenetics and Evolution*, 164, 107268.
- Li, L. & Ortiz, C., 2014, 'Pervasive nanoscale deformation twinning as a catalyst for efficient energy dissipation in a bioceramic armour', *Nature Materials*, 13(5), 501–507.
- Li, L., Weaver, J.C. & Ortiz, C., 2015, 'Hierarchical structural design for fracture resistance in the shell of the pteropod *Clio pyramidata*', *Nature Communications*, 6(1), 6216.
- Li, M., Song, H., Tian, L., Woods, A.D., Dai, X. & Song, H., 2018, 'Lower Triassic deep sea carbonate precipitates from South Tibet, China', *Sedimentary Geology*, 376, 60–71.
- Li, X.W., Ji, H.M., Yang, W., Zhang, G.P. & Chen, D.L., 2017, 'Mechanical properties of crossed-lamellar structures in biological shells: A review', *Journal of the Mechanical Behavior of Biomedical Materials*, 74, 54–71.
- Liao, Z., Bao, L., Fan, M., Gao, P., Wang, X., Qin, C. & Li, X., 2015, 'In-depth proteomic analysis of nacre, prism, and myostracum of *Mytilus* shell', *Journal of Proteomics*, 122, 26–40.
- Lifshitz, R., 2007, 'What is a crystal?', *Zeitschrift für Kristallographie*, 222(6), 313–317.
- Liu, R., Huang, S., Zhang, X., Song, Y., He, G., Wang, Z. & Lian, B., 2021, 'Bio-mineralisation, characterization, and stability of calcium carbonate containing organic matter', *RSC Advances*, 11(24), 14415–14425.
- Loh, H.-C., Divoux, T., Gludovatz, B., Gilbert, P.U.P.A., Ritchie, R.O., Ulm, F.-J. & Masic, A., 2020, 'Nacre toughening due to cooperative plastic deformation of stacks of co-oriented aragonite platelets', *Communications Materials*, 1(1), 77.
- Lopes-Lima, M., Burlakova, L.E., Karatayev, A.Y., Mehler, K., Seddon, M. & Sousa, R., 2018, 'Conservation of freshwater bivalves at the global scale: diversity, threats and research needs', *Hydrobiologia*, 810(1), 1–14.

- Lopes-Lima, M., Rocha, A., Gonçalves, F., Andrade, J. & Machado, J., 2010, 'Microstructural characterization of inner shell layers in the freshwater bivalve *Anodonta cygnea*', *Journal of Shellfish Research*, 29(4), 969–973.
- Lopez, E., Vidal, B., Berland, S., Camprasse, S., Camprasse, G. & Silve, C., 1992, 'Demonstration of the capacity of nacre to induce bone formation by human osteoblasts maintained in vitro', *Tissue and Cell*, 24(5), 667–679.
- Lowenstam, H.A. & Weiner, S., 1989, *On biomineralization*, Oxford Univ. Press, New York, NY.
- Luo, C., Yang, X. & Li, J., 2023, 'Tensile and compressive mechanical properties of nanocrystalline calcite with grain size effect', *Journal of Mechanics*, 39, 442–450.
- Ma, Y., Cohen, S.R., Addadi, L. & Weiner, S., 2008, 'Sea urchin tooth design: An “all-calcite” polycrystalline reinforced fiber composite for grinding rocks', *Advanced Materials*, 20(8), 1555–1559.
- MacClintock, C., 1967, 'Shell structure of patelloid and bellerophonoid gastropods (Mollusca)', *Bulletin of the Peabody Museum of National History, Yale University*, 22, 1–140.
- MacKinnon, D.I., 1977, 'The formation of muscle scars in articulate brachiopods', *Philosophical Transactions of the Royal Society of London. B, Biological Sciences*, 280(970), 1–27.
- Magdams, U. & Gies, H., 2004, 'Single crystal structure analysis of sea urchin spine calcites: Systematic investigations of the Ca/Mg distribution as a function of habitat of the sea urchin and the sample location in the spine', *European Journal of Mineralogy*, 16(2), 261–268.
- Mandera, S., Coronado, I., Fernández-Díaz, L., Mazur, M., Cruz, J.A., Januszewicz, B., Fernández-Martínez, E., Cózar, P. & Stolarski, J., 2023, 'Earthworm granules: A model of non-classical biogenic calcium carbonate phase transformations', *Acta Biomaterialia*, 162, 149–163.
- Mann, K., Poustka, A.J. & Mann, M., 2008, 'The sea urchin (*Strongylocentrotus purpuratus*) test and spine proteomes', *Proteome Science*, 6(1), 22.
- Mann, S., 1995, 'Biomineralization and biomimetic materials chemistry', *Journal of Materials Chemistry*, 5(7), 935.
- Mann, S., 2001, 'Biomineralization: Principles and concepts in bioinorganic materials chemistry'.
- Manuel, J.L. & Dadswell, M.J., 1993, 'Swimming of juvenile sea scallops, *Placopecten magellanicus* (Gmelin): A minimum size for effective swimming?', *Journal of Experimental Marine Biology and Ecology*, 174(2), 137–175.
- Marie, B., Joubert, C., Tayalé, A., Zanella-Cléon, I., Belliard, C., Piquemal, D., Cochennec-Laureau, N., Marin, F., Gueguen, Y. & Montagnani, C., 2012, 'Different secretory repertoires control the biomineralization processes of prism and nacre deposition of the pearl oyster shell', *Proceedings of the National Academy of Sciences*, 109(51), 20986–20991.
- Marie, B., Le Roy, N., Marie, A., Dubost, L., Milet, C., Bedouet, L., Becchi, M., Zanella-Cléon, I., Jackson, D., Degnan, B., Luquet, G. & Marin, F., 2009, 'Nacre evolution: A proteomic approach', *MRS Proceedings*, 1187, 1187-KK01-03.
- Marin, F., Le Roy, N. & Marie, B., 2012, 'The formation and mineralization of mollusk shell', *Front. Biosci.*, 4(3), 1099–1125.
- Marin, F., Luquet, G., Marie, B. & Medakovic, D., 2007a, 'Molluscan shell proteins: Primary structure, origin, and evolution', *Current Topics in Developmental Biology*, vol. 80, pp. 209–276, Elsevier.
- Marin, F., Pokroy, B., Luquet, G., Layrolle, P. & De Groot, K., 2007b, 'Protein mapping of calcium carbonate biominerals by immunogold', *Biomaterials*, 28(14), 2368–2377.

- Märkel, K., Röser, U. & Stauber, M., 1989, 'On the ultrastructure and the supposed function of the mineralizing matrix coat of sea urchins (Echinodermata, Echinoida)', *Zoomorphology*, 109(2), 79–87.
- Marsh, R.L., Olson, J.M. & Guzik, S.K., 1992, 'Mechanical performance of scallop adductor muscle during swimming', *Nature*, 357(6377), 411–413.
- Matsukuma, A., 1996, 'A new genus and four new species of Chamidae (Mollusca, Bivalvia) from the Indo-West Pacific with reference to transposed shells', *Bulletin du Muséum National d'Histoire Naturelle Section A. Zoologie, biologie et écologie animales*, 18, 23–53.
- Matsukuma, A., Hamada, N. & Scott, P.H., 1997, '*Chama pulchella* (Bivalvia : Heterodonta) with transposed shell and normal dentition', *Venus (Japanese Journal of Malacology)*, 56(3), 221–231.
- McCammon, H.M., 1971, 'Behavior in the brachiopod *Terebratulina septentrionalis* (Couthouy)', *Journal of Experimental Marine Biology and Ecology*, 6(1), 35–45.
- McLachlan, A., Jaramillo, E., Defeo, O., Dugan, J., De Ruyck, A. & Coetzee, P., 1995, 'Adaptations of bivalves to different beach types', *Journal of Experimental Marine Biology and Ecology*, 187(2), 147–160.
- Melancon, S., Fryer, B.J., Ludsins, S.A., Gagnon, J.E. & Yang, Z., 2005, 'Effects of crystal structure on the uptake of metals by lake trout (*Salvelinus namaycush*) otoliths', *Canadian Journal of Fisheries and Aquatic Sciences*, 62(11), 2609–2619.
- Meldrum, F.C. & Cölfen, H., 2008, 'Controlling mineral morphologies and structures in biological and synthetic systems', *Chemical Reviews*, 108(11), 4332–4432.
- Mergelsberg, S.T., Ulrich, R.N., Xiao, S. & Dove, P.M., 2019, 'Composition systematics in the exoskeleton of the american lobster, *Homarus americanus* and implications for Malacostraca', *Frontiers in Earth Science*, 7, 69.
- Meyers, M.A., Chen, P.-Y., Lin, A.Y.-M. & Seki, Y., 2008, 'Biological materials: Structure and mechanical properties', *Progress in Materials Science*, 53(1), 1–206.
- Mikkelsen, P.M., 2011, 'Speciation in modern marine bivalves (Mollusca: Bivalvia): Insights from the published record', *American Malacological Bulletin*, 29(1–2), 217–245.
- Miller, A.I. & Sepkoski, J.J., 1988, 'Modeling bivalve diversification: The effect of interaction on a macroevolutionary system', *Paleobiology*, 14(4), 364–369.
- Milliman, J.D., Gastner, M. & Müller, J., 1971, 'Utilization of magnesium in coralline algae', *Geological Society of America Bulletin*, 82(3), 573.
- Millman, B.M., 1967, 'Mechanisms of contraction in molluscan muscle', *American Zoologist*, 7(3), 583–591.
- Min, L., Wei-min, C., Nai-gang, L. & Ling-Dong, W., 2004, 'A numerical study of indentation using indenters of different geometry', *Journal of Materials Research*, 19(1), 73–78.
- Mittal, N., Ansari, F., Gowda, V. K., Brouzet, C., Chen, P., Larsson, P.T., Roth, S.V., Lundell, F., Wågberg, L., Kotov, N.A. & Söderberg, L.D., 2018, 'Multiscale control of nanocellulose assembly: Transferring remarkable nanoscale fibril mechanics to macroscale fibers', *ACS Nano*, 12(7), 6378–6388.
- Mohammadi, P., Gandier, J.-A., Wagermaier, W., Miserez, A. & Penttilä, M., 2021, 'Bioinspired functionally graded composite assembled using cellulose nanocrystals and genetically engineered proteins with controlled biomineralization', *Advanced Materials*, 33(42), 2102658–2102658.
- Mohd Norsham, I.N., Baharin, S.N.A., Raoov, M., Shahabuddin, S., Jakmunee, J. & Sambasevam, K.P., 2020, 'Optimization of waste quail eggshells as biocomposites for polyaniline in ammonia gas detection', *Polymer Engineering & Science*, 60(12), 3170–3182.
- Moine, T. le, 2022, *Characterization of the microstructure and the texture of calcium carbonate crystals in bivalve shells* – PhD thesis, Ludwig-Maximilians-Universität, München .

- Moore, S.W., Manzari, M.T. & Shen, Y.-L., 2010, 'Nanoindentation in elastoplastic materials: insights from numerical simulations', *International Journal of Smart and Nano Materials*, 1(2), 95–114.
- Morand, N., 2020, 'The exploitation of molluscs and other invertebrates in Alexandria (Egypt) from the Hellenistic period to Late Antiquity: food, usage, and trade', *Anthropozoologica*, 55(1), 1.
- Mortensen, T., 1927, *Handbook of the echinoderms of the British Isles*, Oxford university Press, London.
- Morton, B., 2001, 'The evolution of eyes in the Bivalvia', *Oceanography and Marine Biology: An Annual Review*, 39, 165–205.
- Morton, B. & Machado, F.M., 2019, 'Predatory marine bivalves: A review', *Advances in Marine Biology*, vol. 84, pp. 1–98, Elsevier.
- Moureaux, C., Pérez-Huerta, A., Compère, P., Zhu, W., Leloup, T., Cusack, M. & Dubois, P., 2010, 'Structure, composition and mechanical relations to function in sea urchin spine', *Journal of Structural Biology*, 170(1), 41–49.
- Moynihan, M.A., Amini, S., Goodkin, N.F., Tanzil, J.T.I., Chua, J.Q.I., Fabbro, G.N., Fan, T.-Y., Schmidt, D.N. & Miserez, A., 2021, 'Environmental impact on the mechanical properties of *Porites* spp. corals', *Coral Reefs*, 40(3), 701–717.
- Mucci, A. & Morse, J.W., 1984, 'The solubility of calcite in seawater solutions of various magnesium concentration, It= 0.697 m at 25 C and one atmosphere total pressure', *Geochimica et Cosmochimica Acta*, 48(4), 815–822.
- Muller, D.A., 2009, 'Structure and bonding at the atomic scale by scanning transmission electron microscopy', *Nature Materials*, 8(4), 263–270.
- Nakahara, H. & Bevelander, G., 1970, 'An electron microscope study of the muscle attachment in the mollusc *Pinctada radiata*', *Texas reports on biology and medicine*, 28(3), 279–286.
- Nakahara, H. & Bevelander, G., 1971, 'The formation and growth of the prismatic layer of *Pinctada radiata*', *Calcified tissue research*, 7(1), 31–45.
- Nakahara, H., Kakei, M. & Bevelander, G., 1980, 'Fine structure and amino acid composition of the organic "envelope" in the prismatic layer of some bivalve shells', *Venus (Japanese Journal of Malacology)*, 39(3), 167–177.
- Nalepka, K., Berent, K., Checa, A., Machniewicz, T., Harris, A., Nalepka, P., Strag, M., Maj, Ł., Szkudlarek, A., Bieda, M. & Sztwiertnia, K., 2020, *Twin-based toughening mechanisms in Pinna nobilis shell*.
- Nanakoudis, A., 2019, *SEM: Types of electrons and the information they provide*, Thermo Fisher Scientific, Microscopy Blog.
- Narinc, D., Aygun, A., Karaman, E. & Aksoy, T., 2015, 'Egg shell quality in Japanese quail: Characteristics, heritabilities and genetic and phenotypic relationships', *Animal*, 9(7), 1091–1096.
- Nash, M.C. & Adey, W., 2017, 'Multiple phases of mg-calcite in crustose coralline algae suggest caution for temperature proxy and ocean acidification assessment: Lessons from the ultrastructure and biomineralization in *Phymatolithon* (Rhodophyta, Corallinales)', C. Hurd (ed.), *Journal of Phycology*, 53(5), 970–984.
- Nash, M.C., Adey, W. & Harvey, A.S., 2021, 'High magnesium calcite and dolomite composition carbonate in *Amphiroa* (Lithophyllaceae, Corallinales, Rhodophyta): Further documentation of elevated Mg in Corallinales with climate change implications', M. Roleda (ed.), *Journal of Phycology*, 57(2), 496–509.
- Nebelsick, J.H., Dynowski, J.F., Grossmann, J.N. & Tötze, C., 2015, 'Echinoderms: Hierarchically organized light weight skeletons', in C. Hamm (ed.), *Evolution of lightweight structures*, Biologically-Inspired Systems., vol. 6, pp. 141–155, Springer Netherlands, Dordrecht.

- Neumann, M. & Eppe, M., 2007, 'Monohydrocalcite and Its relationship to hydrated amorphous calcium carbonate in biominerals', *European Journal of Inorganic Chemistry*, 2007(14), 1953–1957.
- Newnham, R.E., 2004, *Properties of materials: Anisotropy, symmetry, structure*, Oxford University Press.
- Nickel, K.G., Klang, K., Lauer, C. & Buck, G., 2017, 'Sea urchin spines as role models for biological design and integrative structures', in S. Heuss-Aßbichler, G. Amthauer & M. John (eds.), *Highlights in Applied Mineralogy*, pp. 273–284, De Gruyter.
- Nickel, K.G., Presser, V., Schultheiß, S., Berthold, C., Kohler, C., Nebelsick, J., Grossmann, N., Stegmaier, T., Finckh, H. & Vohrer, A., 2009, 'Seeigelstachel als Modell für stoffdurchlässige Einschlagschutzsysteme', pp. 29–39.
- Nicol, D., 1952, 'Nomenclatural review of genera and subgenera of Chamidae', *Journal of the Washington Academy of Sciences*, 42(5), 154–156.
- Niemiec, M. & Kim, K., 2024, 'Lifetime engineering of bioelectronic implants with mechanically reliable thin film encapsulations', *Progress in Biomedical Engineering*, 6(1), 012001.
- Nindiyasari, F., Ziegler, A., Griesshaber, E., Fernández-Díaz, L., Huber, J., Walther, P. & Schmahl, W.W., 2015, 'Effect of hydrogel matrices on calcite crystal growth morphology, aggregate formation, and co-orientation in biomimetic experiments and biomineralization environments', *Crystal Growth & Design*, 15(6), 2667–2685.
- Nishida, K., Nakashima, R., Majima, R. & Hikida, Y., 2011, 'Ontogenetic changes in shell microstructures in the cold seep-associated bivalve, *Conchocele bisecta* (Bivalvia: Thyasiridae)', *Paleontological Research*, 15(4), 193–212.
- Nishikawa, S. & Kikuchi, S., 1928, 'Diffraction of cathode rays by calcite', *Nature*, 122(3080), 726–726.
- Nissen, H.-U., 1969, 'Crystal orientation and plate structure in echinoid skeletal units', *Science*, 166(3909), 1150–1152.
- Nolze, G., Winkelmann, A. & Neumann, R.S., 2017, *Significant improvement of the orientation resolution by EBSD-pattern matching*, 7–11.
- Norkko, J., Norkko, A., Thrush, S.F. & Cummings, V.J., 2005, 'Detecting growth under environmental extremes: Spatial and temporal patterns in nucleic acid ratios in two Antarctic bivalves', *Journal of Experimental Marine Biology and Ecology*, 326(2), 144–156.
- Norris, R.D. & Hull, P.M., 2012, 'The temporal dimension of marine speciation', *Evolutionary Ecology*, 26(2), 393–415.
- Nudelman, F. & Sommerdijk, N.A.J.M., 2012, 'Biomineralization as an inspiration for materials chemistry', *Angewandte Chemie International Edition*, 51(27), 6582–6596.
- Nunzi, M.G. & Franzini-Armstrong, C., 1981, 'The structure of smooth and striated portions of the adductor muscle of the valves in a scallop', *Journal of Ultrastructure Research*, 76(2), 134–148.
- Oberling, J.-J., 1964, 'Observations on some structural features of the pelecypod shell', *Mitt. Natur. Ges. Bern*, 20, 1–60.
- Odintsova, N., Dyachuk, V., Kiselev, K. & Shelud'ko, N., 2006, 'Expression of thick filament proteins during ontogenesis of the mussel *Mytilus trossulus* (Mollusca: Bivalvia)', *Comparative Biochemistry and Physiology Part B: Biochemistry and Molecular Biology*, 144(2), 238–244.
- Odintsova, N.A., Dyachuk, V.A. & Karpenko, A.A., 2007, 'Development of the muscle system and contractile activity in the mussel *Mytilus trossulus* (Mollusca, Bivalvia)', *Russian Journal of Developmental Biology*, 38(3), 190–196.
- Okazaki, K., 1960, 'Skeleton formation of sea urchin larvae', *Embryologia*, 5(3), 283–320.

- Okazaki, K., Dillaman, R.M. & Wilbur, K.M., 1981, 'Crystalline axes of the spine and test of the sea urchin *Strongylocentrotus purpuratus*: Determination by crystal etching and decoration', *The Biological Bulletin*, 161(3), 402–415.
- Oliver, P.G. & Holmes, A.M., 2006, 'The Arcoidea (Mollusca: Bivalvia): A review of the current phenetic-based systematics', *Zoological Journal of the Linnean Society*, 148(3), 237–251.
- Oliver, W.C. & Pharr, G.M., 1992, 'An improved technique for determining hardness and elastic modulus using load and displacement sensing indentation experiments', *Journal of materials research*, 7(6), 1564–1583.
- O'Toole-Howes, M., Ingleby, R., Mertesdorf, M., Dean, J., Li, W., Carpenter, M.A. & Harper, E.M., 2019, 'Deconvolution of the elastic properties of bivalve shell nanocomposites from direct measurement and finite element analysis', *Journal of Materials Research*, 34(16), 2869–2880.
- Palumbi, S.R., 1994, 'Genetic divergence, reproductive isolation, and marine speciation', *Annual Review of Ecology and Systematics*, 25(1), 547–572.
- Pan, Zhao, Tucker, Zhou, Jiang, Wang, Zhao, Sun, Han, & Yan, 2019, 'Biom mineralization of Monohydrocalcite Induced by the Halophile *Halomonas smyrnensis* WMS-3', *Minerals*, 9(10), 632.
- Paniagua, R., Royuela, M., Garcia-Anchuelo, R. & Fraile, B., 1996, 'Ultrastructure of invertebrate muscle cell types', *Histology and histopathology*.
- Park, T., Woo, J., Lee, D.-J., Lee, D.-C., Lee, S., Han, Z., Chough, S.K. & Choi, D.K., 2011, 'A stem-group cnidarian described from the mid-Cambrian of China and its significance for cnidarian evolution', *Nature Communications*, 2(1), 442.
- Pasquini, L., Molinari, A., Fantazzini, P., Dauphen, Y., Cuif, J.-P., Levy, O., Dubinsky, Z., Caroselli, E., Prada, F., Goffredo, S., Di Giosia, M., Reggi, M. & Falini, G., 2015, 'Isotropic microscale mechanical properties of coral skeletons', *Journal of The Royal Society Interface*, 12(106), 20150168.
- Pastorino, G., 1991, 'The genus *Chama* Linné (Bivalvia) in the marine Quaternary of northern Patagonia, Argentina', *Journal of Paleontology*, 65(5), 756–760.
- Patton, M.L., Brown, S.T., Harman, R.F. & Grove, R.S., 1991, 'Effect of the anemone *Corynactis californica* on subtidal predation by sea stars in the Southern California Bight', *Bulletin of Marine Science*, 48(3), 623–634.
- Pearce, C.M., Manuel, J.L., Gallager, S.M., Manning, D.A., O'Dor, R.K. & Bourget, E., 2004, 'Depth and timing of settlement of veligers from different populations of giant scallop, *Placopecten magellanicus* (Gmelin), in thermally stratified mesocosms', *Journal of Experimental Marine Biology and Ecology*, 312(1), 187–214.
- Pearse, J.S. & Pearse, V.B., 1975, 'Growth zones in the echinoid skeleton', *American Zoologist*, 15(3), 731–751.
- Peck, L.S., Brockington, S. & Brey, T., 1997, 'Growth and metabolism in the Antarctic brachiopod *Liothyrella uva*', *Philosophical Transactions of the Royal Society of London. Series B: Biological Sciences*, 352(1355), 851–858.
- Peck, L.S. & Harper, E., 2010, 'Variation in size of living articulated brachiopods with latitude and depth', *Marine Biology*, 157, 2205–2213.
- Peel, J.S., 2015, 'Failed predation, commensalism and parasitism on lower Cambrian linguliformean brachiopods', *Alcheringa: An Australasian Journal of Palaeontology*, 39(2), 149–163.
- Peharda, M., Black, B.A., Purroy, A. & Mihanović, H., 2016, 'The bivalve *Glycymeris pilosa* as a multidecadal environmental archive for the Adriatic and Mediterranean Seas', *Marine Environmental Research*, 119, 79–87.

- Peharda, M., Crnčević, M., Bušelić, I., Richardson, C.A. & Ezgeta-Balić, D., 2012, 'Growth and longevity of *Glycymeris nummaria* (Linnaeus, 1758) from the eastern Adriatic, Croatia', *Journal of Shellfish Research*, 31(4), 947–950.
- Peharda, M., Walliser, E.O., Markulin, K., Purroy, A., Uvanović, H., Janeković, I., Župan, I., Vilibić, I. & Schöne, B.R., 2019, '*Glycymeris pilosa* (Bivalvia) – A high-potential geochemical archive of the environmental variability in the Adriatic Sea', *Marine Environmental Research*, 150, 104759.
- Peng, Y., Shi, G.R., Gao, Y., He, W. & Shen, S., 2007, 'How and why did the Lingulidae (Brachiopoda) not only survive the end-Permian mass extinction but also thrive in its aftermath?', *Palaeogeography, Palaeoclimatology, Palaeoecology*, 252(1–2), 118–131.
- Peng, Y., Xu, X. & Liang, Y., 2023, 'Influence of an axial-electromagnetic field treatment device with a solenoid structure on crystallization fouling on the tube side of a shell-and-tube heat exchanger', *Entropy*, 25(7), 962.
- Perricone, V., Cesarano, P., Mancosu, A., Asnicar, D., Bravi, S. & Marmo, F., 2023, 'Echinoid skeleton: An insight on the species-specific pattern of the *Paracentrotus lividus* plate and its microstructural variability', *Journal of The Royal Society Interface*, 20(199), 20220673.
- Peter, N.J., Griesshaber, E., Reisecker, C., Hild, S., Oliveira, M.V.G., Schmahl, W.W. & Schneider, A.S., 2023, 'Biocrystal assembly patterns, biopolymer distribution and material property relationships in *Mytilus galloprovincialis*, Bivalvia, and *Haliotis glabra*, Gastropoda, shells', *Materialia*, 28, 101749.
- Peters, B.H. & Campbell, A.C., 1987, 'Morphology of the nervous and muscular systems in the heads of pedicellariae from the sea urchin *Echinus esculentus* L', *Journal of Morphology*, 193(1), 35–51.
- Piez, K.A., 1961, 'Amino acid composition of some calcified proteins', *Science*, 134(3482), 841–842.
- Pineda, M.C., McQuaid, C.D., Turon, X., López-Legentil, S., Ordóñez, V. & Rius, M., 2012, 'Tough adults, frail babies: an analysis of stress sensitivity across early life-history stages of widely introduced marine invertebrates', T. Harder (ed.), *PLoS ONE*, 7(10), e46672.
- Plateau, F., 1883, 'Recherches sur la force absolue des muscles des Invertébrés: 2. Force absolue des muscles adducteurs des mollusques lamellibranches', *Bulletin de l'Académie Royale des Sciences, des Lettres et des Beaux-Arts de Belgique*, 6(9/10), 226–259.
- Plesch, B., 1976, 'Shell attachment in the pond snail *Lymnaea stagnalis* (L.)', *Cell and Tissue Research*, 171(3).
- Plotnick, R.E., 1990, 'Paleobiology of the arthropod cuticle', *Short Courses in Paleontology*, 3, 177–196.
- Politi, Y., Arad, T., Klein, E., Weiner, S. & Addadi, L., 2004, 'Sea urchin spine calcite forms via a transient amorphous calcium carbonate phase', *Science*, 306(5699), 1161–1164.
- Ponder, W.F., Lindberg, D.R. & Ponder, J.M., 2019, *Biology and Evolution of the Mollusca, Volume 1*, CRC Press.
- Popov, S.V., 2014, 'Formation of bivalve shells and their microstructure', *Paleontological Journal*, 48(14), 1519–1531.
- Poppe, G. & Goto, Y., 1993, *European Seashells, volume II (Scaphopoda, Bivalvia, Cephalopoda): 1-221*, ConchBooks, Wiesbaden.
- Porter, S.M., 2010, 'Calcite and aragonite seas and the de novo acquisition of carbonate skeletons: Calcite and aragonite seas and carbonate skeletons', *Geobiology*, 8(4), 256–277.
- Prezant, R.S., Dickinson, G.H., Chapman, E.J., Mugno, R., Rosen, M.N. & Cadmus, M.B., 2022, 'Comparative assessment of shell properties in eight species of cohabiting unionid bivalves', *Freshwater Mollusk Biology and Conservation*, 25(1).
- Qiao, L., Feng, Q.L. & Liu, Y., 2008, 'A novel bio-vaterite in freshwater pearls with high thermal stability and low dissolubility', *Materials Letters*, 62(12–13), 1793–1796.

- Rams, J., Plugaru, R. & Piqueras, J., 1999, 'Cathodoluminescence from mechanically cracked porous silicon', *Materials Science and Engineering: B*, 68(2), 126–129.
- Rathi, P.A., 2023, *Modes of carbonate crystal organization at muscle attachment sites of bivalve shells*, Master thesis, Ludwig-Maximilians-Universität, München.
- Raup, D.M., 1959, 'Crystallography of echinoid calcite', *The Journal of Geology*, 67(6), 661–674.
- Raup, D.M., 1960, 'Ontogenetic variation in the crystallography of echinoid calcite', *Journal of Paleontology*, 34(5), 1041–1050.
- Raup, D.M., 1962a, 'The phylogeny of calcite crystallography in echinoids', *Journal of Paleontology*, 36(4), 793–810.
- Raup, D.M., 1962b, 'Crystallographic data in echinoderm classification', *Systematic Zoology*, 11(3), 97.
- Raup, D.M., 1965, 'Crystal orientations in the echinoid apical system', *Journal of Paleontology*, 39(5), 934–951.
- Raut, H.K., Schwartzman, A.F., Das, R., Liu, F., Wang, L., Ross, C.A. & Fernandez, J.G., 2020, 'Tough and strong: Cross-lamella design imparts multifunctionality to biomimetic nacre', *ACS nano*, 14(8), 9771–9779.
- Reeve, L.A., 1847, *Monograph of the genus Chama.*, vol. 4, L. Reeve & Co., London.
- Reimer, L., 1985, 'Imaging with secondary and backscattered electrons', *Scanning Electron Microscopy*, Springer Series in Optical Sciences., vol. 45, pp. 227–271, Springer Berlin Heidelberg, Berlin, Heidelberg.
- Reindl, S., 1996, 'Arcoid and limopoid bivalves (Mollusca: Pteriomorpha)', *Veliger*, 39(2), 101–116.
- Reindl, S. & Haszprunar, G., 1996, 'Fine structure of caeca and mantle of arcoid and limopoid bivalves (Mollusca: Pteriomorpha)', *Veliger*, 39, 101–116.
- Renard, K. & Jacques, P.J., 2012, 'On the relationship between work hardening and twinning rate in TWIP steels', *Materials Science and Engineering: A*, 542, 8–14.
- Reynolds, D.J., Butler, P.G., Williams, S.M., Scourse, J.D., Richardson, C.A., Wanamaker, A.D., Austin, W.E.N., Cage, A.G. & Sayer, M.D.J., 2013, 'A multiproxy reconstruction of Hebridean (NW Scotland) spring sea surface temperatures between AD 1805 and 2010', *Palaeogeography, Palaeoclimatology, Palaeoecology*, 386, 275–285.
- Richardson, J.R., 1986, 'Brachiopods', *Scientific American*, 255(3), 100–107.
- Ritchie, R.O., 2011, 'The conflicts between strength and toughness', *Nature Materials*, 10(11), 817–822.
- Ritchie, R.O., 2021, 'Toughening materials: Enhancing resistance to fracture', *Philosophical Transactions of the Royal Society A: Mathematical, Physical and Engineering Sciences*, 379(2203), 20200437.
- Ritter, A.-C., Mavromatis, V., Dietzel, M., Kwiecien, O., Wiethoff, F., Griesshaber, E., Casella, L.A., Schmahl, W.W., Koelen, J., Neuser, R.D., Leis, A., Buhl, D., Niedermayr, A., Breitenbach, S.F.M., Bernasconi, S.M. & Immenhauser, A., 2017, 'Exploring the impact of diagenesis on (isotope) geochemical and microstructural alteration features in biogenic aragonite', S. Lokier (ed.), *Sedimentology*, 64(5), 1354–1380.
- Robinson, J., 2014, 'The muscles, body wall and valve-opening mechanism of extant craniid (inarticulated) brachiopods', *Journal of Natural History*, 48(21–22), 1231–1252.
- Rosenberg, G.D. & Hughes, W.W., 1991, 'A metabolic model for the determination of shell composition in the bivalve mollusc, *Mytilus edulis*', *Lethaia*, 24(1), 83–96.

- Rousseau, M., 2018, 'Nacre: A biomineral, a natural biomaterial, and a source of bio-inspiration', in S. Heuss-Assbichler, G. Amthauer & M. John (eds.), *Highlights in Applied Mineralogy*, pp. 285–300, De Gruyter, Berlin.
- Rowley, A.F., Coates, C.J. & Whitten, M.W. (eds.), 2022, *Invertebrate pathology*, Oxford University Press, Oxford.
- Rudwick, M.J.S., 1961, "'Quick" and "catch" adductor muscles in brachiopods', *Nature*, 191(4792), 1021–1021.
- Rudwick, M.J.S., 1970, *Living and fossil brachiopods*, Hutchinson Univ. Libr, London.
- Rüegg, J.C., 1971, 'Smooth muscle tone', *Physiological Reviews*, 51(1), 201–248.
- Runnegar, B., 1984, 'Crystallography of the foliated calcite shell layers of bivalve molluscs', *Alcheringa: An Australasian Journal of Palaeontology*, 8(4), 273–290.
- Runnegar, B. & Bentley, C., 1983, 'Anatomy, ecology and affinities of the Australian early cambrian bivalve *Pojetaia runnegari* Jell', *Journal of Paleontology*, 57(1), 73–92.
- Runnegar, B. & Pojeta, J., 1985, 'Origin and diversification of the Mollusca', *Evolution*, pp. 1–57, Elsevier.
- Ruska, E., 1987, 'The development of the electron microscope and of electron microscopy', *Reviews of modern physics*, 59(3), 627.
- Sakai, M. & Bradt, R.C., 1993, 'Fracture toughness testing of brittle materials', *International Materials Reviews*, 38(2), 53–78.
- Sakharova, N.A., Fernandes, J.V., Antunes, J.M. & Oliveira, M.C., 2009, 'Comparison between Berkovich, Vickers and conical indentation tests: A three-dimensional numerical simulation study', *International Journal of Solids and Structures*, 46(5), 1095–1104.
- Salas, C., Marina, P., Checa, A.G. & Rueda, J.L., 2012, 'The periostracum of *Digitaria digitaria* (Bivalvia: Astartidae): Formation and structure', *Journal of Molluscan Studies*, 78(1), 34–43.
- Salem, A.A., Kalidindi, S.R., Doherty, R.D. & Semiatin, S.L., 2006, 'Strain hardening due to deformation twinning in α -titanium: Mechanisms', *Metallurgical and Materials Transactions A*, 37(1), 259–268.
- Saleuddin, A.S.M. & Wilbur, K.M., 1983, 'The mode of formation and the structure of the periostracum', *The Mollusca*, pp. 199–234, Academic Press.
- Sanchez-Navas, A., Martin-Algarra, A., Sanchez-, M., Jimenez-Lopez, C., Nieto, F. & Ruiz-Bustos, A., 2013, 'Crystal growth of inorganic and biomediated carbonates and phosphates', in S.O. Ferreira (ed.), *Advanced Topics on Crystal Growth*, InTech.
- Sancho Vaquer, A., Griesshaber, E., Checa, A.G., Salas, C., Harper, E.M. & Schmahl, W.W., 2023, *Carbonate crystal microstructure and shape utilization for the formation of foliated, prismatic, vesicular and chalk calcite in Ostreoida shells.*, Conference abstract for Bivalves - Where are we going?
- Sancho Vaquer, A., Griesshaber, E., Salas Casanova, C., Harper, E.M., Checa, A.G. & Schmahl, W.W., 2025, 'The diversity of crystals that form Ostreoida shells: their size, morphology, and assembly characteristics', *Crystals*.
- Santhanam, R., 2018, *Biology and ecology of edible marine bivalve molluscs*, 1st edn., Apple Academic Press, Waretown.
- Saruwatari, K., Matsui, T., Mukai, H., Nagasawa, H. & Kogure, T., 2009, 'Nucleation and growth of aragonite crystals at the growth front of nacre in pearl oyster, *Pinctada fucata*', *Biomaterials*, 30(16), 3028–3034.
- Sato, K. & Sasaki, T., 2015, 'Shell microstructure of Protobranchia (Mollusca: Bivalvia): Diversity, new microstructures and systematic implications', *Malacologia*, 59(1), 45–103.

- Schäffer, T.E., Ionescu-Zanetti, C., Proksch, R., Fritz, M., Walters, D.A., Almqvist, N., Zaremba, C.M., Belcher, A.M., Smith, B.L., Stucky, G.D., & others, 1997, 'Does abalone nacre form by heteroepitaxial nucleation or by growth through mineral bridges?', *Chemistry of Materials*, 9(8), 1731–1740.
- Schindelin, J., Arganda-Carreras, I., Frise, E., Kaynig, V., Longair, M., Pietzsch, T., Preibisch, S., Rueden, C., Saalfeld, S., Schmid, B., Tinevez, J.-Y., White, D.J., Hartenstein, V., Eliceiri, K., Tomancak, P. & Cardona, A., 2012, 'Fiji: An open-source platform for biological-image analysis', *Nature Methods*, 9(7), 676–682.
- Schlotheuber Née Brunner, J.J., Maier, B., Kirner, F., Sturm, S., Cölfen, H. & Sturm, E.V., 2021, 'Self-assembled faceted mesocrystals: Advances in optimization of growth conditions', *Crystal Growth & Design*, 21(10), 5490–5495.
- Schmahl, W.W., Griesshaber, E., Kelm, K., Ball, A., Goetz, A.J., Xu, D., Kreitmeier, L. & Jordan, G., 2012a, 'Towards systematics of calcite biocrystals: Insight from the inside', *Zeitschrift für Kristallographie - Crystalline Materials*, 227(8), 604–611.
- Schmahl, W.W., Griesshaber, E., Kelm, K., Goetz, A., Jordan, G., Ball, A., Xu, D., Merkel, C. & Brand, U., 2012b, 'Hierarchical structure of marine shell biomaterials: biomechanical functionalization of calcite by brachiopods', *Zeitschrift für Kristallographie-Crystalline Materials*, 227(11), 793–804.
- Schmahl, W.W., Griesshaber, E., Neuser, R.D., Goetz, A.J. & Lüter, C., 2008, 'Electron backscatter diffraction study of brachiopod shell calcite – microscale phase and texture analysis of a polycrystalline biomaterial', *Particle & Particle Systems Characterization*, 25(5–6), 474–478.
- Schmahl, W.W., Sancho Vaquer, A., Checa, A.G. & Griesshaber, E., 2025a, 'The very specific texture motif of the oyster shell turbostratic foliated microstructure (Manuscript in preparation)'.
- Schmahl, W.W., Yin, X., Lastam, J., Griesshaber, E., Hoerl, S., Sturm, E. & Vaquer, A.S., 2025b, 'Statistical analysis of EBSD data confirms pronounced classical and non-classical pervasive crystallographic twinning in rotaliid foraminiferal calcite', *Scientific Reports*, 15(1), 14852.
- Schwartz, A.J., Kumar, M., Adams, B.L. & Field, D.P. (eds.), 2009, *Electron Backscatter Diffraction in Materials Science*, Springer US, Boston, MA.
- Sear, R.P., 2012, 'The non-classical nucleation of crystals: Microscopic mechanisms and applications to molecular crystals, ice and calcium carbonate', *International Materials Reviews*, 57(6), 328–356.
- Sear, R.P., 2014, 'Quantitative studies of crystal nucleation at constant supersaturation: Experimental data and models', *CrystEngComm*, 16(29), 6506–6522.
- Seilacher, A., 1979, 'Constructional morphology of sand dollars', *Paleobiology*, 5(3), 191–221.
- Semenoff Tian Chansky, P., 1974, 'Données nouvelles sur la microstructure de certains Tétracoralliaires', *Trudy Instituta Geologii i Geofiziki, Mosco*, 1, 132–144.
- Seto, J., Ma, Y., Davis, S.A., Meldrum, F., Gourrier, A., Kim, Y.-Y., Schilde, U., Sztucki, M., Burghammer, M., Maltsev, S., Jäger, C. & Cölfen, H., 2012, 'Structure-property relationships of a biological mesocrystal in the adult sea urchin spine', *Proceedings of the National Academy of Sciences*, 109(10), 3699–3704.
- Setoguchi, H., Okazaki, M. & Suga, S., 1989, 'Calcification in higher plants with special reference to cystoliths', in R.E. Crick (ed.), *Origin, Evolution, and Modern Aspects of Biomineralization in Plants and Animals*, pp. 409–418, Springer US, Boston, MA.
- Shadwick, R.E. & Gosline, J.M., 1983, 'Molecular biomechanics of protein rubbers in molluscs', *Metabolic Biochemistry and Molecular Biomechanics*, pp. 399–430, Elsevier.
- Shapkin, N.P., Khalchenko, I.G., Panasencko, A.E. & Drozdov, A.L., 2017, *Sea urchin skeleton: Structure, composition, and application as a template for biomimetic materials*, 020006, Depok, Jawa Barat, Indonesia.

- Sharma, N., Mondal, S., Ganguly, S. & Giri, A., 2023, 'Substrate- and life habit-induced morphological convergence and divergence in Recent marine bivalve communities', *Biological Journal of the Linnean Society*, 140(1), 120–129.
- Shi, G.R. & Shen, S., 2000, 'Asian-Western Pacific Permian brachiopoda in space and time: Biogeography and extinction patterns', *Developments in Palaeontology and Stratigraphy*, vol. 18, pp. 327–352, Elsevier.
- Shin, Y.A., Yin, S., Li, X., Lee, S., Moon, S., Jeong, J., Kwon, M., Yoo, S.J., Kim, Y.-M., Zhang, T., Gao, H. & Oh, S.H., 2016, 'Nanotwin-governed toughening mechanism in hierarchically structured biological materials', *Nature Communications*, 7(1), 10772.
- Shtukenberg, A.G., Punin, Y.O., Gunn, E. & Kahr, B., 2012, 'Spherulites', *Chemical Reviews*, 112(3), 1805–1838.
- Sigel, A., Sigel, H. & Sigel, R.K.O., 2008, *Biom mineralization: From nature to application*, John Wiley & sons, Chichester.
- Silva, F.R.S.D., Borges, A.L.D.O., Toldo Jr., E.E., Fick, C., Puhl, E., Oliveira, V.C.B. & Cruz, F.E.G.D., 2023, 'Threshold of motion and orientation of bivalve shells under current flow', *Brazilian Journal of Geology*, 53(1), e20220080.
- Silve, C., Lopez, E., Vidal, B., Smith, D.C., Camprasse, S., Camprasse, G. & Couly, G., 1992, 'Nacre initiates biomineralization by human osteoblasts maintained In Vitro', *Calcified Tissue International*, 51(5), 363–369.
- Silyn-Roberts, H. & Sharp, R.M., 1986, 'Crystal growth and the role of the organic network in eggshell biomineralization', *Proceedings of the Royal Society of London. Series B. Biological Sciences*, 227(1248), 303–324.
- Simkiss, K., 1988, 'Molluscan skin (excluding cephalopods)', *Form and Function*, pp. 11–35, Elsevier.
- Simkiss, K. & Wilbur, K.M., 1989, *Biom mineralization: cell biology and mineral deposition*, Academic press, San Diego New York Berkeley [etc.].
- Simonet Roda, M., Griesshaber, E., Angiolini, L., Rollion-Bard, C., Harper, E.M., Bitner, M.A., Milner Garcia, S., Ye, F., Henkel, D., Häussermann, V., & et al., 2022, 'The architecture of Recent brachiopod shells: diversity of biocrystal and biopolymer assemblages in rhynchonellide, terebratulide, thecideide and craniide shells', *Marine Biology*, 169(1).
- Simonet Roda, M., Griesshaber, E., Ziegler, A., Rupp, U., Yin, X., Henkel, D., Häussermann, V., Laudien, J., Brand, U. & Eisenhauer, A., 2019a, 'Calcite fibre formation in modern brachiopod shells', *Scientific Reports*, 9(1), 598.
- Simonet Roda, M., Ziegler, A., Griesshaber, E., Yin, X., Rupp, U., Greiner, M., Henkel, D., Häussermann, V., Eisenhauer, A., Laudien, J. & Schmahl, W.W., 2019b, 'Terebratulide brachiopod shell biomineralization by mantle epithelial cells', *Journal of Structural Biology*, 207(2), 136–157.
- Skic, A., Kołodziej, P., Stropek, Z., Beer-Lech, K., Drabik, K., Skic, K. & Branco, R., 2024, 'Analysis of the mechanical properties of femurs and eggshells of two selected Japanese quail lines under quasi-static and impact loading conditions', *Advances in Science and Technology Research Journal*, 18(7), 437–446.
- Skinner, A.F. & Weicker, N., 1992, 'ESR dating of *Chione cancellata* and *Chama sinuosa*', *Quaternary Science Reviews*, 11(1–2), 225–229.
- Smaal, A.C., Ferreira, J.G., Grant, J., Petersen, J.K. & Strand, Ø. (eds.), 2019, *Goods and services of marine bivalves*, Springer International Publishing, Cham.
- Smith, A.B., 1978, 'A functional classification of the coronal pores of regular echinoids', *Paleontology*, 21(4), 759–789.
- Smith, A.B., 1980, 'Stereom microstructure of the echinoid test', *Special Papers in Palaeontology*, 25(25), 1–81.

- Smith, A.B., 1991, 'Biomineralization in echinoderms', in J.G. Carter (ed.), *Skeletal Biomineralization: Patterns, Processes and Evolutionary Trends*, Springer US, Boston, MA.
- Smith, A.M., Freeman, D.F., Dixon-Anderson, I.S. & Lee, D.E., 2024, 'Review of skeletal carbonate mineralogy of brachiopods with new material from New Zealand', *New Zealand Journal of Marine and Freshwater Research*, 58(3), 498–529.
- Smolowitz, R., 2021, 'Mollusca: Bivalvia', in E.E.B. LaDouceur (ed.), *Invertebrate Histology*, 1st edn., pp. 163–183, Wiley.
- Song, F., Soh, A.K. & Bai, Y.L., 2003, 'Structural and mechanical properties of the organic matrix layers of nacre', *Biomaterials*, 24(20), 3623–3631.
- Spann, N., Harper, E.M. & Aldridge, D.C., 2010, 'The unusual mineral vaterite in shells of the freshwater bivalve *Corbicula fluminea* from the UK', *Naturwissenschaften*, 97(8), 743–751.
- Squire, J., 1992, 'The structures of striated and smooth muscles related to their function', *Muscle Contraction and Cell Motility: Molecular and Cellular Aspects*, pp. 87–131, Springer.
- Stanley, S.M., 1969, 'Bivalve mollusk burrowing aided by discordant shell ornamentation', *Science*, 166(3905), 634–635.
- Stanley, S.M., 1970, *Relation of shell form to life habits of the Bivalvia (Mollusca)*, vol. 125, Geological Society of America.
- Stanley, S.M., 1972, 'Functional morphology and evolution of byssally attached bivalve mollusks', *Journal of Paleontology*, 165–212.
- Stanley, S.M., 1975, 'Adaptive themes in the evolution of the Bivalvia (Mollusca)', *Annual Review of Earth and Planetary Sciences*, 3, 361.
- Stanley, S.M., 1981, 'Infaunal survival: alternative functions of shell ornamentation in the Bivalvia (Mollusca)', *Paleobiology*, 7(3), 384–393.
- Stauber, M. & Märkel, K., 1988, 'Comparative morphology of muscle-skeleton attachments in the Echinodermata', *Zoomorphology*, 108(3), 137–148.
- Stenzel, H.B., 1971, 'Oysters.', *Treatise on Invertebrate Paleontology, Part N, Bivalvia 3*, N953–N1224.
- Stevens, K., Griesshaber, E., Schmahl, W., Casella, L.A., Iba, Y. & Mutterlose, J., 2017, 'Belemnite biomineralization, development, and geochemistry: The complex rostrum of *Neohibolites minimus*', *Palaeogeography, Palaeoclimatology, Palaeoecology*, 468, 388–402.
- Stokesbury, K.D.E. & Himmelman, J.H., 1996, 'Experimental examination of movement of the giant scallop, *Placopecten magellanicus*', *Marine Biology*, 124, 651–660.
- Stokesbury, K.D.E., O'Keefe, C.E. & Harris, B.P., 2016, 'Fisheries sea scallop, *Placopecten magellanicus*', *Developments in Aquaculture and Fisheries Science*, vol. 40, pp. 719–736, Elsevier.
- Stolarski, J., Coronado, I., Murphy, J.G., Kitahara, M.V., Janiszewska, K., Mazur, M., Gothmann, A.M., Bouvier, A.-S., Marin-Carbonne, J., Taylor, M.L., Quattrini, A.M., McFadden, C.S., Higgins, J.A., Robinson, L.F. & Meibom, A., 2021, 'A modern scleractinian coral with a two-component calcite–aragonite skeleton', *Proceedings of the National Academy of Sciences*, 118(3), e2013316117.
- Stott, K.J., Austin, W.E.N., Sayer, M.D.J., Weidman, C.R., Cage, A.G. & Wilson, R.J.S., 2010, 'The potential of *Arctica islandica* growth records to reconstruct coastal climate in north west Scotland, UK', *Quaternary Science Reviews*, 29(13–14), 1602–1613.
- Strag, M., Maj, Ł., Bieda, M., Petrzak, P., Jarzębska, A., Gluch, J., Topal, E., Kutukova, K., Clausner, A., Heyn, W., Berent, K., Nalepka, K., Zschech, E., Checa, A.G. & Sztwiertnia, K., 2020, 'Anisotropy of mechanical properties of *Pinctada margaritifera* mollusk shell', *Nanomaterials*, 10(4), 634.

- Strathmann, R.R., 1981, 'The role of spines in preventing structural damage to echinoid tests', *Paleobiology*, 7(3), 400–406.
- Struve, A., 1898, 'Ein Beitrag zur Kenntnis des festen Gerüsts der Steinkorallen', *Russisch-Kaiserliche Mineralogische Gesellschaft zu St. Petersburg Verhandlungen (Series 2)*, 35, 43–115.
- Studart, A.R., 2012, 'Towards high-performance bioinspired composites', *Advanced Materials*, 24(37), 5024–5044.
- Studencka, B., 2018, 'A new look at the bivalve *Anomia ephippium* Linnaeus, 1758 from the Miocene of the Central Paratethys: An example from the Nowy Sacz Basin in Poland', *Acta geologica Polonica*, 68, 635–650.
- Su, X., Kamat, S. & Heuer, A.H., 2000, 'The structure of sea urchin spines, large biogenic single crystals of calcite', *Journal of Materials Science*, 35(22), 5545–5551.
- Sun, Y.-Y., Zhang, Q., Fan, L., Han, D.-D., Li, L., Yan, L. & Hou, P.-Y., 2022, 'Engineering the interface of organic/inorganic composite solid-state electrolyte by amino effect for all-solid-state lithium batteries', *Journal of Colloid and Interface Science*, 628, 877–885.
- Suzuki, M. & Nagasawa, H., 2013, 'Mollusk shell structures and their formation mechanism', *Canadian Journal of Zoology*, 91(6), 349–366.
- Suzuki, M., Nakayama, S., Nagasawa, H. & Kogure, T., 2013, 'Initial formation of calcite crystals in the thin prismatic layer with the periostracum of *Pinctada fucata*', *Micron*, 45, 136–139.
- Swaddiwudhipong, S., Hua, J., Tho, K.K. & Liu, Z.S., 2006, 'Equivalency of Berkovich and conical load-indentation curves', *Modelling and Simulation in Materials Science and Engineering*, 14(1), 71–82.
- Tang, S., Dong, Z., Ke, X., Luo, J. & Li, J., 2021, 'Advances in biomineralization-inspired materials for hard tissue repair', *International Journal of Oral Science*, 13(1), 42.
- Tatara, M.R., Charuta, A., Krupski, W., Łuszczewska-Sierakowska, I., Korwin-Kossakowska, A., Sartowska, K., Szpetnar, M. & Horbańczuk, J.O., 2015, 'Interrelationships between morphological, densitometric and mechanical properties of eggs in Japanese quails (*Coturnix japonica*)', *The Journal of Poultry Science*, 53(1), 51–57.
- Taylor, J., Kennedy, W. & Hall, A., 1969, 'The shell structure and mineralogy of the Bivalvia. Introduction. Nuculacea - Trigonacea', *Bulletin of the British Museum (Natural History), Zoology*, Supplement 3.
- Taylor, J., Kennedy, W. & Hall, A., 1973, 'The shell structure and mineralogy of the Bivalvia. II. Lucinacea-Clavagellacea, conclusions', *Bulletin of the British Museum (Natural History), Zoology*, 22, 255–294.
- Taylor, J. & Layman, M., 1972, 'The mechanical properties of bivalve (Mollusca) shell structures', *Palaeontology*, 15, 73–87.
- Taylor, J.D. & Kennedy, W.J., 1970, 'The shell structure and mineralogy of *Chama pellucida* Broderip', *The Veliger*, 11(4), 391–395.
- Taylor, P.D., Lombardi, C. & Cocito, S., 2015, 'Biomineralization in bryozoans: Present, past and future: Bryozoan biomineralization', *Biological Reviews*, 90(4), 1118–1150.
- Tebble, N., 1976, *British bivalve seashells: A handbook for identification*, 2nd edn., Royal Scottish Museum, Edinburgh.
- Teruel, J.D.D., Alcolea, A., Hernández, A. & Ruiz, A.J.O., 2015, 'Comparison of chemical composition of enamel and dentine in human, bovine, porcine and ovine teeth', *Archives of Oral Biology*, 60(5), 768–775.
- Tevesz, M.J.S. & McCall, P.L., 1979, 'Evolution of Substratum Preference in Bivalves (Mollusca)', *Journal of Paleontology*, 53(1), 112–120.
- Thayer, C.W., 1975, 'Diductor muscles of brachiopods: Active or passive?', *Paleobiology*, 1(1), 44–47.

- Thomas, R.D.K., 1975, 'Functional morphology, ecology, and evolutionary conservatism in the Glycymerididae (Bivalvia)', *Palaeontology*, 18, 217–254.
- Thomas, R.D.K., 1978, 'Shell form and the ecological range of living and extinct Arcoida', *Paleobiology*, 4(2), 181–194.
- Thomsen, J., Haynert, K., Wegner, K.M. & Melzner, F., 2015, 'Impact of seawater carbonate chemistry on the calcification of marine bivalves', *Biogeosciences*, 12(14), 4209–4220.
- Tompa, A.S. & Watabe, N., 1976, 'Ultrastructural investigation of the mechanism of muscle attachment to the gastropod shell', *Journal of Morphology*, 149(3), 339–351.
- Towe, K.M., 1967, 'Echinoderm calcite: Single crystal or polycrystalline aggregate', *Science*, 157(3792), 1048–1050.
- Tremblay, I. & Guderley, H.E., 2014, 'Scallops show that muscle metabolic capacities reflect locomotor style and morphology', *Physiological and Biochemical Zoology*, 87(2), 231–244.
- Tremblay, I. & Guderley, H.E., 2017, 'Possible prediction of scallop swimming styles from shell and adductor muscle morphology', *Journal of Shellfish Research*, 36(1), 17–30.
- Tremblay, I., Samson-Dô, M. & Guderley, H.E., 2015, 'When behavior and mechanics meet: Scallop swimming capacities and their hinge ligament', *Journal of Shellfish Research*, 34(2), 203–212.
- Trimby, P., Al-Mosawi, M., Al-Jawad, M., Micklethwaite, S., Aslam, Z., Winkelmann, A. & Piazzolo, S., 2024, 'The characterisation of dental enamel using transmission Kikuchi diffraction in the scanning electron microscope combined with dynamic template matching', *Ultramicroscopy*, 260, 113940.
- Troncoso, O.P., Torres, F.G., Arroyo, J., Gonzales, K.N., Fernández-García, M. & López, D., 2020, 'Mechanical properties of calcite- and aragonite-based structures by nanoindentation tests', *Bioinspired, Biomimetic and Nanobiomaterials*, 9(2), 112–121.
- Trotter, J., 1993, 'Functional morphology of force transmission in skeletal muscle: A brief review', *Cells Tissues Organs*, 146(4), 205–222.
- Trotter, J., Kadler, K. & Holmes, D., 2000, 'Echinoderm collagen fibrils grow by surface-nucleation-and-propagation from both centers and ends', *Journal of molecular biology*, 300(3), 531–540.
- Trueman, E., 1966, 'The fluid dynamics of the bivalve molluscs, *Mya* and *Margaritifera*', *Journal of Experimental Biology*, 45(2), 369–382.
- Trueman, E.R., 1983, 'Locomotion in molluscs', *The Mollusca*, pp. 155–198, Elsevier.
- Trueman, E.R., Brand, A.R. & Davis, P., 1966, 'The dynamics of burrowing of some common littoral bivalves', *Journal of Experimental Biology*, 44(3), 469–492.
- Tsafnat, N., Fitz Gerald, J.D., Le, H.N. & Stachurski, Z.H., 2012, 'Micromechanics of sea urchin spines', C.M. Aegerter (ed.), *PLoS ONE*, 7(9), e44140.
- Tyler, P.A. & Gage, J.D., 1984, 'The reproductive biology of echinothuriid and cidarid sea urchins from the deep sea (Rockall Trough, North-East Atlantic Ocean)', *Marine Biology*, 80(1), 63–74.
- Ubukata, T., 1994, 'Architectural constraints on the morphogenesis of prismatic structure in Bivalvia', *Paleontology*, 37(2), 241–261.
- Ubukata, T., 2005, 'Theoretical morphology of bivalve shell sculptures', *Paleobiology*, 31(4), 643–655.
- Ullah, H., Khan, R.U. & Silberschmidt, V.V., 2024, 'Assessing pseudo-ductile behavior of woven thermoplastic composites under tension and bending', *Composites Science and Technology*, 248, 110465.

- Uttam, P., Kumar, V., Kim, K.-H. & Deep, A., 2020, 'Nanotwinning: Generation, properties, and application', *Materials & Design*, 192, 108752.
- Vance, R.R., 1978, 'A mutualistic interaction between a sessile marine clam and its epibionts', *Ecology*, 59(4), 679–685.
- Varkoulis, A., Voulgaris, K., Zaoutsos, S., Stratakis, A. & Vafidis, D., 2020, 'Chemical composition and microstructural morphology of spines and tests of three common sea urchins species of the sublittoral zone of the Mediterranean Sea', *Animals*, 10(8), 1351.
- Veis, A., 2005, 'A window on biomineralization', *Science*, 307(5714), 1419–1420.
- Vekilov, P.G., 2010, 'The two-step mechanism of nucleation of crystals in solution', *Nanoscale*, 2(11), 2346.
- Vendrasco, M., Porter, S., Kouchinsky, A., Li, G. & Fernandez, C., 2010, 'Shell microstructures in early mollusks', *Festivus*, 42.
- Venier, P., Gerdol, M., Domeneghetti, S., Sharma, N., Pallavicini, A. & Rosani, U., 2019, 'Biotechnologies from marine bivalves', *Goods and Services of Marine Bivalves*, pp. 95–112, Springer, Cham.
- Vermeij, G.J., 1977, 'The mesozoic marine revolution: Evidence from snails, predators and grazers', *Paleobiology*, 3(3), 245–258.
- Verween, A., Vincx, M. & Degraer, S., 2007, 'The effect of temperature and salinity on the survival of *Mytilopsis leucophaeata* larvae (Mollusca, Bivalvia): The search for environmental limits', *Journal of Experimental Marine Biology and Ecology*, 348(1–2), 111–120.
- Vidavsky, N., Addadi, S., Schertel, A., Ben-Ezra, D., Shpigel, M., Addadi, L. & Weiner, S., 2016, 'Calcium transport into the cells of the sea urchin larva in relation to spicule formation', *Proceedings of the National Academy of Sciences*, 113(45), 12637–12642.
- Vinn, O., Holmer, L.E. & Wilson, M.A., 2024, 'Evolution of brachiopod symbiosis in the early Paleozoic', *Historical Biology*, 36(7), 1274–1294.
- Volmer, M. & Weber, A., 1926, 'Keimbildung in übersättigten Gebilden', *Zeitschrift für Physikalische Chemie*, 119U(1), 277–301.
- Voultsiadou, E., Koutsoubas, D. & Achparaki, M., 2010, 'Bivalve mollusc exploitation in Mediterranean coastal communities: An historical approach', *Journal of Biological Research*, 13, 35–45.
- Vyatchin, I. & Dyachuk, V., 2025, 'The unique biology of catch muscles: Insights into structure, function, and robotics innovations', *Frontiers in Bioengineering and Biotechnology*, 13, 1478626.
- Wählich, F.C., Peter, N.J., Abad, O.T., Oliveira, M.V.G., Schneider, A.S., Schmahl, W., Griesshaber, E. & Bennewitz, R., 2014, 'Surviving the surf: The tribomechanical properties of the periostracum of *Mytilus* sp.', *Acta biomaterialia*, 10(9), 3978–3985.
- Wainwright, S.A., 1982, *Mechanical design in organisms*, Princeton University Press.
- Wang, J. & Zhang, X., 2016, 'Twinning effects on strength and plasticity of metallic materials', *MRS Bulletin*, 41(4), 274–281.
- Wang, J.T., Yin, D.L., Liu, J.Q., Tao, J., Su, Y.L. & Zhao, X., 2008, 'Effect of grain size on mechanical property of Mg–3Al–1Zn alloy', *Scripta Materialia*, 59(1), 63–66.
- Wang, R.Z., Addadi, L. & Weiner, S., 1997, 'Design strategies of sea urchin teeth: Structure, composition and micromechanical relations to function', *Philosophical Transactions of the Royal Society of London. Series B: Biological Sciences*, 352(1352), 469–480.

- Wang, X., Li, L., Zhu, Y., Song, X., Fang, X., Huang, R., Que, H. & Zhang, G., 2014, 'Aragonite shells are more ancient than calcite ones in bivalves: new evidence based on omics', *Molecular biology reports*, 41, 7067–7071.
- Wang, Y., Liu, Q., Lan, Z.-F., Zhang, B., Zhang, H.-Q., Liu, J.-W. & Ye, F., 2021, 'Strong and tough bioinspired nacre-like B₄C/Al functionally graded materials with eliminated abrupt interfaces', *Composites Communications*, 25, 100741.
- Watabe, N., 1983, 'Shell repair', *The Mollusca*, pp. 289–316, Elsevier.
- Watt, G.R., Wright, P., Galloway, S. & McLean, C., 1997, 'Cathodoluminescence and trace element zoning in quartz phenocrysts and xenocrysts', *Geochimica et Cosmochimica Acta*, 61(20), 4337–4348.
- Weber, J.N., 1969, 'The incorporation of magnesium into the skeletal calcites of echinoderms', *American Journal of Science*, 267(5), 537–566.
- Wehrmeister, U., Jacob, D.E., Soldati, A.L., Loges, N., Häger, T. & Hofmeister, W., 2011, 'Amorphous, nanocrystalline and crystalline calcium carbonates in biological materials: Amorphous, nanocrystalline and crystalline calcium carbonates in biological materials', *Journal of Raman Spectroscopy*, 42(5), 926–935.
- Weiner, S. & Addadi, L., 1997, 'Design strategies in mineralized biological materials', *Journal of Materials Chemistry*, 7(5), 689–702.
- Weiner, S. & Addadi, L., 2011, 'Crystallization pathways in biomineralization', *Annual Review of Materials Research*, 41(1), 21–40.
- Weiner, S. & Dove, P.M., 2003, 'An overview of biomineralization processes and the problem of the vital effect', *Reviews in Mineralogy and Geochemistry*, 54(1), 1–29.
- Weiner, S. & Lowenstam, H., 1986, 'Organization of extracellularly mineralized tissues: A comparative study of biological crystal growth', *Critical Reviews in Biochemistry*, 20(4), 365–408.
- Wejnert, K.E. & Smith, A.M., 2008, 'Within-colony variation in skeletal mineralogy of *Adeonellopsis* sp. (Cheilostomata: Bryozoa) from New Zealand', *New Zealand Journal of Marine and Freshwater Research*, 42(4), 389–395.
- Wernström, J.V., Gąsiorowski, L. & Hejnol, A., 2022, 'Brachiopod and mollusc biomineralisation is a conserved process that was lost in the phoronid–bryozoan stem lineage', *EvoDevo*, 13(1), 17.
- Wilkens, J.L., 1978, 'Adductor muscles of brachiopods: Activation and contraction', *Canadian Journal of Zoology*, 56(2), 315–323.
- Wilkins, N., 1976, 'Genetic variability in marine Bivalvia: Implications and applications in molluscan mariculture'.
- Wilkinson, A.J., Meaden, G. & Dingley, D.J., 2006, 'High-resolution elastic strain measurement from electron backscatter diffraction patterns: New levels of sensitivity', *Ultramicroscopy*, 106(4–5), 307–313.
- Williams, A., Ager, D.V., Grant, R.E., Rowell, A.J., Stehli, F.G., Muir-Wood, H.M. & Elliott, G.F., 1965, 'Part H, Brachiopoda', in R.C. Moore (ed.), *Treatise on Invertebrate Paleontology*, vol. 1, The Geological Society of America & University of Kansas.
- Williams, A., Cohen, B.L., Cusack, M. & Long, S.L., 2000, 'Provenance of Atlantic lingulid brachiopods', *Palaeontology*, 43(6), 999–1018.
- Wilmot, N.V., Barber, D.J., Taylor, J.D. & Graham, A.L., 1992, 'Electron microscopy of molluscan crossed-lamellar microstructure', *Philosophical Transactions of the Royal Society of London. Series B: Biological Sciences*, 337(1279), 21–35.

- Wilt, F.H., 1999, 'Matrix and mineral in the sea urchin larval skeleton', *Journal of Structural Biology*, 126(3), 216–226.
- Wilt, F.H., 2002, 'Biomineralization of the spicules of sea urchin embryos', *Zoological Science*, 19(3), 253–261.
- Wilt, F.H., 2005, 'Developmental biology meets materials science: Morphogenesis of biomineralized structures', *Developmental Biology*, 280(1), 15–25.
- Wilt, F.H., Killian, C.E. & Livingston, B.T., 2003, 'Development of calcareous skeletal elements in invertebrates', *Differentiation*, 71(4–5), 237–250.
- Winkelmann, A., Jablon, B.M., Tong, V.S., Trager-Cowan, C. & Mingard, K.P., 2020, 'Improving EBSD precision by orientation refinement with full pattern matching', *Journal of Microscopy*, 277(2), 79–92.
- Wombacher, F., Eisenhauer, A., Böhm, F., Gussone, N., Regenberg, M., Dullo, W.-C. & Rüggeberg, A., 2011, 'Magnesium stable isotope fractionation in marine biogenic calcite and aragonite', *Geochimica et Cosmochimica Acta*, 75(19), 5797–5818.
- Wood, R., 2018, 'Exploring the drivers of early biomineralization', T.W. Lyons, M.L. Droser, K.V. Lau & S.M. Porter (eds.), *Emerging Topics in Life Sciences*, 2(2), 201–212.
- Wood, R., Ivantsov, A.Y. & Zhuravlev, A.Y., 2017, 'First macrobiota biomineralization was environmentally triggered', *Proceedings of the Royal Society B: Biological Sciences*, 284(1851), 20170059.
- Wright, S.I., Nowell, M.M. & Field, D.P., 2011, 'A review of strain analysis using electron backscatter diffraction', *Microscopy and Microanalysis*, 17(3), 316–329.
- Wu, L., Li, L., Zhou, L., Zhang, T., Liu, Z., Chen, L., Wu, B., Jing, H. & Sun, X., 2022, 'Phalloidin fluorescence and confocal microscopy reveal the musculature development of clam *Ruditapes philippinarum*', *Comparative Biochemistry and Physiology Part B: Biochemistry and Molecular Biology*, 258, 110693.
- Xu, J. & Zhang, G., 2014, 'Biogenic nanospheres of amorphous carbonated Ca–Mg phosphate within the periostracum of the green mussel *Perna viridis*', *Journal of Structural Biology*, 188(3), 205–212.
- Xu, Q., Zheng, J., Yan, X. & Nie, H., 2020, 'Genetic diversity and differentiation of nine populations of the hard clam (*Meretrix petechialis*) assessed by EST-derived microsatellites', *Electronic Journal of Biotechnology*, 48, 23–28.
- Yamaguchi, T. & Kanazawa, K., 2009, 'Plate construction of the spatangoid test', in L. Harris, S. Böttger, C. Walker & M. Lesser (eds.), *Echinoderms: Durham: Proceedings of the 12th International Echinoderm Conference, 7-11 August 2006, Durham, New Hampshire, U.S.A.*, CRC Press.
- Yang, T., Chen, H., Jia, Z., Deng, Z., Chen, L., Peterman, E.M., Weaver, J.C. & Li, L., 2022a, 'A damage-tolerant, dual-scale, single-crystalline microlattice in the knobby starfish, *Protoreaster nodosus*', *Science*, 375(6581), 647–652.
- Yang, T., Jia, Z., Wu, Z., Chen, H., Deng, Z., Chen, L., Zhu, Y. & Li, L., 2022b, 'High strength and damage-tolerance in echinoderm stereom as a natural bicontinuous ceramic cellular solid', *Nature Communications*, 13(1), 6083.
- Yao, S., Jin, B., Liu, Z., Shao, C., Zhao, R., Wang, X. & Tang, R., 2017, 'Biomineralization: From material tactics to biological strategy', *Advanced Materials*, 29(14), 1605903.
- Yao, S., Li, H., Pang, S., Zhu, B., Zhang, X. & Fatikow, S., 2021, 'A review of computer microvision-based precision motion measurement: Principles, characteristics, and applications', *IEEE Transactions on Instrumentation and Measurement*, 70, 1–28.
- Yao, Z., Xia, M., Li, H., Chen, T., Ye, Y. & Zheng, H., 2014, 'Bivalve shell: Not an abundant useless waste but a functional and versatile biomaterial', *Critical Reviews in Environmental Science and Technology*, 44(22), 2502–2530.

- Ye, F., Bitner, M.A. & Shi, G.R., 2023, 'Variation of shell ornamentation with latitude and water depth—A case study using living brachiopods', *Ecology and Evolution*, 13(4), e10006.
- Ye, F., Jurikova, H., Angiolini, L., Brand, U., Crippa, G., Henkel, D., Laudien, J., Hiebenthal, C. & Šmajgl, D., 2019, 'Variation in brachiopod microstructure and isotope geochemistry under low-pH-ocean acidification conditions', *Biogeosciences*, 16(2), 617–642.
- Yin, X., 2020, *Biological and biomimetic mineralization of calcium carbonate* – PhD thesis, Ludwig-Maximilians-Universität, München.
- Yin, X., Griesshaber, E., Checa, A., Nindiyasari-Behal, F., Sánchez-Almazo, I., Ziegler, A. & Schmahl, W.W., 2021, 'Calcite crystal orientation patterns in the bilayers of laminated shells of benthic rotaliid foraminifera', *Journal of Structural Biology*, 213(2), 107707.
- Yin, X., Griesshaber, E., Fernández-Díaz, L., Ziegler, A., García-García, F.J. & Schmahl, W.W., 2019, 'Influence of gelatin-agarose composites and Mg on hydrogel-carbonate aggregate formation and architecture', *Crystal Growth & Design*, 19(10), 5696–5715.
- Ying, X., Barlow, N.J. & Tatiparthi, A., 2022, 'Micro-CT and volumetric imaging in developmental toxicology', *Reproductive and Developmental Toxicology*, pp. 1261–1285, Elsevier.
- Yonge, C.M., 1973, 'Functional morphology with particular reference to hinge and ligament in *Spondylus* and *Plicatula* and a discussion on relations within the superfamily Pertinacea (Mollusca: Bivalvia)', *Philosophical Transactions of the Royal Society of London. B, Biological Sciences*, 267(883), 173–208.
- Yonge, C.M., 1978, 'Significance of the ligament in the classification of the Bivalvia', *Proceedings of the Royal Society of London. Series B, Biological Sciences*, 202(1147), 231–248.
- Yonge, M., 1967, 'Form, habit and evolution in the Chamidae (Bivalvia) with reference to conditions in the rudists (Hippuritacea)', *Philosophical Transactions of the Royal Society of London. Series B, Biological Sciences*, 252(775), 49–105.
- Yu, H.-P. & Zhu, Y.-J., 2024, 'Guidelines derived from biomineralized tissues for design and construction of high-performance biomimetic materials: From weak to strong', *Chemical Society Reviews*, 53(9), 4490–4606.
- Zaefferer, S., 2011, 'A critical review of orientation microscopy in SEM and TEM', *Crystal Research and Technology*, 46(6), 607–628.
- Zange, J., Pörtner, H.-O. & Grieshaber, M.K., 1989, 'The anaerobic energy metabolism in the anterior byssus retractor muscle of *Mytilus edulis* during contraction and catch', *Journal of Comparative Physiology B*, 159(3), 349–358.
- Zhang, G., Brion, A., Willemin, A., Piet, M., Moby, V., Bianchi, A., Mainard, D., Galois, L., Gillet, P. & Rousseau, M., 2017a, 'Nacre, a natural, multi-use, and timely biomaterial for bone graft substitution', *Journal of Biomedical Materials Research Part A*, 105(2), 662–671.
- Zhang, L., Wang, Q., Liao, W., Guo, W., Ye, B., Li, W., Jiang, H. & Ding, W., 2017b, 'Effects of cyclic extrusion and compression on the microstructure and mechanical properties of AZ91D magnesium composites reinforced by SiC nanoparticles', *Materials Characterization*, 126, 17–27.
- Zhang, Z., Zhang, L., Li, C., Xie, X., Li, G., Hu, Z. & Li, S., 2021, 'Research progress of chitosan-based biomimetic materials', *Marine Drugs*, 19(7), 372.
- Zhang, Z., Zhang, Z., Holmer, L.E., Topper, T.P., Pan, B. & Li, G., 2023, *Diversity and evolutionary growth of biomineralized columns in early Cambrian phosphatic-shelled brachiopods*.
- Zhao, C., Ren, L., Liu, Q. & Liu, T., 2015, 'Morphological and confocal laser scanning microscopic investigations of the adductor muscle-shell interface in scallop: Morphological and CLSM investigations', *Microscopy Research and Technique*, 78(9), 761–770.

- Zhao, H., Liu, S., Yang, X. & Guo, L., 2022, 'Role of inorganic amorphous constituents in highly mineralized biomaterials and their imitations', *ACS Nano*, 16(11), 17486–17496.
- Zhao, Y., Han, Z., Yan, H., Zhao, H., Tucker, M.E., Gao, X., Guo, N., Meng, R. & Owusu, D.C., 2021, 'Selective adsorption of amino acids in crystals of monohydrocalcite induced by the facultative anaerobic enterobacter ludwigii SYB1', *Frontiers in Microbiology*, 12, 696557.
- Ziegler, A., Schröder, L., Ogurreck, M., Faber, C. & Stach, T., 2012, 'Evolution of a novel muscle design in sea urchins (Echinodermata: Echinoidea)', P.J. Planet (ed.), *PLoS ONE*, 7(5), e37520.

APPENDICES

A.1 TERMINOLOGY

A.1.1 STRUCTURAL AND CRYSTALLOGRAPHIC TERMINOLOGY

Subsequently, I define the structural and nanomechanical property terms that I use in this study. For further information concerning electron backscatter diffraction (EBSD), see Schwartz et al. (2009), for crystal twin formation see Griesshaber et al. (2013), Hahn & Klapper (2013) and Kogure et al. (2014). For further information concerning nanoindentation testing, see (Fischer-Cripps & Nicholson 2004).

EBSD analysis and evaluation

Microstructure refers to the sizes, morphologies, co- and misorientations, and modes of interlinkage of grains in a material. It is shown with coloured EBSD maps, where similar colours reflect similar crystal orientations and different colours highlight differences in crystal orientation. The acquisition coordinate system is indicated in the a-axes pole figures in Figs. 1a, b and is consistent for all EBSD scans presented in this contribution.

Pole figures are stereographic projections of crystallographic axes orientations measured for all pixels of an EBSD map or selected areas (subsets). The viewing direction of the pole figures is the same as the viewing direction of the corresponding EBSD maps. All pole figures shown here display the lower hemisphere. Showing data points on the lower hemisphere of the stereographic projection ensures that the pole figures are displayed in the same spatial orientation as the corresponding EBSD map. With pole figures I either show individual orientation data points or the density distributions of the orientation data.

Texture or crystallographic preferred orientation relates to the distribution of all crystal orientations within a material. It is illustrated with pole figures which show either the colour-coded orientation data or the contoured version of the density distribution of the a-, b-, and c-axes poles.

Crystal co-orientation statistics is derived from Kikuchi patterns measured at each pixel of an EBSD map. The degree of aragonite/calcite co-orientation within individual crystals is obtained from measurements of the orientational density distribution, the multiple of uniform (random) distribution (MUD) value, the Euler angles or texture component analysis.

The MUD value is calculated by the CHANNEL 5 EBSD software and is an indication of the strength of crystal co-orientation. A high MUD indicates high crystal co-orientation and low MUD values indicate low to random crystallite and/or mineral unit co-orientation. The parameters for data contouring in the pole figures were fixed to a half width of 5 and a cluster size of 3, to maintain

comparability for all measurements shown in this contribution. For a half width of 5 and a cluster size of 3, an MUD value above 700 indicates single-crystallinity, and an MUD value of 1 indicates polycrystallinity. The given MUD values indicate the crystal co-orientation strength for the described section or subset of an EBSD scan and do not apply to the entire volume of a microstructure.

The three orthogonal Euler angles describe the spatial orientation of a crystal in a three-dimensional space. As each angle corresponds to an elemental rotation in the coordinate system, the combination of the three angles can be used to understand the orientation of a crystal. The degree of correlation of Euler angles across a grain or microstructure can be used to describe and compare its co-orientation. This method is described in more detail in Britton et al. (2016).

Texture component analysis compares all measured data points with a reference texture which can be defined via Euler angles, plane and direction or fibre axis. The calculated texture components can be displayed as a map or as a misorientation angle diagram. Texture component analysis is particularly useful for characterising small-angle misorientations, but is also useful for polycrystalline materials (e.g., Boehm-Courjault et al. 2009)

The EBSD band contrast map depicts the signal strength of the Kikuchi pattern at each measurement point in the EBSD scan. It is displayed as a grey-scale component in the map; white to light grey colours indicate a high intensity of the Kikuchi signal, corresponding to strong mineralization, dark grey and black colours point to a weak or absent Kikuchi signal, e.g. when organic matter is scanned.

Grain size statistics are determined via the AZtecCrystal 3.0 software. The bar charts display the area-weighted fractions. For mean value calculations, pseudosymmetries and wild spikes were filtered and border grains were included.

Crystallographic twinning

Twinned crystals are entities in which adjacent crystals of the same phase are intergrown in a regularly recurring orientation relationship. These crystal orientation states are addressed as the twin domains of a twinned crystal. A regular planar interface of two twin domains is called the composition plane and such a twin is called a contact twin. If the interface is not confined to a plane (or planes), the twin is called a penetration twin. Twinning can occur during the initial growth of the crystal, or, it might take place after its formation, resulting from stress or phase transformation. The orientation relationship for the characteristic twin in question is called the twin law.

If a twinned entity contains domains of two orientation states, alternating in succession, it is called a *polysynthetic twin*. In biological materials, such twins do not show perfectly planar and parallel composition planes, as would be required by the definition of Hahn and Klapper (2013), who, however, focused only on inorganic materials.

If a twinned entity contains three intergrown domains that are related by a twin law consisting of mirror operations on (110) and ($\bar{1}10$), then it is called a *cyclic twin*.

If a twinned entity contains three intergrown domains that are related by a twin law consisting of mirror operations on (110) and ($\bar{1}10$), then it is called a *cyclic twin*. If these three orientation states occur multiple times within an entity as striations or fine parallel lines, I term the twinned crystal a *polycyclic twin*.

In this work, the presence of twinned aragonite is proved via the specific misorientation boundary of the twin law. For calcite, the misorientation at the twin boundary is around 60°. For aragonite, the misorientation at the twin boundary is around 64°. For this misorientation angle, characteristic peaks shown in the misorientation angle distribution diagram indicate the presence and frequency of twinning. The presence of twinned aragonite is also indicated by specific crystal misorientations in the corresponding pole figures.

A.1.2 BIOLOGICAL TERMINOLOGY

Here, biological terms for the different biomineralised hard tissues featuring in this work are defined. In-depth analyses provide additional information about bivalve shells (Taylor et al. 1969; Taylor et al. 1973), brachiopod shells (Williams et al. 1965; James et al. 1992) and sea urchin skeletal elements (Smith 1980; Ebert 2007; Förster 2020).

Biological convergence is the process by which unrelated or distantly related organisms develop similar traits or characteristics independently. This happens because these organisms face similar requirements due to their lifestyle, environmental conditions, or ecological roles that require similar solutions, leading to the natural selection of comparable adaptations.

In evolutionary biology, a conservative trait is relatively slow to change over evolutionary time and is similar across different species that share a common ancestor. Closely related species tend to resemble each other in that trait. That trait is either under strong stabilising selection or has a low rate of evolution, leading to its persistence within lineages. Examples of conservative traits include certain morphological features, physiological processes, or behavioural patterns that have remained relatively stable over long periods of evolutionary history.

Bivalved invertebrate shells

The shell surface of many *Chama* bivalves is covered with calcium carbonate ornamentations. These are developed as ribs and are thin spicule- to blade-shaped hard tissue protrusions that are often arranged on the surface of the shell in an ordered pattern (Yonge 1967; Kennedy et al. 1970).

In recent rhynchonellate brachiopods and bivalves, two main types of muscle fibres can be differentiated (MacKinnon 1977; Chantler 1983). The twitch-type striated muscles, causing quick, incomplete closure, feature small muscle cells that interconnect in a banded pattern at a small angle to the fibre axis. In contrast, smooth muscles comprise distinct units of unstriated, separated fibrils that contract slowly and shut the valves. Compared to bivalves, this delayed relaxation or catch mechanism is much weaker in the rhynchonellates (Wilkins 1978; Ackerly 1991).

Sea urchin skeletal elements

The stereom is a crystallised calcium carbonate (in fact, high-Mg calcite) material with a sponge-like structure and appears in modern and fossil echinoderms, such as sea urchin tests and spines. The stereom consists of a mesh of thin cylindrical columns, the *trabeculae*. The stereom has different architectures; it can be rectilinear (trabeculae arranged perpendicular to each other), galleried (interconnected trabeculae arranged parallel to each other, running in one direction only), or labyrinthic (matrix pervaded by ovoid interconnecting pores without internal alignment). Trabecular extensions are thin nodes of trabecular columns that run parallel to the morphological long axis of spines and traverse the cortex layer. Ambulacral test regions are elongated areas of a test in which the sea urchin tube feet are arranged; interambulacral regions are test sections between ambulacra.

Tubercles are ball-and-socket joints forming the attachment sites for spines and pedicellariae to the test plate. They consist of the basal boss, the stereom region adjacent to the test, and a terminal knob, the outermost tubercular stereom section. Pedicellariae are highly evolved and membranous outgrowths connected to the external test surface, where they form the jaws with their pincer-like morphology. Spines are protective mineralised appendages, with the primary spines being long and large and the secondary spines being small. The medulla of a spine is the stereom section that forms the central, co-oriented, portion of the spine. The cortex of the spine is the layer that externally encases the medulla from the shaft to the top.

A.2 INVESTIGATED SAMPLES AND SAMPLE PREPARATION

A.2.1 INVESTIGATED SAMPLES

A.2.1.1 BIVALVE SAMPLES

As mentioned in previous chapters, the class Bivalvia comprises a large variety of species with a high genetic variation and global diversification, especially following the Late Permian mass extinction (Wilkins 1976; Miller & Sepkoski 1988; Xu et al. 2020). Within the molluscan phylum, bivalves are the second most species-rich class after the gastropods (Hughes 1986; Mikkelsen 2011; Bieler et al. 2013). Their widespread distribution is not due to allopatric isolation but rather because of the high gene flow between bivalve populations, as explained by the Marine Speciation Paradox (Bierne et al. 2003; Mikkelsen 2011). Bivalves have occupied a variety of global habitats and can sustain extreme conditions such as the polar seas or abyssal marine regions (Norkko et al. 2005; Krylova et al. 2015; Kamenev et al. 2022; Iglukowska et al. 2023). The following table A.2.1 summarises the bivalve species investigated in this study and illustrates their family relationships.

Table A.2.1. Summary of all bivalve species investigated in this study. The species that are reported in this study are in bold. This table assumes the geographical differentiation between *C. arcana* and *C. pellucida*, recently reported by Harper & Checa (2017).

Order	Family	Species
Arcida	Arcidae	<i>Anadara gibbosa</i>
	Glycymerididae	<i>Glycymeris glycymeris</i>
		<i>Glycymeris nummaria</i>
		<i>Glycymeris pilosa</i>
		<i>Glycymeris bimaculata</i>
Anomalodesmata	Poromyidae	<i>Poromya granulata</i>
Cardiida	Cardiidae	<i>Acanthocardia tuberculata</i>
Carditida	Astartidae	<i>Astarte fusca</i>
		<i>Digitaria digitaria</i>
	Carditidae	<i>Cardita calyculata</i>

Mytilida	Mytilidae	<i>Mytilus edulis</i>
Nuculida	Nuculidae	<i>Nucula nucleus</i>
Ostreida	Pinnidae	<i>Atrina serrata</i>
		<i>Atrina vexillum</i>
		<i>Pinna nobilis</i>
	Ostreidae	<i>Ostrea stentina</i>
	Pteriidae	<i>Pteria penguin</i>
Pectinida	Anomiidae	<i>Anomia ephippium</i>
	Pectinidae	<i>Pecten maximus</i>
		<i>Placopecten magellanicus</i>
		<i>Placopecten yessoensis</i>
Tellinoidea	Tellinidae	<i>Tellina planata</i>
Venerida	Arcticidae	<i>Arctica islandica</i>
	Chamidae	<i>Chama arcana</i>
		<i>Chama gryphoides</i>
	Veneridae	<i>Dosinia scalaris</i>
		<i>Periglypta puerpera</i>
		<i>Timoclea ovata</i>
Unionida	Unionidae	<i>Elliptio crassidens</i>
		<i>Lampsilis cardium</i>

A.2.1.2 OTHER BIOLOGICAL CALCIUM CARBONATE SAMPLES

The EBSD pattern-matching method enables us to re-examine the microstructural properties and single-crystal character of various biological carbonate hard tissues. Not only does this method allow for significantly lower orientation precision, but it also enables a consistent analysis of small-angle misorientation patterns within a wide variety of biological microstructures. Table A.2.2 compiles the non-bivalve biological hard tissues that were evaluated in the present study.

Table A.2.2. Summary of all non-bivalve species and their type of investigated biological hard tissue that featured in this study. The species reported in this study via EBSD and/or other methods are highlighted in bold letters.

Phylum	Order	Species	Investigated hard tissue
Brachiopoda	Terebratulida	<i>Magellania venosa</i>	Shell and muscle scar
		<i>Gryphus vitreus</i>	Shell and muscle scar
		<i>Liothyrella neozelanica</i>	Shell and muscle scar
Echinodermata	Cidaroida	<i>Cidaris cidaris</i>	Sea urchin test and spines
	Camarodonta	<i>Paracentrotus lividus</i>	Sea urchin test and spines
		<i>Heterocentrotus mamillatus</i>	Sea urchin test and spines
	Arbacioida	<i>Arbacia lixula</i>	Sea urchin test and spines
		<i>Coelopleurus maillardi</i>	Sea urchin test and spines
	Spatangoida	<i>Echinocardium cordatum</i>	Sea urchin test
	Clypeasteroida	<i>Clypeaster reticulatus</i>	Sea urchin test
		<i>Arachnoides placenta</i>	Sea urchin spine
	Diadematoidea	<i>Echinothrix diadema</i>	Sea urchin spine
Chordata	Galliformes	<i>Coturnix japonica</i>	Eggshell

A.2.2 SAMPLE PREPARATION

A.2.2.1 SURFACE PREPARATION FOR CONFOCAL MICROSCOPY, EBSD AND NANOINDENTATION MEASUREMENTS

Electron backscatter diffraction (EBSD) is a crystallographic characterisation technique based on scanning electron microscopy. Not only does EBSD enable the quantification and visualisation of individual grains, but it also allows us to analyse the correlation of crystallographic texture, morphology and twinning between neighbouring grains (Griesshaber et al. 2010; Guo et al. 2019). Furthermore, EBSD can be used to identify defects or internal stresses within crystalline samples (Wilkinson et al. 2006; Wright et al. 2011). Since nanoindentation testing also requires flat and even surfaces, samples that were characterised with FE-SEM or EBSD could subsequently be utilized for nanoindentation measurements and Raman spectroscopy.

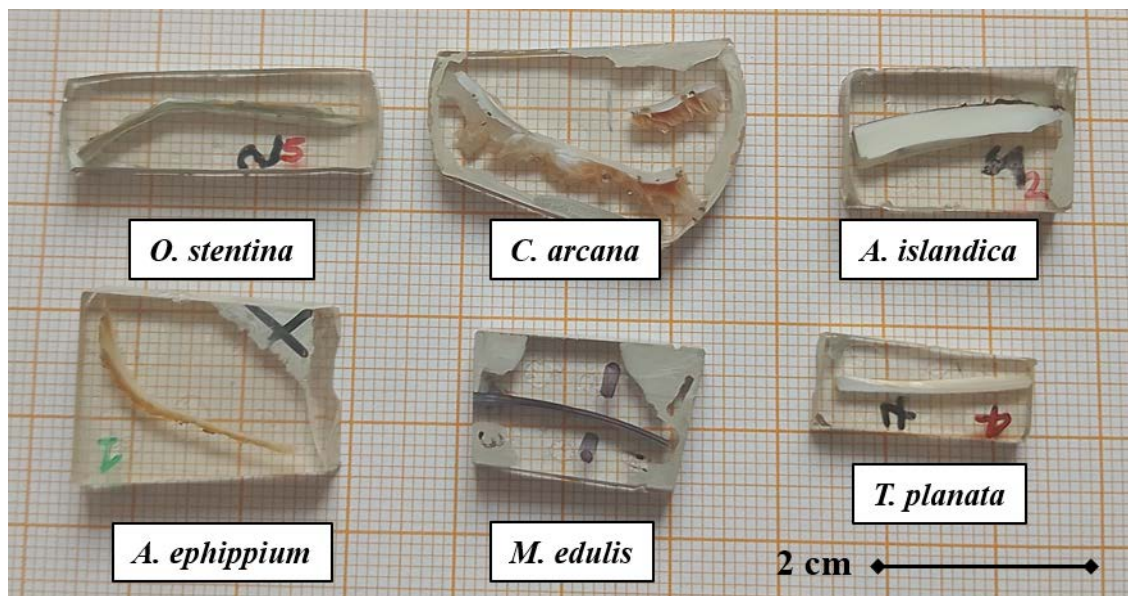


Figure A.2-1. Various bivalve shells embedded into EPON epoxy resin and polished with several manual grinding steps. The samples were tested with nanoindentation and investigated with EBSD. Myostracal pillars of *C. arcana* (top middle) were additionally observed with Raman spectroscopy.

Since the electrons backscatter near the subsurface of the sample, usually within the first few micrometres, specimen surface preparation is critical for the quality and resolution of the EBSD scans. All samples investigated in this study were prepared after an elaborate procedure that was refined through the preparation of hundreds of samples. In the first step, the biological hard tissues are sectioned with a low-speed diamond saw to expose the parts relevant to the aim of the study. The compromised samples were subsequently fixed with double-sided tape and embedded into transparent EPON epoxy resin. After drying, sample surfaces were exposed and polished through several steps of manual and vibratory grinding and polishing. The extent of manual or etch-polishing with colloidal alumina (Buehler Vibro Med 2) was adapted to the composition and characteristics of the sample to

ensure an optimal sample surface (Fig. A.2-1). In this study, the best sample surfaces were achieved when the final grinding step comprised manual polishing with nano-diamond suspensions. Subsequently to polishing, the samples were coated with 4-6 nm of carbon for electron microscopy measurements.

A.2.2.2 SAMPLE PREPARATION FOR CT SCANS

For computerised tomography scans, entire shells of varying sizes were prepared. The shells were dried with the organic matter, such as the two adductor muscles, still intact and attached to the valves. The shells were placed into the centre of transparent plastic sample holders that were tightly packed with polystyrene to prevent sample movement during the scans (Fig. A.2-2). Shells were oriented with the pedicle opening pointing towards the bottom of the tube.



Figure A.2-2. Recent brachiopod shells of *M. venosa* in various sizes, along with the respective sample holders used for CT scanning. Shells were placed into the centre of the plastic tubes.

Samples were measured at the Institute of Biomedical Engineering at the Technische Universität München using a Phoenix V|tome|x S 240. Data evaluation was performed using the Fiji imaging processing package, an open-source platform of ImageJ for biological data analysis (Schindelin et al. 2012).

A.2.2.3 SAMPLE PREPARATION FOR TGA MEASUREMENTS

Samples of crossed-lamellar, complex crossed-lamellar and myostracal aragonite, as well as foliated calcite, were drilled utilising a high-precision dental drill from the respective shell portions (Fig. A.2-1). Up to 15 mg of powder were obtained for analysis. TGA measurements were performed with a Netzsch STA 449 F1. The samples were heated from room temperature to 600 °C at a constant rate of

10 °C per minute in a static-air atmosphere. Approximately 20 mg of each sample was used for TGA analysis in an open aluminium oxide crucible. Each sample was measured twice, except for one. The error margin for individual measurements is ± 0.05 wt%; however, crossed-lamellar and myostracal layers of *G. pilosa* showed small heterogeneities.

No prior drying of the samples was performed. The weight loss between 25 °C and 100 °C is attributed to adsorbed water. Separate measurements on pure inorganic carbonate samples (calcite and aragonite) under the same conditions showed decarbonisation beginning around 500 °C, with a weight loss of 0.03 wt.% at 540 °C for both samples. Therefore, the study reports mass loss between 100 °C and 540 °C, as detailed in Figure 2.3-AP4.

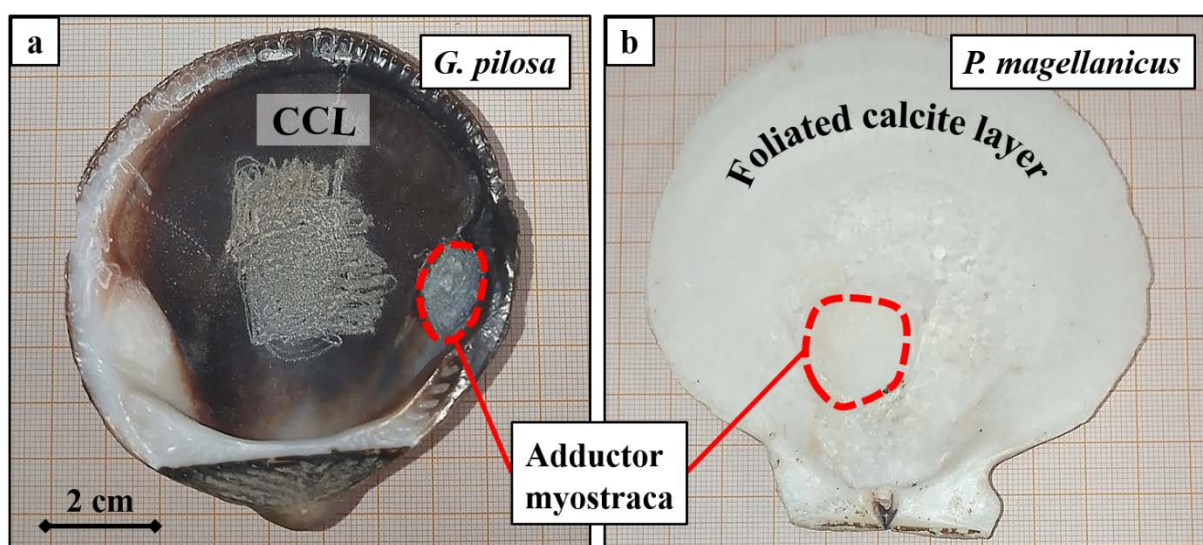


Figure A.2-3. Shells of *G. pilosa* (a) and *P. magellanicus* (b) showcasing the shell areas that were drilled for thermogravimetric analysis. Adductor muscle scars are highlighted with red circles.

B APPLIED METHODS

B.1 ELECTRON MICROSCOPY

Electron microscopy uses electron beams focused onto the sample surface, thus generating high-resolution images of the microstructural organisation of biological and non-biological samples. The evolution of functioning electron microscopes was driven by many significant inventions and discoveries, such as developing a basic electron gun (Braun 1897), unravelling the wave properties of particles (De Broglie 1924) or discovering that electrons can be focused using electromagnetic lenses (Busch 1926). Ruska and Knoll developed one of the first versions of a working electron microscope in 1931 and later awarded the 1986 Nobel Prize in Physics (Ruska 1987). With two electromagnetic lenses, it resembled a rudimental version of a modern transmission electron microscope.

Today's electron microscopes feature highly advanced setups to analyse specific sample properties such as morphology, chemical composition, crystallographic orientation, topology, etc. Despite their different applications, they follow a plain principle: As a focused electron beam hits and interacts with the sample, various signals are produced. When detected, these signals can be used to gather information about the sample or create maps. Recent advances in hard- and software development have led to a distinct increase in data quality and, thus, resolution. While the highest achievable resolution for light microscopes is around 200 nm, due to the objective lens size and light wavelength, electron microscopes can go far beyond that. Thus, unprecedented analysis techniques and the advancement in electron optics allow imaging and spectroscopy within atomic resolution (Muller 2009). The following chapters describe the fundamentals of scanning electron microscopy (SEM), the type of electron microscopy used in this study, and electron backscatter diffraction (EBSD), an SEM-based technique used to study the crystallographic microstructure of various materials.

B.1.1 FUNDAMENTALS OF SCANNING ELECTRON MICROSCOPY (SEM)

Scanning electron microscopy (SEM) allows the imaging and characterisation of specimen morphologies and microstructures on a micro- to nanometer scale. Due to its diverse applications and non-destructive mode of operation, SEM is used in various fields such as biology, materials science, geology and medical science. A typical SEM configuration includes an electron source, lenses, specimen chamber, and detectors, as illustrated in Fig. B.1-1.

Modern microscopes use Schottky-emission electron guns that apply a strong electric field to a heated metal surface, such as ZrO-coated tungsten single crystals. Due to the lowering potential barrier (Schottky effect), thermoelectrons are emitted from the cathode (Fransen et al. 1999). Apertures and

lenses focus the electrons onto the sample surface, where the specimen is irradiated in a defined raster scan. Scanning electron microscopes usually work under a vacuum to generate a consistent electron beam and avoid unimpeded interaction of the accelerated electrons within the electron beam column. As the finely focused beam hits the sample surface, the emitted signals, such as secondary (SE) and backscattered electrons (BSE), are collected by designated detectors. The amplification and quantification of the scanned measurement point signals allow the construction of maps illustrating the sample morphology and microstructure.

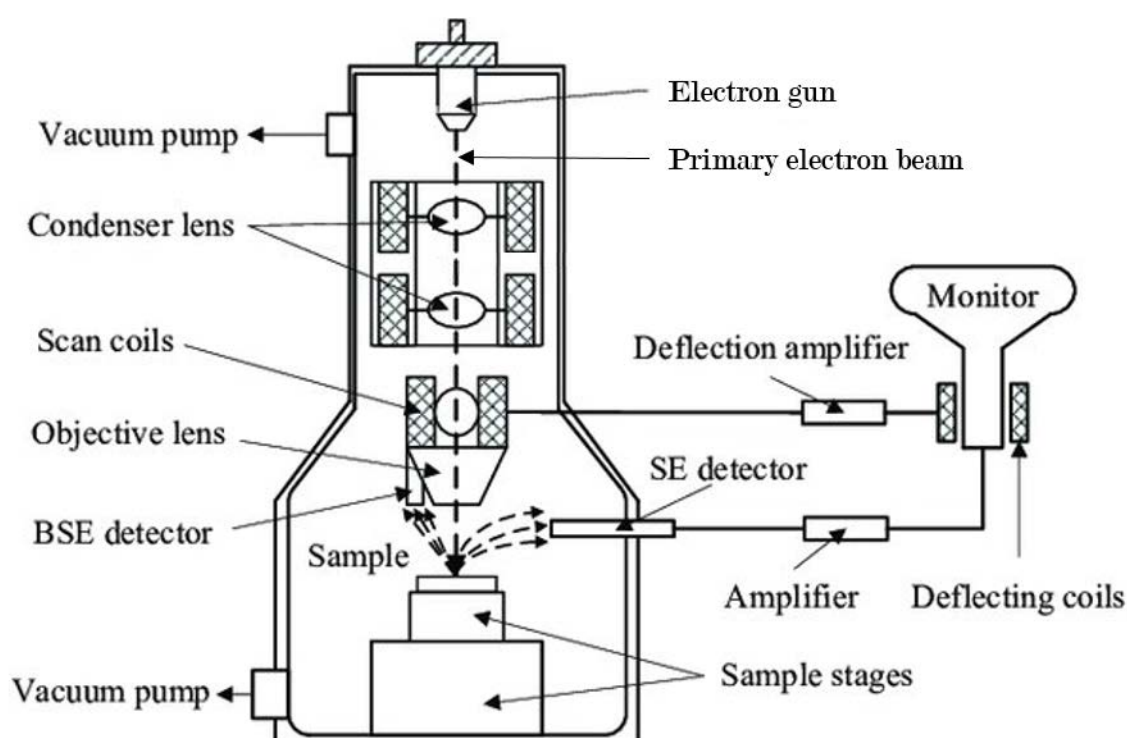


Figure B.1-1. Schematic drawing of the SEM setup (modified after Yao et al. 2021). Electromagnetic coils and lenses focus the electron beam on the specimen for scanning. The detectors measure the incoming secondary and backscattered electrons of each successively scanned specimen point, leading to the creation of an image on the monitor.

As mentioned above, the interaction between the primary electron beam and the sample can generate several different signals (Fig. B.1-2): SE and BSE, Auger electrons, transmitted electrons (if the specimen is sufficiently thin), characteristic X-rays and photons. Depending on the sample density and accelerating voltage, the signals come from different penetration depths. Auger electrons give chemical information about the sample surface, SE produce surface topography contrasts (Reimer 1985), and the cathodoluminescence emitted by some samples can provide information about the trace element distribution and mechanically induced defects (Watt et al. 1997; Rams et al. 1999). Energy-dispersive X-ray spectroscopy (EDX) allows the mapping of chemical element distributions for the investigated sample surface. Connecting the information gathered by different SEM modes can, thus, provide a comprehensive overview of the different sample characteristics.

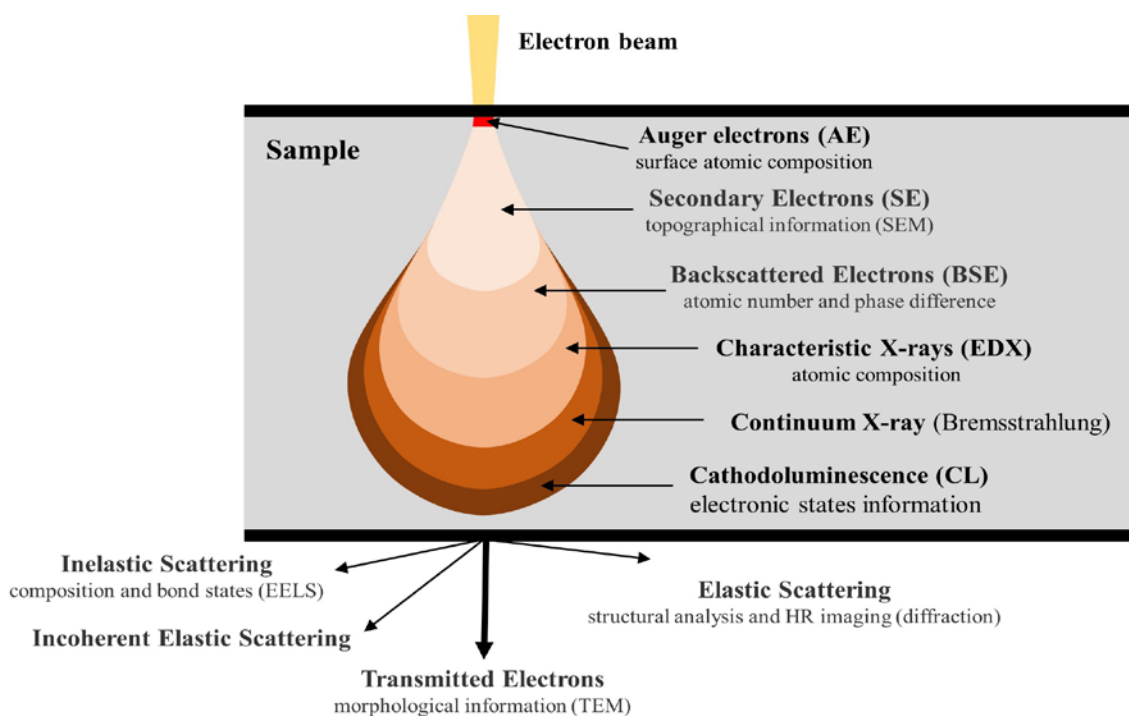


Figure B.1-2. Overview of the signals generated when the primary electron beam interacts with a (relatively) thin sample. In the case of a thick specimen, there are no transmitted electrons, and the signal gets absorbed within the material. Adapted from Nanakoudis (2019).

For the investigation of biological hard tissues, the most powerful signal type is the backscattered electrons. For one, they are highly sensitive to elements (heavy elements backscatter electrons more strongly than light elements) and can, therefore, be used to map chemical composition contrasts in SEM images. Secondly, electron backscatter diffraction (EBSD) measurements provide pivotal information about the crystallographic texture of the sample. This technique is described in more detail in the following chapter.

B.1.2 ELECTRON BACKSCATTER DIFFRACTION (EBSD) ANALYSIS

The history of EBSD began in 1928 at the University of Tokyo, where Nishikawa and Kikuchi observed the diffraction of an electron beam by a calcite crystal (Nishikawa & Kikuchi 1928). The first ever published electron backscatter pattern was recorded on photographic plates. It comprised pairs of parallel black and white lines of poor quality, most likely due to the low vacuum that was realisable at this time. Through recent developments in scanning electron microscopy and EBSP detection, EBSD has since become a powerful tool for understanding the crystallography and internal microstructures of crystalline materials. Opposed to BSE imaging, EBSD allows the identification of grain orientation within a map and can reveal the crystallographic texture of a sample.

Generally, electron backscatter patterns are obtained by illuminating a crystalline specimen with a stationary electron beam in the SEM. The sample surface is oriented at a high tilting angle (usually

70°) to the beam to diffract the pattern into a detector (Fig. B.1-3a). For modern microscopes, the detector is usually a flat phosphor screen paired with a fully digital charge-coupled device. This setup allows a good resolution while maintaining high analysis speed. The detected electron backscatter patterns can be interpreted as a gnomonic projection of the crystal lattice, where each Kikuchi band can be attributed to the diffracting crystal plane forming it (Fig. B.1-3b). The intensity, direction and intersections of the Kikuchi bands are characteristic of particular crystalline phases and orientations and can be indexed to determine and characterise the microstructure. When scanning a map and indexing the obtained Kikuchi patterns, the resulting EBSD map can, therefore, illustrate grain size and morphology as well as the general microstructure of the scanned area. Using sophisticated analysis tools provided by crystallographic software such as Oxford Instrument's AZtecCrystal 3.0, gives insights about grain boundary properties (i.e., twinning), internal misorientations or the development of crystallographic texture.

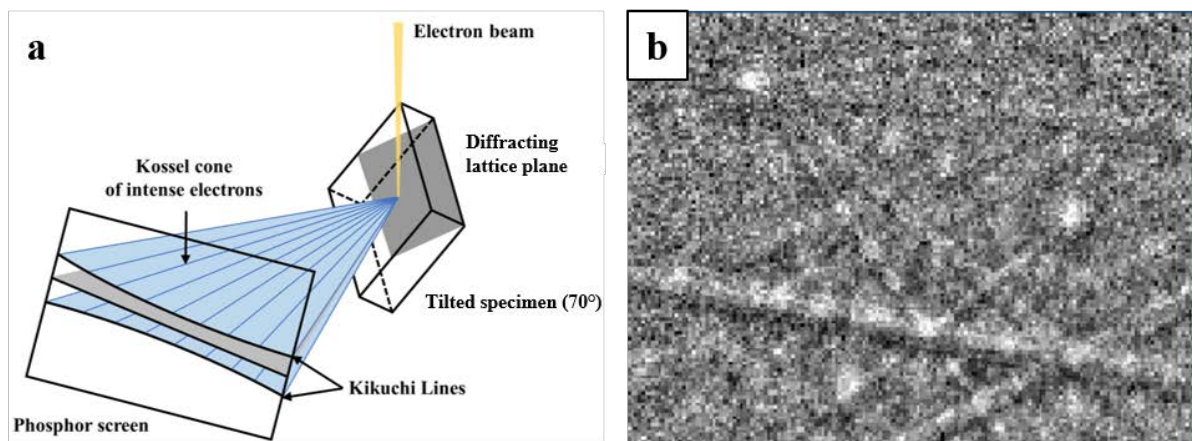


Figure B.1-3. Schematic diagram showing how the Kikuchi cones can diffract from the specimen plane after illumination with an electron beam, and the phosphor screen detecting them (a, modified after (Yin 2020)). Measuring a *Glycymeris pilosa* myostracal shell layer at 20 kv with a Hitachi SU5000 FE-SEM creates a typical electron backscatter pattern for aragonite (b). Kikuchi band width, intensity and pathways give information about the material properties of the scanned point. To enhance the band visibility, the Kikuchi pattern was resolved with 4x4 binning, reducing its resolution to 168x128 pixels.

Although conventional EBSD analysis is a powerful tool for sample characterisation and analysis, the investigation of biological hard tissues has been challenging for two main reasons: Firstly, the sample preparation for EBSD requires finesse as it comprises multiple preparation steps that might damage or even destroy the surface of the hard tissue and, thus, impair the quality of the measurement. Secondly, biological composite materials often comprise small crystals and a high amount of organic material encapsulating the individual grains. The organic matter controls or guides the growth and microstructure of the biological hard tissue, however, it significantly tarnishes the Kikuchi pattern quality of the surrounding crystals. For specific samples, this can lead to poor data quality, resulting in an EBSD map with many zero-solution pixels. The increasingly popular post-processing method of EBSD pattern-matching can be used to retrospectively index, repair, or refine blurry Kikuchi patterns, thus improving the quality and precision of the measurement.

B.1.3 EBSD DATA EVALUATION VIA PATTERN MATCHING

The collection and evaluation of EBSD patterns can be performed via two different methods. The conventional EBSD pattern indexing technique uses the Hough transform (Krieger Lassen et al. 1992; Engler et al. 2023) to detect the position of Kikuchi bands. These bands are indexed using crystallographic parameters such as interplanar angles (Engler et al. 2023). Since this method directly stores the indexed orientations rather than the entire information of the detected EBSD pattern, it is relatively quick, and datasets occupy less space. However, the plain indexation is often inaccurate, leading to an average angular precision variation between 0.5° and 1° . Additionally, if a data point with poor Kikuchi band quality, e.g. at grain boundaries or areas featuring a high organic content, is not indexed by the EBSD evaluation software, it is saved as a zero solution pixel and, thus, its crystallographic information is lost.

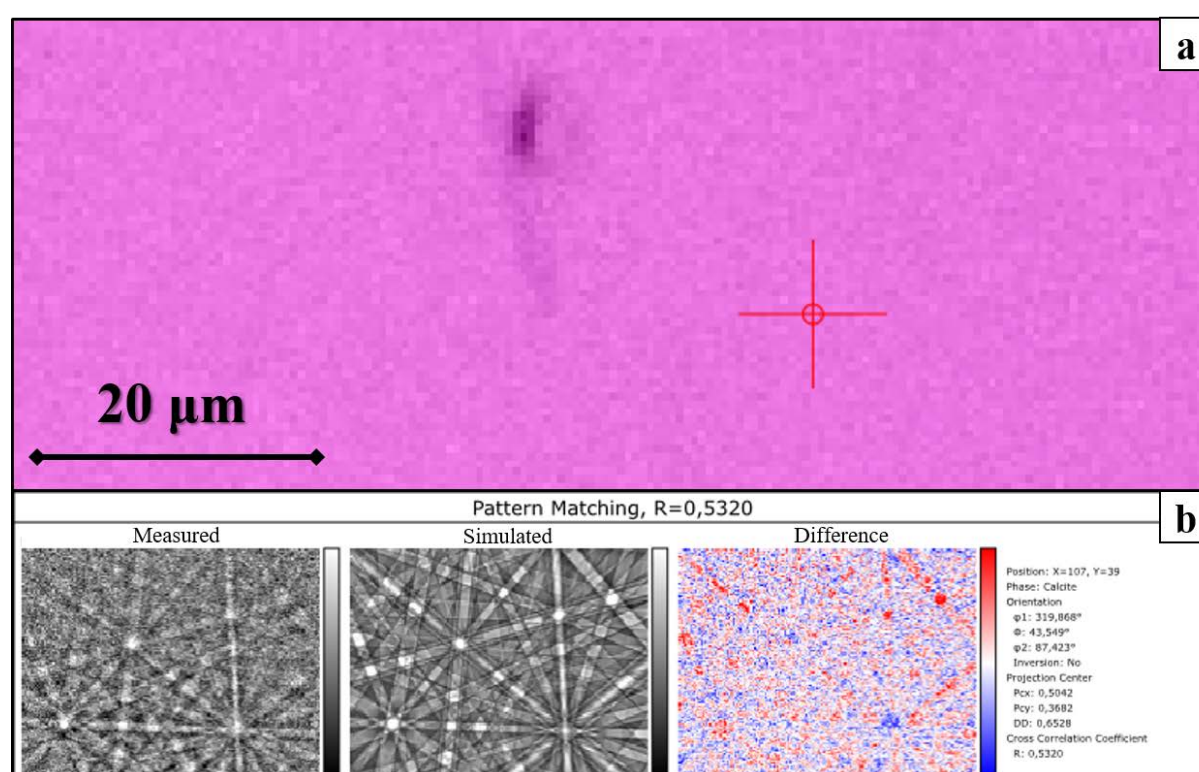


Figure B.1-4. Set up for the projection parameter calibration of the EBSD pattern matching method for a calcite single crystal. For a single data point (indicated by red cross in a), the projection parameters of the electron backscatter pattern calculated from dynamical simulations (middle pattern in b) are refined with the measured pattern (left pattern in b). Upon reaching the maximum cross correlation coefficient and minimising the difference between measurement and simulation (right pattern in b), the parameters are saved to the calibration list that will be used for the refinement sweep.

The recently developed EBSD pattern matching technique tries to overcome the limitations of the conventional method by storing the detected Kikuchi patterns for every data point of the measurement, together with the indexed orientation. While this takes longer than conventional measurements and generates huge file sizes that slow down the evaluation process, it allows post-measurement data refinement. The first step for the refinement is the generation of a pattern simulation

that can be regarded as a reference. For aragonite, I used the unit cell parameters $a = 4.97 \text{ \AA}$, $b = 7.96 \text{ \AA}$ and $c = 5.75 \text{ \AA}$ and for calcite, I used the unit cell parameters $a = b = 4.99 \text{ \AA}$ and $c = 17.07 \text{ \AA}$. Once the dynamically generated simulation pattern of the respective mineral phase is generated, the projection parameters are calibrated by maximising the cross-correlation coefficient with the measured pattern (Fig. B.1-4). Depending on the complexity of the measurement and the number of present phases, the projection parameter calibration may be repeated several times, creating a calibration list that can later be used for the refinement sweep of the entire dataset.

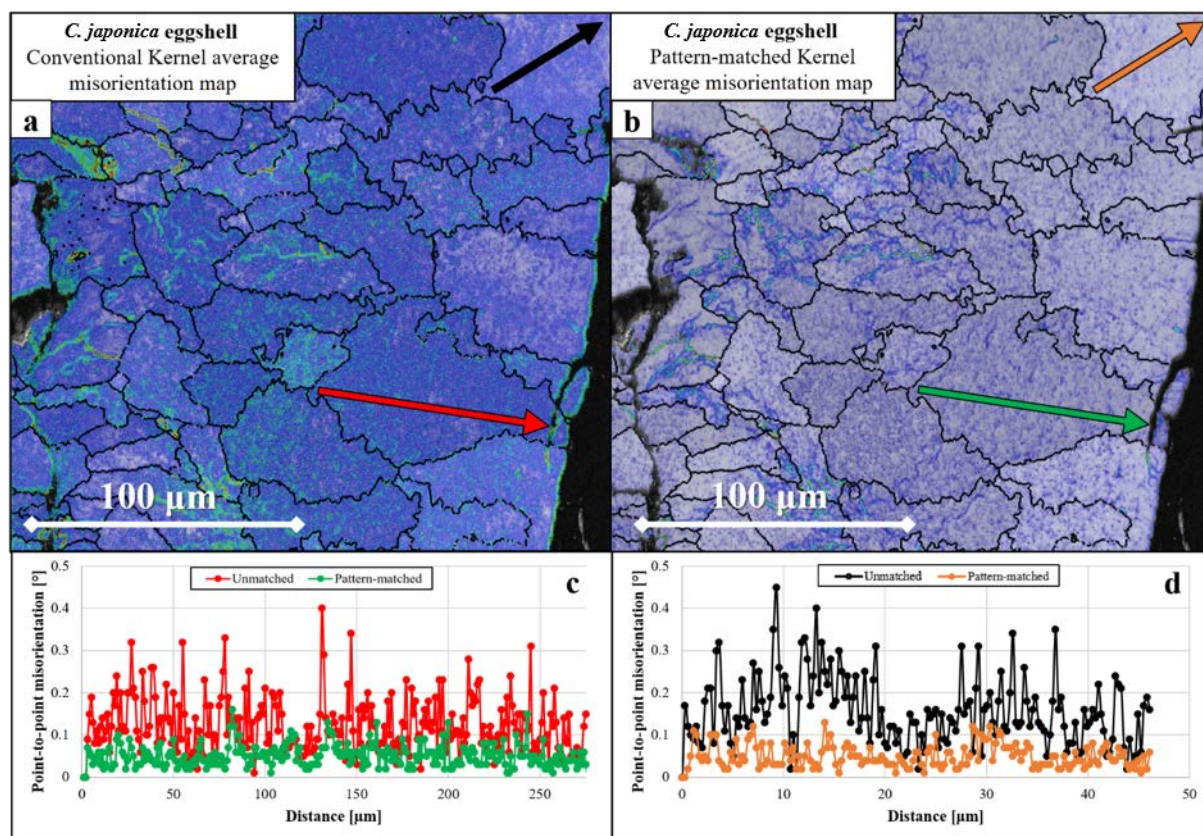


Figure B.1-5. Comparison of Kernel average misorientation maps (Kernel size 5x5, misorientation range 0-2°) and misorientation angle profiles for a measurement on a *C. japonica* eggshell evaluated conventionally and by EBSD pattern-matching. Conventional EBSD data analysis (a) yields a high angular precision variation of 0.5°-1° and, thus, small-angle misorientation within the eggshell are not as well-visible as in the same measurement refined by pattern matching (b). The two misorientation profiles implemented in each map quantitatively reveal the angular differences of the two methods (c, d). The measurement is from a collaboration with Shahrouz Amini and Jingxiao Zhong from the Max-Planck Institute of Colloids and Interfaces, Potsdam.

After the setup is completed, the pattern matching sweep, consisting of three steps, can be performed. Firstly, (i) the dataset is re-indexed with the selected phases. This step allows the post-measurement integration of phases that were not considered during the initial measurement but is optional due to the perpetuity of this process. Afterwards, (ii) the indexed pixels are refined using the projection parameters and simulated Kikuchi patterns. Only the solved patterns with a high cross-correlation coefficient are saved to the pattern-matched dataset. In a last step, (iii) a repair sweep is performed for zero solution datapoints. Depending on the band contrast or nearest neighbours, the crystallographic orientation of the falsely unsolved pixels can be restored. This is particularly important

for grain boundary regions, as overlapping patterns along these boundaries can result in a poor-quality pattern. Since not enough Kikuchi bands of either phase will be detected along these areas, grain boundary regions are difficult to reliably investigate with Hough-based indexing methods.

Finally, the pattern-matched dataset is stored as a separate file to avoid overwriting the raw data, including the measured EBSD patterns. For measurements on biomineralised hard tissues, such as bones, eggshells or teeth, the pattern matching method can improve the angular precision variation to $0.1\text{-}0.2^\circ$, especially enhancing the understanding of low-angle misorientations within individual grains (Fig. B.1-5)

B.2 CONFOCAL SCANNING LASER MICROSCOPY (CSLM)

Confocal scanning laser microscopy (CLSM) enables fast and automated analyses of large sample surfaces and is an ideal technique for creating sharp and descriptive optical overview images that are rich in contrast. In CLSM, the sample is illuminated by a point laser source that scans a set area non-destructively. A small aperture at the objective lens obstructs most of the light reflected from out-of-focus objects and narrows down the depth of focus, albeit at the cost of decreased signal intensity (Fig. B.2-1). Producing blur-free images and 3D surface reconstructions, confocal laser microscopes are a powerful tool for surface characterisation and high-resolution optical microscopy.

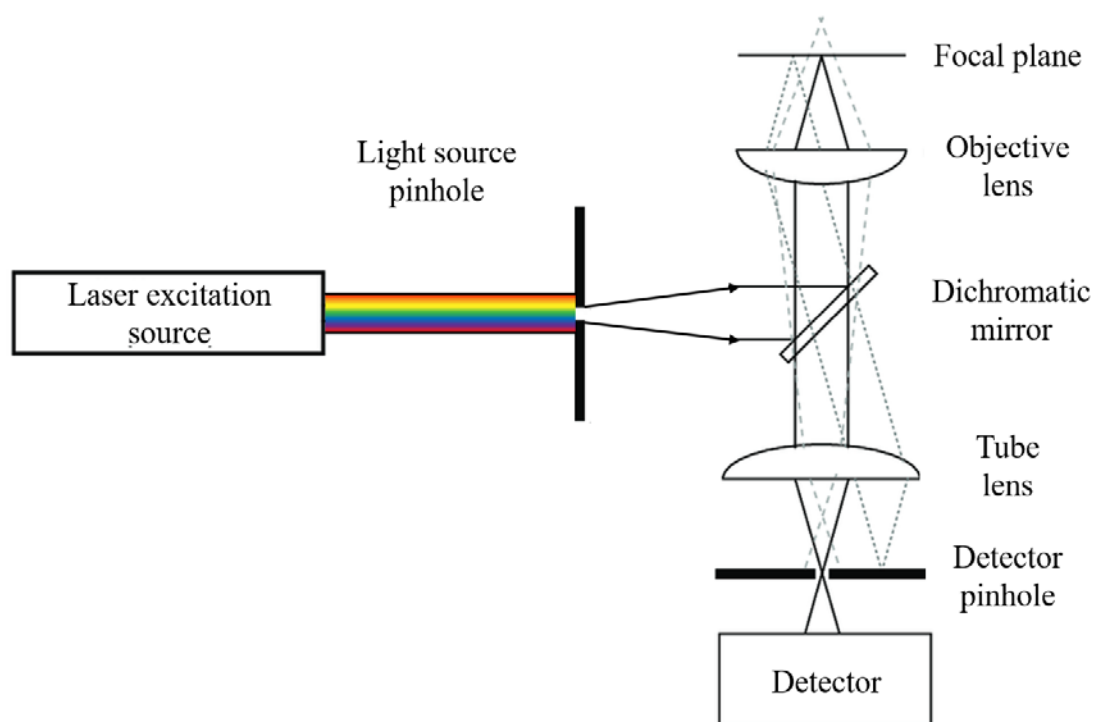


Figure B.2-1. Illustration of the operation principle of a confocal laser microscope. The light source is filtered by a light source pinhole, reflected by a dichromatic mirror and focused onto the sample surface with an objective lens, creating a small excitation volume. Filtered by the detector pinhole, out-of-focus signals are blocked from detection, allowing high-resolution scans.

Samples were imaged with a Keyence 3D laser scanning confocal microscope (VK-X1000 series), equipped with a white coaxial light-emitting diode light and a 661-nm red semiconductor laser, and a Keyence digital microscope (VHX-7000). The white light was used for focus variation measurements and the laser was used for confocal measurements. Overview images were created by stitching multiple focus variation images of a predefined raster. Combining multiple two-dimensional focus variation and laser-confocal measurements into 3D models, the MultiFileAnalyzer Program was used to display the quality and characteristics of sample surfaces.

B.3 THERMOGRAVIMETRIC ANALYSIS (TGA)

Thermogravimetric Analysis (TGA) is a highly precise technique that allows the monitoring of a substance's mass as it is heated or cooled in a controlled environment. In essence, a thermogravimetric analyser comprises a sample pan connected to a precision balance and a tempering device, such as a furnace or cooler. The mass of the substance is usually quantified by a “hangdown” sample pan located below the scale. Thus, the sample holder needs to be both corrosion-resistant and inert to phase transitions over a large temperature scan. Most pans are manufactured from metals or ceramics and can usually hold up to 100 μm of substance. Depending on the experimental setup and investigated material, TGA measurements can be conducted with dynamic or static air conditions under atmospheric air or inert gas.

Due to the controllable tempering rate, the small amount of required material and the high measurement precision, TGA is applied in a variety of scientific fields. Conventional TGA involves the generation of a thermal curve that displays the mass change with temperature or time. Calculating the relative mass changes within defined temperature regions allows the quantification and characterisation of certain reaction processes. For example, performing TGA for biological hard tissues in a temperature region between 100°C and 540°C allows us to compare the organic content of different materials. When complementing TGA with other thermal analysis techniques, such as differential scanning calorimetry, phase changes, reactions, and decompositions can be quantified in a single measurement, allowing a quick and precise characterisation of heat flow and sample properties (Fig. B.3-1).

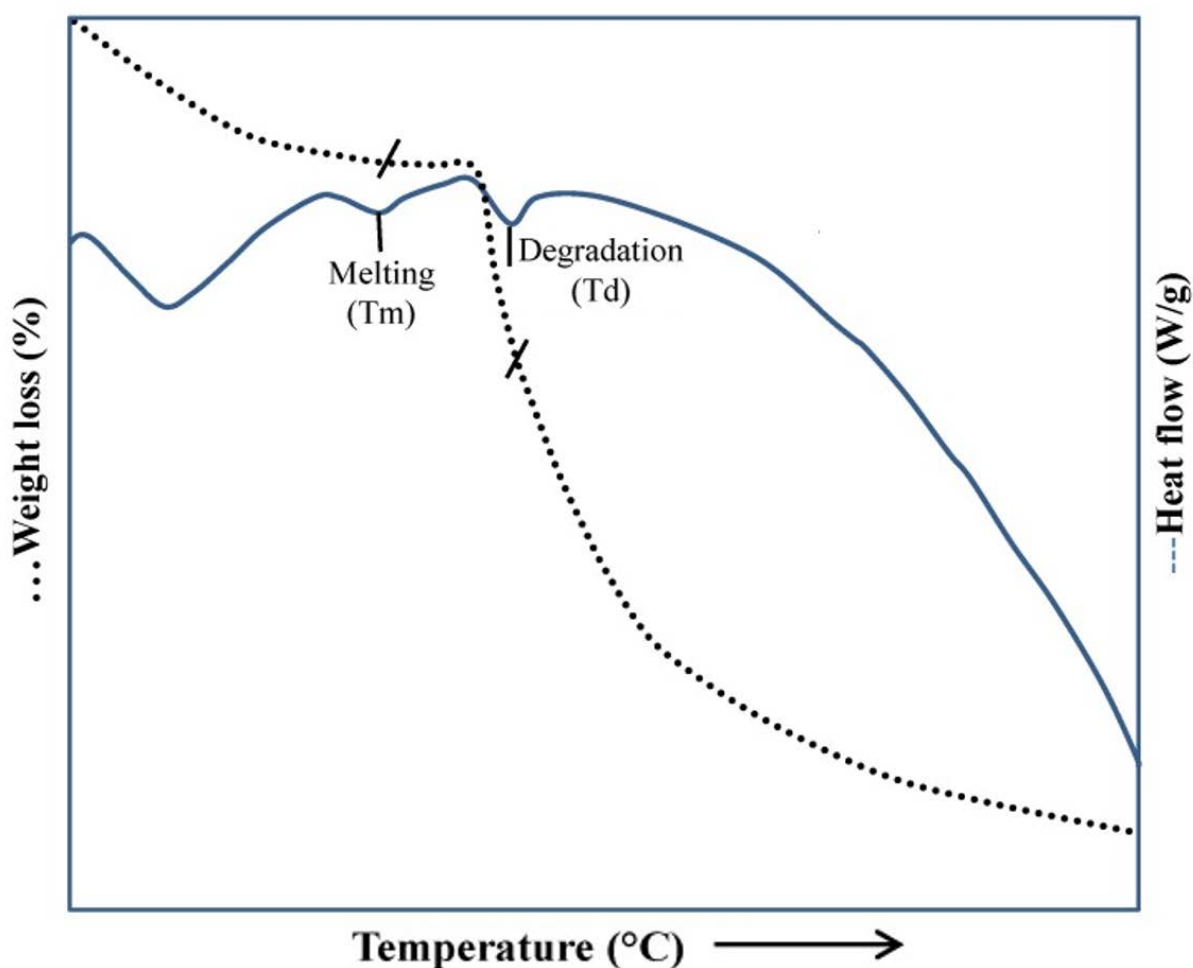


Figure B.3-1. Thermogravimetric analysis - differential scanning calorimetry thermogram of inulin showing the changes in weight loss (black dots) and heat flow (blue line) with increasing temperature (modified after Leyva-Porras *et al.*, 2019).

B.4 MICRO-COMPUTED TOMOGRAPHY (MICRO-CT)

Micro-computed tomography (Micro-CT) is an imaging technique that compiles a series of two-dimensional X-ray images into three-dimensional models. As the prefix in micro-CT indicates, the pixel size of the scanned cross-section images is in the micrometre range. Slice by slice, the sample is captured and, after every scan, rotated slightly until reaching a half or full turn. A conical X-ray beam is transmitted through the sample and detected by the 2D screen arranged behind the sample. During reconstruction, a computational process transforms or stacks the singular images into a three-dimensional model (Fig. B.4-1). Due to its non-destructive nature, high image resolution and quick measurement setup, micro-CT tomography is a widespread analysis technique in biomedical and material science.

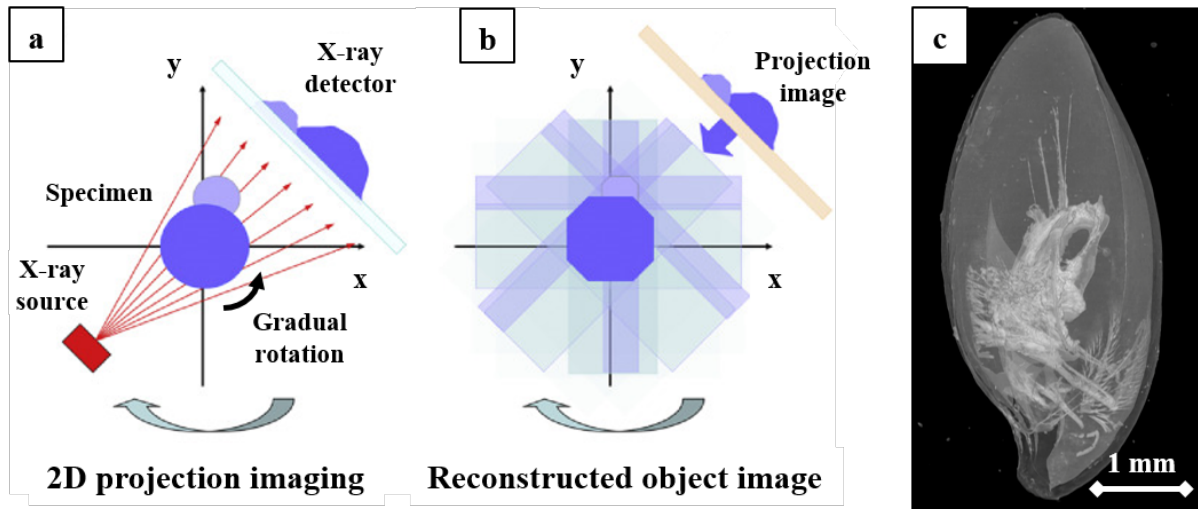


Figure B.4-1. Illustration highlighting the principle of micro-CT scanning. Using X-ray projection imaging, a multitude of images are created and recorded from varying angles (a). In the second step, the radiography images are reconstructed using computed tomography processing methods such as back-projection (b). The reconstruction and combination of all angular scans give a three-dimensional scanned model that can showcase different material properties, such as the distribution of organic material and adductor muscles in undamaged *M. venosa* brachiopod shells (c). The micro-CT illustrations (a, b) are modified after Ying *et al.*, (2022).

B.5 NANOINDENTATION TESTING

Nanoindentation is based on continuously pressing a probe of fixed load into a smooth sample surface to create nanosized displacement marks. Depending on the nanomechanical material properties, the indentation depth will be large for soft samples and small for hard samples. Other than hardness, nanoindentation can also give information about a material's stiffness, fracture toughness, delamination, tensile strength and stress relaxation. Different nanoindentation probes may be used for different fields of work, the most important of which include a spherical probe, the Vickers indenter, and the Berkovich indenter. Since they are considered very sharp and ensure precise control over the indentation process, Berkovich indenters are the most commonly used indentation tips (Fischer-Cripps & Nicholson 2004). For analysis with a Berkovich tip, the hardness H is related to the indenter load P , the contact depth of penetration, h_c , and a constant that attributes the projected area of contact for the standard angle of $\theta = 65.27^\circ$.

$$H = \frac{P}{24.5 h_c^2} \quad \text{B.1-1}$$

Modern nanoindenters, such as the instruments used in this study, can not only measure the total displacement depth against the applied force but also give immediate and detailed displacement feedback during the measurement (Fig. B.5-1a). Evaluating the dislocation activity throughout the loading and unloading cycle can give information about the surface quality of the sample as well as irregular deformation activities. The latter include pile-ups or sink-ins (which can be prevented by preparing a smooth sample surface) and pop-in events, all of which may distort the obtained

nanomechanical properties (Fig. B.5-1b). Some nanoindenters, such as the Hysitron TI 950 TriboIndenter used for a majority of the nanoindentation measurements reported in this thesis, feature integrated in-situ scanning probe microscopy, allowing pre- and post-observation of the material surfaces.

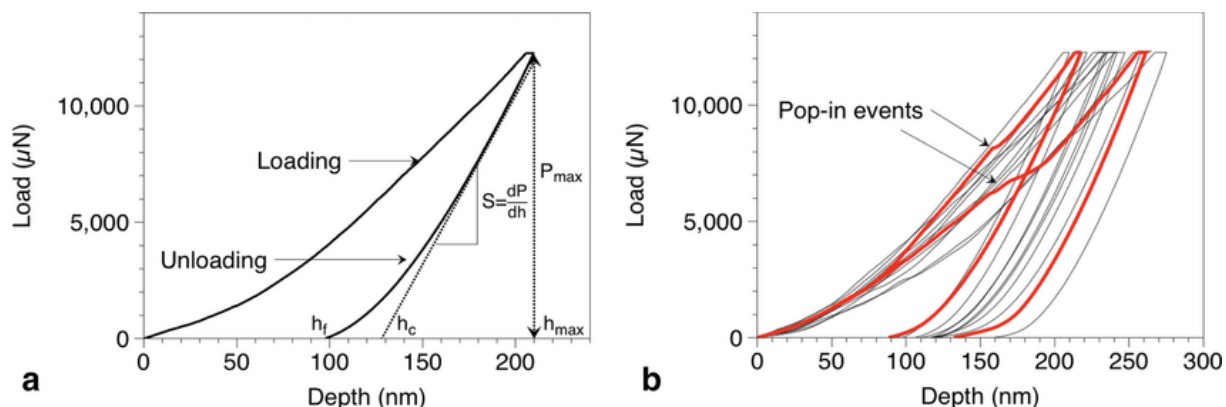


Figure B.5-1. Examples of a regular nanoindentation cycle (a) and pop-in events (b) measured for corals on the Hysitron TI-950 TriboIndenter used for the majority of measurements reported in this thesis. The stiffness can be calculated by the measured load and indentation depth. Pop-in events, caused by free movement of the indenter during cracking, induce displacements which can affect the calculations of the nanomechanical properties (b). Adapted from Moynihan et al. (2021).

Measurements were conducted on two nanoindentation instruments. Samples of *G. bimaculata*, *G. nummaria*, *D. scalaris* as well as the aragonitic and calcitic single crystal references were tested at the Institute for Energy- and Climate Research (IEK-2), Forschungszentrum Jülich, using a Nanoindenter G200X (KLA, USA). All other measurements featured in this thesis were tested using a Triboindenter TI-950 nanomechanical tester (Hysitron, USA) at the Max-Planck Institute of Colloids and Interfaces, Potsdam.

ACKNOWLEDGEMENTS

The most important thing I have learned within the scope of my thesis is probably the value and significance of the people who have guided and supported me. I owe my sincere gratitude and appreciation to everyone who has accompanied me in finishing my dissertation.

First and foremost, I want to thank my Dokoreltern for their immense help and incredible support during this time. I am very grateful to have the two of you, Dr. Erika Griesshaber and Prof. Wolfgang W. Schmahl, as my supervisors, and I appreciate all the constructive discussions and guidance. I owe you deep thankfulness not only for the countless hours that you passionately dedicated to a better understanding of our world, but also for being an exceptional role model and granting me this opportunity. Despite the ups and downs of my graduation, I could not have wished for better supervisors.

I am also grateful for all the discussions and exchanges with Prof. Antonio G. Checa from the University of Granada, who not only provided me with immense support through his expertise and proficiency but also motivated me in my research with his contagious curiosity and thirst for knowledge. Also, I thank him for his willingness to conduct a second review for this work.

Further thanks are given to Dr. Shahrouz Amini from the MPIKG Potsdam, who was always there to help and inspired me greatly through his creativity and expertise. In particular, I thank him and his group for their collaboration and for allowing me to perform measurements at the Max-Planck-Institute. I appreciate not only the interesting discussions and good cooperation with Dr. Jingxiao Zhong, Tingting Zhu, and, in particular, Dr. Chiara Micheletti, but also want to thank them for making me feel welcome during my time in Golm. Likewise, I owe thanks to Dr. Nicolas Peter from the Forschungszentrum Jülich for his help with nanoindentation measurements, the inspiring discussions and the great collaboration.

I owe further thanks to the mineralogy department and, in particular, Daniel Weller of the Ludwig-Maximilians-Universität München. Not only did he allow me to use the laser confocal scanning microscopes on a short-term basis for various projects, but he was also always happy to help and give valuable advice. I would also like to thank Dr. Klaus Achterhold from the Munich Institute of Biomedical Engineering of the Technical University Munich for his help in obtaining and visualising micro-CT data of brachiopod shells. I also appreciate the help of Dr. Aimó Winkelmann from the AGH University of Krakow in applying the pattern matching technique to our biomineralised samples.

For their valuable ideas, inspiring discussions, and assistance with some of the bivalve samples analysed in this thesis, I acknowledge Prof. Elizabeth Harper from the University of Cambridge and Prof. Carmen Salas from the University of Málaga. I would like to extend my gratitude to Dr. Melita Peharda from the Institute of Oceanography and Fisheries in Split, Prof. N. Lagos Suárez from the University of Santo Tomas in Santiago, Dr. Serge Gofas from the University of Málaga and Dr.

Yannicke Dauphin from the National History Museum in Paris for providing additional bivalve samples. I acknowledge Dr. Verena Häussermann from the PUCV in Valparaiso and Dr. Maria Aleksandra Bitner from the Polish Academy of Sciences for providing brachiopod samples and offering valuable feedback on the manuscript. I would like to thank Prof. Carsten Lüter from the Museum für Naturkunde Berlin, Dr. Ekin Tilic from the Senckenberg Institute in Frankfurt/Main, and Dr. Mike Reich from the Natural History Museum in Braunschweig for their assistance with selecting and sending sea urchin specimens.

Thanks to all my current and past colleagues in the Sektion Kristallographie of the Ludwig-Maximilians-Universität. In particular, I would like to thank Fabio Joseph, Niclas Reitberger, Jana Zuncke, and Anna Sancho Vaquer for their constant support and for providing valuable friendship and welcome distractions both inside and outside the office. I owe special thanks to Prof. Elena Sturm for her guidance and unwavering support, particularly during challenging times. However, I am also grateful for the support of Dr. Melanie Kaliwoda, Prof. Peter Gille and Prof. Sandro Jahn, who have encouraged me during various periods of my academic cycle and graduation. Additionally, I would like to thank my other colleagues and friends at the institute. I thoroughly enjoyed and learned a lot from this multidisciplinary group, and I acknowledge all the contacts I made throughout this significant period of my life.

Zu guter Letzt möchte ich aus ganzem Herzen meiner Familie und meinen tollen Freunden danken. Ich bin zutiefst glücklich, so viele außergewöhnliche Menschen in meinem Umfeld zu haben und wäre ohne eure Unterstützung nie so weit gekommen. Besonders danke ich meiner Mama für ihre bedingungslose Liebe und ihren Beistand in all diesen Jahren. Ich schätze sehr, dass du immer für mich da bist und mich in allem unterstützt. Weiterhin danke ich meinem Bruder aus ganzem Herzen dafür, mir in allen Belangen zur Seite zu stehen und ein unverzichtbarer Teil meines Lebens zu sein. Außerdem danke ich meinem Papa und meinen Großeltern zutiefst für ihre stetige Unterstützung und Aufmunterung in allen Lebenslagen. Auch wenn ich sie gar nicht alle aufzählen kann, möchte ich all meine Freunde anerkennen, die während der letzten drei Jahre und darüber hinaus ein großer Anker in meinem Leben waren und mich immer wieder ermutigt und aufgeheitert haben. Danke für alles.

LIST OF PUBLICATIONS AND MANUSCRIPTS

Peer-reviewed Articles

Hoerl, S., Griesshaber, E., Checa, A.G. & Schmahl, W.W., 2024a, 'The biological crystals in chamid bivalve shells: Diversity in morphology and crystal arrangement pattern', *Crystals*, 14(7), 649.

Hoerl, S., Le Moine, T., Peter, N.J., Amini, S., Griesshaber, E., Wang, J., Harper, E.M., Salas, C., Checa, A.G., Schwaiger, R. & Schmahl, W.W., 2024b, 'Crystal organisation and material properties of *Chama* and *Glycymeris myostraca* and shells', *Materialia*, 36, 102149.

Hoerl, S., Griesshaber, E., Weller, D., Amini, S., Häussermann, V., Bitner, M.A., Achterhold, K., Pfeiffer, F., Schmahl, W.W., 2025a, Crystal organisation of muscle attachment sites of bivalved marine organisms: a juxtaposition between brachiopod and bivalved mollusc shells, *Crystals*, 15(7), 649

Hoerl, S., Micheletti, C., Amini, S., Griesshaber, E., Hess, K.-U., Checa, A.G., Peharda, M. & Schmahl, W.W., 2025b, 'Correlation between nanomechanical properties and microstructural design concepts of bivalve muscle attachment sites', *Materials & Design*, 113845.

Hoerl, S., Griesshaber, E., Checa, A.G., Winkelmann, A., Förster, F., Alsheikha, O., Hidalgo, F., Sturm, E., Jahn, S. & Schmahl, W.W., 2025c, 'Evaluating the single crystallinity of sea urchin calcite', *Acta Biomaterialia*, S174270612500220X.

Castro-Claros, J.D., Yin, X., Salas, C., Griesshaber, E., **Hoerl, S.**, Checa, A.G. & Schmahl, W.W., 2024, 'Biomaterial crystallographic preferred orientation in Solenogastres molluscs (Aplacophora) is controlled by organic templating', *Scientific Reports*, 14(1), 10309.

Schmahl, W.W., Yin, X., Lastam, J., Griesshaber, E., **Hoerl, S.**, Sturm, E. & Vaquer, A.S., 2025, Statistical analysis of EBSD data confirms pronounced classical and non-classical pervasive crystallographic twinning in rotaliid foraminiferal calcite, *Scientific Reports*, 15(1):14852.

Sturm, S., Çalışkanoglu, A.Z., Beiers, L.M., **Hoerl, S.**, Döblinger, M., Cimorelli, C., Camara, A.S.B., Müller-Caspary, K., Dingwell, D.B., Sturm, E., 2025, Exploring structure and recrystallization processes upon the formation of apatite based synthetic fulgurite, *European Journal of Mineralogy* (in submission)

Oral Presentations at Conferences

Microstructure, texture and material properties of *Chama* spp. and *Glycymeris* spp. myostraca

Hoerl, S.; Griesshaber, E.; Peter, N.; Amini, S.; Salas, C.; Checa, A.G.; Harper, E.M.; Schmahl, W.W.

Bivalves – Where are we going? Cambridge, UK, 5–8 September 2023

Organization and material properties of bivalve shell and myostraca microstructures

Hoerl, S.; Griesshaber, E.; Amini, S.; Peter, N.; Salas, C.; Checa, A.G.; Schmahl, W.W.

Biomineral structures: synthesis and growth, organization, evolution. Granada, Spain, 6–7 November 2023